Do happier lab animals lead to better science? *p. 624*

Live imaging of neurogenesis in the brain *pp. 639 & 658*

Electron microscopy of fragile materials *p. 675*

Science

$15
9 FEBRUARY 2018
sciencemag.org

AAAS

EVOLUTION OF AGILITY

Secrets of hummingbird flight

pp. 636 & 653

CONTENTS

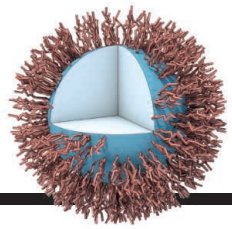

633 & 679
Noninvasive optogenetics

9 FEBRUARY 2018 • VOLUME 359 • ISSUE 6376

NEWS

IN BRIEF

IN DEPTH

FEATURES

624

INSIGHTS

PERSPECTIVES

POLICY FORUM

Published by AAAS

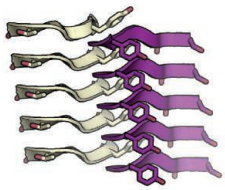

698
Kinked β sheets stack together

652
Folding mitotic chromosomes

ON THE COVER

A violet-crowned woodnymph (*Thalurania colombica colombica*) maneuvers in flight. Hummingbirds are known for their ability to rapidly accelerate, decelerate, and turn on a dime. Species vary in aerial maneuvering performance, and different aspects of maneuverability evolve as a result of various biomechanical traits. This framework may apply to other organisms and to the design of more maneuverable aircraft. See pages 636 and 653.
Photo: Glenn Bartley/BIA/Minden Pictures

SCIENCE (ISSN 0036-8075) is published weekly on Friday, except last week in December, by the American Association for the Advancement of Science, 1200 New York Avenue, NW, Washington, DC 20005. Periodicals mail postage (publication No. 484460) paid at Washington, DC, and additional mailing offices.

Domestic individual membership, including subscription (12 months): $165 ($74 allocated to subscription). Domestic institutional subscription (51 issues): $1808; Foreign postage extra: Mexico, Caribbean (surface mail) $55; other countries (air assist delivery): $89. First class, airmail, student, and emeritus rates on request. Canadian rates with GST available upon request, GST #125488122. Publications Mail Agreement Number 1069624. **Printed in the U.S.A.**
Change of address: Allow 4 weeks, giving old and new addresses and 8-digit account number. **Postmaster:** Send change of address to AAAS, P.O. Box 96178, Washington, DC 20090–6178. **Single-copy sales:** $15 each plus shipping and handling; bulk rate on request. **Authorization to reproduce** material for internal or personal use under circumstances not falling within the fair use provisions of the Copyright Act is granted by AAAS to libraries and others who use Copyright Clearance Center (CCC) Pay-Per-Use services provided that $35.00 per article is paid directly to CCC, 222 Rosewood Drive, Danvers, MA 01923. The identification code for *Science* is 0036-8075. *Science* is indexed in the *Reader's Guide to Periodical Literature* and in several specialized indexes.

Science
AAAS
1200 New York Avenue, NW, Washington, DC 20005
Clarendon House, Clarendon Road, Cambridge, UK CB2 8FH

SUBSCRIPTION SERVICES For change of address, missing issues, new orders and renewals, and payment questions: 866-434-AAAS (2227) or 202-326-6417, FAX 202-842-1065. Mailing addresses: AAAS, P.O. Box 96178, Washington, DC 20090-6178 or AAAS Member Services, 1200 New York Avenue, NW, Washington, DC 20005

INSTITUTIONAL SITE LICENSES 202-326-6730 **REPRINTS:** Author Inquiries 800-635-7181 **COMMERCIAL INQUIRIES** 803-359-4578 **PERMISSIONS** 202-326-6765, permissions@aaas.org **AAAS Member Central Support** 866-434-2227 www.aaas.org/membercentral.

Science serves as a forum for discussion of important issues related to the advancement of science by publishing material on which a consensus has been reached as well as including the presentation of minority or conflicting points of view. Accordingly, all articles published in *Science*—including editorials, news and comment, and book reviews—are signed and reflect the individual views of the authors and not official points of view adopted by AAAS or the institutions with which the authors are affiliated.

INFORMATION FOR AUTHORS See www.sciencemag.org/authors/science-information-authors

Published by AAAS

EDITORIAL

War and peace in the nuclear age

The ongoing confrontation with North Korea is a reminder that the world must prevent nuclear weapons from ever being used again. North Korea's development of a nuclear arsenal and delivery systems that could threaten the U.S. mainland, South Korea, and Japan has heightened the possibility of a disastrous conflict with hundreds of thousands of casualties. If constructive dialogue does not happen soon, the United States and North Korea may ratchet up tensions and take increasingly provocative actions. The decision by North and South Korea to field a combined team in the Winter Olympics gives hope for broader engagement, but diplomacy by scientists might be one step toward a more lasting rapprochement.

Science diplomacy was born as a response to nuclear weapons. The central question of whether nuclear war is inevitable in a world of deterrence was examined in "Living with Nuclear Weapons," which was produced by the Harvard Nuclear Study Group in 1983. The solution was for nations to take continual steps to reduce the risk of nuclear war. With enough time and gradual efforts to transform political relationships, even nuclear disarmament might become possible.

A series of nongovernmental engagements called "Track II" diplomacy began in the 1980s and included nuclear scientists, policy experts, and retired military leaders in the Committee on International Security and Arms Control (CISAC) of the U.S. National Academy of Sciences. This committee had regular meetings with a similarly composed group of experts under the Soviet Academy of Sciences. Both sides briefed their governments. These dialogues turned out to be enormously valuable when a "window of opportunity" for arms control and reductions emerged in Reykjavik, Iceland. There, in 1986, U.S. President Reagan and USSR General Secretary Gorbachev discussed the elimination of nuclear weapons. Several Soviet scientists who were engaged in the Track II diplomacy effort turned out to be Gorbachev's key advisers. Even though negotiations were ultimately unsuccessful, this summit made the aspirational goal more than a pipe dream.

Sadly, that sentiment seems to be lost today. The 2015 Iran nuclear deal, brokered in part by two physicists—Ali Akbar Salehi, head of the Atomic Energy Organization of Iran, and Ernest Moniz, then the U.S. Secretary of Energy—is now threatened by possible U.S. withdrawal from this milestone in science diplomacy.

Nevertheless, scientists could play an integral role in building trust with North Korea and averting miscalculations that could lead to nuclear war. The scientists and engineers who lead North Korea's nuclear weapons and ballistic missile programs are accorded considerable prestige by their government. I propose bringing together North Korea's science leaders and a group of prominent U.S. nuclear scientists and security experts outside of government for a dialogue on nuclear safety and security. Perhaps Chinese scientists who have been involved with U.S. scientists from CISAC in Track II dialogues would be willing to host the first meeting. The U.S. side might include distinguished scientific leaders who have previously engaged with North Korea on nuclear issues, such as former Los Alamos National Laboratory Director Siegfried Hecker, a plutonium expert at Stanford University. It could also include a bipartisan group of scientists with previous high-level government experience, such as Moniz, who is now at the Nuclear Threat Initiative, and Harvard University's Ashton Carter, a physicist and former U.S. Secretary of Defense under President Obama. The current Secretary of Defense, General James Mattis, might be one source of experts credible to the current administration. If the dialogue achieved nothing more than reinforcing deterrence and reducing the risk of actions that could be misinterpreted and lead to conflict, it would be well worthwhile. It might even accelerate serious governmental negotiations for a permanent diplomatic solution.*

–E. William Colglazier

Reagan and Gorbachev sign the 1987 nuclear treaty.

"...scientists could play an integral role in building trust... and averting miscalculations..."

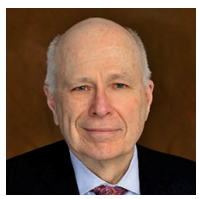

E. William Colglazier is the editor-in-chief of Science & Diplomacy, *Center for Science Diplomacy, American Association for the Advancement of Science, Washington, DC, USA. bcolglaz@aaas.org*

*This editorial was derived from E. William Colglazier, War and peace in the nuclear age, *Science & Diplomacy*, vol. 6, no. 4 (December 2017).

10.1126/science.aat0593

6000 Number of comments posted since 2013 on PubMed Commons, a website where scientists could discuss the 28 million articles indexed in the PubMed database. The site, which did not allow anonymous comments, is closing because of low participation.

IN BRIEF

Edited by **Jeffrey Brainard**

SCIENCE POLICY

Puerto Rico data source under threat

Debris from Hurricane Maria, which struck Puerto Rico in September 2017, remained 4 months later.

A proposal before the Puerto Rican legislature this week would gut the Puerto Rican Institute of Statistics (PRIS), an independent government agency designed to review and analyze statistical data about the island. The measure, part of a larger reorganization proposed by Governor Ricardo Rosselló, would outsource many of PRIS's functions to the private sector. Statisticians, researchers, business groups, and even U.S. congressional representatives have spoken out against the move, saying it threatens the independence and trustworthiness of data on Puerto Rico during an economic crisis and ongoing hurricane recovery efforts. "Objective statistical data are critical, especially in these times for Puerto Rico," says Steve Pierson, director of science policy for the American Statistical Association in Alexandria, Virginia. "From so many angles, this does not seem like a good proposal." But Rosselló maintains that outsourcing PRIS's functions—while encouraging the U.S. federal government to extend more of its statistical services to the island—will streamline data collection and free it from political influence by removing it from local government management. "That would give [the data] the highest level of independence at this time when we need the most clarity," he asserts.

Support for interim CDC head

PUBLIC HEALTH | Public health specialists are lobbying for Anne Schuchat, currently interim director of the Centers for Disease Control and Prevention (CDC), to become the agency's permanent head. Schuchat, who has worked at CDC since 1988, replaced Brenda Fitzgerald after she resigned 31 January following a report in Politico that she had invested in tobacco companies after taking the job 6 months ago. Schuchat should be given "strong consideration to be the permanent CDC director," the Association of Schools and Programs of Public Health, which represents many of the biggest U.S. academic centers, wrote to the Department of Health and Human Services, CDC's parent organization, on 2 February. Schuchat previously served as an interim director from January through July 2017.

Massive rocket's maiden flight

SPACE FLIGHT | The United States's most powerful rocket since the Saturn V lifted off from the Kennedy Space Center in Florida on 6 February. The test launch of the Falcon Heavy, developed by private space company SpaceX, could foreshadow new opportunities in astronomy and space exploration. The 70-meter-tall rocket is designed to carry payloads of up to 64,000 kilograms

SpaceX's Falcon Heavy could carry larger probes.

PHOTOS: (LEFT TO RIGHT) ALVIN BAEZ/REUTERS PICTURES; JOE SKIPPER/REUTERS PICTURES

Published by AAAS

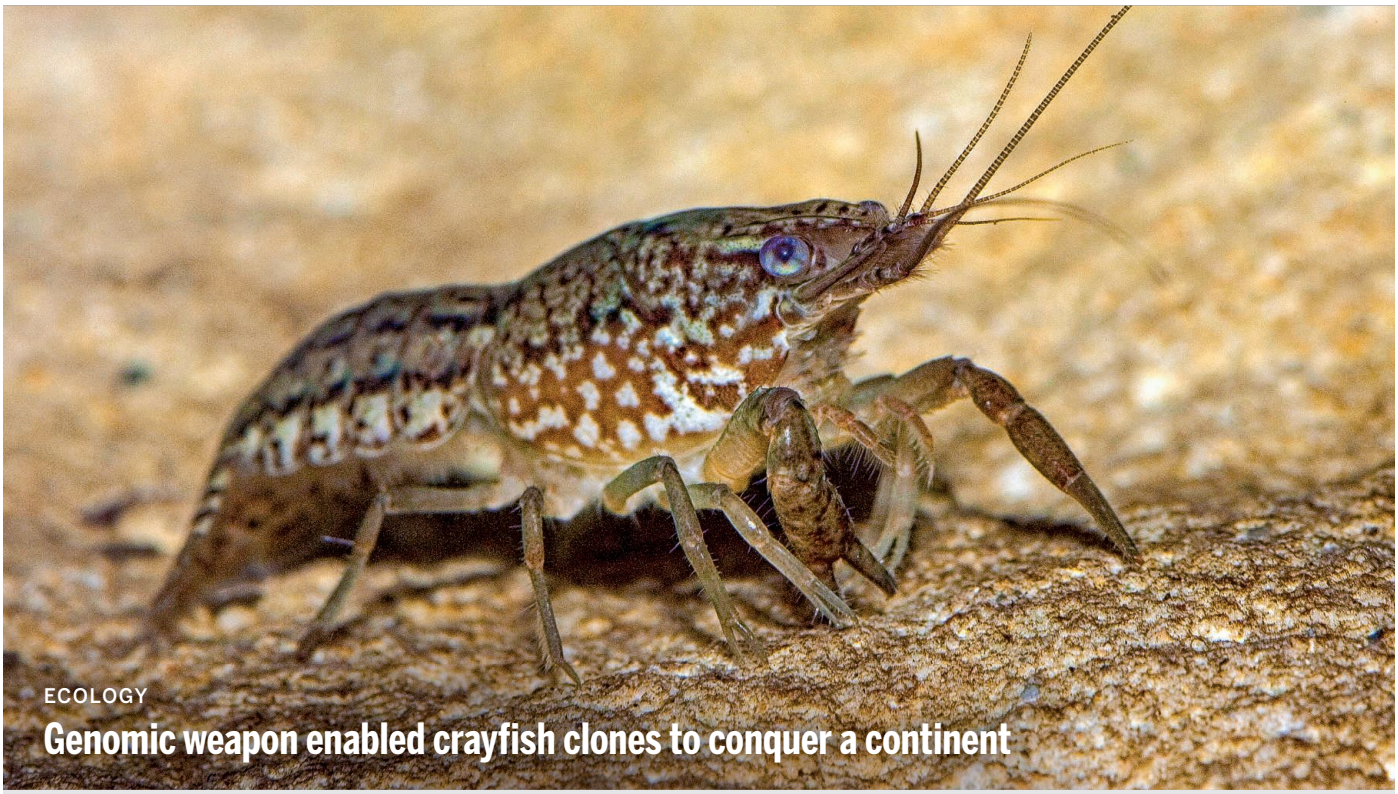

ECOLOGY

Genomic weapon enabled crayfish clones to conquer a continent

A genomic study has verified that crayfish imported to Germany as aquarium pets produced offspring that reproduce asexually. Since that event decades ago, the clones have spread throughout Europe and into Madagascar, where they threaten seven native crayfish. The marbled crayfish's secret weapon is three copies of its genome, one of which is quite different from the other two and may enable this crustacean to adapt to a variety of habitats. Frank Lyko, a molecular geneticist at the German Cancer Research Center in Heidelberg, and colleagues conducted the sequencing, the first of a decapod, a group that includes shrimp, lobsters, prawns, and crabs, and reported it this week in *Nature Ecology & Evolution*. The crayfish's clonal spread may parallel that of cancer cells, and Lyko wants to see what changes, epigenetic or otherwise, enhance the clones' ability to survive and thrive.

to low-Earth orbit, more than twice the payload of any existing rocket. That could allow scientists to loft more ambitious orbiting observatories and send heavier, more sophisticated missions to Mars and beyond. The Falcon Heavy employs reusable boosters, which help lower launch costs. NASA continues to develop a more expensive and powerful rocket, the Space Launch System, in part to return astronauts to the moon.

Cuban science adviser dies

CUBAN SCIENCE | Physicist Fidel Castro Díaz-Balart, the eldest son of Fidel Castro, committed suicide 1 February after undergoing months of treatment for depression, Cuba's state media has reported. He was 68. Fidelito, as Castro Díaz-Balart was affectionately known in Cuba, was a prominent figure in the nation's research scene, serving as science adviser to Cuban President Raul Castro and as a vice president of the Cuban Academy of Sciences. Castro Díaz-Balart's latest scientific project ruffled some feathers among Cuban scientists. In 2015, he established the Center for Advanced Studies of Cuba south of Havana, which aimed to make the nation competitive in nanotechnology. It consumed the lion's share of state funding for physics in recent years—but few scientists were willing to work at the remote site. However, says one prominent official who knew him well, "His depression was related to the death of his father," who died in November 2016.

Turkey arrests doctors

FREE SPEECH | Eleven members of the Turkish Medical Association's board are facing prosecution in Turkey on charges of terrorism after the group condemned the country's military incursion into northern Syria and called for peace. In a statement released after Turkey attacked Kurdish militants in Afrin, Syria, in January, the association warned that "war is a man-made public health problem" and called on Turkey's government to end military operations in its war-torn neighbor. President Recep Tayyip Erdoğan, who has cracked down on critics since a foiled coup in 2016, accused the association of treason and labeled its members "terrorist lovers"; Ankara considers the Kurdish militants to be terrorists. Some board members and doctors belonging to the association have gone into hiding after reportedly receiving death threats in response to the statement. All of the 11 doctors, arrested in late January, have been released on bail. In 2016, Erdoğan's government jailed and dismissed university faculty members who signed a similar petition.

Environmental nominee withdraws

SCIENCE POLICY | U.S. President Donald Trump's highly controversial nominee to lead a key White House environmental panel this week removed herself from consideration. Kathleen Hartnett White, a former Texas state regulator, had been

PHOTO: HUETTER, C./PICTURE ALLIANCE/ARCO IMAGES G/NEWSCOM

PEER REVIEWS

Don't use as intended

Scientists have shared reviews online in recent weeks describing how they've used ordinary products sold by Amazon to meet their research needs. Reviews have been gathered under the hashtag #ReviewforScience. Some are ... odd. Others are gross. Most are entertaining. Some examples:

"Luxury" condoms

"Useful membrane through which to feed hematophagous insects."
Jules Bristow, entomologist

Electric coffee grinder

"Works overall quite well for grinding zebra, springbok, and elephant fecal samples for hormone extraction. Not as great for very goopy samples, or would have given 5/5."
Carrie Cizauskas, wildlife disease ecologist

Nail polish

"Must-have in any tropical rainforest first aid kit! Apply topically over entrance to bot fly pupae until maggot dies, then extract. Coloured polish helps track infestation over course of field season. Also festive."
Aerin Jacob, conservation scientist

Garbage bags

"The best thing about these trash bags is how well a 5'6" frog scientist can fit inside to stay dry and warm during a tropical storm. Highly recommended for other similar-sized field researchers."
Jonathan Kolby, ecologist

Ground coffee, 48-ounce can

"The can is sturdy & perfect for hyper-quenching flowing lava. It holds enough water to take your sample from 1800°F to ambient temp in no time flat. No idea what the coffee tastes like."
Jess Phoenix, volcano scientist

Play-Doh

"Perfect for orienting & securing small skulls, teeth, or other museum specimens for photography without staining the specimen. Downside is that your kids may steal it when you're not looking."
Lisa Whitenack, biologist

Hammer drill kit

"NOT powerful enough to run a 3" concrete boring bit through frozen peat to extract permafrost sediment cores."
Noam Ross, ecologist

picked to chair the White House's Council on Environmental Quality (CEQ), which coordinates federal environmental policy. She came under fire from senators in both parties for what they characterized as her extreme views and disregard for science. Hundreds of scientists had signed a letter calling on Trump to dump the nominee. Hartnett White's "record made it clear that she did not accept basic scientific facts, put industry interests above the public, and would not carry out the mission of CEQ," said Kathleen Rest, executive director of the Union of Concerned Scientists in Cambridge, Massachusetts, which helped organize the scientists' letter.

Russian film touts leaders' genes

GENETICS | Scientists have pounced on a documentary about the infamous Siege of Leningrad, Russia, during World War II that they say strays into science fiction. *Siege Blood, Genetics*, which premiered in Russia in late January, asserts that President Vladimir Putin and other leaders have strong leadership skills because of genes they inherited from survivors of the siege, which claimed more than 1 million lives. Produced with financial support from a pro-Kremlin political party, Just Russia, the film suggests that Putin's mother and other residents of Leningrad (now St. Petersburg) avoided starvation during the nearly 900-day siege thanks to favorable genetic mutations. Putin's father, who served in the Red Army, also experienced the siege after he was wounded and returned home. The documentary highlights research by Oleg Glotov, a geneticist at the Ott Research Institute of Obstetrics and Gynecology in St. Petersburg (*Science*, 5 June 2015, p. 1068), who reported that some siege survivors carry alleles associated with efficient metabolism. But the film treads into questionable territory by suggesting that those alleles gave Putin and other descendants of survivors "a single manner of behavior" and "a high degree of responsibility for everything happening in the country and the city." Yury Chernoff, a cell biologist at the Georgia Institute of Technology in Atlanta, says, "The passing of new gene variants during [the] siege is not proven and seems unlikely." And it's vanishingly unlikely, geneticists say, that those alleles would have shaped descendants' behavior.

PUBLIC HEALTH

Flu hits United States hard as virus dodges vaccine

Percent of U.S. outpatient visits for influenzalike illness

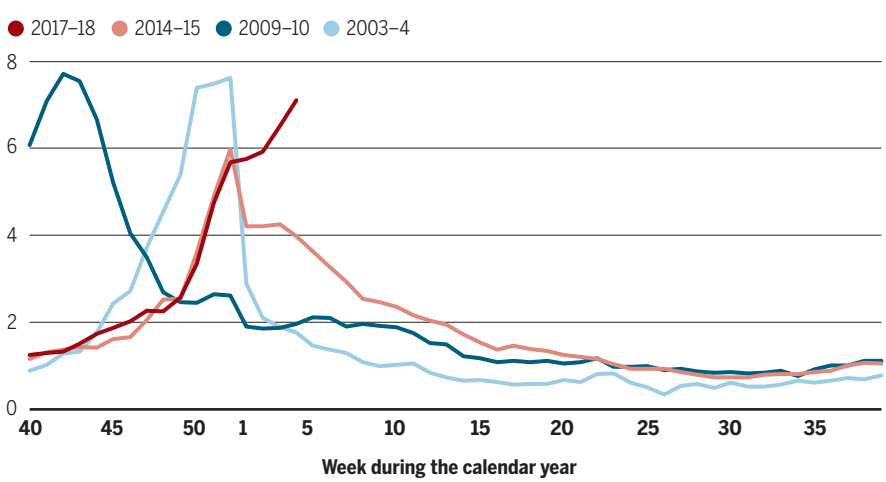

CREDITS: (GRAPHIC) J. YOU/*SCIENCE*; (DATA) U.S. CENTERS FOR DISEASE CONTROL AND PREVENTION

Influenza is walloping the United States harder than usual this winter. The U.S. Centers for Disease Control and Prevention reports that in late January the virus was widespread in 48 of 50 states and that 7.1% of outpatient visits nationwide were for influenzalike illness. In the past 15 years, only two U.S. flu seasons had a week with a higher percentage of such visits, which are used as a proxy for flu because few cases are tested for the virus. Health officials blame some of this year's spike in apparent flu cases on the primary influenza subtype in circulation, which has a history of dodging vaccine-induced immunity. Yet health officials still are urging people to receive the vaccine because it can reduce the severity of symptoms even when it fails to prevent the disease.

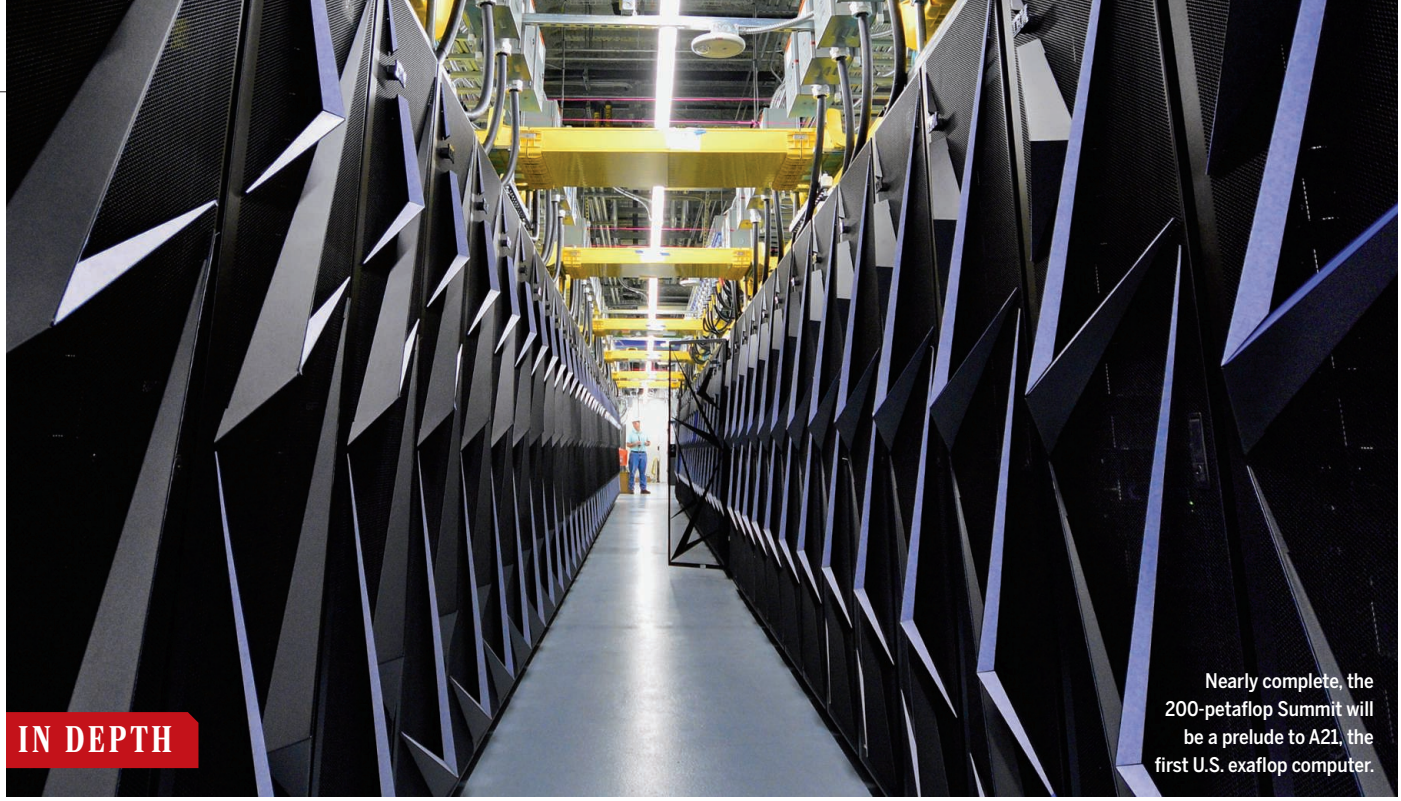

IN DEPTH

Nearly complete, the 200-petaflop Summit will be a prelude to A21, the first U.S. exaflop computer.

PHOTO: LYNN FREENY/DEPARTMENT OF ENERGY VIA FLICKR

SUPERCOMPUTING

Design for U.S. exascale computer takes shape

Competition with China accelerates plans for next great leap in supercomputing power

By **Robert F. Service**

In 1957, the launch of the Sputnik satellite vaulted the Soviet Union to the lead in the space race and galvanized the United States. U.S. supercomputer researchers are today facing their own Sputnik moment—this time with China. After dominating the supercomputing rankings for decades, the United States is now so far behind that the combined power of the top two machines in China easily outpaces that of all 21 supercomputers operated by the U.S. Department of Energy (DOE), the country's top supercomputing funder.

But now, U.S. supercomputing researchers are striking back. Engineers at DOE's Oak Ridge National Laboratory in Tennessee have nearly completed Summit, a computer with twice the power of the top Chinese machine, the Sunway TaihuLight in Wuxi. When fully commissioned this summer, Summit will churn out 200 million billion floating-point operations per second (petaflops). Even more promising, scientists are meeting in Knoxville, Tennessee, this week to get their first detailed look at designs for the next U.S. behemoth, its first 1000-petaflop—1 exaflop or exascale—supercomputer, to be built by 2021 at Argonne National Laboratory in Lemont, Illinois. That's 2 years earlier than planned. "It's a pretty exciting time," says Aiichiro Nakano, a physicist at the University of Southern California in Los Angeles who uses supercomputers to model materials made by layering stacks of atomic sheets like graphene.

Called A21, the Argonne computer will be built by Intel and Cray and is expected to supercharge simulations of everything from the formation of galaxies to the turbulent flows of gas in combustion. "With exascale we can put a lot more physics in there," says Choong-Seock Chang, a physicist at the Princeton Plasma Physics Laboratory in New Jersey who plans to use A21 to model the plasma physics inside a fusion reactor.

> ***"With exascale we can put a lot more physics in there."***
>
> **Choong-Seock Chang**, Princeton Plasma Physics Laboratory

China and possibly Japan are still likely to reach the exascale promised land first (see sidebar, p. 618). But if it's completed on schedule, A21 could keep the United States from slipping too far behind. The faster pace reflects a change of strategy by DOE officials last fall. Initially, the agency set up a "two lanes" approach to overcoming the challenges of an exascale machine, in particular a potentially ravenous appetite for electricity that could require the output of a small nuclear plant.

The agency had been funding two machines, both stepping stones to the exascale, that would take different approaches to cutting the energy demand. IBM and its partner NVIDIA, the makers of Summit, have focused on marrying central processing units (CPUs) with graphical processing units, which are faster and more efficient for calculations involved in complex visual simulations. Intel and Cray, meanwhile, have long aimed to increase the number of CPU "cores" operating in parallel and creating fast links between them. Their strategy was meant to lead to a 180-petaflop sister for Summit, called Aurora, to be built at Argonne.

In 2015, DOE expected Aurora to be finished this year, with the first U.S. exascale machine appearing in 2023. Then China announced a 5-Year Plan that spelled out the goal of an exascale machine by the end of 2020. The United States wasn't just falling behind, it was about to be lapped.

"There was a lot of stress in the U.S. DOE, National Nuclear Security Agency, and in-

dustry," Chang says. DOE changed tacks. It scrapped plans for Aurora, and replaced it with A21, a machine five times bigger. That pushed the launch date back to 2021, but because it was to be the first U.S. exascale machine, it also effectively pushed up the U.S. timeline by 2 years.

Skipping the intermediate step of Aurora is risky, says Kenneth Jansen, an aerospace engineer at the University of Colorado in Boulder. "It means one of the stepping stones is not going to be there." Still, others say it's a risk worth taking. "This is the right way to do it," says Thom Dunning, a computational chemist at the University of Washington in Seattle.

Details of A21's architecture remain closely guarded to protect proprietary technology. But scientists writing software for the new machine will be given detailed briefings on the new architecture after they sign nondisclosure agreements. Some of the first briefings are taking place this week in Knoxville at the second annual Exascale Computing Project meeting.

Researchers already familiar with the plans say the machine is unlike any they've ever seen before. "A21 is a very different architecture," Chang says. In general terms, he says, the design focuses on decreasing the need to move data long distances between processors, an energetically expensive process. He says the new machine will likely require 25 to 30 megawatts of power, only about twice that of Summit. Asked whether he thinks Intel will be able to pull off the new architecture, Chang says, "I am confident they will."

Scaling up

Since 2013, China has operated the most powerful supercomputer in the world. Summit is likely to reclaim the title for the United States this year. China is on track to unveil the first exascale computer in 2020.

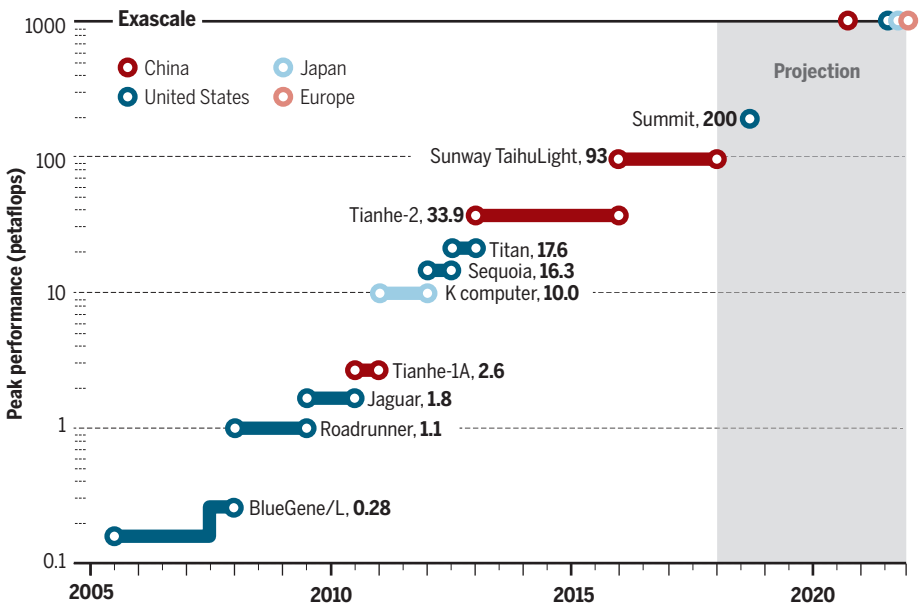

One outside challenge could be money. Congress has yet to pass the fiscal 2018 budget, and instead has funded the government through a series of continuing resolutions that keep funding levels the same as the prior year while forbidding the launch of new projects, such as building the A21 machine. For now, that's not a problem, because DOE is still able to support the underlying scientific developments as part of its existing Exascale Computing Project, says Jack Dongarra, a supercomputing expert at the University of Tennessee in Knoxville. But soon it will be time to start fabricating chips for A21, which is expected to cost between $300 million and $600 million, according to market research firm Hyperion Research. "In 2021 will the budget be there to do this?" asks Horst Simon, a supercomputing expert and deputy director of the Lawrence Berkeley National Laboratory in Berkeley, California. "I don't know." ■

China's planned exascale computer threatens Summit's position at the top

This summer, when engineers flip the switch on Summit, a supercomputer being assembled at Oak Ridge National Laboratory in Tennessee, the machine is expected to be the most powerful in the world. That would return the United States to the top of the supercomputing rankings for the first time since June 2013, when it lost the top spot to Tianhe-2, a machine housed at China's National Supercomputer Center in Guangzhou.

"Of course, we hoped we could have [the top machine] for a longer time," says Depei Qian, a computer scientist at Beihang University in Beijing. "But the government agencies understand that no country can be No. 1 forever."

In the global game of supercomputing leapfrog, China is likely to take back the title from the United States when it builds the first exascale computer: a machine capable of 1 billion billion floating-point operations per second, or 1 exaflop. Under the country's 13th 5-Year Plan, released in 2015, China is committed to launching its first exascale supercomputer by the end of 2020. That could put it a full year ahead of A21, the first U.S. exascale supercomputer, planned for launch in 2021 (see main story, p. 617). Japan is also aiming for an exascale machine with a successor to its K supercomputer at the RIKEN Advanced Institute for Computational Science in Kobe, though the head of the project has said that its delivery could slip to 2021 or 2022. Finally, the European Union could cross the exascale threshold in 2021, according to market research firm Hyperion Research.

But that won't be the end of the race. The four supercomputing powers are convinced they need to push the frontiers in order to compete in a wide range of scientific disciplines, defense technology, industrial technology, and computer products. "Everybody is moving as fast as they can," says Jack Dongarra, a supercomputing expert at the University of Tennessee in Knoxville who keeps close tabs on international supercomputing efforts. And once they cross one threshold, he says, "then it's on to the next one." —*Robert F. Service*

With additional reporting by Dennis Normile.

CREDITS: (GRAPHIC) K. SUTLIFF/*SCIENCE*; (DATA) TOP500

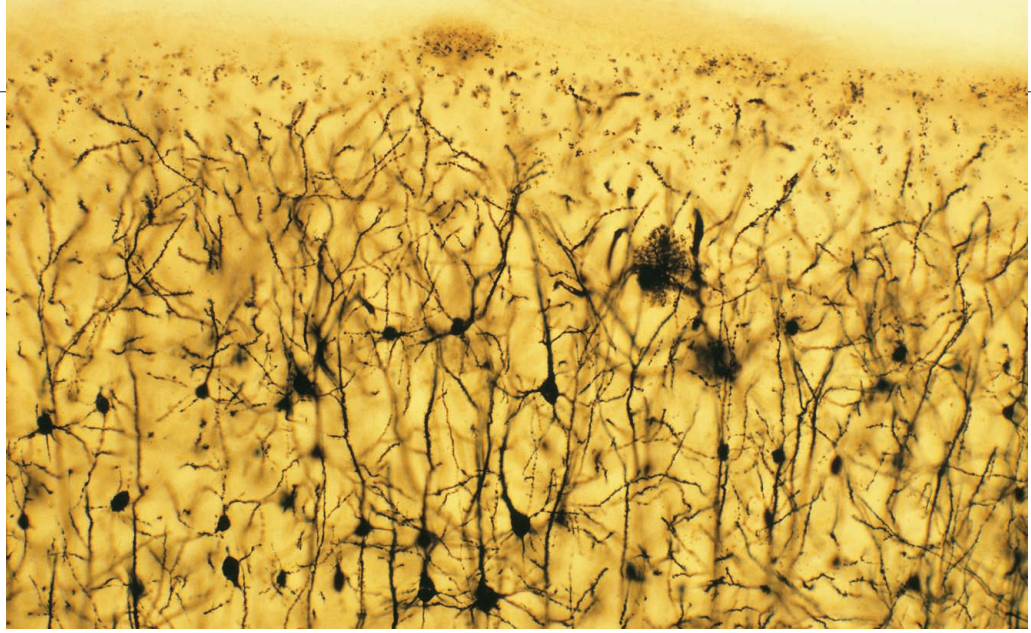

The cerebral cortex has both shared and distinctive gene activity patterns in patients with major mental disorders.

PHOTO: CNRI/SCIENCE SOURCE

NEUROSCIENCE

Psychiatrists begin to map genetic architecture of mental disorders

Gene expression findings from study of hundreds of human brains could lead to diagnostic tests, therapies

By **Roni Dengler**

Mental illness affects one in six U.S. adults, but scientists' sense of the underlying biology of most psychiatric disorders remains nebulous. That's frustrating for physicians treating the diseases, who must also make diagnoses based on symptoms that may only appear sporadically. No laboratory blood test or brain scan can yet distinguish whether someone has depression or bipolar disorder, for example.

Now, however, a large-scale analysis of postmortem brains is revealing distinctive molecular traces in people with mental illness. This week, an international team of researchers reports on p. 693 that five major psychiatric disorders have patterns of gene activity that often overlap but also vary in disease-specific—and sometimes counterintuitive—ways. The findings, they say, might someday lead to diagnostic tests and novel therapies, and one has already inspired a clinical trial of a new way to treat overactive brain cells in autism.

Outsiders say the data mark a milestone in psychiatry. "This [work] is changing fundamental views about the nature of psychiatric illness," says Kenneth Kendler, a psychiatric geneticist at Virginia Commonwealth University in Richmond.

Researchers have long known that genes influence mental illness. Five years ago, for example, the global Psychiatric Genomics Consortium found that people with autism, schizophrenia, bipolar disorder, depression, and attention-deficit hyperactivity disorder frequently share certain DNA variations. But that 2013 study did not say how those genetic alterations might lead to symptoms.

Dan Geschwind, a neurologist and neuroscientist at the University of California, Los Angeles (UCLA), who spearheaded the new work, wanted to know what happens at the molecular level in the brains of people with these disorders. He, his UCLA colleague Mike Gandal, and their team analyzed gene expression patterns from the cerebral cortex, the brain's outer layer, of 700 postmortem patients with autism, schizophrenia, bipolar disorder, depression, or alcoholism and compared the patterns with those from the brains of 293 matched healthy controls. For another control, they also looked at cortical gene expression in 197 patients with inflammatory bowel disease, which should help exclude general disease processes shared by non–central nervous system conditions.

The analysis revealed that certain psychiatric diseases are more similar biologically than their characteristic symptoms indicate. Bipolar disorder is commonly considered a mood disorder, like depression, so it stands to reason that the underlying biology of both ailments would be comparable. But the genomic data told a different story: Bipolar disorder overlapped the most in cortical gene activity with schizophrenia. "This is not what clinicians would've expected," Kendler says. "It certainly suggests the idea that these are sharply different kinds of disorders is not valid."

In another surprise, Geschwind, Gandal, and their colleagues found essentially zero correlation in gene activity patterns between alcoholism and the other four disorders. Many studies in identical twins, who have largely identical DNA, had suggested that the genetic risk factors for major depression and alcohol use disorder are similar, Kendler says. Yet the new work suggests that's not the case.

Another series of tantalizing findings hinted at autism's molecular roots. The study showed, for example, that many genes in the cerebral cortex are active in both schizophrenia and autism—but they are far more active in autism. The finding suggests that gene overexpression might play a role in autism's symptoms. Meanwhile, genes linked to neuronal firing were turned down in autism, as well as in schizophrenia and bipolar disorder—suggesting that changes in brain cell communication play a role in all three conditions.

Another cluster of gene activity that stood out in autism points to overactive microglia, a subset of brain immune cells that protect against inflammation. Based on that, Gandal is leading a small clinical trial that will test whether an antibiotic can keep these cells in a resting state in adults with autism.

Jordan Smoller, a psychiatric geneticist at Harvard Medical School in Boston who led the 2013 study of genetic variants in mental disorders, says the field needs to dive even deeper than the new work by focusing on gene expression from single cells, rather than the large brain area examined in the current analysis. That could help researchers zero in on specific cell types driving the disorders, he suggests.

Nonetheless, Smoller applauds the trend in psychiatric genomics toward large consortia that can tackle big problems with masses of data. "The message [from the new study] is a broadly hopeful one," Kendler adds. "We're beginning to see the bits of the puzzle starting to slowly get clearer." ■

INFECTIOUS DISEASE

Use of cholera vaccines expands, raising hopes

Swelling supplies and a better formulation bolster response to widespread outbreaks

By **Kai Kupferschmidt**

Around the world, cholera is on the march. In Yemen, which is mired in a civil war, the devastating waterborne illness has sickened more than a million people since October 2016 and continues to spread. Outbreaks are ravaging Zambia, Tanzania, Zimbabwe, and several other African countries. Haiti is still suffering from an epidemic that began in 2010. And last month, after torrential rains flooded parts of Kinshasa, the capital of the Democratic Republic of the Congo (DRC), cases spiked there. "For reasons we do not understand, cholera seems to go through cycles of severe seasons," says David Sack, an infectious disease expert at Johns Hopkins University's Bloomberg School of Public Health in Baltimore, Maryland.

But a countermeasure is gaining momentum as well. A vaccine against *Vibrio cholerae*, the causative bacterium, has been around for 20 years, but questions have long swirled about its usefulness in outbreaks, and it has been in short supply. That is changing. The global cholera vaccine stockpile, established by the World Health Organization (WHO) and partners in 2013, has attracted additional manufacturers, and now an easier to use formulation should help health workers respond to outbreaks. Many think this may be the year in which the stockpile starts to reduce cholera's overall toll. "We are reaching an extremely important point where the scale of the campaigns may be sufficiently large to show impact in controlling the disease," says Francisco Luquero, an epidemiologist with Doctors without Borders in Geneva, Switzerland.

In 2013, only about 200,000 doses from the 2-million-dose stockpile were shipped. But as the vaccine has become an option, demand has soared and manufacturers have increased their output. Last year, more than 12 million doses were shipped—and many more were requested by affected countries (see graph, below).

About 2.4 million doses will soon be sent to the DRC, where the current outbreak is the worst in 20 years. That's enough to vaccinate 1.2 million of the country's most at-risk people, and, experts hope, enough to curb the outbreak there. "Kinshasa is definitely my No. 1 concern right now," says Dominique Legros, a cholera expert at WHO in Geneva.

The campaign in Kinshasa will use the new vaccine formulation called Euvichol-Plus, which started shipping early this year. The vaccine is delivered in small plastic tubes rather than glass vials, making it easier to distribute. "It's 25% cheaper, 30% less volume, and 50% less weight," says Seth Berkley, head of Gavi, the Vaccine Alliance in Geneva, which is funding the stockpile. "I think that it is a game changer," Luquero says. "It is clearly making vaccination even more feasible in the conditions where we work." In another improvement over current vaccines, which are most effective in adults, new vaccines in the works may also protect children under 5.

Mass vaccinations were long seen as too slow to stop fast-moving chol-

A surging stockpile

Demand for cholera vaccine from the global stockpile has soared since it was established in 2013. Supply has grown rapidly with it.

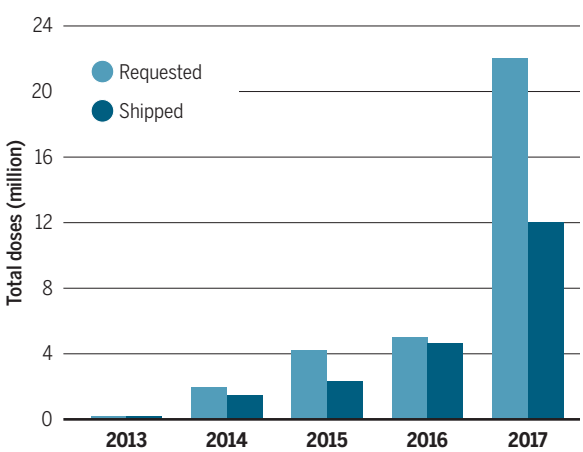

As stocks of oral cholera vaccine rise, mass campaigns, like this one in South Sudan in 2014, become more feasible.

era outbreaks, and many worried they could distract aid workers from treating patients and providing clean drinking water. Studies in Haiti, Guinea, and other countries are confirming that large campaigns are feasible, safe, and effective in outbreaks, while other evidence suggests available doses can be stretched when supplies run short. Recent studies in Bangladesh and Sudan suggest that a single dose confers almost the same protection in the short term as the customary two doses. A report this week in *The New England Journal of Medicine* on a 2016 vaccination campaign in Zambia bolsters that case. The researchers compared 66 people who had cholera with 330 healthy controls and calculated that a single dose offered about 89% protection. "What you gain from the second dose in terms of protection may be marginal," says Luquero, one of the study authors. WHO's Strategic Advisory Group of Experts on Immunization has green-lighted the use of a single dose in emergency settings.

A bigger change may be coming. To date, cholera vaccine, like the other two vaccines in the stockpile for yellow fever and meningitis A, has been used mostly reactively, to stop an outbreak once it begins. But Gavi funding for the stockpile for 2014 to 2018 also included money for some preventive campaigns with the aim of "strengthening the evidence base for periodic, preemptive campaigns." In November, Gavi's board is set to decide whether the alliance will start funding the routine use of cholera vaccines in places where the disease is endemic, such as Bangladesh. That could massively increase the demand for vaccine, creating a further incentive for manufacturers.

Routine vaccination could have global benefits as well. An analysis of hundreds of cholera genomes last year showed that outbreaks in Africa and Latin America originate again and again from introductions of Asian strains (*Science*, 10 November 2017, pp. 785 and 789). Vaccinating against cholera in Asia could help keep the disease from spreading to other continents, Sack says. "In the long run, we want to prevent outbreaks, not just reduce the severity of outbreaks after they have started."

No one thinks improved vaccines or a bigger stockpile will be a panacea. In conflict-torn places such as Yemen, vaccines don't help if vaccinators cannot reach those who need them. And more important, cholera could be vanquished worldwide if everyone had access to safe drinking water. The United Nations estimates that 2 billion people do not. ■

IMAGE: SCIENCE PICTURE CO/SCIENCE SOURCE

BIOMEDICINE

Gene therapy field hit by fresh safety concern

Animal studies show dangerous side effects from virus increasingly used to deliver DNA to treat diseases

By **Jocelyn Kaiser**

A virus that buoyed the gene therapy field when it led to dramatic benefits in babies born with a fatal neuromuscular condition is under scrutiny. The success of the virus—a "vector" for therapeutic DNA—raised hopes that a similar approach could treat other diseases. But an animal study now suggests that the high doses of virus needed may not always be as safe as believed.

In the new research, researchers injected a handful of young monkeys and pigs with many copies of adeno-associated virus 9 (AAV9), a normally harmless virus that infects neurons. Within days, some of the animals developed severe liver and neuron damage.

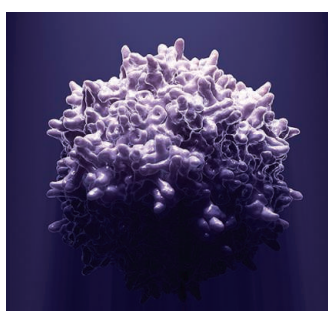

An adeno-associated virus used to ferry a gene into cells was toxic to animals at high doses.

The results, which briefly sent the stock prices of several gene therapy companies plummeting, drew attention in part because they come from the lab of veteran gene therapy researcher James Wilson at the University of Pennsylvania. Wilson led a 1999 trial in which a teenager died from an immune reaction to a different AAV vector, and the new data have him urging researchers planning to treat patients with high-dose AAV9 gene therapy to watch for side effects. They also prompted him to resign from the board of a company pursuing such a trial to treat Duchenne muscular dystrophy.

He and others in the gene therapy field say, however, that ongoing clinical trials with the gene carrier should not be halted. "This is a big deal, potentially," says Terence Flotte of the University of Massachusetts Medical School in Worcester, who is editor-in-chief of *Human Gene Therapy*, which published the new study online on 29 January. However, Flotte writes in a commentary, the community should not "overreact."

AAV9 has proved better than some other vectors at spreading through muscle and neural tissue; at high doses it can even cross the blood-brain barrier to reach spinal neurons and the brain. In the first human trial with AAV9, 15 babies with a severe form of spinal muscular atrophy, a neurodegenerative disease, that typically kills by age 2, received an infusion of the viruses carrying a missing gene called *SMN*. Most of the children can now sit up, and two are walking (*Science*, 3 November 2017, p. 582).

But in Wilson's study, three young rhesus macaques that received a high-dose intravenous infusion of a similar AAV9 carrying *SMN* developed signs of liver toxicity, and one had to be euthanized. Three piglets given the same treatment had motor neuron damage, had trouble walking, and were also euthanized. The team saw similar side effects in one monkey when it tested an AAV9 variant carrying a different gene. Wilson and colleagues note that at least five planned or ongoing clinical trials are using high IV doses of AAV9 or other AAVs. These and other studies "should include careful monitoring for similar toxicities," they write.

In the accompanying commentary, Flotte and a co-author say that AAV9 gene therapy trials should continue because they could save lives. He notes reasons why the finding may not apply to the human trials: Wilson's team injected a different version of AAV9 in their experiments; their study used a human version of *SMN*, which could make it toxic to the animals; and the researchers didn't rule out the possibility that the treatment was contaminated. Wilson agrees, saying he does not want to "derail anything at this point."

Gene therapy researcher R. Jude Samulski of the University of North Carolina in Chapel Hill, who has never seen such toxic effects in his primate studies with AAV9, predicts that many labs will now request Wilson's vector and repeat his experiments. "If this is truly a concern, it needs to be reproducible," he says. ■

A new tobacco industry–funded foundation will study "harm reduction" strategies, including e-cigarettes.

RESEARCH FUNDING

Tobacco giant's research largesse ignites controversy

Philip Morris's $1 billion effort to promote studies of "harm reduction" prompts some researchers to call for a boycott

By **Martin Enserink**

Utrecht University (UU) in the Netherlands thought it had nothing to be ashamed of when it accepted a €360,000 research grant from Philip Morris International (PMI) last September. The tobacco giant had agreed to fund a study on cigarette smuggling that had obvious public health importance, and the lead researcher, law professor John Vervaele, would enjoy complete academic freedom. Sure, there had been a "thorough debate" about the grant, Vervaele said in a press release, "but the tobacco industry is not illegal. The illicit tobacco trade is."

But the announcement sparked a firestorm of criticism from outside groups, including associations of pulmonologists and oncologists and the Dutch Cancer Society. A university should not take money from an industry whose products kill an estimated 7 million people annually, they argued. And on 17 January, UU made a U-turn, announcing that it would sever ties with PMI and pay for the study itself. By then, the topic had become so controversial that Vervaele was no longer allowed to speak to the press.

Similar battles seem bound to emerge at academic institutes elsewhere in the months and years ahead, because PMI is planning to spend a lot more money. The UU grant came from PMI Impact, a $100 million program to fight illegal trade by funding both research and enforcement. Much more money will come through the controversial Foundation for a Smoke-Free World, a New York City–based independent foundation launched last September, to which PMI has pledged to donate almost $1 billion over the next 12 years—most of it for research.

PMI, the maker of Marlboro and other tobacco brands, says it supports the foundation because the company wants to end the production and use of combustible cigarettes and help smokers switch to less dangerous alternatives, which PMI is heavily investing in. But many scientists and public health experts say the new foundation is, well, a smokescreen, set up to protect PMI's interests. In a 25 January statement, the deans of 17 schools of public health in the United States and Canada said they would not collaborate with the foundation; an official at the World Health Organization (WHO) in Geneva, Switzerland, has called the foundation a "deeply alarming development."

To the consternation of many public health researchers, the foundation is headed by a former top WHO official, Derek Yach, who was instrumental in developing the Framework Convention on Tobacco Control, a global pact aimed at curbing smoking. Yach left WHO in 2007 to work for PepsiCo; with his new job, his "journey to the Dark Side is now complete," Stanton Glantz, director of the Center for Tobacco Control Research and Education at the University of California, San Francisco, recently wrote. But an editorial in *The Lancet* called Yach a "respected public health leader" and said a complete boycott of the foundation would be a "mistake."

Accepting tobacco money for research was widely seen as acceptable until the 1990s. But revelations about the way the industry hid data on the risks of smoking from the public and used science to sow confusion and doubt made such funding increasingly taboo for academics. Many universities now shun direct industry funding, and some journals no longer publish tobacco-funded research. Major funders such as the Wellcome Trust and Bloomberg Philanthropies bar their grant recipients from also accepting tobacco money.

But Yach says industry and scientists should work together on "harm reduction" strategies for reducing tobacco's health risks. Harm reduction advocates see promise in e-cigarettes, most of which vaporize nicotine and reduce the inhalation of other toxic compounds. Some have also promoted "heat-not-burn" cigarettes and snus, a powdered tobacco sold in Sweden that is usually placed under the upper lip. The products are meant to complement antitobacco strategies such as taxes, advertising bans, and plain packaging, which have been shown to prevent young people from lighting up but do less to help current smokers quit.

Many tobacco control experts are reluctant to embrace the products, however, because their long-term health effects are unclear; some worry, for instance, that vaping could become a "gateway drug" to smoking. An advisory panel to the U.S. Food and Drug Administration on 25 January voted not to allow PMI to market iQOS, its heat-not-burn product, as less risky than ordinary cigarettes. Also last month, a report from the U.S. National Academies of Sciences, Engineering, and Medicine on e-cigarettes identified an array of questions about harm reduction that researchers need to address.

But public funding to help settle those questions is in short supply, says Brad Rodu, a harm reduction advocate at the

PHOTO: ISTOCK.COM/DIEGO_CERVO

University of Louisville in Kentucky who for years has relied on tobacco money. The new foundation will help fill that void, says Yach, especially in developing countries. "Our focus is clear, and we're unashamed of it," he says: "It's the billion people who smoke." In addition, the foundation plans to assess tobacco companies' actions to promote smoking cessation and to help tobacco farmers find new livelihoods if demand dwindles.

Critics question PMI's declared commitment to harm reduction. The company has fought antitobacco measures in court and is aggressively marketing cigarettes to young people, says Joanna Cohen of Johns Hopkins University's Bloomberg School of Public Health in Baltimore, Maryland. "If they really wanted a smoke-free world, they would stop doing those things right away." Tobacco control researcher Michael Siegel of Boston University says he's all in favor of harm reduction, but accepting tobacco money makes researchers "pawns" in a public relations strategy. He calls the foundation "a scam."

WHO's Vera Luiza da Costa e Silva, head of the tobacco convention's secretariat, sees another risk: By funding research into nontraditional tobacco products, PMI hopes to influence how those products are regulated in the future, as it has done for cigarettes, she wrote in a statement this past September. The new foundation is "an attempt to breach" the convention, Da Costa e Silva said.

Yach says much of the criticism is based on misconceptions. The foundation's bylaws guarantee complete independence from PMI, he notes. To prevent the foundation from becoming a public relations tool, PMI isn't even allowed to mention its funding in its own publications. Those who say that the industry should simply stop making cigarettes tomorrow "have to understand how their business models work," Yach says. "Companies will continue their current products until they see a tipping point."

The big question is how many researchers will want a share of PMI's $1 billion. "I would be very surprised if reputable researchers applied," says Martin McKee of the London School of Hygiene & Tropical Medicine. But Yach says he's already received 50 to 60 proposals from around the world, including from U.S. medical schools. The foundation will issue a formal call for proposals for centers of excellence after a workshop later this month, and expects to award its first major grants within a few months. Yach isn't expecting the criticism to ease anytime soon, however. "The thing I do worry about is harassment of grantees and staff, the very ad hominem attacks," he says. "That is unacceptable behavior." ■

ATMOSPHERIC CHEMISTRY

As polar ozone mends, UV shield closer to equator thins

Short-lived chemicals may be the culprit

By **April Reese**

Thirty years after nations banded together to phase out chemicals that destroy stratospheric ozone, the gaping hole in Earth's ultraviolet (UV) radiation shield above Antarctica is shrinking. But new findings suggest that at midlatitudes, where most people live, the ozone layer in the lower stratosphere is growing more tenuous—for reasons that scientists are struggling to fathom.

"I don't want people to panic or get overly worried," says William Ball, an atmospheric physicist at the Physikalisch-Meteorologisches Observatorium Davos World Radiation Centre in Switzerland. "But there is something happening in the lower stratosphere that's important to understand."

Several recent studies, including one last month in *Geophysical Research Letters*, point to a robust recovery of stratospheric ozone concentrations over Antarctica—the long-awaited payoff after the Montreal Protocol in 1987 mandated a global phaseout of chlorofluorocarbons and other ozone-eating compounds.

> ***"The potential for harm ... may actually be worse than at the poles."***
>
> **Joanna Haigh**, Imperial College London

But recent evidence indicates that the global ozone layer is still at risk. In an analysis published today in *Atmospheric Chemistry and Physics*, Ball and colleagues combined satellite data and two atmospheric chemistry models to examine ozone at midlatitudes, from Earth's surface on up through the troposphere and the stratosphere. They found that from 1998 to 2016, ozone in the lower stratosphere ebbed by 2.2 Dobson units—a measure of ozone thickness—even as concentrations in the upper stratosphere rose by about 0.8 Dobson units. "We saw it at almost every latitude and every altitude below about 25 kilometers," Ball says. "That made us very concerned that perhaps this was something very real that no one looked at before."

The ozone layer's total thickness—not just concentrations in the upper stratosphere—is vital for absorbing UV light. "What matters most for UV at Earth's surface is the total column amount of ozone overhead," says the National Oceanic and Atmospheric Administration's Sean Davis, a co-author in Boulder, Colorado. Although previous studies had suggested a decline in lower stratospheric ozone, no one had combined satellite data to look across such a wide swath of the globe and so far down in the ozone layer.

Ball and his colleagues suspect the culprit is "very short-lived substances," or VSLSs: ozone-eating chemicals such as dichloromethane that break down within 6 months after escaping into the air. Researchers had long assumed that VSLSs' short lifetime would keep them from reaching the stratosphere, but a 2015 study suggested that the substances may account for as much as 25% of the lower stratosphere's ozone losses. Whereas many VSLSs are of natural origin—marine organisms produce dibromomethane, for example—use of humanmade dichloromethane, an ingredient in solvents and paint removers, has doubled in recent years. "We should study [VSLSs] more completely," says Richard Rood, an atmospheric scientist at the University of Michigan in Ann Arbor. But because the compounds are released in small quantities, he says, "They're going to be difficult to measure."

He and others say it's vital to determine what's destroying ozone over the populous midlatitudes. "The potential for harm ... may actually be worse than at the poles," says Joanna Haigh, co-director of the Grantham Institute at Imperial College London. "The decreases in ozone are less than we saw at the poles before the Montreal Protocol was enacted, but UV radiation is more intense in these regions."

Ball and others emphasize that the Montreal Protocol has been a resounding success. "I don't think it in any way says there's something fundamentally wrong with how we've been dealing with the ozone problem," Rood says. "What it says to me is that we're now looking at effects that are more subtle than that original problem we were taking on" when the Montreal Protocol was adopted. ■

April Reese is a freelance journalist in Santa Fe.

THE HAPPINESS PROJECT

Advocates are pushing to enrich the lives of rodents and fish in the lab, but critics worry about the impact on research

By **David Grimm**, *in Ann Arbor, Michigan*

PHOTO: AUSTIN THOMASON/MICHIGAN PHOTOGRAPHY

A mouse at the University of Michigan in Ann Arbor is transferred from cage to cage in a tube, rather than being hoisted by its tail—a common, but stressful maneuver.

If they weren't in the windowless basement of a cavernous biomedical research building, the "Aquatic Suites" might sound like a cushy vacation destination. But the zebrafish here at the University of Michigan (UM) still have it pretty good. In a large room full of aquaria, the striped, pinkie-size swimmers flit past fake green plants, white plastic tunnels, and multicolored marbles that may remind them of the bottoms of lakes and streams. These simple accoutrements are a luxury for creatures typically housed with little more than food and the water they swim in. And the enrichments may make the animals better at what they do: serving as important models for human disease.

For decades, lab animals such as rodents and fish have lived in barren enclosures: a small plastic box, few—if any—companions, and little else. The smaller the number of variables, the thinking went, the greater the accuracy of the experiment. But a growing number of studies suggests that this approach may have backfired. Only one in nine drugs that works in animals ever succeeds in human clinical trials, and labs often struggle to reproduce one another's results. Could the environment these creatures live in be part of the problem?

That's what a new group of advocates argues. "We're trying to control these animals so much, they're no longer useful," says Joseph Garner, a behavioral scientist who runs a program to improve the value and welfare of lab animals at Stanford University in Palo Alto, California. "If we want animals to tell us about stuff that's going to happen in people, we need to treat them more like people."

Garner and others are pushing scientists to enrich the lives of the creatures in their care by giving them toys, companions, and opportunities to exercise and explore—in short, a life more like they would have in the wild. These proponents are driven by both a concern for the welfare of lab animals and a desire to make their contributions to research more meaningful. And they're beginning to conduct experiments that show that such enrichments not only benefit animals, but science as well.

However, other researchers fear that adding extras to animal cages could muddy experiments and exacerbate the reproducibility crisis. And given the tens of millions of rodents and fish in U.S. labs alone, they blanch at the cost. "There's nothing natural about what we're doing, and adding a few tubes to a cage is not going to change that," says Jonathan Godbout, a neuroscientist at The Ohio State University (OSU) in Columbus who studies aging and stress in mice. "The more we spend on this stuff, the less research we can do."

LABORATORY ANIMALS didn't always live such a barren lifestyle. Researchers began breeding rats for scientific experiments in the mid-1800s, and early cages allowed the rodents to burrow and run on wheels. But by the 1960s, in an effort to standardize care and limit variables, labs began to prioritize small, cheap, and sterile enclosures. There was little regard for the animals' natural habits, as long as they were free of obvious pain and suffering. The goal, in essence, was to create furry test tubes.

Today, lab mice live in shoebox-size cages hundreds of thousands of times smaller than their natural ranges, and rats can't forage or even stand upright. Both spend their days blasted by ventilation and bright fluorescent lighting that disrupts their day-night cycles. "We're doing the exact opposite of what we should be doing to make these animals happy," Garner says. Lab animals tend to be obese, have weak immune systems, and develop cancer—all before scientists do any experiments on them.

The first hints that enrichment could help came in the 1940s. In 1947, psychologist Donald Hebb found that rats he raised with his daughters and gave free rein in his home were better learners than lab-raised rodents. In the 1960s, researchers showed that lab rats provided with wooden blocks and a rotating assortment of mazes developed larger sensory regions of their brains.

Yet the only enclosures that changed were those of nonhuman primates. Amendments to the U.S. Animal Welfare Act in 1985 required labs to promote the psychological well-being of the monkeys and chimpanzees in their care, giving them more space, toys, and comrades. The U.S. National Research Council's 1996 *Guide for the Care and Use of Laboratory Animals* went further, prompting animal care staff to add perches, blankets to make nests, and even music and movies. But rodents and fish were largely ignored.

Building a better mouse house

Mice and rats have traditionally been housed in relatively barren cages, with only food, water, and basic bedding material. But advocates hope that enriching their environment with objects for play, exercise, and shelter will give the animals a better life—and make them better research models.

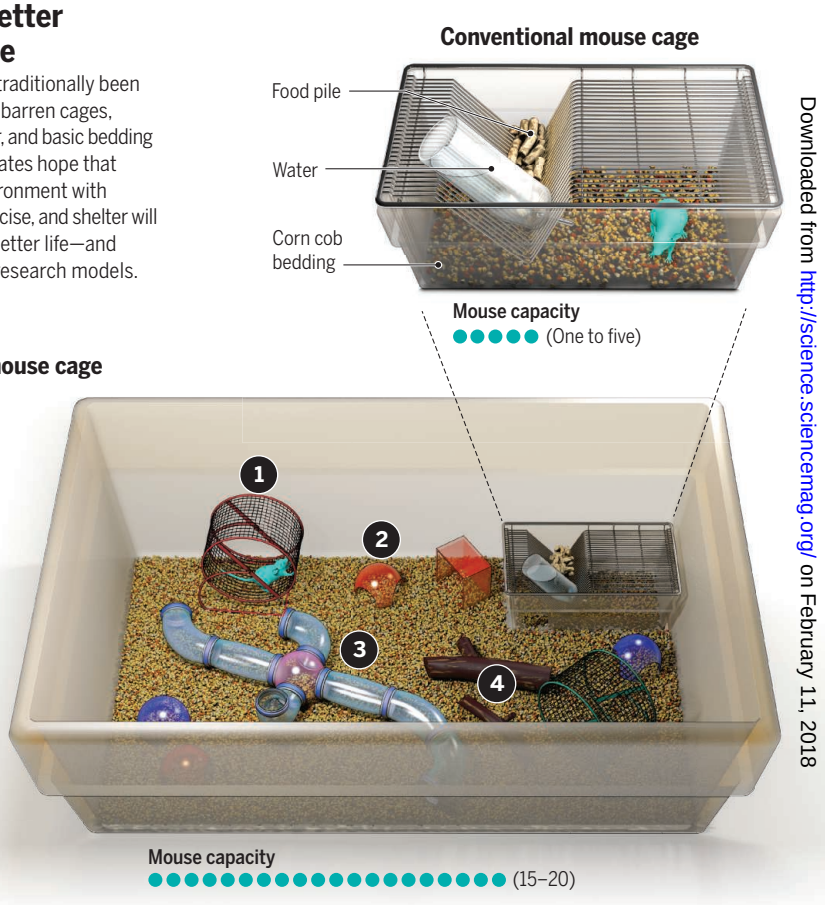

GRAPHIC: V. ALTOUNIAN/*SCIENCE*

Then, in 2000, neuroscientist Anthony Hannan at the University of Melbourne in Australia decided to spice up the lives of his lab mice. Inspired by research that showed enrichment could spark the growth of new neurons, he provided the rodents with cardboard for making nests, brightly colored balls for play, and ladders and ropes to climb. Remarkably, the animals were much slower to develop symptoms of a Huntington-like disease than their counterparts in standard housing—the first demonstration that enrichment could significantly influence neurological disorders.

"Before we did this work, everyone thought Huntington's was 100% genetic," says Hannan, whose team has gone on to show similar results in rodent models of autism, depression, and Alzheimer's disease.

In the past decade, a growing body of work has suggested that rodents and other animals have complex mental lives and can experience a range of emotions once only attributed to people. Scientists have learned more about the power of enrichment, too. In 2010, cancer biologist Lei Cao—inspired by a family member who had died of cancer—wondered whether she could combat it by looking beyond drugs or genes. Her team at OSU created a 1-square-meter enclosure filled with so many mazes, running wheels, and bright red, blue, and orange igloos that her daughter dubbed it "Disneyland for Mice."

When injected with cancer cells, animals housed there developed tumors 80% smaller than those in control mice, or no tumors at all. Cao even discovered a possible mechanism: A stimulating environment seemed to activate the brain's hypothalamus, which regulates hormones that affect everything from mood to cancer proliferation. "We showed that there's a hard science behind enrichment," she says. "You can't just treat the body—you have to treat the mind."

Such findings fit with what we know about how we ourselves respond to our environment. Stress, depression, and lack of social support can boost the risk of cancer in people, and less active individuals are more likely to develop diseases like Huntington later in life.

In the past few years, a host of other studies has demonstrated the power of enrichment. Giving rodents and other animals toys, exercise, and companions appears to reduce their susceptibility to epilepsy, multiple sclerosis, and addiction. Research published last year showed that enrichment helps mice fight infections and sharpens rats' memories.

The growing literature inspired the National Research Council to update its guide in 2011. Like similar guidelines in Europe, it states that all naturally social species should be socially housed if possible, and advocates enrichment for all lab animals, not just nonhuman primates.

Yet scientists can avoid these guidelines if they successfully argue that enrichment will compromise their studies, and universities vary in how they apply enrichment. Showing that enrichment produces happier, healthier lab animals is, after all, not the same as demonstrating that it yields better science. Some researchers want more evidence that enrichment boosts the quality of experimental results.

"My mind could be changed by good science," Godbout says. "If someone comes out with clear-cut data that enrichment impacts the kind of work we do, then of course we'd follow it."

That's what efforts like the fish experiment at UM are trying to provide.

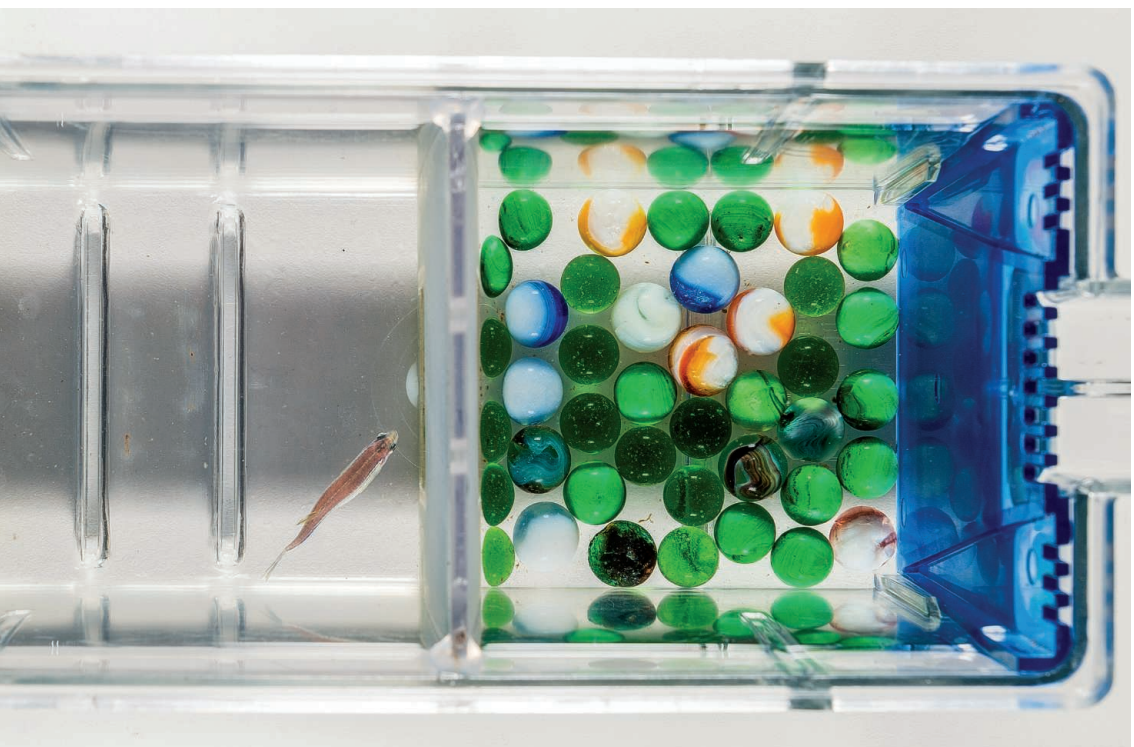

A fish at the University of Michigan in Ann Arbor gets to choose between an empty tank and one filled with marbles.

PHOTO: AUSTIN THOMASON/MICHIGAN PHOTOGRAPHY

BACK IN THE AQUATIC SUITES, veterinarian Jennifer Lofgren is peering into a zebrafish tank. There's a transparent plastic divider in the middle, with a hole to swim through. On one side is an enrichment—multicolored marbles lining the bottom—while the other side is empty. The idea is to see where fish spend more time, and thus which enrichment, if any, they prefer. "We can't just throw random objects like treasure chests in there because we think it looks cool," Lofgren says. "We want to put some science behind it."

That's the goal of the university's Refinement & Enrichment Advancements Laboratory (REAL), an unusual program Lofgren co-founded in 2014. REAL's team of vets and animal care technicians aims to "understand the lived experience of the animal," she says, and to nurture what it has evolved to do. The marbles, for example, might reduce the fish's anxiety by making the tank feel a bit more like the wild. (They're also easier to clean than gravel.)

Stress can affect a wide range of physiologies and behaviors, and researchers are beginning to test whether the additions make the animals better models for depression—and, in the case of these particular fish—retinal regeneration. "If we provide subpar welfare," Lofgren says, "we are also providing subpar science."

Across campus, she and her team are also trying to improve the lives of rabbits. In a fancy, heavily glassed building once owned by biotech giant Pfizer sits a room filled with 50 white bunnies in metal cages the size of large laundry baskets.

Most are housed alone, as has been the standard for decades.

"The going theory is that you can't socially house rabbits, because they'll tear each other apart," says Lofgren, even though the animals live in teeming warrens in the wild. For the past few years, her group has been getting some animals to share cages by providing enrichment: hay-filled paper bags they can "forage" through, plastic keys to gnaw on, and other accoutrements. "Now, they're playing together and snuggling up with each other," she says.

Once they've firmed up the enrichments, Lofgren and colleagues will explore how they affect research results. These animals are used in studies of cardiovascular disease, and isolated rabbits sometimes have irregular circadian rhythms, which can influence heart rate, blood pressure, and hormone levels. "We want to study the impact of diet and drugs on atherosclerosis, not the impact of these other variables," says Patrick Lester, the vet in charge of the rabbits. "If we can eliminate them, we can create a cleaner signal."

The bunnies don't appreciate every addition, and there's an easy way to tell. "They'll pee on it, and shove it into a corner," Lofgren says. Enrichments that the animals like are added to a database that REAL shares across campus and with other labs, including those in the United States that house some 150,000 rabbits. Lofgren says a recent webinar on their rabbit work attracted 90 institutions. "They get back in touch and say, 'Oh my gosh, it actually worked!'"

Other labs are forging their own paths. At the University of Minho in Braga, Portugal, animal facility manager Magda João Castelhano Carlos has helped develop PhenoWorld, a sort of McMansion for rats with exercise rooms fitted with running wheels, dining areas with food and water, and experimental spaces with levers for cognition testing. The rodents must learn how to open the tunnels that lead to each room, giving them daily challenges. The animals engage in more natural play behavior, Carlos says, and are better models for psychiatric disorders because they're not unnaturally depressed or anxious.

Similarly, some rats at the University of British Columbia in Vancouver, Canada, can stand, climb ladders, and burrow in real soil in four-level cages created by biologist Daniel Weary and postdoc Joanna Makowska. "Our dream," Weary says, "is that our animals live a better life with us than if they had never been born."

Despite the boon to animals, some worry that when it comes to research, such enrichments could do more harm than good.

A CASE IN POINT is a strategy pioneered by Lofgren's group to ease a major trauma in the life of a lab mouse. Imagine a giant reaching into your house every week, hoisting you up by your legs, and plopping you into a new home. That's what the lab mice in a room stacked with nearly 900 cages on UM's medical campus deal with every time staff pick them up to clean their enclosures. "It's one of the most stressful things you can do to them," Lofgren says.

To ease that stress, her group adds plastic tubes to some cages. The goal is to get the rodents accustomed to the tubes and to spending time in them. Then, when cleaning time comes, the animal care staff wait for the mice to enter the tubes (or gently nudge them in), and transfer the whole shebang to a new enclosure. If it works, Lofgren says her team will apply the practice across campus.

But there's no free lunch here: With 49,000 mouse cages at the university, the kinder, gentler cleaning would add considerable expense. The 49,000 tubes would have to be sterilized, and cleaning each cage could take up to 10 times longer.

> ***"If we want animals to tell us about stuff that's going to happen in people, we need to treat them more like people."***
>
> **Joseph Garner**, Stanford University

Such numbers concern some scientists, including Godbout. "If you're paying $1 per cage now, and then suddenly it's $2 per cage, how do you afford that," he asks, "especially when our budgets are not keeping pace?"

Godbout and others also worry that far from improving research, enrichment could compromise it. If a lab is studying the impact of stress on the growth of new neurons, for example, and then it lets mice exercise on a running wheel—which has been shown to spark neuron growth—the study could be jeopardized, Godbout says. And if every lab uses a different enrichment, it could complicate the ability to reproduce another lab's experiments, and thus add to, not fix, the reproducibility crisis.

What's more, says John Crabbe, a behavioral geneticist at the Portland Veterans Affairs Medical Center in Oregon who researches alcoholism in mice, just because an enrichment works for one type of disorder doesn't mean it should be applied to all. "If you show it works in tumor studies, I have no trouble with it being the guideline for tumor studies," he says. "But don't generalize it to psychiatric disease."

Godbout says he's all for giving lab animals the best life possible, but he argues that—in a world where they get as much food as they want and don't have to worry about being eaten by predators—they're already living a good life. "You don't need an amusement park to keep them happy."

Hannan acknowledges that enrichment can make studies more expensive. But he argues that the strategy would lead to better studies more likely to translate to human health, saving time and money in the long run. "Less research could be done," he says, "but it would be better research."

Persuading the doubters will take time, in part because money for studies is scarce. The National Institutes of Health in Bethesda, Maryland, doesn't support enrichment research because it doesn't directly relate to the health and well-being of humans, says Patricia Brown, director of the agency's Office of Laboratory Animal Welfare. "We would if we could," she says. "A happy mouse is a better model."

The REAL program gets the vast share of its financing from UM funds designed to improve animal care and use, and a few small organizations offer grants for such work. Hannan's seminal Huntington study came out of his own pocket. "We never could have gotten a grant to do it," he says, "so we just did it."

Still, the chorus for enrichment is growing. "More and more, people are reaching out to us," Lofgren says. "We're starting to see some real momentum." More than 160 papers were published on rodent enrichment in 2016 versus a handful at the turn of the millennium; at the 2016 meeting of the American Association for Laboratory Animal Science, 83 out of 171 rodent presentations focused on enrichment—more than twice the number at the 2009 meeting.

Meanwhile, REAL continues to explore what makes animals happy. Lofgren plans to line the walls of UM's sheep runs with photos of contented sheep, for example, because studies suggest that the animals recognize each others' faces. She and her fellow enrichment advocates hope that one day, work like this will be become the rule, rather than the exception, both for the sake of science and for the animals themselves. "We owe it to these creatures to give them the best lives possible," Lofgren says. "They're giving us the best they can. So we should be doing the best we can." ■

CHINA'S AI IMPERATIVE

The country's massive investments in artificial intelligence are disrupting the industry—and strengthening control of the populace

By **Christina Larson**, *in Beijing*

In a gleaming high-rise here in northern Beijing's Haidian district, two hardware jocks in their 20s are testing new computer chips that might someday make smartphones, robots, and autonomous vehicles truly intelligent. A wiry young man in an untucked plaid flannel shirt watches appraisingly. The onlooker, Chen Yunji, a 34-year-old computer scientist and founding technical adviser of Cambricon Technologies here, explains that traditional processors, designed decades before the recent tsunami of artificial intelligence (AI) research, "are slow and energy inefficient" at processing the reams of data required for AI. "Even if you have a very good algorithm or application," he says, its usefulness in everyday life is limited if you can't run it on your phone, car, or appliance. "Our goal is to change all lives."

In 2012, the seminal Google Brain project required 16,000 microprocessor cores to run algorithms capable of learning to identify a cat. The feat was hailed as a breakthrough in deep learning: crunching vast training data sets to find patterns without guidance from a human programmer. A year later, Yunji and his brother, Chen Tianshi, who is now Cambricon's CEO, teamed up to design a novel chip architecture that could enable portable consumer devices to rival that feat—making them capable of recognizing faces, navigating roads, translating languages, spotting useful information, or identifying "fake news."

Developers hope artificial intelligence–optimized chips like the Cambricon-1A will enable mobile devices to learn on their own.

Tech companies and computer science departments around the world are now pursuing AI-optimized chips, so central to the future of the technology industry that last October Sundar Pichai, CEO of Google in Mountain View, California, told The Verge that his guiding question today is: "How do we apply AI to rethink our products?" The Chen brothers are by all accounts among the leaders; their Cambricon-1A chip made its commercial debut last fall in a Huawei smartphone billed as the world's first "real AI phone." "The Chen brothers are pioneering in terms of specialized chip architecture," says Qiang Yang, a computer scientist at Hong Kong University of Science and Technology (HKUST) in China.

Such groundbreaking advances far from Silicon Valley were hard to imagine only a few years ago. "China has lagged behind the U.S. in cutting-edge hardware design," says Paul Triolo, an analyst at the Eurasia Group in Washington, D.C. "But it wants to win the AI chip race." The country is investing massively in the entire field of AI, from chips to algorithms. The Chen brothers, for example, developed their chip while working at the Institute of Computing Technology of the Chinese Academy of Sciences here, and the academy backed them with seed funding when they spun out Cambricon in 2016. (The company is now worth $1 billion.)

Last summer, China's State Council issued an ambitious policy blueprint calling for the nation to become "the world's primary AI innovation center" by 2030, by which time, it forecast, the country's AI in-

PHOTOS: (CLOCKWISE FROM TOP LEFT) STR/AFP/GETTY IMAGES; JIN KE—IMAGINECHINA VIA AP IMAGES

Some firms in China now use artificial intelligence–powered facial recognition programs to confirm employee identities (far left) and authorize digital payments at fast-food restaurants (middle left). The Chinese government has begun using facial scans to identify pedestrians and jaywalkers (middle right), and even to dispense limited amounts of toilet paper in public restrooms (far right).

PHOTOS: (LEFT TO RIGHT) REX FEATURES VIA AP IMAGES; WANG ZHAO/AFP/GETTY IMAGES

dustry could be worth $150 billion. "China is investing heavily in all aspects of information technology," from quantum computing to chip design, says Raj Reddy, a Turing Award–winning AI pioneer at Stanford University in Palo Alto, California, and Carnegie Mellon University in Pittsburgh, Pennsylvania. "AI stands on top of all these things."

In recent months, the central government and Chinese industry have been launching AI initiatives one after another. In one of the latest moves, China will build a $2.1 billion AI technology park in Beijing's western suburbs, the state news service Xinhua reported last month. Whether that windfall will pay off for the AI industry may not be clear for years. But the brute numbers are tilting in China's favor: The U.S. government's total spending on unclassified AI programs in 2016 was about $1.2 billion, according to In-Q-Tel, a research arm of the U.S. intelligence community. Reddy worries that the United States is losing ground. "We used to be the big kahuna in research funding and advances."

China's advantages in AI go beyond government commitment. Because of its sheer size, vibrant online commerce and social networks, and scant privacy protections, the country is awash in data, the lifeblood of deep learning systems. The fact that AI is a young field also works in China's favor, argues Chen Yunji, by encouraging a burgeoning academic effort that has put China within striking distance of the United States, long the leader in AI research. "For traditional scientific fields, Chinese [scientists] have a long way to go to compete with the U.S. or Europe. But for computer science, it's a relatively new thing. Young people can compete. Chinese can compete." In an editorial last week in *The Boston Globe*, Eric Lander, president of the Broad Institute in Cambridge, Massachusetts, warned that the United States has at best a 6-month lead over China in AI. "China played no role in launching the AI revolution, but is making breathtaking progress catching up," he wrote.

The fierce global competition in AI has downsides. University computer science departments are hollowing out as companies poach top talent. "Trends come and go, but this is the biggest one I've ever seen—a professor can go into industry to make $500,000 to $1 million" a year in the United States or China, says Michael Brown, a computer scientist at York University in Toronto, Canada.

In a more insidious downside, nations are seeking to harness AI advances for surveillance and censorship, and for military purposes. China's military "is funding the development of new AI-driven capabilities" in battlefield decision-making and autonomous weaponry, says Elsa Kania, a fellow at the Center for a New American Security in Washington, D.C. In the field of AI in China, she warned in a recent report, "The boundaries between civilian and military research and development tend to become blurred."

JUST AS OIL fueled the industrial age, data are fueling advances of the AI age. Many practical AI advances are "more about having a large amount of continually refreshed data and good-enough AI researchers who can make use of that data, rather than some brilliant AI theoretician who doesn't have as much data," says computer scientist Kai-Fu Lee, founder of Sinovation Ventures, a venture capital firm here. And China, as *The Economist* recently put it, is "the Saudi Arabia of data."

Every time someone enters a search query into Baidu (China's Google), pays a restaurant tab with WeChat wallet, shops on Taobao (China's Amazon), or catches a ride with Didi (China's Uber), among a plethora of possibilities, those user data can be fed back into algorithms to improve their accuracy. A similar phenomenon is happening in the United States, but China now has 751 million people online, and more than 95% of them access the internet using mobile devices, according to the China Internet Network Information Center. In 2016, Chinese mobile payment transactions totaled $5.5 trillion, about 50 times more than in the United States that year, estimates iResearch, a consulting firm in Shanghai, China.

Baidu, which runs China's dominant search engine, both gathers and exploits much of these data. In parking garages under its futuristic glass-and-steel complex in northern Beijing, cars crowned with LIDAR sensors troll around on test runs for collecting mapping data that will feed Baidu's autonomous driving lab. In the main lobby, staffers' faces are scanned to open the security gates. Of China's tech titans—Baidu, Alibaba, and Tencent—Baidu was the first to pour resources into AI. It now employs more than 2000 AI researchers, including staff in California and Seattle, Washington.

A few years ago, Baidu added an AI-powered image search to its mobile app, allowing a user to snap a photo of a piece of merchandise for the search engine to identify, and then look up price and store information.

Early object recognition programs focused on outlines. But many objects—for example, plates of food in a restaurant—have basically the same outline. What's needed is more precise detection of interior patterns, or "textures," says Feng Zhou, a data scientist in Cupertino, California, who heads Baidu's new Fine-Grained Image Recognition Lab. Now, Baidu's AI image search can distinguish between, for instance, a stewed tofu dish called mapo tofu and fried tofu dishes. (A U.S. equivalent might be detecting the difference between oatmeal and rice.) Better algorithms have helped, Zhou says, but so has an abundance of training data uploaded by internet users.

The data deluge is also transforming academia. "When the AI textbooks were written, we didn't have access to that kind of data," Yang says. "About 5 years ago, we decided that classroom education was not sufficient. We needed to have partnerships with industry, because the big technology companies not only have lots and lots of data, but also a variety of data sources and many interesting contexts to apply AI." Today, a group of HKUST professors and Ph.D. students work on AI projects with Tencent, China's social media giant. They have access to data from WeChat, the company's ubiquitous social network, and are developing "intelligent" chat capabilities for everything from customer service to Buddhist spiritual advice.

Such collaborations are vulnerable, however, as China's academic outposts struggle to keep faculty members capable of designing new AI algorithms from decamping to industry. "University students know that AI is a very cool thing, which might also make you rich," Chen Yunji says.

The Chinese government is also drinking from the data firehose—and is honing AI as a tool for staying in power. The State Council's AI road map explicitly acknowledges AI's importance to "significantly elevate the capability and level of social governance, playing an irreplaceable role in effectively maintaining social stability."

Some worry that the government's embrace of AI could further stifle dissent in China. Enhanced technology for recognizing context and images allows for more effective real-time censorship of online communications, according to a report from The Citizen Lab, a research outfit at the University of Toronto. Also at the heart of this debate is facial recognition technology, which is powered by AI algorithms that analyze minute details of a person's face in order to pick it out from among thousands or millions of potential matches.

Facial recognition is now used routinely in China for shopping and to access some public services. For example, at a growing number of Kentucky Fried Chicken restaurants in China, customers can authorize digital payment by facial scan. Baidu's facial recognition systems confirm passenger identity at certain airport security gates. Recent AI advances have made it possible to identify individuals not only in up-close still photos, but also in video—a far more complex scientific task.

China's attitude toward such advances contrasts with the U.S. response. When the U.S. Customs and Border Protection last May revealed plans to use facial matching to verify the identities of travelers on select flights leaving the United States, a public debate erupted. In an analysis, Jay Stanley of the American Civil Liberties Union in Washington, D.C., warned of the potential for "mission creep": With new AI technologies, "you can subject thousands of people an hour to face recognition when they're walking down the sidewalk without their knowledge, let alone permission or participation."

In China the government is already deploying facial recognition technology in Xinjiang, a Muslim-majority region in western China where tensions between ethnic groups erupted in deadly riots in 2009. Reporters from *The Wall Street Journal* who visited the region late last year found surveillance cameras installed every hundred meters or so in several cities, and they noted facial recognition checkpoints at gas stations, shopping centers, mosque entrances, and elsewhere. "This is the kind of thing that makes people in the West have nightmares about AI and society," says Subbarao Kambhampati, president of the Association for the Advancement of Artificial Intelligence (AAAI) in Palo Alto and a computer scientist at Arizona State University in Tempe. In China, he says, "people are either not worried, or not able to have those kinds of conversations."

CHINA'S AI RESEARCHERS show no signs of slowing down. In October 2016, a White House report found that Chinese researchers now publish more deep learning–related papers in all journals than researchers from any other country. When adjusted for publication impact factor, the United States still produced the most influential AI-related papers, followed by the United Kingdom, with China only narrowly behind, according to a recent McKinsey Global Institute analysis.

Kambhampati adds that before 2012 or so, submissions from China to major AI conferences "used to be quite small." At AAAI's annual meeting earlier this week in New Orleans, Louisiana, he says, accepted papers from China nearly equaled those from the United States. "For the longest time, there was a general feeling that China was always second-rate in technology. That may have been true, but it's also changing quite quickly."

The government wants the boom to continue. At the end of 2017, the science ministry issued a 3-year plan to guide AI development, and named several large companies as "national champions" in key fields: for example, Baidu in autonomous driving, and Tencent in computer vision for medical diagnosis. Zha Hongbin, a professor of machine intelligence at Peking University here who consults for the government, says China plans to expand the number of universities offering dedicated machine learning and AI departments.

In the meantime, industry continues to bet heavily on AI. Last October, for instance, Alibaba announced plans to invest $15 billion in research over 3 years to build seven labs in four countries that will focus on quantum computing and AI.

A decade ago, China's best AI researchers might have left for plum jobs in Silicon Valley. Instead, increasing numbers of them are staying at home to lift the nation's AI industry, says Xia Yan, a 30-year-old data scientist who co-founded Momenta, an autonomous driving startup here. "Many of us are choosing to go from an academic background to running a company," Xia says. "We want to see our work in the real world. It's a new era." ■

Christina Larson is a freelance journalist in Beijing.

Closing the intelligence gap

The United States leads China in private investment in artificial intelligence (AI) and in the number and experience of its scientists. But Chinese firms may gain an advantage from having more data—including data not in the public domain—for honing algorithms.

	UNITED STATES	CHINA
Years experience of the nation's data scientists	More than half have more than 10 years.	Forty percent have less than 5 years.
AI patent applications, 2010–2014	15,317 (First in world)	8410 (Second)
Number of workers in AI positions	850,000 (First)	50,000 (Seventh)
Percent of private AI investment (2016)	66% (First)	17% (Second)
Global ranking of data openness	No. 8	No. 93

DATA: ASTAMUSE; LINKEDIN; MCKINSEY GLOBAL INSTITUTE

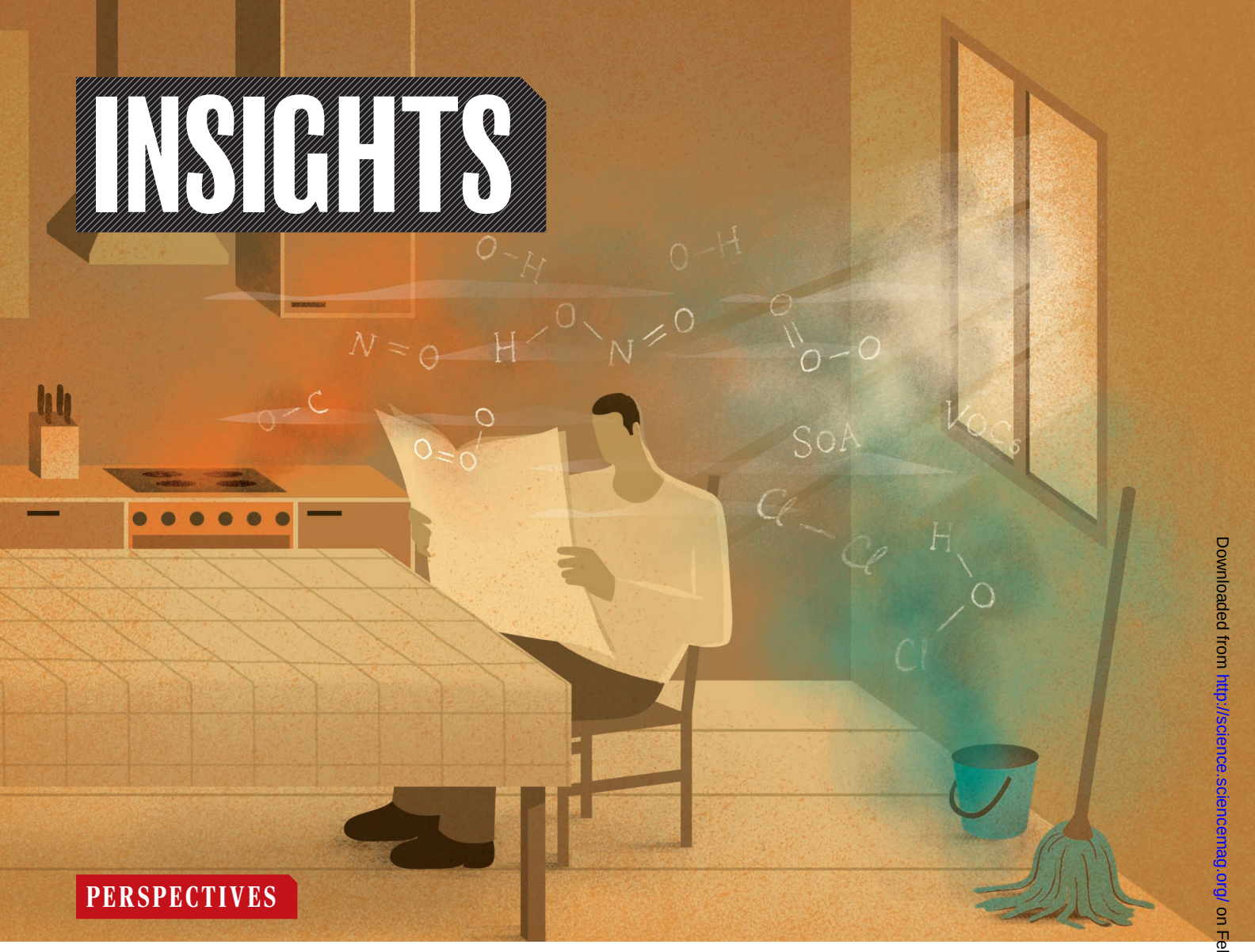

ATMOSPHERIC CHEMISTRY

An indoor chemical cocktail

The chemistry that determines human exposure to indoor pollutants is incompletely understood

By **Sasho Gligorovski**[1] *and* **Jonathan P. D. Abbatt**[2]

In the past 50 years, many of the contaminants and chemical transformations that occur in outdoor waters, soils, and air have been elucidated. However, the chemistry of the indoor environment in which we live most of the time—up to 90% in some societies—is not nearly as well studied. Recent work has highlighted the wealth of chemical transformations that occur indoors. This chemistry is associated with 3 of the top 10 risk factors for negative health outcomes globally: household air pollution from solid fuels, tobacco smoking, and ambient particulate matter pollution (*1*). Assessments of human exposure to indoor pollutants must take these reactive processes into consideration.

A few studies illustrate the nature of multiphase chemistry in the indoor environment. As Sleiman *et al*. have shown (*2*), a highly carcinogenic class of compounds—the tobacco-specific nitrosamines—forms via the reaction of gas-phase nitrous acid (HONO) with cigarette nicotine that is adsorbed onto indoor surfaces similar to those in a typical smoker's room. HONO is also produced indoors directly by other combustion sources such as gas stoves and by the gas-surface reactions of gaseous nitrogen oxides on walls, ceilings, and carpets (*3*). Likewise, carcinogenic polycyclic aromatic hydrocarbons (PAHs) and their often more toxic oxidation products are mobile, existing both on the walls of most dwellings and in the air (*4*); PAHs arise from combustion sources such as smoking and inefficient cookstoves. This is a particularly important issue in developing countries, where the adverse health effects from cooking with solid fuels is a leading cause of disease (*1*). As another example, use of chlorine bleach to wash indoor surfaces promotes oxidizing conditions not just on the surfaces being washed but throughout the indoor space (*5*). Reactive chlorinated gases (such as HOCl and Cl_2) evaporate from the washed surface, can oxidize other surfaces in a room, and may be broken apart by ultraviolet (UV) light to form reactive radicals.

[1]*State Key Laboratory of Organic Geochemistry, Guangzhou Institute of Geochemistry, Chinese Academy of Sciences, Guangzhou 510 640, China.* [2]*Department of Chemistry, University of Toronto, 80 St. George Street, Toronto M5S 3H6, Canada. Email: jabbatt@chem.utoronto.ca; gligorovski@gig.ac.cn*

Reactive chemicals in an indoor environment arise from cooking, cleaning, humans, sunlight, and outdoor pollution.

It is not only human activities such as cooking, smoking, and cleaning that affect the indoor environment. The mere presence of humans affects the oxidative ability of the air. Wisthaler and Weschler (*6*) have shown that human occupancy can dramatically affect ozone levels, such that concentrations of this oxidant dropped by half within 30 minutes when two people entered a test chamber similar in size to a typical indoor room. At the same time, the concentrations of various carbonyl compounds increased. The reactions are so fast that many chemically reactive oils on human skin may be transformed into more oxidized molecules on time scales of tens of minutes (*7*). Recent measurements in heavily occupied spaces such as classrooms illustrate the wealth of human emissions of not only naturally formed molecules (such as small organic acids) but also personal care products (such as siloxanes) (*8, 9*). A key uncertainty is the degree to which indoor environments are oxidizing. Outdoor light levels drive the production of radicals, such as hydroxyl (OH), which act as atmospheric cleansing agents. Without high levels of UV light indoors, what levels of OH will be present? Gómez Alvarez *et al.* have reported the detection of indoor OH radicals, formed from the sunlight-driven decomposition of nitrous acid (*10*); they observed OH concentrations similar to those that form outdoors.

These findings have placed emphasis on indoor radical chemistry. It remains unclear, however, whether light is necessarily involved, or whether dark sources of OH from the oxidation of gas-phase alkenes by ozone dominate instead. In particular, terpene oils, which are components of cleaning, fragrances, and cooking materials, are widely present indoors. Ozonolysis of such alkenes leads to the formation of highly reactive molecules, the Criegee intermediates. The latter sometimes decompose to form OH radicals but in other circumstances may react with a wide range of other indoor constituents. In 2017, Berndt *et al.* reported the direct mass spectrometric measurement of gas-phase Criegee intermediates (*11*); this work opened up the potential for measuring such species in indoor environments. Criegee intermediates may also form when indoor surfaces that are coated with chemically unsaturated skin cells and cooking oils are exposed to ozone. Although largely unstudied, such chemistry may form highly reactive and potentially harmful products, including peroxides and ozonides, on indoor surfaces (*12*).

The atmospheric chemistry field has undergone a dramatic transformation in its understanding of how volatile organic compounds (VOCs) are oxidized (*13*). Highly oxidized organic compounds arise via autoxidation mechanisms initiated by either ozone or radical attack. Reaction with a single oxidant molecule can form multiple oxygenated functional groups on an organic reactant within seconds, changing it from a volatile gas to a molecule that will condense to form secondary organic aerosol (SOA) particles (*14*). Given that levels of VOCs, such as terpenes, can be much higher indoors than outdoors, this pathway may be an important indoor aerosol formation mechanism. Because of very high levels of outdoor pollution, VOC concentrations in industrially developing areas such as China may be much higher than in European and North American homes.

The building science research community has long identified the importance of ventilation for the state of indoor environments. Open windows expose us to outdoor air, whereas well-sealed houses are subject to emissions from furnishings, building materials, chemical reactions, and people and their activities. Climate change (*15*) and outdoor air pollution are leading to efforts to better seal off indoor spaces, slowing down exchange of outdoor air. The purpose may be to improve air conditioning, build more energy-efficient homes, or prevent the inward migration of outdoor air pollution. As exposure to indoor environments increases, we need to know more about the chemical transformations in our living and working spaces, and the associated impacts on human health. ■

REFERENCES AND NOTES

1. S. S. Lim *et al.*, *Lancet* **380**, 2224 (2012).
2. M. Sleiman *et al.*, *Proc. Natl. Acad. Sci. U.S.A.* **107**, 6576 (2010).
3. A. Gandolfo, L. Rouyer, H. Wortham, S. Gligorovski, *Appl. Catal. B* **209**, 429 (2017).
4. C. J. Weschler, W. W. Nazaroff, *Indoor Air* **22**, 356 (2012).
5. J. P. S. Wong, N. Carslaw, R. Zhao, S. Zhou, J. P. D. Abbatt, *Indoor Air* **27**, 1082 (2017).
6. A. Wisthaler, C. J. Weschler, *Proc. Natl. Acad. Sci. U.S.A.* **107**, 6568 (2010).
7. S. Zhou, M. W. Forbes, Y. Katrib, J. P. D. Abbatt, *Environ. Sci. Technol. Lett.* **3**, 170 (2016).
8. S. Liu, S. L. Thompson, H. Stark, P. J. Ziemann, J. L. Jimenez, *Environ. Sci. Technol.* **51**, 5454 (2017).
9. X. Tang, P. K. Misztal, W. W. Nazaroff, A. H. Goldstein, *Environ. Sci. Technol.* **50**, 12686 (2016).
10. E. Gómez Alvarez *et al.*, *Proc. Natl. Acad. Sci. U.S.A.* **110**, 13294 (2013).
11. T. Berndt, H. Herrmann, T. Kurtén, *J. Am. Chem. Soc.* **139**, 13387 (2017).
12. S. Zhou, M. W. Forbes, J. P. D. Abbatt, *Environ. Sci. Technol.* **50**, 11688 (2016).
13. J. D. Crounse, L. B. Nielsen, S. Jørgensen, H. G. Kjaergaard, P. O. Wennberg, *J. Phys. Chem. Lett.* **4**, 3513 (2013).
14. M. Ehn *et al.*, *Nature* **506**, 476 (2014).
15. W. W. Nazaroff, *Environ. Res. Lett.* **8**, 015022 (2013).

ACKNOWLEDGMENTS

J.P.D.A. is supported by the Alfred P. Sloan Foundation. S.G. is supported by the Chinese Academy of Sciences.

10.1126/science.aar6837

NEUROSCIENCE

Toward an optically controlled brain

Noninvasive deep brain stimulation can be achieved by optical triggers

By **Neus Feliu,[1,2] Erwin Neher,[3] Wolfgang J. Parak[1,4,5]**

Neurons can be modified with light-gated ion channels, which cause them to become excited upon illumination (*1, 2*). This discovery has given rise to the field of optogenetics, with impressive examples such as triggering the beat of a heart with light (*3*). There is, however, one technical limitation: Light-gated ion channels are typically stimulated with blue-green light, which is heavily scattered by tissue. Thus, deep brain stimulation, focused on small regions, is a major challenge. On page 679 of this issue, Chen *et al.* (*4*) use transgenic mice implanted with upconverting nanoparticles (NPs) to locally activate light-gated ion channels and modulate neuronal activity, even deep inside the brain. This method might eventually lead the way for clinical applications to optically control neuronal dysfunctions, such as Parkinson's disease or even paralysis.

The brain is a gigantic assembly of interconnected neurons. A neuron "fires" a nerve impulse when a sufficient amount of Na^+ ions enter the cell through membrane-bound ion channels. Neuronal Na^+ channels are unusual in that they open even more as Na^+ ions pass through, rendering the inside of the cell increasingly positively charged (meaning that these channels are voltage-gated). Thus, a wave of positive charge spreads along the nerve fiber as a nerve impulse. Likewise, communication between

[1]*Fachbereich Physik und Chemie and Center for Hybrid Nanostructures, Universität Hamburg, Hamburg, Germany.* [2]*Department of Laboratory Medicine, Karolinska Institutet, Stockholm, Sweden.* [3]*Max-Planck-Institut für biophysikalische Chemie, Göttingen, Germany.* [4]*CIC BiomaGUNE, San Sebastián, Spain.* [5]*Institute of Nano Biomedicine and Engineering, Shanghai Jiao Tong University, Shanghai, China. Email: wolfgang.parak@uni-hamburg.de*

neurons happens via neurotransmitters, which open ion channels in the receiving neuron, rendering their potential either more positive or more negative (meaning that these channels are ligand-gated). Therefore, opening and closing ion channels is the key to controlling neuronal impulses.

Seemingly the most straightforward way to interface with the brain is via an electrical connection (*5*). This has been achieved by the introduction of electrodes, which upon application of voltage pulses may trigger nerve impulses by controlling voltage-gated ion channels. Such techniques are already used in clinical practice—for example, to control the tremor associated with Parkinson's disease (*6*). But, to alter brain activity in a substantial and targeted way, one would need electrodes for many groups of neurons in different regions of the brain, which would complicate how the electrodes are wired outside of the head. The sheer number of neurons and the size of conventional electrode arrays (which are huge compared with a neuron) severely limit clinical applications.

The use of light may overcome these limitations. Light can be focused, and local illumination inside tissue is possible. Upconverting NPs have been used as transducers to improve problems of light scattering by tissues. The special feature of these upconverting NPs is the conversion of near-infrared (NIR) light, which is much less scattered by tissue, into visible light (*7*). Because of their chemical nature, such NPs are highly efficient light absorbers. Thus, if upconverting NPs are close to light-gated ion channels, they absorb NIR light and in turn emit visible light to stimulate the light-gated ion channels (see the figure). Chen *et al.* used transgenic mice engineered to express light-gated ion channels in their neurons and implanted them with upconverting NPs. Upon NIR excitation, green-blue light emitted by the NPs locally activated light-gated ion channels in the animals' brains. Using this approach, the authors could control behavioral patterns of mice, such as the expression of fear, simply by external NIR illumination.

However, the question of how such a technique can be extrapolated to humans remains unclear. The technique might be used to treat the tremor of patients with Parkinson's disease with on-demand optical stimulation of the relevant regions in the brain. A number of challenges must be overcome before this technique can be used in patients. Specifically, neurons have to be transfected with light-gated ion channels. This can be achieved by direct injection of genetic vectors, or by targeted delivery to specific regions of the brain. This is a substantial challenge, which any optogenetics-based approach faces. Moreover, NPs acting as transducers must be placed close to the target neurons. Chen *et al.* achieved this by local injection, which has limited spatial accuracy, and thus stimulation extended to relatively large regions of the brain. Conversely, targeted delivery of NPs via blood is limited by the blood-brain barrier, which restricts the entry of substances from blood vessels into brain tissue. It may even be possible to transfect neurons so that they synthesize the required NPs. This has been demonstrated in bacteria for fluorescent NPs (*8*) and magnetic NPs (*9*).

Additionally, the plasticity of the brain has to be taken into account. Neuronal networks undergo continuous changes (for example, this is the reason our brain can "learn") (*10*). Thus, the stimulation pattern and placement of NPs may have to be adjusted over time. Furthermore, NPs are readily taken up (endocytosed) by cells in the brain (*11*). This would change their distance to membrane-bound ion channels, which may in turn prohibit stable long-term stimulation. Thus, it will be important to understand distance dependence of NP–ion channel signaling.

Potent upconverting NPs are also needed, which are brighter and photostable. Modern colloidal chemistry offers a huge range of functional NP materials (*12*), and thus there is hope for brighter NPs, particularly in a biological environment. Chen *et al.* used NIR intensities at the limit of tolerable tissue heating, which also demonstrates the need for more sensitive NPs. Furthermore, NPs may change properties over time, such as structural degradation and loss of functional properties, which may be tackled with different materials and surface coatings (*13*). Long-term toxicity studies also need to be carried out.

Despite such challenges, it may be possible to optically excite well-defined groups of neurons deep inside the human brain. Eventually, techniques may also be developed that use fluorescent NIR or magnetic resonance imaging probes for the recording of neural activity, as has been demonstrated by measuring oxygen consumption (*14*). However, issues with the intensity of the signals is a technical hurdle. Although Chen *et al.* have taken a big step toward noninvasive manipulation of brain activity, the complexity of the brain imposes an imminent challenge, and future developments in understanding brain circuits are still needed. ■

Activating neurons with light

With technological advances, it might be possible to optically stimulate neurons deep in the human brain. This could aid treatment of patients with Parkinson's disease.

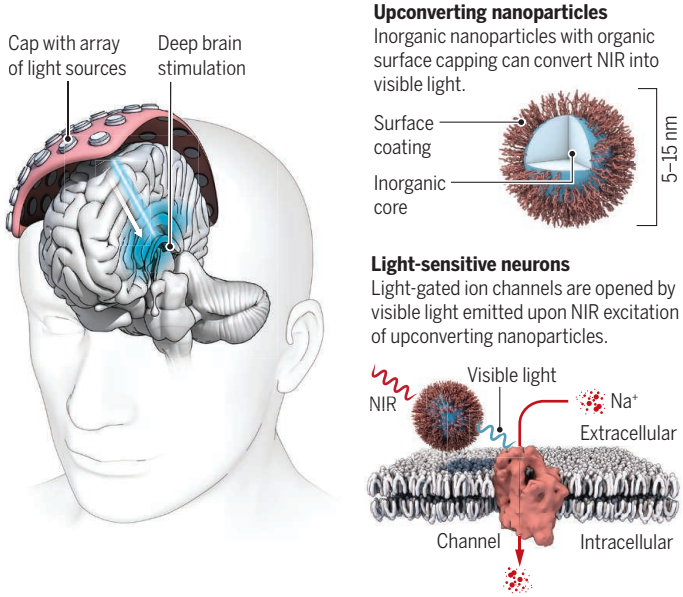

GRAPHIC: C. BICKEL/*SCIENCE*

REFERENCES AND NOTES

1. P. Hegemann, G. Nagel, *EMBO Mol. Med.* **5**, 173 (2013).
2. E. G. Govorunova, O. A. Sineshchekov, R. Janz, X. Liu, J. L. Spudich, *Science* **349**, 647 (2015).
3. A. B. Arrenberg, D. Y. R. Stainier, H. Baier, J. Huisken, *Science* **330**, 971 (2010).
4. S. Chen *et al.*, *Science* **359**, 679 (2018).
5. S. Marchesan, M. Melchionna, M. Prato, *ACS Nano* **9**, 9441 (2015).
6. M. Wadman, *Science* 10.1126/science.aan6920 (2017).
7. S. Wilhelm, *ACS Nano* **11**, 10644 (2017).
8. D. O. Plaza, C. Gallardo, Y. D. Straub, D. Bravo, J. M. Pérez-Donoso, *Microb. Cell Fact.* **15**, 76 (2016).
9. I. Kolinko *et al.*, *Nat. Nanotechnol.* **9**, 193 (2014).
10. A. Pascual-Leone, A. Amedi, F. Fregni, L. B. Merabet, *Annu. Rev. Neurosci.* **28**, 377 (2005).
11. M. Nazarenus *et al.*, *Beilstein J. Nanotechnol.* **5**, 1477 (2014).
12. W. J. Parak, *Science* **334**, 1359 (2011).
13. N. Feliu *et al.*, *Chem. Soc. Rev.* **45**, 2440 (2016).
14. S. A. Sheth *et al.*, *Neuron* **42**, 347 (2004).

ACKNOWLEDGMENTS

W.J.P. acknowledges the Deutsche Forschungsgemeinschaft (DFG grant PA 794/21-1) and N.F. acknowledges the Swedish Governmental Agency for Innovation Systems (Vinnova).

10.1126/science.aar7379

Cholesterol crystals impede nerve repair

Cholesterol deposits in phagocytic cells disrupt the repair of demyelinated axons

By **Yanan Chen** *and* **Brian Popko**

Damage to the myelin sheath that surrounds nerve axons represents the pathological hallmark of the neurological disorder multiple sclerosis (MS) and is thought to contribute to a number of other nervous system maladies (*1*). Remyelination, a regenerative process that forms new myelin sheaths around demyelinated axons, restores nerve function and reverses the clinical manifestations associated with demyelination (*2*). Although remyelination occurs efficiently in young individuals, this restorative process proceeds less well with age (*2*). Inefficient remyelination results in axonal loss and progressive worsening of neurological symptoms. On page 684 of this issue, Cantuti-Castelvetri *et al.* (*3*) report that insufficient clearance (phagocytosis) of damaged myelin by aged macrophages results in the accumulation of cholesterol crystals in these cells, which elicits a maladaptive inflammatory response that is associated with impaired remyelination. Understanding this process may reveal new therapeutic opportunities for MS and other demyelinating disorders.

Central nervous system (CNS) myelin is a multilayered membrane that is formed and maintained by oligodendroglial cells. The electrical insulative properties of myelin allow rapid transmission of nerve impulses and are critical for normal nervous system function in higher vertebrates. Moreover, myelin provides metabolic support to axons, which extend far from the nutritive resources of neuronal cell bodies (*4*). When the myelin sheath is damaged or lost, nerve conduction velocity is greatly diminished, resulting in neurological symptoms, and the demyelinated axons display increased vulnerability to degeneration. Remyelination in the CNS is initiated by the differentiation of oligodendrocyte progenitor cells (OPCs) into new oligodendrocytes (*5*). Failure of OPC differentiation is the main contributor to reduced remyelination in older individuals (*2*). Consequently, therapeutic strategies to enhance OPC differentiation could have clinical impact for demyelinating disorders.

Department of Neurology, Center for Peripheral Neuropathy, University of Chicago, Chicago, IL 60637, USA. Email: bpopko@neurology.bsd.uchicago.edu

Demyelinated lesions contain a number of inhibitors of OPC differentiation (*2*), such that the damaged myelin needs to be cleared by phagocytes, which are CNS-resident microglia and infiltrating macrophages. Compared to phagocytes from young animals, macrophages from older animals display a reduced capacity to ingest myelin (*6*). In a landmark study that utilized heterochronic parabiosis, where old and young mice are joined surgically to create a shared circulatory system, a youthful systemic environment stimulated OPC differentiation and enhanced remyelination in the CNS of conjoined old mice (*7*). This effect was attributed to the enhanced clearance of myelin debris in the older animals by young macrophages.

Cantuti-Castelvetri *et al.* investigated the mechanism responsible for the decline in phagocytic potential of older macrophages. When examined by transmission electron microscopy, macrophages in demyelinated CNS lesions of older animals displayed intracellular cholesterol crystals at a far greater frequency than phagocytes in CNS samples from young mice. Moreover, macrophages from mice defective in cholesterol efflux exhibited increased crystal deposition as well as impaired demyelinated lesion repair. These findings suggest that the blockage of cholesterol transport in macrophages in aged individuals is associated with impaired CNS regeneration. The underlying mechanism for this age-associated decline in cholesterol efflux remains unclear. After demyelinating injury, cholesterol from the lipid-rich myelin debris engulfed by phagocytes is metabolized to oxysterols (*8*). These metabolites activate the heterodimeric transcription factor, liver X receptor (LXR)–retinoid X receptor (RXR). LXR up-regulates the expression of genes associated with cholesterol transport, such as the lipid transporters adenosine triphosphate (ATP)–binding cassette A1 (*Abca1*) and *Abcg1* and apolipoprotein E (*ApoE*) (see the figure). APOE is the primary CNS lipoprotein, which interacts with ABCA1 and ABCG1 to facilitate cholesterol efflux by way of lysosomes into the extracellular space. Cantuti-Castelvetri *et al.* observed that the amount of endogenous oxysterols as well as the expression of *Abca1*, *Abcg1*, and *ApoE* were reduced in the demyelinated lesions of

Macrophage cholesterol efflux and remyelination

After a demyelinating insult, large amounts of lipids are released that inhibit OPC differentiation and remyelination. Phagocytes, such as macrophages, from young animals efficiently process the myelin lipids, whereas macrophages from older animals display impaired cholesterol efflux. This results in cholesterol crystallization and an inflammatory response that impedes remyelination.

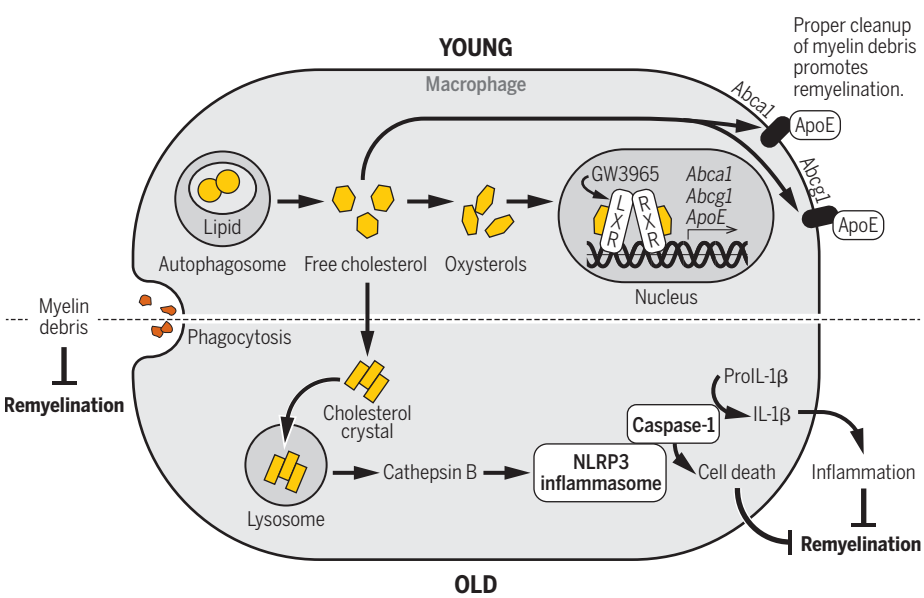

GRAPHIC: V. ALTOUNIAN/*SCIENCE*

old mice, indicating that the LXR signaling pathway is diminished when mice age.

RXR is a key regulator of lipid metabolism and immune function in macrophages (*9*). Similar to LXR, RXR signaling pathways are significantly down-regulated in aged myelin-phagocytic human monocytes (precursor cells that differentiate into macrophages) (*6*). Furthermore, the macrophage-specific ablation of RXR signaling results in decreased myelin clearance and delayed remyelination, suggesting a possible role for RXR-regulated cholesterol efflux in remyelination (*6*).

Cantuti-Castelvetri *et al*. show that the formation of cholesterol crystals in the lysosomes of phagocytes is associated with the limited recovery of demyelinated lesions displayed by mice deficient in LXR signaling. Cholesterol crystals are thought to destabilize the lysosome, resulting in leakage of cathepsin B and induction of inflammation through activation of NLRP3 (NACHT, LRR, and PYD domains containing protein 3) inflammasome activity. They found that NLRP3 inflammasome activity recruits and activates caspase-1, which promotes the release of the inflammatory cytokine interleukin-1β (IL-1β) in the demyelinated lesion (see the figure). Nevertheless, it remains unclear how inflammasome activation diminishes remyelination in aged animals. It is possible that unresolved inflammation (caused by defective cholesterol efflux) delays the conversion of macrophages from proinflammatory to anti-inflammatory, a switch that drives OPC differentiation (*10*). Another possibility is that the regenerative environment is compromised because of the inflammatory (pyroptotic) death of macrophages mediated by caspase-1.

"The study...highlights an interesting parallel between the molecular defects of macrophages in older demyelinated lesions and the development of atherosclerosis..."

The study of Cantuti-Castelvetri *et al*. also highlights an interesting parallel between the molecular defects of macrophages in older demyelinated lesions and the development of atherosclerosis, in which plaques comprised of molecules, including cholesterol, build up in arteries. The prevailing model of atherosclerosis pathogenesis centers on the inability of macrophages to effectively mobilize cholesterol through LXR-RXR–mediated efflux (*8*). Thus, LXR and RXR have become potential therapeutic targets in the effort to restore cholesterol homeostasis in atherosclerosis. Several LXR agonists, including GW3965, have been developed to stimulate cholesterol efflux from lipid-laden macrophages and inhibit the development of atherosclerosis (*11*). Encouragingly, Cantuti-Castelvetri *et al*. show that the administration of GW3965 to older mice with demyelinated CNS lesions resulted in enhanced clearance of myelin debris, reduced cholesterol-crystal formation in associated phagocytes, and significantly improved remyelination. LXR agonists promote the remyelination of rat cerebellar cultures that have been experimentally demyelinated (*12*). Similarly, the RXR agonist 9-*cis*-retinoic acid enhances remyelination in aged mice, and the RXR agonist bexarotene confers a gene-expression profile associated with phagocytes from younger individuals and enhanced myelin-debris clearance by phagocytes from MS patients (*6*, *13*). Bexarotene is being tested in an MS clinical trial (European Union Clinical Trials Register no. 2014-003145-99).

The discovery of the link between cholesterol crystal–laden macrophages and inflammasome activation in demyelinated lesions provides a deeper understanding of remyelination failure in MS patients, particularly as the disease progresses. Currently, there are numerous approved drugs for MS, all of which modulate immune responses to some extent. Although beneficial, these drugs fail to curtail the progressive neurodegeneration that occurs in this chronic neurological disorder (*14*). New therapeutic approaches designed to provide neuroprotection (*15*) and enhanced remyelination, such as by targeting LXR-RXR (*2*), would likely complement the current anti-inflammatory drugs to provide increased clinical benefit. ■

REFERENCES AND NOTES

1. S. L. Hauser *et al*., *Ann. Neurol*. **74**, 317 (2013).
2. R. J. M. Franklin, C. ffrench-Constant, *Nat. Rev. Neurosci*. **18**, 753 (2017).
3. L. Cantuti-Castelvetri *et al*., *Science* **359**, 684 (2018).
4. M. Simons, K.-A. Nave, *Cold Spring Harb. Perspect. Biol*. **8**, a020479 (2015).
5. D. E. Bergles, W. D. Richardson, *Cold Spring Harb. Perspect. Biol*. **8**, a020453 (2015).
6. M. S. Natrajan *et al*., *Brain* **138**, 3581 (2015).
7. J. M. Ruckh *et al*., *Cell Stem Cell* **10**, 96 (2012).
8. K. J. Moore *et al*., *Nat. Rev. Immunol*. **13**, 709 (2013).
9. T. Rőszer *et al*., *Trends Endocrinol. Metab*. **24**, 460 (2013).
10. V. E. Miron *et al*., *Nat. Neurosci*. **16**, 1211 (2013).
11. C. Hong, P. Tontonoz, *Nat. Rev. Drug Discov*. **13**, 433 (2014).
12. D. Meffre *et al*., *Proc. Natl. Acad. Sci. U.S.A*. **112**, 7587 (2015).
13. J. K. Huang *et al*., *Nat. Neurosci*. **14**, 45 (2011).
14. C. A. Dendrou, L. Fugger, *Curr. Opin. Immunol*. **49**, 37 (2017).
15. S. W. Way, B. Popko, *Lancet Neurol*. **15**, 434 (2016).

ACKNOWLEDGMENTS

B.P. is supported by grants from the National Institutes of Health (NS034939, NS099334), the National Multiple Sclerosis Society (RG-1501-02797), and the Dr. Miriam and Sheldon G. Adelson Medical Research Foundation.

10.1126/science.aar7369

EVOLUTION

How hummingbirds stay nimble on the wing

Videos of more than 200 hummingbirds reveal the evolutionary basis of their maneuvering skills

By **Peter C. Wainwright**

Like other modes of locomotion, powered flight is characterized by an ability to quickly change direction and speed. This ability—termed maneuverability—has far-reaching implications for animal success and survival (*1*, *2*) but is challenging to study because it includes a wide range of distinct behaviors and is characterized by spontaneity. As a result, understanding of maneuverability is incomplete at best (*2*–*4*). On page 653 of this issue, Dakin *et al*. (*5*) probe the evolution of flight maneuverability in hummingbirds, which can hover with precision and skillfully use a wide range of acrobatic maneuvers (see the photos). They show that a small number of underlying traits can explain much of the diversity of maneuvering flight in hummingbirds.

Maneuverability involves rapid integration of sensory information by the central nervous system, as well as the physical ability of the animal to elude obstacles as it moves through its environment, often at breakneck speed. Both the complexity and diversity of these maneuvers is difficult to study. This is why Dakin *et al*. did not challenge hummingbirds with a series of specific locomotor tasks. Rather, by extending a recent trend in the study of animal flight (*6*, *7*), they used video recorders to document the diversity and performance of specific maneuvers used by birds housed in an enclosure as they flew about, perched, and fed from a source of artificial nectar. The research team included more than 200 birds from 25 species in the survey, which yielded flight behavior profiles for each species under study. These profiles proved to be largely diagnostic of species: Different spe-

Department of Evolution and Ecology, University of California, Davis, Davis, CA 95616, USA. Email: pcwainwright@ucdavis.edu

PHOTOS: ANAND VARMA

Photographs of Inagua woodstar hummingbirds (*Calliphlox lyrura*) show their complex flight maneuvers.

cies preferred to use some maneuvers more than others and tended to be particularly good at their favored maneuvers.

Larger hummingbird species have disproportionately large muscle capacity and wing size, which generally resulted in higher maneuverability. However, other traits accounted for variation among species in the ability to perform some maneuvers. For example, the use of rotational maneuvers was largely determined by the surface area of the wings and by the muscle capacity. Forward acceleration, velocity, and deceleration were accounted for mostly by muscle capacity. Wing shape was only a major factor in determining variation in some aspects of turning performance. In combination, slight changes in body size, flight muscle capacity, wing size, and wing shape account for much of the variation in flight tendencies and the performance of different maneuvers among hummingbirds.

Given that the birds in this study were not being challenged to perform maneuvers at the limits of their abilities, it is remarkable that a handful of underlying traits accounted for 25 to 40% of the evolution in most performance metrics. This could indicate that hummingbirds operate near their limits even when not severely challenged, or that even flying around enclosures in relaxed conditions they show tendencies and abilities that parallel their maximum flight capacity.

Given the importance of flight to the hummingbird lifestyle, one could easily imagine that flight performance has diversified in response to different ecological conditions encountered by species. However, the species included in Dakin *et al.*'s study showed very strong phylogenetic conservation of flight behavior and performance. This finding suggests that ecological diversity in the major hummingbird lineages must have another functional basis. Future studies should aim to identify the role of flight ability evolution in hummingbird diversification. With more than 330 species, there is much ecological diversity to account for (*8*).

Researchers are now in a strong position to determine the adaptive importance of diversity in the use of maneuvering behaviors among hummingbird species. One may wonder why there is diversity in flight performance at all. Typically, diversity in a major functional system arises because of tradeoffs associated with underlying traits. These trade-offs may or may not also relate directly to flight performance. For example, body size, the most potent driver of maneuvering performance in the present study, has numerous impacts on hummingbird biology, including their energy needs, reproductive success, and performance in long-distance migration. Thus, the body mass of a species reflects the interaction of many factors, including flight performance. Differences among species in the consequences of body size will lead to differences in flight performance. Other important flight traits may have fewer additional implications for fitness, such as the shape of the wing. Thus, wing shapes may more closely track the aspects of flight performance that are most important to the ecology of the species.

Dakin *et al.* provide a blueprint for how to begin to understand the relative importance of different maneuvers to different hummingbird species. Getting from observations of the sort they made to characterizing locomotion in wild birds will require the development of tiny data loggers that can be affixed to these tiny birds but do not interfere with flight. With such devices, researchers would be able to determine the flight tendencies and performance of birds in the course of their everyday life. Dakin *et al.* have deepened our understanding of how traits shape flight performance, setting the stage for others to explain how diversity in maneuverability and other aspects of flight performance relate to species ecology (*9*–*11*). ■

REFERENCES

1. A. M. Wilson *et al.*, *Nature* **498**, 185 (2013).
2. R. B. Langerhans *et al.*, *Evolution* **58**, 2305 (2004).
3. D. R. Irschick, T. Garland, *Annu. Rev. Ecol. Evol. Syst.* **32**, 367 (2001).
4. M. H. Dickinson, F. O. Lehmann, S. P. Sane, *Science* **284**, 1954 (1999).
5. R. Dakin *et al.*, *Science* **359**, 653 (2018).
6. S. A. Combes *et al.*, *J. Exp. Biol.* **215**, 903 (2012).
7. K. M. Sholtis, R. M. Shelton, T. L. Hedrick, *PLOS ONE* **10**, e0125659 (2015).
8. J. A. McGuire *et al.*, *Curr. Biol.* **24**, 910 (2014).
9. S. P. Sane, *J. Exp. Biol.* **206**, 4191 (2003).
10. M. H. Dickinson *et al.*, *Science* **288**, 100 (2000).
11. A. M. Heers, K. P. Dial, *Evolution* **69**, 305 (2014).

10.1126/science.aar7615

QUANTUM OPTICS

When quantum optics meets topology

Single photons are routed around bends in photonic crystals with little backscattering

By **Alberto Amo**

Routing photons at the micrometer scale remains one of the greatest challenges of integrated quantum optics. The main difficulty is the scattering losses at bends and splitters in the photonic circuit. Current approaches imply elaborate designs, quite sensitive to fabrication details (*1*). Inspired by the physics underlying the one-way transport of electrons in topological insulators, on page 666 of this issue, Barik *et al.* (*2*) report a topological photonic crystal in which single photons are emitted and routed through bends with negligible loss. The marriage between quantum optics and topology promises new opportunities for compact quantum optics gating and manipulation.

Topology describes the properties of a system that remain unchanged under smooth deformations. Its hallmark is the emergence of chiral edge states at the interface between materials characterized by different topological indices. The importance of these edge states resides in the fact that transport through them is protected against disorder and distortions. Topology is changing our understanding of transport phenomena in a wide variety of media, the most celebrated example being the conducting states of the quantum Hall effect, which serve to route electric currents in a chip with negligible backscattering.

In the case of photons, the study of topological phases is a particularly rich field of research (*3*). One of the main motivations has been that inducing topological routing in artificial lattices would be a great step forward in the implementation of on-chip optical circuits with low losses. However, to obtain topological phases of the quantum Hall type, time-reversal symmetry needs to be broken by applying an external magnetic field. Although still feasible (*4*), this is very hard to implement for photons. The reason is that they interact very weakly with magnetic materials, particularly at visible and near-infrared wavelengths.

In 2005, Kane and Mele discovered in graphene a topological phase known as the quantum spin Hall effect (*5*). Even in the absence of an external magnetic field, electronic bands with topological properties are possible when the spin-orbit coupling of electrons is sufficiently strong (*6*). One-way channels appear at the edges of such materials, their group velocity being locked to the spin of electrons: Spin-up and spin-down electrons travel in opposite directions. Thus, they can only be backscattered if their spin is flipped, something that is not possible if the material is free of magnetic impurities. This prediction triggered the search for the so-called electronic topological insulators, experimentally evidenced 2 years later (*7*).

Can these concepts be transferred to photonic systems? Khanikaev and coworkers showed it theoretically in 2013 for bianisotropic metamaterials (*8*), which are actually quite hard to fabricate. Wu and Hu came up with a much simpler proposal that uses dielectric materials (*9*). Their idea is based on a hexagonal lattice of dielectric rods in a slab. If the rods in each hexagon are displaced either inward or outward, a photonic gap appears in the transmission spectrum of the material. When the displacement is inward, the bands, characterized by dipole and quadrupole photonic modes, are topologically trivial. When the rods are displaced outward, the dipole or quadrupole character of the bands is inverted in a mechanism related to the spin-orbit coupling of the Kane and Mele topological phase (*5*).

If the two kinds of lattice are brought together, the required band inversion results in the gap being closed exactly at the interface, defining a topological channel (see the figure). In reality, there are two different channels involving photons of opposite circular polarizations moving in opposite directions, similar to the behavior of electrons of opposite spin in a topological insulator. The idea is so simple that it can be applied to almost any physical platform that can be structured and supports waves. For example, it has been implemented in acoustic (*10*) and microwave lattices (*11*).

Barik *et al.* report such an implementation for photons at near-infrared wavelengths. Instead of dielectric rods, they use a semiconductor slab with triangular holes arranged in two types of hexagons, which form direct- and inverted-band photonic crystals (see the figure). By embedding a quantum emitter in the semiconductor, they can couple single photons to the topological channel formed at the interface between the two kinds of crystal. Photons of opposite polarizations are emitted in opposite directions, as was reported previously for a cleverly designed photonic crystal (*12*).

Université de Lille, CNRS, UMR 8523, Laboratoire de Physique des Lasers, Atomes et Molécules (PhLAM), F-59000 Lille, France. Email: alberto.amo@univ-lille1.fr

Topological photonic crystals

At the boundary between the two types of hexagonal clusters (blue and red), the energies of photonic bands with dipole and quadrupole symmetries invert, which defines a topological interface channel (white). Photons of opposite circular polarizations (σ− and σ+) propagate in the channel in opposite directions. The circuit shown connects three quantum dots (black).

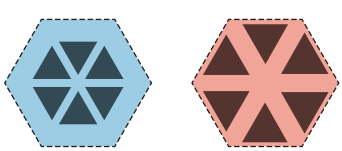

Shrunken cluster resulting in a direct-band photonic crystal.

Expanded cluster giving rise to a band-inverted photonic crystal.

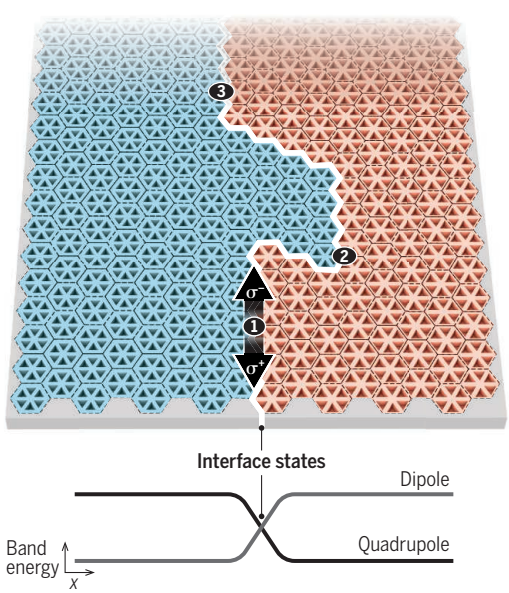

GRAPHIC: V. ALTOUNIAN/*SCIENCE*

The crucial difference is that in the work of Barik *et al.*, the transport is topological, and photons can be routed through bends with negligible backscattering. This feature opens up an exciting new playground for the implementation of integrated quantum networks. Efficient manipulation of photons at the quantum level requires low-loss routers and beam splitters, which are now easily accessible owing to the technology developed by Barik *et al.* Possible upcoming steps based on this kind of topological circuit include on-chip optical isolation, generation of emitter-emitter entanglement, and the implementation of integrated quantum gates (*13*).

Before getting to these applications, some challenges must be overcome. The topological protection of the phase discovered by Kane and Mele (*5*) actually relies on the fermionic nature of electrons, which flip their spin under a fermionic time-reversal transformation. This is not the case for photons, which are bosons. To circumvent this problem, Wu and Hu (*9*) introduced an additional symmetry in the system, a hexagonal geometry. The combination of time-reversal symmetry and the hexagonal C_{6v} geometry mimics the fermionic time-reversal behavior. A price must be paid, in that the topological channel is not immune to disorder in the shape of the hexagons forming the lattice. Only those bends with C_{6v} symmetry (60°, 120°, 240°, and 300°) are immune to backscattering. How these constraints affect the extension to larger and more elaborate quantum networks remains an open question.

Haldane ended his Nobel prize lecture in December 2016 (*14*) by pointing out that "a large experimental and theoretical effort is underway to find and characterise [...] new [topological] materials, study entanglement, and dream of new 'quantum information technologies.'" The work of Barik *et al.* is an important step in this direction. ■

REFERENCES

1. A. Y. Piggott *et al.*, *Nat. Photonics* **9**, 374 (2015).
2. S. Barik *et al.*, *Science* **359**, 666 (2018).
3. L. Lu, J. D. Joannopoulos, M. Soljačić, *Nat. Photonics* **8**, 821 (2014).
4. Z. Wang, Y. Chong, J. D. Joannopoulos, M. Soljačić, *Nature* **461**, 772 (2009).
5. C. L. Kane, E. J. Mele, *Phys. Rev. Lett.* **95**, 226801 (2005).
6. B. A. Bernevig, S.-C. Zhang, *Phys. Rev. Lett.* **96**, 106802 (2006).
7. M. König *et al.*, *Science* **318**, 766 (2007).
8. A. B. Khanikaev *et al.*, *Nat. Mater.* **12**, 233 (2013).
9. L.-H. Wu, X. Hu, *Phys. Rev. Lett.* **114**, 223901 (2015).
10. C. He *et al.*, *Nat. Phys.* **12**, 1124 (2016).
11. S. Yves *et al.*, *Nat. Commun.* **8**, 16023 (2017).
12. I. Söllner *et al.*, *Nat. Nanotechnol.* **10**, 775 (2015).
13. P. Lodahl *et al.*, *Nature* **541**, 473 (2017).
14. www.nobelprize.org/nobel_prizes/physics/laureates/2016/haldane-lecture-slides.pdf.

10.1126/science.aar7396

DEVELOPMENT

Revising concepts about adult stem cells

Imaging adult neurogenesis reveals surprising behavior of progenitor cells

By **Magdalena Götz**

The term "stem cells" is one of the most disputed terms in science. The general definition that stem cells are at the origin of a lineage, self-renewing and multipotent—generating all cell types of a given tissue or even organism (if totipotent)—is agreed upon. But how many cell divisions are required to be called a stem cell? Among the adult stem cells, hematopoietic stem cells are the champions because they can repopulate the immune systems of five generations of mice, living beyond the life of the organism from which they originated. But what about neural stem cells (NSCs), the founder cells of all cells in the central nervous system? Are a few cell cycles of self-renewal, such as nine in embryonic neurogenesis of the neocortex (*1*), sufficient to call them stem cells? And how many different cell types need to be generated by a stem cell? Do cells making only neurons, as occurs in embryonic neurogenesis, qualify as stem cells (*2*)? However, when cultured in vitro, they generate neurons and several other glial cell types, which qualifies them as multipotent (*2*). This is also the case for adult NSCs, but their behavior in vivo is even less well understood. On page 658 of this issue, Pilz *et al.* (*3*) track, for the first time, adult NSCs live in the mammalian brain, gaining exciting new insights that prompt revision of how we define stem cells.

During development, NSCs are radial glial cells (RGCs) defined by their radial morphology and glial hallmarks. Interestingly, adult NSCs also resemble RGCs in morphology and share traits with mature astroglial cells (*2*). However, the adult mammalian brain is largely devoid of NSCs, which are restricted to a few niches, such as the dentate gyrus (DG). This poses the fascinating question of when and how it is determined that neurogenesis continues in one region of the brain but not another. Adult NSCs persist, owing to RGCs dividing in specific modes and becoming quiescent (nondividing) at surprisingly early developmental stages (*4*). This highlights one of many differences between embryonic and adult neurogenesis, namely the speed of cell division (*5*). Adult RGCs divide slowly and generate neurons in specific niches, whereas the generation of glial cells prevails in the remaining adult brain. Conversely, embryonic neurogenesis is widespread and precedes gliogenesis. During developmental neurogenesis, the newly generated neurons connect and mature together, whereas neurons generated in adulthood need to integrate into a preexisting network. This integration serves as a role model for neuronal replacement therapies, such as those aiming to replace degenerated neurons in Parkinson's disease or after stroke (*6*, *7*).

> ***"TAPs are key not only for regulating the output of adult neurogenesis but also in development and evolution when they become more frequent."***

But how does all this occur? How often do RGCs truly self-renew? How hierarchical is lineage progression, and are RGCs the only cells to self-renew? From analyses in fixed brains, it is predicted that RGCs generate an intermediate, transit-amplifying progenitor (TAP). These cells amplify their own population before going on to generate neurons. TAPs have lost the radial morphology and glial hallmarks of NSCs, but little is known about how often they divide and in which mode.

These processes can best be understood by direct observation. Because regions of adult neurogenesis are buried deep in the brain of mammals, live imaging of adult neurogenesis was first performed in zebrafish, a species with an everted telencephalon that exposes adult NSCs to the brain surface (*8*). This revealed the unexpected direct conversion of an RGC into a neuron without any cell divi-

Institute of Stem Cell Research, Helmholtz Center Munich and Biomedical Center, Ludwig-Maximilians University, Munich, Germany. Email: magdalena.goetz@helmholtz-muenchen.de

Constructing neural cell lineages

Adult neurogenesis is restricted to a few niches in the mammalian brain, including the DG. RGCs are NSCs, the origin of neural lineage trees that are capable of asymmetric or symmetric divisions to self-renew. However, Pilz *et al*. reveal that RGC progeny, nonradial cells or TAPs, can also undergo asymmetric or symmetric divisions to self-renew or amplify the cell population. Thus, these TAPs have some stem cell characteristics.

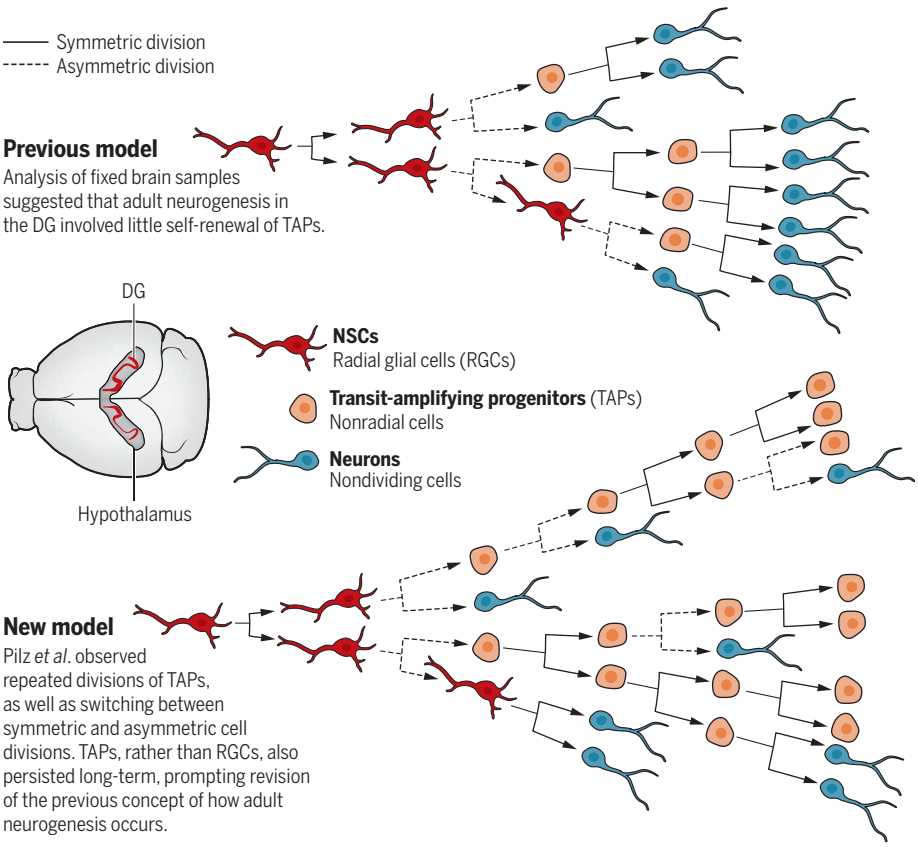

sion, but the extent to which this also occurs in mammals is unknown.

Pilz *et al*. imaged adult neurogenesis in the mammalian DG by removing the overlying neocortex to get visual access to RGCs sparsely labeled by Achaete-scute homolog 1 (Ascl1)–driven expression of green fluorescent protein. Dividing RGCs and all their progeny were followed by daily imaging for up to several months. The RGCs underwent typically two to three cell divisions with initial symmetric or asymmetric self-renewing divisions (producing two or one RGCs, respectively), followed by a final self-depleting symmetric division generating two nonradial daughter cells (see the figure). This is consistent with previous clonal analysis in mouse brain sections (*9*, *10*), whereas others have proposed long-term RGC self-renewal (*11*). Importantly, the imaging analysis followed Ascl1-expressing RGCs, whereas other subtypes of RGCs that do not express Ascl1 may be more prone to long-term self-renewal.

The biggest surprise came when observing the direct progeny of the RGCs that were expected to amplify the population by dividing symmetrically. However, Pilz *et al*. demonstrated that they also divide asymmetrically, producing a neuronal daughter and an apparently self-renewing mother cell. As they divided much more than RGCs and with the ability to stochastically switch between asymmetric (with one differentiating daughter) and symmetric (self-renewing or amplifying) division, their behavior may qualify them as NSCs. Thus, TAPs are becoming more similar to stem cells, as in other organs (*12*). These findings also have repercussions for the part of the definition that asserts that stem cells are the origin of a lineage. Because cells not at the top of the lineage tree, like TAPs, meet some criteria of stem cells, this part of the definition may also need to be revisited, including reconsidering the unidirectional aspect of lineage trees.

Another interesting observation was an early wave of cell death during adult neurogenesis, apparently regulated by intrinsic factors. This is deduced from the observation that entire branches of a lineage are prone to die and that cell death occurs independent of location. This fascinating finding provokes questions about what these intrinsic factors might be.

These data also allow for further comparisons between neurogenesis in development and adulthood. No in vivo imaging is available for neurogenesis in mammalian embryos, but in the developing zebrafish, amplification by TAPs is rare, and if TAPs exist, they divide only once (*13*, *14*). However, the sequence of symmetric self-renewing divisions of RGCs followed by asymmetric divisions generating a neuron and an RGC is also prevailing in developmental neurogenesis. Interestingly, while RGCs in adult neurogenesis obey this rule, TAPs do not.

However, especially in the developing mammalian brain, there are some regions with a large population of TAPs, such as in the telencephalon. In these regions, TAPs also exhibit an intriguing behavior, with increasingly faster cell cycles in each subsequent round of cell division, whereas RGCs divide much slower (*15*). In the adult DG, RGCs divide as fast as TAPs, which do not change their cell cycle duration with subsequent divisions. Moreover, adult DG TAPs switch between symmetric and asymmetric division—a behavior unprecedented in the nervous system so far. Thus, the behavior of TAPs is another difference between embryonic and adult neurogenesis.

TAPs are key not only for regulating the output of adult neurogenesis but also in development and evolution when they become more frequent. Indeed, there is little lineage amplification in adult zebrafish forebrain neurogenesis, allowing the direct conversion of RGCs to neurons that was not observed in the adult mammalian DG. Thus, the mechanisms regulating the emergence of indirect neurogenesis with an ever-enlarging and stem cell–like TAP population are of prime importance for brain expansion and for neuronal output in adult neurogenesis. Given that such TAPs can readily replenish the stem cells at the origin of the lineage tree in some organs (*12*), such as the intestine, it is important to watch them in an injury paradigm and be prepared for further surprises. ■

REFERENCES

1. P. Gao *et al.*, *Cell* **159**, 775 (2014).
2. M. Götz *et al.*, *Glia* **63**, 1452 (2015).
3. G.-A. Pilz *et al.*, *Science* **359**, 658 (2018).
4. S. Falk, M. Götz, *Curr. Opin. Neurobiol.* **47**, 188 (2017).
5. N. Urbán, F. Guillemot, *Front. Cell Neurosci.* **8**, 396 (2014).
6. J. T. Gonçalves, S. T. Schafer, F. H. Gage, *Cell* **167**, 897 (2016).
7. S. Falkner *et al.*, *Nature* **539**, 248 (2016).
8. J. S. Barbosa *et al.*, *Science* **348**, 789 (2015).
9. F. Calzolari *et al.*, *Nat. Neurosci.* **18**, 490 (2015).
10. A. Sierra *et al.*, *Cell Stem Cell* **16**, 488 (2015).
11. M. A. Bonaguidi *et al.*, *Cell* **145**, 1142 (2011).
12. J. Beumer, H. Clevers, *Development* **143**, 3639 (2016).
13. R. McIntosh *et al.*, *Open Biol.* **7**, 160312 (2017).
14. P. Engerer *et al.*, *EMBO J.* **36**, 1134 (2017).
15. G.-A. Pilz *et al.*, *Nat. Comm.* **4**, 2125 (2013).

10.1126/science.aar7732

GRAPHIC: K. SUTLIFF/*SCIENCE*

QUANTUM OPTICS

Superradiators created atom by atom

Collective emission is observed from atoms dropping singly through a resonator field

By **Dieter Meschede**

High radiation rates are usually associated with macroscopic lasers. Laser radiation is "coherent"—its amplitude and phase are well-defined—but its generation requires energy inputs to overcome loss. Excited atoms spontaneously emit in a random and incoherent fashion, and for N such atoms, the emission rate simply increases as N. However, if these atoms are in close proximity and coherently coupled by a radiation field, this microscopic ensemble acts as a single emitter whose emission rate increases as N^2 and becomes "superradiant," to use Dicke's terminology (*1*). On page 662 of this issue, Kim *et al.* (*2*) show the buildup of coherent light fields through collective emission from atomic radiators injected one by one into a resonator field. There is only one atom ever in the cavity, but the emission is still collective and superradiant. These results suggest another route toward thresholdless lasing.

The spontaneous emission from a single atom can be modeled as a quantum antenna without preferred emission direction. The radiation field of individual atomic emitters is also considered "incoherent" because no well-defined phase exists. Embedding an atom into the field of a small-volume optical resonator provides some directionality because the radiation is injected mainly into the geometrically determined cavity field [the Purcell effect (*3*)].

A rather different limit is realized in a conventional laser oscillator (see the figure, bottom panel). In order to maintain coherent oscillations, all members of the microscopic antenna ensemble (the macroscopic polarization of the laser medium) must be fully synchronized with the local phase of the laser wave. Coherent laser light is then driven by this phased array and emitted in a direction determined by the mirror assembly.

Laser radiation is a threshold process. The laser switches on when there is sufficient energy to self-organize the ensemble in such a way that the polarization continuously drives the field. The threshold is conditioned on the rate of stimulated emission induced by the field of the laser resonator that must overcome the losses suffered by competition from spontaneous fluorescence. Above the threshold, additionally supplied energy will dominantly feed the laser field and not be lost. In conventional lasers, the number of photons populating the laser resonator field is already very large at threshold.

Cooperative radiation effects do not fundamentally need to overcome any threshold and do not depend on any mirror geometry. Atom ensembles can always show an effective interaction through the constructive or destructive interaction of their individual contributions. What matters is that the atoms couple phase-coherently to a joint mode of the radiation field. For example, such phase-coherent emitters located within a single half wavelength create a superradiant emitter whose emission scales as N^2. A commentary on superradiance by Scully and Svidzinsky (*4*) noted applications such as quantum memories.

In recent years, control of atomic emitters coupled to a radiation field has seen much experimental progress, such as providing the phase control required for synchronized interaction of atoms and radiation fields. A resonator field not only geometrically facilitates phase-controlled atom-field coupling but also enhances the electromagnetic field amplitude at the emitter. In this situation, stimulated emission into the resonator field can increase to the level that threshold conditions are rendered almost negligible. The effective interaction of two atoms coupled to a joint radiation field is shown in the figure, top panel (*5*). The atomic radiation fields interfere constructively for full-wavelength spacing and destructively for half-wavelength spacing, like phased arrays of radio antennae used to control emission patterns.

Kim *et al.* have now shown how to build up coherent light fields by collective emission from atomic radiators injected one by one into a resonator field (see the figure, middle panel). Phase-stable lasers induce dipole emitters with a superposition of the atomic ground and excited state. Insertion at selected positions supports constructive interference. In their experiment, only a single emitter (a barium atom) is present in the cavity at any time. Nonetheless, the radiation field exhibits the properties of collective emission, the N^2 emission rate. The long-lived resonator field stores the radiation field and effectively couples every atomic dipole with its preceding and following neighbors.

The threshold for the superradiant buildup of a coherent radiation field is again negligible, a consequence of injecting a controlled stable polarization that drives the laser field from the beginning. Such thresholdless lasing is of interest probably not for high-power but for low-power applications. Attempts have been made to reduce thresholds by geometrically optimizing the ratio of stimulated and spontaneous emission. The present experiment may point out alternative routes. ■

Enhancing emission

The radiation of single atoms can be focused and amplified with superradiance or lasing. Kim *et al.* now show that single atoms falling through a cavity can also superradiate with negligible threshold.

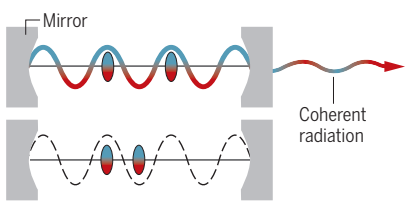

Interfering atomic radiators: Two phase-coherently driven atoms emit their radiation field into the cavity constructively (superradiantly) for 2π phase difference and destructively (no emission) for π phase difference.

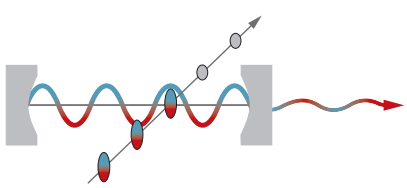

Cavity memory effects: Stimulated emission causes traversing atomic dipoles to deliver their radiation field into the resonator field. Subsequent atoms show collective radiation phenomena because the long-lived cavity field stores the field and thus memorizes preceding atoms.

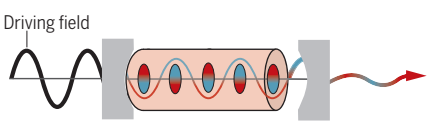

Lasing: Conventional devices use the macroscopic polarization of a laser medium to drive the laser field. The polarization and coherent laser field switch on in a self-organized way at threshold.

GRAPHIC: N. CARY/*SCIENCE*

Institut für Angewandte Physik, Universität Bonn, 53115 Bonn, Germany. Email: meschede@uni-bonn.de

REFERENCES

1. R. Dicke, *Phys. Rev.* **93**, 99 (1954).
2. J. Kim, D. Yang, S.-h. Oh, K. An, *Science* **359**, 662 (2018).
3. E. M. Purcell, *Phys. Rev.* **69**, 37 (1946).
4. M. O. Scully, A. A. Svidzinsky, *Science* **325**, 1510 (2009).
5. R. Reimann *et al.*, *Phys. Rev. Lett.* **114**, 023601 (2015).

10.1126/science.aas9067

POLICY FORUM

DATA AND DEVELOPMENT

Open data sharing and the Global South–Who benefits?

Limited capacity, deep mistrust pose challenges to sharing

By **David Serwadda,[1,2] Paul Ndebele,[3] M. Kate Grabowski,[2,4] Francis Bajunirwe,[5] Rhoda K. Wanyenze[1]**

A growing number of government agencies, funding organizations, and publishers are endorsing the call for increased data sharing, especially in biomedical research, many with an ultimate goal of open data. Open data is among the least restrictive forms of data sharing, in contrast to managed access mechanisms, which typically have terms of use and in some cases oversight by the data generators themselves. But despite an ethically sound rationale and growing support for open data sharing in many parts of the world, concerns remain, particularly among researchers in low- and middle-income countries (LMICs) in Africa, Latin America, and parts of Asia and the Middle East that comprise the Global South. Drawing on our perspective as researchers and ethicists working in the Global South, we see opportunities to improve community engagement, raise awareness, and build capacity, all toward improving research and data sharing involving researchers in LMICs.

The Scholarly Publishing and Academic Resource Coalition defines open data as being "freely available on the internet permitting any user to download, copy, analyze… without financial, legal or technical barriers other than those inseparable from gaining access to the internet itself." Many of the broad challenges surrounding data sharing are not entirely new. Such challenges have been explored within the context of social, policy, and research norms of the time, resulting in approaches to equitable international collaborations involving researchers in LMICs, including data sharing standards through managed access that helped ensure appropriate recognition. But more recently, as a result of changing technology that has made data collection, storage, and sharing more feasible, along with changing social and research norms driving toward openness and sharing, this prior equilibrium has been disturbed, with equitable collaboration less easily assured.

Although it is arguable that most obstacles to open data sharing are not exclusive to the Global South, stark resource inequities and, in some cases, histories of colonial oppression, present a markedly different landscape, often characterized by limited capacity and deep mistrust, for acceptance and implementation of open data policies.

[1]*Makerere University School of Public Health, Kampala, Uganda.* [2]*Rakai Health Sciences Program, Kalisizo, Uganda.* [3]*Medical Research Council of Zimbabwe, Harare, Zimbabwe.* [4]*Department of Pathology, Johns Hopkins University, Baltimore, MD, USA.* [5]*Department of Community Health, Mbarara University for Science and Technology, Mbarara, Uganda. Email: dserwada@imul.com*

A field researcher for INDEPTH collects data in the village of Kokmua in Ghana, September 2007.

PHOTO: SHAUL SCHWARZ/CONTRIBUTOR/GETTY IMAGES

PARACHUTES AND FREE RIDERS

North-South research collaborations are almost universally funded by Northern donors with upstream flow of specimens and data from the South and rarely vice versa. Open data effectively makes the resources collected in one country freely available to others. African scientists have expressed concern that open data compromises national ownership and reopens the gates for "parachute-research" (i.e., Northern researchers absconding with data to their home countries). Other LMIC researchers have articulated fears over free-riding scientists using the data collected by others for their own career advancement (*1*, *2*).

Studies on data sharing among LMIC researchers have found that although they are generally supportive of data sharing, there is considerably less enthusiasm for open data. There are concerns about data misuse, violations of patient privacy through participant reidentification, and possible humiliation and exploitation of the researchers themselves (*3*, *4*). Lack of awareness and experience with data sharing outside of trusted collaborations were also identified as obstacles to public data release (*1*).

Capacity building efforts, such as the National Institutes of Health (NIH) Fogarty International Center, have done much to alleviate stereotypes of the parachute researcher symbolic of Northern colonial science. Indeed, the Council for International Organizations of Medical Science ethical guidelines for human research acknowledges an essential role for capacity development in ethical international collaborations (*5*). However, open data may jeopardize capacity building in the absence of risk management. Research data are used not only to advance science, but also to train new investigators, increasing national autonomy and equity. It is inevitable that open data sharing will give rise to scenarios where Southern investigators do not publish all intended analyses from data sets before investigators at more well-resourced institutions in the North do so first. This is because of disadvantages inherent to LMICs, including poor digital literacy, inadequate infrastructure, and minimal investment in data science training. Additionally, many researchers in resource-poor settings have limited time to publish scientific manuscripts because a disproportionate amount of energy is spent on implementing studies and programs for Northern collaborators.

Although a major objective of open data sharing is to increase the numbers and diversity of scientists addressing societal problems, this also means that open data will result in researchers using and interpreting data from communities to which they have no connections. In an ideal world, these external users would engage local researchers and communities to ensure that their science is not harmful to local communities and to avoid misinterpretation of results. In reality, such interactions may not be practical, potentially imperiling rather than promoting public health. We recognize that not all projects will necessitate local expertise and some research findings may not have direct implications for community well-being, but Northern researchers using open data should strive to conduct ethical studies relevant to local communities and return results to them.

CREDIT, CAPACITY, AND ENGAGEMENT

So how can Northern researchers using open data from LMICs avoid the pitfalls of colonial science and move open data forward ethically and equitably? First, there is an urgent need to increase awareness of the benefits and risks of open data among scientists and other stakeholders in biomedical research in the Global South. Such efforts could be undertaken by funding bodies such as NIH or Wellcome Trust, which have spearheaded research ethics awareness and training on data sharing in many LMICs. Strategies to mitigate risk from open data while ensuring equity could be incorporated into these future trainings.

With respect to capacity development, there must be a paradigm shift in how we recognize and credit research contributions. Journals requiring open data sharing should formally recognize the persons or groups who provide the primary data. This could be done through a taxonomy of contributorship delineating authorship roles (*6*). Any taxonomic contributions to data curation should include at least one author from the country where the data originate, which ideally would be mandated by the International Committee of Medical Journal Editors. Academic institutions, donors, and industry must formally recognize open data contributions and reward them in promotion and grant reviews. Without any direct benefits to data generators, there will be limited incentive for researchers to participate in open data initiatives. Increasing awareness and use of data repository software such as Dataverse, which facilitates scholarly citing of data, could aid in providing such credit.

Substantial increased donor investment in management of open data sets, training in data analysis, and infrastructure for data handling and storage in LMICs would improve equity and reciprocity. Governments of LMICs, which have historically invested very little in biomedical sciences, should be core funders of these activities as well.

Ensuring community engagement and feedback in the era of open data will be challenging but is possible. Northern institutional review boards (IRBs) could play a critical role in determining whether local expertise is needed and whether a dissemination plan for results is necessary. However, it is more likely that deidentified secondary analyses using open data will not undergo IRB review. In these instances, publishers could play an important role in facilitating community engagement. One solution would be to make research findings open access to IP addresses originating in the source country (some journals already do this). Journals could require authors to provide data curators or ministries of health with the findings as a condition of publication, and ensure diversity and country or regional representation within the peer-review process. Evaluations and research are also needed to document the benefits and potential challenges arising from open access in communities providing data.

"There is no stopping data sharing...But it is... not without risk to...ethical international research collaborations..."

Although organizations such as the European Union Horizon 2020 program and the British Medical Research Council, among others, have developed data sharing policies and guidelines, there is a need to generate an international policy framework in which countries from LMICs fully participate to find solutions workable for all stakeholders (*7*). The World Health Organization (WHO) is one such organization that could help bring countries from the South and North together to formulate policies and guidelines. The WHO and research funding agencies could also facilitate country-level adaptations, capacity development, and operationalization of data sharing policies in LMICs, which are currently lacking. Once established, policies as well as adequate financial support for data sharing should be incorporated into research grants and material transfer agreements, ensuring that the necessary resources, procedures, and legal frameworks are in place prior to studies.

Some data sharing initiatives involving researchers in LMICS, such as the Malaria Genomic Epidemiology Network (MalariaGEN), Human Heredity and Health in Africa (H3Africa), International Network for the Demographic Evaluation of Populations and Their Health (INDEPTH), and the Southern African Treatment and Resistance Network (SATuRN) collaborations, actively engage in data dissemination between countries in the Global South, not just from South to North. However, these are predominantly through managed data sharing mechanisms. Other efforts are promoting open data in LMICs, but these almost exclusively aggregate national statistics to increase government transparency (e.g., African Information Highway, Kenya Open Data Initiative). The African Academy of Sciences (AAS), in partnership with F1000Research, announced plans to launch in 2018 a platform to enable AAS-funded and -affiliated researchers to publish quickly, without obstacles. The Bill & Melinda Gates Foundation and Wellcome Trust already host similar platforms, but they are not widely used yet. Additional efforts to encourage and sustain open data sharing are needed in the Global South. Future open data initiatives should be bottom-up, led by Southern researchers with investment from their own governments. International advocacy will be required to enhance LMIC investments in research capacity to make such sustainable data sharing objectives realities.

There is no stopping data sharing in biomedical research. Efforts to do so—which this is not—would be in vain. But it is worth noting that it is not without risk to important elements of ethical international research collaborations, including capacity development and community engagement. The global scientific community in the North and South must ensure that those societies providing and collecting the data, particularly in resource-limited settings, benefit from their contributions. Otherwise, we risk imperiling that which we seek to promote. ■

REFERENCES AND NOTES

1. S. G. Denny, B. Silaigwana, D. Wassenaar, S. Bull, M. Parker, *J. Empir. Res. Hum. Res. Ethics* **10**, 290 (2015).
2. K. Hate *et al.*, *J. Empir. Res. Hum. Res. Ethics* **10**, 239 (2015).
3. P. Y. Cheah *et al.*, *J. Empir. Res. Hum. Res. Ethics* **10**, 278 (2015).
4. S. Bull, N. Roberts, M. Parker, *J. Empir. Res. Hum. Res. Ethics* **10**, 225 (2015).
5. Council for International Organization of Medical Sciences, *International Ethical Guidelines for Health-Related Research Involving Humans* (2016).
6. L. Allen, J. Scott, A. Brand, M. Hlava, M. Altman, *Nature* **508**, 312 (2014).
7. I. Jao *et al.*, *J. Empir. Res. Hum. Res. Ethics* **10**, 264 (2015).

ACKNOWLEDGMENTS

All authors draw upon their experiences as participants in the 9th Annual Research Ethics Conference held by the Ugandan National Council for Science and Technology in Kampala, Uganda, in July 2017. The authors acknowledge J. Lessler and J. Hansen for their comments and feedback.

10.1126/science.aap8395

BOOKS *et al.*

ECONOMICS

Data rich

If liberal democracies can resist the urge to micromanage the economy, big data could catalyze a new capitalism

By **Andrew W. Lo**

Capitalism is a powerful tool: By compressing enormous amounts of information regarding supply and demand into a single number—the market price—buyers and sellers are able to make remarkably intelligent decisions simply by engaging in self-interested behavior. But in a big-data world, where a supercomputer can fit into our pocket and a simple Internet search allows us to find every product under the Sun, do we still need it?

In *Reinventing Capitalism in the Age of Big Data*, Viktor Mayer-Schönberger and Thomas Ramge argue that big data will transform our economies on a fundamental level. Money will become obsolete, they argue, replaced by metadata. Instead of a single market price for each commodity, sophisticated matching algorithms will use a bundle of specifications and personal preferences to select just the right product for you. Artificial intelligence powered by machine-learning techniques will relentlessly negotiate the best possible transaction on your behalf. Capital will still be important, they concede, but increasingly just for its signaling content. "Venture informers" might even replace venture capitalists.

Reinventing Capitalism in the Age of Big Data
Viktor Mayer-Schönberger and Thomas Ramge
Basic Books, 2018. 283 pp.

Mayer-Schönberger, professor of internet governance and regulation at Oxford University, and Ramge, a writer for *The Economist*, believe that the untold gigabytes of data we generate daily will catalyze a restructuring of the economy into one of small, flexible firms that quickly adapt to changing economic conditions. However, this isn't so much a reinvention of capitalism as a new release—"Capitalism 2.0"—with more complex market signals and optimization algorithms.

The authors' vision of the future is of a decentralized economy with thick markets of small data-rich firms, reminiscent of Germany's famous Mittelstand and Adam Smith's "nation of shopkeepers." This may sound like a utopia, but if it is, it's a carefully tended one.

Although they believe that large "superstar" information companies are merely a temporary phenomenon that profits from regulatory arbitrage, Mayer-Schönberger and Ramge are wary of the concentration of data in the hands of too few. Their remedy is aggressive antitrust action and a mandate for companies to share proprietary data proportional to market share.

The reviewer is at the MIT Sloan School of Management, Massachusetts Institute of Technology, Cambridge, MA 02142, USA. Email: alo-admin@mit.edu

Big data could catalyze a shift toward small firms that can adapt quickly to economic conditions.

Mayer-Schönberger and Ramge caution that liberal democracies might be tempted to use big-data capitalism to bring the economy under the greater control of the state, citing an experiment conducted in Chile in the 1970s as an example. During the Allende administration, we learn, much of the country's production decisions were placed under government control, directed by a complex cybernetic model named Cybersyn. Although the technological capacity to fully manage an economy didn't exist at that time, the Chilean system managed some partial successes before it was ended after an America-backed coup d'état in 1973.

This brings us to an important conundrum in *Reinventing Capitalism*'s thesis: The same technologies that could bring us a decentralized, big-data world could also bring about a resurgence in central planning and totalitarianism.

The high-growth, high-tech economy of Communist China is now the envy of many countries. Could this emerge as an alternative to big-data capitalism? The authors seem to think so, as they articulate in a chapter entitled "Unbundling Work." Here, they discuss the potential realization of the Marxist slogan: "From each according to his abilities, to each according to his needs." They do not, however, explore the darker implications of proceeding down this path.

Clearly technophiles, the authors focus on the positive roles that technologies can and do play in shaping society. But to venerate Moore's law without acknowledging Murphy's law is a mistake. Threats to privacy and cybersecurity, increases in systemic risk, automation-driven unemployment, and manipulation of elections and public opinion by social media hacks are new realities that we'll need to reckon with in the coming years.

Technological advances also create a form of inequality in their own right—an elitism that separates the technologically savvy from the less sophisticated. Will the high priests of data science become the new bourgeoisie, eventually leading to another Marxian dialectic in which the proletariat will have nothing to lose but their blockchains?

Reinventing Capitalism is a thought-provoking book that takes current trends in business, economics, and the information sciences and extrapolates them in a surprising manner. Nevertheless, its conclusion should not be taken as a prediction of the future, but rather as an idealistic sketch of one possible outcome. ■

10.1126/science.aar6309

COLLABORATION

Better together

A pair of policy experts highlights tension in team science and, inadvertently, in the study of scientific teams

The Strength in Numbers
The New Science of Team Science
Barry Bozeman and Jan Youtie
Princeton University Press, 2017. 239 pp.

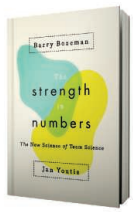

By **Stephen M. Fiore**

Science has long been reputed to be the fortress of the lone thinker, but scientists are increasingly challenged to be more collaborative and interdisciplinary in their research. Experts in science policy, Barry Bozeman and Jan Youtie have long studied various aspects of scientific collaboration. After years of focusing on primary research, their new book, *The Strength in Numbers*, aims to translate their findings for those who are actually doing scientific research. Reading less like an academic article and more like a "how to" guide, it introduces data and anecdotes about the challenges experienced by individuals working in science teams.

Painting in broad brushstrokes, the book begins with an overview of some of the research conducted on science collaboration, providing an idiosyncratic perspective that focuses primarily on science policy. For those unfamiliar with this body of work, this section provides an introduction to an often-inaccessible literature.

More useful for those interested in improving the practice of science is when the authors discuss findings from surveys and interviews with scientists who have had experience working on teams. To frame this, Bozeman and Youtie adapt the traditional "input-process-output" model found in organizational research, using context and people as inputs, collaboration as a process factor, and research effectiveness as an output. We learn that one's career stage can alter perceptions of collaborations in that, for example, junior colleagues are sometimes expected to accommodate the goals of more senior researchers. We also learn how university-industry relationships can influence team process and outcomes by, for example, producing publishing delays due to intellectual property concerns. Anecdotes bring life to the abstract framework. Even if overly simplistic, this is a useful approach because heuristic categorizations are more easily remembered by stakeholders.

As is clear from the study of science teams, tension is part of group dynamics—the behavioral, emotional, and cognitive processes that emerge when we interact to achieve some goal. But, when stepping back to view this book from a broader perspective, a different set of tensions emerges around how to do research on scientific collaborations.

Methods have varied from qualitative to quantitative, ranging from ethnographies of researchers embedded in centers, to interviews and surveys of scientists, to interventions meant to create changes, to bibliometric and network science approaches. Each serves a purpose, but implicit in Bozeman and Youtie's book is a kind of framing that dismisses some approaches in favor of others.

Can social science research on teamwork in other domains be used to understand and improve team effectiveness in the sciences? Bozeman and Youtie equivocate on this. Although they claim that the social sciences have informed their thinking and recommendations, the book offers scant discussion of the vast and diverse literature on teamwork.

The authors also dismiss more than a decade of research conducted by others in the burgeoning field known as the "science of team science" (SciTS). For a more robust discussion of this field, and how social science theory can contribute to our understanding of research collaborations, one should consult the National Academies 2015 report on science team effectiveness.

Perhaps most useful is the concluding chapter, which provides recommendations for managing science collaborations. With a mix of affect-laden verbiage (e.g., tyrannical) and functional processes (e.g., directive), the reader is given five management approaches. But this is all prelude to what is arguably the authors' main point—providing a description of "consultative collaboration management" (CCM)—which, they argue, is the "gold standard" for managing research collaborations. CCM, a strategy of the authors' creation, identifies core features that are most likely to support team functioning (e.g., "trust" and "open disagreement") and successful scientific outcomes (e.g., "effective communication").

Although CCM provides useful heuristic guidance, calling it the "gold standard" for research collaboration is premature. When viewed from the perspective of a science of team science, the book's recommendations would not pass muster as evidence. First, Bozeman and Youtie's data are from a sample of scientists who have worked on teams, not data from a sample of science teams. As such, they do not, and cannot, link aggregated team member attitudes about collaborations with team-level research outcomes. Second, and more important, CCM has not been validated to test its claims across science teams.

The Strength in Numbers succeeds in translating data into one approach for understanding team science. Ultimately, however, any collaboration recommendations worth considering must reflect a more robust evidentiary base. ■

Collaborative efforts like the research being conducted by this international team in the northern Arctic Ocean basin would likely benefit from a clearer understanding of what makes scientific teams successful.

PHOTO: ZHONGYONG GAO, THIRD INSTITUTE OF OCEANOGRAPHY, STATE OCEANIC ADMINISTRATION (SOA)

The reviewer is in the Department of Philosophy, University of Central Florida, Orlando, FL 32816, USA. Email: sfiore@ist.ucf.edu

10.1126/science.aap9897

A bison grazes in Poland's Białowieża Forest.

LETTERS

Edited by **Jennifer Sills**

Białowieża Forest: Political stands

In his News Feature "Last stands" (8 December 2017, p. 1240), E. Stokstad discusses the arguments between foresters and ecologists over how much logging to allow in Poland's Białowieża Forest. This conflict is no longer only about environmental values and priorities, but also the broader political stakes.

Białowieża Forest, with its wild roaming bison, has always been important to the Polish people. For the new conservative government, the Forest has become a battleground with the EU for the hearts and minds of Poland's electorate, as a symbol of national identity. The Minister of Environment simply could not be seen to back down. Complying with the EU's demands to cease logging in Białowieża (*1*) would have constituted surrendering national self-determination. The situation was exacerbated by the Minister having previously lost face over another EU decision regarding the Via Baltica highway (*2*).

The dispute over Białowieża epitomizes the struggle between the Polish Government's nationalism and the transnational interests of the EU. In doing so, it echoes other nationalist governments' lack of concern for international environmental issues, most notably including U.S. President Trump's withdrawal of the United States from the Paris Agreement, which may have irreparable consequences for the future of our planet.

Natural science alone seems unable to inform environmental decisions that stem primarily from politicians' core beliefs and those of their electorates. There is an urgent and growing need for integrated approaches with social science to identify environmental solutions that address both national and transnational concerns (*3*).

Malgorzata Blicharska[1]* and Richard J. Smithers[2]
[1]Natural Resources and Sustainable Development, Department of Earth Sciences, Uppsala University, 75 236 Uppsala, Sweden. [2]Ricardo Energy and Environment, Harwell, Didcot, OX11 0QR, UK.
*Corresponding author.
E-mail: malgorzata.blicharska@geo.uu.se

REFERENCES

1. Court of Justice of the EU, Order of the Court in Case C-441/17R (2017); http://curia.europa.eu/juris/liste.jsf?language=en&jur=C,T,F&num=C-441/17%20R&td=ALL.
2. S. Fuller, *Soc. Movement Stud.* **12**, 335 (2013).
3. H. Hackmann *et al.*, *Nat. Clim. Change* **4**, 653 (2014).

10.1126/science.aar7173

Białowieża Forest: Logging data lacking

In his News Feature "Last Stands" (8 December 2017, p. 1240), E. Stokstad describes the fierce conflict over the protection of Europe's most primeval forest area, the Białowieża Forest, now facing an outbreak of the spruce bark beetle (*Ips typographus*). The question of how to respond to this outbreak boils down to deciding whether active measures should be taken to protect biodiversity, or whether it should be allowed to evolve solely by natural processes, including periodic bark beetle outbreaks. We agree with Stokstad that the above question is essentially one of values and, as such, lies beyond the scope of the natural sciences. However, the use of sanitary and salvage logging as measures of biodiversity protection should certainly rest on solid scientific evidence—yet a research conference recently organized by the Polish Academy of Sciences has shown that evidence in favor of such measures is weak, at best (*1*).

This conference brought to light a general lack of controlled, replicated studies concerning the efficacy of efforts to contain bark beetle outbreaks by means of sanitary logging in lowland old-growth forests. Although the Polish State Forests administration managing the Białowieża Forest has recently initiated such study by establishing a "reference" area, its soundness is questionable because it lacks proper replication (*2*). Study design issues are further complicated by the Białowieża Forest's mosaic of protected and managed tree stands. Bark beetles spread rapidly, so it remains unclear whether sanitary logging limited to unprotected areas can restrain the outbreak (*3*). Relevant meta-analyses are also scant, and those currently available actually point to adverse effects of salvage logging on biodiversity (*4*, *5*).

The above methodological weaknesses must be urgently tackled, preferably by large-scale, replicated studies. In the Białowieża Forest, this can only be achieved through trans-border collaboration with the Belarusian side, which manages two-thirds of the tree stands. The Polish and Belarusian Academies of Sciences have already started collaboration on this issue (*1*). We surely need to learn the right lessons from the current outbreak, given that the next one will inevitably come; with the encroachment of global warming, outbreaks are occurring with increased frequency (*6*).

Marek Konarzewski,[1] Romuald Zabielski,[2] Rafał Kowalczyk,[3] Jerzy Duszyński[4]*
[1]Institute of Biology, University of Białystok, 15-245 Białystok, Poland. [2]Faculty of Veterinary Medicine, Warsaw University of Life Sciences–SGGW, 02-787 Warsaw, Poland. [3]Mammal Research Institute, Polish Academy of Sciences, 17-230 Białowieża, Poland. [4]Nencki Institute of Experimental Biology, Polish Academy of Sciences, 02-093 Warsaw, Poland.
*Corresponding author. E-mail: president@pan.pl

REFERENCES

1. Managing bark beetle outbreak in Białowieża Primeval Forest (2017); www.youtube.com/watch?v=fFCDbAp24sk.
2. L. Fahse, M. Heurich, *Ecol. Model.* **222**, 1833 (2011).
3. S. H. Hurlbert, *Ecol. Monogr.* **54**, 87 (1984).
4. S. Thorn *et al.*, *J. Appl. Ecol.* 10.1111/1365-2664.12945 (2017).
5. A. Chaudahary *et al.*, *Sci. Rep.* **6**, 23954 (2016).
6. R. Seidl, *BioScience* **64**, 1159 (2014).

10.1126/science.aat0295

Transport expansion threatens the Arctic

The expansion of transport infrastructure endangers many wild places, particularly in the tropics ("Roads to riches or ruin?," W. F. Laurance and I. Burgués Arrea, Perspectives, 27 October 2017, p. 442). Opening transport

PHOTO: RAFAŁ KOWALCZYK

routes through the Arctic is also likely to damage fragile ecosystems and potentially exacerbate global climate change.

Aided by unparalleled ice retreat (*1*), Russia, the United States, Germany, and Scandinavian countries have accelerated navigation and exploration of the Arctic (*2*). In the summer of 2017, China completed its first navigation of the Northwest Passage (*3*). Through its New Silk Road Initiatives, which include cooperation with Russia for the "Silk Road on ice" (*4*), the country has seized the opportunity to increase its involvement in Arctic affairs. Nearly half of China's gross domestic product is shipping dependent, and the lure of shorter routes has driven growing interest in Arctic shipping.

Shipping can, however, exacerbate environmental pollution. In Scandinavia, ship emissions increase deposition of nitrate by 30 to 50% and sulphate by 10 to 25% (*5*), endangering human health and increasing ocean acidification. Deposition of black carbon aerosols can reduce albedo, accelerating snowmelt and ice loss (*6*). With limited infrastructure and poor weather, accidental spills of oil and chemicals are major concerns. For example, the 1989 Exxon Valdez oil spill has had lasting impacts in the Arctic due to difficulties of cleaning up in icy waters (*7*). Concerns have increased after recent tragic spills (*8*). Foreign species can also be introduced through ballast or wastewater discharges (*9*). Shipping through areas of critical ecological concern such as whale foraging zones or migration corridors may threaten wildlife, for example, the North Atlantic right whale (*10*).

With limited implementation of the Paris Agreement, particularly from the United States, Arctic shipping could be easier in the future. Nevertheless, the International Maritime Organization's Polar Code includes waste management, improving infrastructure, and routing agreements (*11*). Strict enforcement of such international codes and national laws will be necessary to minimize environmental impacts on Arctic environments (*12*).

Hong Yang,[1,2]* Mingguo Ma,[1] Julian R. Thompson,[3] Roger J. Flower[3]

[1]Chongqing Engineering Research Center for Remote Sensing Big Data Application, Chongqing Key Laboratory of Karst Environment, School of Geographical Sciences, Southwest University, Chongqing, 400715, China. [2]Department of Geography and Environmental Science, University of Reading, Reading, RG6 6AB, UK. [3]UCL Department of Geography, University College London, London, WC1E 6BT, UK.
*Corresponding author.
Email: hongyanghy@gmail.com

REFERENCES

1. Y. Aksenov *et al.*, *Mar. Policy* **75**, 300 (2017).
2. Y. R. Zhang, Q. Meng, L. Y. Zhang, *Mar. Pol.* **73**, 53 (2016).
3. Central Government of P. R. of China, "China successfully finished the first navigation of the Northwest Passage in Arctic" (2017); www.gov.cn/xinwen/2017-09/07/content_5223349.htm [in Chinese].
4. *Xinhua*, "Interview: 'Silk Road on Ice' to enhance Russia-China cooperation in Arctic: Russian expert" (2017); http://news.xinhuanet.com/english/2017-11/27/c_136782902.htm.
5. S. B. Dalsøren, Ø. Endresen, I. S. Isaksen, G. Gravir, E. Sørgård, *J. Geophys. Res. Atmos.* **112**, D02310(2007).
6. J. Browse *et al.*, *Geophys. Res. Lett.* **40**, 4459 (2013).
7. World Wildlife Fund, "20 years on, Arctic unprepared for another Exxon Valdez" (2009); http://wwf.panda.org/?159442/20-years-on-Arctic-unprepared-for-another-Exxon-Valdez.
8. A. Jernelov, *Nature* **466**, 182 (2010).
9. L. Jing, B. Chen, B. Zhang, H. Peng, *Environ. Rev.* **20**, 83 (2012).
10. N. Hong, *Res. Transport. Econ.* **35**, 50 (2012).
11. International Maritime Organization, "Guidelines for ships operating in polar waters" (2010); www.imo.org/en/Publications/Documents/Attachments/Pages%20from%20E190E.pdf.
12. H. Yang, X. Huang, J. R. Thompson, R. J. Flower, *Science* **347**, 834 (2015).

10.1126/science.aar5443

RESEARCH

DNA used to order nanoparticle assembly

Lin et al., *p. 669*

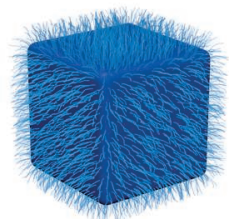

IN *SCIENCE* JOURNALS

Edited by **Stella Hurtley**

NEURODEVELOPMENT

A window on hippocampal neurogenesis

Addition of new neurons to the adult brain is key to the hippocampal functions of learning and memory. Pilz *et al.* labeled individual progenitor cells in the mouse hippocampus and watched them in situ for the next 2 months (see the Perspective by Götz). The results revealed the developmental progression as progenitor cells gave rise to mature cells of the dentate gyrus. —PJH

Science, this issue p. 658; see also p. 639

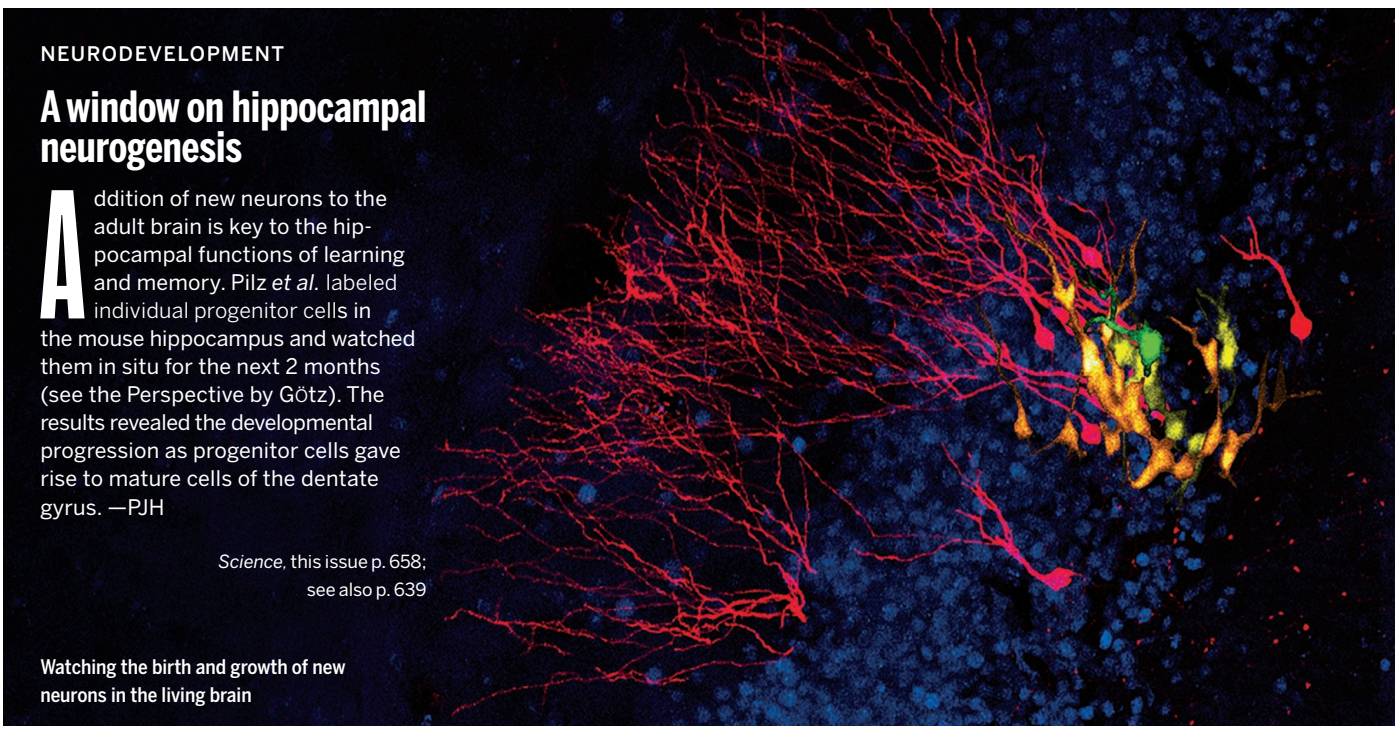

Watching the birth and growth of new neurons in the living brain

PSYCHIATRIC GENOMICS

Genes overlap across psychiatric disease

Many genome-wide studies have examined genes associated with a range of neuropsychiatric disorders. However, the degree to which the genetic underpinnings of these diseases differ or overlap is unknown. Gandal *et al*. performed meta-analyses of transcriptomic studies covering five major psychiatric disorders and compared cases and controls to identify coexpressed gene modules. From this, they found that some psychiatric disorders share global gene expression patterns. This overlap in polygenic traits in neuropsychiatric disorders may allow for better diagnosis and treatment. —LMZ

Science, this issue p. 693

PROTEIN BIOCHEMISTRY

Interactions of LARKS protein domains

More than 1500 human proteins contain long, disordered stretches of "low complexity"—strings of just a few of the 20 common amino acids. The functions of these low-complexity domains have been unclear. Hughes *et al*. present atomic-resolution structures that suggest that short segments of two such domains can bind weakly to each other by forming a pair of kinked β-sheets. Because aromatic amino acid side chains stabilize these interactions, the interacting motifs are termed LARKS, for low-complexity, aromatic-rich, kinked segments. Numerous proteins associated with membraneless organelles of biological cells contain low-complexity domains housing multiple LARKS. —SMH

Science, this issue p. 698

CANCER

Safer without PUMA

Gastrointestinal toxicity is a major cause of side effects from chemotherapy and radiation that can decrease quality of life and limit the dosing of cancer treatments. Tumor suppressor p53 plays a major role in chemotherapy-induced intestinal cell death, but inhibiting p53 is not safe because its loss would worsen cancer growth. Leibowitz *et al*. blocked only the detrimental function of p53 by inhibiting its downstream effector, PUMA. A small-molecule inhibitor of PUMA protected intestinal cells in mice and in human colon organoids but did not protect cancer cells. The approach may thus provide a viable strategy for intestinal protection in cancer patients. —YN

Sci. Transl. Med. **10**, eaam7610 (2018).

QUANTUM OPTICS

Building up to superradiance, one by one

Superradiance is a quantum phenomenon that occurs when emitters are sufficiently close to change spontaneous emission. Controlling the position and state of emitters within an atomic ensemble, however, is technically challenging. Kim *et al*. show that spatial correlations can be replaced by temporal

CREDITS: (TOP TO BOTTOM) Q.-Y. LIN *ET AL.*; GREGOR PILZ AND SARA BOTTES/BRAIN RESEARCH INSTITUTE, UNIVERSITY OF ZURICH

Published by AAAS

correlations to achieve superradiance (see the Perspective by Meschede). They dropped prepared atoms into a high-quality optical cavity and found that the number of photons within the cavity built up superradiantly as the atoms dropped through one by one. The method provides a versatile platform for generating nonclassical states of light. —ISO

Science, this issue p. 662; see also p. 641

CARDIOVASCULAR BIOLOGY

Protecting the heart by destabilizing mRNA

The CCR4-NOT complex removes polyadenylate tails from mRNAs that then undergo degradation. Yamaguchi *et al.* found that this complex was required to prevent cardiomyocyte death (see the Focus by Das). Mice deficient in a component of this complex had cardiac dysfunction and died of heart failure. Cardiomyocytes from these mice had less deadenylated *Atg7* mRNA, which resulted in the activation of cell death–associated genes. These results raise the possibility of cardiovascular side effects for autophagy-promoting drugs, which have been explored for the treatment of various diseases. —WW

Sci. Signal. **11**, eaan3638; see also eaar6364 (2018).

MATERIALS SCIENCE

Crystallography of sensitive materials

High-resolution transmission electron microscopy is an invaluable tool for looking at the crystalline structures of many materials. However, the need for high beam doses, especially as a sample is rotated to find the crystal axes, can lead to damage, particularly in fragile materials. Zhang *et al.* combined a state-of-the-art direct-detection electron-counting camera with ways to limit the overall electron dose to analyze delicate materials such as metal organic frameworks. With this approach, they could see the benzene rings in a UiO-66 linker and the coexistence of ligand-free (metal-exposing) and ligand-capped surfaces in UiO-66 crystals. —MSL

Science, this issue p. 675

BIOMECHANICS

Making quick turns

Hummingbirds are well known for their impressive maneuvering during flight. Dakin *et al.* used a computer vision approach to characterize the details of flight in >200 hummingbirds from 25 species (see the Perspective by Wainwright). Larger species had enhanced agility owing to increased muscle mass. In all species, muscles dictated transitional movement, whereas wing shape facilitated sharp turns and rapid rotations. Species, and individuals within species, played on their strengths by combining inherent traits and learned skills. —SNV

Science, this issue p. 653; see also p. 636

QUANTUM OPTICS

Connecting quantum emitters

Exploiting topological properties of a system allows certain properties to be protected against the disorder and scattering caused by defects. Barik *et al.* demonstrate a strong light-matter interaction in a topological photonic structure (see the Perspective by Amo). They created topological edge states at the interface between two photonic, topologically distinct regions and coupled them to a single quantum emitter. The chiral nature of single-photon emission was used to inject single photons of opposite polarization into counterpropagating topological edge states. Such a topological quantum optics interface may provide a powerful platform for developing robust integrated quantum optical circuits. —ISO

Science, this issue p. 666; see also p. 638

IN OTHER JOURNALS

Edited by **Sacha Vignieri** *and* **Jesse Smith**

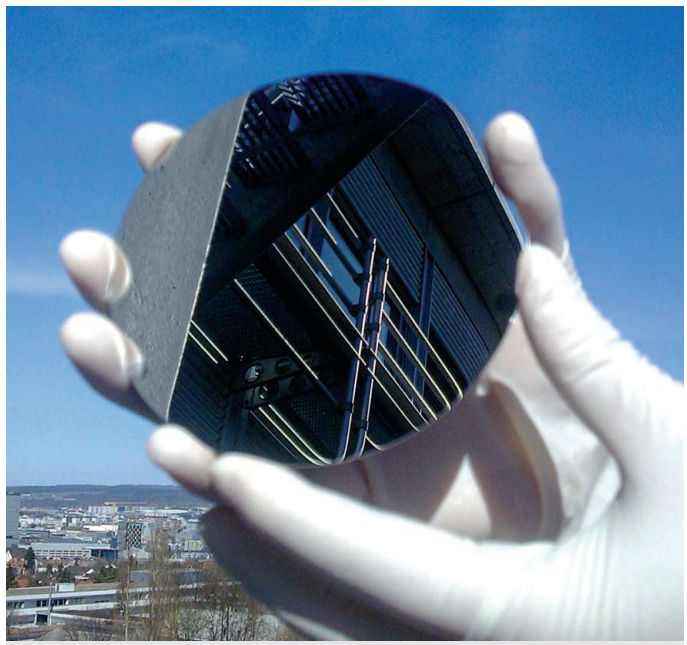

Large-area hexagonal boron nitride nanomesh can be grown on a single-crystalline rhodium thin film substrate (shown here).

NANOMATERIALS

Scalable h-BN sheets

Growth of two-dimensional material in situ is a scalable route for device production, especially if the films can be transferred to another substrate. Cun *et al.* grew single crystals of hexagonal boron nitride (h-BN) on ~10-cm rhodium films supported on silicon wafers. After electrochemical treatment with an organic acid and spin-coating with a polymer layer, the h-BN was electrochemically exfoliated by generating hydrogen bubbles at the rhodium surface. These films could be transferred onto a germanium surface to prevent their high-temperature oxidation. Films in which nanovoids had been introduced into h-BN functioned as freestanding membranes after removal of the polymer support. —PDS

Nano Lett. 10.1021/acs.nanolett.7b04752 (2018).

CELL BIOLOGY

Migration without a nucleus

When cells migrate, they normally do so by adopting a characteristic polarized morphology with the nucleus seemingly pushing from behind. The internal cytoskeleton forms well-organized arrays, and the mechanics within the cell, as well as the interactions with the surface on which the cell is moving, are well understood. It has been assumed that the nucleus itself is important for directed migration. Graham *et al.* examined the migration of enucleated mammalian cells and found that the nucleus was dispensable for directed migration, at least along flat surfaces. When it came to migration in three-dimensional (3D) environments, the lack of a nucleus was important. It seems

PHOTO: H. CUN *ET AL.*, *NANO LETT.* 10.1021/ACS.NANOLETT.7B04752 (2018)

Brittle stars detect light with a network of opsin-containing cells.

PHOTORECEPTION

Unfocused eyes in the stars

Imagine having a whole-body-surface visual system. The brittle star *Ophiocoma wendtii* and its relatives are decorated with a surface layer of calcite hemispheres. Although these have been implicated in light focusing, there has been little anatomical evidence of an underlying photoreceptor network. Sumner-Rooney *et al.* found a comprehensive network connecting opsin-containing cells across the entire body surface of the stars. However, these cells project past the calcite structures, which apparently are not acting as microlenses, as previously thought. The projecting photoreceptors are thus not eyes in the sense of image-forming vision. Rather, the opsin-containing cells detect high-contrast light changes, evidently to coordinate shade-seeking, predator avoidance, and color-changing reflexes. —CA

Proc. R. Soc. B **285**, 20172590 (2018).

that the mechanical interactions between the cytoskeleton and the nucleoskeleton provide the physical robustness required for cells to push their way through 3D environments. —SMH

J. Cell Biol. 10.1083/jcb.201706097 (2018).

LUNG DISEASE

COPD risk: Clues from the tree branches

Chronic obstructive pulmonary disease (COPD) is estimated to affect 250 million people worldwide. Smoking is a major risk factor, but intrinsic host factors likely also play a role. Smith *et al.* hypothesized that variations in central airway tree branching might affect COPD risk. They studied large multiethnic populations by chest computed tomography (CT) and found variant branching patterns in one-quarter of the study participants. Certain branch variants were associated with COPD susceptibility and with broad structural changes in the lungs. Thus, variations in central airway anatomy detected by CT scans could potentially identify individuals at risk of COPD. Whether such scans will prevent COPD and/or improve patient care will require future longitudinal studies. —PAK

Proc. Natl. Acad. Sci. U.S.A. 10.1073/pnas.1715564115 (2018).

EDUCATION

Chemistry assessments go 3D

Student assessments should support meaningful learning while supplying faculty with information about what students know. Underwood *et al.* provide an evidence-based approach to modifying typical assessment questions to align them with the three-dimensional learning framework of the Next Generation Science Standards. Specifically, the Three-Dimensional Learning Assessment Protocol (3D-LAP) can be used to help identify the core concept of the assessment question (core idea), the criteria to evaluate students' ability to use this knowledge (scientific practices), and how that knowledge can relate to other science disciplines (crosscutting concepts). The 3D-LAP enables faculty to adapt their existing assessments to elicit stronger evidence about what students know and can do, ultimately making this process easier and less time-consuming than designing questions from scratch. —MMc

J. Chem. Educ. 10.1021/acs.jchemed.7b00645 (2017).

IMMUNOTHERAPY

Monocytes may shed light on melanoma therapy

Checkpoint blockade immunotherapy has shown considerable promise for the control of metastatic melanoma. Despite the success stories, there are still many patients who do not respond at all. Thus, identification of molecular markers to predict which patients could have beneficial treatment outcomes is key. Krieg *et al.* used high-dimensional single-cell mass cytometry to analyze the peripheral blood of melanoma patients. Samples were analyzed before and after the patients' 12-week course of treatment with PD-1 immunotherapy. Those patients who responded better had increased activation and frequency of monocytes (defined as $CD14^{+}CD16^{-}HLA\text{-}DR^{hi}$ cells) in their blood before starting treatment. The researchers propose that monocyte profiling could be used to stratify patients before commencing PD-1 immunotherapy. —PNK

Nat. Med 10.1038/nm.4466 (2018).

DRUG DELIVERY

Synergistic approach to localized delivery

An improved remedy for osteoarthritis could involve localized delivery of an agent to the affected joints to reduce the disease progression, rather than the current use of systemic or local delivery of drugs that only treat the symptoms. Maudens *et al.* explored the potential for long-term delivery of kartogenin, a pathway activator that enhances articular cartilage protection, by combining two ideas for slow drug release. Using wet milling, they prepared nanocrystals of kartogenin, which dissolve over time, and then embedded them in biodegradable polymer microparticles. The drug-loaded particles were tested in vitro with human synoviocytes and in vivo in a mouse model, in which prolonged delivery and bioactivity of kartogenin were observed. —MSL

Small 10.1002/smll.201703108 (2018).

PHOTO: SARAH DAVIES

ALSO IN *SCIENCE* JOURNALS

Edited by **Stella Hurtley**

SYNTHETIC BIOLOGY

Toward programmed therapeutics

Advances in synthetic biology are enabling the development of new gene and cell therapies. Kitada *et al*. review recent successes in areas such as cancer immunotherapy and stem cell therapy, point out the limitations of current approaches, and describe prospects for using synthetic biology to overcome these challenges. Broader adoption of these therapies requires precise, context-specific control over cellular behavior. Gene circuits can be built to give sophisticated control over cellular behaviors so that therapeutic functions can, for example, be programmed to activate in response to disease biomarkers. —VV

Science, this issue p. 651

TISSUE REGENERATION

Keeping cholesterol at bay

A decline in tissue repair is a universal hallmark of aging. The failure to regenerate myelin sheaths in multiple sclerosis lesions contributes to chronic progressive disease and disability. Understanding the cause and preventing this failure is a key goal in regenerative medicine. Cantuti-Castelvetri *et al*. report that the self-limiting inflammatory response, which is necessary for remyelination to occur, is maladaptive in the central nervous system (CNS) of old mice (see the Perspective by Chen and Popko). Cholesterol-rich myelin debris overwhelmed the efflux capacity of phagocytes, resulting in a transition of free cholesterol into crystals, thereby inducing lysosomal rupture and inflammasome stimulation. Thus, drugs being developed to promote cholesterol clearance in human atherosclerosis lesions may also be good candidates for regenerative medicine in the CNS. —SMH

Science, this issue p. 684; see also p. 635

MOLECULAR BIOLOGY

Tracking mitotic chromosome formation

How cells pack DNA into fully compact, rod-shaped chromosomes during mitosis has fascinated cell biologists for more than a century. Gibcus *et al*. delineated the conformational transition trajectory from interphase chromatin to mitotic chromosomes minute by minute during the cell cycle. The mitotic chromosome is organized in a spiral staircase architecture in which chromatin loops emanate radially from a centrally located helical scaffold. The molecular machines condensin I and II play distinct roles in these processes: Condensin II is essential for helical winding, whereas condensin I modulates the organization within each helical turn. —SYM

Science, this issue p. 652

NEUROSCIENCE

Stimulating deep inside the brain

Noninvasive deep brain stimulation is an important goal in neuroscience and neuroengineering. Optogenetics normally requires the use of a blue laser inserted into the brain. Chen *et al*. used specialized nanoparticles that can upconvert near-infrared light from outside the brain into the local emission of blue light (see the Perspective by Feliu *et al*.). They injected these nanoparticles into the ventral tegmental area of the mouse brain and activated channelrhodopsin expressed in dopaminergic neurons with near-infrared light generated outside the skull at a distance of several millimeters. This technique allowed distant near-infrared light to evoke fast increases in dopamine release. The method was also used successfully to evoke fear memories in the dentate gyrus during fear conditioning. —PRS

Science, this issue p. 679; see also p. 633

OPTICS

Seeding a laser amplifier

Amplification of femtosecond laser pulses requires a lasing medium or a nonlinear crystal. The chemical properties of the lasing medium or adherence to momentum conservation rules in the nonlinear crystal constrain the frequency and the bandwidth of the amplified pulses. Vampa *et al*. seeded modulation instability in a laser crystal pumped with femtosecond near-infrared pulses. This provided a method for the high gain amplification of broadband and short laser pulses up to intensities of 1 terawatt per square centimeter. The method avoids constraints related to doping and phase matching and can be expected to be applied to a wide pool of glasses and crystals. —ISO

Science, this issue p. 673

PROTEIN TARGETING

When do you really need SRP?

Proteins destined for the cell exterior are recruited during synthesis to the surface of the endoplasmic reticulum (ER) by the signal recognition particle (SRP). The classic view suggests that SRP recognizes signal sequences at the beginning of proteins. Working in yeast, Costa *et al*. found that many proteins with cleavable signal peptides were efficiently targeted during synthesis in the absence of SRP. In contrast, proteins with internal targeting signals universally depended on SRP and were susceptible to aberrant mitochondrial targeting in its absence. These studies establish the full physiological role of SRP in ensuring accurate and efficient protein targeting in the secretory pathway. —SMH

Science, this issue p. 689

ATMOSPHERIC CHEMISTRY

Do we know the air we breathe indoors?

Many people spend most of their lives indoors, yet air pollution studies tend to focus on outdoor air. In a Perspective, Gligorovski and Abbatt highlight recent advances in understanding the reactions that occur in indoor living environments—for example, owing to smoking and the use of cookstoves and cleaning agents. Even the mere presence of humans in a room changes the air chemistry. Because of these reactions, humans are exposed to a bewildering array of chemicals with little-known health impacts. —JFU

Science, this issue p. 632

AUTOIMMUNITY

At home in the pancreas

Type 1 diabetes (T1D) is associated with enrichment of autoreactive $CD8^+$ T cells that target pancreatic islet cells. Culina *et al*. studied islet-reactive $CD8^+$ T cells reactive to the zinc transporter $8_{186–194}$ ($ZnT8_{186–194}$) and other islet epitopes in healthy individuals and T1D patients. These epitopes showed equivalent functionality and similar frequencies and naive phenotypes in the peripheral circulation across both groups. In contrast, $ZnT8_{186–194}$-reactive $CD8^+$ T cells were enriched in the pancreases of T1D patients relative to those of healthy controls and showed cross-reactivity to an epitope from the commensal *Bacteroides stercoris*. Thus, incomplete central tolerance may allow the survival of these islet-reactive $CD8^+$ T cells in the periphery, and proinflammatory

conditions in the islets may contribute to T1D progression. —CNF

Sci. Immunol. **3**, eaao4013 (2018).

NEUROSCIENCE

A brain rhythm for speech integration

Spoken communication demands coordination between auditory and motor aspects of language processing. Assaneo and Poeppel measured brain oscillations while humans listened to speech produced at different rates. Neural synchrony across auditory and motor speech areas was selectively enhanced at 4.5 Hz, a frequency corresponding to the mean syllable rate generated across human languages. Neural network simulations validated the findings, revealing an oscillatory mechanism for coupling sensory and motor codes of speech patterning. —KSL

Sci. Adv. 10.1126/sciadv.aao3842 (2018).

NANOMATERIALS

Programmed nanoparticle stacking

A polymer pore template can control the order of assembly of nanoparticles into well-defined stacks and create superlattices. Lin *et al*. used DNA strands on gold nanoparticles to control interparticle distance. The DNA strands contained modified adenines with more rigid ribose groups that formed stronger base pairs. The height of the stacks of three different types of gold nanoparticle could be changed with different solvents, which in turn changed their optical response. —PDS

Science, this issue p. 669

REVIEW SUMMARY

SYNTHETIC BIOLOGY

Programming gene and engineered-cell therapies with synthetic biology

Tasuku Kitada,* Breanna DiAndreth,* Brian Teague,* Ron Weiss†

BACKGROUND: Gene and engineered-cell therapies promise new treatment modalities for incurable or difficult-to-treat diseases. First-generation gene and engineered-cell therapies are already used in the clinic, including an ex vivo gene-replacement therapy for adenosine deaminase deficiency, chimeric antigen receptor (CAR) T cell therapies for certain types of leukemias and lymphomas, an adeno-associated virus gene therapy for inherited retinal diseases, and investigational therapies for β-thalassemia, sickle cell disease, hemophilia, and spinal muscular atrophy. Despite these early successes, safety concerns may hamper the broader adoption of some of these approaches: For example, overexpression of a therapeutic gene product with a narrow therapeutic window may be toxic, and excessive activation of T cells can be fatal. More-sophisticated control over cellular activity would allow us to reliably "program" cells with therapeutic behaviors, leading to safer and more effective gene and engineered-cell therapies as well as new treatments.

ADVANCES: Recent advances in synthetic biology are enabling new gene and engineered-cell therapies. These developments include engineered biological sensors that can detect disease biomarkers such as microRNAs and cell-surface proteins; genetic sensors that respond to exogenous small molecules; and new methods for interacting with various components of the cell—editing DNA, modulating RNA, and interfacing with endogenous signaling networks. These new biological modules have therapeutic potential on their own and can also serve as building blocks for sophisticated synthetic gene "circuits" that precisely control the strength, timing, and location of therapeutic function. This advanced control over cellular behavior will facilitate the development of treatments that address the underlying molecular causes of disease as well as provide viable therapeutic strategies in situations where the biomolecular targets have been previously considered "undruggable."

Recent publications have demonstrated several strategies for designing complex therapeutic genetic programs by combining basic sensor, regulatory, and effector modules. These strategies include (i) external small-molecule regulation to control therapeutic activity postdelivery, (ii) sensors of cell-specific biomarkers that activate therapeutic activity only in diseased cells and tissues, and/or (iii) feedback control loops that maintain homeostasis of bodily systems. Example therapeutic systems include a genetic circuit that senses two specific cell-surface markers to activate CAR T cells only in the presence of target cancer cells, a circuit that programmatically differentiates pancreatic progenitor cells into insulin-secreting β-like cells, and a gene network that senses the amount of psoriasis-associated cytokines to release immunomodulatory proteins only during flare-ups. These proof-of-concept systems may lead to new treatments that are dramatically safer and more effective than current therapies.

ON OUR WEBSITE

Read the full article at http://dx.doi.org/10.1126/science.aad1067

OUTLOOK: Rapid progress in synthetic biology and related fields is bringing therapeutic gene circuits ever closer to the clinic. Ongoing efforts in modeling and simulating mammalian genetic circuits will reduce the number of circuit variants that need to be tested to achieve the desired behavior. The platforms used to test genetic circuits are also evolving to more closely resemble the actual human environment in which the circuits will operate. Human organoid, tissue-on-a-chip, and whole-blood models will enable higher-throughput circuit characterization and optimization in a more physiologically relevant setting. Progress in nucleic acid delivery will improve the safety and efficiency with which therapeutic nucleic acids are introduced to target cells, and new methods for immunomodulation will suppress or mitigate unwanted immune responses. Together, these advances will accelerate the development and adoption of synthetic biology-based gene and engineered-cell therapies. ■

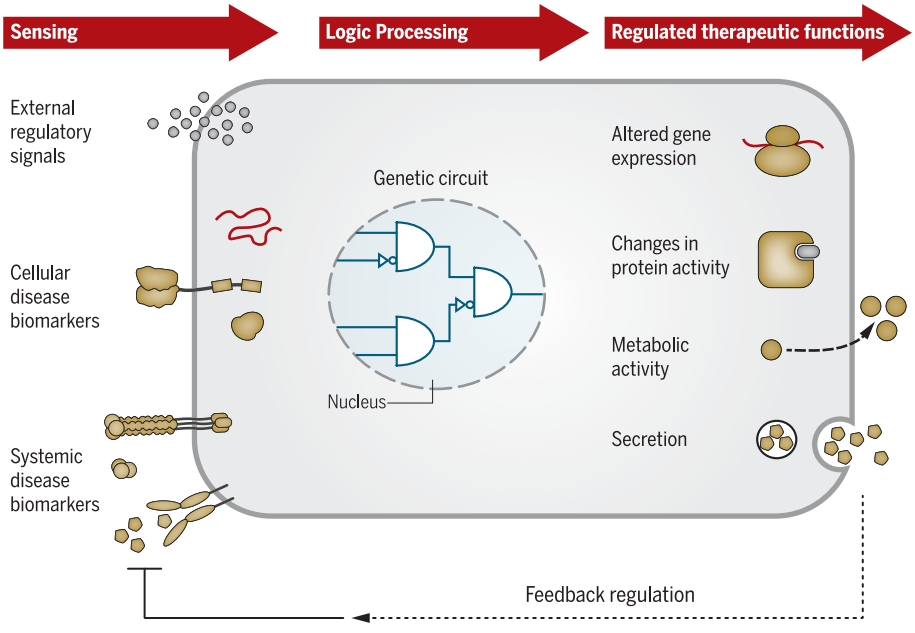

Programming gene and engineered-cell therapies with synthetic biology to improve human health. Genetically encoded therapeutic programs can regulate the dosage, localization, or timing of therapeutic function by sensing and processing externally administered signals as well as cell-specific and systemic disease biomarkers. These synthetic gene networks may lead to gene and engineered-cell therapies that are safer and more effective and that can address a broader class of diseases than current approaches.

Synthetic Biology Center, Department of Biological Engineering, Massachusetts Institute of Technology, Cambridge, MA 02139, USA.
*These authors contributed equally to this work.
†Corresponding author. Email: rweiss@mit.edu
Cite this article as T. Kitada *et al.*, *Science* **359**, eaad1067 (2018). DOI: 10.1126/science.aad1067

REVIEW

SYNTHETIC BIOLOGY

Programming gene and engineered-cell therapies with synthetic biology

Tasuku Kitada,*† Breanna DiAndreth,* Brian Teague,* Ron Weiss‡

Gene and engineered-cell therapies promise to treat diseases by genetically modifying cells to carry out therapeutic tasks. Although the field has had some success in treating monogenic disorders and hematological malignancies, current approaches are limited to overexpression of one or a few transgenes, constraining the diseases that can be treated with this approach and leading to potential concerns over safety and efficacy. Synthetic gene networks can regulate the dosage, timing, and localization of gene expression and therapeutic activity in response to small molecules and disease biomarkers. Such "programmable" gene and engineered-cell therapies will provide new interventions for incurable or difficult-to-treat diseases.

Gene and engineered-cell therapies use nucleic acids to repair or augment a cell's genetic "program" to change its behavior in a therapeutically useful manner. For example, transducing the hematopoietic stem cells of β-thalassemia patients with a functional β-globin locus may cure their disease (*1*), and genetically modifying a cancer patient's T cells ex vivo with a chimeric antigen receptor (CAR) may allow them to destroy tumor cells when transplanted back in vivo (*2*). These approaches represent a new wave of rational therapeutic design and open exciting new avenues to treat, or even cure, previously intractable diseases (*3*).

However, although gene and engineered-cell therapies are starting to demonstrate promising clinical results, an important limitation of many current approaches is that they provide little control over the strength, timing, or cellular context of the therapeutic effect. This lack of control may hamper broader adoption of these approaches: For example, existing gene therapies usually rely on overexpression of a therapeutic gene product, which may not be appropriate for interventions that have a narrow therapeutic window or require a graded or time-varying response. Clinical trials of engineered cancer-fighting T cells have reported a number of fatal or life-threatening adverse events, including cytokine release syndrome and neurotoxicity related to excessive activation of engineered T cells (*2*). Therapeutics that are activated in response to small molecules or disease biomarkers may prove safer and more effective than current treatments as well as enable new treatments for diseases that are difficult to treat with current approaches.

Synthetic Biology Center, Department of Biological Engineering, Massachusetts Institute of Technology, Cambridge, MA 02139, USA.
*These authors contributed equally to this work.
†Present address: Candriam Investors Group, B-1000 Brussels, Belgium.
‡Corresponding author. Email: rweiss@mit.edu

The field of synthetic biology aims to develop such sophisticated, programmable control over cellular behavior. Synthetic biologists build new biological systems by combining traditional engineering concepts (computer-aided design, modularity, abstraction, feedback control) with new design rules specifically suited to engineering biology (for example, codon optimization and strategies to avoid toxicity caused by the expression of transgenes) (*4*). As the field has developed, synthetic systems have evolved from simple transcriptional regulatory networks in prokaryotes (*5*, *6*) to complex multimodal biological circuits in every branch of life, including mammalian systems both in vitro and in vivo (*7*). Many recent advances have biomedical potential, such as detecting cancer cells by means of their microRNA (miRNA) signature (*8*) and maintaining insulin homeostasis with engineered transplanted cells (*9*). These developments promise a new generation of gene and engineered-cell therapies based on sophisticated synthetic biology methods.

This Review discusses the progress of and prospects for bringing mammalian synthetic biology from the bench to the bedside. We begin by mapping out approaches for controlling cellular behavior at the DNA, RNA, and protein levels, discussing a number of biological modules that might be applied in gene and engineered-cell therapies. Next, we review several strategies that gene circuits can use to control the strength, timing, and context of a therapeutic effect. We conclude by discussing several remaining challenges for the field of mammalian synthetic biology, including better tools for predictive biological design and more clinically relevant testing platforms. Taken together, recent advances promise precise, context-specific control over cellular behavior, leading to new or improved therapies for a host of diseases.

Biological modules: Building blocks for therapeutic circuits

One of the most important principles of engineering, modularity, allows engineers to design complex systems by combining simpler functional units with defined inputs and outputs. These simpler units, or modules, can be designed, tested, and characterized independently before being integrated together. Biological systems can similarly be thought of as a hierarchical connection of many simpler units (*10*), the simplest of which are molecular interactions. For example, transcription can be thought of as a module with two "inputs" (a DNA molecule containing a promoter and a transcription factor) and one "output" (an RNA molecule). These molecular interfaces allow bioengineers to create synthetic modules that interact with endogenous cellular processes, and they support the creation of more-complex synthetic systems by means of the composition of these modules.

Like all abstractions, this definition of biological modularity ignores many important details for the sake of conceptual simplicity. By focusing initially on the modules' inputs and outputs, this abstraction can make designing complex "biological programs" more tractable: The overall desired behavior of a system is expressed as a composite set of logic operations (Fig. 1A), which in turn are decomposed into modules that encode appropriate logical relationships and whose inputs and outputs can be properly connected. For instance, imagine a "second-generation" monogenic gene therapy that allows a clinician to control the strength and timing of transgene expression by administering an appropriate small-molecule drug. The overall behavior of this therapy can be expressed by a simple Boolean AND gate, in which the therapy is only "ON" if both the DNA and the small molecule are present. We begin by decomposing the overall desired system behavior, "DNA AND small-molecule drug → protein," into a set of molecular modules. The required "AND" logic can be implemented in many ways (Fig. 1C): For example, the program's transcription module could be one that requires a small-molecule drug–activated transcription factor for transgene transcription (*11*). Alternatively, we could insert a drug-sensitive ribozyme in the transgene's 5′ untranslated region (UTR), which regulates the transcript's degradation rate (*12*). Choosing an appropriate strategy requires deeper consideration of the clinical requirements, biological dynamics, and cellular context of the eventual therapeutic circuit.

The effective design of gene circuits requires a broad understanding of the available modules, and thus we begin this Review with a survey of synthetic modules that are particularly useful for gene and engineered-cell therapies. The survey groups modules together on the basis of their output, classifying them as directly affecting the abundance or activity of DNA, RNA, or proteins (Fig. 1C). This structure reflects our focus on therapeutic applications, as it is often useful to map a module's functional effect to the molecular basis of a disease. For example, patients with spinal muscular atrophy (SMA) have decreased levels of correctly spliced survival of motor neuron (SMN) mRNA, and therefore, modules that affect mRNA could be utilized. Amounts of the

functional full-length SMN splice isoform could be restored by increasing pre-mRNA production with a synthetic transcription factor or by targeting a splicing silencer region with a splice-switching oligonucleotide (*13*, *14*). For each category of modules, we discuss several recent examples, emphasizing both their utility in engineering synthetic gene circuits and their applicability in a clinical context.

Biological modules that control DNA

Biological modules that act on DNA (Fig. 1C) have the potential to be powerful therapies, because editing a cell's genome can cause permanent changes in its phenotype. For example, targeted DNA cleavage and subsequent repair of gene regulatory elements may one day treat β-hemoglobinopathies (*15*, *16*). Although gene-editing tools based on zinc-finger nucleases and transcription activator-like effector (TALE) nucleases have been used in several clinical trials (*17*, *18*), recent advances in CRISPR systems are generating excitement because their targets are specified with a guide RNA (gRNA) by using simple base-pairing rules instead of laborious protein engineering. CRISPR-enabled gene editing is already generating encouraging results in animal models (*19*–*21*); for example, Tabebordbar *et al*. used a Cas nuclease from *Staphylococcus aureus*, SaCas9, to excise a mutated intron in the *mdx* mouse model of Duchenne muscular dystrophy. The CRISPR system has also been extended to enable direct base editing (*22*, *23*) and targeted DNA demethylation (*24*, *25*).

Gene-editing tools, including Cas nucleases, can also be targeted to exogenous DNA that encodes the synthetic gene circuit itself as part of the biological program or as a safety mechanism. For example, a recent effort used a Cas9 system as a DNA-based memory recording device (*26*). The Cas9 transgene was placed under control of a nuclear factor κB (NF-κB)–responsive promoter, and the nuclease was targeted to the DNA sequence encoding the gRNA. When cells containing this memory device were implanted in vivo, the number of mutations in the gRNA sequence reflected the intensity and duration of NF-κB–mediated inflammation. A similar self-targeting strategy might be used as a "self-destruct" component of a gene circuit, enabling the destruction of DNA-encoded therapies if unintended adverse effects arise or when the therapy is no longer required. For example, our group created a Cas9-based "safety switch" (*27*), where Cas9 cleaves circuit-related DNA upon the addition of a small molecule. The circuit is therefore only expressed in cells where the circuit DNA is present "AND NOT" the small molecule–induced gRNA-loaded Cas9 (Fig. 1C).

Biological modules that control RNA

Many different cellular processes regulate the production, stability, conformation, splicing, and translation of RNA (*28*). The broad range of processes that involve RNA make it a compelling target for engineering efforts, and dysfunctions in these processes make synthetic systems that interact with RNA of considerable therapeutic interest. For example, a synthetic splice-switching oligonucleotide (Fig. 1C) was approved by the U.S. Food and Drug Administration (FDA) for the treatment of SMA (*14*), and a synthetic small interfering RNA (siRNA), which targets transthyretin (TTR) mRNAs for degradation, demonstrated strong clinical benefits in a trial for patients with TTR amyloidosis (*29*). These successes suggest that more-sophisticated synthetic biological modules that control the abundance and activity of RNA may have broad therapeutic potential.

One way to control the abundance of RNA is by regulating its transcription from DNA. Synthetic transcription modules (Fig. 1C) in mammalian systems have typically been built by fusing DNA binding domains with activation and repression domains (*30*). For example, Zhang *et al*. created synthetic transcriptional activators by attaching the potent synthetic activation domain, VP64, to TALE DNA binding domains designed to target sequences upstream of endogenous genes (*31*). Customizing the DNA binding specificity of synthetic transcription factors has become even easier with the development of catalytically "dead" dCas9, which still binds DNA but does not cleave it. For instance, dCas9-based transcriptional activation systems designed to target the 5′ long terminal repeat of dormant HIV proviral DNA have been used to induce HIV in cell culture models of latency (*32*).

Additionally, the abundance, availability, and translational or catalytic activity of RNA can be modified directly by interactions with other biomolecules. For example, Chen *et al*. created a

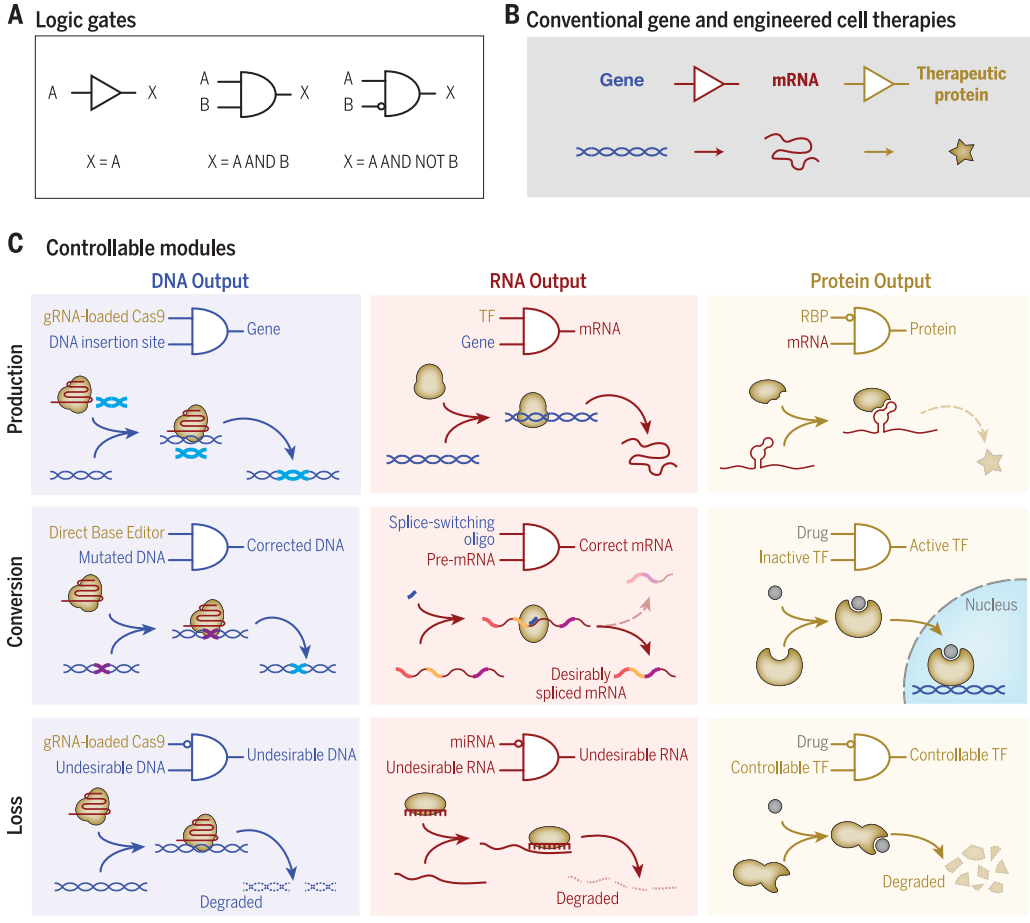

Fig. 1. Building blocks for therapeutic programs. (**A**) Logic gates with inputs (A and/or B) and outputs (X) can be used to represent molecular processes and reactions. (**B**) Conventional gene and cell therapies require just one exogenous molecular input and lack precise control over the output. Such modules function as buffer gates (i.e., control devices whose output levels correspond to their input levels), because the RNA output will be produced in any cell that the DNA input is delivered to and the therapeutic protein will be translated correspondingly. (**C**) Engineerable modules can regulate the production, conversion, or loss of specific DNA (blue), RNA (red), or protein (yellow) species by using more than one molecular input. TF, transcription factor; RBP, RNA-binding protein.

synthetic RNA device that deactivates an adjacent ribozyme upon binding theophylline (*12*). When inserted into the 3′UTR of a transcript encoding interleukin-15 (IL-15) in a mouse cytotoxic T cell line (CTLL-2), the theophylline switch implements a logic AND module: Only in the presence of both the RNA transcript and theophylline is IL-15 expressed. This enabled control over IL-15–mediated proliferation of these T cells in mice to improve clonal expansion after adoptive transfer. More recently, orthologs of the RNA-guided RNA-targeting CRISPR-Cas effector Cas13 have been used in mammalian cells to both knock down and directly edit endogenous mRNA transcripts with high specificity (*33*, *34*). Such programmable RNA-binding proteins enable precise posttranscriptional regulation of endogenous RNAs, which has exciting therapeutic implications.

Finally, just as siRNAs can be used to target endogenous mRNAs for degradation (Fig. 1C), synthetic biological modules can regulate RNA abundance by interfacing with endogenous host RNA-degradation machinery. For example, engineered mRNAs containing miRNA target sites in their 3′UTRs can be used as miRNA sensors because their abundance (and the abundance of the translated protein) is inversely related to the amount of cognate miRNA in the cell. This approach was used to control the replication of an engineered herpes simplex virus 1 (HSV-1) oncolytic virus by inserting miR-124 target sites into the 3′UTR of an essential viral early gene (*35*). Because miR-124 is expressed in neurons, but not glioblastoma cells, viral replication occurred in cancerous cells but not in healthy neuronal tissue.

Biological modules that control proteins

Proteins are a biochemically diverse molecular species that transduce information, catalyze synthesis and conversion of other biomolecules, and serve as structural components inside and outside the cell. Because of this functional diversity, clinicians have been able to use protein "biologics" (i.e., complex drugs manufactured in and isolated from living cells) to treat diseases, including autoimmune, metabolic, and cardiovascular disorders as well as cancer (*36*). Synthetic biology promises to improve upon these therapies by providing precise control over the abundance, localization, and activity of therapeutic proteins, making them safer and more effective.

Because most gene circuits express proteins from RNA, any of the strategies discussed above for controlling RNA abundance can also be used to modulate protein levels. Additionally, an mRNA's translation can be influenced by its interactions with other proteins and small molecules. For example, the archaeal ribosomal protein L7Ae binds the box C/D kink turn (K turn) and related K-loop RNA motifs, and this binding has been shown to strongly inhibit translation of the RNA (*37*, *38*). This module therefore produces a protein output when the logic function "mRNA AND NOT L7Ae" is true (Fig. 1C). Endogenous RNAs can be modulated in this way as well, by means of programmable RBPs such as the Pumilio/fem-3 mRNA-binding factors (PUF) (*39*), pentratricopeptide repeat (PPR) proteins (*40*) and, more recently, RNA-targeting Cas effector proteins (*33*, *41*–*46*). Together, these new tools are rapidly expanding the list of RNAs whose translation can be controlled by engineered systems.

Finally, a protein's abundance and activity can be modulated by fusing it to domains that respond to small molecules (Fig. 1C). For example, a number of modular degradation domains are stabilized by small-molecule ligands, allowing for direct external control of protein levels (*47*–*49*). Banaszynski *et al.* fused one of these domains to the cytokine tumor necrosis factor–α (TNF-α) and then used the small-molecule ligand Shield-1 to control the strength and timing of the cytokine's expression in mice. The fusion protein was expressed from a strain of vaccinia virus that preferentially replicates in tumor cells. When Shield-1 was administered 3 days after viral delivery, TNF-α expression was localized primarily to the tumor cells, demonstrating control over both the localization and timing of an otherwise toxic gene product (*50*). Another recent example is the synthetic thyroid hormone homeostasis system developed by Saxena *et al.* (*51*), which uses the hormone-binding domain of human thyroid receptor alpha fused to a DNA binding domain to activate a reporter transgene in response to thyroid hormone. When they replaced the reporter transgene with a thyroid-stimulating hormone receptor antagonist, the construct was able to restore thyroid hormone homeostasis in a mouse model of Graves' disease. This last example of a prototype therapeutic gene circuit uses feedback to modulate the level of its therapeutic output: The output of the circuit decreases thyroid activity, which reduces thyroid hormone amounts that are, in turn, the input to the circuit. This negative feedback is one strategy that therapeutic gene circuits can use to control the strength, timing, and context of their therapeutic output. Such control strategies, and gene circuits that implement them, are the subject of the next section of this Review.

Genetically encoded therapeutic programs

Although recent years have witnessed an increase in the number of successful gene and engineered-cell therapy trials for various diseases, more-precise regulation of the dosage, localization, or timing of a treatment's therapeutic activity may lead to improved safety and efficacy profiles for existing treatments as well as enable new modes of therapeutic intervention. For instance, implanted cells engineered with "prosthetic" gene circuits may one day treat autoimmune disorders by sensing systemic disease-associated biomarkers and secreting immune-modulating proteins in response (*52*). In this section, we describe three synthetic biology strategies to more precisely control gene and engineered-cell therapies. In the first strategy, a synthetic gene circuit's activity is externally modulated by small molecules, affording a clinician precise control over the intensity and timing of therapeutic functions. In the second strategy, gene circuits sense intracellular and extracellular biomarkers to spatially restrict therapeutic activities to diseased cells and tissues. Finally, in the third strategy, gene circuits use feedback control loops to adaptively modulate the activity levels of therapies to treat diseases caused by disrupted homeostasis. For each strategy, we examine several recently reported gene circuits, exploring how therapeutic requirements drive the design of synthetic biology solutions. Together, these examples highlight how synthetic biology could pave the way to safer and more-effective gene and engineered-cell therapies.

Small molecule–based regulation of gene and engineered-cell therapies

Successful clinical translation of gene and engineered-cell therapies would be facilitated by the ability of a clinician to control the activity of a therapy once it has been administered to a patient. In some settings, external control can decrease the likelihood that excessive activity of an engineered-cell or gene therapy results in harm to the patient. For example, serious adverse events have been recorded in a number of recent CAR T cell cancer immunotherapy trials (*2*). CAR T cell therapy is a potent new cancer treatment in which a patient's T cells are harvested, genetically engineered with a CAR against a tumor antigen, expanded, and reinfused into the patient. Unfortunately, in some patients, through a not yet fully characterized process linked to excessive activation of the infused cells, CAR T cell therapy can cause severe neurotoxicity or cytokine release syndromes that have proved fatal (*2*).

One possible way to address such problems is to engineer gene circuits whose activities are regulated by the administration of small molecules. Gene and engineered-cell therapies may persist in the body for a relatively long period of time, whereas small molecules typically have short half-lives in vivo and thus can be used to precisely control the activities of gene and engineered-cell therapies. For example, to enable external control over cytotoxic T cell function, Wu *et al.* created a CAR whose activation was dependent on a rapamycin analog (rapalog) (*53*). CAR proteins are typically composed of a single-chain variable fragment (scFv) fused to activating domains of the T cell–receptor CD3ζ intracellular domain and costimulatory domains such as CD28 or 4-1BB (Fig. 2A). Wu *et al.* modified the original CAR to develop an ON-switch CAR system consisting of two modular transmembrane proteins: one containing the extracellular scFv domain, a 4-1BB costimulation domain, and an FKBP domain; and the other composed of the CD3ζ T cell activator, a second 4-1BB domain, and an FRB domain. The FKBP and FRB domains interact to create a complete receptor only when rapalog is present (Fig. 2A). Small molecule–dependent activation of the ON-switch CAR T cell was demonstrated in vitro using a cell-killing assay, as well as by tumor clearance in a xenograft mouse model of CD19-positive lymphoma, establishing the proof of concept of a titratable CAR T cell system.

The key to this circuit's function is the careful design of the split CAR. In particular, the CAR's activity is controlled by rapalog posttranslationally. This allows for a timely response to the small molecule and might allow the CAR T cells to be shut down rapidly in patients experiencing cytokine release syndrome or neurotoxicity. This strategy is advantageous over a design in which a small molecule controls the transcription of a CAR: In such a scenario, full activation of the CAR T cell would be delayed by the transcription and translation processes necessary to produce the receptor, and shut off of T cell activity would be slow because of the time required for the CAR protein to be degraded.

Although small-molecule control over gene circuit activity has obvious safety benefits, the same strategy can also be used more broadly to control therapeutic gene circuit behavior to facilitate new modes of therapeutic interventions. For example, Saxena *et al.* developed a synthetic gene network that uses increasing concentrations of vanillic acid (VA) to differentiate pancreatic progenitor cells into insulin-producing β-like cells (*54*) (Fig. 2B). Saxena *et al.* use discrete concentrations (zero, moderate, and high) of VA to sequentially establish three distinct patterns of gene expression, resulting in an OFF-ON-OFF pattern for *Ngn3*; an ON-OFF-ON pattern for *Pdx1*; and an OFF-OFF-ON pattern for *MafA*, which encode three transcription factors that drive cell differentiation. Two different VA sensors enable the circuit's concentration-dependent response: MOR9-1, which is activated by VA, and $VanA_1$, which is inhibited by high concentrations of VA. Plasmids encoding the circuit were transfected into pancreatic progenitor cells, which were differentiated from induced pluripotent stem cells (iPSCs) by using growth factors and small-molecule inducers. In the absence of VA, circuit-containing pancreatic progenitor cells express endogenous *Pdx1*, but no genes from the circuit (*Pdx1*: ON, *Ngn3*: OFF, *MafA*: OFF). At moderate concentrations of VA, the odorant receptor MOR9-1 is activated, and this in turn generates moderate concentrations of activated endogenous CREB1. Activated CREB1 binds the highly sensitive P_{CRE} promoter, inducing expression of the synthetic transcription factor $VanA_1$, which in turn activates transcription of both *Ngn3* and a synthetic miRNA against endogenous *Pdx1* mRNA (*Pdx1*: OFF, *Ngn3*: ON, *MafA*: OFF). This drives differentiation of the pancreatic progenitor cells into endocrine progenitor cells. Finally, at high concentrations of VA and, therefore, high levels of activated CREB1, the less sensitive P_{CREm} promoter is activated and induces *Pdx1* and *Maf1*, while $VanA_1$ is inhibited by the high concentration of VA. Inhibition of $VanA_1$ stops induction of *Ngn3* and *Pdx1* miRNA (*Pdx1*: ON, *Ngn3*: OFF, *MafA*: ON), producing β-like cells. By changing the concentration of one exogenous molecule, three different gene expression signatures are generated, guiding the stepwise differentiation of pancreatic progenitor cells into β-like cells.

An important feature of this lineage-control network is the tight integration between the synthetic gene network and endogenous machinery for transmitting information and effecting changes to cell state. The VA-activated G protein–coupled receptor MOR9-1 is expressed from a transgene, but it transmits information to the rest of the synthetic gene circuit by means of endogenous species: a G protein, adenylyl cyclase, kinase, and transcription factor. This takes advantage of the signal-amplification properties of the endogenous signaling network (*55*). Additionally, the three circuit-encoded effector genes that drive cell differentiation, *Ngn3*, *Pdx1*, and *MafA*, also drive transcription from their endogenous loci. These feedback loops, initially activated by the synthetic gene network, serve as signal amplifiers and help the combined gene network achieve the intermediate states that are necessary to drive the pancreatic progenitor cell's differentiation.

Even though the synthetic gene circuit that Saxena *et al.* describe operates in vitro, circuits that guide multistage (trans)differentiation by using discrete concentrations of a single small molecule may be useful for in vivo therapeutic applications as well. For instance, there is continued interest in using cell-based therapies to repair damaged or diseased tissues in situ, but engraftment of immature cells into existing structures remains a challenge (*56*). Such therapies generally involve creation of patient-specific PSCs, then implanting them into damaged tissue. Engineering these cells with a gene circuit that directs an engineered–stem cell's differentiation in vivo could

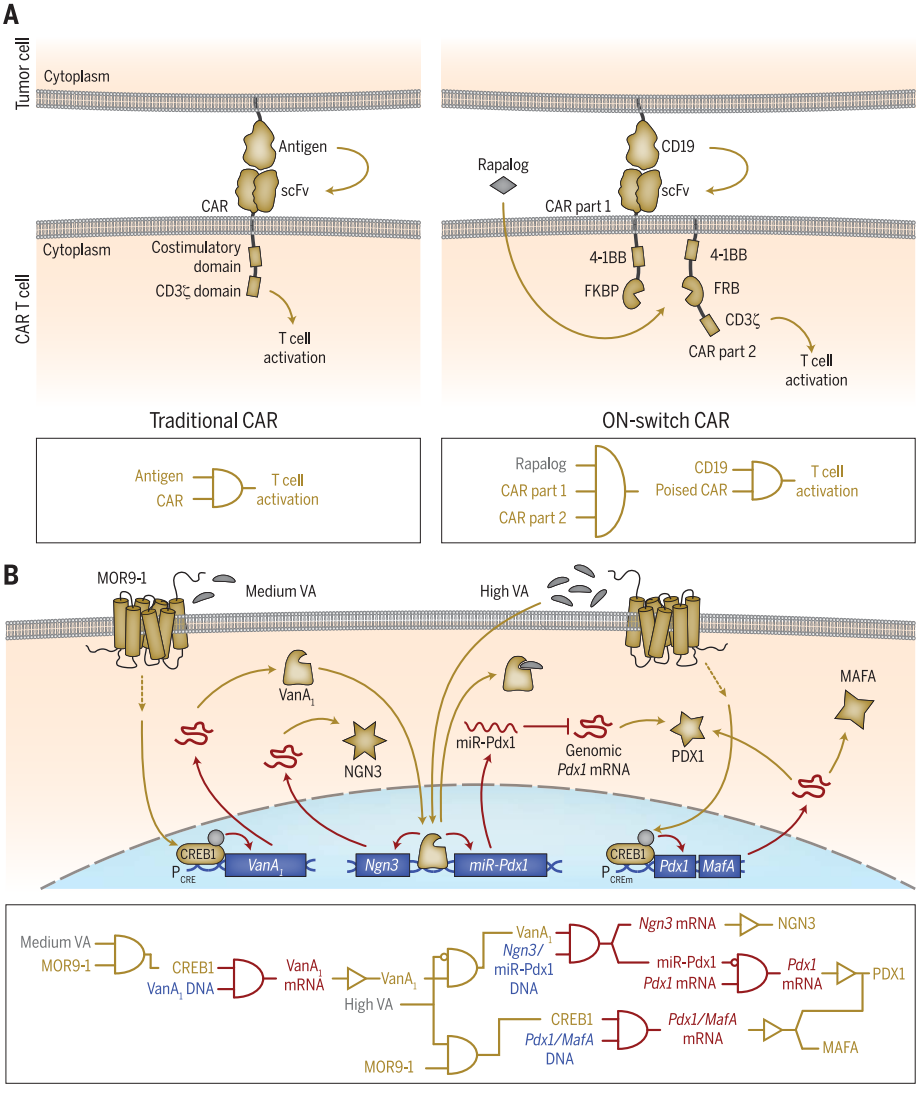

Fig. 2. Small-molecule regulation enables control over strength of therapeutic activity and facilitates new applications. (**A**) Traditional CARs are activated when the T cell encounters a target antigen. ON-switch CARs respond to antigens only when a small molecule, such as rapalog, is administered. (**B**) The pancreatic progenitor-to–β-like cell differentiation circuit is controlled by VA. Increasing levels of VA establish three different gene-expression profiles for the transcription factors PDX1, NGN3, and MAFA to drive differentiation. The final concentration of PDX1 is a summation of translation from two mRNA sources akin to a wired-OR operation in electronic logic circuits. Dashed arrows indicate multiple steps. The same drawing conventions are used as in Fig. 1.

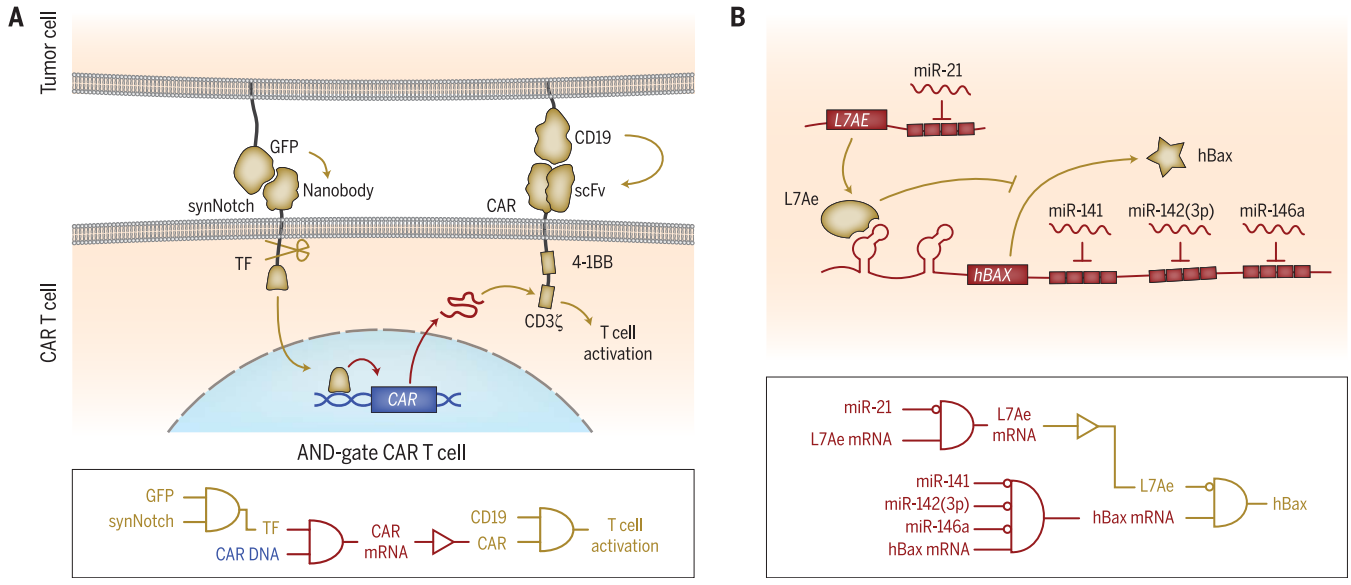

Fig. 3. Genetically encoded therapeutic programs incorporate cell-specific biomarkers for localized activity. (**A**) In an AND-gate CAR T cell, the activation of a synNotch receptor by a first antigen induces the expression of a CAR, which in turn is activated by a second antigen to ultimately activate the T cell. (**B**) RNA-encoded miRNA-classifier circuit selectively kills cancer cells characterized by high levels of miR-21 and low levels of miR-141, miR-142(3p), and miR-146a. The same drawing conventions are used as in Fig. 1.

improve the likelihood that it engrafts successfully. This strategy would be particularly powerful when combined with ex vivo gene editing for monogenic disorders: For example, Duchenne muscular dystrophy could potentially be treated by (i) generating iPSCs from a patient, (ii) correcting the mutated *DMD* gene, which encodes dystrophin, and then (iii) implanting the iPSCs into the patient's muscles and directing their differentiation into mature myofibers. For transdifferentiation, an analogous approach might involve delivering a similar multistage gene circuit to damaged tissues in vivo, which could guide the direct and efficient conversion of one cell type to another. Activating such a circuit in specific cell types is the subject of the next section.

Sensing biomarkers for localized therapeutic activity

Circuits that use endogenous cellular biomarkers to regulate their activity can enable gene and engineered-cell therapies to be more context specific, activating only in the proper cellular environment. This additional specificity can increase potency and reduce off-target activation, making gene and engineered-cell therapies safer and more effective.

CAR T cell–based cancer immunotherapy, dicussed above, is a particularly ripe target for biomarker-based gene and engineered-cell therapies. Because an antigen targeted by a CAR is rarely expressed exclusively on tumor cells, T cell activation is sometimes observed in tissues other than the tumor, leading to adverse events in clinical trials. For example, leukemia patients who were administered autologous T cells engineered with CARs against CD19 experienced cancer remission but also long-term depletion of normal $CD19^+$ B cells (*57*). The engineered effector cells in these trials are potently activated by the tumor antigen, but, if their activation could be made more specific, they may serve as the basis for safer therapeutics.

One approach to improving the specificity of engineered CAR T cells is to make them recognize multiple antigens instead of just one. Roybal *et al.* did so by engineering a CAR T cell system that could recognize two independent antigens (*58*), which was based on a synthetic Notch juxtacrine sensor developed by Morsut *et al.* (*59*). The native Notch receptor recognizes a cognate ligand and releases an intracellular domain that activates endogenous gene expression. Morsut *et al.* replaced both the extracellular ligand-binding domain and the intracellular transactivation domain, creating a synthetic Notch receptor (a "synNotch") whose signaling is orthogonal to native cellular machinery. Roybal *et al.* then used the synNotch receptor platform to engineer CAR T cells with improved specificity (*58*). Their system is composed of several modules: (i) a synNotch receptor, which binds to a tumor antigen and releases a synthetic transactivator; (ii) the DNA encoding a CAR, which is activated by the synNotch transactivator; and (iii) the CAR itself, which binds to a second tumor antigen and activates the T cell. This results in a very specific AND gate: Only T cells presented with both the synNotch ligand and the CAR ligand are activated (Fig. 3A). As a proof of concept, Roybal *et al.* built a synNotch sensor for green fluorescent protein (GFP) and a CAR specific to CD19 (*58*). When they implanted a CD19- and GFP-expressing xenograft into mice and injected their engineered T cells, the tumor was cleared. Notably, the AND-gate T cells did not elicit a response against tumor cells that only express GFP or CD19, demonstrating the specificity of the engineered T cells.

The dual-antigen CAR T cell system is a promising platform for personalized medicine because both the synNotch receptor and the CAR can be engineered with virtually any ligand-binding domain. In the future, it may be possible to engineer T cells that precisely target a patient's tumor by using synNotch receptors and CARs or T cell receptors that recognize specific cell-surface markers or major histocompatibility complex epitopes expressed on that patient's tumor cells (*60*). There are also opportunities to add other effectors to the output of the circuit: Because synNotch can activate any exogenous gene, it would be straightforward to expand the circuit with other modules that, for example, modulate the properties of T cells. Indeed, in a recent publication, Roybal *et al.* engineered synNotch T cells that express the T helper type 1 (T_H1) specific transcription factor T-bet upon recognition of the CD19 antigen (*61*). These synNotch T cells differentiated into interferon-γ (IFN-γ)–secreting T_H1 cells when cocultured with leukemia cells ectopically expressing CD19 but not when cocultured with control leukemia cells.

There are biomarkers besides cell-surface antigens that can be used to distinguish cancer cells from healthy tissues. Intracellular biomarkers, such as miRNAs, can also be detected by gene circuits, providing specificity to broadly cytotoxic anticancer mechanisms that may otherwise have considerable off-tumor activity. In this vein, in collaborations with the laboratories of Benenson, Saito, and Xie, we have created several "cancer-classifier" circuits that use endogenous miRNA expression signatures to distinguish between HeLa cells and healthy cells and activate apoptosis selectively in malignant HeLa cells, while sparing surrounding cells. The original circuit was built using plasmid DNA by Benenson and our group

(8) and was subsequently modified by Lapique and Benenson to reduce leaky output expression by introducing a recombinase-mediated delay in expression of the toxic load (62). In a related project, with Xie's group, we demonstrated HeLa and HEK (human embryonic kidney) cell classification using a cross-repressed TALE repressor circuit (63). This circuit architecture decreased leaky expression and improved the signal-to-noise ratio of cell-type classification. More recently, we implemented another version of the classifier based on the original circuit design (8) but which used only posttranscriptional regulation (Fig. 3B) (64). This allowed us to encode the circuit entirely in synthetic mRNA, a safer therapeutic modality compared to DNA (65). The RNA-encoded circuit consists of mRNA for the RNA-binding protein L7Ae with target sites for miR-21 in its 3′ UTR region and a second mRNA encoding the proapoptotic hBax protein regulated by an upstream K-turn motif and followed by target sites for miR-141, miR-142(3p), and miR-146a. L7Ae binds the K-turn motif and represses expression of hBax. Thus, hBax is expressed only in cells with high levels of miR-21 and low levels of miR-141, miR-142(3p), and miR-146a, a signature specific for HeLa cells. When this mRNA-encoded circuit was transfected into a coculture of HeLa and HEK cells in vitro, the circuit induced apoptosis specifically in HeLa cells.

Several features make miRNA sensing a particularly attractive strategy for designing cell-type classifier circuits. First, current sequencing methods make holistic comparisons of miRNA signatures from different tissues rapid, inexpensive, and reliable. Second, miRNA-sensing modules are easy to design, function potently, and can be combined in tandem to create more-complex logic. One caveat is that miRNA abundance does not always correlate well with miRNA-sensor activity (66). Thus, experimental verification of sensor libraries may be critical for predictable and accurate design of cell type–classifier circuits.

Feedback control for augmented homeostasis

Gene circuits that sense and respond to disease biomarkers by means of feedback loops can regulate therapeutic functions so that they are activated only at the right intensity and time. Such a feature could be particularly beneficial when systemic modes of interventions are used for treatment of disorders related to disrupted homeostasis (67). For example, diet-induced obesity may be treated with this approach. Although the primary treatment is a change in the patient's lifestyle and dietary habits, pharmacological and surgical interventions can assist weight loss by suppressing appetite and reducing fat absorption. One such intervention is treatment with pramlintide, an analog of amylin, which aids in blood glucose regulation and promotes satiety. Pramlintide is approved by the FDA for the treatment of type 1 and type 2 diabetes in patients who use mealtime insulin, but it has also been investigated as an adjunct to lifestyle intervention in obesity treatment (68). Because pramlintide is a peptide, it can be synthesized via a transgene, which makes it an attractive effector module for a gene circuit to treat diet-induced obesity.

To enable autonomous dosing of pramlintide, Rössger *et al.* created a feedback loop that coupled its expression to a sensor for an appropriate metabolite. They built such a sensor, dubbed the lipid-sensing receptor (LSR), by fusing the ligand-binding domain of peroxisome proliferator-activated receptor alpha (PPARα) to the phloretin-responsive repressor TtgR (Fig. 4A) (69), which allowed the LSR to bind to a synthetic promoter containing the TtgR operator. The PPARα subunit recruits transcriptional coactivators in the presence of fatty acids, and corepressors in their absence, expressing the transgene strongly in the ON state but abolishing its expression in the OFF state. The DNA binding domain TtgR provides another level of control because its binding to the TtgR operator sequence is repressed by phloretin, an apple-derived small molecule found in many cosmetics. The small-molecule control could serve as an external way to tune system response or abrogate circuit activity. Thus, the LSR forms a logical two-input AND gate with one inverted input, in which the transgene under LSR control is active only when lipids are present but phloretin is absent. In cell culture, this sensor was highly sensitive to exogenous fatty acids, with transgene expression increasing over 100-fold in response to some treatments, such as with rapeseed oil.

Delivery is one of the major obstacles in translating such advances into clinically useful therapeutics. To deliver their prosthetic gene circuit, Rössger *et al.* (69) engineered the human fibrosarcoma cell line HT-1080 to express LSR and LSR-controlled pramlintide transgene, then encapsulated the cells in alginate–poly-L-lysine beads and injected them intraperitoneally into mice. The alginate encapsulation protects the implanted cells from the host immune response but provides them with access to host metabolism. When obese mice fed a high-fat diet were implanted with the cells, they showed high concentrations of circulating pramlintide and corresponding decreases in blood fat, food intake, and body weight. Prosthetic gene circuits have also been developed to regulate urate (70), blood pressure (71), blood pH (72), thyroid hormones (51), enterohepatic signaling (73), blood glucose (9), and insulin (74).

In addition to metabolic disorders, feedback control of therapeutic gene circuits is also appropriate for chronic diseases that flare up occasionally but for which prophylactic treatment has safety concerns. One example is psoriasis, a common autoimmune disorder that causes inflamed skin lesions and whose comorbidities include psoriatic arthritis, Crohn's disease, metabolic syndrome, and cardiovascular disease (75). The inflammation characteristic of psoriasis is caused by overexpression of cytokines such as TNF-α and IL-22. Existing therapies include antibodies against TNF-α or T_H1- and T_H17-related cytokines as well as various oral or topical treatments, but long-term suppression of the immune system is associated with side effects such as infection (76). Recent phase 2 trials of anti-psoriatic and anti-inflammatory cytokines IL-4 and IL-10 have shown efficacy in treating psoriasis (77, 78), but the short half-lives of these compounds means that they require almost continuous administration to be efficacious.

To address these challenges, Schukur *et al.* used a feedback-regulation strategy to engineer a gene circuit that senses TNF-α and IL-22 and drives the expression of IL-4 and IL-10 (Fig. 4B) (52). The sensing half of the circuit shares a similar "serial sensor" design with the synNotch CAR: The endogenous TNF-α receptor activates expression of an IL-22 receptor IL-22RA by means of an endogenous NF-κB signaling cascade; the IL-22RA transgene then senses IL-22 and communicates the signal to the nucleus through an endogenous JAK-STAT (Janus kinase–signal transducers and activators of transcription) cascade. Finally, synthetic STAT3-responsive promoters activate expression of IL-4 and IL-10. The circuit therefore encodes a logical two-input AND gate: The therapeutic outputs (IL-4 and IL-10) are expressed only in the presence of TNF-α and IL-22. In a cultured human-cell assay, the activity was reversible, with production of IL-4 and IL-10 falling after the withdrawal of TNF-α and IL-22, which is a precondition for reacting to changing amounts of pathological cytokines during a psoriatic flare-up. HEK-293T cells engineered with the homeostatic circuit were encapsulated in alginate–poly-L-lysine and injected intraperitoneally into mice, where the prosthetic gene circuit successfully controlled inflammation caused by topical application of imiquimod, a common model for psoriatic lesions. The sensors also responded to cytokines in the blood of psoriasis patients, suggesting that they are sensitive enough to detect circulating TNF-α and IL-22 in humans.

Perspective

Synthetic biology is poised to improve gene- and engineered-cell–based treatments for many diseases by providing precise control over the intensity, timing, and context of therapeutic intervention. Synthetic biology–inspired modules such as safety-switches and gene editing technologies are being introduced to clinical trials, and more-sophisticated gene circuits may one day enable advanced therapies like direct in vivo transdifferentiation. However, although complex synthetic systems have been demonstrated by a growing number of proofs of concept in the lab, challenges remain in developing synthetic biology–enabled therapies. This section explores several of these challenges, including designing synthetic gene networks that meet specified performance goals, translating them from in vitro testing environments to an in vivo therapeutic context, and delivering them efficiently into the patient. We also discuss recent advances in all three areas, which together are moving synthetic biology closer to the clinic.

Despite synthetic biology's explosive development in the past decade, it is still challenging to build gene circuits that behave as anticipated (79), often requiring many design-build-test iterations before a synthetic gene network meets its performance goals. One common reason is

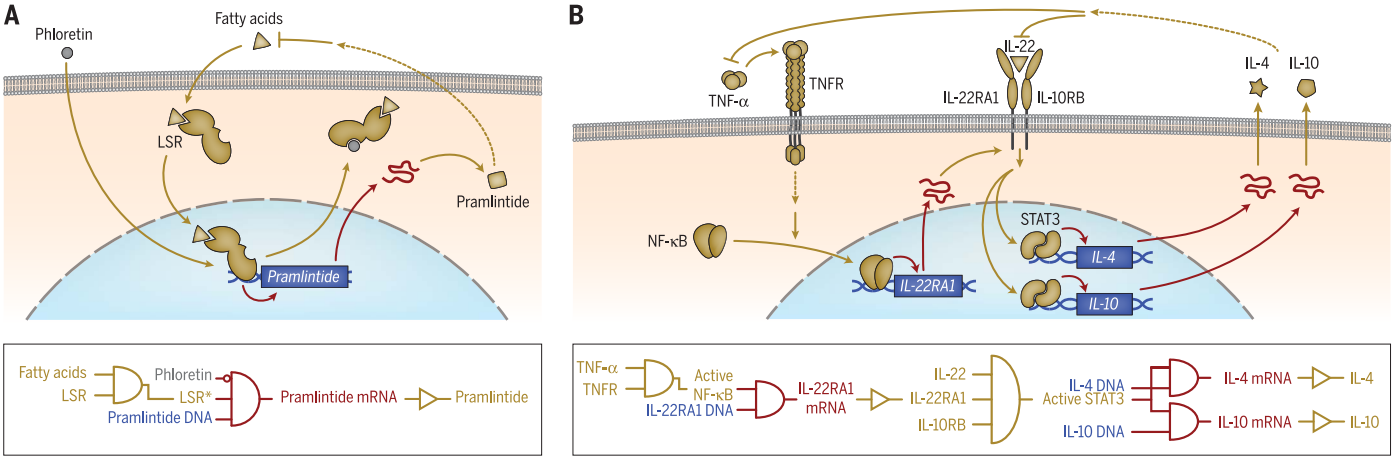

Fig. 4. Gene circuits that use feedback regulation to sense systemic biomarkers and secrete systemically acting effector molecules enable homeostasis. (**A**) A closed-loop circuit to treat obesity responds to fatty acids and produces pramlintide to slow gastric emptying, reduce glucagon, and modulate satiety. (**B**) A cytokine converter circuit to treat psoriasis responds to inflammatory signals TNF-α and IL-22 and produces anti-psoriatic and anti-inflammatory cytokines, IL-4 and IL-10, respectively. Dashed arrows indicate multiple steps. The same drawing conventions are used as in Fig. 1.

unaccounted for context effects: Genetic circuits operate using host-cell resources, which vary from cell to cell and form a finite pool from which all cellular processes (both native and engineered) must draw. Resource competition and other contextual effects can lead to modules that have different behavior depending on other modules in the circuit and circuits that have different behavior depending on the cell type in which they operate (*80*). Characterizing genetic modules in multiple cell types or specific contexts of interest as well as in combination with different modules might help to better account for this context sensitivity when designing larger circuits and systems. In parallel, by developing a deeper understanding of how cellular environments influence the behavior of synthetic modules, bioengineers may design modules and circuits that are better insulated from the cellular context.

One manifestation of context sensitivity is the poor agreement observed anecdotally between circuit performance in vitro and in vivo. Mammalian gene circuits are typically developed in cell lines cultured in artificial environments, which facilitates rapid testing of many circuit variants. Although these culture systems are experimentally tractable, they do a poor job recapitulating the heterogeneous, dynamic in vivo environment in which a therapeutic circuit must ultimately operate. For instance, differences in intracellular biomolecule amounts between cell lines and primary cells (*81*) could be debilitating for synthetic gene circuits whose proper function depends sensitively on the concentrations of their modules' inputs.

Bridging this gap in circuit behavior may be possible using in vitro test systems that more closely resemble the environment inside the body. Promising technologies include organoids, which are three-dimensional "organ buds" grown in vitro, and "organ-on-a-chip" systems where cells are grown in microfluidic systems that mimic tissue properties. Both of these platforms have shown utility in emulating disease pathologies (*82*, *83*). For example, Ogawa *et al.* created cholangiocyte organoids from iPSCs of cystic fibrosis (CF) patients that recapitulated important aspects of the CF disease phenotype (*84*). Whereas organoids derived from normal iPSCs could regulate cyst swelling through cystic fibrosis transmembrane conductance regulator (CFTR)–mediated fluid transfer, this capability was lost in organoids derived from CF patients' cholangiocytes. The researchers then demonstrated that cyst swelling could be rescued in the diseased organoids by modulators of CFTR. Such organoids may one day facilitate testing of therapeutic synthetic gene circuits in a setting that closely mimics relevant disease pathologies. Another approach might be to characterize genetic circuits embedded in engineered "designer cells" by using human whole-blood culture systems (*52*, *85*). These systems simulate the environment that the engineered cells will be exposed to in a patient, helping to more accurately predict their performance in vivo. For example, engineered HEK-293T cells encapsulated in alginate and cocultured with whole blood were able to respond to the TNF-α produced by primary immune cells stimulated with bacterial lipopolysaccharides (*85*). The continuing development of such platforms will enable high-throughput circuit characterization and optimization in more physiologically relevant settings.

A complementary approach to address gene circuits' unwanted context sensitivity is to develop biological modules and circuit designs that are better insulated from cellular context, for example, by minimizing spurious interactions (crosstalk) with other molecular species or by reducing reliance on host factors and processes. Such modules and designs should be easier to model computationally and may better maintain their behavior as they are moved from model systems to in vivo use. One design technique to achieve this is to import modules and molecules from other organisms that are expected to have minimal crosstalk with native mammalian molecular networks. For example, a modified form of the *Escherichia coli* transcription factor TetR and its cognate DNA sequence have found broad use in mammalian systems (*11*). Although this module relies on endogenous transcription machinery, there is minimal nonspecific interaction between TetR and other DNA sequences in mammalian cells, which allows for some degree of logical insulation of the module from the cellular context. Another design strategy is to use modules whose interaction partners can be controlled more rationally, such as CRISPR-Cas and RNA-interference modules whose binding is based on Watson-Crick base pairing; although in both cases, off-target binding effects are still being studied.

Both of these approaches to building more–predictable gene circuits can be supported by advances in computer-aided design tools. Better software for designing and simulating biological circuits could reduce the number of circuit variants that need to be built and tested, leading to faster and cheaper development of synthetic-biology therapies. Early efforts to simulate the behavior of synthetic gene networks relied on mechanistic models that captured each species' production, transport, binding, etc. (*86*), but these models' predictive power decreased as the size of the gene networks grew. Some recent efforts have taken a less mechanistic, more phenomenological approach: For example, Nielsen *et al.* developed a software package, Cello, that automates the design of biological circuits whose desired behavior is expressed in the digital logic design language Verilog (*87*). Of the 60 circuits that they designed in *E. coli*, 45 performed correctly for every predicted output. Cello builds circuits by using a library of genetic modules with well-characterized input-output relationships, combining modules together by mapping the output

range of one module to the input range of another. Notably, circuit predictions became more accurate after incorporation of constraints to exclude combinations of modules that behaved unpredictably as well as mechanisms to insulate individual modules.

This phenomenological approach parallels recent progress in modeling and predicting the behavior of mammalian gene circuits from Davidsohn *et al.* (*88*), who adopted a hybrid phenomenological and mechanistic strategy for modeling transcriptional cascades in transiently transfected mammalian cells. Because such experimental systems never reach a steady state, Davidsohn *et al.* used a set of rate functions to model the production and loss of each transcriptional product. By characterizing several input-output relationships of regulatory parts and then keeping track of their evolution over time, the investigators achieved predictions with a 1.6-fold mean error over a 261-fold range in output. Such a hybrid approach may enable more-advanced and -predictive biodesign and modeling tools for therapeutic gene networks.

Finally, a key hurdle to therapeutic deployment of synthetic gene circuits is safe and efficient delivery into a patient's body. One promising approach for delivery directly into patient cells is to use adeno-associated virus (AAV) because it efficiently delivers genetic material to cells in the human body with minimal immune response (*3*). Although AAV has been used in several recent gene therapy clinical trials (*3*), the nucleic acid packaging capacity of AAV is only approximately 5 kb (*89*), which is too small for many of the synthetic gene circuits described above (although AAV codelivery is being investigated). Other viral vectors, such as HSV-1, have a much larger packaging capacity, well over 100 kb, but their immunogenicity limits their applications (*90*).

A number of alternative nucleic acid delivery methods are also under development. One approach is to introduce purified DNA or mRNA into cells using physical forces, such as electroporation, or synthetic carriers, such as zwitterionic lipids or cationic polymers (*91*). These methods are not subject to the same packaging-capacity limits as viral vectors and, furthermore, can be produced in a completely cell-free manner, simplifying the manufacturing process and reducing the risk of unexpected contaminants in the final product. Unfortunately, nonviral delivery systems have their own challenges: Mechanical methods such as electroporation work well in vitro but are difficult to use in human subjects, and synthetic carrier-based delivery of large nucleic acids often triggers an undesirable immune response (*65*). Chemically modified nucleic acid vectors and biodegradable synthetic carriers that have reduced toxicity owing to their rapid elimination represent a promising step forward in advancing these systems into the clinic (*65*, *92*).

By contrast, engineered-cell therapies deliver genetic material to cells ex vivo and then use the engineered cells as "living therapeutics." In methods based on adoptive cell transfer, a patient's own cells are extracted, engineered, and expanded in a laboratory, then transplanted back into the patient. This approach allows for efficient ex vivo delivery of genetic material and has seen recent successes in clinical trials, including CAR T cell–based cancer therapies (*2*) and engineered hematopoietic stem cells used to treat β-thalassemia (*1*) and adenosine deaminase severe combined immunodeficiency (*93*). Alternately, genetically engineered cells can be microencapsulated in a biocompatible polymer matrix, such as alginate, and transplanted directly into the body (*67*), as described in the diet-induced obesity and psoriasis circuit examples above. Because the encapsulated cells do not provoke an immune response, these prosthetic genetic circuits can be tested and optimized in vitro in the same cell line in which they will operate in vivo, increasing the likelihood that the therapeutic circuit will function as desired.

More broadly, synthetic biology–based therapies carry the risk that either the delivery vector or the proteins expressed by the gene may cause T cells to become reactive or induce so-called antidrug antibodies (ADAs) (*94*). The consequences of an immune response can vary from a reduction in therapeutic efficacy all the way to a life-threatening reaction. For example, a T cell response to nonhuman proteins in ex vivo engineered-cell therapies may cause those cells to be destroyed, blunting the efficacy of the therapeutic. On the other hand, ADAs against human proteins or nonhuman proteins expressed by gene therapies in situ could lead to a severe autoimmune response. To address these issues, strategies have been developed to suppress or mitigate the immune responses against therapies. For example, administration of corticosteroids was used to dampen the T cell response to AAV capsids in a clinical trial in which factor IX was expressed in hemophilia B patients (*95*). Notably, the expression levels of factor IX were sustained for several years in those patients who were promptly treated with steroids after a T cell response (*96*). More recently, Kishimoto *et al.* coadministered therapeutic biologics and poly(lactic-co-glycolic acid)–encapsulated rapamycin nanoparticles to mice and nonhuman primates to induce immunological tolerance toward the biologics and prevented antidrug immune responses (*97*, *98*). A recent clinical trial used this strategy to induce tolerance against a yeast uricase enzyme for the treatment of gout (*99*). In the future, it may be possible to encode mechanisms to prevent antidrug immune responses in therapeutic gene circuits themselves.

The rapid development of our ability to manipulate biological systems using synthetic genes has direct implications for medicine. More than two decades after the first gene therapy trial was initiated (*100*), we have witnessed several regulatory approvals of gene- and engineered-cell–based therapies (*101*, *102*). The advancement of gene and engineered-cell therapies into the clinic brings with it opportunities for synthetic biologists to create new treatments using synthetic gene circuits. These circuits promise to make gene and engineered-cell therapies both safer and more effective as well as enable treatment options for diseases, genetic and otherwise, that are currently intractable. Taken together, these prospects will continue to propel synthetic biology into the clinic, where it can have a major impact on human health.

REFERENCES AND NOTES

1. M. Cavazzana-Calvo *et al.*, Transfusion independence and *HMGA2* activation after gene therapy of human β-thalassaemia. *Nature* **467**, 318–322 (2010). doi: 10.1038/nature09328; pmid: 20844535
2. W. A. Lim, C. H. June, The principles of engineering immune cells to treat cancer. *Cell* **168**, 724–740 (2017). doi: 10.1016/j.cell.2017.01.016; pmid: 28187291
3. L. Naldini, Gene therapy returns to centre stage. *Nature* **526**, 351–360 (2015). doi: 10.1038/nature15818; pmid: 26469046
4. A. L. Slusarczyk, A. Lin, R. Weiss, Foundations for the design and implementation of synthetic genetic circuits. *Nat. Rev. Genet.* **13**, 406–420 (2012). doi: 10.1038/nrg3227; pmid: 22596318
5. M. B. Elowitz, S. Leibler, A synthetic oscillatory network of transcriptional regulators. *Nature* **403**, 335–338 (2000). doi: 10.1038/35002125; pmid: 10659856
6. T. S. Gardner, C. R. Cantor, J. J. Collins, Construction of a genetic toggle switch in *Escherichia coli*. *Nature* **403**, 339–342 (2000). doi: 10.1038/35002131; pmid: 10659857
7. W. C. Ruder, T. Lu, J. J. Collins, Synthetic biology moving into the clinic. *Science* **333**, 1248–1252 (2011). doi: 10.1126/science.1206843; pmid: 21885773
8. Z. Xie, L. Wroblewska, L. Prochazka, R. Weiss, Y. Benenson, Multi-input RNAi-based logic circuit for identification of specific cancer cells. *Science* **333**, 1307–1311 (2011). doi: 10.1126/science.1205527; pmid: 21885784
9. M. Xie *et al.*, β-cell-mimetic designer cells provide closed-loop glycemic control. *Science* **354**, 1296–1301 (2016). doi: 10.1126/science.aaf4006; pmid: 27940875
10. L. H. Hartwell, J. J. Hopfield, S. Leibler, A. W. Murray, From molecular to modular cell biology. *Nature* **402** (Suppl), C47–C52 (1999). doi: 10.1038/35011540; pmid: 10591225
11. A. D. Ryding, M. G. Sharp, J. J. Mullins, Conditional transgenic technologies. *J. Endocrinol.* **171**, 1–14 (2001). doi: 10.1677/joe.0.1710001; pmid: 11572785
12. Y. Y. Chen, M. C. Jensen, C. D. Smolke, Genetic control of mammalian T-cell proliferation with synthetic RNA regulatory systems. *Proc. Natl. Acad. Sci. U.S.A.* **107**, 8531–8536 (2010). doi: 10.1073/pnas.1001721107; pmid: 20421500
13. M. Nizzardo *et al.*, Spinal muscular atrophy phenotype is ameliorated in human motor neurons by SMN increase via different novel RNA therapeutic approaches. *Sci. Rep.* **5**, 11746 (2015). doi: 10.1038/srep11746; pmid: 26123042
14. R. S. Finkel *et al.*, Treatment of infantile-onset spinal muscular atrophy with nusinersen: A phase 2, open-label, dose-escalation study. *Lancet* **388**, 3017–3026 (2016). doi: 10.1016/S0140-6736(16)31408-8; pmid: 27939059
15. L. Ye *et al.*, Genome editing using CRISPR-Cas9 to create the HPFH genotype in HSPCs: An approach for treating sickle cell disease and β-thalassemia. *Proc. Natl. Acad. Sci. U.S.A.* **113**, 10661–10665 (2016). doi: 10.1073/pnas.1612075113; pmid: 27601644
16. E. A. Traxler *et al.*, A genome-editing strategy to treat β-hemoglobinopathies that recapitulates a mutation associated with a benign genetic condition. *Nat. Med.* **22**, 987–990 (2016). doi: 10.1038/nm.4170; pmid: 27525524
17. P. Tebas *et al.*, Gene editing of *CCR5* in autologous CD4 T cells of persons infected with HIV. *N. Engl. J. Med.* **370**, 901–910 (2014). doi: 10.1056/NEJMoa1300662; pmid: 24597865
18. W. Qasim *et al.*, Molecular remission of infant B-ALL after infusion of universal TALEN gene-edited CAR T cells. *Sci. Transl. Med.* **9**, eaaj2013 (2017). doi: 10.1126/scitranslmed.aaj2013; pmid: 28123068
19. M. Tabebordbar *et al.*, In vivo gene editing in dystrophic mouse muscle and muscle stem cells. *Science* **351**, 407–411 (2016). doi: 10.1126/science.aad5177; pmid: 26721686
20. C. E. Nelson *et al.*, In vivo genome editing improves muscle function in a mouse model of Duchenne muscular dystrophy. *Science* **351**, 403–407 (2016). doi: 10.1126/science.aad5143; pmid: 26721684
21. C. Long *et al.*, Postnatal genome editing partially restores dystrophin expression in a mouse model of muscular dystrophy. *Science* **351**, 400–403 (2016). doi: 10.1126/science.aad5725; pmid: 26721683

22. A. C. Komor, Y. B. Kim, M. S. Packer, J. A. Zuris, D. R. Liu, Programmable editing of a target base in genomic DNA without double-stranded DNA cleavage. *Nature* **533**, 420–424 (2016). doi: 10.1038/nature17946; pmid: 27096365
23. N. M. Gaudelli *et al*., Programmable base editing of A•T to G•C in genomic DNA without DNA cleavage. *Nature* **551**, 464–471 (2017). pmid: 29160308
24. X. Xu *et al*., A CRISPR-based approach for targeted DNA demethylation. *Cell Discov.* **2**, 16009 (2016). doi: 10.1038/celldisc.2016.9; pmid: 27462456
25. S. Morita *et al*., Targeted DNA demethylation in vivo using dCas9-peptide repeat and scFv-TET1 catalytic domain fusions. *Nat. Biotechnol.* **34**, 1060–1065 (2016). doi: 10.1038/nbt.3658; pmid: 27571369
26. S. D. Perli, C. H. Cui, T. K. Lu, Continuous genetic recording with self-targeting CRISPR-Cas in human cells. *Science* **353**, aag0511 (2016). doi: 10.1126/science.aag0511; pmid: 27540006
27. S. Kiani *et al*., Cas9 gRNA engineering for genome editing, activation and repression. *Nat. Methods* **12**, 1051–1054 (2015). doi: 10.1038/nmeth.3580; pmid: 26344044
28. K. S. Manning, T. A. Cooper, The roles of RNA processing in translating genotype to phenotype. *Nat. Rev. Mol. Cell Biol.* **18**, 102–114 (2017). doi: 10.1038/nrm.2016.139; pmid: 27847391
29. D. Adams, paper presented at the First European Meeting for ATTR Amyloidosis for Doctors and Patients, Paris, France, 2 Nov 2017.
30. I. Sadowski, J. Ma, S. Triezenberg, M. Ptashne, GAL4-VP16 is an unusually potent transcriptional activator. *Nature* **335**, 563–564 (1988). doi: 10.1038/335563a0; pmid: 3047590
31. F. Zhang *et al*., Efficient construction of sequence-specific TAL effectors for modulating mammalian transcription. *Nat. Biotechnol.* **29**, 149–153 (2011). doi: 10.1038/nbt.1775; pmid: 21248753
32. J. K. Bialek *et al*., Targeted HIV-1 latency reversal using CRISPR/Cas9-derived transcriptional activator systems. *PLOS ONE* **11**, e0158294 (2016). doi: 10.1371/journal.pone.0158294; pmid: 27341108
33. O. O. Abudayyeh *et al*., RNA targeting with CRISPR-Cas13. *Nature* **550**, 280–284 (2017). pmid: 28976959
34. D. B. T. Cox *et al*., RNA editing with CRISPR-Cas13. *Science* **358**, 1019–1027 (2017). doi: 10.1126/science.aaq0180; pmid: 29070703
35. L. Mazzacurati *et al*., Use of miRNA response sequences to block off-target replication and increase the safety of an unattenuated, glioblastoma-targeted oncolytic HSV. *Mol. Ther.* **23**, 99–107 (2015). doi: 10.1038/mt.2014.177; pmid: 25200130
36. M. S. Kinch, An overview of FDA-approved biologics medicines. *Drug Discov. Today* **20**, 393–398 (2015). doi: 10.1016/j.drudis.2014.09.003; pmid: 25220442
37. H. Saito *et al*., Synthetic translational regulation by an L7Ae-kink-turn RNP switch. *Nat. Chem. Biol.* **6**, 71–78 (2010). doi: 10.1038/nchembio.273; pmid: 20016495
38. J. A. Stapleton *et al*., Feedback control of protein expression in mammalian cells by tunable synthetic translational inhibition. *ACS Synth. Biol.* **1**, 83–88 (2012). doi: 10.1021/sb200005w; pmid: 23651072
39. T. Quenault, T. Lithgow, A. Traven, PUF proteins: Repression, activation and mRNA localization. *Trends Cell Biol.* **21**, 104–112 (2011). doi: 10.1016/j.tcb.2010.09.013; pmid: 21115348
40. Y. Yagi, T. Nakamura, I. Small, The potential for manipulating RNA with pentatricopeptide repeat proteins. *Plant J.* **78**, 772–782 (2014). doi: 10.1111/tpj.12377; pmid: 24471963
41. G. Tamulaitis *et al*., Programmable RNA shredding by the type III-A CRISPR-Cas system of *Streptococcus thermophilus*. *Mol. Cell* **56**, 506–517 (2014). doi: 10.1016/j.molcel.2014.09.027; pmid: 25458845
42. R. H. J. Staals *et al*., RNA targeting by the type III-A CRISPR-Cas Csm complex of *Thermus thermophilus*. *Mol. Cell* **56**, 518–530 (2014). doi: 10.1016/j.molcel.2014.10.005; pmid: 25457165
43. M. R. O'Connell *et al*., Programmable RNA recognition and cleavage by CRISPR/Cas9. *Nature* **516**, 263–266 (2014). doi: 10.1038/nature13769; pmid: 25274302
44. O. O. Abudayyeh *et al*., C2c2 is a single-component programmable RNA-guided RNA-targeting CRISPR effector. *Science* **353**, aaf5573 (2016). doi: 10.1126/science.aaf5573; pmid: 27256883
45. A. A. Smargon *et al*., Cas13b is a type VI-B CRISPR-associated RNA-guided RNase differentially regulated by accessory proteins Csx27 and Csx28. *Mol. Cell* **65**, 618–630.e7 (2017). doi: 10.1016/j.molcel.2016.12.023; pmid: 28065598
46. J. S. Gootenberg *et al*., Nucleic acid detection with CRISPR-Cas13a/C2c2. *Science* **356**, 438–442 (2017). doi: 10.1126/science.aam9321; pmid: 28408723
47. L. A. Banaszynski, L.-C. Chen, L. A. Maynard-Smith, A. G. L. Ooi, T. J. Wandless, A rapid, reversible, and tunable method to regulate protein function in living cells using synthetic small molecules. *Cell* **126**, 995–1004 (2006). doi: 10.1016/j.cell.2006.07.025; pmid: 16959577
48. K. M. Bonger, L.-C. Chen, C. W. Liu, T. J. Wandless, Small-molecule displacement of a cryptic degron causes conditional protein degradation. *Nat. Chem. Biol.* **7**, 531–537 (2011). doi: 10.1038/nchembio.598; pmid: 21725303
49. H. K. Chung *et al*., Tunable and reversible drug control of protein production via a self-excising degron. *Nat. Chem. Biol.* **11**, 713–720 (2015). doi: 10.1038/nchembio.1869; pmid: 26214256
50. L. A. Banaszynski, M. A. Sellmyer, C. H. Contag, T. J. Wandless, S. H. Thorne, Chemical control of protein stability and function in living mice. *Nat. Med.* **14**, 1123–1127 (2008). doi: 10.1038/nm.1754; pmid: 18836461
51. P. Saxena, G. Charpin-El Hamri, M. Folcher, H. Zulewski, M. Fussenegger, Synthetic gene network restoring endogenous pituitary-thyroid feedback control in experimental Graves' disease. *Proc. Natl. Acad. Sci. U.S.A.* **113**, 1244–1249 (2016). doi: 10.1073/pnas.1514383113; pmid: 26787873
52. L. Schukur, B. Geering, G. Charpin-El Hamri, M. Fussenegger, Implantable synthetic cytokine converter cells with AND-gate logic treat experimental psoriasis. *Sci. Transl. Med.* **7**, 318ra201 (2015). doi: 10.1126/scitranslmed.aac4964; pmid: 26676608
53. C.-Y. Wu, K. T. Roybal, E. M. Puchner, J. Onuffer, W. A. Lim, Remote control of therapeutic T cells through a small molecule-gated chimeric receptor. *Science* **350**, aab4077 (2015). doi: 10.1126/science.aab4077; pmid: 26405231
54. P. Saxena *et al*., A programmable synthetic lineage-control network that differentiates human IPSCs into glucose-sensitive insulin-secreting beta-like cells. *Nat. Commun.* **7**, 11247 (2016). doi: 10.1038/ncomms11247; pmid: 27063289
55. U. S. Bhalla, R. Iyengar, Emergent properties of networks of biological signaling pathways. *Science* **283**, 381–387 (1999). doi: 10.1126/science.283.5400.381; pmid: 9888852
56. J. Meng, F. Muntoni, J. E. Morgan, Stem cells to treat muscular dystrophies–Where are we? *Neuromuscul. Disord.* **21**, 4–12 (2011). doi: 10.1016/j.nmd.2010.10.004; pmid: 21055938
57. J. N. Kochenderfer *et al*., B-cell depletion and remissions of malignancy along with cytokine-associated toxicity in a clinical trial of anti-CD19 chimeric-antigen-receptor-transduced T cells. *Blood* **119**, 2709–2720 (2012). doi: 10.1182/blood-2011-10-384388; pmid: 22160384
58. K. T. Roybal *et al*., Precision tumor recognition by T cells with combinatorial antigen-sensing circuits. *Cell* **164**, 770–779 (2016). doi: 10.1016/j.cell.2016.01.011; pmid: 26830879
59. L. Morsut *et al*., Engineering customized cell sensing and response behaviors using synthetic Notch receptors. *Cell* **164**, 780–791 (2016). doi: 10.1016/j.cell.2016.01.012; pmid: 26830878
60. C. A. Klebanoff, S. A. Rosenberg, N. P. Restifo, Prospects for gene-engineered T cell immunotherapy for solid cancers. *Nat. Med.* **22**, 26–36 (2016). doi: 10.1038/nm.4015; pmid: 26735408
61. K. T. Roybal *et al*., Engineering T cells with customized therapeutic response programs using synthetic Notch receptors. *Cell* **167**, 419–432.e16 (2016). doi: 10.1016/j.cell.2016.09.011; pmid: 27693353
62. N. Lapique, Y. Benenson, Digital switching in a biosensor circuit via programmable timing of gene availability. *Nat. Chem. Biol.* **10**, 1020–1027 (2014). pmid: 25306443
63. Y. Li *et al*., Modular construction of mammalian gene circuits using TALE transcriptional repressors. *Nat. Chem. Biol.* **11**, 207–213 (2015). doi: 10.1038/nchembio.1736; pmid: 25643171
64. L. Wroblewska *et al*., Mammalian synthetic circuits with RNA binding proteins for RNA-only delivery. *Nat. Biotechnol.* **33**, 839–841 (2015). pmid: 26237515
65. U. Sahin, K. Karikó, Ö. Türeci, mRNA-based therapeutics—Developing a new class of drugs. *Nat. Rev. Drug Discov.* **13**, 759–780 (2014). doi: 10.1038/nrd4278; pmid: 25233993
66. G. Mullokandov *et al*., High-throughput assessment of microRNA activity and function using microRNA sensor and decoy libraries. *Nat. Methods* **9**, 840–846 (2012). doi: 10.1038/nmeth.2078; pmid: 22751203
67. B. C. Heng, D. Aubel, M. Fussenegger, Prosthetic gene networks as an alternative to standard pharmacotherapies for metabolic disorders. *Curr. Opin. Biotechnol.* **35**, 37–45 (2015). doi: 10.1016/j.copbio.2015.01.010; pmid: 25679308
68. L. J. Aronne, A. E. Halseth, C. M. Burns, S. Miller, L. Z. Shen, Enhanced weight loss following coadministration of pramlintide with sibutramine or phentermine in a multicenter trial. *Obesity (Silver Spring)* **18**, 1739–1746 (2010). doi: 10.1038/oby.2009.478; pmid: 20094043
69. K. Rössger, G. Charpin-El-Hamri, M. Fussenegger, A closed-loop synthetic gene circuit for the treatment of diet-induced obesity in mice. *Nat. Commun.* **4**, 2825 (2013). doi: 10.1038/ncomms3825; pmid: 24281397
70. C. Kemmer *et al*., Self-sufficient control of urate homeostasis in mice by a synthetic circuit. *Nat. Biotechnol.* **28**, 355–360 (2010). doi: 10.1038/nbt.1617; pmid: 20351688
71. K. Rössger, G. Charpin-El Hamri, M. Fussenegger, Reward-based hypertension control by a synthetic brain-dopamine interface. *Proc. Natl. Acad. Sci. U.S.A.* **110**, 18150–18155 (2013). doi: 10.1073/pnas.1312414110; pmid: 24127594
72. D. Ausländer *et al*., A synthetic multifunctional mammalian pH sensor and CO_2 transgene-control device. *Mol. Cell* **55**, 397–408 (2014). doi: 10.1016/j.molcel.2014.06.007; pmid: 25018017
73. P. Bai *et al*., A synthetic biology-based device prevents liver injury in mice. *J. Hepatol.* **65**, 84–94 (2016). doi: 10.1016/j.jhep.2016.03.020; pmid: 27067456
74. H. Ye *et al*., *Self-adjusting synthetic gene circuit for correcting insulin resistance. Nat. Biomed. Eng.* **1**, 0005 (2017). doi: 10.1038/s41551-016-0005; pmid: 28480128
75. W.-H. Boehncke, M. P. Schön, Psoriasis. *Lancet* **386**, 983–994 (2015). doi: 10.1016/S0140-6736(14)61909-7; pmid: 26025581
76. A. Menter *et al*., Adalimumab therapy for moderate to severe psoriasis: A randomized, controlled phase III trial. *J. Am. Acad. Dermatol.* **58**, 106–115 (2008). doi: 10.1016/j.jaad.2007.09.010; pmid: 17936411
77. K. Ghoreschi *et al*., Interleukin-4 therapy of psoriasis induces Th2 responses and improves human autoimmune disease. *Nat. Med.* **9**, 40–46 (2003). doi: 10.1038/nm804; pmid: 12461524
78. K. Asadullah *et al*., Interleukin 10 treatment of psoriasis: Clinical results of a phase 2 trial. *Arch. Dermatol.* **135**, 187–192 (1999). doi: 10.1001/archderm.135.2.187; pmid: 10052405
79. J. A. N. Brophy, C. A. Voigt, Principles of genetic circuit design. *Nat. Methods* **11**, 508–520 (2014). doi: 10.1038/nmeth.2926; pmid: 24781324
80. D. Del Vecchio, Modularity, context-dependence, and insulation in engineered biological circuits. *Trends Biotechnol.* **33**, 111–119 (2015). doi: 10.1016/j.tibtech.2014.11.009; pmid: 25544476
81. C. Pan, C. Kumar, S. Bohl, U. Klingmueller, M. Mann, Comparative proteomic phenotyping of cell lines and primary cells to assess preservation of cell type-specific functions. *Mol. Cell. Proteomics* **8**, 443–450 (2009). doi: 10.1074/mcp.M800258-MCP200; pmid: 18952599
82. H. Clevers, Modeling development and disease with organoids. *Cell* **165**, 1586–1597 (2016). doi: 10.1016/j.cell.2016.05.082; pmid: 27315476
83. E. W. Esch, A. Bahinski, D. Huh, Organs-on-chips at the frontiers of drug discovery. *Nat. Rev. Drug Discov.* **14**, 248–260 (2015). doi: 10.1038/nrd4539; pmid: 25792263
84. M. Ogawa *et al*., Directed differentiation of cholangiocytes from human pluripotent stem cells. *Nat. Biotechnol.* **33**, 853–861 (2015). doi: 10.1038/nbt.3294; pmid: 26167630
85. L. Schukur, B. Geering, M. Fussenegger, Human whole-blood culture system for ex vivo characterization of designer-cell function. *Biotechnol. Bioeng.* **113**, 588–597 (2016). doi: 10.1002/bit.25828; pmid: 26348251
86. J. T. MacDonald, C. Barnes, R. I. Kitney, P. S. Freemont, G.-B. V. Stan, Computational design approaches and tools for synthetic biology. *Integr. Biol.* **3**, 97–108 (2011). doi: 10.1039/c0ib00077a; pmid: 21258712
87. A. A. K. Nielsen *et al*., Genetic circuit design automation. *Science* **352**, aac7341 (2016). doi: 10.1126/science.aac7341; pmid: 27034378

88. N. Davidsohn *et al*., Accurate predictions of genetic circuit behavior from part characterization and modular composition. *ACS Synth. Biol.* **4**, 673–681 (2015). doi: 10.1021/sb500263b; pmid: 25369267
89. J. Y. Dong, P. D. Fan, R. A. Frizzell, Quantitative analysis of the packaging capacity of recombinant adeno-associated virus. *Hum. Gene Ther.* **7**, 2101–2112 (1996). doi: 10.1089/hum.1996.7.17-2101; pmid: 8934224
90. A. L. Epstein, Progress and prospects: Biological properties and technological advances of herpes simplex virus type 1-based amplicon vectors. *Gene Ther.* **16**, 709–715 (2009). doi: 10.1038/gt.2009.42; pmid: 19369969
91. H. Yin *et al*., Non-viral vectors for gene-based therapy. *Nat. Rev. Genet.* **15**, 541–555 (2014). doi: 10.1038/nrg3763; pmid: 25022906
92. M. A. Maier *et al*., Biodegradable lipids enabling rapidly eliminated lipid nanoparticles for systemic delivery of RNAi therapeutics. *Mol. Ther.* **21**, 1570–1578 (2013). doi: 10.1038/mt.2013.124; pmid: 23799535
93. J. Hoggatt, Gene therapy for "Bubble Boy" disease. *Cell* **166**, 263 (2016). doi: 10.1016/j.cell.2016.06.049; pmid: 27419862
94. C. Kloks *et al*., A fit-for-purpose strategy for the risk-based immunogenicity testing of biotherapeutics: A European industry perspective. *J. Immunol. Methods* **417**, 1–9 (2015). doi: 10.1016/j.jim.2015.01.003; pmid: 25602137
95. A. C. Nathwani *et al*., Adenovirus-associated virus vector-mediated gene transfer in hemophilia B. *N. Engl. J. Med.* **365**, 2357–2365 (2011). doi: 10.1056/NEJMoa1108046; pmid: 22149959
96. A. C. Nathwani *et al*., Long-term safety and efficacy of factor IX gene therapy in hemophilia B. *N. Engl. J. Med.* **371**, 1994–2004 (2014). doi: 10.1056/NEJMoa1407309; pmid: 25409372
97. R. A. Maldonado *et al*., Polymeric synthetic nanoparticles for the induction of antigen-specific immunological tolerance. *Proc. Natl. Acad. Sci. U.S.A.* **112**, E156–E165 (2015). doi: 10.1073/pnas.1408686111; pmid: 25548186
98. T. K. Kishimoto *et al*., Improving the efficacy and safety of biologic drugs with tolerogenic nanoparticles. *Nat. Nanotechnol.* **11**, 890–899 (2016). doi: 10.1038/nnano.2016.135; pmid: 27479756
99. E. Sands, paper presented at the Annual European Congress of Rheumatology, Madrid, Spain, 15 June 2017.
100. R. M. Blaese *et al*., T lymphocyte-directed gene therapy for ADA$^-$ SCID: Initial trial results after 4 years. *Science* **270**, 475–480 (1995). doi: 10.1126/science.270.5235.475; pmid: 7570001
101. A. Aiuti, M. G. Roncarolo, L. Naldini, Gene therapy for ADA$^-$ SCID, the first marketing approval of an ex vivo gene therapy in Europe: Paving the road for the next generation of advanced therapy medicinal products. *EMBO Mol. Med.* **9**, 737–740 (2017). doi: 10.15252/emmm.201707573; pmid: 28396566
102. E. Dolgin, Epic $12 billion deal and FDA's approval raise CAR-T to new heights. *Nat. Biotechnol.* **35**, 891–892 (2017). doi: 10.1038/nbt1017-891; pmid: 29019995

ACKNOWLEDGMENTS

We thank S. Kiani for critical discussions. This work was supported by research grants to R.W. from the Defense Advanced Research Projects Agency (DARPA-BAA-11-23), the NIH (CA207029), and the NSF (CNS-1446607), and by the Ragon Institute of Massachusetts General Hospital (MGH), Massachusetts Institute of Technology (MIT), and Harvard. B.D. was supported by a fellowship from the NSF (GRFP 1122374). T.K., B.D., and R.W. are listed as coinventors on patents (granted or pending) assigned to MIT that relate to methods in mammalian synthetic biology.

10.1126/science.aad1067

Cite as: J. H. Gibcus *et al.*, *Science* 10.1126/science.aao6135 (2018).

A pathway for mitotic chromosome formation

Johan H. Gibcus,[1]* Kumiko Samejima,[2]* Anton Goloborodko,[3]* Itaru Samejima,[2] Natalia Naumova,[1] Johannes Nuebler,[3] Masato T. Kanemaki,[4] Linfeng Xie,[5] James R. Paulson,[5] William C. Earnshaw,[2]† Leonid A. Mirny,[3]† Job Dekker[1,6]†

[1]Program in Systems Biology, Department of Biochemistry and Molecular Pharmacology, University of Massachusetts Medical School, 368 Plantation Street, Worcester, MA 01605, USA. [2]Wellcome Centre for Cell Biology University of Edinburgh, King's Buildings, Max Born Crescent Edinburgh EH9 3BF, Scotland, UK. [3]Institute for Medical Engineering and Science, and Department of Physics, Massachusetts Institute of Technology, Cambridge, MA 02139, USA. [4]Division of Molecular Cell Engineering, National Institute of Genetics, Research Organization of Information and Systems (ROIS), and Department of Genetics, SOKENDAI, Yata 1111, Mishima, Shizuoka 411-8540, Japan. [5]Department of Chemistry, University of Wisconsin-Oshkosh, 800 Algoma Blvd, Oshkosh, WI 54901, USA. [6]Howard Hughes Medical Institute, 4000 Jones Bridge Road, Chevy Chase, MD 20815-6789, USA.

*These authors contributed equally to this work.

†Corresponding author. Email: bill.earnshaw@ed.ac.uk (W.C.E.); leonid@MIT.edu (L.A.M.); job.dekker@umassmed.edu (J.D.)

Mitotic chromosomes fold as compact arrays of chromatin loops. To identify the pathway of mitotic chromosome formation, we combined imaging and Hi-C of synchronous DT40 cell cultures with polymer simulations. We show that in prophase, the interphase organization is rapidly lost in a condensin-dependent manner and arrays of consecutive 60 kb loops are formed. During prometaphase ~80 kb inner loops are nested within ~400 kb outer loops. The loop array acquires a helical arrangement with consecutive loops emanating from a central spiral-staircase condensin scaffold. The size of helical turns progressively increases during prometaphase to ~12 Mb. Acute depletion of condensin I or II shows that nested loops form by differential action of the two condensins while condensin II is required for helical winding.

Chromosomes dramatically change their conformation as cells progress through the cell cycle. Throughout most of interphase, chromosomes of vertebrates display two layers of organization: topologically associating domains (TADs) (*1*, *2*) and A- and B-compartments (*3*). At a finer scale, chromatin looping between promoters, enhancers and CTCF-bound sites (*4*, *5*) facilitates gene regulation. During mitosis, these features disappear and chromosomes are compacted into dense arrays of randomly positioned consecutive chromatin loops (*6–9*).

Although the organization of these two states is now increasingly understood, much less is known about how cells convert from one state into the other. Previous microscopy observations revealed that chromosomes become recognizable during prophase and form linearly organized structures where sister chromatids are initially mixed (*10–13*). By late prophase, sister chromatid arms separate and each chromatid is thought to be organized as an array of loops that emanate from an axial core containing condensin complexes and topoisomerase II alpha (*14–18*). During prometaphase, the chromatids shorten and become thicker (*11*), ultimately forming fully condensed metaphase chromosomes (*19*). How compaction of loop arrays occurs during prometaphase is not known.

Here we employ a chemical-genetic system for highly synchronous entry of DT40 cells into prophase. DT40 cells are karyotypically stable, near diploid (fig. S1) and have been extensively used for analysis of mitotic chromosome organization (*20*). Use of chemical genetics (*21*) in this cell system allowed us to apply Hi-C with high temporal resolution and to determine how chromosome conformation changes as cells disassemble the interphase nucleus and form mitotic chromosomes (*22*, *23*). These data, combined with polymer simulations (*24*, *25*) and direct imaging reveal a mitotic chromosome morphogenesis pathway with distinct transitions, including compartment and TAD loss, loop array formation by late prophase and chromosome shortening during prometaphase through growing and winding of loops around a central helical scaffold. Using an auxin-inducible degron approach (*26*, *27*) we then identify distinct key roles for condensin I and II in this pathway.

Results

Synchronous progression into mitosis

To obtain cultures of cells that synchronously enter mitosis we arrested cells in G_2 by selectively inhibiting CDK1. We stably expressed a variant of *Xenopus laevis* CDK1 cDNA (CDK1as) harboring a F80G mutation in DT40 cells (*22*, *28*). This mutation renders CDK1as sensitive to inhibition by the ATP analog 1NM-PP1 (*22*). We then disrupted the endogenous CDK1 gene using CRISPR/Cas9. Growing cells for 10 hours in the presence of 1NM-PP1 efficiently arrested >90% of cells in

G_2 as indicated by FACS (table S1 and fig. S2) and by microscopy analysis of chromosome and nuclear morphology (Fig. 1A). Washing out 1NM-PP1 led to rapid release of cells from the G_2 arrest and synchronous entry into prophase.

This system allowed us to study chromosome morphogenesis by harvesting cells at sequential time points for imaging and Hi-C analysis as they synchronously progress through mitosis. For some cultures collected at later time points (30 - 60 min), we added nocodazole 30 min prior to their release from the 1NM-PP1 arrest, to block the metaphase-anaphase transition (see Methods). All time courses described here were performed in duplicate and results were highly concordant. DAPI staining showed the expected chromosome condensation and individualization in prophase (Fig. 1A). Nuclear envelope breakdown (NEBD) occurred around t = ~7 - 10 min as evidenced by staining for Lamin B1, which diffuses into the cytoplasm upon NEBD (fig. S3) (*29*) and by measuring the association of previously cytoplasmic condensin I subunits with the chromosomes (CAPD2, CAPG1, CAPH and increased levels of SMC2 and SMC4; fig. S4, A and B). Previous studies, and our proteomic analysis (fig. S4B) show that by late prophase, cohesin (SMC1 and SMC3) has dissociated from the arms of sister chromatids, which separate, but remain aligned (*11*, *12*, *30*, *31*). Chromosome shortening subsequently occurred during prometaphase and at the late time points fully condensed chromosomes were observed (Fig. 1A).

Loss of compartments and TADs in prophase

Hi-C analysis showed that G_2-arrested cells display all features characteristic of vertebrate interphase cells (*8*). First, chromosomes form territories as indicated by relatively high levels of intra-chromosomal interactions (*3*). Second, chromosomes display the characteristic pattern of active A- and inactive B- compartments as revealed by the plaid pattern of Hi-C interactions (*3*) (Fig. 1B). The locations of these compartments in G_2 resembled those detected in exponentially growing cells, though the compartment signal strength was stronger and the pattern sharper in the synchronous cells likely as a result of uniformity in cell cycle stage. Third, TADs were readily visible in the Hi-C interaction maps as squares of relatively high interaction frequencies along the diagonal (Fig. 1C). TAD boundaries were similar in position and strength to those in non-synchronous cells as determined using an insulation score calculated from a 250 kb sliding window (*32*) (fig. S5). Finally, we analyzed how contact frequency (P) of contacts between locus pairs depends on their genomic distance (s). $P(s)$ decays with genomic distance and this relationship changes with cell cycle stages (*8*). For G_2 cells, we found $P(s)$ to be highly similar to that observed previously in non-synchronous cells (figs. S6 and S7). Together, these analyses show that G_2 chromosomes, which are composed of two closely aligned and likely catenated sister chromatids, are organized similarly to G_1 chromosomes (*8*).

This interphase chromosomal organization was rapidly lost upon release of cells into prophase. As soon as 5 min after release we detected a marked reduction in the typical plaid pattern of long-range interactions, indicating a loss of compartments (Fig. 1B). By 10 min (late prophase) compartments were mostly gone. At the same time, TADs were also lost (Fig. 1C and fig. S8).

We used eigenvector decomposition to quantify the disappearance of compartments (*33*). The first eigenvector readily captured compartments at t = 0 and 2.5 min, but starting at t = 5 min it explained progressively less of the variance in the Hi-C interaction maps, indicating weakening of the compartment structure. By t = 7.5 min the strength of the first eigenvector fell to 17% (from 80% at t = 0 min) and by t = 10 min, it no longer captured compartments. Loss of compartments was also quantified by calculating the ratio of A-to-A or B-to-B interactions over A-to-B interactions over the time course. From t = 0 to t = 2.5 min and onward this fraction decreased steadily, indicating that preferential interactions within compartments are lost (Fig. 1D and fig. S9).

The strength of TADs can be quantified using the insulation score, which indicates the amount of contacts formed across a locus up to a certain distance (*32*). TAD boundaries have a low score (indicative of high insulation), whereas loci inside TADs show a high score value (no insulation). The genome-wide variance of insulation scores provides a quantitative measure of the presence of TADs (*8*). Starting at t = 2.5 min the variance of the insulation profiles progressively decreased, indicating loss of TADs (Fig. 1C and fig. S5B). By t = 7.5 min the variance was reduced more than 2-fold and by t = 10 min no TADs were detected. This conclusion was confirmed by plotting the average Hi-C interaction pattern at and around TAD boundaries identified in G_2 at different time points during mitosis (Fig. 1C). Insulation is strongest in G_2 and by late prophase insulation values are near background levels (quantified in fig. S10). We conclude that compartments and TADs disappear rapidly during early prophase.

By late prophase, when sister arms have resolved (*11*, *34*), and around the time of nuclear envelope breakdown (t ~ 7.5-10 min), the Hi-C maps are characterized by a general decay of contact frequency P with genomic distance s (Fig. 2A). The shape of the $P(s)$ curve changes as prophase progresses. In G_2 cells, it is shallow ($P(s) \sim s^{-0.5}$) up to a distance of several hundred kb, reflecting compaction within TADs (*35*, *36*), but for larger distances the decay becomes steeper. During prophase, the initial shallow decay extends for longer-range interactions, with a steeper drop at 2 Mb at t = 10 min, suggesting a higher degree of compaction. As we demonstrate below, this decay and shape are consistent with formation of a linearly arranged, layered organization of the chromosome (*8*), where

the size of each layer corresponds to the position of the steep drop in the $P(s)$ curve.

Appearance of a second diagonal band in Hi-C maps from prometaphase cells

At t = 15 min, when cells have entered prometaphase, the Hi-C maps produce a $P(s)$ curve with a drop at 2 Mb. Strikingly, a distinct second diagonal band appears, running in parallel with the primary diagonal for all loci and chromosomes (Fig. 1B and fig. S11). This second diagonal represents increased interaction frequencies between any pair of loci separated by around 3 Mb. At 15 min, this feature is clearly observed in $P(s)$ plots as a local peak at ~3 Mb (Fig. 3A and figs. S6 and S7). As cells progress through prometaphase, the position of the drop in $P(s)$ and the position of the second diagonal migrate to larger genomic distances (Fig. 3A and figs. S6 and S7). By t = 60 min, when compact metaphase chromosomes have formed, the second diagonal is positioned at ~12 Mb and appears more diffuse. The second diagonal appears in all chromosomal maps and its position is independent of chromosome size over two orders of magnitude (fig. S11). The appearance and movement of the second diagonal is not dependent or affected by nocodazole: no nocodazole was added to the t = 15 min sample, and a replicate Hi-C dataset obtained from a culture collected at t = 30 min in the absence of nocodazole was nearly identical to the data obtained in the presence of nocodazole (table S2 and figs. S7 and S8). Together, these $P(s)$ curves reveal a periodicity of interactions that reflects chromosome structure at the scale of megabases.

The only known regular periodic structural feature of chromosomes is helical coiling, which was first described in 1880 (*37*) and can be observed in certain chromosome preparations (*10*, *38–40*). Experimentally induced banding of the chromosome arms is much more irregular (*41*). In helical chromosomes with a pitch (the length of a complete turn) of ~3 Mb, each locus is in relatively close proximity to loci located one turn up or down the chromosome, i.e., 3 Mb up or downstream along the DNA. The progressive movement of the second diagonal band to larger distances during prometaphase would reflect an increased "winding up" and shortening of the helix.

Although this is the first Hi-C data revealing the helical coiling of chromosomes, the chicken DT40 late prometaphase (t = 60 min) Hi-C contact maps strongly resemble those for mitotic human HeLa S3 chromosomes that we had reported earlier (*8*). In fact, re-analysis of mitotic HeLa S3 Hi-C data in more detail by deeper sequencing revealed a weak second diagonal band at ~10 Mb distance (fig. S12), suggesting this periodic folding is a conserved feature of vertebrate mitotic chromosomes.

Testing models of chromosomes

Previous studies suggested that mitotic chromosomes are organized as arrays of consecutive loops emanating from a condensin-rich scaffold, forming a polymer bottlebrush (*42*, *43*), with a layered organization of loops (*6*, *19*, *44*). To understand chromosome organization at different stages of compaction we built coarse-grained models of chromosomes as arrays of loops aiming to reproduce $P(s)$ curves of Hi-C data, separately for each time point. In these models, a chromosome is represented by a cylinder with an axial scaffold; loop bases are arranged consecutively along the scaffold, and each chromatin loop, emanating from the scaffold in a particular direction, is represented by a blob of loci (Fig. 2B, see supplementary materials). Loops are regularly placed along the axis, with angular positions determined by a stochastic model; loop sizes are exponentially distributed and bases of loops are not positioned at defined genomic sequences or loci (*8*). Analysis of condensin ChIP data for DT40 cells (*45*) supports sequence-independent positioning for >95% of loops (supplementary materials, fig. S13; see discussion). For specific models of loop arrangements, presented below, the $P(s)$ curve can be found analytically as the return probability of a stochastic process describing angular positions of loops (see supplementary materials, section "Coarse-grained model of contact probability decay in mitotic chromosomes"). The resulting $P(s)$ always has three regions (Fig. 2B): (i) the intra-loop region at short separations, where two loci are likely to be within the same loop and $P(s)$ reflects the internal organization of loops; (ii) the "intra-layer" region at larger genomic separations, where loci are located on different loops within the same axial layer of the cylindrical chromosome and $P(s)$ reflects the specific arrangement of loops relative to each other; (iii) the "inter-layer" that appears as a steep drop in contact frequency at large genomic distances, where loci are located in loops that are so distant along the scaffold that their blobs can no longer overlap. In the $P(s)$ plot of experimental Hi-C data throughout mitosis, the intra-layer region and the drop-off can be readily discerned (Fig. 2, A and C).

Prophase chromosomes

The coarse-grained models show that the relative orientation of consecutive loops strongly affects the shape of the $P(s)$ curve in the intra-layer region. If the orientations of consecutive loops are independent of each other, the contact frequency $P(s)$ does not decay with genomic distance in the intra-layer region, as any pair of loops within a layer are equally likely to interact (Fig. 2C). In contrast, introducing correlations between orientations of consecutive loops, i.e., forcing neighboring loops to project in similar directions, makes them follow an angular random walk. The angular random walk is a 1D random walk on a circle and has a return probability of $P(s) \sim s^{-0.5}$ until the full turn is made by the walk.

The $P(s)\sim s^{-0.5}$ decay followed by a drop is in good agreement with the late prophase Hi-C data (t = 7-10 min – Fig. 2C). Taken together, these results suggest that by late prophase chromosomes are already organized into arrays of consecutive loops with correlated angular orientations.

We developed detailed polymer models to test whether specific classes of conformations can reproduce experimental Hi-C data, though they do not prove mechanisms by which these structures form. Further, all our simulations produce equilibrium models and do not reflect kinetics of chromosome folding. In these models, chromatin is represented as a 10 nm fiber (*46*, *47*), where one monomer corresponds to one nucleosome (Fig. 2D), allowing us to simulate up to 40 Mb of chromatin. Prophase chromosomes are modeled as arrays of consecutive loops of exponentially distributed length and random genomic locations, emanating from a flexible scaffold, as would result from a loop extrusion process (*48*). The loop array is further condensed by imposing poor solvent conditions to the density observed in electron microscopy (one nucleosome per 11×11×11nm cube, i.e., ~40% volume fraction) (*49*), while preserving the overall cylindrical shape of the chromosome (Fig. 2D). We systematically varied two parameters: the average loop size and the linear loop density along the chromosomal scaffold (Fig. 2E). For all combinations, we generated equilibrium conformations, simulated a Hi-C experiment, and evaluated its ability to reproduce $P(s)$ curves from Hi-C data for different time points during prophase (Fig. 2, E to H).

These polymer models can accurately reproduce $P(s)$ (20 kb < s < 4 Mb) for all prophase time points, in agreement with the prediction of the coarse-grained model (Fig. 2C). The best matching models for later prophase time points, when sister chromatids are separate and lie side-by-side, have gradually increasing average loop size: from 40-50 kb at t = 5 min to ~60-70 kb at t = 10 min (Fig. 2H), reproducing the gradually shifting position of the drop-off from 2 to 3.5Mb (i.e., increase of the layer size), while maintaining about the same ~50 loops per layer and ~250 loops per μm. These results are consistent with a model where loop arrays are formed early in prophase, and loop sizes grow gradually, e.g., by merging smaller adjacent loops (*25*). Thus, both coarse grained modes and polymer simulations indicate that by late prophase, chromosomes fold as dense arrays of loops, with consecutive loops positioned with correlated radial orientations.

Prometaphase spirals

A striking feature of prometaphase Hi-C data is the appearance of the second diagonal band, which appears as a distinct peak on the $P(s)$ curves (Fig. 3A). This feature cannot be explained by interactions between sister chromatids, as these become minimal in prometaphase, and simulations show that no amount of overlap between sisters gives rise to such periodic pattern in interactions (fig. S14). As argued above, periodic interactions seen by Hi-C are most readily explained by a helical organization of mitotic loop arrays, which has been observed microscopically (*6*, *10*, *40*, *50*). Two classes of chromosome architecture can give rise to periodicity in contact frequencies: an "external" helix when the whole chromosome is folded into a solenoid (*50*) (the solenoid model), and a "staircase" model in which consecutive loops wind in a helical order around a centrally located scaffold ("internal" helix). We note that by "scaffold" we do not necessarily imply a solid integrated structure stretching from one end of the chromosome to the other. The "scaffold" could equally be a dynamic association of smaller complexes linked by DNA that pack with helical symmetry. By modeling we examined these classes of architectures and the continuum of models in between them.

To explore whether an internal helix can arise through reorganization of loop orientations, while preserving the cylindrical morphology of the whole chromosome, we extended our coarse-grained prophase model (Fig. 2B) by adding a preferred angular orientation for each loop: (1) as in prophase, the orientation of each loop is correlated with its neighbors; (2) these loops have preferred, but not fixed, orientations that follow a helical path, thus winding around the chromosomal scaffold (Fig. 3B). Loops in this spiral staircase model follow an angular Ornstein-Uhlenbeck random walk with bias toward preferred positions, and $P(s)$ can be found analytically (*51*) (supplementary materials, section "Coarse-grained model of contact probability decay in mitotic chromosomes – loops with spiral staircase orientation"). This coarse-grained model yields a $P(s)$ curve that closely follows the experimental prometaphase $P(s)$ and displays both the $P(s)\sim s^{-0.5}$ decay and the narrow peak corresponding to the second diagonal band (Fig. 3C). These results indicate that, (i) the emergent second diagonal band in Hi-C data can result from a spiral organization, and (ii) such organization can arise from preferred orientations of loops around the central scaffold. Further support for a centrally located spiraling scaffold is provided by analysis of chromosome shape and SMC2-mAID-GFP, CAP-H-mAID-GFP or CAP-H2-mAID-GFP localization along mitotic chromosomes from colchicine arrested DT40 cells (Fig. 3B and figs. S15 and S16). We observe a pattern of condensin localization that is consistent with a helical path of the scaffold.

Detailed polymer modeling allowed us to explore a broader range of architectures, with both external and internal helices, and to obtain quantitative estimates of loop sizes and other aspects of organization. Two aspects of the prometaphase organization must be captured by any model: (i) a higher linear density of chromatin of up to 50-70 Mb/μm, necessitating an evolution of the loop architecture; and (ii) spiraling of the scaffold. The higher density of loops can be

achieved by a nested loop organization where several smaller (inner) loops are organized consecutively within each larger (outer) loop whose bases form the central axis (Fig. 3D). The presence of nested loops is an essential feature for prometaphase models, as models with a single layer of loops could not reproduce Hi-C $P(s)$ curves even when other parameters were varied (fig. S14B). To model helical architecture we made the scaffold follow a helical path in 3D, while allowing loops to adopt their equilibrium conformations within an otherwise cylindrical chromosome (Fig. 3D).

We systematically varied the model parameters, such as geometry of the spiral scaffold and loop sizes (Fig. 3E). This also probed different lengths and widths of chromosomes as the volume density was kept constant. For t = 30 min the best agreement was achieved for a relatively narrow internal spiral staircase-like scaffold (R=30-60nm) (Fig. 3, F and G). This spiral is much more narrow than the ~300nm diameter of the chromatid, and has a small pitch (the height of one turn, 100-200nm) (Fig. 3H). Interestingly, this spiral arrangement of loop bases can achieve helical winding of loops that reproduces the second diagonal in the interaction maps and the peak on the $P(s)$ curves for t = 15, 30 and 60 min (Fig. 3, F to H). Wider spiraling of the scaffold (Fig. 3G, III) approximating external helix architectures (*50*) failed to accurately reproduce $P(s)$ (fig. S14C). Taken together, coarse-grained and polymer models that agree with Hi-C data overwhelmingly support the spiral staircase ("internal" helix) architecture of the scaffold (I and II in Fig. 3G), and subsequent helical winding of loops.

Fitting consecutive time points probed by Hi-C, we found that the linear chromatin density of the best-matching models continued to grow throughout prometaphase, in agreement with the observed steadily shortening of mitotic chromosomes (Figs. 1A and 3H and fig. S18). Simulations show that shifting the peak in $P(s)$ to larger genomic distances representing the second diagonal in consecutive time points (Fig. 3A) can be achieved by increasing the radius of the helical scaffold from 30 to 100 nm, the radius of the chromatid from 300 to 360 nm, and increasing the pitch from 100 to 250 nm, while maintaining a constant outer and inner loop size (~400 kb and ~80 kb respectively) (Fig. 3H). These changes lead to the increase in amount of DNA (Mb) per turn of the spiral from ~3 Mb in early prometaphase up to ~12 Mb by late prometaphase.

Comparison of the dimensions of our best models with direct microscopic measurements of prometaphase chromosomes prepared according to the Hi-C protocol reveals good agreement between experiment and predictions (fig. S17).

Condensins are critical for prophase chromosome morphogenesis

To determine the role of condensin complexes in chromosome morphogenesis, we fused a minimal auxin inducible degron domain (mAID) to SMC2 (supplementary materials, table S3). In the presence of the plant F-box protein osTIR1, addition of auxin induces rapid proteasome-dependent degradation of the SMC2-mAID protein, thus disrupting both condensin I and II complexes (*18*, *26*, *27*). Incubation of cells for 3 hours in the presence of auxin during the1NM-PP1-induced G_2–arrest (supplementary materials) reduced SMC2 levels to <5% (fig. S19). Remarkably, this did not affect global chromosome organization as compartments and TADs were comparable to those in WT G_2 arrested cells (Fig. 4A and fig. S20). Cells entered prophase rapidly after washout of 1NM-PP1, and the onset of NEBD, as indicated by DAPI staining, occurred as in wild type at ~7-10 min (fig. S21).

Chromosomes in SMC2-depleted cells did not form well-resolved chromatids as cells progressed to prometaphase, confirming previous observations (fig. S21) (*18*, *52*–*54*). Chromatin in such cells lacks functional condensin (*55*, *56*), but nonetheless achieves a normal degree of chromatin compaction despite the absence of individualized chromosomes (*57*). FACS analysis confirmed that these cells are incapable of normal mitotic exit. They ultimately undergo mitotic slippage, forming tetraploid interphase cells (fig. S2).

Hi-C analysis revealed that in the absence of SMC2, interphase compartments and TADs were still present and largely unaffected by late prophase, at a time when they were completely disassembled in WT (t = 10 min, Fig. 4A and fig. S20A). NEBD and spindle assembly did occur; indicating cells progressed to physiological prometaphase. In prometaphase (t = 45 min and t = 75 min), compartments and TADs progressively weakened, but remained detectable (Fig. 4A and figs. S22 and S23). No second diagonal, characteristic for WT prometaphase ever appeared in Hi-C maps (Fig. 4A), instead $P(s)$ curves show little change from G_2 (figs. S20A and S24 to S26). Preferential A-to-A interactions and B-to-B interactions became progressively weaker (figs. S20A and S22A). Analysis of the variation of the insulation score along chromosomes indicated that TAD boundaries were reduced in strength but not eliminated (Fig. 4A and fig. S23). Further, removal of cohesin (SMC1/3) and CTCF from chromatin, as assessed by chromatin enrichment for proteomics (ChEP) (*58*) was delayed and reduced compared to WT (fig. S4D). This may explain the incomplete loss of TAD boundaries. Combined, these data reveal that condensin is not required for TAD and compartment architecture during interphase. In its absence, mitotic chromatin is compacted but chromosomes do not become individualized or acquire the normal mitotic morphology, while partially preserving elements of interphase architecture. This indicates (i) that compaction and formation of rod shaped mitotic chromosomes are two separate processes, as assumed by our model; and (ii) a critical role for

condensin is in the formation of proper morphology and internal organization of mitotic chromosomes, and in disassembly of the interphase architecture (*59*).

Condensin I and II play distinct roles in chromosome morphogenesis

Next, we determined the roles of condensin I and II separately. Condensin I and II bind chromatin independently (*52*, *56*, *60*, *61*), and recent in vitro mitotic chromosome assembly experiments show that they can act independently (*62*). Therefore, depletion of one condensin complex is unlikely to affect the other, though we cannot rule out more subtle interplay between the complexes. We fused auxin inducible degron domains to the condensin II-specific kleisin CAP-H2 (CAP-H2-mAID) or the condensin I-specific kleisin CAP-H (CAP-H-mAID) in CDK1as DT40 cells (supplementary methods). Addition of auxin lead to >95% protein depletion in G_2–arrested CAP-H-mAID or CAP-H2-mAID cells (fig. S19). Cells were then released from the G_2 block and chromosome conformation was determined by microscopy and Hi-C as cells progressed through mitosis.

Depleting either condensin I or II alone led to less severe phenotypes than depleting both together (fig. S21). In contrast to cells lacking both condensin I and II (SMC2-mAID), these cells exited mitosis within 3 hours after entry into prophase (fig. S2).

Comparison of Hi-C interaction matrices (Fig. 4, B and C, and fig. S20, B and C) and $P(s)$ curves (Fig. 5, A and B, and figs. S24, B and C; S25; and S26) for CAP-H and CAP-H2 depleted cells in late prometaphase (t = 30 min and 60 min) shows that they capture different aspects of the WT architecture. The $P(s)$ curve for CAP-H2-depleted cells, where only condensin I remains active, matches that of the intra-layer organization of WT up to ~6 Mb, and lacks the second diagonal band (Fig. 5B). The $P(s)$ curve for CAP-H depleted cells (active condensin II), matches that of WT only for the long-range organization (6-20 Mb), including the second diagonal band (Fig. 5B). CAP-H depleted cells have a much lower contact frequency between loci separated less than 6 Mb than do WT and CAP-H2 depleted cells. Thus, condensin I and II play distinct roles at different structural levels, in mitotic chromosome morphogenesis, providing a mechanistic explanation for earlier microscopic studies (*60*, *61*, *63*, *64*).

Helical winding during prometaphase requires condensin II

In condensin II-depleted cells, both A- and B-compartments and TADs were lost starting around the prophase-prometaphase transition (t = 10 - 15 min; Fig. 4B and figs. S20 and S22). In late prometaphase (t = 30 - 60 min), chromosomes in these cells were longer and narrower than WT chromosomes, as previously observed (*60*, *63*, *64*) (fig. S21). $P(s)$ curves for t = 10 and 15 min (early prometaphase) resembled those in WT for late prophase (t = 10 min; compare Fig. 5A with Fig. 2A), displaying a mild decay followed by a steep drop that is characteristic for a densely packed loop array (Fig. 2B). Most strikingly, CAP-H2 depletion prevented emergence of the second diagonal band in prometaphase in Hi-C contact frequency maps and $P(s)$ plots (Figs. 4B and 5B and fig. S20B and S24B).

The close similarity between CAP-H2 prometaphase and WT prophase Hi-C, and lack of the second diagonal, allowed us to model CAP-H2 chromosomes as a prophase-like array of a single layer of loops emanating from a flexible, non-helical scaffold. By systematically varying the loop size and the degree of linear compaction, we obtained excellent agreement with experimental $P(s)$ curves for ~40-60 kb loops, and a linear density of 15 Mb/μm for all prometaphase time points (Fig. 5, D and E). This linear density is 3-4 times smaller than that of WT prometaphase chromosomes (50-70 Mb/μm). These simulations indicate that in the absence of condensin II, prometaphase chromosomes form extended prophase-like loop arrays and do not progress to further longitudinal shortening and helical winding.

Condensin I modulates the internal organization of prometaphase helical layers

Cells depleted for CAP-H (fig. S19) seemed to progress through prophase normally: Hi-C data show a rapid loss of compartments and TADs (Fig. 4C and figs. S20C, S22, and S23) and by late prophase individual chromosomes were discerned by DAPI staining (fig. S21). Deviation from the WT morphogenesis pathway was observed during prometaphase, i.e., after NEBD, when the bulk of condensin I normally loads in WT (fig. S4, B and C). A second diagonal was observed at 30 min indicating helical winding of the chromatids (Fig. 4C and fig. S20C) but this was located at a genomic distance of ~12 Mb, which in WT cells was only observed at t = 60 min. Therefore, the progression to larger helical turns during prometaphase is accelerated in cells lacking CAP-H.

Despite a spiral organization, loss of condensin I leads to a different loop arrangement and folding, as seen from differences in the $P(s)$ curves: the intra-layer arrangement of loops shows a characteristic $P(s) \sim s^{-0.5}$ from 400 kb to ~3 Mb, with $P(s)$ for the s < 400 kb region having a different slope, possibly reflecting a different intra-loop organization. These features are captured well by the coarse-grained model with 200-400 kb loops emanating with correlated angular orientations from a spiral scaffold (Fig. 5G). This loop size agrees well with the sizes of outer loops in the best models for WT chromosomes at t = 60 min (Fig. 3H).

Strikingly, when we matched the t = 30 min $P(s)$ curve with the simulations of prometaphase chromosomes with helical scaffolds and nested loops, the best match was

achieved with either a single layer of 200 kb loops, or a nested system of loops, with 400 kb outer loops and 200 kb inner loops (Fig. 5F). Together these results suggest that CAP-H (condensin I) is essential for formation of short (60-80 kb) inner loops but is dispensable for ~200-400 kb outer loops emanating from a helical staircase scaffold. The helical arrangement appears weaker in condensin I depleted chromosomes, as illustrated by the reduced strength of the second diagonal and reduced peaks in the $P(s)$ plots. One possible reason for this could be the much larger loop sizes in condensin I depleted chromosomes that may allow larger disorder in their angular arrangement. Taken together, our data obtained with CAP-H and CAP-H2 depleted cells support the formation of nested loops during prometaphase.

Discussion

We delineate a folding pathway from interphase to metaphase at minute time resolution. Hi-C data reveal a periodic pattern of interactions that we show to be consistent with a spiral staircase model of mitotic chromosome folding. This model unifies many disparate observations made over the last several decades. We demonstrate that mitotic chromosomes have nested loops that are formed by differential action of condensin I and II, with condensin II being required for helical coiling of mitotic chromosomes. Finally, we find that condensins are required for the timely loss of the interphase nuclear architecture.

A mitotic chromosome morphogenesis pathway

The data and modeling presented here suggest a chromosome morphogenesis pathway by which cells convert interphase chromosome organization into compacted mitotic chromosomes (Fig. 6). Together, our imaging and Hi-C data, coarse-grained models and polymer simulations, and previous observations (*11*) reveal that interphase features such as compartments and TADs are lost within minutes upon entry into prophase, in a condensin-dependent process and by late prophase, chromosomes are organized as radial loop arrays. The mechanism by which TADs and compartments are lost is not known, but our data show that condensin is required. Additional contributing factors could include loss of CTCF and cohesin binding (fig. S4, B and C) and increased levels of loop extrusion that can erase boundaries even when CTCF is still bound (supplementary materials, fig. S27). Importantly, activation of the mitotic kinase cascade is not sufficient to disassemble interphase chromatin organization without the action of condensin.

Our models that achieve best agreement with Hi-C data show that during prophase, condensin II-dependent loops grow from 30-40 kb to 60 kb in size, leading to a ~2-fold increase in linear chromatin density from ~7 Mb/μm to 15 Mb/μm. Condensins at loop bases form a chromosomal scaffold (*19*, *62*), which may be a dynamic, rather than static structure, and loops are arranged consecutively along it (one loop every ~5 nm of the axis). Interestingly, the radial arrangement of loops around the central flexible scaffold is not random, with consecutive loops projecting in similar directions i.e., with an angularly correlated arrangement.

Chromosomes shorten along their longitudinal axis and become wider during prometaphase. Our simulations show that condensin II loops continue to grow to 200-400 kb by 30 min and 400-700 kb by 60 min, accompanied by an increase in the linear chromatin density, which reaches 60 Mb/μm. However, two important reorganizations take place during prometaphase. First, large condensin II-mediated loops are subdivided into smaller 80 kb loops in a condensin I-dependent process, thus producing a nested loop arrangement with ~400 kb outer loops and ~80 kb inner loops. Second, the loop array acquires a helical arrangement as evidenced by the appearance of a second diagonal band in Hi-C maps for all loci and chromosomes. Models show that this helical arrangement of loops can be achieved if the scaffold forms a narrow helical "spiral staircase" inside an otherwise homogeneous cylindrical chromosome. Interestingly, the radius, the height of each turn (pitch) and kb/turn of this helix continue to grow through prometaphase, and this growth is to some extent restrained by condensin I. An emerging model of the prometaphase chromosome thus has a central helical scaffold formed by condensin II (*62*) that organizes 200-400 kb outer loops, that are further subdivided into 80 kb condensin I-mediated inner loops in order to achieve a high volume density.

Chromosomes in DT40 cells range in size from almost 200 Mb to less than 1 Mb. Our Hi-C analysis shows that the organization of prophase and prometaphase chromosomes is largely independent of their length: the size of loops and the amount of DNA per helical turn is the same for all chromosomes larger than 10-20 Mb (fig. S11). For the chromosomes that are shorter than one turn of the helix (which together contain <6% of the chicken genome) we do not see the second diagonal in the Hi-C maps, indicating that, as expected, the scaffold is too short and cannot complete a full helical turn. (fig. S11). Simulating the structure of short (<10-20 Mb) chromosomes is difficult because most of their chromatin is close to a telomere or a centromere, which may affect its organization, and our models do not describe how DNA is arranged at the tips of the chromosomes.

Comparison to previous and classical studies

While specific details of this model emerge from an unbiased fitting of models to the data, the emerging organization and its quantitative characteristics agree with earlier studies. First, the 60-80 kb sizes of the inner loops are remarkably

similar to values suggested by an extensive survey of the literature (*44*), measurements from electron microscopy (*6*, *19*) and Hi-C analysis of mitotic HeLa cells (*8*). Similarly, changes of linear density from prophase to prometaphase in the best models (from 15 Mb/μm to 50 Mb/μm) are consistent with prophase chromosomes being at least two-fold longer than metaphase chromosomes (*11*, *61*).

Second, helical prometaphase chromosomes have long been observed in certain chromosome preparations (*10*, *37*, *38*, *40*), and this has led to diverse models for how mitotic chromosomes are folded. Our analysis of Hi-C data indicates that the prometaphase chromosome is organized around a helical central region or scaffold: loops emanate with helical packing from a centrally located "spiral staircase" scaffold. Modeling shows that other helical arrangements of loop arrays, e.g., coiling of the entire loop array itself (*40*, *50*, *65*, *66*), are not consistent with our Hi-C data.

Our helical scaffold/loop model unifies a range of models and observations made over the years. It explains how a helical chromatin packing arrangement can be achieved while scaffold proteins such as condensins and topoisomerase II are localized centrally (*15–17*), within a cylindrical chromatid that is not obviously helical when visualized with a DNA dye such as DAPI (*67*). Interestingly, by late prometaphase we estimate the height of one helical turn to be around 200 nm, which is also the size of the layer (12 Mb layer at linear density 60 Mb/um), and is consistent with microscope observations suggesting that consecutive genomic loci follow a helical gyre with a pitch of ~250 nm within the cylindrical shape of chromatids (*68*).

Possible mechanisms

Such loop arrangements can naturally emerge due to a process of loop extrusion. Loop extrusion has been hypothesized as a mechanism of chromosome compaction (*69*, *70*) and most recently examined by simulations (*25*, *48*, *71*) and supported by single-molecule studies (*72*). In this process, each condensin starts forming a progressively larger loop until it dissociates or stops being blocked by neighboring condensins or other DNA-binding proteins. A recent study demonstrated that this process can form an array of consecutive loops (*8*) with condensins forming a central scaffold in the middle of a cylindrical chromosome (*48*), essential features of mitotic chromosomes. We note that sister chromatids are resolved by late prophase (*11–13*) indicating that the formation of loop arrays occurs as sister chromatid arms become separated.

Another aspect of loop extrusion is that loop sizes are established by a dynamic process of condensin exchange, without a need for barrier elements or specific loading sites (*25*). This is consistent with our Hi-C data that suggests that loop bases are not positioned at specific reproducible positions (e.g., scaffold or matrix attachment regions - (*73*, *74*)) in a population of cells. Analysis of published chromatin immunoprecipitation data for SMC2 in mitotic DT40 cells (*45*) shows a low level of condensin binding throughout the genome and only very few loci enriched in condensin binding: only 289 sites show more than a 5-fold enrichment compared to DNA input and 4,617 sites show over 2-fold enrichment. These numbers are much lower than the 16,000 inner loops our data and models predict. Interestingly, the condensin-enriched sites do show a Hi-C interaction pattern consistent with them being at the bases of loops slightly more frequently than other loci (supplementary materials, fig. S13). Based on these analyses, we estimate that over 95% of mitotic loops are not positioned at specific loci.

Simulations show that loop extrusion slowly approaches steady state by exchanging condensins and gradually increasing loop sizes during this process (*25*). This is consistent with gradual growth of loops up to 500 kb by slowly-exchanging condensin II, and relatively rapid formation of 60-80 kb inner loops by the more rapidly exchanging condensin I (*75*).

Formation of nested loops was critical for our polymer simulations to reproduce prometaphase Hi-C data because only this allowed a higher linear chromatin density. In this architecture, the outer loop bases are located at the central scaffold, while the inner, nested loop bases are radially displaced. Our analysis of condensin I or II depletion reveals that condensin II generates outer loops and condensin I generates inner loops. Our simulations reveal that this nested loop arrangement can be explained by the longer half-life of condensin II and shorter half life of condensin I on chromatin as measured by FRAP (*75*) (supplementary materials, movie S1). Indeed, nested loops only form in prometaphase, when condensin I gains access to chromatin. Thus, loop extrusion models can explain the nested loop arrangement of condensed mitotic chromosomes.

Why condensin II-based scaffolds only acquire helicity in prometaphase, and not in prophase is not known, but this could involve interactions with other proteins, such as DNA topoisomerase IIalpha or KIF4A. Our estimates of the radius of the prometaphase scaffold of 30-100 nm is consistent with a 50 nm length of SMC coiled coils that can interact with each other through HEAT repeats (*76*) which are known for ability to self-assemble into a helical "spiral staircase" (*77*). Gradual formation of such a HEAT-mediated staircase and binding of other factors can explain how the pitch and the radius of the helix increase in time.

We note that mitotic chromatin still condenses in the absence of both condensin I and II, although individualized rod-shaped chromosomes are not formed and cells cannot progress into anaphase. This indicates that there are other mechanisms by which chromatin fibers become compacted during mitosis. Our simulations also show that to achieve agreement

with Hi-C data, chromatin should also be condensed (computationally analogous to poor solvent conditions) forming densely packed chromatin loops within mitotic chromosomes analogous to the dense packing of chromatin observed in mitotic chromosomes by electron microscopy (*46*, *78*, *79*). The molecular basis for this compaction is not known but may involve mitosis-specific chromatin modifications (*80*, *81*) or active motor proteins such as KIF4A (*82*, *83*).

The chromosome morphogenesis pathway described here, and the identification of distinct architectural roles for condensin I and II in organizing chromosomes as nested loop arrays winding around a helical "spiral staircase" scaffold within a cylindrical chromatid can guide future experiments to uncover the molecular mechanisms by which these complexes, and other key components such as topoisomerase IIalpha and KIF4A, act in generating, (re-)arranging and condensing chromatin loops to build the mitotic chromosome.

Methods summary

DT40 Cell cultures synchronously entering mitosis were analyzed by Hi-C, imaging and proteomics to determine the structure of chromosomes. Hi-C data were used to quantify chromosome compartmentalization and to derive relationships between contact frequency P and genomic distance s. Coarse grained models and equilibrium polymer simulations were performed to test models of prophase and prometaphase chromosome organization against Hi-C data, and to identify best fitting parameters for size of loops, helical turn and pitch, linear density (Mb/micron chromosome length). Imaging of chromosome dimensions and condensin localization were performed to validate model predictions. Cell lines expressing condensin subunits fused to auxin-inducible degron domains were used to efficiently deplete these subunits prior to cells entering mitosis. Hi-C and imaging analysis were then performed to assess the effects of depletion of condensins on mitotic chromosome formation. Detailed procedures for all methods are described in the supplementary materials.

REFERENCES AND NOTES

1. J. R. Dixon, S. Selvaraj, F. Yue, A. Kim, Y. Li, Y. Shen, M. Hu, J. S. Liu, B. Ren, Topological domains in mammalian genomes identified by analysis of chromatin interactions. *Nature* **485**, 376–380 (2012). doi:10.1038/nature11082 Medline
2. E. P. Nora, B. R. Lajoie, E. G. Schulz, L. Giorgetti, I. Okamoto, N. Servant, T. Piolot, N. L. van Berkum, J. Meisig, J. Sedat, J. Gribnau, E. Barillot, N. Blüthgen, J. Dekker, E. Heard, Spatial partitioning of the regulatory landscape of the X-inactivation centre. *Nature* **485**, 381–385 (2012). doi:10.1038/nature11049 Medline
3. E. Lieberman-Aiden, N. L. van Berkum, L. Williams, M. Imakaev, T. Ragoczy, A. Telling, I. Amit, B. R. Lajoie, P. J. Sabo, M. O. Dorschner, R. Sandstrom, B. Bernstein, M. A. Bender, M. Groudine, A. Gnirke, J. Stamatoyannopoulos, L. A. Mirny, E. S. Lander, J. Dekker, Comprehensive mapping of long-range interactions reveals folding principles of the human genome. *Science* **326**, 289–293 (2009). doi:10.1126/science.1181369 Medline
4. S. S. Rao, M. H. Huntley, N. C. Durand, E. K. Stamenova, I. D. Bochkov, J. T. Robinson, A. L. Sanborn, I. Machol, A. D. Omer, E. S. Lander, E. L. Aiden, A 3D map of the human genome at kilobase resolution reveals principles of chromatin looping. *Cell* **159**, 1665–1680 (2014). doi:10.1016/j.cell.2014.11.021 Medline
5. A. Sanyal, B. R. Lajoie, G. Jain, J. Dekker, The long-range interaction landscape of gene promoters. *Nature* **489**, 109–113 (2012). doi:10.1038/nature11279 Medline
6. W. C. Earnshaw, U. K. Laemmli, Architecture of metaphase chromosomes and chromosome scaffolds. *J. Cell Biol.* **96**, 84–93 (1983). doi:10.1083/jcb.96.1.84 Medline
7. M. P. Marsden, U. K. Laemmli, Metaphase chromosome structure: Evidence for a radial loop model. *Cell* **17**, 849–858 (1979). doi:10.1016/0092-8674(79)90325-8 Medline
8. N. Naumova, M. Imakaev, G. Fudenberg, Y. Zhan, B. R. Lajoie, L. A. Mirny, J. Dekker, Organization of the mitotic chromosome. *Science* **342**, 948–953 (2013). doi:10.1126/science.1236083 Medline
9. T. Nagano, Y. Lubling, C. Várnai, C. Dudley, W. Leung, Y. Baran, N. Mendelson Cohen, S. Wingett, P. Fraser, A. Tanay, Cell-cycle dynamics of chromosomal organization at single-cell resolution. *Nature* **547**, 61–67 (2017). doi:10.1038/nature23001 Medline
10. Y. Ohnuki, Structure of chromosomes. I. Morphological studies of the spiral structure of human somatic chromosomes. *Chromosoma* **25**, 402–428 (1968). doi:10.1007/BF02327721 Medline
11. Z. Liang, D. Zickler, M. Prentiss, F. S. Chang, G. Witz, K. Maeshima, N. Kleckner, Chromosomes progress to metaphase in multiple discrete steps via global compaction/expansion cycles. *Cell* **161**, 1124–1137 (2015). doi:10.1016/j.cell.2015.04.030 Medline
12. K. Nagasaka, M. J. Hossain, M. J. Roberti, J. Ellenberg, T. Hirota, Sister chromatid resolution is an intrinsic part of chromosome organization in prophase. *Nat. Cell Biol.* **18**, 692–699 (2016). doi:10.1038/ncb3353 Medline
13. L. L. Moore, M. B. Roth, HCP-4, a CENP-C-like protein in *Caenorhabditis elegans*, is required for resolution of sister centromeres. *J. Cell Biol.* **153**, 1199–1208 (2001). doi:10.1083/jcb.153.6.1199 Medline
14. K. W. Adolphs, S. M. Cheng, J. R. Paulson, U. K. Laemmli, Isolation of a protein scaffold from mitotic HeLa cell chromosomes. *Proc. Natl. Acad. Sci. U.S.A.* **74**, 4937–4941 (1977). doi:10.1073/pnas.74.11.4937 Medline
15. W. C. Earnshaw, M. M. Heck, Localization of topoisomerase II in mitotic chromosomes. *J. Cell Biol.* **100**, 1716–1725 (1985). doi:10.1083/jcb.100.5.1716 Medline
16. S. M. Gasser, U. K. Laemmli, The organisation of chromatin loops: Characterization of a scaffold attachment site. *EMBO J.* **5**, 511–518 (1986). Medline
17. Y. Saitoh, U. K. Laemmli, Metaphase chromosome structure: Bands arise from a differential folding path of the highly AT-rich scaffold. *Cell* **76**, 609–622 (1994). doi:10.1016/0092-8674(94)90502-9 Medline
18. K. Samejima, I. Samejima, P. Vagnarelli, H. Ogawa, G. Vargiu, D. A. Kelly, F. de Lima Alves, A. Kerr, L. C. Green, D. F. Hudson, S. Ohta, C. A. Cooke, C. J. Farr, J. Rappsilber, W. C. Earnshaw, Mitotic chromosomes are compacted laterally by KIF4 and condensin and axially by topoisomerase IIα. *J. Cell Biol.* **199**, 755–770 (2012). doi:10.1083/jcb.201202155 Medline
19. J. R. Paulson, U. K. Laemmli, The structure of histone-depleted metaphase chromosomes. *Cell* **12**, 817–828 (1977). doi:10.1016/0092-8674(77)90280-X Medline
20. M. Okada, T. Hori, T. Fukagawa, The DT40 system as a tool for analyzing kinetochore assembly. *Subcell. Biochem.* **40**, 91–106 (2006). Medline
21. A. C. Bishop, K. Shah, Y. Liu, L. Witucki, C. Kung, K. M. Shokat, Design of allele-specific inhibitors to probe protein kinase signaling. *Curr. Biol.* **8**, 257–266 (1998). doi:10.1016/S0960-9822(98)70198-8 Medline
22. H. Hochegger, D. Dejsuphong, E. Sonoda, A. Saberi, E. Rajendra, J. Kirk, T. Hunt, S. Takeda, An essential role for Cdk1 in S phase control is revealed via chemical genetics in vertebrate cells. *J. Cell Biol.* **178**, 257–268 (2007). doi:10.1083/jcb.200702034 Medline
23. K. Samejima, H. Ogawa, C. A. Cooke, D. F. Hudson, F. Macisaac, S. A. Ribeiro, P. Vagnarelli, S. Cardinale, A. Kerr, F. Lai, S. Ruchaud, Z. Yue, W. C. Earnshaw, A promoter-hijack strategy for conditional shutdown of multiply spliced essential cell cycle genes. *Proc. Natl. Acad. Sci. U.S.A.* **105**, 2457–2462 (2008). doi:10.1073/pnas.0712083105 Medline
24. G. Fudenberg, M. Imakaev, C. Lu, A. Goloborodko, N. Abdennur, L. A. Mirny, Formation of chromosomal domains by loop extrusion. *Cell Reports* **15**, 2038–

2049 (2016). doi:10.1016/j.celrep.2016.04.085 Medline
25. A. Goloborodko, J. F. Marko, L. A. Mirny, Chromosome compaction by active loop extrusion. *Biophys. J.* **110**, 2162–2168 (2016). doi:10.1016/j.bpj.2016.02.041 Medline
26. A. J. Holland, D. Fachinetti, J. S. Han, D. W. Cleveland, Inducible, reversible system for the rapid and complete degradation of proteins in mammalian cells. *Proc. Natl. Acad. Sci. U.S.A.* **109**, E3350–E3357 (2012). doi:10.1073/pnas.1216880109 Medline
27. K. Nishimura, T. Fukagawa, H. Takisawa, T. Kakimoto, M. Kanemaki, An auxin-based degron system for the rapid depletion of proteins in nonplant cells. *Nat. Methods* **6**, 917–922 (2009). doi:10.1038/nmeth.1401 Medline
28. E. Sonoda, M. Takata, Y. M. Yamashita, C. Morrison, S. Takeda, Homologous DNA recombination in vertebrate cells. *Proc. Natl. Acad. Sci. U.S.A.* **98**, 8388–8394 (2001). doi:10.1073/pnas.111006398 Medline
29. S. D. Georgatos, A. Pyrpasopoulou, P. A. Theodoropoulos, Nuclear envelope breakdown in mammalian cells involves stepwise lamina disassembly and microtubule-drive deformation of the nuclear membrane. *J. Cell Sci.* **110**, 2129–2140 (1997). Medline
30. I. C. Waizenegger, S. Hauf, A. Meinke, J. M. Peters, Two distinct pathways remove mammalian cohesin from chromosome arms in prophase and from centromeres in anaphase. *Cell* **103**, 399–410 (2000). doi:10.1016/S0092-8674(00)00132-X Medline
31. A. Losada, M. Hirano, T. Hirano, Cohesin release is required for sister chromatid resolution, but not for condensin-mediated compaction, at the onset of mitosis. *Genes Dev.* **16**, 3004–3016 (2002). doi:10.1101/gad.249202 Medline
32. E. Crane, Q. Bian, R. P. McCord, B. R. Lajoie, B. S. Wheeler, E. J. Ralston, S. Uzawa, J. Dekker, B. J. Meyer, Condensin-driven remodelling of X chromosome topology during dosage compensation. *Nature* **523**, 240–244 (2015). doi:10.1038/nature14450 Medline
33. M. Imakaev, G. Fudenberg, R. P. McCord, N. Naumova, A. Goloborodko, B. R. Lajoie, J. Dekker, L. A. Mirny, Iterative correction of Hi-C data reveals hallmarks of chromosome organization. *Nat. Methods* **9**, 999–1003 (2012). doi:10.1038/nmeth.2148 Medline
34. S. Abe, K. Nagasaka, Y. Hirayama, H. Kozuka-Hata, M. Oyama, Y. Aoyagi, C. Obuse, T. Hirota, The initial phase of chromosome condensation requires Cdk1-mediated phosphorylation of the CAP-D3 subunit of condensin II. *Genes Dev.* **25**, 863–874 (2011). doi:10.1101/gad.2016411 Medline
35. W. Schwarzer *et al.*, Two independent modes of chromosome organization are revealed by cohesin removal. *bioRxiv* (2016) (available at http://biorxiv.org/content/early/2016/12/15/094185.abstract).
36. E. P. Nora, A. Goloborodko, A.-L. Valton, J. H. Gibcus, A. Uebersohn, N. Abdennur, J. Dekker, L. A. Mirny, B. G. Bruneau, Targeted degradation of CTCF decouples local insulation of chromosome domains from genomic compartmentalization. *Cell* **169**, 930–944.e22 (2017). doi:10.1016/j.cell.2017.05.004 Medline
37. J. Baranetzky, Die Kerntheilung in den Pollenmutterzellen einiger Tradescantien. *Bot. Zeitung* **38**, 281–296 (1880).
38. Y. Kuwada, Chromosome structure: A critical review. *Cytologia* **10**, 213–256 (1939). doi:10.1508/cytologia.10.213
39. C. L. Woodcock, L. L. Frado, J. B. Rattner, The higher-order structure of chromatin: Evidence for a helical ribbon arrangement. *J. Cell Biol.* **99**, 42–52 (1984). doi:10.1083/jcb.99.1.42 Medline
40. E. B. de la Tour, U. K. Laemmli, The metaphase scaffold is helically folded: Sister chromatids have predominantly opposite helical handedness. *Cell* **55**, 937–944 (1988). doi:10.1016/0092-8674(88)90239-5 Medline
41. J. M. Craig, W. A. Bickmore, Chromosome bands—Flavours to savour. *BioEssays* **15**, 349–354 (1993). doi:10.1002/bies.950150510 Medline
42. J. Paturej, S. S. Sheiko, S. Panyukov, M. Rubinstein, Molecular structure of bottlebrush polymers in melts. *Sci. Adv.* **2**, e1601478 (2016). doi:10.1126/sciadv.1601478 Medline
43. J. F. Marko, E. D. Siggia, Polymer models of meiotic and mitotic chromosomes. *Mol. Biol. Cell* **8**, 2217–2231 (1997). doi:10.1091/mbc.8.11.2217 Medline
44. K. J. Pienta, D. S. Coffey, A structural analysis of the role of the nuclear matrix and DNA loops in the organization of the nucleus and chromosome. *J. Cell Sci. Suppl.* **1984**, 123–135 (1984). doi:10.1242/jcs.1984.Supplement_1.9 Medline
45. J. H. Kim, T. Zhang, N. C. Wong, N. Davidson, J. Maksimovic, A. Oshlack, W. C. Earnshaw, P. Kalitsis, D. F. Hudson, Condensin I associates with structural and gene regulatory regions in vertebrate chromosomes. *Nat. Commun.* **4**, 2537 (2013). doi:10.1038/ncomms3537 Medline
46. H. D. Ou, S. Phan, T. J. Deerinck, A. Thor, M. H. Ellisman, C. C. O'Shea, ChromEMT: Visualizing 3D chromatin structure and compaction in interphase and mitotic cells. *Science* **357**, eaag0025 (2017). doi:10.1126/science.aag0025 Medline
47. Y. Nishino, M. Eltsov, Y. Joti, K. Ito, H. Takata, Y. Takahashi, S. Hihara, A. S. Frangakis, N. Imamoto, T. Ishikawa, K. Maeshima, Human mitotic chromosomes consist predominantly of irregularly folded nucleosome fibres without a 30-nm chromatin structure. *EMBO J.* **31**, 1644–1653 (2012). doi:10.1038/emboj.2012.35 Medline
48. A. Goloborodko, M. V. Imakaev, J. F. Marko, L. Mirny, Compaction and segregation of sister chromatids via active loop extrusion. *eLife* **5**, e14864 (2016). doi:10.7554/eLife.14864 Medline
49. D. G. Booth, A. J. Beckett, O. Molina, I. Samejima, H. Masumoto, N. Kouprina, V. Larionov, I. A. Prior, W. C. Earnshaw, 3D-CLEM reveals that a major portion of mitotic chromosomes is not chromatin. *Mol. Cell* **64**, 790–802 (2016). doi:10.1016/j.molcel.2016.10.009 Medline
50. J. B. Rattner, C. C. Lin, Radial loops and helical coils coexist in metaphase chromosomes. *Cell* **42**, 291–296 (1985). doi:10.1016/S0092-8674(85)80124-0 Medline
51. B. D. Hughes, *Random Walks and Random Environments* (Clarendon Press, 1995; https://global.oup.com/academic/product/random-walks-and-random-environments-9780198537885?cc=us&lang=en&).
52. T. Hirota, D. Gerlich, B. Koch, J. Ellenberg, J.-M. Peters, Distinct functions of condensin I and II in mitotic chromosome assembly. *J. Cell Sci.* **117**, 6435–6445 (2004). doi:10.1242/jcs.01604 Medline
53. T. Ono, Y. Fang, D. L. Spector, T. Hirano, Spatial and temporal regulation of condensins I and II in mitotic chromosome assembly in human cells. *Mol. Biol. Cell* **15**, 3296–3308 (2004). doi:10.1091/mbc.E04-03-0242 Medline
54. D. F. Hudson, P. Vagnarelli, R. Gassmann, W. C. Earnshaw, Condensin is required for nonhistone protein assembly and structural integrity of vertebrate mitotic chromosomes. *Dev. Cell* **5**, 323–336 (2003). doi:10.1016/S1534-5807(03)00199-0 Medline
55. S. Ohta, J.-C. Bukowski-Wills, L. Sanchez-Pulido, Fde. L. Alves, L. Wood, Z. A. Chen, M. Platani, L. Fischer, D. F. Hudson, C. P. Ponting, T. Fukagawa, W. C. Earnshaw, J. Rappsilber, The protein composition of mitotic chromosomes determined using multiclassifier combinatorial proteomics. *Cell* **142**, 810–821 (2010). doi:10.1016/j.cell.2010.07.047 Medline
56. S. Ohta, L. F. Montaño-Gutierrez, F. de Lima Alves, H. Ogawa, I. Toramoto, N. Sato, C. G. Morrison, S. Takeda, D. F. Hudson, J. Rappsilber, W. C. Earnshaw, Proteomics analysis with a nano random forest approach reveals novel functional interactions regulated by SMC complexes on mitotic chromosomes. *Mol. Cell. Proteomics* **15**, 2802–2818 (2016). doi:10.1074/mcp.M116.057885 Medline
57. K. Samejima *et al.*, Rapid degradation and 3D CLEM of condensin reveal chromatin compaction uncoupled from chromosome architecture in mitosis. *bioRxiv* (2017) (available at http://biorxiv.org/content/early/2017/08/09/173633.abstract).
58. G. Kustatscher, K. L. H. Wills, C. Furlan, J. Rappsilber, Chromatin enrichment for proteomics. *Nat. Protoc.* **9**, 2090–2099 (2014). doi:10.1038/nprot.2014.142 Medline
59. M. Yanagida, Clearing the way for mitosis: Is cohesin a target? *Nat. Rev. Mol. Cell Biol.* **10**, 489–496 (2009). doi:10.1038/nrm2712 Medline
60. T. Ono, A. Losada, M. Hirano, M. P. Myers, A. F. Neuwald, T. Hirano, Differential contributions of condensin I and condensin II to mitotic chromosome architecture in vertebrate cells. *Cell* **115**, 109–121 (2003). doi:10.1016/S0092-8674(03)00724-4 Medline
61. L. C. Green, P. Kalitsis, T. M. Chang, M. Cipetic, J. H. Kim, O. Marshall, L. Turnbull, C. B. Whitchurch, P. Vagnarelli, K. Samejima, W. C. Earnshaw, K. H. A. Choo, D. F. Hudson, Contrasting roles of condensin I and condensin II in mitotic chromosome formation. *J. Cell Sci.* **125**, 1591–1604 (2012). doi:10.1242/jcs.097790 Medline
62. K. Shintomi, F. Inoue, H. Watanabe, K. Ohsumi, M. Ohsugi, T. Hirano, Mitotic chromosome assembly despite nucleosome depletion in *Xenopus* egg extracts. *Science* **356**, 1284–1287 (2017). doi:10.1126/science.aam9702 Medline
63. K. Shintomi, T. Hirano, The relative ratio of condensin I to II determines chromosome shapes. *Genes Dev.* **25**, 1464–1469 (2011).

doi:10.1101/gad.2060311 Medline
64. T. Zhang, J. R. Paulson, M. Bakhrebah, J. H. Kim, C. Nowell, P. Kalitsis, D. F. Hudson, Condensin I and II behaviour in interphase nuclei and cells undergoing premature chromosome condensation. *Chromosome Res.* **24**, 243–269 (2016). doi:10.1007/s10577-016-9519-7 Medline
65. A. S. Belmont, J. W. Sedat, D. A. Agard, A three-dimensional approach to mitotic chromosome structure: Evidence for a complex hierarchical organization. *J. Cell Biol.* **105**, 77–92 (1987). doi:10.1083/jcb.105.1.77 Medline
66. A. S. Belmont, S. Dietzel, A. C. Nye, Y. G. Strukov, T. Tumbar, Large-scale chromatin structure and function. *Curr. Opin. Cell Biol.* **11**, 307–311 (1999). doi:10.1016/S0955-0674(99)80041-6 Medline
67. K. Maeshima, U. K. Laemmli, A two-step scaffolding model for mitotic chromosome assembly. *Dev. Cell* **4**, 467–480 (2003). doi:10.1016/S1534-5807(03)00092-3 Medline
68. Y. G. Strukov, Y. Wang, A. S. Belmont, Engineered chromosome regions with altered sequence composition demonstrate hierarchical large-scale folding within metaphase chromosomes. *J. Cell Biol.* **162**, 23–35 (2003). doi:10.1083/jcb.200303098 Medline
69. K. Nasmyth, Disseminating the genome: Joining, resolving, and separating sister chromatids during mitosis and meiosis. *Annu. Rev. Genet.* **35**, 673–745 (2001). doi:10.1146/annurev.genet.35.102401.091334 Medline
70. A. D. Riggs, DNA methylation and late replication probably aid cell memory, and type I DNA reeling could aid chromosome folding and enhancer function. *Philos. Trans. R. Soc. Lond. B Biol. Sci.* **326**, 285–297 (1990). doi:10.1098/rstb.1990.0012 Medline
71. E. Alipour, J. F. Marko, Self-organization of domain structures by DNA-loop-extruding enzymes. *Nucleic Acids Res.* **40**, 11202–11212 (2012). doi:10.1093/nar/gks925 Medline
72. T. Terekawa *et al.*, The Condensin Complex Is A Mechanochemical Motor That Translocates Along DNA. *bioRxiv* (2017) (available at http://www.biorxiv.org/content/early/2017/05/13/137711).
73. J. Mirkovitch, S. M. Gasser, U. K. Laemmli, Scaffold attachment of DNA loops in metaphase chromosomes. *J. Mol. Biol.* **200**, 101–109 (1988). doi:10.1016/0022-2836(88)90336-1 Medline
74. P. N. Cockerill, W. T. Garrard, Chromosomal loop anchorage of the kappa immunoglobulin gene occurs next to the enhancer in a region containing topoisomerase II sites. *Cell* **44**, 273–282 (1986). doi:10.1016/0092-8674(86)90761-0 Medline
75. D. Gerlich, T. Hirota, B. Koch, J.-M. Peters, J. Ellenberg, Condensin I stabilizes chromosomes mechanically through a dynamic interaction in live cells. *Curr. Biol.* **16**, 333–344 (2006). doi:10.1016/j.cub.2005.12.040 Medline
76. S. H. Yoshimura, T. Hirano, HEAT repeats - versatile arrays of amphiphilic helices working in crowded environments? *J. Cell Sci.* **129**, 3963–3970 (2016). Medline
77. B. Kobe, T. Gleichmann, J. Horne, I. G. Jennings, P. D. Scotney, T. Teh, Turn up the HEAT. *Structure* **7**, R91–R97 (1999). doi:10.1016/S0969-2126(99)80060-4 Medline
78. E. Robbins, N. K. Gonatas, The ultrastructure of a mammalian cell during the mitotic cycle. *J. Cell Biol.* **21**, 429–463 (1964). doi:10.1083/jcb.21.3.429 Medline
79. M. Eltsov, K. M. Maclellan, K. Maeshima, A. S. Frangakis, J. Dubochet, Analysis of cryo-electron microscopy images does not support the existence of 30-nm chromatin fibers in mitotic chromosomes in situ. *Proc. Natl. Acad. Sci. U.S.A.* **105**, 19732–19737 (2008). doi:10.1073/pnas.0810057105 Medline
80. B. J. Wilkins, N. A. Rall, Y. Ostwal, T. Kruitwagen, K. Hiragami-Hamada, M. Winkler, Y. Barral, W. Fischle, H. Neumann, A cascade of histone modifications induces chromatin condensation in mitosis. *Science* **343**, 77–80 (2014). doi:10.1126/science.1244508 Medline
81. A. Zhiteneva, J. J. Bonfiglio, A. Makarov, T. Colby, P. Vagnarelli, E. C. Schirmer, I. Matic, W. C. Earnshaw, Mitotic post-translational modifications of histones promote chromatin compaction in vitro. *Open Biol.* **7**, 170076 (2017). doi:10.1098/rsob.170076 Medline
82. M. Mazumdar, S. Sundareshan, T. Misteli, Human chromokinesin KIF4A functions in chromosome condensation and segregation. *J. Cell Biol.* **166**, 613–620 (2004). doi:10.1083/jcb.200401142 Medline
83. M. Takahashi, T. Wakai, T. Hirota, Condensin I-mediated mitotic chromosome assembly requires association with chromokinesin KIF4A. *Genes Dev.* **30**, 1931–1936 (2016). doi:10.1101/gad.282855.116 Medline
84. A. Maritan, C. Micheletti, A. Trovato, J. R. Banavar, Optimal shapes of compact strings. *Nature* **406**, 287–290 (2000). doi:10.1038/35018538 Medline
85. J. Cox, M. Mann, MaxQuant enables high peptide identification rates, individualized p.p.b.-range mass accuracies and proteome-wide protein quantification. *Nat. Biotechnol.* **26**, 1367–1372 (2008). doi:10.1038/nbt.1511 Medline
86. B. Schwanhäusser, D. Busse, N. Li, G. Dittmar, J. Schuchhardt, J. Wolf, W. Chen, M. Selbach, Global quantification of mammalian gene expression control. *Nature* **473**, 337–342 (2011). doi:10.1038/nature10098 Medline
87. J. R. Wiśniewski, M. Y. Hein, J. Cox, M. Mann, A "proteomic ruler" for protein copy number and concentration estimation without spike-in standards. *Mol. Cell. Proteomics* **13**, 3497–3506 (2014). doi:10.1074/mcp.M113.037309 Medline
88. S. G. Landt, G. K. Marinov, A. Kundaje, P. Kheradpour, F. Pauli, S. Batzoglou, B. E. Bernstein, P. Bickel, J. B. Brown, P. Cayting, Y. Chen, G. DeSalvo, C. Epstein, K. I. Fisher-Aylor, G. Euskirchen, M. Gerstein, J. Gertz, A. J. Hartemink, M. M. Hoffman, V. R. Iyer, Y. L. Jung, S. Karmakar, M. Kellis, P. V. Kharchenko, Q. Li, T. Liu, X. S. Liu, L. Ma, A. Milosavljevic, R. M. Myers, P. J. Park, M. J. Pazin, M. D. Perry, D. Raha, T. E. Reddy, J. Rozowsky, N. Shoresh, A. Sidow, M. Slattery, J. A. Stamatoyannopoulos, M. Y. Tolstorukov, K. P. White, S. Xi, P. J. Farnham, J. D. Lieb, B. J. Wold, M. Snyder, ChIP-seq guidelines and practices of the ENCODE and modENCODE consortia. *Genome Res.* **22**, 1813–1831 (2012). doi:10.1101/gr.136184.111 Medline
89. J. M. Belton, R. P. McCord, J. H. Gibcus, N. Naumova, Y. Zhan, J. Dekker, Hi-C: A comprehensive technique to capture the conformation of genomes. *Methods* **58**, 268–276 (2012). doi:10.1016/j.ymeth.2012.05.001 Medline
90. B. R. Lajoie, J. Dekker, N. Kaplan, The hitchhiker's guide to Hi-C analysis: Practical guidelines. *Methods* **72**, 65–75 (2015). doi:10.1016/j.ymeth.2014.10.031 Medline
91. W. C. Warren, L. W. Hillier, C. Tomlinson, P. Minx, M. Kremitzki, T. Graves, C. Markovic, N. Bouk, K. D. Pruitt, F. Thibaud-Nissen, V. Schneider, T. A. Mansour, C. T. Brown, A. Zimin, R. Hawken, M. Abrahamsen, A. B. Pyrkosz, M. Morisson, V. Fillon, A. Vignal, W. Chow, K. Howe, J. E. Fulton, M. M. Miller, P. Lovell, C. V. Mello, M. Wirthlin, A. S. Mason, R. Kuo, D. W. Burt, J. B. Dodgson, H. H. Cheng, A new chicken genome assembly provides insight into avian genome structure. *G3* **7**, 109–117 (2017). doi:10.1534/g3.116.035923 Medline
92. Y. Zhang, R. P. McCord, Y.-J. Ho, B. R. Lajoie, D. G. Hildebrand, A. C. Simon, M. S. Becker, F. W. Alt, J. Dekker, Spatial organization of the mouse genome and its role in recurrent chromosomal translocations. *Cell* **148**, 908–921 (2012). doi:10.1016/j.cell.2012.02.002 Medline
93. I. M. Flyamer, J. Gassler, M. Imakaev, H. B. Brandão, S. V. Ulianov, N. Abdennur, S. V. Razin, L. A. Mirny, K. Tachibana-Konwalski, Single-nucleus Hi-C reveals unique chromatin reorganization at oocyte-to-zygote transition. *Nature* **544**, 110–114 (2017). doi:10.1038/nature21711 Medline
94. J. Kihoon, K. Hong, S. Satchell, *Defining Single Asset Price Momentum in Terms of a Stochastic Process* (2012), vol. 2.
95. P. Eastman, J. Swails, J. D. Chodera, R. T. McGibbon, Y. Zhao, K. A. Beauchamp, L.-P. Wang, A. C. Simmonett, M. P. Harrigan, C. D. Stern, R. P. Wiewiora, B. R. Brooks, V. S. Pande, OpenMM 7: Rapid development of high performance algorithms for molecular dynamics. *PLOS Comput. Biol.* **13**, e1005659 (2017). doi:10.1371/journal.pcbi.1005659 Medline
96. P. Eastman, V. S. Pande, Efficient nonbonded interactions for molecular dynamics on a graphics processing unit. *J. Comput. Chem.* **31**, 1268–1272 (2010). Medline
97. J. Nuebler, G. Fudenberg, M. Imakaev, N. Abdennur, L. Mirny, Chromatin Organization by an Interplay of Loop Extrusion and Compartmental Segregation. bioRxiv (2017) (available at http://biorxiv.org/content/early/2017/10/03/196261.abstract).
98. J. Molnár, Á. Póti, O. Pipek, M. Krzystanek, N. Kanu, C. Swanton, G. E. Tusnády, Z. Szallasi, I. Csabai, D. Szüts, The genome of the chicken DT40 bursal lymphoma cell line. *G3* **4**, 2231–2240 (2014). doi:10.1534/g3.114.013482 Medline

ACKNOWLEDGMENTS

Supported by grants from the National Human Genome Research Institute (HG003143) and the National Institutes of Health Common Fund (DK107980) to J. Dekker and L. Mirny. J. Dekker is an investigator of the Howard Hughes Medical Institute. Work in the Mirny lab was also supported by the National

Science Foundation (Physics of Living Systems, 1504942), and the National Institute of General Medical Sciences (GM114190). Work in the Earnshaw lab was funded by Wellcome, of which W.C.E. is a Principal Research Fellow (Grant 107022). The Wellcome Centre for Cell Biology is supported by core funding from the Wellcome Trust [203149]. M.T.K. was supported by JSPS KAKENHI Grant (16K15095), and research grants from Mochida Memorial Foundation for Medical and Pharmaceutical Research, SGH Foundation, The Sumitomo Foundation, and The Canon Foundation. Sorting of GFP positive and negative cells was performed in the Flow Cytometry facility, Institute of Immunology & Infection Research, Edinburgh with assistance of Dr. Martin Waterfall. We thank Dr. Hakan Ozadam for assistance with Hi-C data processing. All Hi-C data has been submitted to GEO and will be publicly available upon publication (accession number GSE102740). This paper is dedicated to the memory of Donald S. Coffey, who pioneered the study of chromatin loops in the nucleus. **Author contributions:** KS generated cell lines, established cell synchronization protocols, performed synchronized timecourses and performed imaging analyses. JHG and NN performed Hi-C analyses. AG and JN performed polymer simulations. LAM and AG designed and analyzed coarse grained models, with A.G. serving as the lead modeler. AG analyzed condensin chromatin immunoprecipitation data. LX and JRP prepared 1NM-PP1. IS performed chromatin enriched proteomics analyses. MTK provided constructs for cell line engineering. MTK is a coinventor on a provisional patent application no. PCT/JP2016/059174 relating to auxin-inducible degron (AID) technology filed by National Institute of Genetics. AG, JHG, KS, JN, WCE, LAM and JD designed the project and analyzed data. All contributed to writing the manuscript.

SUPPLEMENTARY MATERIALS

www.sciencemag.org/cgi/content/full/science.aao6135/DC1
Materials and Methods
Figs. S1 to S27
Tables S1 to S4
References (*85*–*98*)
Movie S1

10 August 2017; accepted 9 January 2018
Published online 18 January 2018
10.1126/science.aao6135

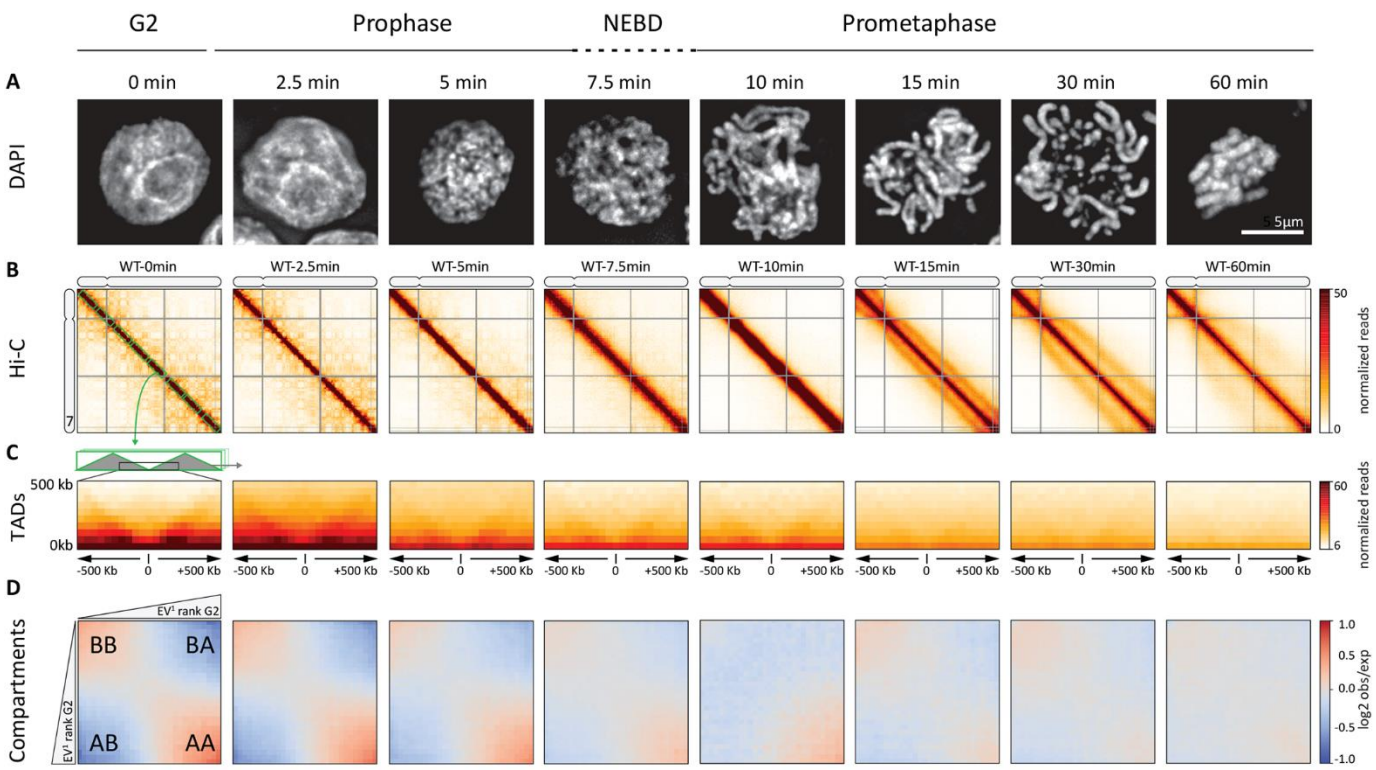

Fig. 1. Chromosome morphogenesis during synchronous mitosis. (**A**) Representative DAPI images of nuclei and chromosomes in CDK1as DT40 cells taken at indicated time points (in minutes) after release from 1NM-PP1-induced G_2 arrest show mitotic chromosome formation. Bar indicates 5 micron. (**B**) Hi-C interaction maps of chromosome 7 (binned at 100 kb) from cells collected indicated time points in prophase and prometaphase show large-scale changes in contact frequencies as cell progress through mitosis (**C**) The average interaction maps center around G_2 TAD boundaries. TAD boundaries disappear. (**D**) Compartmentalization saddle plots: average distance-normalized interaction frequencies between cis-pairs of 100-kb bins arranged by their G_2 eigenvector value. Compartments disappear.

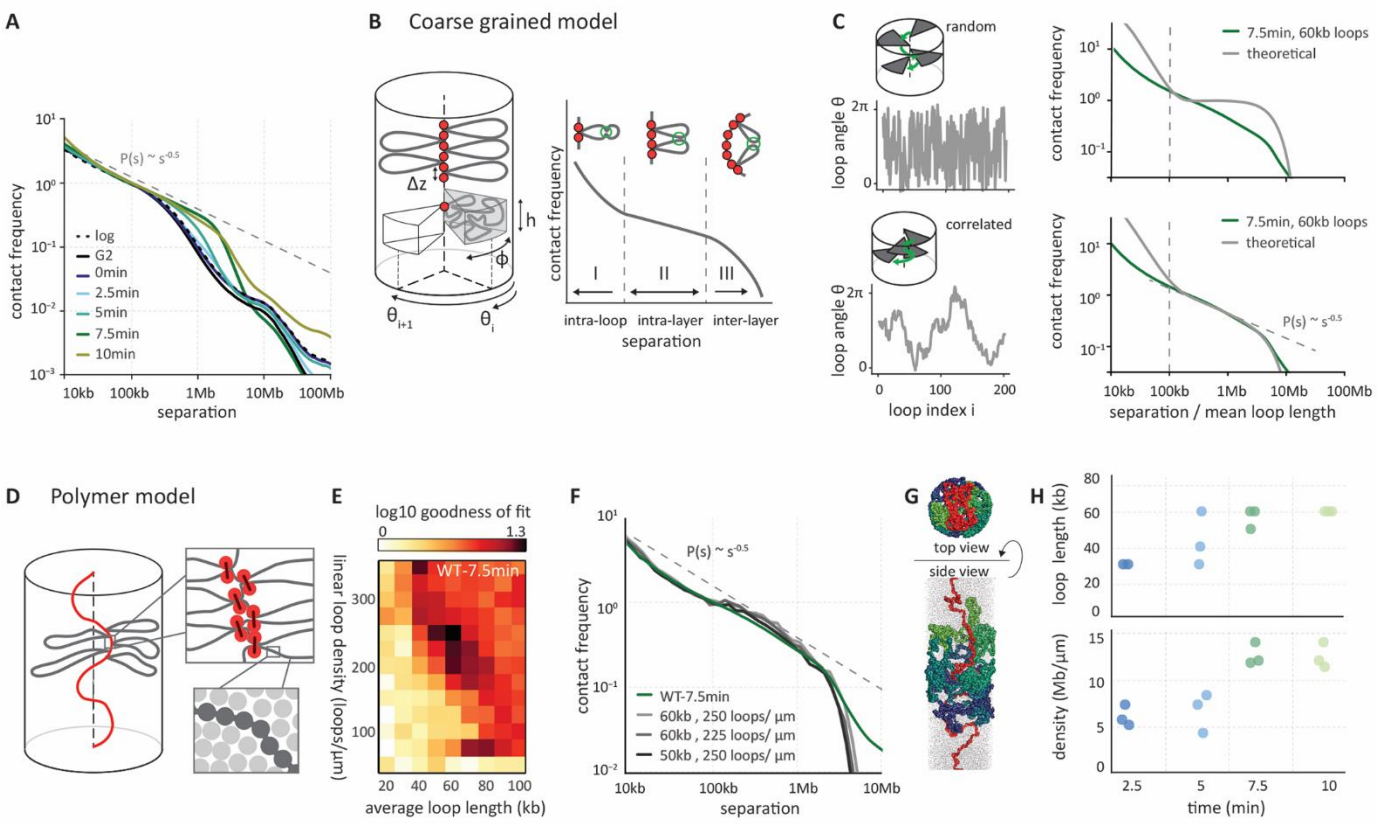

Fig. 2. Prophase chromosomes fold as axially compressed loop arrays. (A) Genome-wide curves of contact frequency $P(s)$ vs genomic distance s, normalized to unity at s = 100 kb. The curves are derived from prophase Hi-C data at the indicated time points after release from G_2 arrest. The dotted line indicates $P(s) = s^{-0.5}$ observed for mitotic chromosomes (*8*). (B) Overview of the coarse grained model of prophase chromosomes. The chromosome is compacted into a series of consecutive loops and compressed into a cylindrical shape. The loop bases form a scaffold at the chromosomal axis, each loop occupies a cylindrical sector of height h and angular size φ, oriented at angle Θ_i. The coarse-grained model predicts the $P(s)$ curve to have three distinct regions: an intra loop (I), intra layer (II) and inter layer (III) regions. (C) The best fitting $P(s)$ predictions by the coarse grained model for late prophase (t = 7.5 min) under two different assumptions on loop orientations: (top panels) uncorrelated and (bottom panels) correlated orientations of consecutive loops. Uncorrelated angular loop orientations lead to a plateau in $P(s)$ in the intra-layer, whereas correlated angles lead to the experimentally observed $P(s) = s^{-0.5}$ (right panels). (D) Polymer models of prophase chromosomes. Chromatin fibers are modeled as chains of particles (dark gray circles), compacted into arrays of consecutive loops (loop bases indicated in orange). Chromosomes are compacted into a cylinder with a density of one nucleosome per 11×11×11nm cube (lower right). (E) Goodness of fit for simulated vs experimental $P(s)$. Polymer simulations were performed for a range of loop densities and loop lengths, and for each simulation $P(s)$ was calculated. The heatmap shows the quality of a match between the predicted and experimental $P(s)$ curves at late prophase (t = 7.5 min). (F) $P(s)$ derived from late prophase Hi-C experiments (green line) and the best fitting polymer models (grayscale lines). Average loop size and linear density of loops along the chromosome axis are listed. (G) Top and side view of the best fitting polymer model of late prophase chromosomes. Loops bases are shown in red and several loops rendered in different colors. (H) The average loop size and linear density of the 3 best-fitting models of prophase chromosomes at different time points.

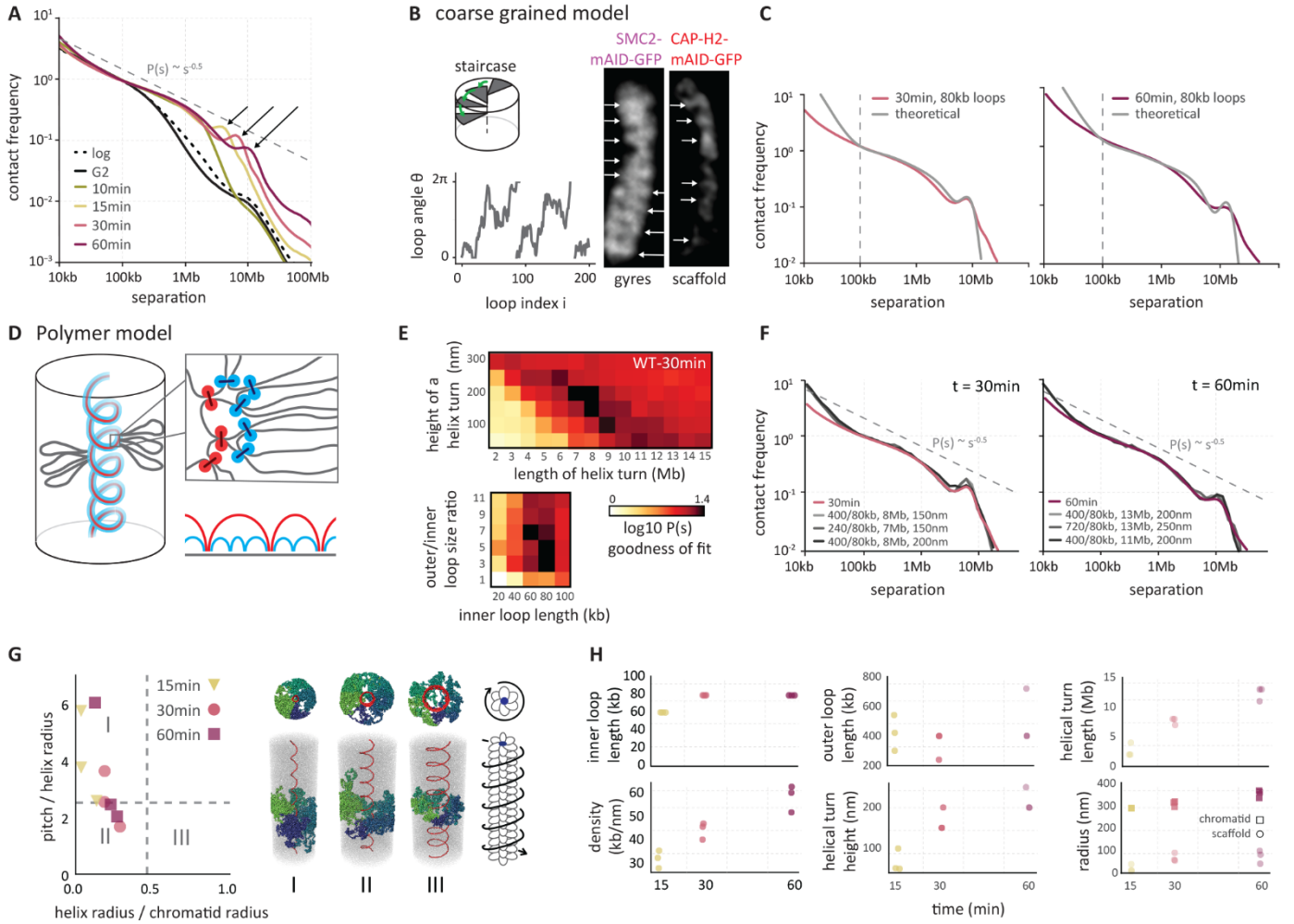

Fig. 3. Helical organization of prometaphase chromosomes. (A) Genome-wide curves of contact frequency $P(s)$ vs genomic distance (separation, s), normalized to unity at s = 100 kb. The curves are derived from Hi-C data obtained from prometaphase cells (t = 10-60 min after release from G_2 arrest). The dashed line indicates $P(s) = s^{-0.5}$. Arrows indicate positions of a local peak in $P(s)$ representing the second diagonal band observed in Hi-C interaction maps. (B) The coarse grained model of prometaphase chromosomes with staircase loop arrangement. Left, top: the staircase loop arrangement implies that loops rotate in genomic order around a central scaffold (see supplementary materials). Left, bottom: angles of adjacent loops are correlated and steadily increasing, reflecting helical arrangement of loops. Right: this helical arrangement can be observed as gyres by DNA staining and a helical scaffold can be observed in cells expressing GFP-tagged condensins. (C) The best fitting $P(s)$ predictions by the staircase coarse grained model for late prometaphase t = 30 min (30 min; left panel) and t = 60 min (60 min, right panel) after release from G_2 arrest (Hi-C data: colored lines; model; gray lines). (D) Polymer model of prometaphase chromosomes. Chromosomes are modeled as arrays of consecutive nested loops with a helical scaffold (outer loops in red, inner loops in blue, also indicated diagrammatically bottom right). (E) Goodness of fit for simulated vs experimental $P(s)$. Polymer simulations were performed varying the helix height (nm), the size of a helical turn (Mb), and the sizes of inner and outer loops. For each simulation $P(s)$ was calculated. The heatmaps show the quality of the best match between the predicted and experimental $P(s)$ at prometaphase (t = 30 min), when two out of four parameters were fixed to the specified values. (F) $P(s)$ derived from prometaphase Hi-C experiments (colored lines) and the best fitting polymer models (gray lines). Left panel: t = 30 min, right panel t = 60 min after release from G_2 arrest. Average size of outer and inner loops, the length of a helix turn and the helical pitch are indicated. (G) Parameters of the helical scaffolds from the best fitting polymer models. A-axis: ratio of the radius of the helical scaffold to that of the whole chromatid; Y-axis: ratio of the pitch to the helix radius. The dashed lines show the corresponding values (0.46 and 2.5122) for the optimal space-filling helix (*84*). Classical solenoid configurations are predicted to be in sector III, while the "spiraling staircase" configurations are in I and II. On the right, three examples of models of type I, II and III are shown with loops bases in red and several individual loops rendered in different colors. Also shown is a schematic of a prometaphase chromosome with the helical winding of loops indicated by arrow around the loop array. (H) Parameters of the best 3 models of prometaphase chromosomes at different time points.

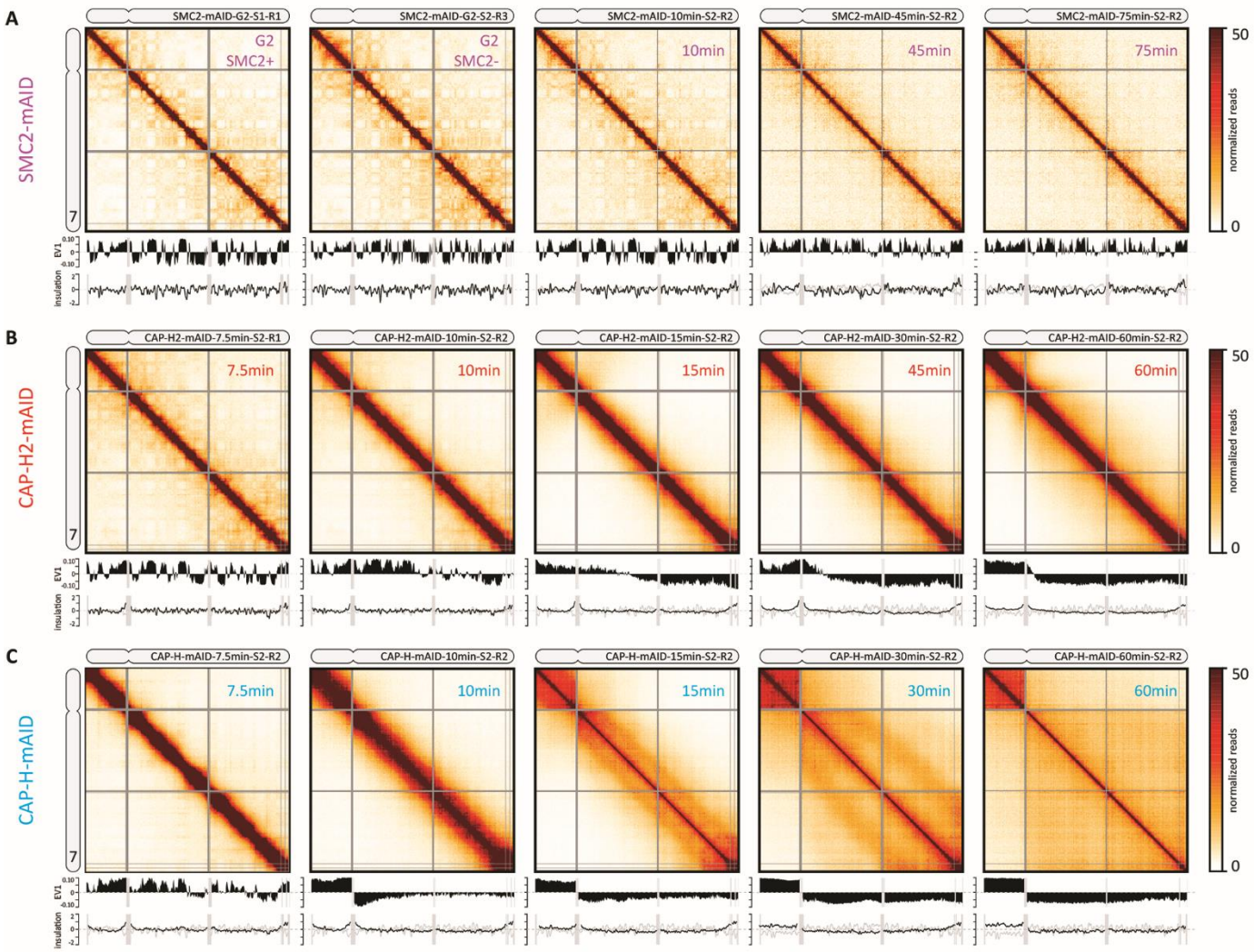

Fig. 4. Defects in chromosome morphogenesis in condensin depleted cells. (**A** to **C**). Hi-C interaction frequency maps (binned at 100 kb) for chromosome 7 at indicated time points (top right in each heatmap) after release from G_2 arrest. The first plot below each Hi-C interaction map displays the compartment signal (Eigenvector 1). The bottom graph shows the insulation score (TADs; binned at 50 kb). (A) SMC2-mAID cells were treated with auxin for three hours prior to release from G_2 arrest to deplete SMC2. SMC2+: Hi-C interaction map for G_2-arrested cells prior to auxin treatment. SMC2-: Hi-C interaction map for G_2-arrested cells after three hours of auxin treatment. (B) Hi-C data for CAP-H2-mAID cells treated for three hours with auxin prior to release from G_2 arrest to deplete CAP-H2. (C). Hi-C data for CAP-H-mAID cells treated for three hours with auxin prior to release from G_2 arrest to deplete CAP-H.

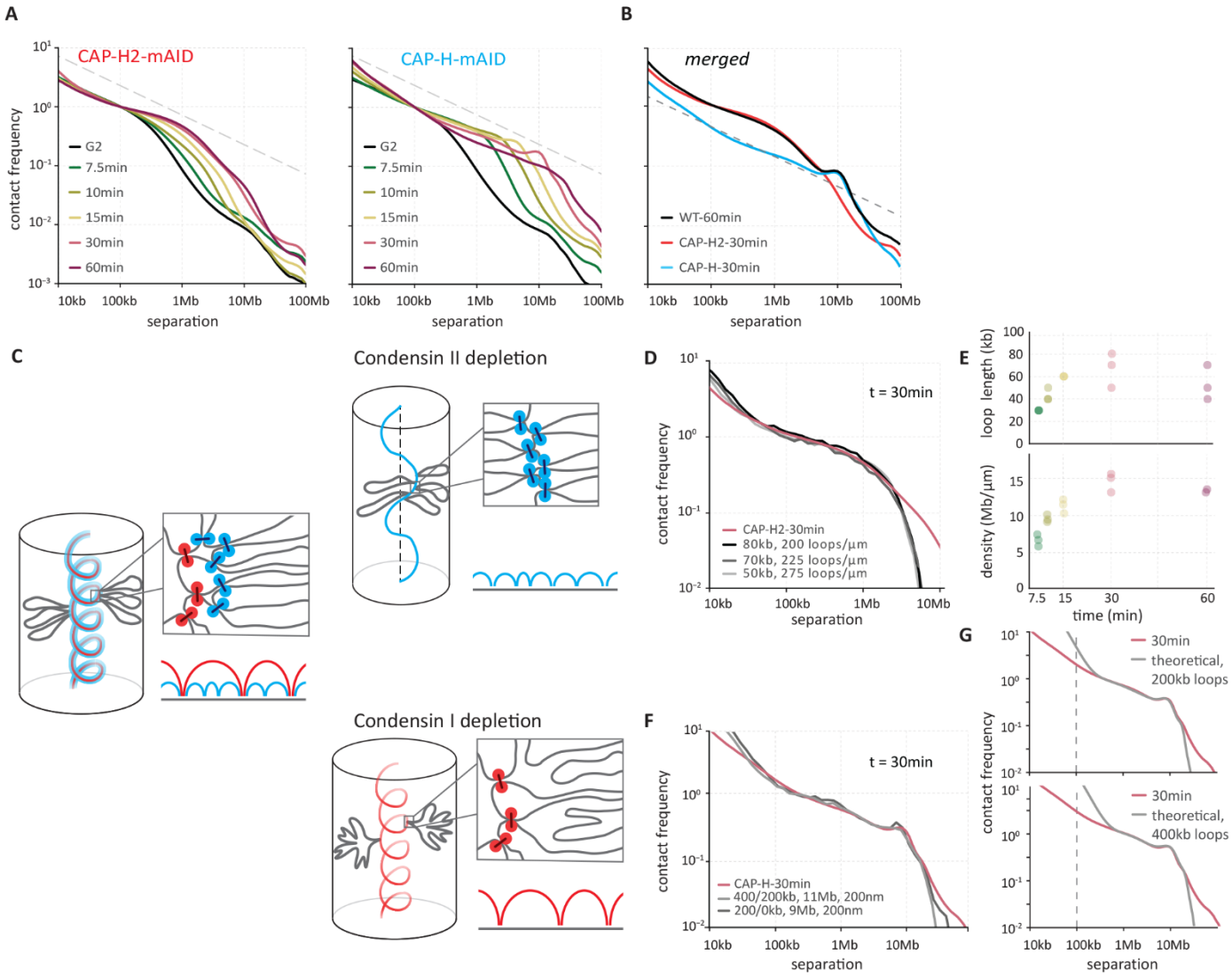

Fig. 5. Distinct roles for condensin I and II in mitotic chromosome formation. (**A**) Genome-wide curves of contact frequency $P(s)$ vs genomic distance s, normalized to unity at s = 100 kb. The curves are $P(s)$ derived from Hi-C data obtained from CAP-H2-depleted (left panel) and CAP-H-depleted cells (right panel), at t = 7-60 min after release from G_2 arrest. Dashed line indicates $P(s) = s^{-0.5}$. (**B**) Overlayed $P(s)$ curves of WT, CAP-H- and CAP-H2-depleted chromosomes show independent contributions of two condensin complexes to short- and long-distance contacts. (**C**) Polymer models of CAP-H2 (top) and CAP-H (bottom) depleted chromosomes. Top: depletion of CAP-H2 is modeled via removal of outer loops and relaxation of the helix. Bottom: depletion of CAP-H is modeled via removal of the inner loops, while preserving the helical arrangement of the scaffold. Condensin II loop anchors are shown in red, condensin I loop anchors are shown in blue. (**D**) $P(s)$ derived from late prometaphase CAP-H2 depletion Hi-C experiments (red line) and the three best fitting polymer models (grayscale lines). The average loop size and linear density of loops along the chromosome axis are indicated. (**E**) The average loop size and linear DNA density of the 3 best-fitting models of CAP-H2-depleted chromosomes at different time points. (**F**) $P(s)$ derived from late prometaphase CAP-H depletion Hi-C experiments (blue line) and the best fitting polymer models with and without nested inner loops (grayscale lines). The average size of outer and inner loops, the length of a helix turn in Mb and the helical pitch are indicated. (**G**) The best fitting $P(s)$ predictions by the staircase coarse grained model for late prometaphase CAP-H depletion Hi-C experiments at t = 30 min after release of G_2 arrest (gray lines; experimental P(s): red lines. Top: loop size is 200 kb, bottom: loop size is 400 kb.

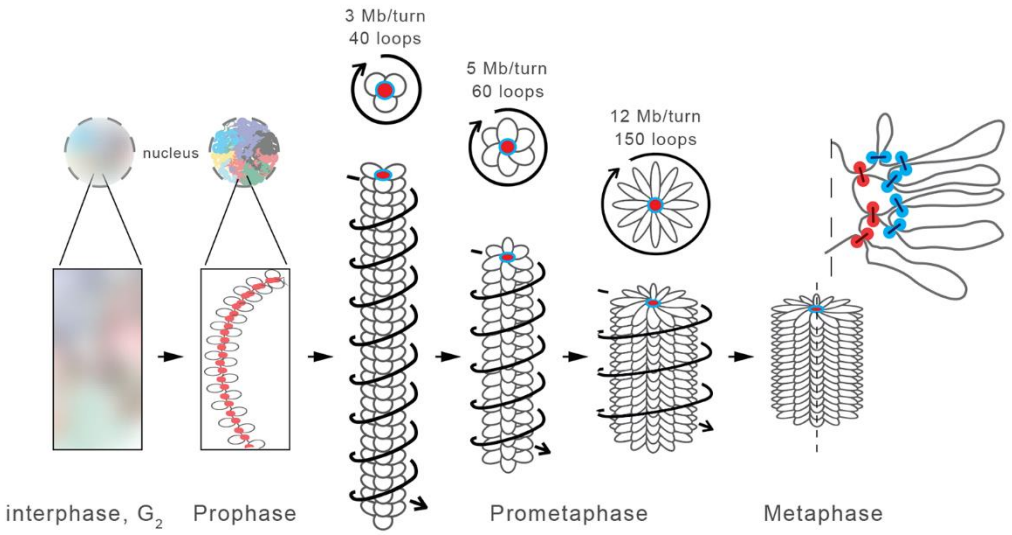

Fig. 6. A mitotic chromosome morphogenesis pathway. In prophase, condensin II compacts chromosomes into arrays of consecutive loops and sister chromatids split along their length. The scaffold of condensin II-mediated loop bases is indicated in red. Upon nuclear envelope breakdown and entry into prometaphase, condensin II-mediated loops become increasingly large as they split into smaller ~80 kb loops by condensin I. Chromosomes are shown as arrays of loops (only inner loops can be observed microscopically; top: cross-section, bottom: side view. For clarity, loops are indicated as separate entities pointing in one direction, while in reality loops are unstructured and can mix). The nested arrangements of centrally located condensin II-mediated loop bases and more peripherally located condensin I-mediated loop bases are indicated in red and blue respectively. During prometaphase central scaffold acquires a helical arrangement with loops rotating around the scaffold as steps in a "spiral staircase" (helical path of loops is indicated by arrows). As prometaphase progresses outer loops grow and the number of loops per turn increases and chromosomes shorten to form the mature mitotic chromosome.

RESEARCH ARTICLE

BIOMECHANICS

Morphology, muscle capacity, skill, and maneuvering ability in hummingbirds

Roslyn Dakin,[1]*† Paolo S. Segre,[1]*‡ Andrew D. Straw,[2] Douglas L. Altshuler[1]§

How does agility evolve? This question is challenging because natural movement has many degrees of freedom and can be influenced by multiple traits. We used computer vision to record thousands of translations, rotations, and turns from more than 200 hummingbirds from 25 species, revealing that distinct performance metrics are correlated and that species diverge in their maneuvering style. Our analysis demonstrates that the enhanced maneuverability of larger species is explained by their proportionately greater muscle capacity and lower wing loading. Fast acceleration maneuvers evolve by recruiting changes in muscle capacity, whereas fast rotations and sharp turns evolve by recruiting changes in wing morphology. Both species and individuals use turns that play to their strengths. These results demonstrate how both skill and biomechanical traits shape maneuvering behavior.

A hallmark of powered flight is maneuverability, defined as the ability to actively change speed and/or direction (*1*). These maneuvers are often used in pursuit, escape, and collision avoidance (*2*–*5*). Selection on these behaviors is predicted to recruit a variety of underlying physiological and morphological traits (*6*, *7*). However, understanding how animals achieve high performance is challenging because of the sheer diversity of behaviors and the versatility with which any given maneuver, such as a banked turn, is used (*1*, *8*). Previous experimental studies have used a reductionist approach by constraining animals to complete a predefined task (*9*–*11*). Although this can elucidate important biomechanical mechanisms, it cannot capture the degrees of freedom inherent in diverse maneuvering behaviors or the correlations among these behaviors (*1*, *3*–*5*). Thus, it remains a challenge to link maneuvering performance to its underlying traits (*12*–*15*).

We used computer vision to track individual hummingbirds (*16*, *17*), highly agile fliers (*4*, *18*) that can hover and fly backward, and we developed a method to quantify the phenotypic architecture of maneuverability as a multidimensional performance space. The first step is to extract maneuvers that can be classified into three geometric categories (table S1): body translations, body rotations, and complex turns (*17*). As an example, shown in Fig. 1A is a sequence that begins with a sharp turn known as a pitch-roll turn (PRT), that occurs when a bird pitches up to decelerate, rolls about the longitudinal axis, and then accelerates again in a new direction. This sequence also includes two translational maneuvers (AccHor, acceleration, and DecHor, deceleration), as well as another complex turn, Arc, which is defined as a smooth arcing turn with no change in vertical position. Using this method to identify a large number of maneuvers from a single species, the Anna's hummingbird (*Calypte anna*), we previously found that solo birds performed similarly to vigorously competing birds in the same environment (*17*). Furthermore, performance variation within this species in all three types of maneuvers (translations, rotations, and turns) could be explained by individual differences in muscle capacity. By contrast, morphology was only correlated with certain features of turns; narrower wing shapes were associated with the use of Arc turns and high centripetal accelerations. However, *C. anna* has only limited variation in traits known to influence flight efficiency and force production, such as body mass, wing size, and wing shape (*19*–*21*). Thus, it was not clear whether these results generalize beyond *C. anna* or whether performance differences at broader taxonomic levels can be understood by using this framework.

In the hummingbird family, there are at least 337 other species with body mass spanning an order of magnitude and wing sizes and shapes that can vary nonisometrically (*22*–*24*). Thus, evolution provides an opportunity to examine the independent contributions of size and shape by generating repeated changes in these traits (Fig. 1). The hummingbird family also includes montane taxa that must cope with the additional challenge of flight in low-density air (*23*, *25*). To understand how these factors influence maneuverability, we recorded flight maneuvers and morphology from 207 individuals representing 25 neotropical species found at high and low elevation (Fig. 1D). Each bird was recorded alone for 30 min in a large chamber, motivated by the captive environment (supplementary materials, materials and methods, and movie S1). Because we were interested in separating the within- and between-species effects of morphology, we used a different large sample of 263 birds in load-lifting studies to obtain species-average values for body mass, wing size, wing shape, and muscle capacity (supplementary materials, materials and methods, and figs. S1 and S2).

In nature, the ability to outmaneuver competitors, predators, and prey depends on strategic and sensory considerations as well as force production (*5*, *26*–*28*). A key problem in evolutionary physiology is how to measure meaningful variation in noisy behavioral phenotypes (*6*, *8*). We designed our maneuvering assay to capture a broad range of performance levels from each bird, leveraging the large sample sizes shown in Fig. 1B to recover an accurate signal of individual variation, as defined by moderate to high intertrial repeatability (*17*). Thus, the analysis does not focus on a single maximal performance value, owing to the constraint of testing performance in a chamber and because it is not possible to unequivocally determine individual variation in maxima for voluntary behaviors.

From the maneuvering trials, we extracted stereotypical maneuvers defined in table S1 that represent the three general categories of translations, rotations, and turns (Fig. 1B). Each maneuver was used by all 25 species. The translational maneuvers included linear accelerations (AccHor) and decelerations (DecHor) limited to the horizontal (*xy*) plane, as well as accelerations that represent monotonic increases in total (*xyz*) velocity (Vel). To calculate performance on these translations, we took the maximum value attained during each maneuver (Fig. 1C) and then found the average for each bird over a 30-min trial. The body rotational maneuvers included sequences when the birds pitched upward (PitchU), pitched downward (PitchD), or made yaw turns (Yaw). We calculated the average rate of body rotation from each maneuver (Fig. 1C), followed by the trial average. For smooth Arc turns, we calculated the turn radius in the *xy* plane (Arc_{radius}), the average velocity in the *xy* plane ($Arc_{vel,avg}$), and the maximum centripetal acceleration ($Arc_{cent,max}$). For sharp PRTs, we calculated the magnitude of heading change in degrees ($PRT_{degrees}$) and the duration in seconds (PRT_{time}). In each case, we calculated a bird's trial average as its performance phenotype. Last, as a measure of the use of different turn strategies, we calculated the percentage of a bird's complex turns that were sharp PRTs (PRT%).

We first asked whether the performance metrics of distinct behaviors are correlated, either negatively, because of trade-offs, or positively, because of general capacities such as muscle size or neural architecture that may influence multiple behaviors (*6*, *7*). We found strong positive correlations,

[1]Department of Zoology, University of British Columbia, Vancouver, BC V6T1Z4, Canada. [2]Department of Animal Physiology, Neurobiology and Behavior, Faculty of Biology, University of Freiburg, Freiburg, D-79104, Germany.
*These authors contributed equally to this work. †Present address: Smithsonian Migratory Bird Center, Washington, DC 20008, USA. ‡Present address: Department of Biology, Hopkins Marine Station, Stanford University, Pacific Grove, CA 93950, USA.
§Corresponding author. Email: doug@zoology.ubc.ca

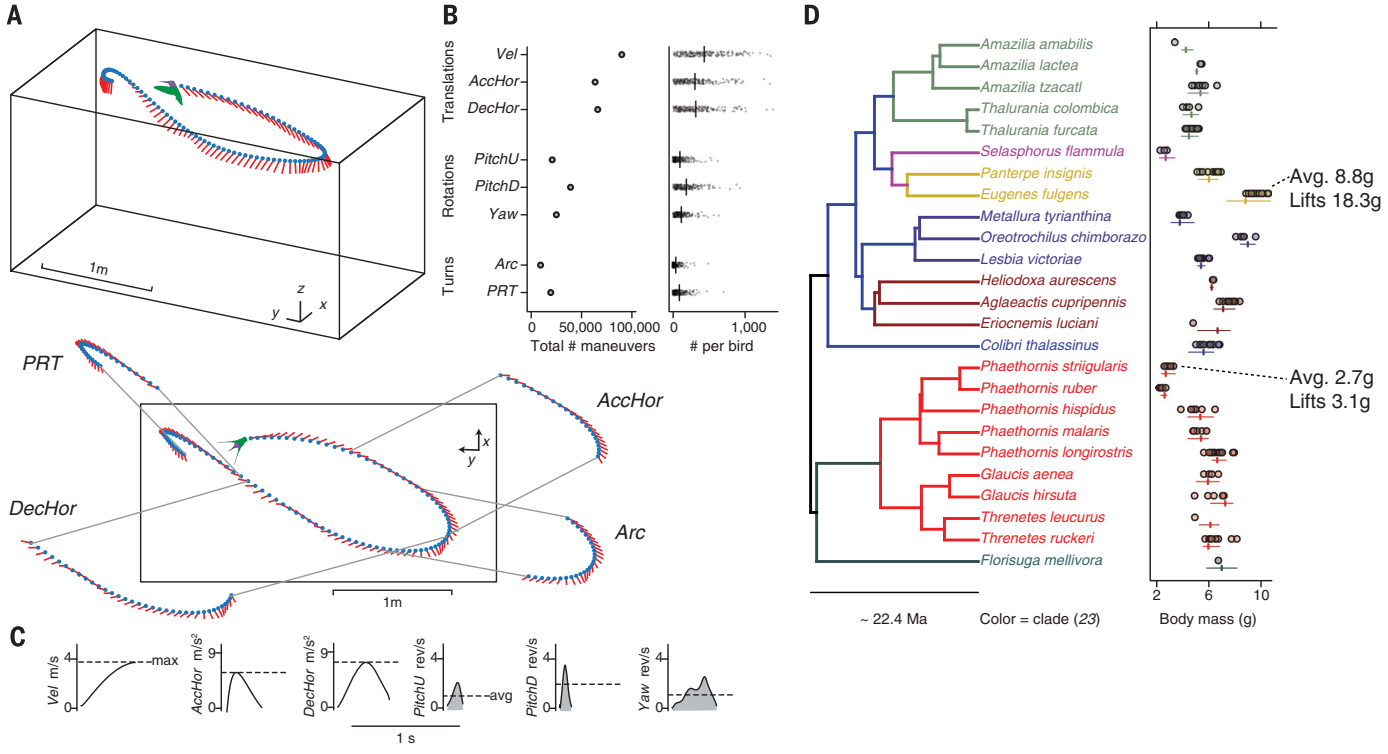

Fig. 1. Flight performance and evolution of Central and South American hummingbirds. (**A**) A tracking system recorded body position (blue dots) and orientation (red lines) at 200 frames per second. These data were used to identify stereotyped translations, rotations, and complex turns. The sequence in (A) and movie S1 shows a bird performing a pitch-roll turn (PRT) followed by a deceleration (DecHor), an arcing turn (Arc), and an acceleration (AccHor). The sequence duration is 2.5 s, and every 5th frame is shown. (**B**) The number of translations, rotations, and turns recorded in this study (vertical ticks show the means). (**C**) Example translations and rotations illustrating the performance metrics. (**D**) We obtained performance metrics for 207 individuals from 25 species, ranging in mass from ~2 to 10 g. The phylogenetic tree at left was derived from a recent multilocus analysis (*23*), with eight principal clades denoted by color. The vertical ticks in (D) show the mean and range for 263 individuals assessed for species average muscle capacity and morphological traits (figs. S1 and S2). The bird in (A) is not drawn to scale. Alternative smoothing of tracking data is provided in figs. S3 and S4 and movie S2.

especially for the rotations and translations (Fig. 2A). This could be caused by coupling owing to constraints of the flight chamber; for example, what accelerates fast may be constrained to decelerate fast in a relatively confined space. If so, we would expect correlations for paired maneuvers within the same bout of flight to be as strong as the corresponding correlations for trial average performance among individuals. Instead, nearly all of the within-flight bout correlations are much weaker than the corresponding correlations among birds (Fig. 2B and fig. S5). This demonstrates how maneuverability is a suite of correlated behaviors that covary among individuals, similar to other behavioral syndromes (*7*, *29*). Moreover, it shows that our assay of voluntary performance in captivity can reveal the structure of individual behavioral differences.

This also raises the question of whether species differ in these behavioral phenotypes. To test this possibility, we used a discriminant function (DF) analysis to find the combination of behavioral variables that would best distinguish the 25 species. The results indicate that species differ primarily in their performance of complex turns and rotations (Fig. 3A and fig. S6). On the basis of a cross-validation test, we found that birds could be classified to the correct species 34% of the time

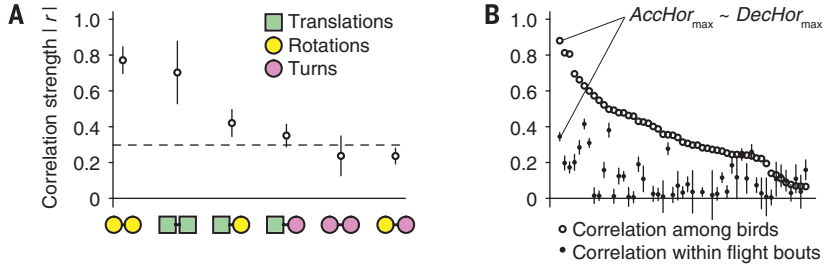

Fig. 2. Performance of different maneuvers is positively correlated. (**A**) If birds differ in overall maneuverability, we expect trial-average performance to be positively correlated among individuals. Positive correlations are particularly strong for the rotations and translations [means ± 95% confidence intervals (CIs), n = 200 individuals]. The dashed line is the average for all correlations. (**B**) Positive correlations could be caused by coupling due to constraints of flight in a confined space; if so, it would generate strong within-flight bout correlations. Each column in (B) compares the strength of the average within-flight bout correlation (± 95% CI) with the corresponding among-individual correlation. This shows that most of the strong covariance among maneuvers is not due to coupling within bouts of flight. Full analysis is provided in fig. S5.

by using their maneuvers alone, more than expected by chance (Cohen's κ = 0.30) (Fig. 3A), indicating that differences among species in maneuvering style are subtle but significant. For comparison, the same sample could be classified to the correct species 65% of the time by using morphological traits (κ = 0.61) (Fig. 3B). An analysis of phylogenetic structure indicated that on average, closely related species have similar morphologies and maneuvering styles (Fig. 3).

What mechanisms determine these evolved differences? Given that many maneuvers involve reorienting the body (*10*, *15*, *27*, *30*), we asked whether performance changes with body mass

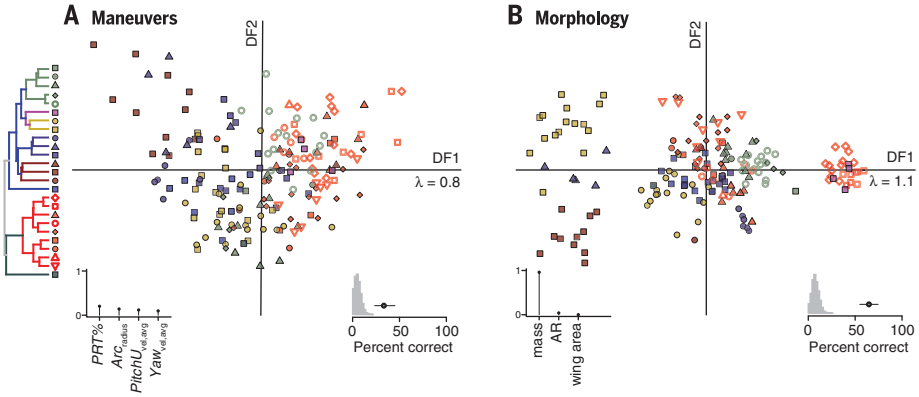

Fig. 3. Species differ in maneuvers and morphology. (**A** to **B**) We used discriminant functions (DFs) to classify 25 species based on (A) maneuvering and (B) morphological phenotypes (n = 180 birds). Each species is represented by a different color-symbol combination. The x axis (DF1; arbitrary units) accounts for most of the variation in the data space [33% in (A); 85% in (B)]. In both (A) and (B), DF1 has a Pagel's λ significantly greater than 0, indicating that closely related species resemble each other more than species drawn at random (all $P < 0.03$). (Left insets) The top DF1 loadings, demonstrating that species mainly differ in (A) their performance of complex turns and rotations and (B) body mass. (Right insets) The results of cross-validation, as the median percent of test data that was classified to the correct species (±95% central range). In both (A) and (B), classification accuracy was significantly better than expected (inset histograms = 10,000 randomized permutations). However, morphological classification was nearly twice as accurate, demonstrating that the species differ more in morphology than maneuvering style. Additional loadings are available in fig. S6.

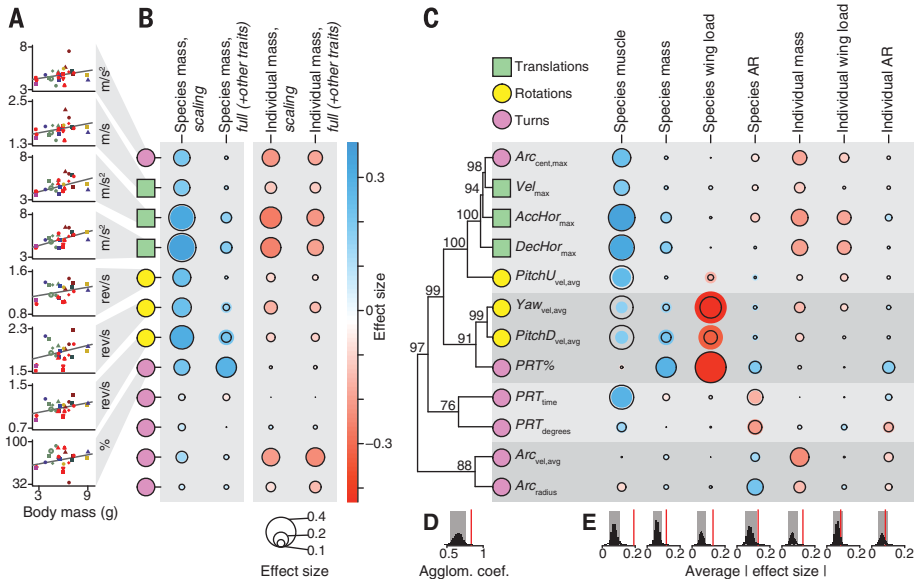

Fig. 4. Different flight maneuvers are determined by different biomechanical traits. (**A**) Species mass is positively associated with several maneuvers. (**B**) Effect sizes from scaling models (mass only) and full models (mass + other traits). Each row is a maneuver, ordered to match (C). Effect sizes are standardized to be comparable across traits (columns) and maneuvers (rows). The positive effects of species mass (blue) are attenuated when the other traits are added in the full model, except for PRT%. The negative effects of individual mass (red) are consistent. (**C**) Results of the full models show how maneuvers are clustered according to their associations with different biomechanical traits. AR stands for wing aspect ratio, a measure of wing shape. The bootstrap support (percent) is shown for each node in the dendrogram. (**D**) The agglomerative coefficient measures the strength of clustering and is significantly greater than that of randomized data (black histogram; shading shows the 95% central range for 10,000 permutations). (**E**) The mean effect magnitude for each trait, averaged across all maneuvers. The outlined circles in (B) and (C) show the results of analyses that account for phylogenetic relationships (n = 187 birds, except 180 for Arc). Full analysis is provided in figs. S7 to S9.

(*1*, *8*). Using a recent multilocus phylogeny for cross-species comparisons (*23*), we modeled each performance metric, entering species-average body mass and individual mass (relative to conspecifics) as predictors. Analyzing both levels of biological variation is necessary to test whether the "within-species" effects of a trait are broadly consistent. Moreover, it also tests whether the "between-species" and within-species effects of a trait diverge, as a result of other compensatory traits (*8*, *31*). This analysis also accounted for the elevation where the species reside and were tested. We found that hummingbird species with greater body mass perform faster translations, centripetal accelerations, and rotations (Fig. 4A and movie S1). However, within a species, heavier individuals tend to perform slower translations and centripetal accelerations (Fig. 4B).

To determine the reason for this scaling result, we reran the analysis above but added muscle capacity and wing morphological traits as additional predictors (Fig. 4C). These "full models" revealed that enhanced translational and centripetal accelerations can be attributed to greater species muscle capacity rather than body mass per se, whereas enhanced rotational speeds can be attributed to a combination of greater muscle capacity and lower wing loading (Fig. 4C). This result explains why hummingbird maneuverability scales positively with species mass, even though mass has the opposite effect on individual performance: Larger species can achieve maneuverability through the evolution of disproportionate increases in muscle capacity and wing size (*24*). One exception is PRT%, the only metric showing a strong relationship with species mass independent of the other traits, to which we will return later.

The distinct trait effects shown in Fig. 4C suggested that different maneuvers rely on different biomechanical traits. To quantitatively test this hypothesis, we used hierarchical clustering to group the performance metrics according to trait effect sizes and found strong support for four terminal groups (Fig. 4D). The first cluster includes all three translational maneuvers, the centripetal accelerations, and the upward rotations; these maneuvers largely depend on the effect of species muscle capacity. A second cluster includes the downward and yaw rotations and the relative use of turns, which largely depend on species wing loading. The third and fourth clusters include the size and speed of turns, which are the features most strongly associated with species aspect ratio (AR), a measure of wing shape. Thus, species-level evolutionary changes in muscle capacity and wing morphology affect different, correlated suites of behaviors.

Our analysis identifies burst muscle or the engine capacity of a species as having the strongest overall effect on multiple maneuvers (Fig. 4E). This extends our previous result that muscle capacity variation determines individual performance within a species (*17*). We measured load-lifting and maneuvering using different individuals, which provides a strong test of the hypothesis that evolved changes in muscle capacity influence

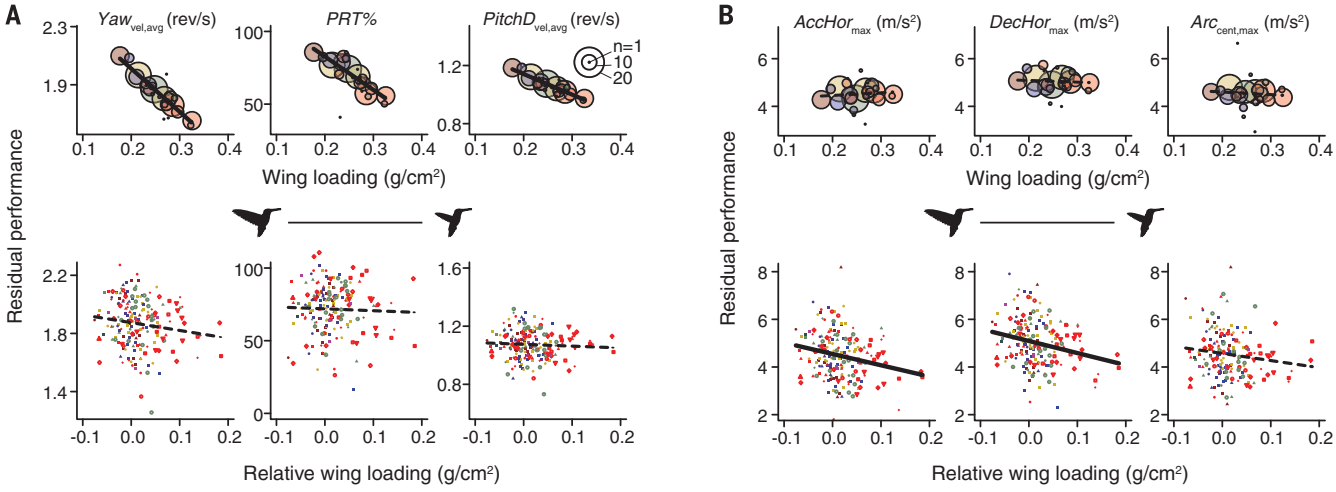

Fig. 5. Species and individual wing size affect different maneuvers. Partial effect plots illustrate the relative effect of wing loading given the other effects in the statistical model. Dotted lines indicate nonsignificant effects. (**A**) Yaw rotations, the use of complex turns, and downward rotations are strongly dependent on species wing loading (top row). However, these same maneuvers are not significantly associated with an individual's wing loading relative to conspecifics (bottom row). (**B**) Horizontal acceleration, deceleration, and centripetal acceleration are not associated with species wing loading (top row); however, these are the metrics that are most strongly associated with individual wing loading (bottom row). Colors indicate clade, as in Fig. 1. Bubble diameters represent the sample sizes for the 25 species.

performance. Muscle capacity differences among and within species are likely both due to variation in muscle size (*32*–*34*) because, as the evidence to date indicates, small birds have flight muscles composed exclusively of fast oxidative glycolytic fibers (*35*).

It is thought that the flight performance envelope is also determined by wing size (*36*). Specifically, a larger wing area relative to body mass (lower wing loading) is predicted to enhance acceleration and turning performance (*37*, *38*). We found that evolved interspecific differences in hummingbird wing loading are strongly associated with two of the rotational maneuvers and the use of sharp, pitch-roll turns (Fig. 5A). Therefore, sharp turns and fast rotations—the same behaviors that best differentiate species (fig. S6)—are associated with disproportionate increases in wing size (*24*). We also found that individuals with higher wing loading relative to their conspecifics tend to perform slower accelerations (Fig. 5B). Given that muscle capacity is the primary species-level trait associated with accelerations (Fig. 4C), this result suggests that evolved changes in muscle capacity can compensate for relatively small wings. A corollary is that smaller wings are not always detrimental because they may have efficiency advantages, depending on the environment and mode of flight.

Our results also illustrate why the effects of individual wing size and body mass were not detected in a previous study of just one species (*17*): They are too weak to detect in small samples (Fig. 5B and fig. S10), highlighting the need for large sample sizes. With respect to individual body mass, birds often experience fluctuations of 10 to 20% within hours (*39*, *40*). Our analysis predicts that these body mass fluctuations will affect translational and centripetal accelerations in many species.

Although wing shape determines efficiency (*41*), it has relatively weak effects on maneuverability, with the only significant result being a positive association between individual aspect ratio (AR) and the use of sharp pitch-roll turns, PRT% (Fig. 4C). The direction of this result is surprising because we previously found that AR was negatively associated with PRT% within one species (*C. anna*) (*17*). Further analysis here explains why: AR has either a negative, neutral, or positive association with PRT%, depending on the species (fig. S11). In hummingbirds, an individual's AR often changes dramatically as a result of damage to the wings and molt, and these changes can even exceed the variation among species (*42*). Many individuals in this study had wings that were naturally damaged or molting, capturing a wide range of AR values (fig. S1). Our results therefore raise the possibility that maneuvering flight is either robust to these transitory changes in wing shape, or it may be affected in different ways, depending on the species, its morphology, and its use of different behaviors. These hypotheses could be tested through a combination of natural and experimental alterations of wing phenotypes.

The only aspect of maneuvering that differed among elevations, independent of other traits, was the use of complex turns; species captured and tested at high elevation used proportionately fewer sharp PRTs and more smooth Arcs (Fig. 6A). This is consistent with a previous result that low-elevation birds reduce their use of PRTs when moved to high elevation (*25*), and so it suggests a shared constraint. Complex turns are also associated with morphological evolution; heavier species and those with lower wing disk loading use proportionately more sharp turns and fewer smooth Arcs (Fig. 6B). This could be due to biomechanical differences that influence the efficiency of Arc and PRT maneuvers (such as wingbeat frequency, inertia, and/or mass distribution). Another hypothesis is suggested by the fact that individuals use more Arcs in the presence of another bird (*17*). Smaller species and those with higher wing loading may use arcing turns more often for a tactical or safety advantage. These hypotheses could be tested by manipulating mass and wing phenotypes during competition among different species (*13*).

How does the use of a behavior relate to its performance? We define maneuvering fatigue as any process that causes the individuals that use a particular maneuver more often to perform it at a lower level. Conversely, maneuvering skill is any process that causes the individuals that use a maneuver more often to perform it at a higher level. Our results show that performance and frequency of use are often related and that skill predominates. All else being equal, birds that perform more pitch-downward and -upward rotations, and more total velocity increases, perform these respective maneuvers more rapidly; birds that perform more sharp PRT turns also do so for larger heading changes in less time (fig. S12). We used further analysis of PRT% to test the use of complex turns at both the species and individual level. Species that use proportionately more Arcs tend to perform their Arcs with greater centripetal acceleration (Fig. 6B); they are able redirect more turning force laterally while maintaining altitude. This trend is also recapitulated within species (Fig. 6C). Thus, the complex turns demonstrate that both species and individuals play to their strengths. How do these preferences for particular maneuvers arise? Are they driven by physiological and/or ecological differences, or do they represent random or neutral variation? These questions could be addressed by examining species differences in sensory systems

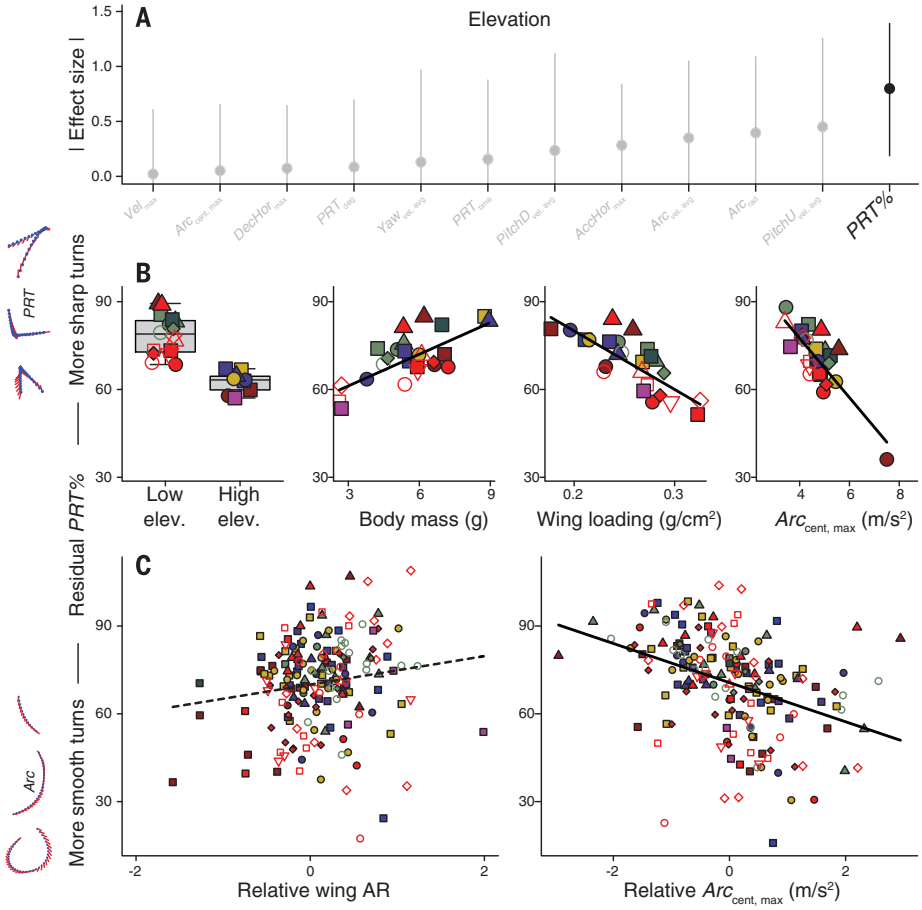

Fig. 6. Complex turns are associated with the environment, morphology, and skill. (**A**) The use of sharp versus smooth turns, PRT%, was the only behavior that differed among high- and low-elevation species. Effect sizes account for phylogenetic relationships (±95% highest posterior density intervals). (**B** and **C**) Partial effect plots illustrate the relative effect of each variable on PRT%, given the other effects in the statistical model (n = 180 individuals). (B) All else being equal, low-elevation species, larger-mass species, and those with lower wing loading use proportionately more sharp PRTs (and fewer Arcs). (C) Individuals with longer wings (high AR) use more sharp turns, although further analysis shows how this association can vary, depending on the species (fig. S11). Species and individuals that perform Arcs with greater centripetal acceleration also use proportionately more Arcs [(B) and (C), rightmost column], indicating that skill predominates over fatigue in the use of these complex turn maneuvers. Results are robust to removing the high-leverage species with n = 1 individual in (B).

and the development of locomotor ability, as well as functional ecology.

A key result of our comparative analysis is that evolved changes in the wings primarily determine turns and rotations, whereas evolved changes in muscle capacity primarily determine translations. This indicates that different flight maneuvers evolve by recruiting different traits. Our method provides a framework to now investigate the underlying genetic changes and adaptive fitness landscapes that have shaped the evolution of maneuvering flight. For birds, the relevant ecological factors may include predation, competition, and socially selected displays as well as elevational habitat (*1*, *18*, *25*, *33*). An important next step is to determine how translations, rotations, and turns are used in other behavioral contexts and how suites of maneuvering behaviors are used by other flying animals. Such comparisons may reveal performance tradeoffs that favor different maneuvering and morphological phenotypes (*6*). Moreover, the framework we provide can be used to test these ideas in more complex environments, once sufficiently small biologging tools become available. Although we have focused here on maneuvers that are shared among species, going forward it will be important to consider how these behaviors are combined into higher-order sequences and how novel maneuvers and sequences evolve.

REFERENCES AND NOTES

1. R. Dudley, *Integr. Comp. Biol.* **42**, 135–140 (2002).
2. M. F. Land, T. S. Collett, *J. Comp. Physiol.* **89**, 331–357 (1974).
3. S. A. Combes, D. E. Rundle, J. M. Iwasaki, J. D. Crall, *J. Exp. Biol.* **215**, 903–913 (2012).
4. K. M. Sholtis, R. M. Shelton, T. L. Hedrick, *PLOS ONE* **10**, e0125659 (2015).
5. T. Y. Moore, A. A. Biewener, *Integr. Comp. Biol.* **55**, 1188–1197 (2015).
6. T. Garland Jr., P. A. Carter, *Annu. Rev. Physiol.* **56**, 579–621 (1994).
7. V. Careau, T. Garland Jr., *Physiol. Biochem. Zool.* **85**, 543–571 (2012).
8. K. P. Dial, E. Greene, D. J. Irschick, *Trends Ecol. Evol.* **23**, 394–401 (2008).
9. T. L. Hedrick, A. A. Biewener, *J. Exp. Biol.* **210**, 1897–1911 (2007).
10. T. J. G. Read, P. S. Segre, K. M. Middleton, D. L. Altshuler, *J. R. Soc. Interface* **13**, 20160110 (2016).
11. S. Sefati *et al.*, *Proc. Natl. Acad. Sci. U.S.A.* **110**, 18798–18803 (2013).
12. S. J. Arnold, *Integr. Comp. Biol.* **23**, 347–361 (1983).
13. R. B. Srygley, R. Dudley, *J. Exp. Biol.* **174**, 155–166 (1993).
14. D. R. Warrick, *Can. J. Zool.* **76**, 1063–1079 (1998).
15. B. Cheng *et al.*, *J. Exp. Biol.* **219**, 3518–3531 (2016).
16. A. D. Straw, K. Branson, T. R. Neumann, M. H. Dickinson, *J. R. Soc. Interface* **8**, 395–409 (2011).
17. P. S. Segre *et al.*, *eLife* **4**, e11159 (2015).
18. C. J. Clark, *Proc. Biol. Sci.* **276**, 3047–3052 (2009).
19. T. Alerstam, M. Rosén, J. Bäckman, P. G. P. Ericson, O. Hellgren, *PLOS Biol.* **5**, e197 (2007).
20. C. J. Pennycuick, *Oikos* **30**, 165–176 (1978).
21. J. H. Marden, *J. Exp. Biol.* **130**, 235–258 (1987).
22. C. H. Greenewalt, *Trans. Am. Philos. Soc.* **65**, 1–67 (1975).
23. J. A. McGuire *et al.*, *Curr. Biol.* **24**, 910–916 (2014).
24. D. A. Skandalis *et al.*, *Nat. Commun.* **8**, 1047 (2017).
25. P. S. Segre, R. Dakin, T. J. G. Read, A. D. Straw, D. L. Altshuler, *Curr. Biol.* **26**, 3368–3374 (2016).
26. A. M. Wilson *et al.*, *Nature* **498**, 185–189 (2013).
27. R. P. Wilson *et al.*, *eLife* **4**, e06487 (2015).
28. H. C. Howland, *J. Theor. Biol.* **47**, 333–350 (1974).
29. A. Sih, A. M. Bell, J. C. Johnson, R. E. Ziemba, *Q. Rev. Biol.* **79**, 241–277 (2004).
30. I. G. Ros, L. C. Bassman, M. A. Badger, A. N. Pierson, A. A. Biewener, *Proc. Natl. Acad. Sci. U.S.A.* **108**, 19990–19995 (2011).
31. J. M. Cheverud, *Integr. Comp. Biol.* **36**, 44–50 (1996).
32. D. L. Altshuler, R. Dudley, S. M. Heredia, J. A. McGuire, *J. Exp. Biol.* **213**, 725–734 (2010).
33. N. A. Wright, D. W. Steadman, C. C. Witt, *Proc. Natl. Acad. Sci. U.S.A.* **113**, 4765–4770 (2016).
34. A. Lindström, A. Kvist, T. Piersma, A. Dekinga, M. W. Dietz, *J. Exp. Biol.* **203**, 913–919 (2000).
35. K. C. Welch Jr., D. L. Altshuler, *Comp. Biochem. Physiol. B Biochem. Mol. Biol.* **152**, 324–331 (2009).
36. O. B. O. Savile, *Evolution* **11**, 212–224 (1957).
37. A. Hedenström, M. Rosén, *Behav. Ecol.* **12**, 150–156 (2001).
38. J. G. Burns, R. C. Ydenberg, *Behav. Ecol. Sociobiol.* **52**, 128–136 (2002).
39. F. L. Carpenter, D. C. Paton, M. A. Hixon, *Proc. Natl. Acad. Sci. U.S.A.* **80**, 7259–7263 (1983).
40. K. Lilliendahl, *J. Avian Biol.* **33**, 212–218 (2002).
41. J. W. Kruyt, E. M. Quicazán-Rubio, G. F. van Heijst, D. L. Altshuler, D. Lentink, *J. R. Soc. Interface* **11**, 20140585 (2014).
42. P. Chai, *J. Exp. Biol.* **200**, 1527–1536 (1997).

ACKNOWLEDGMENTS

We thank the Los Amigos and La Selva Biological Stations, La Georgina restaurant, Hacienda Guaytara, L. Darkhovsky, A. Quinonez, C. Andrade, J. Saucier, A. Ryskiewicz, S. Chang, E. Kim, M. Van Vlaardingen, C. Witt, O. Ramirez, R. Vargas, A. Camacho, M. Pennell, V. Careau, and three anonymous reviewers. This research was funded by NSF (IOS 0923849) and the Natural Sciences and Engineering Research Council of Canada (402677 and PDF). Data and scripts are available on figshare at https://doi.org/10.6084/m9.figshare.5307136.v3. R.D., P.S.S., and D.L.A. designed the research. A.D.S. and P.S.S. developed the data acquisition techniques. P.S.S. and D.L.A. collected the data. R.D. developed the analysis and figures. R.D. and D.L.A. wrote the manuscript. All authors approved the manuscript.

SUPPLEMENTARY MATERIALS

www.sciencemag.org/content/359/6376/653/suppl/DC1
Materials and Methods
Figs. S1 to S12
Table S1
References (*43*–*64*)
Movies S1 and S2

17 August 2017; accepted 21 December 2017
10.1126/science.aao7104

NEURODEVELOPMENT

Live imaging of neurogenesis in the adult mouse hippocampus

Gregor-Alexander Pilz,[1]* Sara Bottes,[1]* Marion Betizeau,[1,2] David J. Jörg,[3,4] Stefano Carta,[1,6] Benjamin D. Simons,[3,4,5] Fritjof Helmchen,[6] Sebastian Jessberger[1]†

Neural stem and progenitor cells (NSPCs) generate neurons throughout life in the mammalian hippocampus. We used chronic in vivo imaging and followed genetically labeled individual NSPCs and their progeny in the mouse hippocampus for up to 2 months. We show that NSPCs targeted by the endogenous Achaete-scute homolog 1 (Ascl1) promoter undergo limited rounds of symmetric and asymmetric divisions, eliciting a burst of neurogenic activity, after which they are lost. Further, our data reveal unexpected asymmetric divisions of nonradial glia-like NSPCs. Cell fates of Ascl1-labeled lineages suggest a developmental-like program involving a sequential transition from a proliferative to a neurogenic phase. By providing a comprehensive description of lineage relationships, from dividing NSPCs to newborn neurons integrating into the hippocampal circuitry, our data offer insight into how NSPCs support life-long hippocampal neurogenesis.

The hippocampus requires new neurons in the dentate gyrus (DG) throughout life for learning and memory (*1*). Failing or altered hippocampal neurogenesis has been implicated in a variety of diseases such as major depression and age-related cognitive decline (*2*, *3*). On the basis of thymidine analog labeling, in vivo lineage tracing, and cell ablation studies, it has been proposed that radial glia-like (R) progenitor cells are the bona fide stem cells of the adult DG (*4*–*9*). According to the prevailing model of adult hippocampal neurogenesis, R cells self-renew—here defined as generating a daughter cell with equivalent molecular characteristics and potency—and give rise to proliferative nonradial glia-like (NR) cells that divide symmetrically to generate granule cells (*3*). However, the self-renewal capacity and lineage relationships of R cells remain controversial owing to the lack of longitudinal observations of individual R cells and their progeny within their niche (*7*, *8*). Similarly to previous imaging approaches that have probed the dynamics of somatic stem cell behavior in the nonmammalian nervous system and other stem cell niches (*10*–*17*), we used chronic in vivo imaging to track the fate of individual R cells over time within the adult DG.

[1]Laboratory of Neural Plasticity, Faculties of Medicine and Science, Brain Research Institute, University of Zurich, 8057 Zurich, Switzerland. [2]Institute of Neuroinformatics, University of Zurich and Swiss Federal Institute of Technology (ETH) Zurich, 8057 Zurich, Switzerland. [3]Cavendish Laboratory, Department of Physics, University of Cambridge, Cambridge CB3 0HE, UK. [4]Wellcome Trust/Cancer Research UK Gurdon Institute, University of Cambridge, Cambridge CB2 1QN, UK. [5]Wellcome Trust–Medical Research Council Cambridge Stem Cell Institute, University of Cambridge, Cambridge CB2 1QR, UK. [6]Laboratory of Neural Circuit Dynamics, Faculties of Medicine and Science, Brain Research Institute, University of Zurich, 8057 Zurich, Switzerland.
*These authors contributed equally to this work.
†Corresponding author. Email: jessberger@hifo.uzh.ch

Chronic imaging of individual brain stem cells

To label hippocampal R cells, we used mice expressing a tamoxifen (Tam)–regulable Cre recombinase under the control of the endogenous Achaete-scute homolog 1 (Ascl1) promoter crossed with a tdTomato reporter mouse line (Ascl1-tdTomato mice) (*18*). Ascl1-expressing cells constitute an essential population of neural stem and progenitor cells (NSPCs) in the adult DG (*18*–*20*). Adult Ascl1-tdTomato mice were implanted with a cortical window that left the hippocampal formation intact and allowed for two-photon imaging (Fig. 1A and fig. S1A) (*21*). A single Tam injection induced sparse labeling of Ascl1-expressing cells that were classified as R or NR cells on the basis of morphological features and marker expression (Fig. 1, B and C; fig. S2; and movie S1). Only R cells were analyzed as a starting population. Individual clones were imaged every ~12 to 24 hours (unless otherwise indicated) and followed for up to 2 months (Fig. 1, D and E, and fig. S3). Imaged clones (n = 63) were characterized on the basis of behavioral and morphological criteria (methods, fig. S2, movie S2, and table S1), allowing for the construction of individual lineage trees (Fig. 1E, fig. S3, and movie S3). After imaging, the final fate of progeny was confirmed using immunohistochemistry (Fig. 1, E and F, and fig. S4).

In agreement with previous static clonal lineage tracing experiments, we found that in 8- to 9-week-old Ascl1-tdTomato mice, 67% (42/63) of R cells entered the cell cycle and became active during the time course of imaging. Of these active R cells, 88% (37/42) divided within the first 20 days and, as a population, gave rise to both neuronal and glial daughter cells (Fig. 1, D to F, and figs. S3 and S4, A to D) (*19*).

Once activated, cycling R cells divided 2.3 ± 0.1 times and persisted for 9.6 ± 1.4 days on average (Fig. 2A and fig. S3). We did not find Ascl1-targeted R cells that generated neuronal progeny and returned to long-term (>4 weeks) quiescence within the 2-month observational period in any analyzed clones (Fig. 2A and figs. S3 and S4E). This suggests that, once activated, Ascl1-targeted R cells do not reenter long-term quiescence but generate a burst of neurogenic activity before committing to terminal neuronal differentiation and loss (Fig. 2A and figs. S3 and S4, E to H). The average clone size derived from active R cells was 4.8 ± 0.5 cells (Fig. 2B and fig. S3). We found no evidence for terminal differentiation of R cells into astrocytes, which had been suggested for nestin-expressing NSPCs after several rounds of cell division (*8*) (figs. S3 and S4H). Thus, the self-renewal capacity of Ascl1-targeted R cells is temporally limited; this finding is similar to previous results obtained using population-based static analysis of nestin-labeled NSPCs (*8*).

Cell division history is associated with cell fate

We then considered the fate behavior of activated R cells and their progeny. Previously, it has been proposed that the predominant mode of R cell division is asymmetric (*6*–*8*, *22*). However, without access to continuous in vivo cell tracking, evidence for asymmetric fate has been indirect. Morphological analyses of cell body and radial glia-like processes of R cells before and after cell division revealed that the morphology of R cells remained stable (Fig. 2, C and D, and fig. S5A), providing direct evidence for asymmetric cell divisions (*6*–*8*, *22*). Although the majority of observed first cell divisions were asymmetric, generating a R cell and a NR cell (79.3%; Fig. 2, E and F), we found that 13.8% of first R cell divisions expanded the R cell pool through symmetric divisions (Fig. 2, E and G), mirroring the behavior found in static clonal studies of R cells targeted by a nestin promoter (*7*). With the further identification of direct neurogenic cell divisions of R cells (Fig. 2E and figs. S3 and S5, B and C), all three modes of division were observed, reminiscent of the fate behavior described for neural progenitors in the developing neocortex (*23*, *24*). The majority (70.6%) of all R cell divisions led to the generation of NR cells that were identified on the basis of their lack of a radial process, their ability to enter the cell cycle, and their capacity to generate neuronal progeny at later stages during the imaging period (Fig. 2, E and F). In contrast to previously suggested models (*3*), we found not only symmetric, neurogenic cell divisions of NR cells but also a substantial fraction of asymmetric cell divisions (24.2% of all NR divisions), yielding one renewed NR cell and one neuronal daughter cell (Fig. 2, H to J) (*9*). NR cells underwent as many as six rounds of cell division (with an average of 2.9 ± 0.2 divisions); thus, NR cells are a major source of clonal expansion (Fig. 2, H to J, and fig. S3).

Chronic imaging also allowed us to analyze whether division times (T_D) are correlated with previous cell divisions or within clonally related lineages. We analyzed the T_D of R and NR

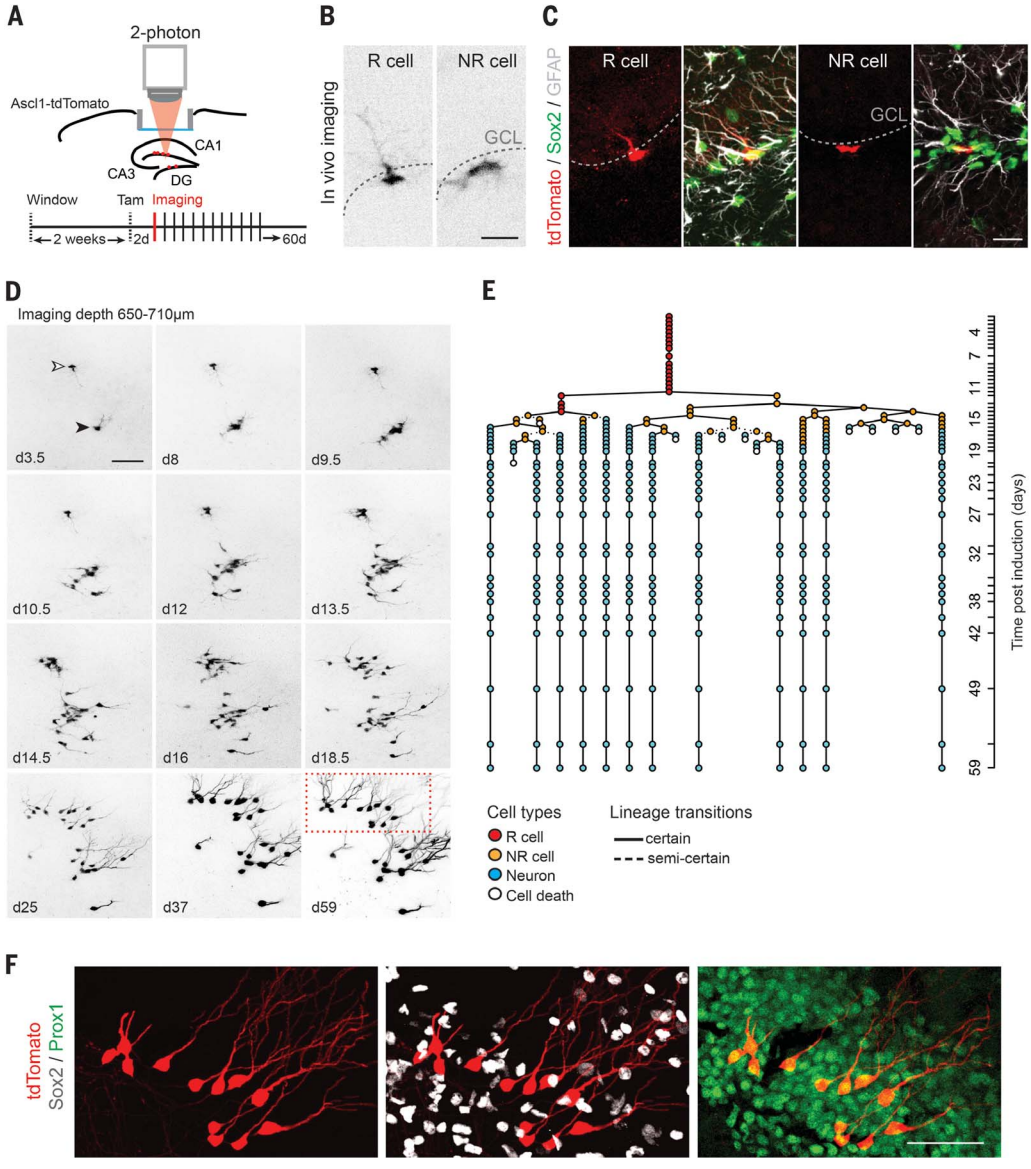

Fig. 1. Chronic in vivo imaging of neurogenesis in the adult DG. (**A**) Scheme illustrating the experimental approach allowing for chronic in vivo imaging of NSPCs in the adult DG of Ascl1-tdTomato mice. (**B**) Representative in vivo images of R and NR cells at 2 days post-induction (dpi). (**C**) Immunostained images showing Sox2-positive (green), Ascl1-tdTomato–labeled (red) R cells with GFAP (glial fibrillary acidic protein)–positive (white) radial processes and NR cells (Sox2-positive and GFAP-negative) in Ascl1-tdTomato mice at 2 dpi. (**D**) Selected imaging time points for two R cells (respectively indicated with open and filled arrowheads) over the course of 2 months, showing the emergence of two neuronal clones. Time points after Tam injection are indicated in each panel. Shown are collapsed *z*-stacks. The clonal expansion of individual R cell progeny and subsequent neuronal maturation can be seen. (**E**) Lineage tree deduced from tracking one R cell [open arrowhead in (D)] and its progeny. Identified cell types are color-coded, and lineage transitions are depicted depending on their certainty (methods). Each circle in the lineage tree represents an imaging time point. The *y* axis shows the duration of the imaging. (**F**) Post hoc immunohistochemical analyses of the clone shown in (D) (boxed area, day 59) confirm neuronal progeny with newborn cells positive for Prox1 (green) and negative for Sox2 (white). The horizontal view of the DG corresponds to the view obtained during in vivo imaging. Scale bars, 20 µm [(B) and (C)] and 50 µm [(D) and (F)]. d, days; GCL, granule cell layer.

divisions and found that, once the cells were activated, T_D remained constant (Fig. 2K). T_D times of sister cells were correlated among R cell daughters, whereas no correlation was detected for daughters of NR cells (Fig. 2, L and M), suggesting segregation of cellular features selectively in R cells that determine the daughter cells' reentry into cell division.

Asymmetric segregation of cell death within clonal lineages

Not all newborn cells survive and become stably integrated into the DG circuitry. Two critical periods of cell death have been described previously: an early phase of cell death within the first days after cell birth and a later phase of neuronal selection that is activity-dependent and occurs about 1 to 3 weeks after new neurons are born (*25*–*27*). Consistent with previous reports, we found an average frequency of cell death among the progeny per lineage of 59.6% and identified two waves of cell death occurring around 1 to 4 and 13 to 18 days after birth, respectively (Fig. 3, A and B) (*25*–*27*). We identified interclonal variability, with some clones showing no cell death, whereas other clones completely disappeared over time (Fig. 3A). Furthermore, we found differences regarding the susceptibility to cell death among individual sublineages when analyzing levels of early cell death (until 7 days after cell birth; Fig. 3, C to F), suggesting that cell death is not evenly distributed among progeny. The underlying cause for the observed subtree-associated variability of cell death remains unknown, but it may involve intrinsic mechanisms—for example, retrotransposon-associated genetic alterations or unequal segregation of aging factors (*28*, *29*)—rather than environmental, niche-dependent factors, such as growth factor availability (*3*). Supporting this interpretation, we found that surviving cells can lie interspersed among death-prone cells (Fig. 3G).

Developmental-like program describes cell fate behavior

Inspection of reconstructed R cell lineages revealed a wide variability in neurogenic potential and fate outcomes (fig. S3). After induction, some R cells differentiated early, giving rise to one or two short-lived neurons, whereas others gave rise to more than 10 surviving neurons (Fig. 2B and figs. S3 and S4F). Despite this variability, some features of R cell fate behavior were conserved among all lineage trees. In particular, we found no instance of an asymmetrical R cell division being followed by a symmetric R cell duplication (Fig. 2E and fig. S3), suggesting either that, once activated, R cells move sequentially from a symmetrically to an asymmetrically dividing phase, or that the proliferative potential of R cells becomes progressively exhausted so that symmetrical duplicative divisions become increasingly scarce. In contrast, variability in the output of dividing NR cells was indicative of a conserved pattern of stochastic

fate, with NR cells choosing between symmetric duplication, asymmetric division, and symmetric differentiation with probabilities independent of the cell generation (Fig. 2H and fig. S3).

Thus, on the basis of these observations, we considered the quantitative fate behavior of R cells. Given the sequential pattern of symmetric and asymmetric divisions, we questioned whether R cells might be following a developmental-like program, switching irreversibly from a phase of proliferative (symmetrical) divisions to a phase of neurogenic (asymmetrical) divisions, as observed during cortical development (Fig. 4A, fig. S6A, and table S2) (*30*). Using a statistical modeling approach, we quantitatively assessed the viability of this hypothesis by fitting the lengths of putative proliferative and neurogenic phases against average clonal properties (methods). This simple developmental-like paradigm yielded predictions of the proliferative output, the cell fate distributions, and the average clonal composition over time that were in agreement with the observed data within the theoretically predicted variability (Fig. 4, B to D, and methods). As a consistency check, we also assessed whether the observed sequential fate pattern could represent the chance outcome of stochastic fate behavior, with R cells becoming progressively biased away from self-renewal toward differentiation over time (figs. S6 and S7). However,

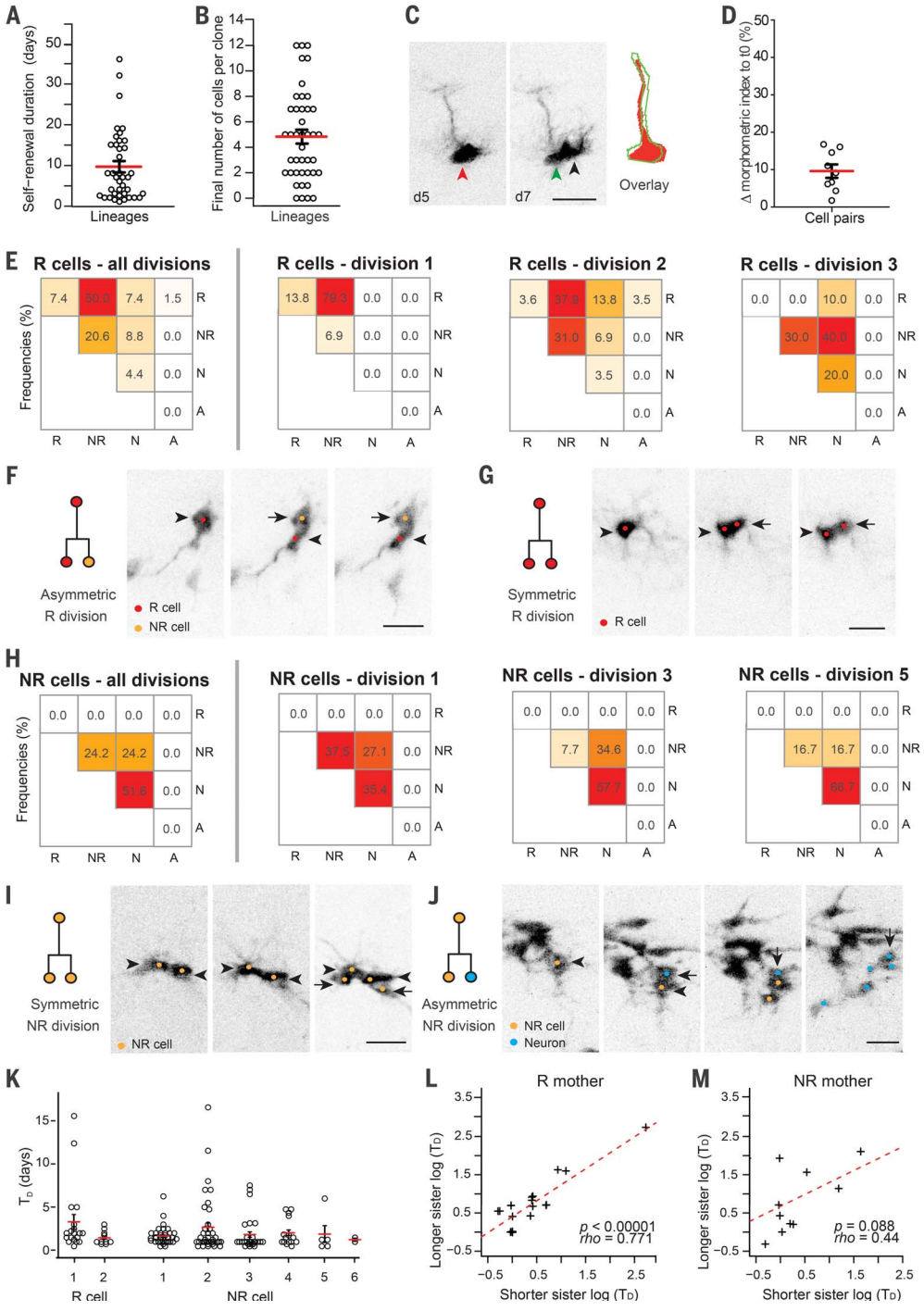

Fig. 2. The mode of NSPC division is associated with individual cell division history. (**A**) Self-renewal duration (time between first and last division in each lineage) of R cells (9.6 ± 1.3 days; n = 39). (**B**) Distribution of the final number of cells per active clone (n = 42 lineages). Open circles represent individual clones. (**C**) Chronic in vivo imaging before and after cell division illustrates asymmetric cell division of R cells. A large overlap is evident in the cellular morphology before (red arrowhead and red outline) and after (green arrowhead and green outline) R cell division. The black arrowhead points at the asymmetrically generated daughter cell. (**D**) A morphometric index (including circularity and process length; details are given in the methods) shows little deviation in cell morphology before and after cell division (9.6 ± 1.8%; n = 9). (**E**) Heat map representing the frequencies of modes of division of R cells (all divisions and division rounds 1 to 3; n = 68 divisions total). The division mode changes from predominantly asymmetric (division 1) to a more symmetric differentiating division (divisions 2 and 3). N, neuron; A, astrocyte. (**F**) Example of an asymmetric division of an R cell (lineage 40; fig. S3). (**G**) Example of a symmetric division of an R cell (lineage 13). Mother cells are indicated with arrowheads and daughter cells with arrows. (**H**) Heat map representing the frequencies of cell division modes of NR cells (all divisions and division rounds 1, 3, and 5; n = 153 divisions). (**I**) Example of a symmetric NR cell division (lineage 1). (**J**) Example of an asymmetric NR cell division (lineage 3). The NR daughter continues to divide. Mother and daughter cells are indicated as in (F) and (G). (**K**) Cell division time (T_D) of R and NR cells for different divisions. (**L**) The times until next cell division of sister cells originating from a single R mother cell are correlated (Pearson's ρ = 0.77; *P < 0.00001; n = 22 pairs). (**M**) The T_D of sister cells originating from a single NR mother are not correlated (Pearson's ρ = 0.44; P = 0.08; n = 16 pairs). Each plus sign represents a pair of sister cells. Red lines, means; error bars, SEM. Scale bars, 20 μm [(C), (F), (G), (I), and (J)].

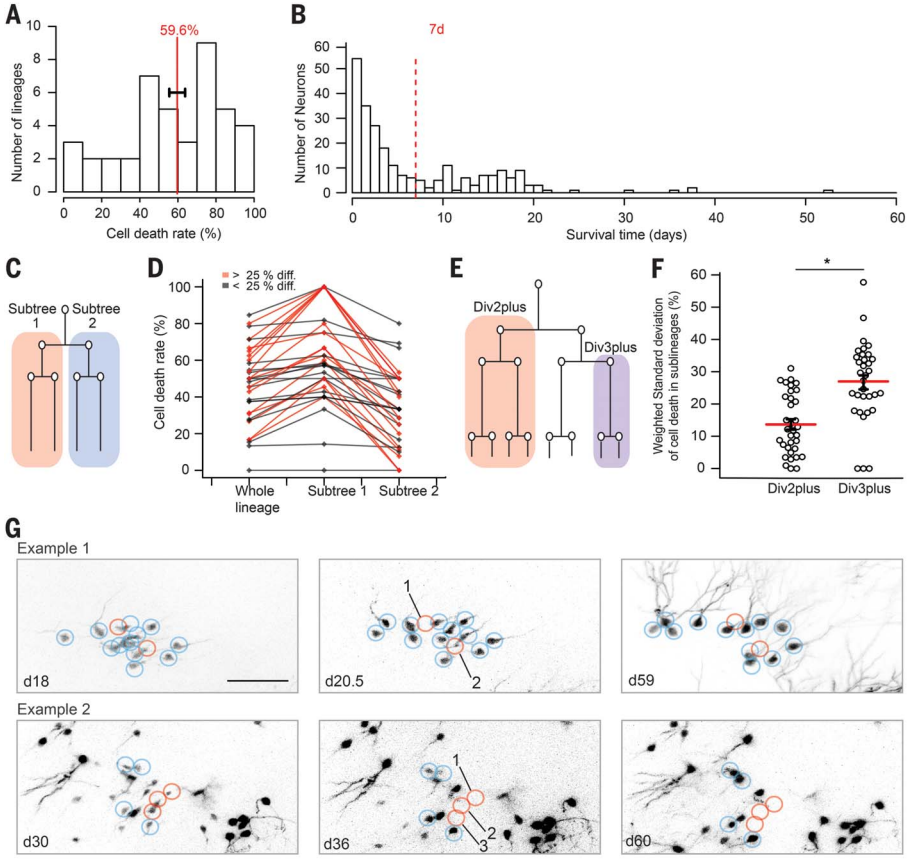

Fig. 3. Chronic in vivo imaging reveals variable susceptibility to cell death. (**A**) The frequency of cell death in all chronically imaged lineages ranges from 0 to 100% (mean = 59.6%, n = 42; error bars, SEM). (**B**) Time point of cell death after last cell division. Two peaks of cell death occur before and after 7 days, with almost no cell death occurring >20 days after birth (n = 242). (**C**) Pictogram depicting the comparison of cell death frequencies in subtrees 1 and 2, derived after the initial R cell division, plus subsequent progeny within that subtree (Div2plus). (**D**) Difference in cell death frequencies in subtrees 1 and 2 in comparison with cell death frequency in the whole lineage [lineages with >25% difference in cell death rate are colored red; only early cell death (until day 7 after birth) was included]. (**E**) Pictogram depicting the comparison of cell death frequencies in the Div2plus subtrees and the subtrees derived from the second division after initial R cell division plus subsequent progeny within those subtrees (Div3plus). (**F**) Cell death frequencies are more asymmetrically distributed among Div3plus than among Div2plus sublineages, as demonstrated by the higher weighted standard deviation to the Div2plus subtree death frequency [Div2plus difference, 13.6 ± 1.6 (n = 34); Div3plus difference, 27 ± 2.2 (n = 33); *P < 0.0001, Wilcoxon rank sum test]. Weighted standard deviation was used to account for differences in subtree sizes within each clone. Red lines, means; error bars, SEM. (**G**) Locations of surviving newborn neurons (blue circles) relative to cells that underwent cell death (red circles). The observed times until death (calculated from the birth of the individual cell) for dying cells are 2.5 days (cells 1 and 2 in example 1) and 13, 3, and 4 days (cell 1, 2, and 3 in example 2). Spatial localizations of surviving and dying cells overlap. Scale bar, 100 μm.

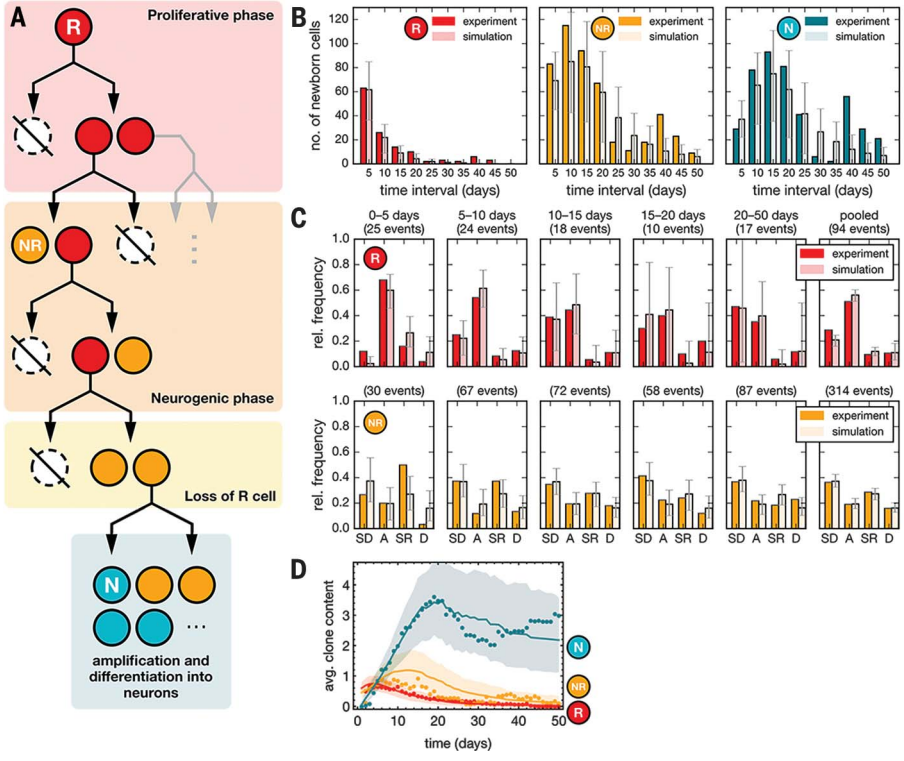

Fig. 4. Modeling-based analysis suggests a developmental-like program for R cell fate behavior. (**A**) In the model paradigm, R cells follow a defined program comprising a proliferative phase (duplications) that switches irreversibly into a neurogenic phase (asymmetric divisions and terminal differentiation). (**B**) Total number of newborn cells in successive time intervals of 5 days after induction from experiments (dark data set) and from simulations (light data set) for R and NR cells and neurons (N) (methods). Cell counts were pooled over 55 lineage trees with nonquiescent R cells and averaged over 500 realizations for each lineage tree, resulting in a total of 27,500 simulations (model parameters are given in table S2). Error bars indicate the range within which 95% of the simulation results fall. (**C**) Relative frequencies of different cell fates in successive time intervals of 5 days after induction from experiments and simulations, as in (B). Later time intervals (20 to 50 days) with small numbers of events have been pooled together. SD, symmetric differentiating divisions; A, asymmetric divisions; SR, symmetric self-renewing divisions; D, cell death. (**D**) Average clone content as a function of time from experiments (dots) and from simulations (lines) for different indicated cell types. Shaded areas indicate the regions within which 95% of the simulation results fall.

given the observed cell fate frequencies and the number of observed lineage trees, we estimated the chance for such an outcome to be only 2.4% (methods). Thus, we conclude that a model in which the sporadic entry of R cells into the cell cycle activates a developmental-like program of fate, leading to a burst of neurogenic activity, provides the most plausible explanation of the lineage data.

In this study, we used chronic imaging of individual R cells and their progeny to characterize the cellular dynamics underlying adult hippocampal neurogenesis. Our data show that, after activation, Ascl1-targeted R cells enter a developmental-like program, eliciting a burst of neurogenic activity. However, self-renewal is temporally limited: We did not observe repeated shuttling between quiescence and proliferation, leading to a loss of activated R cells. These findings do not rule out the previously reported presence of stem cells in the mammalian DG that shuttle back and forth between quiescence and activity, dividing for extended periods (*7*, *31*, *32*). Stem cell heterogeneity has been postulated, and the Ascl1-targeted population analyzed here may not include all subtypes that are capable of generating neuronal progeny in the adult DG (*33*–*35*). Previous data suggested that about 10 to 15% of all granule cells are adult-generated in the mouse hippocampus. This indicates that adult neural stem cells generate 30,000 to 45,000 granule cells during the entire life span (*5*, *36*, *37*), which, as a fraction of the total neuronal population, appears to be lower in the rodent than in the human DG (*38*). We found that, once activated, individual Ascl1-targeted R cells generated 4.8 neurons on average. On the basis of previous estimates that the DG contains ~10,000 R cells in 2-month-old mice (*8*), the total number of cells that can be generated by Ascl1-targeted cells with the principles of clonal expansion described here (~45,000) appears to be sufficient to explain a substantial part of hippocampal neurogenesis. Our in vivo imaging results elucidate the cellular dynamics of physiological adult neurogenesis and form the basis to understand the molecular mechanisms governing the steps from dividing stem cells to newborn neurons.

REFERENCES AND NOTES

1. C. Anacker, R. Hen, *Nat. Rev. Neurosci.* **18**, 335–346 (2017).
2. S. Yun, R. P. Reynolds, I. Masiulis, A. J. Eisch, *Nat. Med.* **22**, 1239–1247 (2016).
3. J. T. Gonçalves, S. T. Schafer, F. H. Gage, *Cell* **167**, 897–914 (2016).
4. D. C. Lagace *et al.*, *J. Neurosci.* **27**, 12623–12629 (2007).
5. I. Imayoshi *et al.*, *Nat. Neurosci.* **11**, 1153–1161 (2008).
6. B. Seri, J. M. García-Verdugo, B. S. McEwen, A. Alvarez-Buylla, *J. Neurosci.* **21**, 7153–7160 (2001).
7. M. A. Bonaguidi *et al.*, *Cell* **145**, 1142–1155 (2011).
8. J. M. Encinas *et al.*, *Cell Stem Cell* **8**, 566–579 (2011).
9. S. Lugert *et al.*, *Cell Stem Cell* **6**, 445–456 (2010).
10. J. S. Barbosa *et al.*, *Science* **348**, 789–793 (2015).
11. D. B. Gurevich *et al.*, *Science* **353**, aad9969 (2016).
12. P. Rompolas, K. R. Mesa, V. Greco, *Nature* **502**, 513–518 (2013).
13. P. Rompolas *et al.*, *Nature* **487**, 496–499 (2012).
14. P. Rompolas *et al.*, *Science* **352**, 1471–1474 (2016).
15. C. Lo Celso *et al.*, *Nature* **457**, 92–96 (2009).
16. Y. Xie *et al.*, *Nature* **457**, 97–101 (2009).
17. L. Ritsma *et al.*, *Nature* **507**, 362–365 (2014).
18. E. J. Kim, J. L. Ables, L. K. Dickel, A. J. Eisch, J. E. Johnson, *PLOS ONE* **6**, e18472 (2011).
19. G. J. Sun *et al.*, *Proc. Natl. Acad. Sci. U.S.A.* **112**, 9484–9489 (2015).
20. J. Andersen *et al.*, *Neuron* **83**, 1085–1097 (2014).
21. G. A. Pilz *et al.*, *J. Neurosci.* **36**, 7407–7414 (2016).
22. H. Suh *et al.*, *Cell Stem Cell* **1**, 515–528 (2007).
23. J. H. Lui, D. V. Hansen, A. R. Kriegstein, *Cell* **146**, 18–36 (2011).
24. M. Götz, W. B. Huttner, *Nat. Rev. Mol. Cell Biol.* **6**, 777–788 (2005).
25. G. Kempermann, D. Gast, G. Kronenberg, M. Yamaguchi, F. H. Gage, *Development* **130**, 391–399 (2003).
26. A. Sierra *et al.*, *Cell Stem Cell* **7**, 483–495 (2010).
27. A. Tashiro, V. M. Sandler, N. Toni, C. Zhao, F. H. Gage, *Nature* **442**, 929–933 (2006).
28. D. L. Moore, G. A. Pilz, M. J. Araúzo-Bravo, Y. Barral, S. Jessberger, *Science* **349**, 1334–1338 (2015).
29. A. R. Muotri *et al.*, *Nature* **435**, 903–910 (2005).
30. P. Gao *et al.*, *Cell* **159**, 775–788 (2014).
31. G. Kempermann, *Cell* **145**, 1009–1011 (2011).
32. N. Urbán *et al.*, *Science* **353**, 292–295 (2016).
33. M. A. Bonaguidi, J. Song, G. L. Ming, H. Song, *Curr. Opin. Neurobiol.* **22**, 754–761 (2012).
34. Z. Chaker, P. Codega, F. Doetsch, *Wiley Interdiscip. Rev. Dev. Biol.* **5**, 640–658 (2016).
35. N. A. DeCarolis *et al.*, *Hippocampus* **23**, 708–719 (2013).
36. G. Kempermann, H. G. Kuhn, F. H. Gage, *Proc. Natl. Acad. Sci. U.S.A.* **94**, 10409–10414 (1997).
37. J. Ninkovic, T. Mori, M. Götz, *J. Neurosci.* **27**, 10906–10911 (2007).
38. K. L. Spalding *et al.*, *Cell* **153**, 1219–1227 (2013).

ACKNOWLEDGMENTS

We thank S. April for help with analyzing R cell morphology and D. L. Moore and D. C. Lie for comments on the manuscript. **Funding:** This work was supported by the European Research Council (to S.J. and F.H.), the Swiss National Science Foundation (BSCGI0_157859 to S.J.), the Zurich Neuroscience Center, and the Wellcome Trust (098357/Z/12/Z to B.D.S.). G.A.P. was supported by a European Molecular Biology Organization Long-Term Fellowship. M.B. was supported by a SystemsX transition postdoctoral fellowship. **Author contributions:** G.A.P. developed the imaging approach, performed imaging, analyzed data, and cowrote the manuscript. S.B. performed imaging, analyzed data, and revised the manuscript. S.C. codeveloped the imaging approach and performed imaging. M.B. analyzed data and revised the manuscript. D.J.J. and B.D.S. contributed to the concept, performed theoretical modeling, and cowrote the manuscript. F.H. contributed to the concept and revised the manuscript. S.J. developed the concept and wrote the manuscript. **Competing interests:** None declared. **Data and materials availability:** The data reported are presented in the main paper and the supplementary materials.

SUPPLEMENTARY MATERIALS

www.sciencemag.org/content/359/6376/658/suppl/DC1
Materials and Methods
Figs. S1 to S7
Tables S1 and S2
References (*39*–*54*)
Movies S1 to S3

27 July 2017; accepted 13 December 2017
10.1126/science.aao5056

Cite as: J. Kim *et al.*, *Science* 10.1126/science.aar2179 (2017).

Coherent single-atom superradiance

Junki Kim, Daeho Yang, Seung-hoon Oh, Kyungwon An*

Department of Physics and Astronomy, Seoul National University, Seoul 08826, Korea.

*Corresponding author. Email: kwan@phya.snu.ac.kr

Superradiance is a quantum phenomenon emerging in macroscopic systems whereby correlated single atoms cooperatively emit photons. Demonstration of controlled collective atom-field interactions has resulted from the ability to directly imprint correlations with an atomic ensemble. Here, we report cavity-mediated coherent single-atom superradiance: single atoms with predefined correlation traverse a high-Q cavity one by one, emitting photons cooperatively with the *N* atoms already gone through the cavity. Enhanced collective photoemission of *N*-squared dependence was observed even when the intracavity atom number was less than unity. The correlation among single atoms was achieved by nanometer-precision position control and phase-aligned state manipulation of atoms by using a nanohole-array aperture. Our results demonstrate a platform for phase-controlled atom-field interactions.

Superradiance is a collective radiation phenomenon by a number of quantum emitters (*1*). In the original prediction, exchange symmetry is present in closely packed emitters whose inter-particle distance is much smaller than the transition wavelength, and therefore dipole-dipole correlation emerges during their spontaneous decay process. The correlation makes the ensemble behave collectively and induces enhanced interaction with the vacuum fields, leading to stronger and faster radiation emission compared to the ordinary spontaneous emission. Early experiments performed with a large number of emitters (as in a dense atomic vapor or in a beam) reported observations consistent with the prediction (*2*, *3*). Recent technical advances have enabled the realization of superradiance in various systems such as a Bose-Einstein condensate (*4*), quantum dots (*5*) and trapped atoms coupled to a cavity (*6*).

The mutual phase correlation among atoms is the key to superradiance. It can make the ensemble behave as a single macro dipole. Moreover, direct control of atomic phases enables controllable collective atom-field interactions. In recent experiments, the phase of atoms in an ensemble was imprinted by a single photon pulse (*7*–*9*) or a frequency-swept laser pulse (*10*). The ensemble then started superradiant emission without a threshold or an initial time delay. The output field in this case follows the given imprinted phase and thus its spatial mode overlaps with the input mode, making it hard to distinguish the input and output fields spatially. This approach works only in the pulsed regime. Observation of a superradiant state in a Bose-Einstein condensate couple to a cavity was another notable work (*11*). However, it relied on self-organization of atoms based on a thermodynamic principle, and thus further tunability could not be attained.

Another approach to achieve controllable superradiance is to prepare emitters in a cavity and to manipulate the quantum state of individual emitters. Ions (*12*), neutral atoms (*13*) and artificial atoms based on superconducting circuits (*14*) have been used in this approach. The results include immediate strong and fast radiation emission and controllability between superradiance and subradiance. However, technical difficulties have limited the number of emitters involved in the superradiance only up to two.

We present an approach to realize phase-controlled superradiance whereby single atoms are prepared in the same quantum superposition of ground and excited states traverse a cavity one by one. The long-lived cavity field then mediates collective interaction among the phase-correlated single atoms separated in time, leading to superradiance. The collective interaction is one-sided in that the emission of a particular atom in the cavity is cooperative only with the preceding atoms. Even when at most only one atom is present in the cavity, tens of atoms participate in the superradiance and the emission intensity is proportional to the square of the number of the participating atoms.

Our system, adapted from (*15*), consists of a supersonic barium atomic beam and a high-Q optical cavity which the atoms resonantly interact with (Fig. 1A). The barium-138 atoms are prepared in a superposition state of the ground and excited states just before they enter the cavity mode by a pump laser propagating perpendicular to the cavity axis as well as to the atomic beam direction. The atomic phase imprinted by the pump laser depends on the position at which the atom traverses the pump laser. The phase of the atom-cavity coupling also alternates 0 and π radian following the standing wave structure of the cavity mode. A checkerboard-pattern nanohole array is used as an atomic beam aperture in order to localize and control the atomic position. The localized atoms then selectively pick up the phase of the pump

laser as well as the cavity field corresponding to their positions prescribed by the array structure. As a result, the atom-field relative phase is the same for every atom traversing the cavity (Fig. 1B). The desired atomic internal state is prepared by the pump laser with a pulse area of $\Theta = \int[\Omega_p(x)/v]dx$, where $\Omega_p(x)$ is the Rabi frequency due to the pump laser and v is velocity of the atom. The atomic state can then be expressed as $|\psi_{atom}\rangle = \sin(\Theta/2)|e\rangle + \cos(\Theta/2)\exp(i\phi)|g\rangle$, where ϕ is the atomic phase imprinted by the pump laser. Atomic correlation between any two of the injected atoms is then given by $\langle\sigma_i^{\dagger}\sigma_j\rangle = \frac{1}{4}\sin^2\Theta$, where $\sigma_i = |g\rangle\langle e|$ is the lowering operator of the i-th atom, showing that the atom-atom correlation is maximized when $\Theta = \pi/2$.

Injected atoms then emit photons into the cavity mode and build up the cavity field. A previous study assuming a lossless cavity expected enhanced collective emission by consecutively injected N atomic dipoles to show explicit N^2 dependence (*16*). The longlasting cavity field links the atoms together and the expected photon number is exactly the same as that of simultaneously injected N dipoles (see fig. S1).

When a cavity has a finite decay, the gain (emission by atoms) and the loss (absorption by atoms as well as the cavity decay) of the cavity field would be balanced in its steady state. The averaged cavity photon number $\langle n\rangle$ in the steady state can be obtained from the quantum master equation (*17*) and it is approximately given by

$$\langle n\rangle \approx \frac{\langle N_c\rangle \rho_{ee} (g\tau)^2}{2-(2\rho_{ee}-1)\langle N_c\rangle (g\tau)^2} + \left(\langle N_c\rangle |\rho_{eg}| g\tau\right)^2 \qquad (1)$$

where $\langle N_c\rangle \equiv r/\gamma_c$ is the mean number of atoms injected into the cavity during the cavity-field decay time $1/\gamma_c$ with r the atomic injection rate, ρ_{ee} and ρ_{eg} are the density matrix elements of atomic state with the subscripts 'e' and 'g' represent excited and ground states, respectively, g is the atom-cavity coupling constant and τ is the atom-cavity interaction time.

The first term, approximately proportional to $\frac{1}{2}\langle N_c\rangle$ when $\langle N_c\rangle(g\tau)^2 << 1$, is due to the non-collective emission of atoms, including spontaneous and stimulated emission as well as the cavity-QED effect. The second term, exhibiting a quadratic dependence on $\langle N_c\rangle$, is due to collective emission, *i.e.* the superradiance. Compared to the case with a lossless cavity (*16*), the number of atoms participating in the superradiance is identified to be $\langle N_c\rangle$ in our case (*17*). When $\langle N_c\rangle >> 1$, the second term dominates the emission and the field state approximately becomes a coherent state $|\alpha\rangle$ with $\alpha = -i\langle N_c\rangle\rho_{eg}g\tau$.

The mean intracavity atom number $\langle N\rangle$ is related to $\langle N_c\rangle$ as $\langle N_c\rangle = \langle N\rangle/(\gamma_c\tau)$. If the cavity-field decay time $1/\gamma_c$ is much larger than τ ($\gamma_c\tau << 1$), $\langle N_c\rangle$ can be much greater than unity even when the mean intracavity atom number $\langle N\rangle$ is less than unity and thus the collective effect can take place. The cavity field mediates the collective behavior among the time-separated $\langle N_c\rangle$ atoms that are going through the cavity individually during the cavity-field decay time, leading to the single-atom superradiance. Around 22 atoms are involved in the collective emission when a single atom is present in the cavity mode on average.

In our experiment, the phase-aligned atomic dipoles prepared with the aforementioned nanohole-array were injected into the cavity and the mean intracavity photon number in the steady state was measured with a single-photon-counting module. The atom-cavity interaction was in the strong coupling regime with $(g, \gamma, \gamma_c) = 2\pi \times (290, 25, 75)$ kHz, where g is the atom-cavity coupling averaged over the atomic distribution centered around the antinodes of the cavity and γ (γ_c) is the atomic polarization (cavity-field) decay rate. The single-atom cooperativity was $C = g^2/\gamma\gamma_c = 44$. The mean travel time of atoms from the pump to the cavity field was about 200 ns whereas the mean atom-cavity interaction time τ = 101 ns. As a comparative counterpart, we also performed the experiment with a 250 μm × 25 μm-sized rectangular atomic beam aperture for the case of atoms with random phases. In the latter case, the atomic beam was injected into the cavity mode with a small tilt angle in order to induce Doppler shifts so as to achieve a uniform atom-field coupling (*18–21*), whose strength is a half of the maximum coupling strength.

The collective emission described by the second term in Eq. 1 is expected to have the quadratic dependence on two parameters, the induced atomic dipole moment $\propto |\rho_{eg}|$ and the atom number $\langle N_c\rangle$. First, we investigated $|\rho_{eg}|$ dependence of collective emission by varying the pump pulse area (Fig. 2). Due to the relation $|\rho_{eg}| = |\frac{1}{2}\sin\Theta|$ for the prepared superposition state, the atomic dipole moment would be maximized with equal ground- and excited-state populations ($\Theta = 0.5\pi$ or 1.5π), and so would be the collective emission. Clear enhancement was observed when the atoms are prepared in the phase-aligned superposition states. The enhancement was more than ten-fold for $\Theta < 0.3\pi$ (also see fig. S2). Combined contributions by ρ_{ee} (non-collective) and $|\rho_{eg}|$ (collective) make $\langle n\rangle$ maximized near $\Theta \approx 0.7\pi$. Due to the small overlap between the pump laser field and the cavity mode (both are Gaussian), the collective emission process is somewhat disturbed by the stray pump field in the cavity when the pump intensity is strong, resulting in the enhancement reduction for $\Theta > \pi$. On the other hand, in the case of random phase, the photon number is given by the non-collective emission only, and thus it is maximized with fully inverted atomic states ($\Theta = \pi$).

The enhancement is strongly dependent on the atomic phase purity. In reality, there are several sources of phase noise. Finite atomic localization sets the lower bound of atomic phase variance. Atomic spontaneous emission into

free space also contributes to phase diffusion of atoms, reducing $|\rho_{eg}|$ by 6%. In addition, the pump laser has a phase uncertainty: the laser phase diffuses in time with a finite laser linewidth. If we intentionally make the pump laser linewidth larger, the superradiant enhancement becomes smaller (see fig. S3). We performed quantum-trajectory simulation as well as quantum master equation calculation with the experimental parameters and our data well agree with the numerical results (*17*) (also see fig. S4).

Figure 3 shows the mean intracavity photon number $\langle n \rangle$ versus the excited state atom number $\langle N \rangle \rho_{ee}$. When the atoms have no dipole moment (Fig. 3B), only the non-collective emission is present. With a small number of atoms, the cavity field is mainly made by spontaneous emission of atoms (dashed line) and its photon number increases linearly to the atom number. As the accumulated photon number gets larger, stimulated emission and absorption become dominant over the spontaneous emission and the system lases for positive inversion ($\rho_{ee} - \rho_{gg} > 0$) or the photon number plateaus for negative inversion ($\rho_{ee} - \rho_{gg} < 0$). Especially for positive inversion, a rapid growth of the photon number starts to occur at $\langle n \rangle \approx 1$, which is the well-known lasing threshold in the conventional lasers (*22*).

However, when atoms have the same phase (Fig. 3A), photon emission is enhanced nonlinearly with its log-log slope getting steeper than unity. The measured intracavity photon numbers are consistently larger than the photon number made only by the cavity-enhanced spontaneous emission (dashed line). When the pump pulse area is 0.5π, corresponding to $|\psi_{atom}\rangle \approx [|e\rangle + \exp(i\phi)|g\rangle]/\sqrt{2}$, the observed log-log slope is 1.66 ± 0.01. After subtracting the contribution by the non-collective emission corresponding to the dashed line, the recalculated log-log slope becomes 1.94 ± 0.04 (see the inset of Fig. 3), which indicates the observed emission is dominantly superradiance proportional to the square of the number of atoms. A near-quadratic growth appears even in the negative inversion case of $\Theta = 0.3\pi$, in which only 21% of atoms are in the excited state with the rest in the ground state. When $\Theta > 0.5\pi$, the atoms have positive population inversion and thus the photon number grows further by stimulated emission beyond the level by the collective emission. In this case, it is impossible to isolate the collective emission effect clearly in the log-log plot.

It is also notable that the log-log slope is almost invariant for a large range of $\langle N_c \rangle$ for $\Theta \leq 0.5\pi$. The theory expects that the quadratic dependence on $\langle N_c \rangle$ would be dominant in the region of $(1 + \cos\Theta)^{-1} < \langle N_c \rangle < (g\tau)^{-2}$ for the perfectly phase-aligned atoms although the practical phase noise would make the domain somewhat reduced. Such a broad-range quadratic growth, occurring independently of $\langle n \rangle$ values, including $\langle n \rangle << 1$ as in (*23*), is a distinctive feature of the present superradiance compared to the drastic slope change occurring near the threshold condition of $\langle n \rangle \approx 1$ in the ordinary lasing case. The absence of the usual lasing threshold or thresholdless lasing in the present superradiance cannot be explained in terms of the so-called β-factor in ordinary lasers based on non-collective emission (*24*). In our case $\beta = (g\tau)^2 \approx 0.034$ in the nanohole-array-aperture case (Figs. 2A and 3A) and 0.011 in the rectangular-aperture case (Figs. 2B and 3B) (*17*). The latter is consistent with the large mean photon number change occurring at the threshold in Fig. 3B ($\Theta > \pi/2$). Note also that the range of superradiance or the maximum number of atoms participating in the collective emission can be easily scaled up by choosing smaller $g\tau$ values (see fig. S5). This feature may provide a new approach in building thresholdless lasers.

The present single-atom superradiance can be viewed as a consequence of one-sided interaction among a series of atoms separated by tens of meters. Note that the photon emitted by a preceding atom interacts with the next atom after traveling $c\tau/\langle N \rangle$ (about 30 m for $\langle N \rangle = 1$) when we unfold mirror refections although their average distance in real space is only hundreds of micrometers. Due to causality, only the preceding atoms can then affect the quantum states of the following atoms. This interaction induces the emission rate of the atom in the cavity to be twice larger than the emission rate per atom in the usual superradiance (*17*) (fig. S6). The time-separated atoms linked by such one-sided interaction can form atom-atom interaction systems, which can serve as a testbed for various quantum many-body physics (*25*).

The present study deepens our understanding on matter-light collective interaction and provides a new insight on the field-mediated long-range (*26*, *27*) interactions. In addition, the phase-controlled many-atom-field interaction based on the nanohole-array technique can be used in non-classical field generation such as optical Schrödinger cat states and highly-squeezed vacuum states (*28*), even in a lossy cavity contrary to the previous studies in the microwave region (*29*), as well as in realizing superabsorption (*30*). The greatly enhanced single-atom emission may be useful in constructing efficient quantum interfaces (*31*).

REFERENCES AND NOTES

1. R. H. Dicke, Coherence in spontaneous radiation processes. *Phys. Rev.* **93**, 99–110 (1954). doi:10.1103/PhysRev.93.99

2. M. Gross, S. Haroche, Superradiance: An essay on the theory of collective spontaneous emission. *Phys. Rep.* **93**, 301–396 (1982). doi:10.1016/0370-1573(82)90102-8

3. N. Skribanowitz, I. P. Herman, J. C. MacGillivray, M. S. Feld, Observation of Dicke superradiance in optically pumped HF gas. *Phys. Rev. Lett.* **30**, 309–312 (1973). doi:10.1103/PhysRevLett.30.309

4. S. Inouye, A. P. Chikkatur, D. M. Stamper-Kurn, J. Stenger, D. E. Pritchard, W.

Ketterle, Superradiant Rayleigh scattering from a Bose-Einstein condensate. *Science* **285**, 571–574 (1999). doi:10.1126/science.285.5427.571 Medline

5. M. Scheibner, T. Schmidt, L. Worschech, A. Forchel, G. Bacher, T. Passow, D. Hommel, Superradiance of quantum dots. *Nat. Phys.* **3**, 106–110 (2007). doi:10.1038/nphys494

6. R. Reimann, W. Alt, T. Kampschulte, T. Macha, L. Ratschbacher, N. Thau, S. Yoon, D. Meschede, Cavity-modified collective Rayleigh scattering of two atoms. *Phys. Rev. Lett.* **114**, 023601 (2015). doi:10.1103/PhysRevLett.114.023601 Medline

7. M. O. Scully, A. A. Svidzinsky, The super of superradiance. *Science* **325**, 1510–1511 (2009). doi:10.1126/science.1176695 Medline

8. R. Röhlsberger, K. Schlage, B. Sahoo, S. Couet, R. Rüffer, Collective Lamb shift in single-photon superradiance. *Science* **328**, 1248–1251 (2010). doi:10.1126/science.1187770 Medline

9. S. J. Roof, K. J. Kemp, M. D. Havey, I. M. Sokolov, Observation of single-photon superradiance and the cooperative Lamb shift in an extended sample of cold atoms. *Phys. Rev. Lett.* **117**, 073003 (2016). doi:10.1103/PhysRevLett.117.073003 Medline

10. M. A. Norcia, M. N. Winchester, J. R. K. Cline, J. K. Thompson, Superradiance on the millihertz linewidth strontium clock transition. *Sci. Adv.* **2**, e1601231 (2016). doi:10.1126/sciadv.1601231 Medline

11. K. Baumann, C. Guerlin, F. Brennecke, T. Esslinger, Dicke quantum phase transition with a superfluid gas in an optical cavity. *Nature* **464**, 1301–1306 (2010). doi:10.1038/nature09009 Medline

12. B. Casabone, K. Friebe, B. Brandstätter, K. Schüppert, R. Blatt, T. E. Northup, Enhanced quantum interface with collective ion-cavity coupling. *Phys. Rev. Lett.* **114**, 023602 (2015). doi:10.1103/PhysRevLett.114.023602 Medline

13. A. Neuzner, M. Körber, O. Morin, S. Ritter, G. Rempe, Interference and dynamics of light from a distance-controlled atom pair in an optical cavity. *Nat. Photonics* **10**, 303–306 (2016). doi:10.1038/nphoton.2016.19

14. J. A. Mlynek, A. A. Abdumalikov, C. Eichler, A. Wallraff, Observation of Dicke superradiance for two artificial atoms in a cavity with high decay rate. *Nat. Commun.* **5**, 5186 (2014). doi:10.1038/ncomms6186 Medline

15. M. Lee, J. Kim, W. Seo, H. G. Hong, Y. Song, R. R. Dasari, K. An, Three-dimensional imaging of cavity vacuum with single atoms localized by a nanohole array. *Nat. Commun.* **5**, 3441 (2014). Medline

16. F. Le Kien, M. O. Scully, H. Walther, Generation of a coherent state of the micromaser field. *Found. Phys.* **23**, 177–184 (1993). doi:10.1007/BF01883622

17. See supplementary materials.

18. W. Choi, J.-H. Lee, K. An, C. Fang-Yen, R. R. Dasari, M. S. Feld, Observation of sub-Poisson photon statistics in the cavity-QED microlaser. *Phys. Rev. Lett.* **96**, 093603 (2006). doi:10.1103/PhysRevLett.96.093603 Medline

19. C. Fang-Yen, C. C. Yu, S. Ha, W. Choi, K. An, R. R. Dasari, M. S. Feld, Observation of multiple thresholds in the many-atom cavity QED microlaser. *Phys. Rev. A* **73**, 041802 (2006). doi:10.1103/PhysRevA.73.041802

20. K. An, R. R. Dasari, M. S. Feld, Traveling-wave atom cavity interaction in the single-atom microlaser. *Opt. Lett.* **22**, 1500–1502 (1997). doi:10.1364/OL.22.001500 Medline

21. H.-G. Hong, W. Seo, Y. Song, M. Lee, H. Jeong, Y. Shin, W. Choi, R. R. Dasari, K. An, Spectrum of the cavity-QED microlaser: Strong coupling effects in the frequency pulling at off resonance. *Phys. Rev. Lett.* **109**, 243601 (2012). doi:10.1103/PhysRevLett.109.243601 Medline

22. G. Björk, A. Karlsson, Y. Yamamoto, Definition of a laser threshold. *Phys. Rev. A* **50**, 1675–1680 (1994). doi:10.1103/PhysRevA.50.1675 Medline

23. J. G. Bohnet, Z. Chen, J. M. Weiner, D. Meiser, M. J. Holland, J. K. Thompson, A steady-state superradiant laser with less than one intracavity photon. *Nature* **484**, 78–81 (2012). doi:10.1038/nature10920 Medline

24. M. Khajavikhan, A. Simic, M. Katz, J. H. Lee, B. Slutsky, A. Mizrahi, V. Lomakin, Y. Fainman, Thresholdless nanoscale coaxial lasers. *Nature* **482**, 204–207 (2012). doi:10.1038/nature10840 Medline

25. P. Lodahl, S. Mahmoodian, S. Stobbe, A. Rauschenbeutel, P. Schneeweiss, J. Volz, H. Pichler, P. Zoller, Chiral quantum optics. *Nature* **541**, 473–480 (2017). doi:10.1038/nature21037 Medline

26. J. S. Douglas, H. Habibian, C.-L. Hung, A. V. Gorshkov, H. J. Kimble, D. E. Chang, Quantum many-body models with cold atoms coupled to photonic crystals. *Nat. Photonics* **9**, 326–331 (2015). doi:10.1038/nphoton.2015.57

27. Z. Meir, O. Schwartz, E. Shahmoon, D. Oron, R. Ozeri, Cooperative Lamb shift in a mesoscopic atomic array. *Phys. Rev. Lett.* **113**, 193002 (2014). doi:10.1103/PhysRevLett.113.193002 Medline

28. D. Yang, J. Kim, M. Lee, Y.-T. Chough, K. An, Generation of an optical Schrödinger-cat-like state in a nonideal cavity by injecting opposite-phase atomic dipoles. *Phys. Rev. A* **94**, 023826 (2016). doi:10.1103/PhysRevA.94.023826

29. S. Deléglise, I. Dotsenko, C. Sayrin, J. Bernu, M. Brune, J.-M. Raimond, S. Haroche, Reconstruction of non-classical cavity field states with snapshots of their decoherence. *Nature* **455**, 510–514 (2008). doi:10.1038/nature07288 Medline

30. K. D. B. Higgins, S. C. Benjamin, T. M. Stace, G. J. Milburn, B. W. Lovett, E. M. Gauger, Superabsorption of light via quantum engineering. *Nat. Commun.* **5**, 4705 (2014). doi:10.1038/ncomms5705 Medline

31. K. Hammerer, A. S. Sørensen, E. S. Polzik, Quantum interface between light and atomic ensembles. *Rev. Mod. Phys.* **82**, 1041–1093 (2010). doi:10.1103/RevModPhys.82.1041

32. H. J. Carmichael, Quantum trajectory theory for cascaded open systems. *Phys. Rev. Lett.* **70**, 2273–2276 (1993). doi:10.1103/PhysRevLett.70.2273 Medline

33. C. Yang, K. An, Quantum trajectory analysis of a thresholdlike transition in the microlaser. *Phys. Rev. A* **55**, 4492–4500 (1997). doi:10.1103/PhysRevA.55.4492

34. M. O. Scully, M. S. Zubairy, *Quantum Optics* (Cambridge Univ. Press, 1997).

35. N. Lu, The coherently pumped laser: The simplest system for lasers without inversion. *Opt. Commun.* **73**, 479–483 (1989). doi:10.1016/0030-4018(89)90466-5

ACKNOWLEDGMENTS

We thank Moonjoo Lee and Hyun-Gue Hong for helpful comments. This work was supported by a grant from Samsung Science and Technology Foundation under Project No. SSTF-BA1502-05. The authors declare no competing financial interests. All data needed to evaluate the conclusions in the paper are present in the paper and/or the supplementary materials.

SUPPLEMENTARY MATERIALS

www.sciencemag.org/cgi/content/full/science.aar2179/DC1
Materials and Methods
Supplementary Text
Figs. S1 to S6
References (*32*–*35*)

15 October 2017; accepted 7 December 2017
Published online 21 December 2017
10.1126/science.aar2179

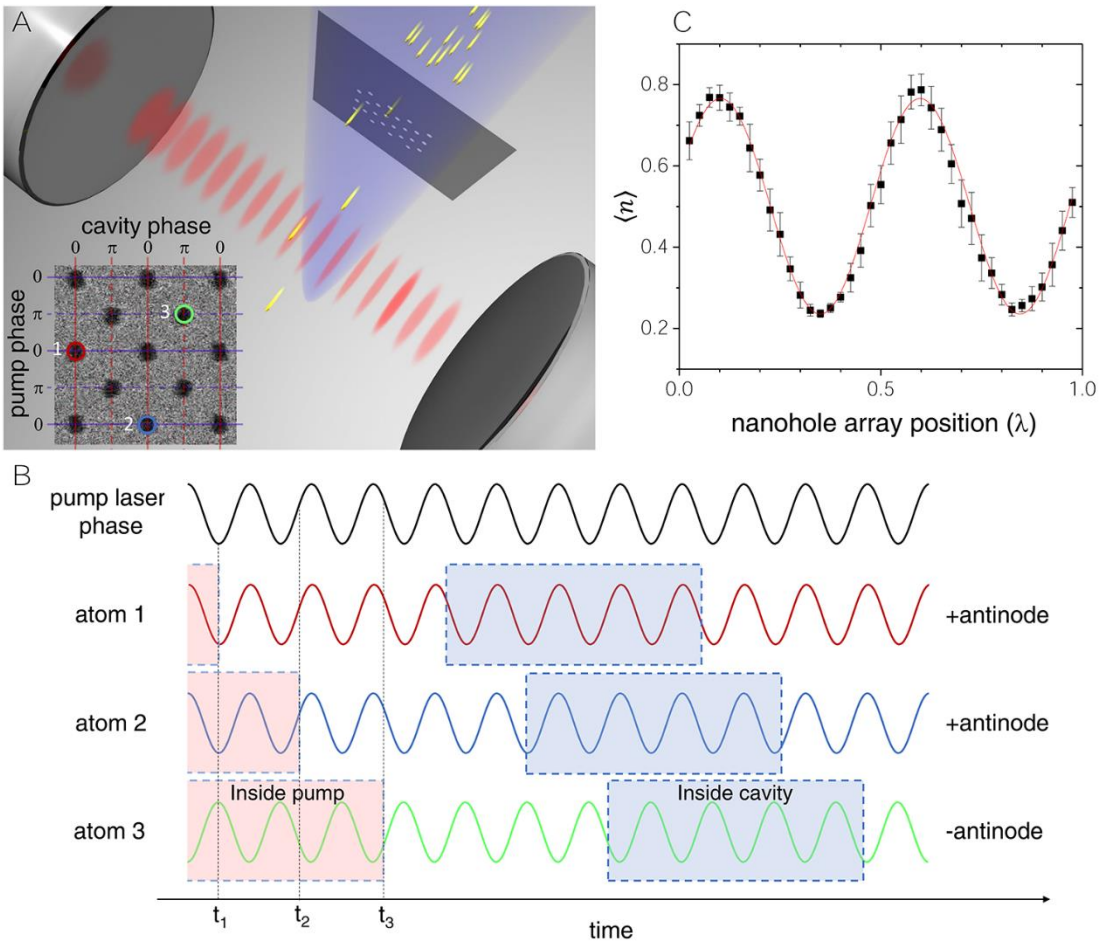

Fig. 1. Phase-controlled atom-cavity interaction with a nanohole-array aperture. (A) Barium atoms (yellow flying spheres) go through a nanohole-array aperture and are prepared in a desired state by a pump laser (blue beam). The atoms interact with the cavity field in a given interaction time τ and emit photons into the cavity mode in both collective and non-collective ways. The inset shows a focused-ion-beam image of the nanohole-array aperture (*17*). The nanohole array dimension is 25λ by 25λ, spanning 19.8 μm both horizontally and vertically. Here λ = 791 nm is the atomic transition wavelength. (B) The atom-cavity relative phase is prescribed by the array structure. Consider three atoms going through nanoholes 1, 2 and 3 as indicated in (A) and then exiting the pump field at time t_1, t_2 and t_3, respectively. The pump laser phase at one of the zero-phase planes is shown with the imprinted atomic phases. Although atom 3 has the opposite imprinted phase to the others, it goes through an antinode opposite in phase to the antinodes that atoms 1 and 2 go through. As a result, all three atoms would have identical atom-cavity relative phases. (C) Varying the nanohole-array position along the cavity axis changes the atomic trajectory from crossing nodes to crossing antinodes, and therefore the cavity mean photon number (black square) varies sinusoidally when pumped by fully excited atoms. The signal visibility is 0.54 and the corresponding effective atomic distribution has a full width at half maximum of 0.29λ. Red solid line is a sinusoidal fit to the data.

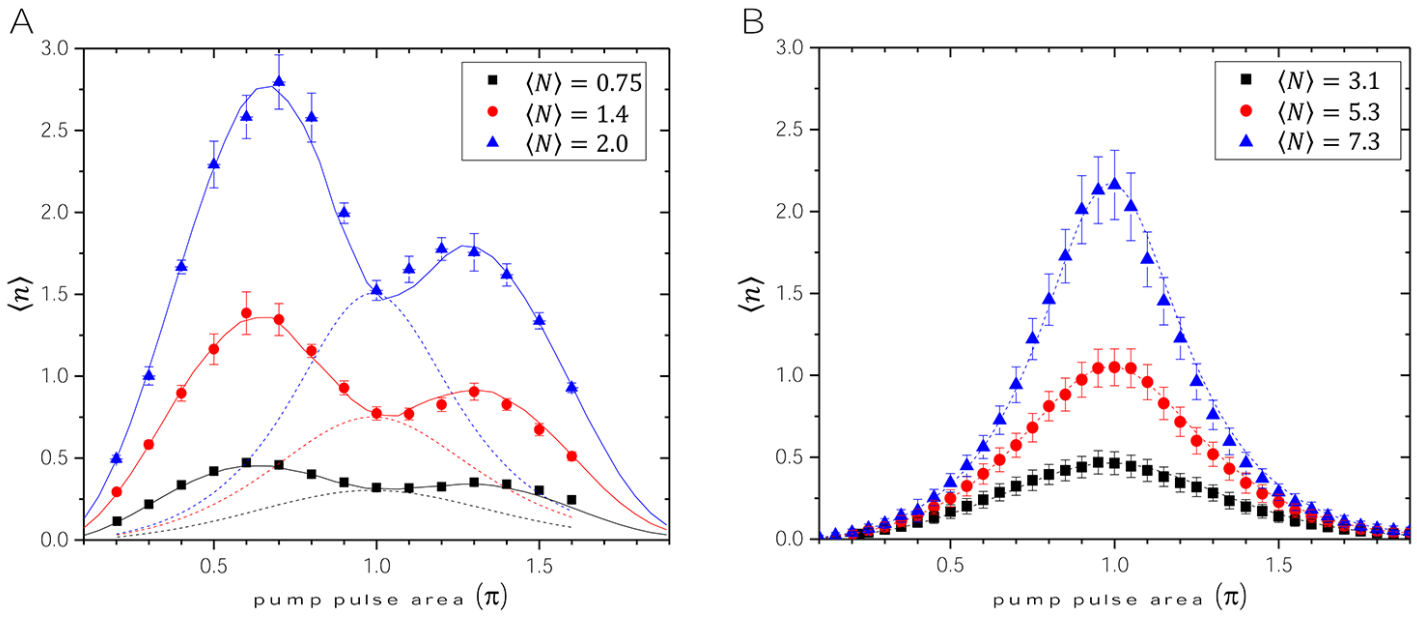

Fig. 2. Intracavity photon number dependence on the atomic state. The intracavity mean photon number $\langle n \rangle$ versus the pump pulse area Θ for various mean atom numbers $\langle N \rangle$ in the cavity with (A) phase-aligned atoms and (B) atoms with random phases. Vacuum Rabi angle $g\tau$ is associated with the cavity-enhanced spontaneous emission probability $\sin^2(g\tau)$ during the atom-cavity interaction time τ for a single atom. The value of $g\tau$ is 0.18 rad for the phase-aligned atoms, averaged over the finite atomic distribution around the antinode of the cavity field, and 0.10 rad for the random phase atoms with a traveling-wave atom-cavity coupling. Solid (dashed) lines are theoretical predictions for the case of phase-aligned (random phase) atoms with the actual experimental parameters (*17*).

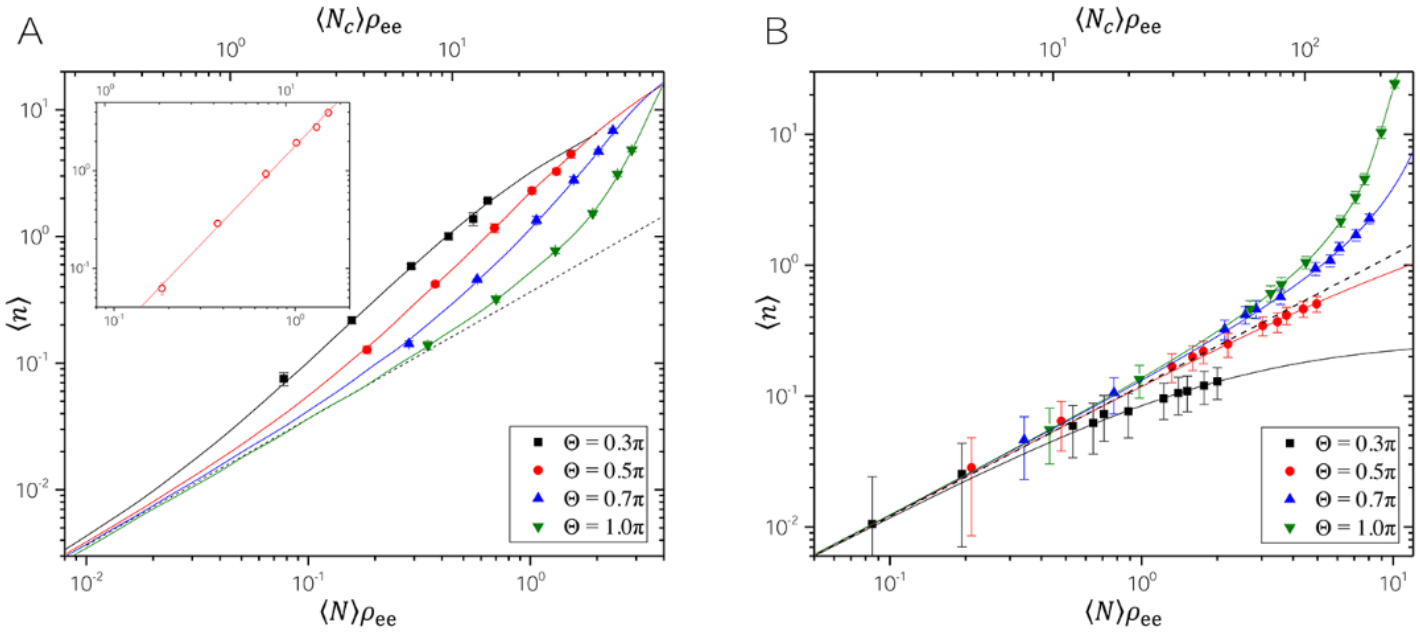

Fig. 3. Intracavity photon number dependence on the number of atoms. The intracavity mean photon number $\langle n \rangle$ versus the excited-state mean atom number $\langle N \rangle \rho_{ee}$ for (**A**) the phase-aligned case and (**B**) the random phase case. We use $\langle N \rangle \rho_{ee}$ instead of just $\langle N \rangle$ for the horizontal axis in order to align the non-collective emission contribution as a common base line. The inset shows $\langle n \rangle$ with the non-collective contribution subtracted for $\Theta = 0.5\pi$ cases and a linear fit to data with the log-log slope of 1.94 ± 0.04. Dashed lines correspond to the expected photon number made only by the cavity-enhanced spontaneous emission of atoms. Solid lines are theoretical predictions with the actual experimental parameters (*17*).

QUANTUM OPTICS

A topological quantum optics interface

Sabyasachi Barik,[1,2] Aziz Karasahin,[3] Christopher Flower,[1,2] Tao Cai,[3] Hirokazu Miyake,[2] Wade DeGottardi,[1,2] Mohammad Hafezi,[1,2,3]* Edo Waks[1,2,3]*

The application of topology in optics has led to a new paradigm in developing photonic devices with robust properties against disorder. Although considerable progress on topological phenomena has been achieved in the classical domain, the realization of strong light-matter coupling in the quantum domain remains unexplored. We demonstrate a strong interface between single quantum emitters and topological photonic states. Our approach creates robust counterpropagating edge states at the boundary of two distinct topological photonic crystals. We demonstrate the chiral emission of a quantum emitter into these modes and establish their robustness against sharp bends. This approach may enable the development of quantum optics devices with built-in protection, with potential applications in quantum simulation and sensing.

The discovery of the quantum Hall effects has inspired developments in similar topological phenomena in a range of platforms, including ultracold neutral atoms (*1*, *2*), photonics (*3*, *4*), and mechanical structures (*5*–*7*). Like their electronic analogs, topological photonic states are distinctive in their directional transport and reflectionless propagation along the interface of two topologically distinct regions. Such robustness has been demonstrated in various electromagnetic systems, ranging from the microwave (*8*, *9*) to the optical (*10*, *11*) domain, opening avenues for a plethora of applications—such as robust delay lines, slow-light optical buffers (*12*), and topological lasers (*13*–*15*)—to develop optical devices with built-in protection. Although the scope of previous work has remained in the classical electromagnetic regime, interesting physics could emerge by bringing topological photonics to the quantum domain. Specifically, integrating quantum emitters into topological photonic structures could lead to robust, strong light-matter interaction (*16*) and the generation of novel states of light and exotic many-body states (*17*–*19*).

We experimentally demonstrated light-matter coupling in a topological photonic crystal. We used an all-dielectric structure (*20*–*22*) to implement topologically robust edge states at the interface between two topologically distinct photonic materials, where the light is transversally trapped in a small area, up to half of the wavelength of light. We show that a quantum emitter efficiently couples to these edge modes and that the emitted single photons exhibit robust transport, even in the presence of a bend. Figure 1A shows the fabricated topological photonic crystal structure. The device is composed of a thin GaAs membrane with epitaxially grown InAs quantum dots at the center that act as quantum emitters (*22*).

The topological photonic structure comprises two deformed honeycomb photonic crystal lattices made of equilateral triangular air holes (fig. S2) on a GaAs membrane (*21*, *22*). Figure 1B shows a close-up image of the interface, where the black dashed lines identify a single unit cell of each photonic crystal. In each region, we perturb the unit cell by concentrically moving the triangular holes either inward (yellow region) or outward (blue region). The corresponding band structures of the two regions are shown in Fig. 1, C and D. The perturbations open two bandgaps exhibiting band inversion at the Γ point (*20*, *21*). Specifically, the region with a compressed unit cell, highlighted in yellow, acquires a topologically trivial bandgap, whereas the expanded region, highlighted in blue, takes on a nontrivial one. We designed both regions so that their bandgaps overlap. Photons within the common bandgap cannot propagate into either photonic crystal. However, because the crystals have different topological band properties, the interface between them supports two topological helical edge modes, traveling in opposite directions, with opposite circular polarizations at the center of the unit cell.

To show the presence of the guided edge mode, we measured the transmission spectrum. We illuminated the left grating ("L") with a 780-nm continuous-wave laser using a pump power of 1.3 μW and collected the emission from the right grating ("R"; Fig. 2A). At this power, the quantum dot ensemble emission became a broad continuum owing to power broadening, resulting in an internal white light source that spanned the wavelength range of 900 to 980 nm. Figure 2B shows the spectrum at the right grating, presented with the band structure simulation (*21*). Light emitted within the topological band efficiently transmitted through the edge mode and propagated to the other grating coupler, whereas photons outside of the bandgap dissipated into bulk modes.

To confirm that the emission originates from guided modes at the interface between the two topological materials, we excited the structure in the middle of the waveguide ("M") and collected the emission at the left and right grating coupler, which we independently calibrated (*22*). Figure 2C shows the transmission spectrum collected from the left coupler as a function of the laser spot position as we scanned the laser along the *y* axis (across the interface indicated by the blue arrow in Fig. 2A). The spectrum attained a maximum transmission within the topological band when the pump excited the center of the structure. When

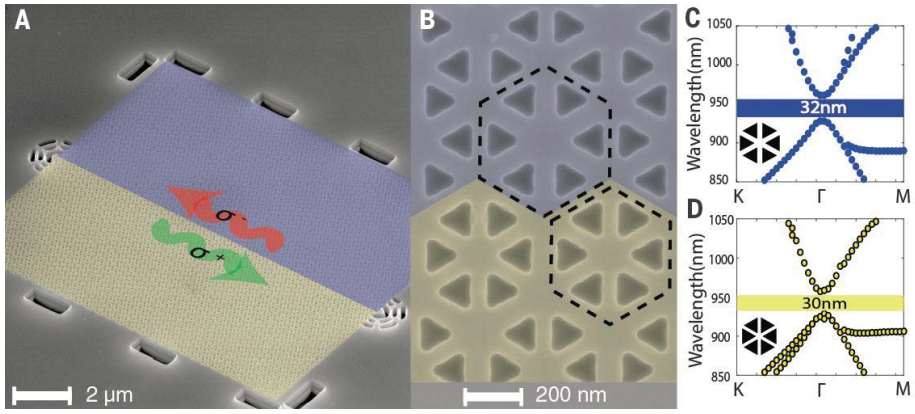

Fig. 1. Fabricated device and band structure. (**A**) Scanning electron microscope image of the device, which is composed of two regions identified by blue and yellow shading, corresponding to two photonic crystals with different topological properties. The interface between the two photonic crystals supports helical edge states with opposite circular polarization (σ^+ and σ^-). Grating couplers at each end of the device scatter light in the out-of-plane direction for collection. (**B**) Close-up image of the interface. Black dashed lines identify a single unit cell of each photonic crystal. (**C** and **D**) Band structures for the transverse electric modes of the two photonic crystals.

[1]Department of Physics, University of Maryland, College Park, MD 20742, USA. [2]Joint Quantum Institute, University of Maryland, College Park, MD 20742, USA. [3]Department of Electrical and Computer Engineering and Institute for Research in Electronics and Applied Physics, University of Maryland, College Park, MD 20742, USA.
*Corresponding author. Email: hafezi@umd.edu (M.H.); edowaks@umd.edu (E.W.)

we displaced the excitation beam by ~1.5 μm along the *y* direction, the transmission vanished, indicating that the photons were coming only from the waveguide.

A key feature of topological edge modes is the chiral nature of the coupling between the helical topological edge mode and the quantum emitter. Specifically, different dipole spins radiatively couple to opposite propagating helical edge states. To demonstrate this helical light-matter coupling, we applied a magnetic field in the out-of-plane (Faraday) direction on the entire sample. This field induced a Zeeman splitting in the quantum dot excited state, resulting in two nondegenerate states that emitted with opposite circular polarizations (fig. S5), denoted as $\sigma^{\pm}$ (Fig. 3A) (*22*, *23*). Although this magnetic field does not play a role in the topological nature of the waveguide, it enabled us to identify the polarization of the dipole by the frequency of emitted photons. By spectrally resolving the emissions, we were able to identify the dipole spin and correlate it with the propagation direction of the emitted photon.

To isolate a single quantum emitter within the topological edge mode, we reduced the power to 10 nW, which is well below the quantum dot saturation power. Using the intensities of the collected light at the two ends, we calculated a lower bound on the coupling efficiency of 68% (table S1), defined as the ratio of the photon emission rate into the waveguide to the total emission rate (*22*). This high efficiency is due to the tight electromagnetic confinement of the guided modes, which enhances light-matter interactions. Figure 3B shows the emission spectrum as a function of magnetic field, where we collected the emission directly from point M indicated in Fig. 2A. As the magnetic field increases, the quantum dot resonance splits into two branches corresponding to the two Zeeman split bright exciton states. We compared this spectrum with the one collected from the left and right gratings (Fig. 3, C and D). At the left grating, we observed only the emission from the σ^- branch, whereas at the right grating, we observed only the emission from the σ^+ branch. These results establish the chiral emission and spin-momentum locking of the emitted photons and provide strong evidence that the emitter is coupling to topological edge states that exhibit unidirectional transport. Such chiral coupling is in direct analogy to one-dimensional systems (*16*, *24*, *25*); however, the waveguided modes of our structure originate from two-dimensional topology. As a result, the topological edge mode should exhibit robustness to certain deformations, such as bends.

To establish this topological robustness, we analyzed the propagation of emitted photons in the presence of a bend. We introduced a 60° bend into the structure, as shown in Fig. 4A, and performed measurements similar to those in Fig. 3. Again, we observed that emitted photons propagate in opposite directions in a chiral fashion and arrive at the grating associated with their respective polarization (Fig. 4, B and C). The preservation of the chiral nature of the emission

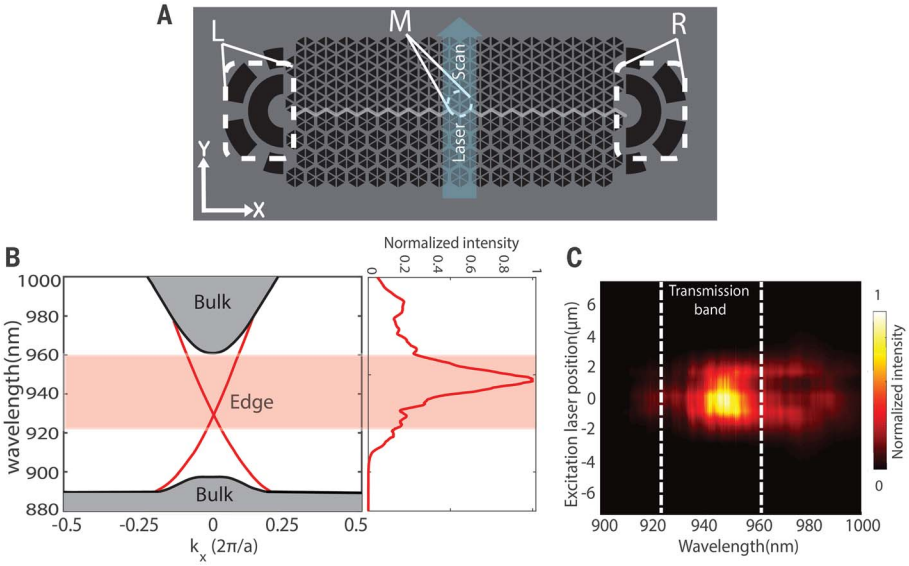

Fig. 2. Transmission characteristics of the topological waveguide. (**A**) A schematic of the excitation scheme identifying the three relevant regions (L, left grating; R, right grating; M, middle of the waveguide). (**B**) Simulated band structure of transverse electromagnetic modes of a straight topological waveguide. The gray region corresponds to bulk modes of the individual topological photonic crystals, and red lines represent modes within the bandgap corresponding to topological edge states. The adjacent panel shows the measured spectrum at the transmitted end of the waveguide. The red shaded region identifies the topological edge band. k_x, reciprocal wave vector; *a*, lattice constant. (**C**) Transmission spectrum at point L as a function of the excitation laser position.

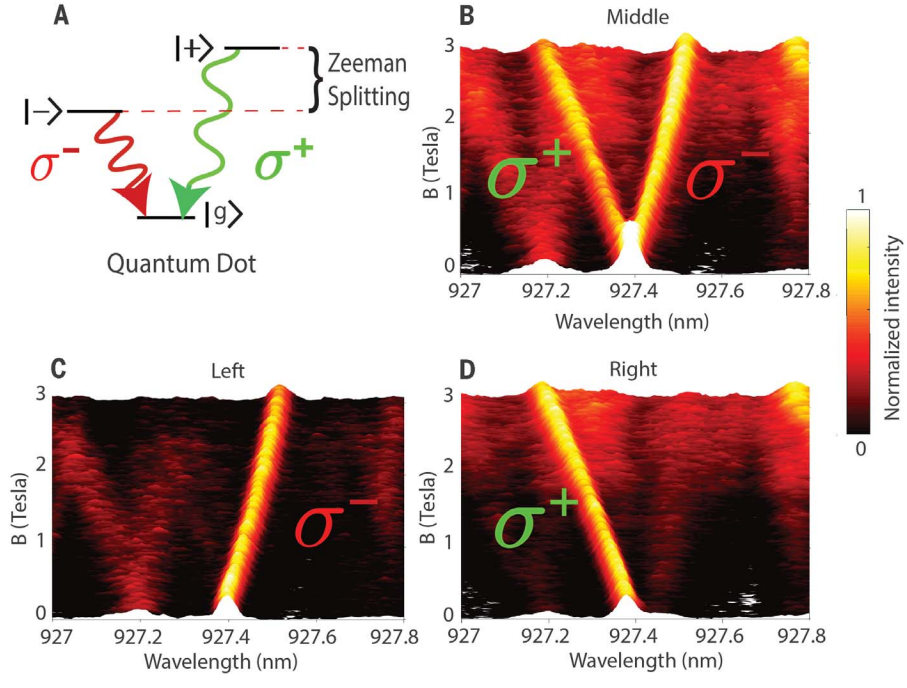

Fig. 3. Chirality in a straight topological waveguide. (**A**) Schematic of quantum dot–level structure in the presence of a magnetic field and radiative transitions with opposite circular polarizations. (**B**) Emission spectrum collected from the excitation region as a function of magnetic field (*B*). (**C** and **D**) Transmission spectra to left and right gratings, respectively.

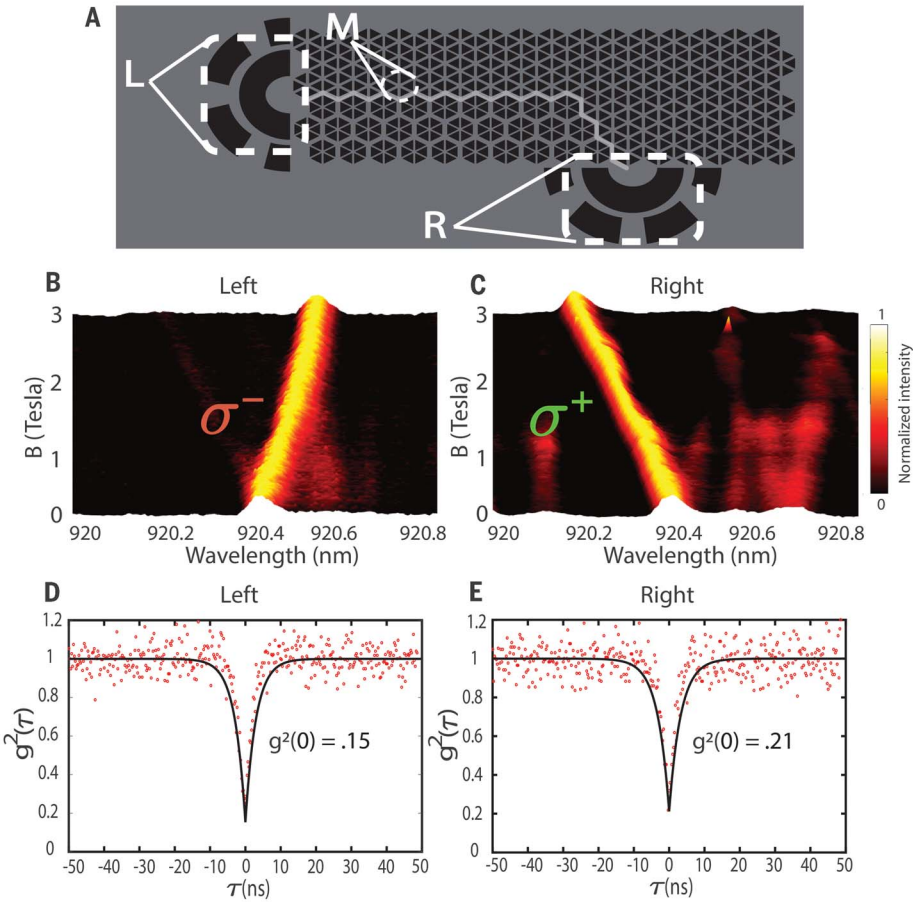

Fig. 4. Robust transport in two dimensions along a bend. (**A**) Schematic of a modified topological waveguide with a bend. (**B** and **C**) Photoluminescence collected from points L and R, respectively, showing only one branch of the quantum dot. (**D** and **E**) Second-order correlation measurement [$g^2(\tau)$, where τ is the time delay] data obtained from points L and R, respectively, showing antibunching. Red dots represent the experimental data, and the black line corresponds to fitting.

demonstrates an absence of back-reflection at the bend, which would result in a strong signal for both polarizations at the left grating. We also confirmed that these routed photons are single photons by performing a second-order correlation measurement for photons collected from both ends of the waveguide, which exhibits strong antibunching (Fig. 4, D and E). The robustness in this system is due to C_{6v} symmetry, and the boundary and disorder can break this symmetry and lead to backscattering of the edge modes. In the supplementary materials, we analyze the effect of certain types of disorder on the transmission properties of the edge modes and show that the unidirectional propagation is robust. The full characterization of robustness, beyond numerical simulations and the tight-binding model (*26*), requires further study.

In this work, we demonstrated coupling between single quantum emitters and topologically robust photonic edge states. Our approach opens new prospects at the interface of quantum optics and topological photonics. In the context of chiral quantum optics, one can explore new regimes of dipole emission in the vicinity of topological photonic structures and exploit the robustness of the electromagnetic modes (*16*). Furthermore, in a chiral waveguide, photon-mediated interactions between emitters are location-independent (*27*). This property could facilitate the coupling of multiple solid-state emitters via photons while overcoming scalability issues associated with random emitter position, enabling large-scale superradiant states and spin-squeezing. Ultimately, such an approach could constitute a versatile platform to explore many-body quantum physics at a topological edge (*28*), create chiral spin networks (*27*, *29*), and realize fractional quantum Hall states of light (*30*, *31*).

REFERENCES AND NOTES

1. J. Dalibard, F. Gerbier, G. Juzeliūnas, P. Öhberg, *Rev. Mod. Phys.* **83**, 1523–1543 (2011).
2. C. Eckardt, *Rev. Mod. Phys.* **89**, 011004 (2017).
3. M. Hafezi, J. M. Taylor, *Phys. Today* **67**, 68–69 (2014).
4. L. Lu, J. D. Joannopoulos, M. Soljačić, *Nat. Photonics* **8**, 821–829 (2014).
5. L. Kane, T. C. Lubensky, *Nat. Phys.* **10**, 39–45 (2014).
6. J. Paulose, B. G. G. Chen, V. Vitelli, *Nat. Phys.* **11**, 153–156 (2015).
7. R. Süsstrunk, S. D. Huber, *Science* **349**, 47–50 (2015).
8. Z. Wang, Y. Chong, J. D. Joannopoulos, M. Soljacić, *Nature* **461**, 772–775 (2009).
9. X. Cheng *et al.*, *Nat. Mater.* **15**, 542–548 (2016).
10. M. Hafezi, S. Mittal, J. Fan, A. Migdall, J. M. Taylor, *Nat. Photonics* **7**, 1001–1005 (2013).
11. M. C. Rechtsman *et al.*, *Nature* **496**, 196–200 (2013).
12. M. Hafezi, E. A. Demler, M. D. Lukin, J. M. Taylor, *Nat. Phys.* **7**, 907–912 (2011).
13. L. Pilozzi, C. Conti, *Phys. Rev. B* **93**, 195317 (2016).
14. G. Harari *et al.*, "Topological lasers," in *Conference on Lasers and Electro-Optics* [OSA Technical Digest (online), Optical Society of America, 2016], FM3A.3.
15. P. St-Jean *et al.*, *Nat. Photonics* **11**, 651–656 (2017).
16. P. Lodahl *et al.*, *Nature* **541**, 473–480 (2017).
17. I. Carusotto, C. Ciuti, *Rev. Mod. Phys.* **85**, 299–366 (2013).
18. J. I. Cirac, H. J. Kimble, *Nat. Photonics* **11**, 18–20 (2017).
19. D. G. Angelakis, Ed., *Quantum Simulations with Photons and Polaritons* (Springer International Publishing, 2017).
20. L. H. Wu, X. Hu, *Phys. Rev. Lett.* **114**, 223901 (2015).
21. S. Barik, H. Miyake, W. DeGottardi, E. Waks, M. Hafezi, *New J. Phys.* **18**, 113013 (2016).
22. Materials and methods are available as supplementary materials.
23. M. Bayer *et al.*, *Phys. Rev. B* **65**, 195315 (2002).
24. J. Petersen, J. Volz, A. Rauschenbeutel, *Science* **346**, 67–71 (2014).
25. I. Söllner *et al.*, *Nat. Nanotechnol.* **10**, 775–778 (2015).
26. T. Kariyado, X. Hu, *Sci. Rep.* **7**, 16515 (2017).
27. H. Pichler, T. Ramos, A. J. Daley, P. Zoller, *Phys. Rev. A* **91**, 042116 (2014).
28. M. Ringel, M. Pletyukhov, V. Gritsev, *New J. Phys.* **16**, 113030 (2014).
29. A. Metelmann, A. A. Clerk, *Phys. Rev. X* **5**, 021025 (2015).
30. R. O. Umucalılar, I. Carusotto, *Phys. Rev. Lett.* **108**, 206809 (2012).
31. M. Hafezi, M. D. Lukin, J. M. Taylor, *New J. Phys.* **15**, 063001 (2013).

ACKNOWLEDGMENTS

The authors acknowledge fruitful discussions with S. Mittal. All data needed to evaluate the conclusions are present in the paper and/or the supplementary materials. This research was supported by the Office of Naval Research, the Air Force Office of Scientific Research–Multidisciplinary University Research Initiative (grant FA9550-16-1-0323), the Sloan Foundation, and the Physics Frontier Center at the Joint Quantum Institute.

SUPPLEMENTARY MATERIALS

www.sciencemag.org/content/359/6376/666/suppl/DC1
Materials and Methods
Supplementary Text
Figs. S1 to S5
Table S1

24 September 2017; accepted 11 December 2017
10.1126/science.aaq0327

Science

REPORTS

Cite as: Q.-Y. Lin *et al.*, *Science* 10.1126/science.aaq0591 (2018).

Building superlattices from individual nanoparticles via template-confined DNA-mediated assembly

Qing-Yuan Lin,[1,3]* Jarad A. Mason,[1,2]* Zhongyang Li,[4]* Wenjie Zhou,[1,2] Matthew N. O'Brien,[1,2] Keith A. Brown,[1,2] Matthew R. Jones,[1,3] Serkan Butun,[4] Byeongdu Lee,[5] Vinayak P. Dravid,[1,3†] Koray Aydin,[4†] Chad A. Mirkin[1,2,3†]

[1]International Institute for Nanotechnology, Northwestern University, Evanston, IL 60208, USA. [2]Department of Chemistry, Northwestern University, Evanston, IL 60208, USA. [3]Department of Materials Science and Engineering, Northwestern University, Evanston, IL 60208, USA. [4]Department of Electrical Engineering and Computer Science, Northwestern University, Evanston, IL 60208, USA. [5]X-ray Science Division, Argonne National Laboratory, 9700 South Cass Avenue, Argonne, IL 60439, USA.

*These authors contributed equally to this work.

†Corresponding author. Email: chadnano@northwestern.edu (C.A.M.); aydin@northwestern.edu (K.A.); v-dravid@northwestern.edu (V.P.D.)

DNA programmable assembly has been combined with top-down lithography to construct superlattices of discrete, reconfigurable nanoparticle architectures on a gold surface over large areas. Specifically, the assembly of individual colloidal plasmonic nanoparticles with different shapes and sizes is controlled by oligonucleotides containing "locked" nucleic acids and confined environments provided by polymer pores to yield oriented architectures that feature tunable arrangements and independently controllable distances at both nanometer and micrometer length scales. These structures, which would be difficult to construct via other common assembly methods, provide a platform to systematically study and control light-matter interactions in nanoparticle-based optical materials. The generality and potential of this approach are explored by identifying a broadband absorber with a solvent polarity response that allows dynamic tuning of visible light absorption.

DNA has become a powerful tool for constructing highly ordered materials from nanoparticle (NP) building blocks (*1*–*3*). Indeed, the tunability afforded by the sequence-specific interactions inherent to oligonucleotides has been leveraged to assemble NPs into many exotic structures, including colloidal crystals that feature over 30 different lattice symmetries, tunable interparticle distances ranging from below 3 nm to above 130 nm, and multiple well-defined crystal habits (*4*–*7*). In contrast to the diversity of structures that have been synthesized in solution, DNA has only been used to generate a relatively limited set of NP structures on surfaces (*8*–*10*). Moreover, the use of DNA—as well as any other bottom-up or combination of bottom-up and top-down assembly technique—to transfer colloidal NPs from solution to a surface has led to either NP monolayers or three-dimensional (3D) extended lattices (*11*–*14*), while the synthesis of isolated nanostructures that incorporate multiple NP sizes, shapes, and/or compositions has remained elusive. The ability to predictably, rapidly, and precisely place individual NPs into desired arrangements—regardless of size, shape, or composition—over large areas on a surface in both two- and three-dimensions would represent a significant advance in structural control, dramatically expanding the range of nanomaterials that can be synthesized and enabling new properties, many of which have likely never even been contemplated because a lack of access to such structures.

With most assembly techniques, it is extremely challenging to control the thermodynamics of interactions both between NPs and between NPs and a surface, as would be required to build discrete, surface-bound architectures with a high level of structural control. Here, by using DNA programmable interactions to direct the layer-by-layer assembly of colloidal NPs within a polymer template, we realize oriented superlattices of multicomponent NP architectures. Confined environments provided by the pores of the polymer template enable the construction of architectures perpendicular to the substrate, while precisely engineered NP-NP interactions mediated by DNA allow architectures to be assembled a single NP at a time with controlled interparticle distances. These NP superlattices can be specified and independently controlled by the two-dimensional (2D) template and the one-dimensional (1D) arrangement of the oriented, NP architecture. Because of the oligonucleotide bonding elements that hold them in place, these architectures undergo reversible structural changes in response to chemical stimuli, allowing interactions with visible light to be dynamically tuned.

To arrange colloidal NPs into desired architectures on a surface (Fig. 1), we used electron-beam lithography (EBL) to pattern a uniform array of pores into a 300-nm thick layer of poly(methyl methacrylate) (PMMA) affixed to a gold-coated silicon substrate (*9*). The selectively exposed gold surfaces at the bottom of each pore were then densely functionalized with oligonucleotides bearing a terminal propylthiol [DNA sequences are provided in table S1 (*15*)]. Complementary oligonucleotides were then hybridized to the single-stranded

DNA at the base of each pore to yield a monolayer of rigid, double-stranded DNA with a short single-stranded region, or "sticky end," at the solution-facing terminus.

Colloidal gold NPs of different shapes and sizes (fig. S1) were similarly modified with DNA. Architectures of DNA-functionalized NPs were then assembled within each pore of the PMMA template in a layer-by-layer fashion by designing the sticky end DNA sequence present on a selected NP to be complementary to that of the previous layer (Fig. 1). To achieve a predictable, thermodynamically favored arrangement of NPs in each layer, the assembly process must be governed by the maximization of canonical Watson-Crick DNA hybridization events between complementary DNA sticky ends—a principle known as the complementary contact model (*3*, *16*). For this interaction to dominate, we needed to mitigate the effects of other nonspecific interactions that compete at low temperatures, such as interactions between non-complementary nucleic acids and between DNA and the PMMA template.

Anisotropic NPs with flat facets and adenine- or guanine-containing sticky ends are particularly prone to a range of noncanonical interactions (*8*, *17*). The impact of these interactions can be reduced by performing the assembly at higher temperatures, but high temperatures may also lead to the dehybridization and desorption of NP layers that have already been assembled (fig. S2) (*8*). Indeed, finding a suitable assembly temperature for the synthesis of architectures in both high yield and high purity proved to be challenging when sticky ends were composed of conventional nucleic acids (fig. S3A).

To increase the strength of Watson-Crick DNA hybridization interactions between sticky ends relative to noncanonical ones, we replaced three adenine nucleotides in sticky end sequences with "locked" versions containing the same base (table S1). Locked nucleic acids (LNA) are modified RNA nucleotides in which the ribose group is rigidified by connecting the 2′ oxygen to the 4′ carbon with a methylene bridge (*18*, *19*). This modification reduces conformational flexibility and increases the strength of canonical base-pairing interactions. Incorporating just three LNA bases into the sticky-end sequences of nanocubes increased the melting temperature associated with canonical hybridization interactions by 9°C, while also decreasing the melting temperature for noncanonical interactions by 1°C (fig. S3B). This 10°C greater window for NP assembly enabled the predictable synthesis of highly uniform superlattices composed of one-, two-, and three-layer NP architectures.

In addition to DNA, the size, shape, depth, and arrangement of PMMA pores provide a critical element of structural control during NP assembly [additional discussion of the relationships between pore design and NP assembly is provided in the Supplementary Text (*15*)]. For example, the depth of each pore, which was determined by the thickness of PMMA, provided a confined environment for the assembly of each NP layer. We could then build 1D architectures a single NP at a time exclusively in a direction perpendicular to the substrate. Additionally, NPs would not assemble in a pore smaller than the NP, whereas multiple NPs would assemble in larger pores (figs. S4 and S5). Choosing a pore size slightly larger than the total size of NP and DNA thus allowed us to assemble uniform monolayers of different size and shape NPs into arrays (Fig. 2) (*9*). The pore shape further offers the ability to align the average orientation of anisotropic NPs, as observed for cubes assembled in square pores and triangular prisms assembled in triangular pores (Fig. 2, B and C, and fig. S37). After assembly, the porous PMMA template could be dissolved and the NP superlattices transferred intact to the solid state for imaging by scanning electron microscopy (SEM) (Fig. 1 and fig. S7).

In addition to monolayers of isolated NPs, we used template-confined, DNA-mediated assembly to synthesize superlattices with 2D periodicity featuring ten different unit cells that each consist of a 1D architecture of either two or three NPs oriented normal to the surface (Fig. 3A and figs. S8 to S17). These 1D architectures include building blocks of the same size and shape, building blocks of decreasing size, and building blocks of different sizes and shapes. Superlattices of these low-symmetry architectures were synthesized over areas of at least 600 μm by 600 μm with high uniformity (Fig. 3, B and D, and fig. S18). Grazing incidence small angle X-ray scattering (GISAXS) confirmed that the superlattices exhibited the expected diffraction patterns—lines in reciprocal space—of a material with 2D periodicity (Fig. 3C and fig. S19). This bottom-up, layer-by-layer assembly process overcame several challenges in the fabrication of multilayer architectures with conventional top-down techniques, such as focused ion beam (FIB) milling (*20*) or EBL stacking (*21*), which require time-consuming, small-scale cutting of materials or complex serial alignment, exposure, development and metal evaporation to form each layer. Here, biomolecular interactions operating at molecular length-scales allow for the rapid, automatic, and precise alignment of each NP layer with tunable interlayer distances (fig. S21).

Not surprisingly, these NP superlattices contained several types of defects analogous to thermodynamically inevitable defects in atomic crystals, including "vacancies," where a NP was missing from a superlattice position, and "interstitials," where an extra NP was present within the superlattice (*22*). Each individual architecture within the superlattice could be resolved by electron microscopy, so these NP defects can be rigorously quantified and used to establish structure-property relations. For example, a representative disk-cube-sphere three-layer superlattice of 773 architectures contained 73% defect-free structures, 1% vacancies, 9% interstitials, and 17%

other defects (Fig. 3D). In general, the number of defects tended to increase as the number of potential competing interactions increased in moving from one to two to three layer structures (figs. S8 to S17). Note that the SEM images depict snapshots of the structures in the perturbed solid-state, a consequence of drying, and the solution-based architectures likely exhibit greater uniformity.

In addition to directing NP assembly, oligonucleotide bonds between NPs are dynamic and undergo reversible contractions and expansions in response to changes in solvent polarity that allow the distance between NPs to be precisely tuned (*23*). Although it is a challenge to accurately measure the distance between NPs of different sizes and shapes in isolated architectures, cross-sectional SEM images of disk-cube-sphere architectures, which were encased in silica to attempt to preserve their solution-phase arrangements (*23*), showed that the average distance between NPs decreased from > 12 nm to < 3 nm when the solvent composition was adjusted from 0 to 80% EtOH in H_2O by volume at constant 0.3 M NaCl (Fig. 4D and fig. S20).

The synthesis of plasmonic NP architectures with structures and stimuli-responsive behavior that are not accessible in lithographically-defined plasmonic nanostructures (*24–26*) provides an opportunity to design materials with emergent optical properties that offer new fundamental insights and previously inaccessible functionalities. As a proof-of-concept demonstration of the potential of our approach, we leveraged the tunability of oligonucleotide bonds to dynamically control light-matter interactions, enabling the exploration of active and reconfigurable plasmonic devices (*27*). Specifically, because the interparticle distances in the DNA-assembled NP superlattices reported here are within a region that should give rise to strong plasmonic coupling, we anticipated that even small changes to the arrangement of and spacing between coupled plasmonic NPs would lead to substantial changes in the absorption spectrum (*24*, *27–29*). It is not readily apparent, however, which NP architectures might offer the largest optical tuning range for a given change in the spacing between NPs.

To predict the effects of structural changes on interactions of light with plasmonic NP superlattices, finite-difference time-domain (FDTD) simulations were performed for multilayer superlattices with different periodicities, NP sizes and shapes, and gap distances, enabling us to screen for absorbers that feature large-magnitude wavelength and amplitude tunabilities (figs. S22 to S25). Based on these simulations, we identified a tunable broadband absorber in the visible regime—not yet realized experimentally and difficult to envision making by conventional lithography or assembly—composed of the following NP architectures: a sphere (60 nm in diameter) placed on top of a cube (76 nm in edge-length) placed on top of a circular disk (105 nm in diameter, 7.5 nm in thickness) and arranged into square arrays with 200-nm periodicity on a 100-nm thick gold substrate (Fig. 4A). FDTD simulations suggested that decreasing gap lengths from 16 to 4 nm within each NP architecture would increase the localized electric field intensity within the nanocavities at larger wavelengths (>690 nm), affording both very large wavelength tunability and amplitude modulation (Figs. 4, B and C, and fig S26).

To experimentally confirm the predicted optical response, the computationally identified NP superlattice—composed of discrete disk-cube-sphere architectures—was synthesized (fig. S27). Absorption spectra were measured with an inverted optical microscope for the superlattice coated with a thin layer of solvent with increasing ratios of EtOH to H_2O (Fig. 4E). As predicted, changing the average coupling distance between NPs led to dramatic changes in the absorption spectra, which are in excellent agreement with simulations—indicating that any defects or inhomogeneities present in the assembled superlattice do not significantly affect its optical properties—and confirmed the high tunability of this reconfigurable absorber (Fig. 4, E and F). Specifically, the superlattice had a 75% increase in the average absorption of light from 550 to 800 nm when decreasing solvent polarity—and decreasing average gap lengths—from 0 to 80% EtOH in H_2O, with a maximum increase of 443% at 732 nm (increased absorption from 14 to 73%). As expected, the changes in optical response could also be observed visually as the color of the surface changed from maroon to dark green to brown as gap lengths decreased (Fig. 4G).

In addition to the amplitude, the absorption band edge λ_{edge}, could be tuned from 650 nm (1.9 eV) to 775 nm (1.6 eV) (Fig. 4, E and F). The 125-nm shift in wavelength represents a wavelength tuning figure of merit (wavelength shift divided by the initial band edge wavelength prior to tuning) of 19%. The tunability reported here exceeds that of stretchable substrates, which have exhibited wavelength tuning of up to 11% in the longer wavelength infrared region (*30*), and is comparable to that achieved recently using temperature responsive polymers (*31*). Importantly, all structural changes, and the changes they induce in optical properties, were reversible for at least five cycles between large and small gaps, with no appreciable changes to absorption spectra observed (Fig. 4H).

The ability to control the arrangement, spacing, and sequence of NPs within each architecture is critical to the realization of tunable broadband absorption. Indeed, superlattices with other sequences of disk, cube, and sphere Au NP architectures are predicted to exhibit very different optical responses with considerably reduced tunability (fig. S22). Beyond tunable absorption, the ability to make responsive plasmonic nanoarchitectures not yet achievable via other techniques should dramatically increase the diversity of

structures and compositions that can now be explored by theorists and experimentalists to access new and useful optical properties. It should be possible to synthesize even more sophisticated architectures through the use of more intricate pore designs, and new DNA sequence designs should enable responsiveness to be extended to light and biological signals, in addition to chemical ones. Additionally, although we have only synthesized three-layer architectures here, the number of NP layers could in principle be increased by using deeper PMMA pores.

REFERENCES AND NOTES

1. C. A. Mirkin, R. L. Letsinger, R. C. Mucic, J. J. Storhoff, A DNA-based method for rationally assembling nanoparticles into macroscopic materials. *Nature* **382**, 607–609 (1996). doi:10.1038/382607a0 Medline
2. D. Nykypanchuk, M. M. Maye, D. van der Lelie, O. Gang, DNA-guided crystallization of colloidal nanoparticles. *Nature* **451**, 549–552 (2008). doi:10.1038/nature06560 Medline
3. M. R. Jones, N. C. Seeman, C. A. Mirkin, Programmable materials and the nature of the DNA bond. *Science* **347**, 1260901 (2015). doi:10.1126/science.1260901 Medline
4. Y. Wang, Y. Wang, D. R. Breed, V. N. Manoharan, L. Feng, A. D. Hollingsworth, M. Weck, D. J. Pine, Colloids with valence and specific directional bonding. *Nature* **491**, 51–55 (2012). doi:10.1038/nature11564 Medline
5. W. Liu, M. Tagawa, H. L. Xin, T. Wang, H. Emamy, H. Li, K. G. Yager, F. W. Starr, A. V. Tkachenko, O. Gang, Diamond family of nanoparticle superlattices. *Science* **351**, 582–586 (2016). doi:10.1126/science.aad2080 Medline
6. W. B. Rogers, W. M. Shih, V. N. Manoharan, Using DNA to program the self-assembly of colloidal nanoparticles and microparticles. *Nat. Rev. Mater.* **1**, 16008 (2016). doi:10.1038/natrevmats.2016.8
7. M. N. O'Brien, H.-X. Lin, M. Girard, M. Olvera de la Cruz, C. A. Mirkin, Programming colloidal crystal habit with anisotropic nanoparticle building blocks and DNA bonds. *J. Am. Chem. Soc.* **138**, 14562–14565 (2016). doi:10.1021/jacs.6b09704 Medline
8. M. N. O'Brien, B. Radha, K. A. Brown, M. R. Jones, C. A. Mirkin, Langmuir analysis of nanoparticle polyvalency in DNA-mediated adsorption. *Angew. Chem. Int. Ed.* **53**, 9532–9538 (2014). doi:10.1002/anie.201405317 Medline
9. Q.-Y. Lin, Z. Li, K. A. Brown, M. N. O'Brien, M. B. Ross, Y. Zhou, S. Butun, P.-C. Chen, G. C. Schatz, V. P. Dravid, K. Aydin, C. A. Mirkin, Strong coupling between plasmonic gap modes and photonic lattice modes in DNA-assembled gold nanocube arrays. *Nano Lett.* **15**, 4699–4703 (2015). doi:10.1021/acs.nanolett.5b01548 Medline
10. M. X. Wang, S. E. Seo, P. A. Gabrys, D. Fleischman, B. Lee, Y. Kim, H. A. Atwater, R. J. Macfarlane, C. A. Mirkin, Epitaxy: Programmable atom equivalents versus atoms. *ACS Nano* **11**, 180–185 (2017). doi:10.1021/acsnano.6b06584 Medline
11. J. Henzie, S. C. Andrews, X. Y. Ling, Z. Li, P. Yang, Oriented assembly of polyhedral plasmonic nanoparticle clusters. *Proc. Natl. Acad. Sci. U.S.A.* **110**, 6640–6645 (2013). doi:10.1073/pnas.1218616110 Medline
12. X. Liu, S. Biswas, J. W. Jarrett, E. Poutrina, A. Urbas, K. L. Knappenberger Jr., R. A. Vaia, P. F. Nealey, Deterministic construction of plasmonic heterostructures in well-organized arrays for nanophotonic materials. *Adv. Mater.* **27**, 7314–7319 (2015). doi:10.1002/adma.201503336 Medline
13. V. Flauraud, M. Mastrangeli, G. D. Bernasconi, J. Butet, D. T. L. Alexander, E. Shahrabi, O. J. F. Martin, J. Brugger, Nanoscale topographical control of capillary assembly of nanoparticles. *Nat. Nanotechnol.* **12**, 73–80 (2017). doi:10.1038/nnano.2016.179 Medline
14. R. A. Hughes, E. Menumerov, S. Neretina, When lithography meets self-assembly: A review of recent advances in the directed assembly of complex metal nanostructures on planar and textured surfaces. *Nanotechnology* **28**, 282002 (2017). doi:10.1088/1361-6528/aa77ce Medline
15. Materials and methods are available as supplementary materials.
16. R. J. Macfarlane, B. Lee, M. R. Jones, N. Harris, G. C. Schatz, C. A. Mirkin, Nanoparticle superlattice engineering with DNA. *Science* **334**, 204–208 (2011). doi:10.1126/science.1210493 Medline
17. V. A. Bloomfield, D. M. Crothers, I. Tinoco, *Nucleic Acids: Structures, Properties, and Functions* (University Science Books, Sausalito, CA, 2000).
18. A. A. Koshkin, S. K. Singh, P. Nielsen, V. K. Rajwanshi, R. Kumar, M. Meldgaard, C. E. Olsen, J. Wengel, LNA (Locked Nucleic Acids): Synthesis of the adenine, cytosine, guanine, 5-methylcytosine, thymine and uracil bicyclonucleoside monomers, oligomerisation, and unprecedented nucleic acid recognition. *Tetrahedron* **54**, 3607–3630 (1998). doi:10.1016/S0040-4020(98)00094-5
19. R. Owczarzy, Y. You, C. L. Groth, A. V. Tataurov, Stability and mismatch discrimination of locked nucleic acid-DNA duplexes. *Biochemistry* **50**, 9352–9367 (2011). doi:10.1021/bi200904e Medline
20. J. Valentine, S. Zhang, T. Zentgraf, E. Ulin-Avila, D. A. Genov, G. Bartal, X. Zhang, Three-dimensional optical metamaterial with a negative refractive index. *Nature* **455**, 376–379 (2008). doi:10.1038/nature07247 Medline
21. N. Liu, H. Guo, L. Fu, S. Kaiser, H. Schweizer, H. Giessen, Three-dimensional photonic metamaterials at optical frequencies. *Nat. Mater.* **7**, 31–37 (2008). doi:10.1038/nmat2072 Medline
22. M. A. Boles, M. Engel, D. V. Talapin, Self-assembly of colloidal nanocrystals: From intricate structures to functional materials. *Chem. Rev.* **116**, 11220–11289 (2016). doi:10.1021/acs.chemrev.6b00196 Medline
23. J. A. Mason, C. R. Laramy, C.-T. Lai, M. N. O'Brien, Q.-Y. Lin, V. P. Dravid, G. C. Schatz, C. A. Mirkin, Contraction and expansion of stimuli-responsive DNA bonds in flexible colloidal crystals. *J. Am. Chem. Soc.* **138**, 8722–8725 (2016). doi:10.1021/jacs.6b05430 Medline
24. N. J. Halas, S. Lal, W.-S. Chang, S. Link, P. Nordlander, Plasmons in strongly coupled metallic nanostructures. *Chem. Rev.* **111**, 3913–3961 (2011). doi:10.1021/cr200061k Medline
25. A. M. Urbas, Z. Jacob, L. D. Negro, N. Engheta, A. D. Boardman, P. Egan, A. B. Khanikaev, V. Menon, M. Ferrera, N. Kinsey, C. DeVault, J. Kim, V. Shalaev, A. Boltasseva, J. Valentine, C. Pfeiffer, A. Grbic, E. Narimanov, L. Zhu, S. Fan, A. Alù, E. Poutrina, N. M. Litchinitser, M. A. Noginov, K. F. MacDonald, E. Plum, X. Liu, P. F. Nealey, C. R. Kagan, C. B. Murray, D. A. Pawlak, I. I. Smolyaninov, V. N. Smolyaninova, D. Chanda, Roadmap on optical metamaterials. *J. Opt.* **18**, 093005 (2016). doi:10.1088/2040-8978/18/9/093005
26. N. I. Zheludev, E. Plum, Reconfigurable nanomechanical photonic metamaterials. *Nat. Nanotechnol.* **11**, 16–22 (2016). doi:10.1038/nnano.2015.302 Medline
27. Z. Qian, D. S. Ginger, Reversibly reconfigurable colloidal plasmonic nanomaterials. *J. Am. Chem. Soc.* **139**, 5266–5276 (2017). doi:10.1021/jacs.7b00711 Medline
28. A. Moreau, C. Ciracì, J. J. Mock, R. T. Hill, Q. Wang, B. J. Wiley, A. Chilkoti, D. R. Smith, Controlled-reflectance surfaces with film-coupled colloidal nanoantennas. *Nature* **492**, 86–89 (2012). doi:10.1038/nature11615 Medline
29. G. M. Akselrod, J. Huang, T. B. Hoang, P. T. Bowen, L. Su, D. R. Smith, M. H. Mikkelsen, Large-area metasurface perfect absorbers from visible to near-infrared. *Adv. Mater.* **27**, 8028–8034 (2015). doi:10.1002/adma.201503281 Medline
30. I. M. Pryce, K. Aydin, Y. A. Kelaita, R. M. Briggs, H. A. Atwater, Highly strained compliant optical metamaterials with large frequency tunability. *Nano Lett.* **10**, 4222–4227 (2010). doi:10.1021/nl102684x Medline
31. T. Ding, V. K. Valev, A. R. Salmon, C. J. Forman, S. K. Smoukov, O. A. Scherman, D. Frenkel, J. J. Baumberg, Light-induced actuating nanotransducers. *Proc. Natl. Acad. Sci. U.S.A.* **113**, 5503–5507 (2016). doi:10.1073/pnas.1524209113 Medline
32. M. N. O'Brien, M. R. Jones, K. A. Brown, C. A. Mirkin, Universal noble metal nanoparticle seeds realized through iterative reductive growth and oxidative dissolution reactions. *J. Am. Chem. Soc.* **136**, 7603–7606 (2014). doi:10.1021/ja503509k Medline
33. M. R. Jones, R. J. Macfarlane, B. Lee, J. Zhang, K. L. Young, A. J. Senesi, C. A. Mirkin, DNA-nanoparticle superlattices formed from anisotropic building blocks. *Nat. Mater.* **9**, 913–917 (2010). doi:10.1038/nmat2870 Medline
34. K. L. Young, M. R. Jones, J. Zhang, R. J. Macfarlane, R. Esquivel-Sirvent, R. J. Nap, J. Wu, G. C. Schatz, B. Lee, C. A. Mirkin, Assembly of reconfigurable one-dimensional colloidal superlattices due to a synergy of fundamental nanoscale forces. *Proc. Natl. Acad. Sci. U.S.A.* **109**, 2240–2245 (2012). doi:10.1073/pnas.1119301109 Medline
35. M. N. O'Brien, M. R. Jones, K. L. Kohlstedt, G. C. Schatz, C. A. Mirkin, Uniform

circular disks with synthetically tailorable diameters: Two-dimensional nanoparticles for plasmonics. *Nano Lett.* **15**, 1012–1017 (2015). doi:10.1021/nl5038566 Medline
36. S. Y. Chou, P. R. Krauss, P. J. Renstrom, Nanoimprint lithography. *J. Vac. Sci. Technol. B* **14**, 4129–4133 (1996). doi:10.1116/1.588605
37. F. Huo, G. Zheng, X. Liao, L. R. Giam, J. Chai, X. Chen, W. Shim, C. A. Mirkin, Beam pen lithography. *Nat. Nanotechnol.* **5**, 637–640 (2010). doi:10.1038/nnano.2010.161 Medline
38. M. R. Jones, R. J. Macfarlane, A. E. Prigodich, P. C. Patel, C. A. Mirkin, Nanoparticle shape anisotropy dictates the collective behavior of surface-bound ligands. *J. Am. Chem. Soc.* **133**, 18865–18869 (2011). doi:10.1021/ja206777k Medline
39. J. M. G. Cowie, M. A. Mohsin, I. J. McEwen, Alcohol-water cosolvent systems for poly(methyl methacrylate). *Polymer* **28**, 1569–1572 (1987). doi:10.1016/0032-3861(87)90360-0
40. E. Auyeung, R. J. Macfarlane, C. H. J. Choi, J. I. Cutler, C. A. Mirkin, Transitioning DNA-engineered nanoparticle superlattices from solution to the solid state. *Adv. Mater.* **24**, 5181–5186 (2012). doi:10.1002/adma.201202069 Medline
41. E. D. Palik, *Handbook of Optical Constants of Solids* (Academic Press, 1998), vol. 3.
42. V. Myroshnychenko, J. Rodríguez-Fernández, I. Pastoriza-Santos, A. M. Funston, C. Novo, P. Mulvaney, L. M. Liz-Marzán, F. J. García de Abajo, Modelling the optical response of gold nanoparticles. *Chem. Soc. Rev.* **37**, 1792–1805 (2008). doi:10.1039/b711486a Medline
43. J. B. Lassiter, F. McGuire, J. J. Mock, C. Ciracì, R. T. Hill, B. J. Wiley, A. Chilkoti, D. R. Smith, Plasmonic waveguide modes of film-coupled metallic nanocubes. *Nano Lett.* **13**, 5866–5872 (2013). doi:10.1021/nl402660s Medline
44. K. Aydin, V. E. Ferry, R. M. Briggs, H. A. Atwater, Broadband polarization-independent resonant light absorption using ultrathin plasmonic super absorbers. *Nat. Commun.* **2**, 517 (2011). doi:10.1038/ncomms1528 Medline
45. D. Wang, A. Yang, W. Wang, Y. Hua, R. D. Schaller, G. C. Schatz, T. W. Odom, Band-edge engineering for controlled multi-modal nanolasing in plasmonic superlattices. *Nat. Nanotechnol.* **12**, 889–894 (2017). doi:10.1038/nnano.2017.126 Medline
46. A. Tittl, P. Mai, R. Taubert, D. Dregely, N. Liu, H. Giessen, Palladium-based plasmonic perfect absorber in the visible wavelength range and its application to hydrogen sensing. *Nano Lett.* **11**, 4366–4369 (2011). doi:10.1021/nl202489g Medline
47. Z. Li, S. Butun, K. Aydin, Ultranarrow band absorbers based on surface lattice resonances in nanostructured metal surfaces. *ACS Nano* **8**, 8242–8248 (2014). doi:10.1021/nn502617t Medline
48. J. W. Park, P. V. Tuong, J. Y. Rhee, K. W. Kim, W. H. Jang, E. H. Choi, L. Y. Chen, Y. Lee, Multi-band metamaterial absorber based on the arrangement of donut-type resonators. *Opt. Express* **21**, 9691–9702 (2013). doi:10.1364/OE.21.009691 Medline
49. L. R. Hirsch, R. J. Stafford, J. A. Bankson, S. R. Sershen, B. Rivera, R. E. Price, J. D. Hazle, N. J. Halas, J. L. West, Nanoshell-mediated near-infrared thermal therapy of tumors under magnetic resonance guidance. *Proc. Natl. Acad. Sci. U.S.A.* **100**, 13549–13554 (2003). doi:10.1073/pnas.2232479100 Medline
50. B. C. Stipe, T. C. Strand, C. C. Poon, H. Balamane, T. D. Boone, J. A. Katine, J.-L. Li, V. Rawat, H. Nemoto, A. Hirotsune, O. Hellwig, R. Ruiz, E. Dobisz, D. S. Kercher, N. Robertson, T. R. Albrecht, B. D. Terris, Magnetic recording at 1.5 Pb m− 2 using an integrated plasmonic antenna. *Nat. Photonics* **4**, 484–488 (2010). doi:10.1038/nphoton.2010.90
51. M. W. Knight, H. Sobhani, P. Nordlander, N. J. Halas, Photodetection with active optical antennas. *Science* **332**, 702–704 (2011). doi:10.1126/science.1203056 Medline
52. X. Liu, T. Tyler, T. Starr, A. F. Starr, N. M. Jokerst, W. J. Padilla, Taming the blackbody with infrared metamaterials as selective thermal emitters. *Phys. Rev. Lett.* **107**, 045901 (2011). doi:10.1103/PhysRevLett.107.045901 Medline
53. N. Liu, M. Mesch, T. Weiss, M. Hentschel, H. Giessen, Infrared perfect absorber and its application as plasmonic sensor. *Nano Lett.* **10**, 2342–2348 (2010). doi:10.1021/nl9041033 Medline
54. O. Neumann, A. S. Urban, J. Day, S. Lal, P. Nordlander, N. J. Halas, Solar vapor generation enabled by nanoparticles. *ACS Nano* **7**, 42–49 (2013). doi:10.1021/nn304948h Medline
55. S. Zhang, W. Fan, N. C. Panoiu, K. J. Malloy, R. M. Osgood, S. R. J. Brueck, Experimental demonstration of near-infrared negative-index metamaterials. *Phys. Rev. Lett.* **95**, 137404 (2005). doi:10.1103/PhysRevLett.95.137404 Medline
56. C. M. Soukoulis, M. Wegener, Past achievements and future challenges in the development of three-dimensional photonic metamaterials. *Nat. Photonics* **5**, 523–530 (2011).
57. Y. Cui, K. H. Fung, J. Xu, H. Ma, Y. Jin, S. He, N. X. Fang, Ultrabroadband light absorption by a sawtooth anisotropic metamaterial slab. *Nano Lett.* **12**, 1443–1447 (2012). doi:10.1021/nl204118h Medline
58. J. A. Bossard, L. Lin, S. Yun, L. Liu, D. H. Werner, T. S. Mayer, Near-ideal optical metamaterial absorbers with super-octave bandwidth. *ACS Nano* **8**, 1517–1524 (2014). doi:10.1021/nn4057148 Medline
59. Z. Li, E. Palacios, S. Butun, H. Kocer, K. Aydin, Omnidirectional, broadband light absorption using large-area, ultrathin lossy metallic film coatings. *Sci. Rep.* **5**, 15137 (2015). Medline
60. Z. L. Sámson, K. F. MacDonald, F. De Angelis, B. Gholipour, K. Knight, C. C. Huang, E. Di Fabrizio, D. W. Hewak, N. I. Zheludev, Metamaterial electro-optic switch of nanoscale thickness. *Appl. Phys. Lett.* **96**, 143105 (2010). doi:10.1063/1.3355544
61. F. Yi, E. Shim, A. Y. Zhu, H. Zhu, J. C. Reed, E. Cubukcu, Voltage tuning of plasmonic absorbers by indium tin oxide. *Appl. Phys. Lett.* **102**, 221102 (2013). doi:10.1063/1.4809516
62. Z. Li, Y. Zhou, H. Qi, Q. Pan, Z. Zhang, N. N. Shi, M. Lu, A. Stein, C. Y. Li, S. Ramanathan, N. Yu, Correlated perovskites as a new platform for super-broadband-tunable photonics. *Adv. Mater.* **28**, 9117–9125 (2016). doi:10.1002/adma.201601204 Medline
63. S. Xiao, U. K. Chettiar, A. V. Kildishev, V. Drachev, I. C. Khoo, V. M. Shalaev, Tunable magnetic response of metamaterials. *Appl. Phys. Lett.* **95**, 033115 (2009). doi:10.1063/1.3182857
64. J.-Y. Ou, E. Plum, J. Zhang, N. I. Zheludev, An electromechanically reconfigurable plasmonic metamaterial operating in the near-infrared. *Nat. Nanotechnol.* **8**, 252–255 (2013). doi:10.1038/nnano.2013.25 Medline
65. H. Zhu, F. Yi, E. Cubukcu, Plasmonic metamaterial absorber for broadband manipulation of mechanical resonances. *Nat. Photonics* **10**, 709–714 (2016). doi:10.1038/nphoton.2016.183
66. Y. Zhao, Q. Hao, Y. Ma, M. Lu, B. Zhang, M. Lapsley, I.-C. Khoo, T. Jun Huang, Light-driven tunable dual-band plasmonic absorber using liquid-crystal-coated asymmetric nanodisk array. *Appl. Phys. Lett.* **100**, 053119 (2012). doi:10.1063/1.3681808
67. H. R. Seren, G. R. Keiser, L. Cao, J. Zhang, A. C. Strikwerda, K. Fan, G. D. Metcalfe, M. Wraback, X. Zhang, R. D. Averitt, Optically modulated multiband terahertz perfect absorber. *Adv. Opt. Mater.* **2**, 1221–1226 (2014). doi:10.1002/adom.201400197
68. Z. Sun, A. Martinez, F. Wang, Optical modulators with 2D layered materials. *Nat. Photonics* **10**, 227–238 (2016). doi:10.1038/nphoton.2016.15
69. M. A. Kats, D. Sharma, J. Lin, P. Genevet, R. Blanchard, Z. Yang, M. M. Qazilbash, D. N. Basov, S. Ramanathan, F. Capasso, Ultra-thin perfect absorber employing a tunable phase change material. *Appl. Phys. Lett.* **101**, 221101 (2012). doi:10.1063/1.4767646
70. A. Tittl, A.-K. U. Michel, M. Schäferling, X. Yin, B. Gholipour, L. Cui, M. Wuttig, T. Taubner, F. Neubrech, H. Giessen, A switchable mid-infrared plasmonic perfect absorber with multispectral thermal imaging capability. *Adv. Mater.* **27**, 4597–4603 (2015). doi:10.1002/adma.201502023 Medline
71. G. Bakan, S. Ayas, T. Saidzoda, K. Celebi, A. Dana, Ultrathin phase-change coatings on metals for electrothermally tunable colors. *Appl. Phys. Lett.* **109**, 071109 (2016). doi:10.1063/1.4961368
72. Y. Cui, J. Zhou, V. A. Tamma, W. Park, Dynamic tuning and symmetry lowering of Fano resonance in plasmonic nanostructure. *ACS Nano* **6**, 2385–2393 (2012). doi:10.1021/nn204647b Medline

ACKNOWLEDGMENTS

This material is based upon work supported by the Center for Bio-Inspired Energy Science, an Energy Frontier Research Center funded by the U.S. Department of Energy, Office of Science, Basic Energy Sciences under Award DE-SC0000989 and the Air Force Office of Scientific Research under Award Numbers FA9550-12-1-0280, FA9550-14-1-0274, and FA9550-17-1-0348. Use of the Center for

Nanoscale Materials, an Office of Science user facility at Argonne National Laboratory, and GISAXS experiments at beamline 12-ID-B at the Advanced Photon Source (APS) at Argonne National Laboratory, were supported by the U. S. Department of Energy, Office of Science, Office of Basic Energy Sciences, under Contract No. DE-AC02-06CH11357. This work made use of the EPIC facility of the NUANCE Center at Northwestern University, which has received support from the Soft and Hybrid Nanotechnology Experimental (SHyNE) Resource (NSF NNCI-1542205); the MRSEC program (NSF DMR-1121262) at the Materials Research Center; the International Institute for Nanotechnology (IIN); the Keck Foundation; and the State of Illinois, through the IIN. Q.-Y.L., Z.L., and M.R.J. gratefully acknowledge support from the Ryan Fellowship at Northwestern University, and M.N.O. gratefully acknowledges the National Science Foundation for a Graduate Research Fellowship. We thank C. Laramy and H. Lin for assistance with some nanoparticle syntheses. The authors declare no competing financial interests. All data are reported in the main text and supplement.

SUPPLEMENTARY MATERIALS

www.sciencemag.org/cgi/content/full/science.aaq0591/DC1
Materials and Methods
Supplementary Text
Figs. S1 to S37
Table S1
References (*32*–*72*)

26 September 2017; accepted 26 December 2017
Published online 18 January 2018
10.1126/science.aaq0591

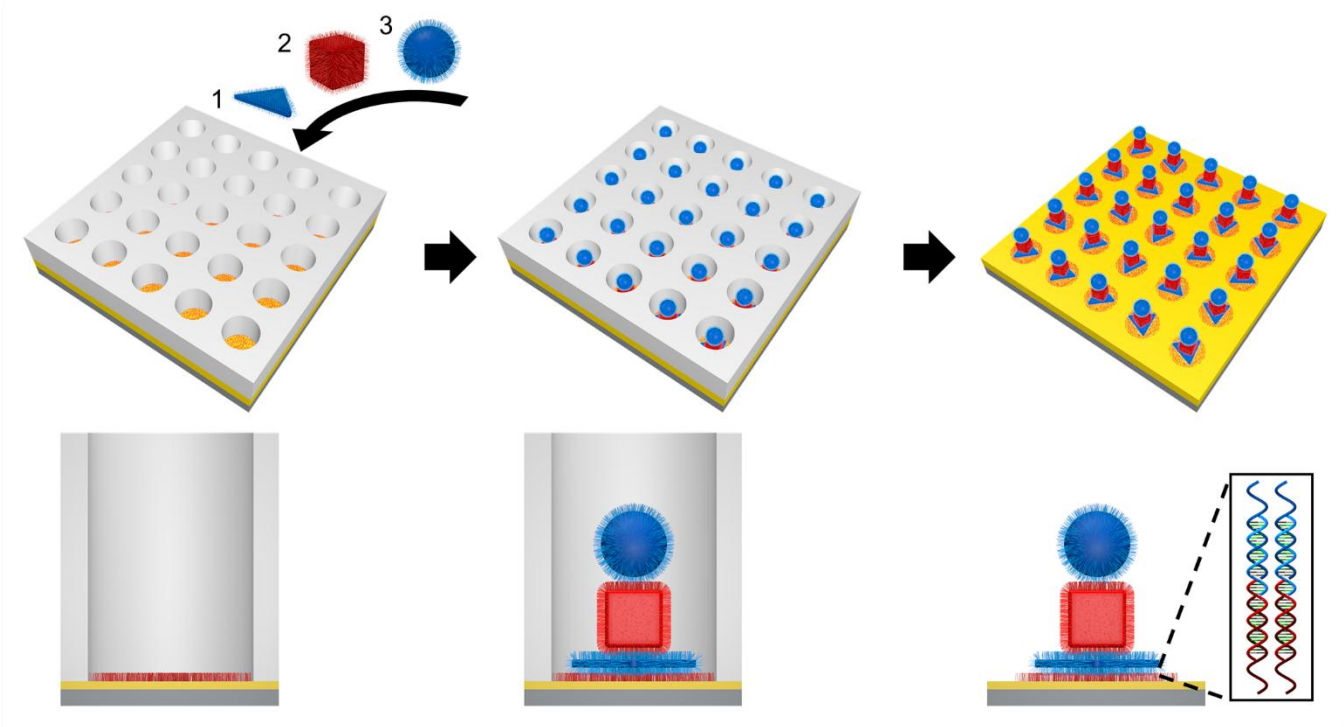

Fig. 1. Programmable assembly of reconfigurable nanoparticle (NP) architectures. To assemble NP architectures within a confined environment, one-dimensional pores are fabricated in a poly(methyl methacrylate) (PMMA)-coated gold substrate using top-down lithography, and the gold surface at the bottom of each pore is densely functionalized with DNA. DNA-functionalized colloidal NPs of controlled size and shape are then assembled in a layer-by-layer fashion by designing each layer of NPs to have a terminal DNA sequence complementary to that of the previous layer. The porous PMMA template is removed to generate NP superlattices with two-dimensional periodicity that are composed of oriented NP architectures. Bottom images depict cross-sectional views of a single pore.

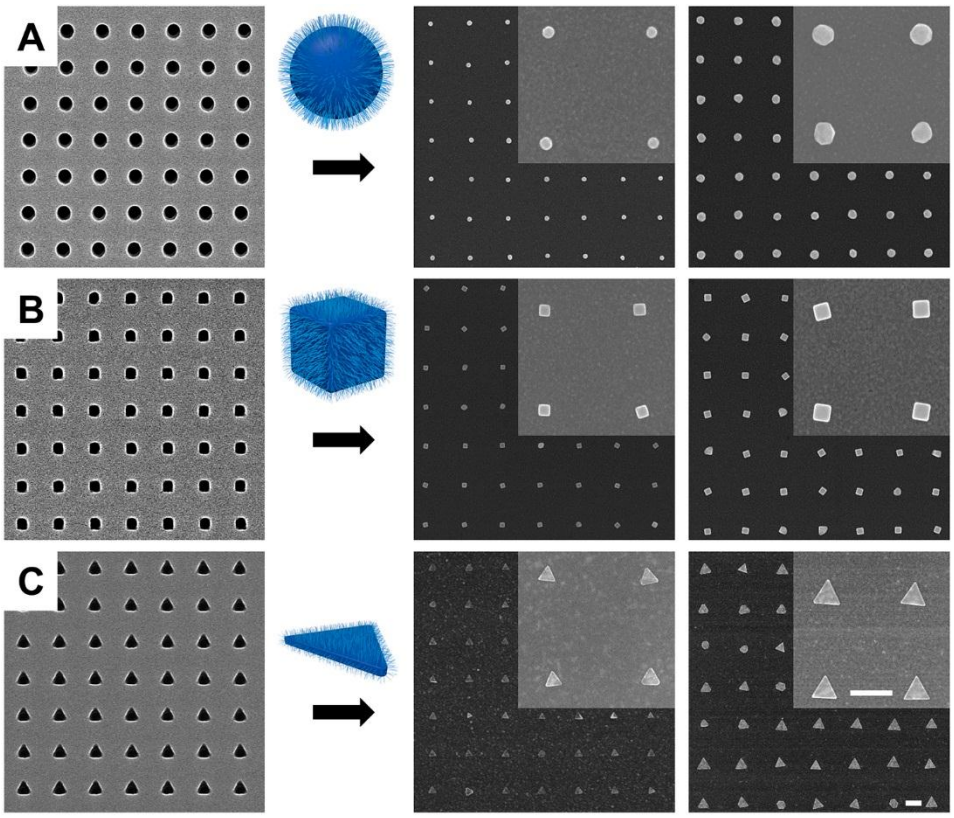

Fig. 2. **Monolayer of DNA-functionalized gold NPs assembled in PMMA templates with different shaped pores.** (**A**) Circular pores (left) are used to assemble a monolayer of gold spheres 60 and 100 nm in diameter (right). (**B**) Square pores (left) are used to assemble a monolayer of gold cubes 55 and 80 nm in edge length (right). (**C**) Triangular pores (left) are used to assemble a monolayer of gold triangular prisms 90 and 165 nm in edge length (right). Note that all SEM images of assembled nanoparticles are shown after the removal of the PMMA template. Scale bars, 200 nm.

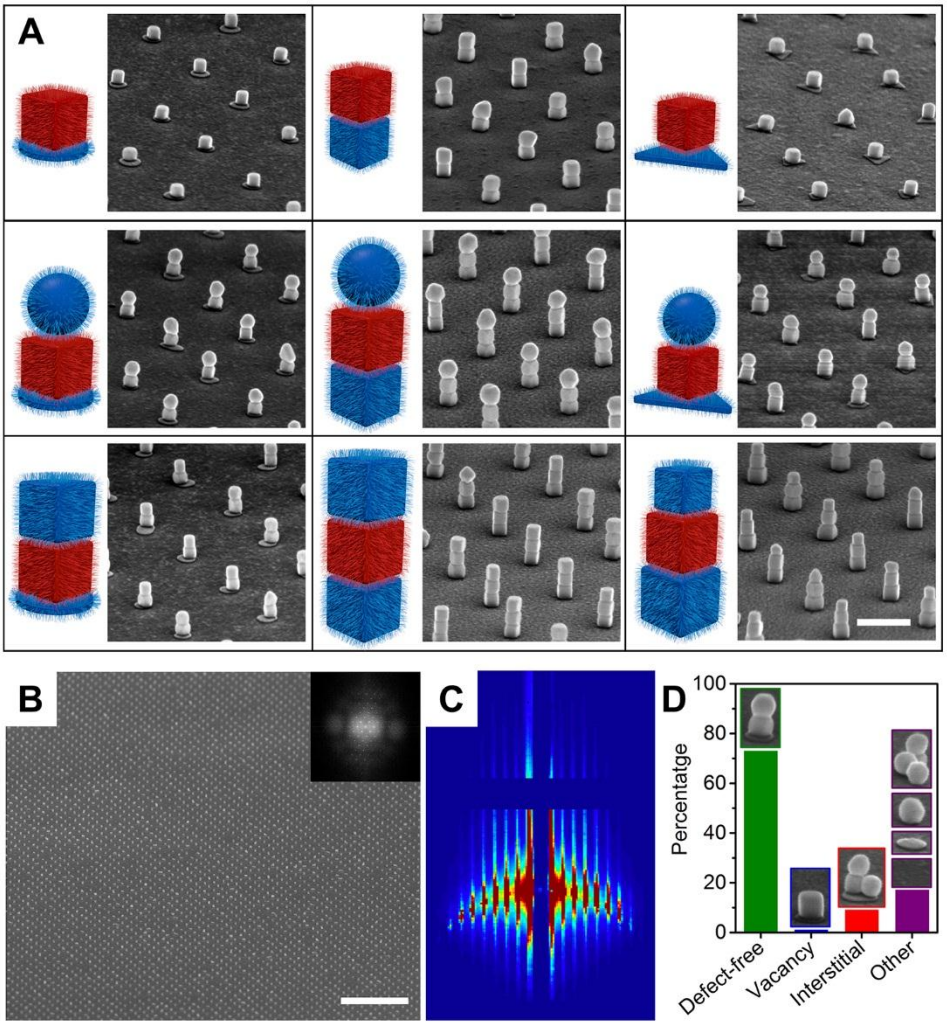

Fig. 3. Synthesis of oriented superlattices of two- and three-layer NP architectures. (**A**) Scanning electron microscopy (SEM) images of oriented superlattices (periodicity = 500 nm) attached to a gold surface after removal of the PMMA template. The superlattices are composed of one-dimensional architectures of gold NPs in the order of: disk-cube, cube-cube, prism-cube, disk-cube-sphere, cube-cube-sphere, prism-cube-sphere, disk-cube-cube, cube-cube-cube (same size), cube-cube-cube (decreasing sizes). Scale bar, 300 nm. (**B**) Large-area SEM image of the disk-cube-sphere superlattice. Inset: fast Fourier transform (FFT) pattern of the SEM image. Scale bar, 4 μm. (**C**) Grazing incidence small-angle x-ray scattering (GISAXS) pattern of the disk-cube-sphere superlattice. (**D**) Defects in the disk-cube-sphere superlattice were quantified through analysis of SEM images that contained 773 individual unit cells within the superlattice.

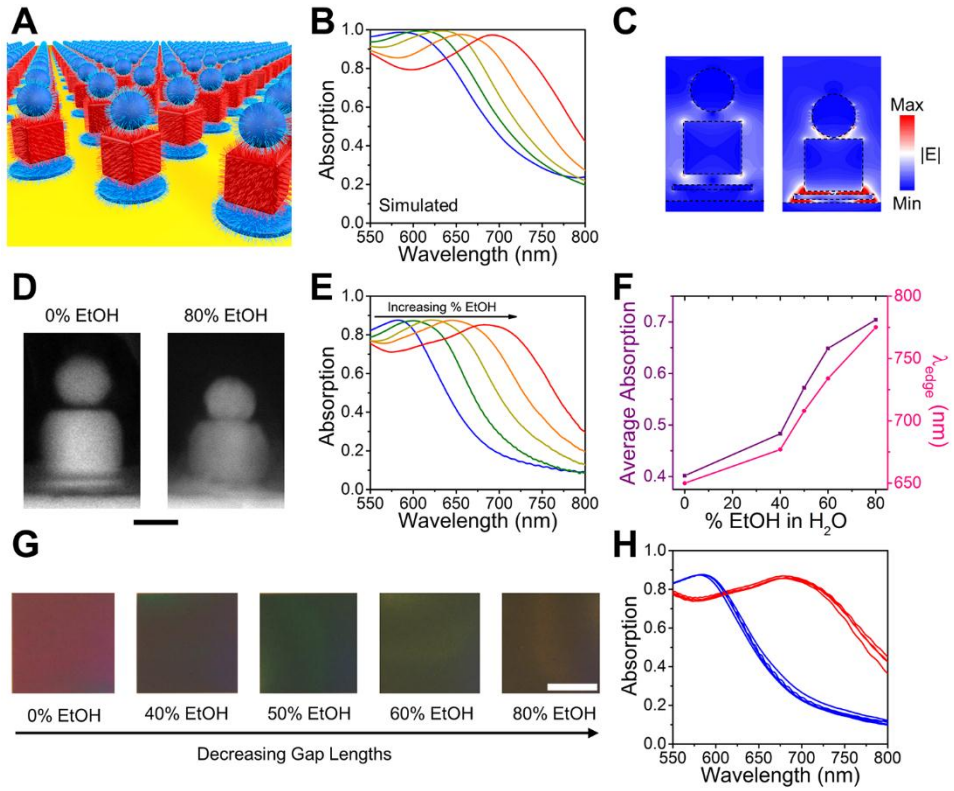

Fig. 4. Reconfigurable optical properties. (**A**) Each unit cell of the NP superlattice consists of a gold surface, circular disk, cube, and sphere, with experimentally matched dimensions. (**B**) Finite-difference time-domain (FDTD) simulations of optical absorption spectra of the disk-cube-sphere superlattice with 16, 10, 8, 6, and 4 nm gap lengths (from blue to red). (**C**) FDTD simulations of electric field distributions, $|E|$, for 16 nm gaps (left) and 4 nm gaps (right) at λ = 690 nm. (**D**) Cross-sectional SEM images of a single disk-cube-sphere architecture after immersing in 0% (left) and 80% (right) EtOH in H_2O at 0.3 M NaCl. Superlattices were encased in silica before imaging to preserve the solution-phase structure in the solid state. Scale bar, 50 nm. (**E**) Experimental optical absorption spectra at 0%, 40%, 50%, 60%, and 80% EtOH in H_2O (from blue to red: increasing % EtOH leads to decreasing average gap lengths). (**F**) Average fraction of light absorbed from 550-800 nm (dark purple) and wavelength of absorption band edge, λ_{edge} (pink). (**G**) Optical images of the disk-cube-sphere superlattice. Scale bar, 100 μm. (**H**) Optical absorption spectra are shown for 5 cycles between 0% (blue) and 80% (red) EtOH in H_2O.

OPTICS

Light amplification by seeded Kerr instability

G. Vampa,[1,2]*† T. J. Hammond,[1]† M. Nesrallah,[1] A. Yu. Naumov,[3] P. B. Corkum,[1,3] T. Brabec[1]*

Amplification of femtosecond laser pulses typically requires a lasing medium or a nonlinear crystal. In either case, the chemical properties of the lasing medium or the momentum conservation in the nonlinear crystal constrain the frequency and the bandwidth of the amplified pulses. We demonstrate high gain amplification (greater than 1000) of widely tunable (0.5 to 2.2 micrometers) and short (less than 60 femtosecond) laser pulses, up to intensities of 1 terawatt per square centimeter, by seeding the modulation instability in an $Y_3Al_5O_{12}$ crystal pumped by femtosecond near-infrared pulses. Our method avoids constraints related to doping and phase matching and therefore can occur in a wider pool of glasses and crystals even at far-infrared frequencies and for single-cycle pulses. Such amplified pulses are ideal to study strong-field processes in solids and highly excited states in gases.

Amplification of mode-locked laser pulses typically proceeds through linear optical pumping of a gain medium followed by stimulated emission at lower photon energies than that of the pump. The medium stores the energy difference, and material damage limits the maximum amplified power. Recently, the quest for ever higher-average powers and broader wavelength tunability has resulted in the exploitation of optical parametric amplification (*1*, *2*)—a second-order nonlinearity in which pump photons are split into pairs of conjugate lower-energy photons, without energy stored in the nonlinear crystal. However, phase matching and absorption of the pump and seed waves limits the center wavelength and the bandwidth of the amplified waves (*3*, *4*). Improving phase matching and transparency requires intense development of new nonlinear crystals. We show that Kerr instability (*5*–*7*), a third-order optical nonlinearity resulting in an intensity-dependent refractive index and common to any material, can compete with the more exploited parametric amplification.

The nonlinear Schrödinger equation with a Kerr third-order nonlinearity admits unstable solutions (*6*, *7*); pumping a nonlinear medium with a sufficiently intense driver leads to weak waves that experience exponential gain as they propagate. When these weak waves are seeded from noise, the continuous wave breaks up into an unstable train of pulses (*6*, *8*), leading to the disintegration of the spatial mode of an optical beam (*9*) or the formation of oceanic (*10*) and optical rogue waves (*11*). Despite the wide occurrence of Kerr instabilities in physics, the theoretical understanding is still limited to instabilities at frequencies comparable with that of the pump (*6*). Recently, a fully analytical theory of Kerr instabilities valid for perturbations of arbitrary frequencies has been developed (*7*) that predicts appreciable gain over a broad spectral range between about zero and twice the pump frequency. Here, we experimentally demonstrate seeded amplification of femtosecond laser pulses in the visible and infrared spectral regions.

By seeding gain at different wavelengths, it is possible to amplify femtosecond laser pulses over more than an octave bandwidth (Fig. 1). A comparison is shown for seed spectra at three different central wavelengths (0.6, 1.4, and 1.8 μm) (Fig. 1, pale colored solid lines) with the corresponding amplified spectra (Fig. 1, bright colors, solid lines). The gain medium is a $Y_3Al_5O_{12}$ (YAG) crystal pumped by long femtosecond pulses from a Ti:sapphire laser. Gain in excess of 1000 is achieved throughout the whole bandwidth spanning 0.5 to 2.2 μm by simply adjusting the angle θ (Fig. 1) between the seed and the pump beams. Not only can the gain be tuned to the desired wavelength, but the spectral bandwidth is also rather large. At 1.4 μm, for example, the 100-nm bandwidth of the seed is fully amplified. Despite the strong nonlinearity and the complex propagation of the pump through the crystal, the seed pulses propagate and amplify without appreciable phase modulation. We measured the amplified pulses with second-harmonic frequency resolved optical gating (SH-FROG). As demonstrated in Fig. 1, insets A to D, the duration of the amplified pulses remains close to the transform limit of the seed, in any case <60 fs, and can even be shorter than the seed by pumping with short pulses (fig. S3). Furthermore, the beam quality is preserved during amplification (fig. S1). Our newly developed theory suggests that single-cycle pulses can potentially be amplified by controlling the pump and seed wavelengths. Therefore, together with automatic phase matching demonstrated below, Kerr amplification offers an interesting new approach to amplifying single-cycle pulses in the visible (*12*, *13*), infrared (*14*–*16*), and even multicycle pulses in the terahertz region (*17*), where amplification schemes are presently nonexistent.

To characterize the gain, in the mathematical limit of continuous-wave seed and pump beams and infinitely extended in space, the amplification

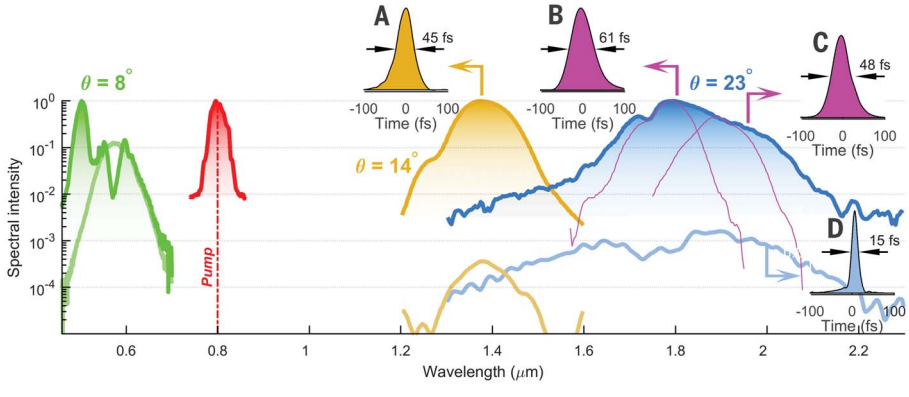

Fig. 1. Amplified spectra and pulse durations. Experimental amplified spectra (bright colors) and seed spectra (pale colors) for amplification around 0.5 μm (green), 1.4 μm (yellow), and 1.8 μm (blue), normalized to corresponding amplified spectra. The pump spectrum at 0.8 μm is shown in red. The angle between the pump and the seed laser beams (θ) is reported close to each amplified spectra. The pulse durations measured with a SHG-FROG are plotted in the insets for amplification spectra centered at (**A**) 1.4 μm, (**B**) 1.75 μm, and (**C**) 1.95 μm and (**D**) for the seed at 1.8 μm. The amplified pulses at 1.4 μm preserve the seed pulse duration of 45 fs [inset (A)]. Although the 1.8-μm seed pulses last only 15 fs (close to transform limit), the angular chirp of the amplification process narrows the spectrum that enters the FROG apparatus, which is positioned a few meters away from the YAG crystal. The measured spectra associated with insets (B) and (C) are plotted with purple lines. Each slice of the spectrum generates transform limited pulses (at 1.75 μm the measured bandwidth is 76 nm, and at 1.85 μm it is 100 nm).

[1]Department of Physics, University of Ottawa, Ottawa, ON K1N 6N5, Canada. [2]Stanford PULSE Institute, SLAC National Accelerator Laboratory, Menlo Park, CA 94025, USA. [3]National Research Council of Canada, Ottawa, ON K1A 0R6, Canada.
*Corresponding author. Email: gvampa@stanford.edu (G.V.); thomas.brabec@uottawa.ca (T.B.) †These authors contributed equally to this work.

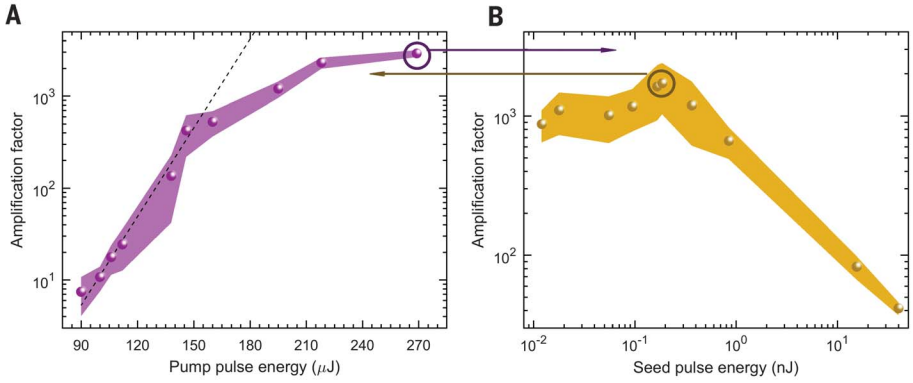

Fig. 2. Dependence of gain on pump and seed powers. (**A**) The amplification factor (the ratio between amplified and seed powers, spectrally integrated) increases exponentially with pump pulse energy, in agreement with theoretical expectation (black dotted line, which is reported in the supplementary materials) (*18*), but saturates for pump energies higher than 150 μJ, which are close to the damage threshold of YAG (~300 μJ, corresponding to a vacuum intensity of 10 TW/cm^2). (**B**) As a function of seed pulse energy, amplification remains high (>1000) for seed energies <0.2 nJ but decreases with a polynomial behavior for higher seed energies. Seed energy is varied at the maximum pump power (purple circles), whereas pump energy is varied at the seed energy just before the onset of saturation (yellow circle). The seed center wavelength is 1.4 μm.

Fig. 3. Angular chirp of the amplified spectrum. Amplified spectrum centered around 1.8 μm as a function of propagation angle, measured in the far field. The angular chirp of 3 μm/rad and the emission angle agree with the theoretical prediction (gray dashed line). It is the angularly integrated spectrum that is plotted as a blue line in Fig. 1.

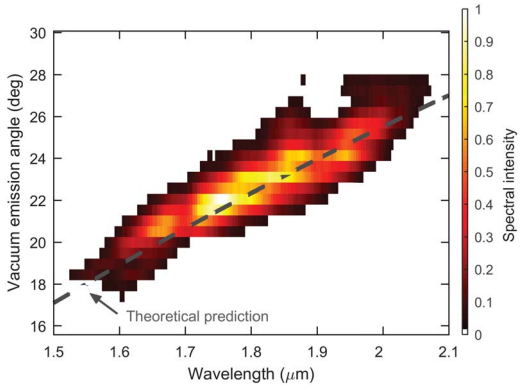

proceeds exponentially with the length of the crystal with intensity gain coefficient (*7*)

$$\bar{g}(\Omega) = \frac{k_{n(+)}k_{n(-)}}{\sqrt{k_p^2 - (\sigma D_u)^2}} \quad (1)$$

Here, $\Omega = \omega - \omega_p$ is the frequency shift between seed (ω) and pump (ω_p), $k_{n(\pm)}(\Omega) = (\omega_p \pm \Omega)\sqrt{n_2 I_p}/c$ is the nonlinear wavevector, and I_p and n_2 are the pump intensity and the nonlinear refractive index, respectively. $k_p^2 = k^2(\omega_p) + k_n^2(0)$ is the total wave vector of the pump given by adding the linear wave vector $k = \omega n(\omega)/c$ to the nonlinear wave vector at the pump wavelength. $\sigma = [k_v(\omega_p) + D_g]/k_p$, where $k_v^2(\omega) = k^2(\omega) + 2k_n^2(\omega)$ is the seed wave vector (the nonlinearity is added twice compared with k_p). $D_{\{g,u\}}$ takes into account the dispersion of the medium to any frequency shift (*7*). Amplification of finite pulses and Gaussian beams modifies this ideal gain factor by taking into account the temporal and spatial geometry (supplementary materials) (*18*).

We measured exponential growth with respect to pump intensity (Fig. 2A), in agreement with the theoretical prediction (Fig. 2A, dashed black line), up to saturation of the gain, which occurs close to the damage threshold of YAG. As a function of seed pulse energy (Fig. 2B), the gain remains constant up to 0.2 nJ and then also saturates. Saturation limits the amplified intensity to 1 TW/cm^2, which is ~10% of the pump intensity (the seed pulses are shorter than the pump, and the seed beam waist at the focus is smaller) (supplementary materials) (*18*). Near saturation, we observed cross-talk between the two similarly intense beams in the reduction of the speckle pattern generated by the pump beam. The maximum amplified energy is 1.6 μJ (from 40-nJ seed and 270-μJ pump), corresponding to an energy conversion efficiency of 0.6%. Chirped pulse amplification (*19*, *20*) can be used to increase the output energy.

We next demonstrated that phase matching still plays a role in Kerr amplification, as it does everywhere in nonlinear optics, by forcing different frequencies to propagate at slightly different directions, with angle $\theta = \sin^{-1}[\kappa_\perp/(k_p + \sigma D_u)]$ with respect to the pump beam. Here, $\kappa_\perp^2 = (k_p^2 - D_u^2)(\sigma^2 - 1)$ is the transverse momentum that experiences maximum gain. In contrast to conventional three- or four-wave mixing processes, however, here phase matching is automatically satisfied (*7*). The measured angular chirp (Fig. 3) matches the theoretical prediction well. Because the chirp is almost linear with wavelength, it will be possible to compensate for the beam divergence that phase matching imposes with a dispersive element placed just after the medium. Furthermore, the angular chirp is only weakly dependent on the pump intensity (fig. S6), suggesting that it is uniform across the amplified beam profile. Matching the transverse momentum of optimum gain is a critical parameter to achieve amplification. Optimum amplification of a desired wavelength is achieved in the experiment by tuning the angle θ (Fig. 1). And as confirmed in Fig. 3, the measured optimum angle coincides with that predicted by theory.

By using near-infrared pump pulses, we have demonstrated seeded amplification by means of Kerr instability of short femtosecond pulses over a widely tunable spectral range. Amplification occurred in a crystal (YAG) whose nonlinear refractive index is of average magnitude. The nonlinearity is at least 100 times stronger in special materials such as chalcogenide glasses (*21*) or graphene (*22*) or at frequencies at which the linear permittivity approaches zero (*23*). In the latter case, a total index change of 170% has been observed. Therefore, high gain amplification seems feasible in only a few micrometers, if not nanometers, of these materials, with gain coefficients as high as $\bar{g} \sim 100\ \mathrm{s\ mm^{-1}}$ (as opposed to ~ 5 mm^{-1}, as in YAG).

Our theory predicts that gain terminates at frequencies for which either $\kappa_\perp^2 < 0$ or $k_p^2 \simeq (\sigma D_u)^2$. In KBr pumped by 2.1-μm femtosecond pulses, the cut-off extends to 14 μm (~21 THz), and to 42 μm (~7.1 THz) in the CW limit, therefore up to far-infrared frequencies, at which nonlinear crystals perform poorly or amplification schemes are inexistent altogether. Neither linear gain media nor $\chi^{(2)}$ nonlinear crystals offer as wide a bandwidth tunability because of limitations in achieving phase matching (*4*) or because of narrow gain profiles. Several nonlinear crystals also absorb mid-infrared light (*24*).

The energy output can be scaled up to arbitrarily high energies by adapting chirped pulse amplification schemes (*19*, *20*). Furthermore, the amplified bandwidth can sustain single-cycle pulses. Therefore, Kerr amplification will result in a shift of design paradigm for next-generation high-intensity laser sources. For the moment, the demonstrated microjoule-level pulse energies are already suitable to trigger strong-field processes in condensed matter—such as high harmonic generation (*25*), ablation and damage (*26*), optically driven currents (*27*), and photoemission (*28*)—and to study highly excited Rydberg states (*29*).

Given the broad occurrence of Kerr nonlinear instabilities in nature (*10*, *11*), our demonstration with femtosecond laser pulses may prove useful to address the spatiotemporal evolution of instabilities in forms other than light over a broad range of frequencies, where the effect of the full linear and nonlinear (*23*) dispersion of the medium becomes important.

REFERENCES AND NOTES

1. R. Baumgartner, R. Byer, *IEEE J. Quantum Electron.* **15**, 432–444 (1979).
2. R. W. Boyd, *Nonlinear Optics* (Academic Press, 2003).
3. C. Manzoni, G. Cerullo, *J. Opt.* **18**, 103501 (2016).
4. B. E. Schmidt *et al.*, *Nat. Commun.* **5**, 3643 (2014).
5. K. Tai, A. Tomita, J. L. Jewell, A. Hasegawa, *Appl. Phys. Lett.* **49**, 236–238 (1986).
6. L. W. Liou, X. D. Cao, C. J. McKinstrie, G. P. Agrawal, *Phys. Rev. A* **46**, 4202–4208 (1992).
7. M. Nesrallah *et al.*, arXiv:1711.04417 [physics.optics] (2017).
8. K. Tai, A. Hasegawa, A. Tomita, *Phys. Rev. Lett.* **56**, 135–138 (1986).
9. D. Kip, M. Soljacic, M. Segev, E. Eugenieva, D. N. Christodoulides, *Science* **290**, 495–498 (2000).
10. C. Kharif, E. Pelinovsky, *Eur. J. Mech. B* **22**, 603–634 (2003).
11. J. M. Dudley, F. Dias, M. Erkintalo, G. Genty, *Nat. Photonics* **8**, 755–764 (2014).
12. E. Goulielmakis *et al.*, *Science* **320**, 1614–1617 (2008).
13. A. Wirth *et al.*, *Science* **334**, 195–200 (2011).
14. G. Krauss *et al.*, *Nat. Photonics* **4**, 33–36 (2010).
15. P. Krogen *et al.*, *Nat. Photonics* **11**, 222–226 (2017).
16. H. Liang *et al.*, *Nat. Commun.* **8**, 141 (2017).
17. M. Tonouchi, *Nat. Photonics* **1**, 97–105 (2007).
18. Materials and methods are available as supplementary materials.
19. D. Strickland, G. Mourou, *Opt. Commun.* **55**, 447–449 (1985).
20. A. Dubietis, G. Jonušauskas, A. Piskarskas, *Opt. Commun.* **88**, 437–440 (1992).
21. F. Smektala, C. Quemard, V. Couderc, A. Barthélémy, *J. Non-Cryst. Solids* **274**, 232–237 (2000).
22. H. Zhang *et al.*, *Opt. Lett.* **37**, 1856–1858 (2012).
23. M. Z. Alam, I. De Leon, R. W. Boyd, *Science* **352**, 795–797 (2016).
24. D. N. Nikogosyan, *Nonlinear Optical Crystals: A Complete Survey* (Springer Science & Business Media, 2006).
25. S. Ghimire *et al.*, *Nat. Phys.* **7**, 138–141 (2011).
26. R. R. Gattass, E. Mazur, *Nat. Photonics* **2**, 219–225 (2008).
27. A. Schiffrin *et al.*, *Nature* **493**, 70–74 (2013).
28. M. Krüger, M. Schenk, P. Hommelhoff, *Nature* **475**, 78–81 (2011).
29. U. Eichmann, A. Saenz, S. Eilzer, T. Nubbemeyer, W. Sandner, *Phys. Rev. Lett.* **110**, 203002 (2013).

ACKNOWLEDGMENTS

We acknowledge valuable financial support from the Air Force Office of Scientific Research (AFOSR) under award FA9550-16-1-0109, the AFOSR Multidisciplinary University Research Initiative grant FA9550-15-1-0037, and from Canada's National Research Council and Natural Sciences and Engineering Research Council. The authors declare no competing financial interests. G.V. thanks B. Schmidt for insightful discussions. All data needed to evaluate the conclusions in the paper are present in the paper and/or the supplementary materials.

SUPPLEMENTARY MATERIALS

www.sciencemag.org/content/359/6376/673/suppl/DC1
Materials and Methods
Supplementary Text
Figs. S1 to S6
References (*30*–*34*)

19 September 2017; accepted 21 December 2017
10.1126/science.aaq0053

Cite as: D. Zhang *et al.*, *Science* 10.1126/science.aao0865 (2018).

Atomic-resolution transmission electron microscopy of electron beam–sensitive crystalline materials

Daliang Zhang,[1]* Yihan Zhu,[2†] Lingmei Liu,[2] Xiangrong Ying,[2] Chia-En Hsiung,[2] Rachid Sougrat,[1] Kun Li,[1]* Yu Han[2,3]*

[1]King Abdullah University of Science and Technology (KAUST), Imaging and Characterization Core Lab, Thuwal 23955-6900, Saudi Arabia. [2]King Abdullah University of Science and Technology (KAUST), Advanced Membranes and Porous Materials Center, Physical Sciences and Engineering Division, Thuwal 23955-6900, Saudi Arabia. [3]King Abdullah University of Science and Technology (KAUST), KAUST Catalysis Center, Physical Sciences and Engineering Division, Thuwal 23955-6900, Saudi Arabia.

*Corresponding author. Email: daliang.zhang@kaust.edu.sa (D.Z.); kun.li@kaust.edu.sa (K.L.); yu.han@kaust.edu.sa (Y.H.)

†Present address: Department of Chemical Engineering, Zhejiang University of Technology, Hangzhou 310014, P.R. China.

High-resolution imaging of electron beam-sensitive materials is one of the most difficult applications of transmission electron microscopy (TEM). The challenges are manifold, including the acquisition of images with extremely low beam doses, the time-constrained search for crystal zone axes, the precise image alignment, and the accurate determination of the defocus value. We develop a suite of methods to fulfill these requirements and acquire atomic-resolution TEM images of several metal organic frameworks that are generally recognized as highly sensitive to electron beams. The high image resolution allows us to identify individual metal atomic columns, various types of surface termination, and benzene rings in the organic linkers. We also apply our methods to other electron beam–sensitive materials, including the organic-inorganic hybrid perovskite $CH_3NH_3PbBr_3$.

Understanding the fundamental structure-property relationships in functional materials is the essence of materials science. High-resolution TEM (HRTEM) is a powerful tool for structure characterization (*1*). However, there are a wide range of materials that are easily damaged by the electron beams (*2*–*5*). Metal organic frameworks (MOFs), which have designable porous structures and fascinating properties (*6*–*8*), represent a typical example of electron beam–sensitive materials. During the few attempts to image MOFs using HRTEM, only the primary channels could be resolved by the limited resolution as a result of beam damage (*2*, *9*–*11*).

The mechanisms of beam damage are complex and vary with the material, primarily including knock-on damage, heating effects, and radiolysis (*3*, *4*, *12*). One means of alleviating beam damage is to reduce the energy of electron beam. HRTEM with low accelerating voltages has successfully imaged carbon nanotube and graphene (*13*–*15*). However, the use of low-energy electrons results in poor image resolution and a short penetration depth, and only prevents knock-on damage. Similarly, the use of cryo-TEM only lessens the heating damage to a certain degree (*11*). An alternative, in-principle more general solution to this issue is to acquire the HRTEM images with a sufficiently low electron dose to capture the structure before damage occurs. Although this idea is straightforward, it is difficult to realize because it requires an extremely sensitive camera to record acceptable images with only a few electrons per pixel. Conventional cameras cannot produce images with a sufficient signal-to-noise ratio under such low dose conditions.

Direct-detection electron-counting (DDEC) cameras have an unprecedentedly high detective quantum efficiency and enable HRTEM at ultralow electron doses (*16*, *17*). Taking advantage of this, structural biologists have boosted the voxel resolution for protein structures using cryo-TEM (*18*). In the field of materials science, however, the potential of DDEC cameras in HRTEM imaging of electron beam–sensitive materials remains largely unexplored, due to some practical obstacles. First, unlike the single-particle cryo-TEM that reconstructs a protein structure from randomly oriented particles, for crystalline materials images should be acquired along specific directions, i.e., along the zone axes of the lattice. With beam-sensitive specimens, the process of finding a zone axis must be accomplished very quickly to minimize the beam irradiation. Second, the electron-counting mode is capable of producing successive short-exposure images, but the images must be precisely aligned to fully restore the high resolution information. Third, it is impossible to acquire a focus series of a beam-sensitive material, even when using a DDEC camera, and thus the interpretation of the image is difficult unless an accurate defocus value can be determined. We reported the use of a DDEC camera to image a MOF material (ZIF-8) with an ultralow electron dose, in which the zone-axis image was obtained by sampling a large number of randomly oriented crystals (*19*). However, this is an inefficient trial-and-error process and success is not guaranteed. In this work, we develop a suite of methods to overcome these obstacles, advancing the HRTEM of beam-sensitive materials to a

nearly routine process.

To design the quantitative HRTEM conditions for MOFs, we first evaluated their stabilities under a 300 KV-accelerated electron beam. The results reveal they began to lose their crystallinity when the cumulative electron dose reached 10-20 $e^- Å^{-2}$, as determined by the fading of the electron diffraction (ED) spots (fig. S1). These values set the upper limits of the cumulative electron dose for both locating a zone axis and the subsequent image acquisition. In our experiments, we used a DDEC camera to acquire images at a reasonably high magnification of 55,000 to achieve atomic resolution (pixel size: 0.57 Å × 0.57 Å) with electron doses of 2-4 e^- per pixel (6-12 $e^- Å^{-2}$). Therefore, the maximum electron dose that can be used to find a zone axis is less than 10 $e^- Å^{-2}$. The conventional, manual method for aligning a zone axis does not meet this threshold, because it requires time-consuming, iterative toggles between the diffraction and imaging modes, often causing the total electron dose to reach hundreds of electrons per $Å^2$.

We developed a simple program to achieve a direct, one-step alignment of the zone axis (figs. S2 and S3). When the electron beam incidence deviates from a zone axis by an angle φ, the zero-order Laue zone of the lattice intersects with the Ewald sphere, forming an arc in the ED that is part of the Laue circle. The radius of the Laue circle is approximately equal to $\sin(\varphi)*(1/\lambda)$, where λ is the wavelength of the beam. Our program first identifies a Laue circle by analyzing the distribution of reflections from an off-axis ED pattern. Different from an earlier software of automatic zone axis alignment (*20*) that estimates the crystal orientation by evaluating the intensities of reflections, our program determines the Laue circle from the positions of reflections to avoid the influence of structure factors or dynamic effects. Once the Laue circle is identified, φ is determined by its radius and λ. The program then decomposes φ into two components, φ_α and φ_β, which correspond to two tilting angles around the α-tilt and β-tilt axes of the double-tilt TEM holder, based on the predetermined directions of the two tilting axes. By applying the program-calculated tilting angles φ_α and φ_β, we can directly tilt the crystal from the initial orientation to align with the zone axis. The whole process requires the acquisition of only two EDs, one for determining the Laue circle and the other for confirming the on-axis orientation; the electron beam is blanked in between while the program does its calculations, and the total dose consumed is far below 1 $e^-/Å^2$. This method requires that the initial crystal orientation is close to a zone axis ($-5° < \varphi < 5°$); otherwise, there are very few reflections observed in ED, making the identification of a Laue circle difficult. In practice, the probability of seeing a Laue circle is > 10% in randomly oriented powder samples.

HRTEM of electron beam–sensitive materials often suffers from a beam-induced specimen motion that results in blurred images. When using a DDEC camera, this issue can be overcome by breaking the total exposure into a stack of successive short-exposure images (frames), on the condition that the drift between frames can be precisely corrected by image alignment. In principle, the exposure of each frame should be as short as possible to minimize specimen motion and statistical errors from the detector. However, beam-sensitive materials require low electron dose rate to avoid structural damage, and consequently, short exposure times result in very noisy frames with poor signal to noise that cannot be aligned using the common methods based on feature matching or phase correlation. To increase the signal to noise, several successive frames can be merged into one, which is equal to using longer exposure and thus detrimental to image resolution, especially when the specimen motion is severe. Image filters can also increase the signal to noise to facilitate image alignment, but the existing filters do not work well with high noise levels (fig. S4).

A general principle of image alignment is to decompose a real-space image into components of different spatial frequencies in the reciprocal space by Fourier transform (FT). Image drift can be determined from the 'phases' variation in the FTs. The difficulty in aligning noisy images lies in the poor signal to noise that affects the accuracy of phase determination. We hypothesize that the impact of noise can be minimized by selectively analyzing pixels in the FT with strong amplitudes, because phase determination of weak pixels is more easily influenced by noise and prone to errors. On the basis of this hypothesis, we developed an "amplitude filter" to confine the phase analysis to 'reliable' strong-amplitude pixels (figs. S5 and S6).

Unlike the common methods that deal with the weak signals of individual frames, the "amplitude filter" starts by integrating the FTs of all the frames in an image stack to pinpoint the strong-amplitude pixels. The workflow is illustrated in Fig. 1 using an HRTEM image stack of MOF UiO-66 (*21*). With extremely low dose (0.033 e^-/pixel) (Fig. 1A), even the reflections are difficult to identify in the FT of each frame (Fig. 1B). We summed the FT amplitude components from all of the frames in the stack, as the reflections have invariable coordinates in the FTs, irrespective of image drift. As shown in Fig. 1C, the "hidden" reflections emerged in the summed FT amplitude pattern (we call it 'amplitude pattern' because it does not contain phase information). We filtered out background and weak pixels that have amplitudes lower than a set threshold from the amplitude pattern. The "amplitudes" of the remaining pixels were combined with the "phases" from the original FT of each frame to generate a series of modified FTs (Fig. 1D), followed by inverse FTs to generate a series of filtered images (Fig. 1E). Finally, the image drift was calculated using iterative cross-correlation based on the filtered images (Fig. 1F), and this information was used to align

the original images in the stack. The drift-corrected, summed image shows rich high-resolution structural details, as evidenced by the appearance of the 1.4 Å reflection in the FT (Fig. 1G). By contrast, the cross-correlation without our "amplitude filter" could not correctly align this image stack until it is 1×1×10 binned, which led to a marked reduction in image resolution in the direction of the image drift (Fig. 1H). The result of merging all of the frames without drift correction is shown in Fig. 1I for comparison.

We are now able to study various MOFs with TEM along different zone axes, and to restore high-resolution information from the obtained images. Results from MOF UiO-66 are presented in Fig. 2. The successful acquisition of HRTEM images from four zone axes, <001>, <011>, <111>, and <013>, demonstrates the effectiveness of our method for zone axis alignment. FTs of these images show that the information transfer is < 2 Å in all directions (Fig. 2), confirming the efficacy of our method for image alignment.

The contrast in HRTEM images varies with the specimen thickness and defocus, making a single image difficult to interpret directly. A common practice in HRTEM is to acquire a series of images with different defocuses for structure reconstruction (*22*, *23*). But this method is not suitable for MOFs because it is impossible to acquire multiple images without causing structural damage, even when using the low-dose conditions. On the other hand, the very low framework density of MOFs greatly decreases their effective scattering thickness; therefore, we can safely apply the weak-phase object approximation to MOFs for a wide range of thicknesses up to ~ 100 nm. Therefore, a single image can be made more interpretable by correcting the "contrast inversion" caused by the contrast transfer function (CTF) of the objective lens, if the absolute defocus of the image is known (*24*). Here we propose that we can take advantage of the "instability" of MOFs to determine the defocus. Specifically, after an HRTEM image is captured, we prolong the beam irradiation to deliberately destroy the crystalline structure, and acquire a focus series of this amorphized area (fig. S7). Using established methods (*22*), we can determine the absolute defocus value of each image in the series and, thus, that of the HRTEM image of MOF for CTF correction.

The success of our methodology has been demonstrated in a case study, in which an HRTEM image of UiO-66 along the <011> axis was acquired, aligned, and CTF-corrected using the methods described above. The sample was heated at 300°C under vacuum for 10 hours to remove the solvent/guest molecules before HRTEM. The imaged area contains a truncated octahedral crystal with an ultra-thin piece of crystal protruding from its lower right corner (Fig. 3A). In the CTF-corrected and denoised image (Fig. 3B and fig. S8), triangular channels encompassed by three metal clusters and three 1,4-benzenedicarboxylic acids (BDC) are identified, and atomic columns of Zr are distinguished within the Zr_6O_8 clusters, in good agreement with the crystal structure of UiO-66. The benzene rings with face-on configurations in the BDC linkers are resolved (Fig. 3B and fig. S8). In addition to the bulk structure, our image reveals detailed local structures. At the truncation surface of the octahedral crystal that corresponds to the fast-growing {100} planes, the crystal growth steps are identified as a number of small {100} and {111} facets (Fig. 3C). Furthermore, the high resolution allows us to investigate the surface termination of this crystal. In the CTF-corrected image, the outermost layer of Zr clusters have dark contrast and can be identified at the crystal surfaces, where the organic linkers are hardly visible because of the weak contrast associated with the low atomic numbers. We performed real-space averaging along the crystal surface to enhance the signal to noise (fig. S9). The results reveal the coexistence of ligand-free (metal-exposing) and ligand-capped surfaces: the major exposed {111} surface terminates with BDC linkers (Fig. 3D); in contrast, the small truncation surface (growth steps) expose Zr clusters at the kink positions between {100} and {111} facets (Fig. 3E).

It has been speculated that upon heating to 300°C, the octahedral $ZrO_4(OH)_4$ clusters in UiO-66 undergo dehydroxylation forming distorted Zr_6O_6 clusters (*25*). In a <110> projection, this distortion gives rise to increased Zr-Zr distances along the in-plane <110> direction (fig. S10). However, the random orientation of this distortion makes it difficult to verify by conventional characterizations. Using HRTEM, we observed the subtle structural change in UiO-66 associated with dehydroxylation (figs. S11 to S13). As revealed in the images, the as-synthesized UiO-66 contains only one type of Zr cluster with uniform Zr-Zr distances of 3.34 Å, whereas the heated UiO-66 contains two types of Zr clusters; one is same as the cluster in the as-synthesized sample and the other has larger Zr-Zr distances of 3.89 Å (Fig. 3, F and G, and fig. S12). This result supports speculation that the Zr clusters in UiO-66 become distorted upon heating (*25*). The appearance of a small number of undistorted clusters (Zr-Zr: 3.34 Å) in the heated UiO-66 (fig. S13) was likely caused by partial re-hydroxylation during the TEM sample preparation process. We note that the exact values of the Zr-Zr distance measured using HRTEM are not very accurate due to the pixel size limitations.

HRTEM images of MOFs ZIF-8 and HKUST-1 (*26*) and a germanosilicate zeolite are presented in figs. S14 and S15, which show good matching with the corresponding crystal structures after CTF-correction. We also successfully acquired HRTEM images of the organic-inorganic hybrid perovskite $CH_3NH_3PbBr_3$, which has emerged as an optoelectronic material and is known to be very sensitive to electron beams. The hybrid perovskites show anomalous I-V

hysteresis in photovoltaic applications (*27*). Ferroelectric effect (*28*) and ion migration (*29*) have been posited to be likely causes for the hysteresis. Our image reveals that $CH_3NH_3PbBr_3$ crystals contain ordered nanometer-sized domains with off-centered CH_3NH_3 cations that have differing orientations. In the two typical domains highlighted in Fig. 4, the CH_3NH_3 cations exhibit normal and parallel configurations (relative to the projection direction), giving rise to in-plane and out-of-plane electric dipoles, respectively. This observation implies the ferroelectric order in this material.

In summary, we developed a suite of methodologies that enable atomic-resolution TEM imaging of electron beam–sensitive crystalline materials, which have traditionally been considered unsuitable for TEM characterization. With this capability, we are able to observe the local structures of MOFs and other fragile materials, significantly expanding the range of applications for HRTEM. It is worth noting that our method for zone axis alignment not only reduces the electron dose, but also enhances the precision of alignment. Its application is not limited to beam-sensitive materials; it is particularly useful for aligning nanosized crystals. Likewise, our method for image alignment can be generally applied to various noisy images with periodic features. This study facilitates investigations in a wide variety of "unstable" materials using HRTEM.

REFERENCES AND NOTES

1. C. L. Jia, M. Lentzen, K. Urban, Atomic-resolution imaging of oxygen in perovskite ceramics. *Science* **299**, 870–873 (2003). doi:10.1126/science.1079121 Medline
2. J. Cravillon, S. Münzer, S.-J. Lohmeier, A. Feldhoff, K. Huber, M. Wiebcke, Rapid Room-Temperature Synthesis and Characterization of Nanocrystals of a Prototypical Zeolitic Imidazolate Framework. *Chem. Mater.* **21**, 1410–1412 (2009). doi:10.1021/cm900166h
3. O. Ugurlu, J. Haus, A. A. Gunawan, M. G. Thomas, S. Maheshwari, M. Tsapatsis, K. A. Mkhoyan, Radiolysis to knock-on damage transition in zeolites under electron beam irradiation. *Phys. Rev. B* **83**, 113408 (2011). doi:10.1103/PhysRevB.83.113408
4. T. Susi, J. Kotakoski, R. Arenal, S. Kurasch, H. Jiang, V. Skakalova, O. Stephan, A. V. Krasheninnikov, E. I. Kauppinen, U. Kaiser, J. C. Meyer, Atomistic description of electron beam damage in nitrogen-doped graphene and single-walled carbon nanotubes. *ACS Nano* **6**, 8837–8846 (2012). doi:10.1021/nn303944f Medline
5. A. Garcia, A. M. Raya, M. M. Mariscal, R. Esparza, M. Herrera, S. I. Molina, G. Scavello, P. L. Galindo, M. Jose-Yacaman, A. Ponce, Analysis of electron beam damage of exfoliated MoS_2 sheets and quantitative HAADF-STEM imaging. *Ultramicroscopy* **146**, 33–38 (2014). doi:10.1016/j.ultramic.2014.05.004 Medline
6. H. Li, M. Eddaoudi, M. O'Keeffe, O. M. Yaghi, Design and synthesis of an exceptionally stable and highly porous metal-organic framework. *Nature* **402**, 276–279 (1999). doi:10.1038/46248
7. H. Furukawa, K. E. Cordova, M. O'Keeffe, O. M. Yaghi, The chemistry and applications of metal-organic frameworks. *Science* **341**, 1230444 (2013). doi:10.1126/science.1230444 Medline
8. O. K. Farha, A. Ö. Yazaydın, I. Eryazici, C. D. Malliakas, B. G. Hauser, M. G. Kanatzidis, S. T. Nguyen, R. Q. Snurr, J. T. Hupp, De novo synthesis of a metal-organic framework material featuring ultrahigh surface area and gas storage capacities. *Nat. Chem.* **2**, 944–948 (2010). doi:10.1038/nchem.834 Medline
9. O. I. Lebedev, F. Millange, C. Serre, G. Van Tendeloo, G. Ferey, First direct imaging of giant pores of the metal-organic framework MIL-101. *Chem. Mater.* **17**, 6525–6527 (2005). doi:10.1021/cm051870o
10. L. K. Zhu, D. L. Zhang, M. Xue, H. Li, S. L. Qiu, Direct observations of the MOF (UiO-66) structure by transmission electron microscopy. *CrystEngComm* **15**, 9356–9359 (2013). doi:10.1039/c3ce41122b
11. C. Wiktor, S. Turner, D. Zacher, R. A. Fischer, G. Van Tendeloo, Imaging of intact MOF-5 nanocrystals by advanced TEM at liquid nitrogen temperature. *Microporous Mesoporous Mater.* **162**, 131–135 (2012). doi:10.1016/j.micromeso.2012.06.014
12. R. F. Egerton, Mechanisms of radiation damage in beam-sensitive specimens, for TEM accelerating voltages between 10 and 300 kV. *Microsc. Res. Tech.* **75**, 1550–1556 (2012). doi:10.1002/jemt.22099 Medline
13. A. Hashimoto, K. Suenaga, A. Gloter, K. Urita, S. Iijima, Direct evidence for atomic defects in graphene layers. *Nature* **430**, 870–873 (2004). doi:10.1038/nature02817 Medline
14. J. C. Meyer, S. Kurasch, H. J. Park, V. Skakalova, D. Künzel, A. Gross, A. Chuvilin, G. Algara-Siller, S. Roth, T. Iwasaki, U. Starke, J. H. Smet, U. Kaiser, Experimental analysis of charge redistribution due to chemical bonding by high-resolution transmission electron microscopy. *Nat. Mater.* **10**, 209–215 (2011). doi:10.1038/nmat2941 Medline
15. L. Guan, K. Suenaga, S. Iijima, Smallest carbon nanotube assigned with atomic resolution accuracy. *Nano Lett.* **8**, 459–462 (2008). doi:10.1021/nl072396j Medline
16. L. Jin, A.-C. Milazzo, S. Kleinfelder, S. Li, P. Leblanc, F. Duttweiler, J. C. Bouwer, S. T. Peltier, M. H. Ellisman, N.-H. Xuong, Applications of direct detection device in transmission electron microscopy. *J. Struct. Biol.* **161**, 352–358 (2008). doi:10.1016/j.jsb.2007.10.007 Medline
17. X. Li, P. Mooney, S. Zheng, C. R. Booth, M. B. Braunfeld, S. Gubbens, D. A. Agard, Y. Cheng, Electron counting and beam-induced motion correction enable near-atomic-resolution single-particle cryo-EM. *Nat. Methods* **10**, 584–590 (2013). doi:10.1038/nmeth.2472 Medline
18. A. Merk, A. Bartesaghi, S. Banerjee, V. Falconieri, P. Rao, M. I. Davis, R. Pragani, M. B. Boxer, L. A. Earl, J. L. S. Milne, S. Subramaniam, Breaking cryo-EM resolution barriers to facilitate drug discovery. *Cell* **165**, 1698–1707 (2016). doi:10.1016/j.cell.2016.05.040 Medline
19. Y. Zhu, J. Ciston, B. Zheng, X. Miao, C. Czarnik, Y. Pan, R. Sougrat, Z. Lai, C.-E. Hsiung, K. Yao, I. Pinnau, M. Pan, Y. Han, Unravelling surface and interfacial structures of a metal-organic framework by transmission electron microscopy. *Nat. Mater.* **16**, 532–536 (2017). doi:10.1038/nmat4852 Medline
20. T. Duden, A. Gautam, U. Dahmen, KSpaceNavigator as a tool for computer-assisted sample tilting in high-resolution imaging, tomography and defect analysis. *Ultramicroscopy* **111**, 1574–1580 (2011). doi:10.1016/j.ultramic.2011.08.003 Medline
21. J. H. Cavka, S. Jakobsen, U. Olsbye, N. Guillou, C. Lamberti, S. Bordiga, K. P. Lillerud, A new zirconium inorganic building brick forming metal organic frameworks with exceptional stability. *J. Am. Chem. Soc.* **130**, 13850–13851 (2008). doi:10.1021/ja8057953 Medline
22. W. Wan, S. Hovmöller, X. Zou, Structure projection reconstruction from through-focus series of high-resolution transmission electron microscopy images. *Ultramicroscopy* **115**, 50–60 (2012). doi:10.1016/j.ultramic.2012.01.013 Medline
23. H. W. Zandbergen, D. Tang, J. Jansen, R. J. Cava, The use of through focus exit wave reconstruction in the structure determination of several intermetallic superconductors. *Ultramicroscopy* **64**, 231–247 (1996). doi:10.1016/0304-3991(96)00015-0
24. X. D. Zou, S. Hovmöller, P. Oleynikov, *Electron Crystallography: Electron Microscopy and Electron Diffraction* (Oxford Univ. Press, 2011), pp. 177–190.
25. L. Valenzano, B. Civalleri, S. Chavan, S. Bordiga, M. H. Nilsen, S. Jakobsen, K. P. Lillerud, C. Lamberti, Disclosing the complex structure of UiO-66 metal organic framework: A synergic combination of experiment and theory. *Chem. Mater.* **23**, 1700–1718 (2011). doi:10.1021/cm1022882
26. S. S. Chui, S. M. Lo, J. P. Charmant, A. G. Orpen, I. D. Williams, A chemically functionalizable nanoporous material. *Science* **283**, 1148–1150 (1999). doi:10.1126/science.283.5405.1148 Medline
27. H. J. Snaith, A. Abate, J. M. Ball, G. E. Eperon, T. Leijtens, N. K. Noel, S. D. Stranks, J. T.-W. Wang, K. Wojciechowski, W. Zhang, Anomalous hysteresis in perovskite solar cells. *J. Phys. Chem. Lett.* **5**, 1511–1515 (2014). doi:10.1021/jz500113x Medline
28. J. Wei, Y. Zhao, H. Li, G. Li, J. Pan, D. Xu, Q. Zhao, D. Yu, Hysteresis analysis based

on the ferroelectric effect in hybrid perovskite solar cells. *J. Phys. Chem. Lett.* **5**, 3937–3945 (2014). doi:10.1021/jz502111u Medline
29. W. Tress, N. Marinova, T. Moehl, S. M. Zakeeruddin, M. K. Nazeeruddin, M. Grätzel, Understanding the rate-dependent J-V hysteresis, slow time component, and aging in $CH_3NH_3PbI_3$ perovskite solar cells: The role of a compensated electric field. *Energy Environ. Sci.* **8**, 995–1004 (2015). doi:10.1039/C4EE03664F
30. F. Brivio, K. T. Butler, A. Walsh, M. van Schilfgaarde, Relativistic quasiparticle self-consistent electronic structure of hybrid halide perovskite photovoltaic absorbers. *Phys. Rev. B* **89**, 155204 (2014). doi:10.1103/PhysRevB.89.155204
31. Z. Xu, L. Yang, C. Xu, Pt@UiO-66 heterostructures for highly selective detection of hydrogen peroxide with an extended linear range. *Anal. Chem.* **87**, 3438–3444 (2015). doi:10.1021/ac5047278 Medline
32. N. L. Torad, M. Hu, Y. Kamachi, K. Takai, M. Imura, M. Naito, Y. Yamauchi, Facile synthesis of nanoporous carbons with controlled particle sizes by direct carbonization of monodispersed ZIF-8 crystals. *Chem. Commun. (Camb.)* **49**, 2521–2523 (2013). doi:10.1039/c3cc38955c Medline
33. F. L. Wang, H. L. Guo, Y. M. Chai, Y. P. Li, C. G. Liu, The controlled regulation of morphology and size of HKUST-1 by "coordination modulation method". *Microporous Mesoporous Mater.* **173**, 181–188 (2013). doi:10.1016/j.micromeso.2013.02.023
34. W. J. Roth, P. Nachtigall, R. E. Morris, P. S. Wheatley, V. R. Seymour, S. E. Ashbrook, P. Chlubná, L. Grajciar, M. Položij, A. Zukal, O. Shvets, J. Čejka, A family of zeolites with controlled pore size prepared using a top-down method. *Nat. Chem.* **5**, 628–633 (2013). doi:10.1038/nchem.1662 Medline
35. J. A. Sichert, Y. Tong, N. Mutz, M. Vollmer, S. Fischer, K. Z. Milowska, R. García Cortadella, B. Nickel, C. Cardenas-Daw, J. K. Stolarczyk, A. S. Urban, J. Feldmann, Quantum size effect in organometal halide perovskite nanoplatelets. *Nano Lett.* **15**, 6521–6527 (2015). doi:10.1021/acs.nanolett.5b02985 Medline
36. W. Wan, J. Sun, J. Su, S. Hovmöller, X. Zou, Three-dimensional rotation electron diffraction: Software RED for automated data collection and data processing. *J. Appl. Crystallogr.* **46**, 1863–1873 (2013). doi:10.1107/S0021889813027714 Medline
37. QSTEM V2, 31; www.qstem.org.
38. M. V. Sidorov, ctfExplorer V0.999a; www.maxsidorov.com/ctfexplorer.
39. R. Kilaas, Optimal and near-optimal filters in high-resolution electron microscopy. *J. Microsc-Oxford* **190**, 45–51 (1998). doi:10.1046/j.1365-2818.1998.3070861.x
40. D. R. G. Mitchell, HRTEM filter V1.3; www.felmi-zfe.at/dm-script/dm-script-database/.
41. X. Liu, H. Xu, L. Zhang, L. Han, J. Jiang, P. Oleynikov, L. Chen, P. Wu, Isomorphous incorporation of tin ions into germanosilicate framework assisted by local structural rearrangement. *ACS Catal.* **6**, 8420–8431 (2016). doi:10.1021/acscatal.6b02032

ACKNOWLEDGMENTS

We thank M. Pan and O. Terasaki for helpful discussions. This work was supported by King Abdullah University of Science and Technology through Competitive Research Grant (URF/1/2570-01) and Center Competitive Funding (FCC/1/1972-19). HRTEM images presented in this paper and the two programs used for zone axis alignment and image alignment are archived in a data repository (https://zenodo.org/record/1133206) for verification purposes only. Interested readers can download the programs after agreeing with the terms and conditions stated there. D. Z., Y. Z., K. L., and Y. H. are inventors on United States Provisional patent applications (62/490,967 and 62/490,968) submitted by King Abdullah University of Science and Technology that cover the methods for crystal zone axis alignment and image alignment.

SUPPLEMENTARY MATERIALS

www.sciencemag.org/cgi/content/full/science.aao0865/DC1
Materials and Methods
Figs. S1 to S16
Table S1
References (*31*–*41*)

12 June 2017; resubmitted 29 September 2017
Accepted 27 December 2017
Published online 18 January 2018

10.1126/science.aao0865

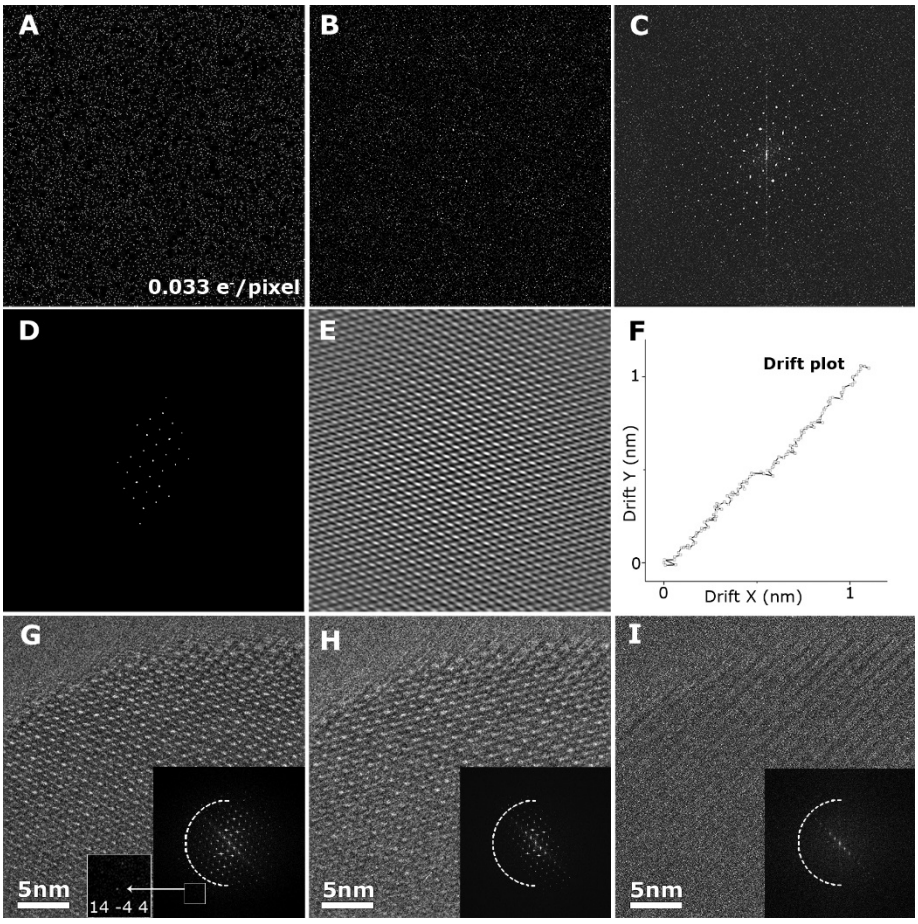

Fig. 1. Alignment of an image stack using the "amplitude filter". (**A**) A single frame and (**B**) the corresponding FT in an HRTEM image stack (120 frames in total) acquired for UiO-66 along the <011> zone axis. (**C**) The FT amplitude pattern formed by summing up the FT amplitude component of all frames. (**D**) Modified FT of a single frame by adopting filtered amplitudes from (C). (**E**) An amplitude-filtered single frame that is produced by inverse FT of (D). (**F**) The image-drift profile determined from filtered frames. (**G**) The drift-corrected image based on (F). (**H**) The drift-corrected image by cross-correlation, where the image stack is 1×1×10 binned to enhance the signal to noise. (**I**) Uncorrected image formed by directly summing up all the frames. In (G)-(I), the corresponding FTs are shown as insets; the half circles represent the frequency of 2 Å. In (G), a local area is zoomed in to highlight the observed 14 -4 4 reflection (d = 1.4 Å).

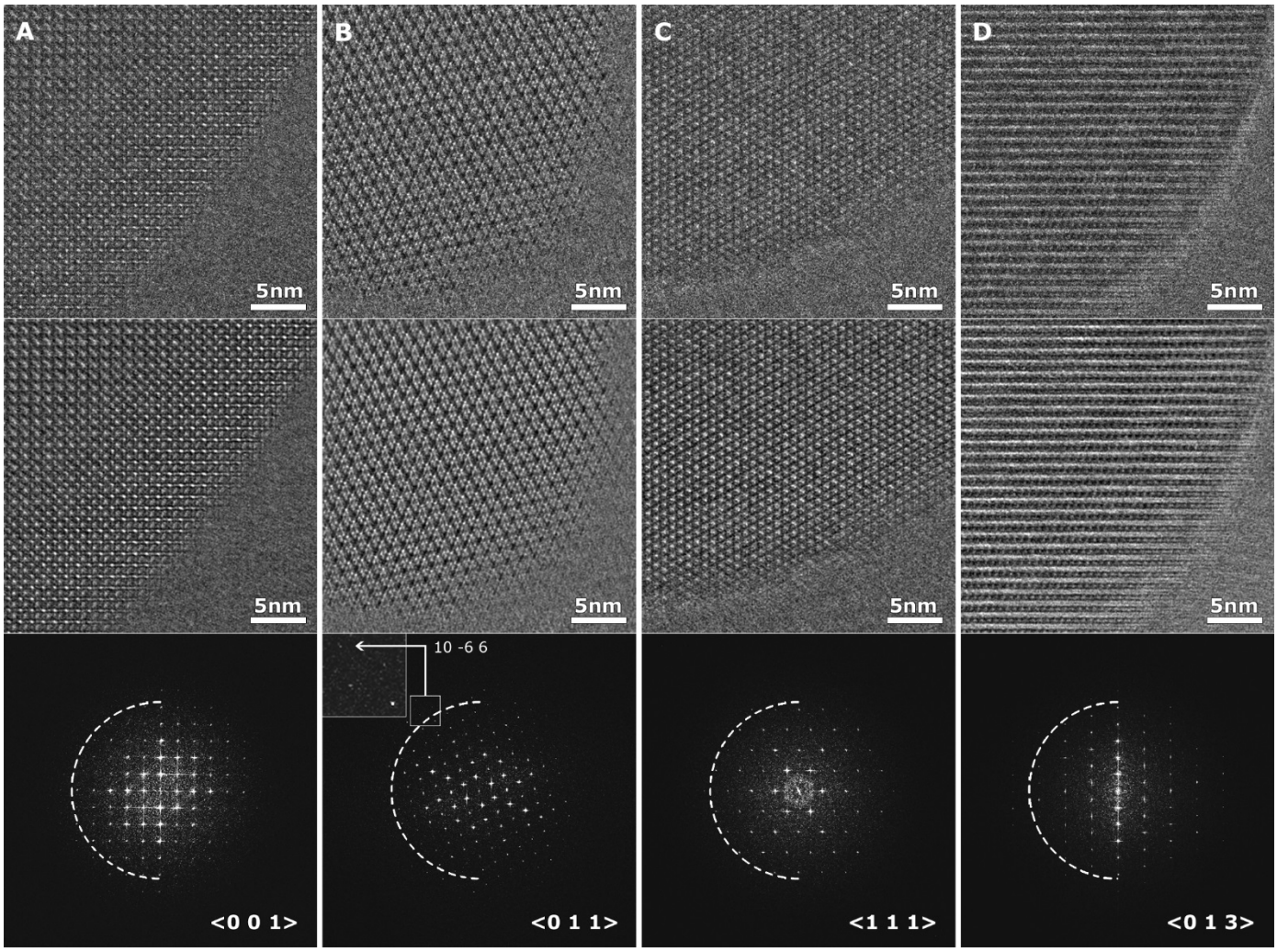

Fig. 2. HRTEM images of UiO-66 acquired from different zone axes: (**A**) <001>, (**B**) <011>, (**C**) <111> and (**D**) <013>. The top, middle, and bottom rows show raw images, denoised images and FTs of the raw images, respectively. The half circles in the FTs represent 2 Å. In all directions, there are reflections observed beyond the circle, indicating that the information transfer is less than 2 Å. As an example, the 10 -6 6 reflection (d = 1.6 Å) is highlighted in (B).

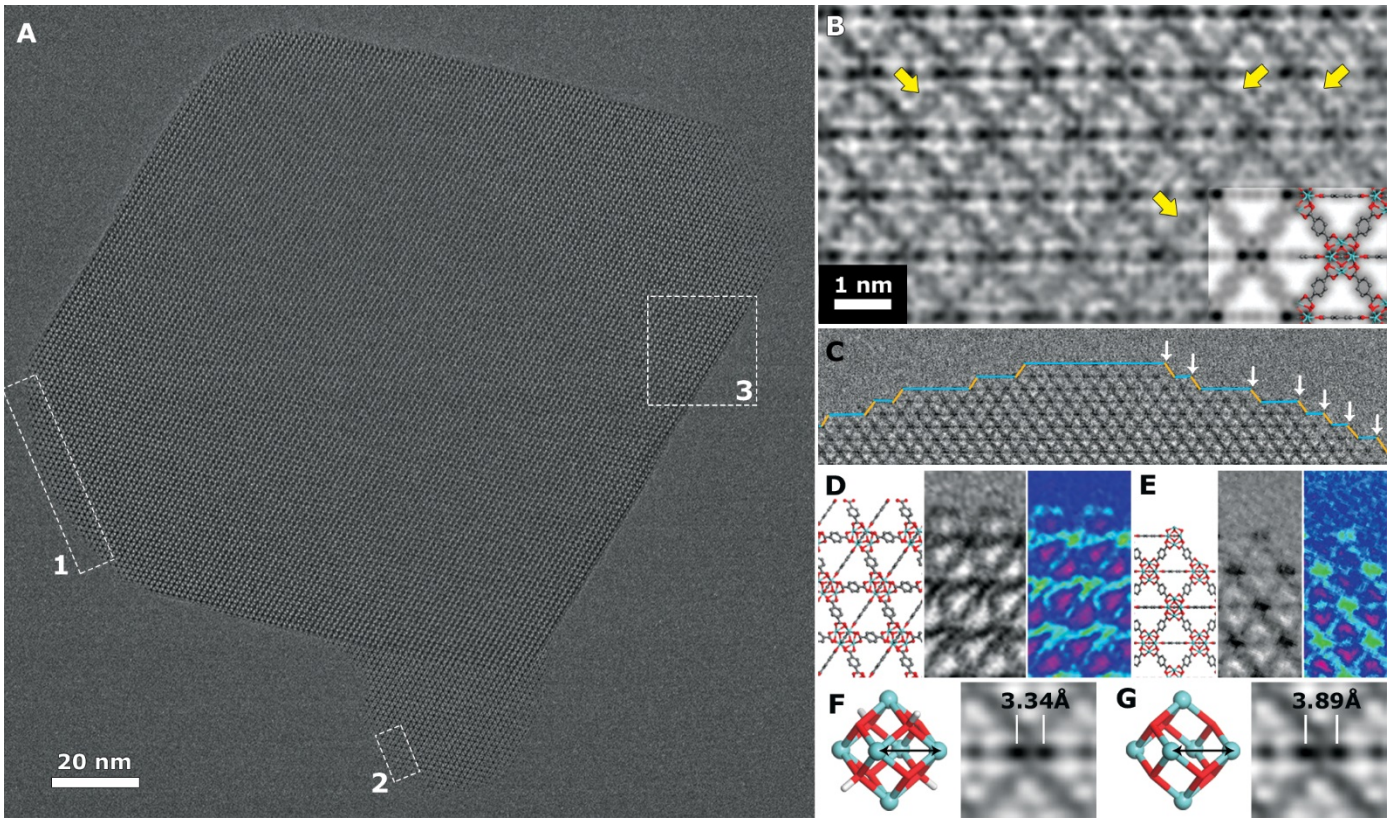

Fig. 3. HRTEM of thermally treated UiO-66. (**A**) Drift-corrected HRTEM image of a truncated octahedral UiO-66 crystal and an ultra-thin piece of crystal with the same <011> orientation. (**B**) CTF-corrected denoised image from the ultra-thin crystal (area 2 in (A)), showing triangular channels, individual Zr atomic columns, and the BDC linkers. The benzene rings in the BDC linkers are indicated by the arrows. Overlays are simulated projected potential maps and a projected structural model of UiO-66 for comparison. (**C**) A truncation surface (area 1 in (A)), showing crystal growth steps involving small {100} facets and {111} facets (labeled in blue and yellow, respectively). The white arrows indicate "kink" positions between {100} and {111} facets. (**D**) Ligand-terminated {111} surface: (left) structural model; (middle) processed HRTEM image by real-space averaging of 5 motifs from area 3 in (A); (right) the averaged image displayed in the rainbow colors to increase the visibility of the ligand contrast. (**E**) Ligand-free (metal-terminated) {100}/{111} kink: (left) structural model; (middle) processed HRTEM image by real-space averaging of 7 motifs from area 1 in (A); (right) the averaged image displayed in the rainbow colors. (**F** and **G**) The structure model (left) and the processed HRTEM image (right) of the (F) hydroxylated and (G) dehydroxylated Zr clusters featuring different Zr-Zr distances. The image processing details are shown in fig. S13.

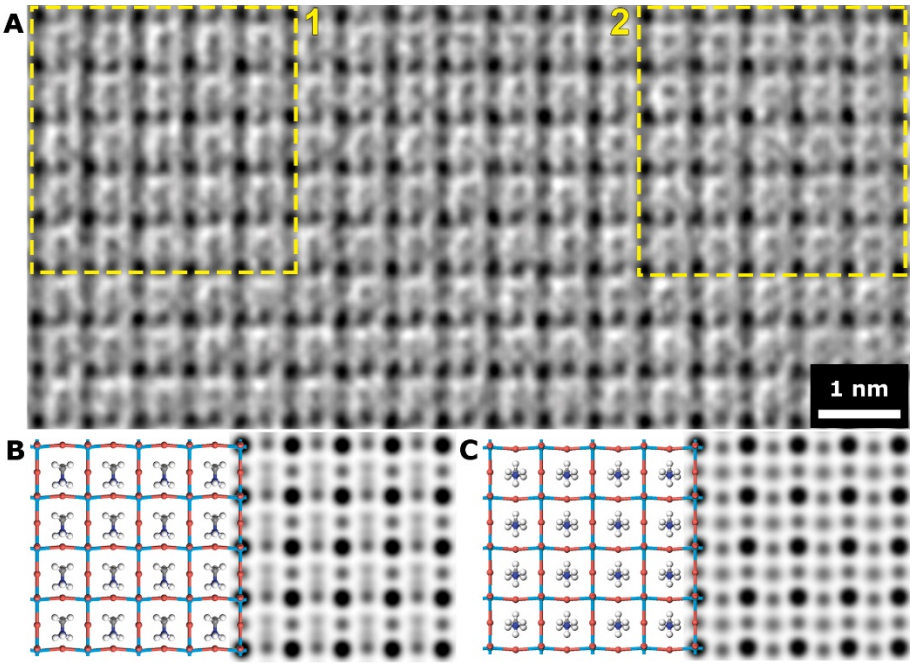

Fig. 4. HRTEM of organic-inorganic hybrid perovskite $CH_3NH_3PbBr_3$. (**A**) CTF-corrected denoised HRTEM image. The raw image is shown in fig. S16. The squares highlight two ordered domains with off-centered CH_3NH_3 cations that have differing orientations. (**B** and **C**) The structural model (left) (*30*) and the simulated projected potential map (right) of $CH_3NH_3PbBr_3$ with different CH_3NH_3 orientations, corresponding to region 1 and 2 in (A), respectively. In (B) and (C), the off-centered CH_3NH_3 cations exhibit normal and parallel configurations (relative to the projection direction), giving rise to in-plane and out-of-plane electric dipoles, respectively.

NEUROSCIENCE

Near-infrared deep brain stimulation via upconversion nanoparticle–mediated optogenetics

Shuo Chen,[1]* Adam Z. Weitemier,[1] Xiao Zeng,[2] Linmeng He,[1] Xiyu Wang,[1] Yanqiu Tao,[1] Arthur J. Y. Huang,[1] Yuki Hashimotodani,[3] Masanobu Kano,[3,4] Hirohide Iwasaki,[5] Laxmi Kumar Parajuli,[5] Shigeo Okabe,[5] Daniel B. Loong Teh,[6] Angelo H. All,[7] Iku Tsutsui-Kimura,[8] Kenji F. Tanaka,[8] Xiaogang Liu,[2,9]* Thomas J. McHugh[1,10]*

Optogenetics has revolutionized the experimental interrogation of neural circuits and holds promise for the treatment of neurological disorders. It is limited, however, because visible light cannot penetrate deep inside brain tissue. Upconversion nanoparticles (UCNPs) absorb tissue-penetrating near-infrared (NIR) light and emit wavelength-specific visible light. Here, we demonstrate that molecularly tailored UCNPs can serve as optogenetic actuators of transcranial NIR light to stimulate deep brain neurons. Transcranial NIR UCNP-mediated optogenetics evoked dopamine release from genetically tagged neurons in the ventral tegmental area, induced brain oscillations through activation of inhibitory neurons in the medial septum, silenced seizure by inhibition of hippocampal excitatory cells, and triggered memory recall. UCNP technology will enable less-invasive optical neuronal activity manipulation with the potential for remote therapy.

Technologies for minimally invasive and remote stimulation of specific neurons deep in the brain have long been desired for the experimental interrogation of neural systems and clinical treatment of neurological disorders. Deep brain stimulation is effective in the alleviation of specific neurological symptoms, but lacks cell-type specificity and requires permanently implanted electrodes (*1*). Potential alternatives for brain tissue–penetrating stimuli include electric (*2*, *3*), magnetic (*2*, *4*, *5*), acoustic (*6*, *7*), and optical signals (*8*). These approaches were largely developed independently of the optogenetic toolbox established over the past decade (*9*) and therefore remain limited to discrete applications. Stimulation of deep brain neurons via light-gated ion channels has hitherto required the insertion of invasive optical fibers because the activating blue-green wavelengths are strongly scattered and absorbed by endogenous chromophores (*10*). The action spectra of red-shifted variants of rhodopsins still fall short of the near-infrared (NIR) optical window (650 to 1350 nm), where light has its maximal depth of penetration (*10*–*15*). Two-photon optogenetic methods allow in vivo stimulation via an NIR laser, but the depth of this focal excitation is restricted to shallow brain areas by light scattering (*16*).

We developed transcranial NIR optogenetic stimulation of specifically labeled neurons in deep brain areas, where tissue-penetrating NIR light is locally converted to visible light at levels sufficient for activating channelrhodopsin-expressing neurons (Fig. 1A). This requires lanthanide-doped upconversion nanoparticles (UCNPs) capable of converting low-energy incident NIR photons into high-energy visible emission with an efficiency orders of magnitude greater than that of multiphoton processes (Fig. 1, B to D) (*17*, *18*). As a result, a continuous-wave (CW) NIR laser diode at low-energy irradiance was sufficient to drive intense upconversion emission by UCNPs. Owing to the ladderlike electronic energy structure of the lanthanide, the emission of UCNPs can be precisely tuned to a particular wavelength by control of energy transfer via selective lanthanide-ion doping (*17*, *18*). Incorporation of Tm^{3+} into Yb^{3+}-doped host lattices leads to blue emission that matches the maximum absorption of channelrhodopsin-2 (ChR2) for neuronal activation, whereas the Yb^{3+}-Er^{3+} couple emits green light compatible with activation of halorhodopsin (NpHR) or archaerhodopsin (Arch) for neuronal inhibition (Fig. 1, C and D, and figs. S1 and S2). UCNP-mediated optogenetics was first proposed in 2011 (*19*) and used for neural stimulation in culture (*20*–*22*) and in *Caenorhabditis elegans* (*23*) and zebrafish larvae (*24*), but its compelling potential for minimally invasive deep brain stimulation in a mammalian system has yet to be demonstrated.

We reasoned that UCNP-mediated optogenetics would be feasible for transcranial stimulation of deep brain neurons in rodents based on an evaluation of (i) the efficiency of NIR upconversion by the nanoparticles (Fig. 1D and fig. S3) and (ii) the transmittance of NIR light in brain tissue (figs. S4 and S5). For ChR2 activation, we synthesized blue-emitting $NaYF_4$ nanocrystals codoped with Yb^{3+}/Tm^{3+} (Fig. 1C). An optically inert shell layer of $NaYF_4$ was epitaxially grown onto the core to eliminate the surface quenching of upconversion luminescence by solvent molecules. The resulting core-shell UCNPs exhibited a characteristic upconversion emission spectrum peaking at 450 and 475 nm upon excitation at 980 nm (Fig. 1D). The conversion yield of NIR to blue light was ~2.5% (Fig. 1D and fig. S3). Applying the Kubelka-Munk theory of light propagation in diffuse scattering media (*25*), we estimated that a 2.0-W 980-nm laser delivered over the mouse skull through an optic fiber (200 μm in diameter) would result in 13.8-mW/mm^2 NIR at a depth of 4.5 mm in the brain. At this intensity, local upconversion by UCNPs would generate 0.34-mW/mm^2 blue-light emission (supplementary text), sufficient to activate ChR2 for cation influx (fig. S6).

We therefore performed in vivo fiber photometry (*26*) to examine NIR upconversion by UCNPs in the ventral tegmental area (VTA) of the mouse brain, a region located ~4.2 mm below the skull. UCNPs were injected into the VTA, and an optic fiber was positioned nearby to record blue emission (Fig. 1, F and G). Upon transcranial delivery of 980-nm CW laser pulses at a peak power of 2.0 W (25-ms pulses at 20 Hz over 1 s), an upconverted emission with a power density of ~0.063 mW/mm^2 was detected (Fig. 1H and fig. S5). This value was in line with our estimates based on the Kubelka-Munk theory when an empirical loss term was included (supplementary text). Further, considering that fiber photometry can only partially capture the emitted photons, this value represents a lower bound but nonetheless exceeds the level sufficient for ChR2 activation (fig. S6).

For the stimulation of a specific brain region, the power of transcranial NIR irradiation can be tuned according to its depth. NIR light is largely transparent, and its limited absorption results in minimal increases in local temperature because of constant circulation; thus, NIR pulses delivered across a wide range of laser energies to living tissue result in little photochemical or thermal damage (*27*, *28*). Nonetheless, at higher powers, it is important to consider a possible heating effect of NIR on the tissue. Our measurements of temperature change in the brain tissue showed that only mild temperature increases were induced under the conditions used in our study (supplementary text, figs. S7 and S8, and table S2). Immunohistochemical assessments further confirmed the absence of cytotoxicity (fig. S9). However, before a NIR strategy is adopted,

[1]Laboratory for Circuit and Behavioral Physiology, RIKEN Brain Science Institute, Wakoshi, Saitama 351-0198, Japan. [2]Department of Chemistry, National University of Singapore, Singapore 117543, Singapore. [3]Department of Neurophysiology, Graduate School of Medicine, The University of Tokyo, 7-3-1 Hongo, Bunkyo-ku, Tokyo 113-0033, Japan. [4]International Research Center for Neurointellegence (WPI), University of Tokyo Institute for Advanced Studies, The University of Tokyo, 7-3-1 Hongo, Bunkyo-ku, Tokyo 113-0033, Japan. [5]Department of Cellular Neurobiology, Graduate School of Medicine, The University of Tokyo, 7-3-1 Hongo, Bunkyo-ku, Tokyo 113-0033, Japan. [6]Singapore Institute for Neurotechnology (SINAPSE), National University of Singapore, Singapore 117456, Singapore. [7]Department of Biomedical Engineering, School of Medicine, Johns Hopkins University, Baltimore, MD 21205, USA. [8]Department of Neuropsychiatry, Keio University School of Medicine, Tokyo 160-8582, Japan. [9]Institute of Materials Research and Engineering, Agency for Science, Technology and Research, Singapore 117602, Singapore. [10]Department of Life Sciences, Graduate School of Arts and Sciences, The University of Tokyo, Tokyo, Japan.
*Corresponding author. Email: shuoshu@gmail.com (S.C.); chmlx@nus.edu.sg (X.L.); tjmchugh@brain.riken.jp (T.J.M.)

Fig. 1. UCNP-mediated NIR upconversion optogenetics for deep brain stimulation. (**A**) Schematic principle of UCNP-mediated NIR upconversion optogenetics. (**B**) Transmission electron microscopy (TEM) images of the silica-coated UCNPs. (Inset) High-resolution TEM image showing the core-shell structure. (**C**) Schematic design of a blue-emitting $NaYF_4$:Yb/Tm@SiO_2 particle. (**D**) Emission spectrum of the $NaYF_4$:Yb/Tm@SiO_2 particles under excitation at 980 nm. (Inset) Upconversion emission intensity of UCNPs [0.18 mg, 200 mg/ml in 900 nl of phosphate-buffered saline (PBS)] as a function of excitation intensity at 980 nm. (**E**) Size distribution of the UCNPs measured by dynamic light scattering. No aggregation is observed in water, PBS, or bovine serum albumin (BSA, 1 mg/ml in PBS) solution. (**F**) Scheme of in vivo fiber photometry for measuring UCNP-mediated NIR upconversion in deep brain tissue. The tip of an optic fiber transmitting NIR excitation light was positioned at various distances from the VTA where UCNPs were injected, and their emission was recorded by a second optic fiber. (**G**) Upconversion emission at the VTA upon 980-nm NIR irradiation (25-ms pulses at 20 Hz, 2.0-W peak power) from varying distances. (**H**) Measured (n = 4 mice) and simulated intensity of upconversion emission at the VTA as a function of the distance from the NIR irradiation source. Data are presented as mean ± SEM.

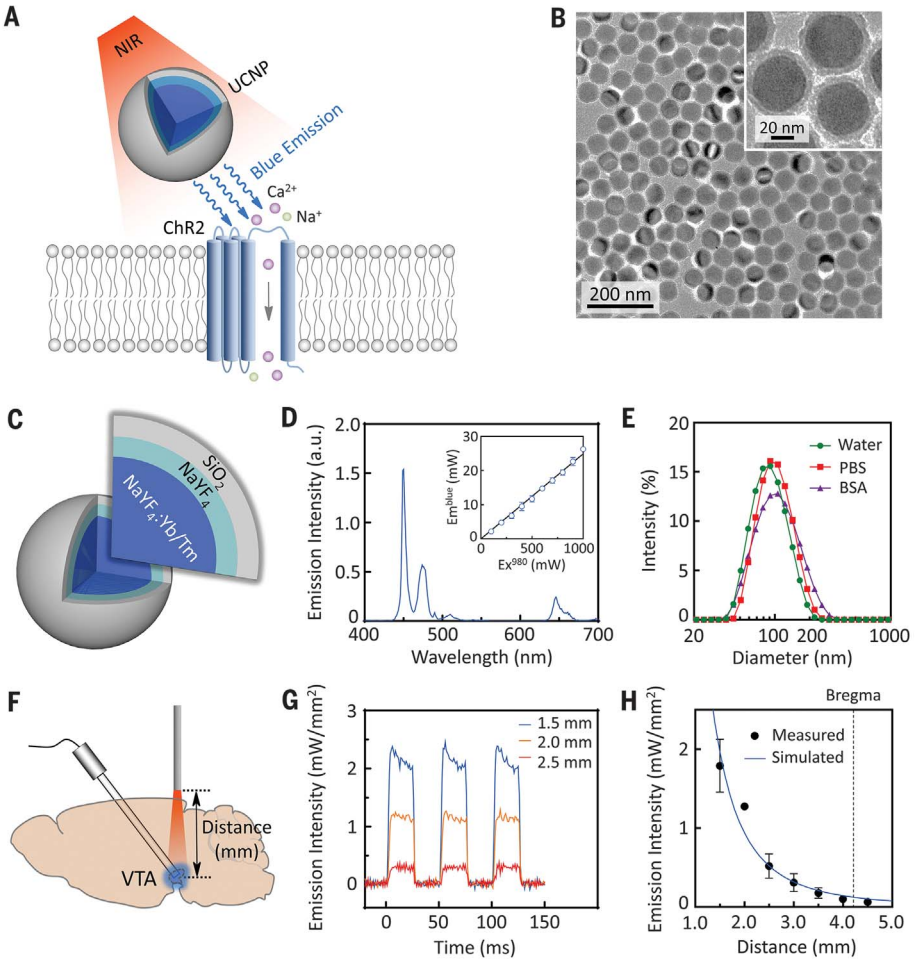

Fig. 2. NIR excitation of VTA DA neurons in vitro. (**A**) Experimental scheme. AAV-DIO-ChR2-EYFP was injected into the VTA of TH-Cre transgenic mice for Cre-dependent expression of ChR2 in DA neurons. Four weeks later, 900 nl of 200 mg/ml blue-emitting $NaYF_4$:Yb/Tm@SiO_2 UCNPs was injected into the VTA. Horizontal acute slices containing the VTA were prepared, and in vitro whole-cell recordings were performed. (**B**) Electron micrographs of UCNPs distributed in the VTA tissue. Black arrows indicate clusters of UCNPs. The upper image shows the distribution of the majority of UCNPs in extracellular space, and the lower image shows the uptake of UCNPs by an axon. (**C**) Voltage-clamp traces of neurons from VTA slice preparations in response to 100-ms NIR stimulation at various intensities. NIR light triggered photocurrents only in ChR2-transfected neurons in the presence of UCNPs. The traces for ChR2(−) and UCNP(−) controls in black were recorded under 8.22-W/mm^2 NIR irradiation. (**D**) Increase in photocurrent amplitude with elevated intensity of the NIR stimulation (n = 6 cells). (**E**) Current-clamp traces of a ChR2-expressing DA neuron in response to trains of 10 NIR pulses at different frequencies (20-ms pulses at 10 and 20 Hz, 10-ms pulses at 50 Hz, 8.22-W/mm^2 peak power) in the presence of UCNPs. Brief red lines indicate NIR pulses. (**F**) Spike probability as a function of the frequency of NIR stimulation (n = 6 cells). Data are presented as mean ± SEM.

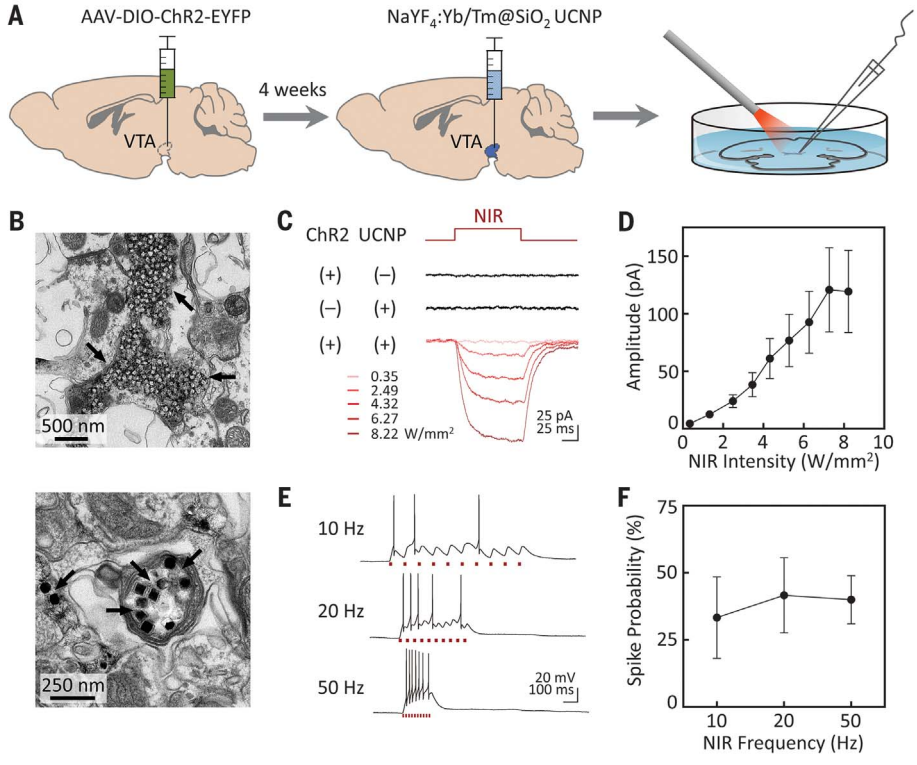

the stimulation parameters should always be optimized for a balance between safety and efficacy.

To optimize the biocompatibility and long-term utility of UCNPs, we decorated the core-shell $NaYF_4$:Yb/Tm nanocrystals with silica ($NaYF_4$:Yb/Tm@SiO2) or poly(acrylic acid) (PAA) ($NaYF_4$:Yb/Tm@PAA). Both coating strategies resulted in monodispersed UCNPs of ~90-nm diameter (Fig. 1, B and E, and figs. S1 and S2) with similar luminescence profiles (Fig. 1D and fig. S1). One month after injection, UCNPs could still be observed at the target site, regardless of the type of coating (figs. S10 and S11), suggesting their long-term stability and low dispersion in tissue. We selected silica-coated UCNPs for in vivo upconversion optogenetics because they showed minimum cytotoxicity compared to the PAA-grafted ones, as indicated by less glial activation and lower macrophage accumulation in the VTA over prolonged exposure (figs. S10 and S11). This is likely a result of the silica coating that chemically stabilizes the nanoparticles and prevents direct contact of their lanthanide-doped core to cells within the tissue (*29*).

We chose the VTA for an initial examination of NIR stimulation because it is a deep brain region with a well-characterized anatomy and function. An adeno-associated virus (AAV) encoding ChR2-EYFP (enhanced yellow fluorescent protein) in a double-floxed inverted open reading frame (DIO) was injected into the VTA of tyrosine hydroxylase (TH)–driven Cre recombinase (TH-Cre) transgenic mice, resulting in Cre-dependent expression of ChR2 in dopamine (DA) neurons (Fig. 2A). Four weeks later, 900 nl of 200 mg/ml blue-emitting $NaYF_4$:Yb/Tm@SiO_2 UCNPs was injected into the VTA. We first assayed UCNP-mediated optogenetic activation of DA neurons in acute slices. Electron microscopy (Fig. 2B and fig. S12) showed that the UCNPs were localized in the injection area without extensive diffusion. The majority were distributed in extracellular spaces in the vicinity of cell membrane and synaptic clefts. A small fraction of UCNPs were taken up by neurons, mainly localized to axons, as well as by microglia. The confinement of UCNPs in the target brain region agrees with our light microscopy results showing that UCNPs exhibited minimal dispersion 1 month after injection (figs. S10 and S11). The 980-nm NIR pulses triggered membrane depolarization sufficient to generate photocurrents and evoke spikes in VTA DA neurons. The photocurrent amplitudes of ChR2 increased in response to elevated intensity of the incident NIR light under voltage clamp (Fig. 2, C and D). In the absence of UCNPs, no inward photocurrent was detected upon NIR irradiation (Fig. 2C). The activation kinetics of ChR2 by NIR upconversion was slower than that of blue light-activated ChR2 (fig. S6) (*30*) but comparable to that of recently reported red-shifted rhodopsins (*10*). NIR irradiation could also evoke action potentials of DA neurons, as shown in current-clamp traces. Trains of NIR illumination at 10 to 50 Hz elicited multiple spikes (Fig. 2E). The spike probability showed no significant dependence on the frequency of the NIR light (Fig. 2F).

We next tested the in vivo utility of UCNP-mediated NIR upconversion optogenetics. We sensitized VTA DA neurons of TH-Cre mice to transcranial NIR stimulation through viral delivery of ChR2 followed by bilateral UCNP injection (Fig. 3A). Anesthetized mice were exposed to transcranial pulsed NIR irradiation (15-ms pulses at 20 Hz, 3 s every 3 min for 30 min, 3.0-W peak power, 15-mW average power) delivered from an optical fiber (200 μm in diameter) placed 2 mm above the skull (1.4-W/mm^2 NIR on the skull surface). NIR-activated DA neurons

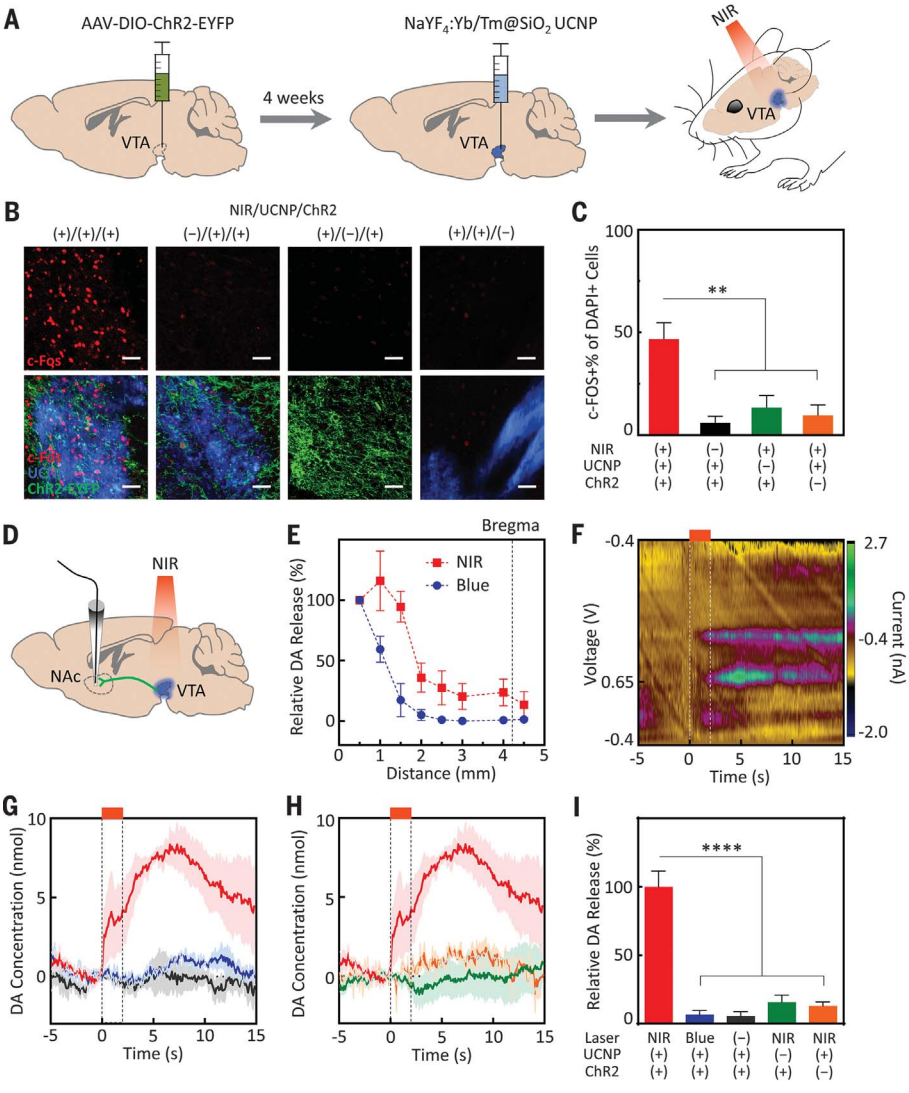

Fig. 3. Transcranial NIR stimulation of VTA DA neurons in vivo. (**A**) In vivo experimental scheme for transcranial NIR stimulation of the VTA in anesthetized mice. (**B**) Confocal images of the VTA after transcranial NIR stimulation under different conditions. Extensive NIR-driven c-Fos (red) expression was observed only in the presence of both UCNPs (blue) and ChR2 expression (labeled with EYFP, green). Scale bars: 100 μm. (**C**) Percentage of c-Fos–positive neurons within cell population indicated by DAPI (4′,6-diamidino-2-phenylindole), corresponding to the four conditions presented in (B) (n = 3 mice each, $F_{3,8}$ = 10.40, P < 0.01). (**D**) Scheme of in vivo FSCV to measure DA transients in ventral striatum during NIR stimulation of the VTA. (**E**) Relative DA signals in ventral striatum under NIR and blue-light stimulation of the VTA as a function of the distance from the light source to the VTA target. (**F**) A trace of background-subtracted current measured by FSCV in the ventral striatum of a nomifensine-pretreated mouse in response to transcranial NIR stimulation of the VTA (15-ms pulses at 20 Hz, 700-mW peak power). Vertical dashed lines marked by a horizontal orange line in between indicate the start and end of 2-s transcranial NIR stimulation. (**G** and **H**) Transient DA concentrations in ventral striatum in response to transcranial VTA stimulation under different conditions. Each color corresponds to a condition shown in (I). Significant DA release temporally locked to NIR stimulation was detected only in the presence of both UCNPs and ChR2 expression. (**I**) Cumulative DA release within 15 s after the start of transcranial stimulation under the five conditions presented in (G) and (H) ($F_{4,10}$ = 32.93, P < 0.0001). Data are presented as mean ± SEM.

were mapped by imaging the expression of c-Fos (Fig. 3, B and C, and fig. S13). Neuronal excitation was only triggered by NIR light in ChR2-transfected mice in the presence of UCNPs, as indicated by the significantly higher proportion of c-Fos–positive cells in areas where UCNP injection and ChR2 expression overlapped. We injected UCNPs to just one side of the VTA and observed NIR-induced c-Fos expression only in the injected hemisphere (fig. S14). We also observed up-regulation of c-Fos expression in the ventral striatum (fig. S15), which receives inputs from VTA DA neurons (*31*), indicating NIR-evoked excitation of postsynaptic structures of the targeted neurons. Control mice with UCNP injection, ChR2 expression, or NIR stimulation alone showed no significant c-Fos expression in either VTA or ventral striatum.

We evaluated the real-time efficacy of NIR-evoked excitation of VTA DA neurons with fast-scan cyclic voltammetry (FSCV) (Fig. 3D). Striatal DA transients reflect the phasic spike activity of VTA DA neurons (*31*) and have therapeutic implications for the treatment of major depression. In nomifensine-pretreated mice with both UCNP injection and ChR2 expression in VTA, we detected DA release that was temporally locked to transcranial NIR stimulation (15-ms pulses at 20 Hz, 700-mW peak power) (Fig. 3F). After a 2-s NIR stimulation, striatal DA release lasted for more than 15 s and peaked at ~5 s after light onset (Fig. 3, F and G). We detected no significant DA release in control mice with omission of NIR stimulation, UCNP injection, or ChR2 expression (Fig. 3, G to I). We compared the efficacy of NIR with blue light in evoking DA release by VTA DA neurons (Fig. 3E). The tip of an optic fiber transmitting NIR or blue light was positioned at various distances from the VTA target for optogenetic activation of DA neurons. When illuminating from a distance of 0.5 mm, NIR and blue light triggered similar amounts of DA release in ventral striatum (Fig. 3E and fig. S16). However, transcranial application of blue light did not result in striatal DA release (Fig. 3, E and I). Furthermore, NIR stimulation showed significantly slower attenuation in DA release with the increase of the distance from fiber tip to VTA (Fig. 3E).

We next expanded the application of in vivo upconversion optogenetics to multiple modes of neural control, including inhibition, as well as to different brain regions. First, we developed green-emitting UCNPs to match the maximum absorption of rhodopsins that hyperpolarize neurons, such as NpHR and Arch, to achieve non-invasive neuronal inhibition. The emission of UCNPs was tuned to ~540 nm by codoping Er^{3+} and Yb^{3+} into the $NaYF_4$ host lattice (Fig. 4A and fig. S1). We then assayed the ability of $NaYF_4$:Yb/Er@SiO_2 UCNPs to inhibit hippocampal activity during chemically induced hyperexcitability. Arch was virally expressed in excitatory neurons in the CA1 and dentate gyrus (DG) regions of the calcium-calmodulin–dependent kinase II (CamKII)–Cre mice, and green-emitting UCNPs were injected into the same region (Fig. 4B). Mice were

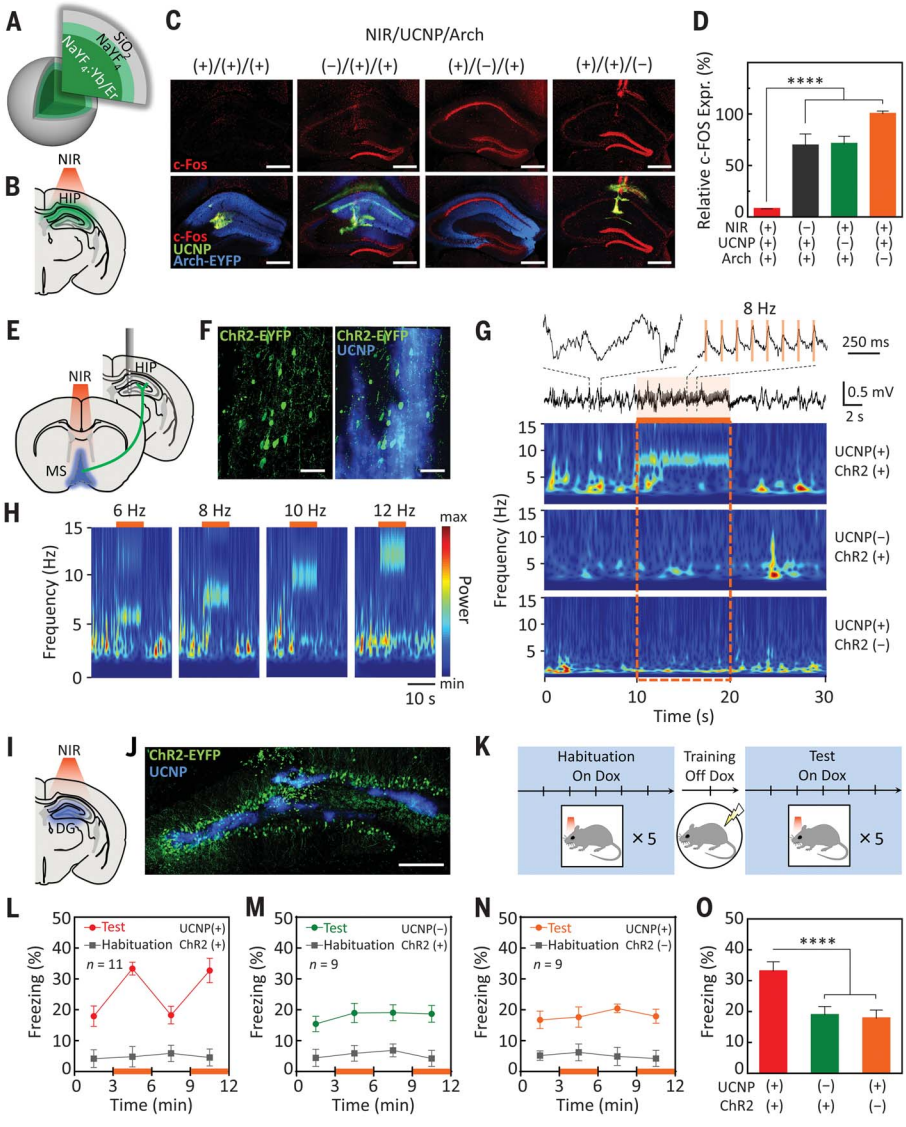

Fig. 4. Expanding in vivo upconversion optogenetics to multiple neural systems. (**A**) Schematic of a green-emitting $NaYF_4$:Yb/Er@SiO_2 particle. (**B**) Illustration of transcranial NIR inhibition of hippocampal (HIP) activity during chemically induced seizure. (**C**) Confocal images of the hippocampus following transcranial NIR stimulation under different conditions. Significant decrease in c-Fos (red) expression was observed only in the presence of both UCNPs (green) and Arch expression (labeled with EYFP, blue). Scale bars: 400 μm. (**D**) c-Fos expression under the four conditions presented in (C) (n = 3 mice each, $F_{3,8}$ = 94.02, P < 0.0001). (**E**) Illustration of transcranial NIR stimulation of medial septum (MS) for generation of theta oscillations. (**F**) Confocal images showing the overlap between ChR2-expressing PV interneurons (labeled by EYFP, green) and UCNPs (blue) in the MS of a PV-Cre mouse. Scale bars: 50 μm. (**G**) Hippocampal LFP in response to 8-Hz transcranial NIR stimulation (15-ms pulses, 10 s, 3.0-W peak power, 360-mW average power) of MS under different conditions. Top: Raw LFP trace from mouse with both UCNP and ChR2 injection. Bottom: Z-scored power in the theta range averaged across 30-s trials in all three conditions. (**H**) Transcranial NIR entrainment of hippocampal theta in a frequency-dependent manner. (**I**) Illustration of transcranial NIR stimulation of hippocampal engram for memory recall. (**J**) Confocal image showing the overlap between UCNPs (blue) and ChR2 expression (labeled with EYFP, green) in the DG of a mouse that underwent habituation, fear conditioning, and test sessions presented in (K). Scale bar: 200 μm. (**K**) Mice were on Dox food and habituated with NIR stimulation (15-ms pulses at 20 Hz, 250-mW peak power) in context A for 5 days, then off Dox food for 2 days and fear conditioned in context B. Mice were put back on Dox food and tested for 5 days in context A with transcranial NIR stimulation. (**L** to **N**) After fear conditioning, only c-fos-tTA mice with both ChR2 expression and UCNP injection showed increased freezing during 3-min NIR-on periods. Orange lines indicate the NIR-on epochs. (**O**) Summary of freezing levels of the three groups during test NIR-on epochs ($F_{2,26}$ = 105.9, P < 0.0001). Data are presented as mean ± SEM.

anesthetized and received the excitotoxin kainic acid (KA) at a dose used to induce seizure. We then applied transcranial low-intensity chronic pulsed NIR irradiation (3-ms pulses at 10 Hz, 120 min, 750-mW peak power, 22.5-mW average power) to inhibit neural activity in the hippocampus. Compared to all controls, mice with Arch expression, UCNP injection, and NIR stimulation showed a significant decrease in KA-induced c-Fos expression in the granule cells of the DG (Fig. 4, C and D), indicating effective silencing of hippocampal neurons by UCNP-mediated Arch activation. When NIR irradiation or Arch delivery was only unilaterally applied, distinct levels of c-Fos expression were observed between the two hemispheres (fig. S17).

Next, we examined if UCNP-mediated optogenetics could be used for noninvasive synchronization of neural activity. We targeted our NIR stimulation to inhibitory neurons in the medial septum, a key node in the network generating the theta oscillation (*32*, *33*). In vivo recordings of hippocampal local field potential (LFP) were performed during transcranial NIR irradiation of anesthetized parvalbumin (PV)–Cre mice with ChR2 expression and UCNP injection targeted to the medial septum (Fig. 4, E and F). Pulsed NIR stimulation in the theta frequency range (6 to 12 Hz) entrained the hippocampal theta oscillation in a frequency-dependent manner (Fig. 4, G and H). Control animals without ChR2 expression or UCNP injection showed no oscillation entrainment upon NIR irradiation (Fig. 4G).

Finally, we used the UCNP-mediated optogenetics to alter behavior of an awake animal by targeting NIR excitation to granule cells in the hippocampus involved in memory recall. Recent studies have demonstrated the neuronal activity–dependent tagging of memory-encoding hippocampal neurons by ChR2 and subsequent optogenetic reactivation of these engrams (*34*). We injected blue-emitting UCNPs into the DG of c-fos-tTA (tetracycline transcriptional activator) transgenic mice and labeled active c-Fos–expressing DG granule cells with ChR2 during the encoding of fear memory in the absence of doxycycline (Dox) (Fig. 4, I to K, and fig. S18). We then applied transcranial NIR stimulation (15-ms pulses at 20 Hz, 250-mW peak power) to reactivate labeled granule cells. NIR irradiation increased freezing behavior of the mice during laser illumination in a safe context (Fig. 4L). Animals with no UCNP injection or ChR2 expression showed no significant change in freezing when NIR irradiation was applied (Fig. 4, M to O). Moreover, the behavioral effect of NIR stimulation in this experiment was observed 2 weeks after the injection of UCNPs, indicating their long-term in vivo utility. This timing is consistent with our findings that no extensive diffusion or degradation of UCNPs was observed 1 month after injection (figs. S10 and S11).

These findings demonstrate that UCNP-mediated optogenetics is a flexible and robust minimally invasive nanotechnology-assisted approach for optical control of in vitro and in vivo neuronal activity. We show spectral tuning of UCNPs for compatibility with the current toolbox of light-activated channels (*9*) that is sufficient for functional activation and inhibition across a variety of deep brain structures. Future characterization of the interaction of UCNPs with neural tissue will allow for better biocompatibility and long-term utility. In parallel, systematic optimization of the dose of UCNP injection and the parameters of NIR stimulation will provide improved accuracy and safety. Such data might also present an upper limit to the adaptability and efficiency of NIR stimulation. Furthermore, refinements of the nanoparticles to establish precise cell-type or intracellular targeting (*17*, *18*), as well as improved delivery methods that would further reduce invasiveness (*35*), will advance the utility of the approach. These methods, combined with the enhanced ability to express light-sensitive channels in the brain, may allow UCNP-mediated neuronal control to complement or extend current approaches to deep brain stimulation and neurological disorder therapies.

REFERENCES AND NOTES

1. A. M. Lozano, N. Lipsman, *Neuron* **77**, 406–424 (2013).
2. E. Dayan, N. Censor, E. R. Buch, M. Sandrini, L. G. Cohen, *Nat. Neurosci.* **16**, 838–844 (2013).
3. N. Grossman *et al.*, *Cell* **169**, 1029–1041.e16 (2017).
4. R. Chen, G. Romero, M. G. Christiansen, A. Mohr, P. Anikeeva, *Science* **347**, 1477–1480 (2015).
5. S. A. Stanley *et al.*, *Nature* **531**, 647–650 (2016).
6. W. Legon *et al.*, *Nat. Neurosci.* **17**, 322–329 (2014).
7. R. Airan, *Science* **357**, 465 (2017).
8. M. R. Hamblin, *BBA Clin.* **6**, 113–124 (2016).
9. L. Fenno, O. Yizhar, K. Deisseroth, *Annu. Rev. Neurosci.* **34**, 389–412 (2011).
10. J. Y. Lin, P. M. Knutsen, A. Muller, D. Kleinfeld, R. Y. Tsien, *Nat. Neurosci.* **16**, 1499–1508 (2013).
11. F. Zhang *et al.*, *Nat. Neurosci.* **11**, 631–633 (2008).
12. O. Yizhar *et al.*, *Nature* **477**, 171–178 (2011).
13. A. S. Chuong *et al.*, *Nat. Neurosci.* **17**, 1123–1129 (2014).
14. N. C. Klapoetke *et al.*, *Nat. Methods* **11**, 338–346 (2014).
15. P. Rajasethupathy *et al.*, *Nature* **526**, 653–659 (2015).
16. R. Prakash *et al.*, *Nat. Methods* **9**, 1171–1179 (2012).
17. G. Chen, H. Qiu, P. N. Prasad, X. Chen, *Chem. Rev.* **114**, 5161–5214 (2014).
18. B.Zhou, B. Shi, D. Jin, X. Liu, *Nat. Nanotechnol.* **10**, 924–936 (2015).
19. K. A. Deisseroth, P. Anikeeva, Upconversion of light for use in optogenetic methods. United States Patent PCT/US2011/059287 (2011).
20. S. Hososhima *et al.*, *Sci. Rep.* **5**, 16533 (2015).
21. S. Shah *et al.*, *Nanoscale* **7**, 16571–16577 (2015).
22. X. Wu *et al.*, *ACS Nano* **10**, 1060–1066 (2016).
23. A. Bansal, H. Liu, M. K. Jayakumar, S. Andersson-Engels, Y. Zhang, *Small* **12**, 1732–1743 (2016).
24. X. Ai *et al.*, *Angew. Chem. Int. Ed. Engl.* **56**, 3031–3035 (2017).
25. T. Vo-Dinh, Ed., *Biomedical Photonics Handbook* (CRC Press, Boca Raton, FL, 2003).
26. L. A. Gunaydin *et al.*, *Cell* **157**, 1535–1551 (2014).
27. A. Bozkurt, B. Onaral, *Biomed. Eng. Online* **3**, 9 (2004).
28. T. A. Henderson, L. D. Morries, *Neuropsychiatr. Dis. Treat.* **11**, 2191–2208 (2015).
29. J. N. Liu, W. B. Bu, J. L. Shi, *Acc. Chem. Res.* **48**, 1797–1805 (2015).
30. E. S. Boyden, F. Zhang, E. Bamberg, G. Nagel, K. Deisseroth, *Nat. Neurosci.* **8**, 1263–1268 (2005).
31. M. J. Wanat, I. Willuhn, J. J. Clark, P. E. Phillips, *Curr. Drug Abuse Rev.* **2**, 195–213 (2009).
32. R. Boyce, S. D. Glasgow, S. Williams, A. Adamantidis, *Science* **352**, 812–816 (2016).
33. L. L. Colgin, *Annu. Rev. Neurosci.* **36**, 295–312 (2013).
34. X. Liu *et al.*, *Nature* **484**, 381–385 (2012).
35. D. Ni *et al.*, *ACS Nano* **8**, 1231–1242 (2014).

ACKNOWLEDGMENTS

We thank S. Wada and T. Tsukihana (RIKEN Center for Advanced Photonics) for technical advice and assistance with laser optics; H. Hirase [RIKEN Brain Science Institute (BSI)] for helpful discussion on in vivo toxicity assay and gifts of antibodies against GFAP (glial fibrillary acidic protein) and Iba1; S. Itohara (RIKEN BSI) for the gift of antibody against Caspase-3; T. Launey (RIKEN BSI) for helpful discussion on electron microscopy; and C. Yokoyama (RIKEN BSI) and F. Xu (University of Science and Technology of China) for comments on the manuscript. This work was supported by JSPS (Japan Society for the Promotion of Science) Postdoctoral Fellowship (16F16386) (S.C.); RIKEN Special Postdoctoral Researchers Program (S.C.); RIKEN BSI (T.J.M.); Grant-in-Aid for Scientific Research on Innovative Areas from MEXT (the Ministry of Education, Culture, Sports, Science and Technology of Japan) (17H05591) (T.J.M.); Grant-in-Aid for Young Scientists B (16K18373) (S.C.); the Singapore Ministry of Education (grant R143000627112, R143000642112) (X.L.); the National Research Foundation of Singapore under its Competitive Research Programme (CRP Award no. NRF-CRP15-2015-03) (X.L.); Grants-in-Aid for Scientific Research (25000015) (M.K.); Grants-in-Aid for Scientific Research (17H01387 and 25117006) (S.O.); and Core Research for Evolutional Science and Technology from the Japanese Science and Technology Agency (JPMJCR14W2) (S.O.). All data necessary to assess the conclusions of this research are available in the text and supplementary materials. Data related to the synthesis and characterization of UCNPs are available via the X.L. laboratory website (http://liuxg.science.nus.edu.sg). Data related to the application of UCNP-mediated optogenetics in the mouse brain are archived on the servers of Laboratory for Circuit and Behavioral Physiology at the RIKEN Brain Science Institute and accessible at http://cbp.brain.riken.jp/chen_et_al. All materials are available upon request.

SUPPLEMENTARY MATERIALS

www.sciencemag.org/content/359/6376/679/suppl/DC1
Materials and Methods
Supplementary Text
Figs. S1 to S18
Tables S1 and S2
References (*36*–*46*)

3 October 2017; accepted 7 December 2017
10.1126/science.aaq1144

Cite as: L. Cantuti-Castelvetri *et al.*, *Science* 10.1126/science.aan4183 (2018).

Defective cholesterol clearance limits remyelination in the aged central nervous system

Ludovico Cantuti-Castelvetri,[1,2,3,4]* Dirk Fitzner,[1,5]* Mar Bosch-Queralt,[1,2,3,4] Marie-Theres Weil,[1,6] Minhui Su,[1,2,3,4] Paromita Sen,[1] Torben Ruhwedel,[7] Miso Mitkovski,[8] George Trendelenburg,[5] Dieter Lütjohann,[9] Wiebke Möbius,[6,7] Mikael Simons[1,2,3,4]†

[1]Max Planck Institute of Experimental Medicine, 37075 Göttingen, Germany. [2]Munich Cluster for Systems Neurology (SyNergy), 81377 Munich, Germany. [3]Institute of Neuronal Cell Biology, Technical University Munich, 80805 Munich, Germany. [4]German Center for Neurodegenerative Disease (DZNE), 81377 Munich, Germany. [5]Department of Neurology, University of Göttingen Medical Center, 37075 Göttingen, Germany. [6]Center Nanoscale Microscopy and Molecular Physiology of the Brain (CNMPB), 37075 Göttingen, Germany. [7]Department of Neurogenetics, Max Planck Institute of Experimental Medicine, 37075 Göttingen, Germany. [8]Light Microscopy Facility, Max Planck Institute of Experimental Medicine, 37075 Göttingen Germany. [9]Institute for Clinical Chemistry and Clinical Pharmacology, University of Bonn, 53127 Bonn, Germany.

*These authors contributed equally to this work.

†Corresponding author. Email: msimons@gwdg.de

Age-associated decline in regeneration capacity limits the restoration of nervous system functionality after injury. In a model for demyelination, we found that old mice fail to resolve the inflammatory response initiated after myelin damage. Aged phagocytes accumulated excessive amounts of myelin debris, which triggered cholesterol crystal formation, phagolysosomal membrane rupture, and stimulated inflammasomes. Myelin debris clearance required cholesterol transporters including apolipoprotein E. Remarkably, stimulation of reverse cholesterol transport was sufficient to restore the capacity of old mice to remyelinate lesioned tissue. Thus, cholesterol-rich myelin debris can overwhelm the efflux capacity of phagocytes, resulting in a phase transition of cholesterol into crystals thereby inducing a maladaptive immune response that impedes tissue regeneration.

Remyelination restores rapid transmission of nerve impulses and axonal function in the CNS of patients with demyelinating diseases such as multiple sclerosis (MS). Although remyelination can occur in MS, age-associated decline in myelin repair contributes to chronic progressive disease and disability (*1*). Thus, understanding the cause of and preventing this decline is a key goal in regenerative medicine (*2*–*4*). So far, epigenetic changes within aging oligodendrocyte progenitor cells and declines in phagocytic capacity of aged blood-derived monocytes have been identified as possible mechanisms (*5*, *6*). We implemented a toxin-induced model, in which a single injection of lysolecithin (lysophosphatidylcholine) induces a focal demyelinating lesion in the white matter of the brain or spinal cord of mice. In lesioned animals, demyelination is complete within 4 days, followed by a repair process that is maximal between 14 to 21 days post injection (dpi) and requires rapid clearance of damaged myelin for regeneration to occur (*7*). We induced focal demyelinating lesions in the corpus callosum of young (3 months) and old (12 months) mice by lysolecithin injections. Lesions were of similar size at 4 dpi, but not at 14 dpi confirming the poor regenerative capacity of old mice (Fig. 1, A to C, and fig. S1, A to E). Sustained immune infiltration, as determined by IBA1-positive and MAC2-positive cells, was detected in old mice at 14dpi (Fig. 1, A and E, and fig. S1G). Myelin debris accumulation within lysosomes of phagocytes (Fig. 1, D and F) and numerous foam cells harboring lipid droplets and needle-shaped cholesterol crystals - a typical hallmark of cholesterol overloading - were found in old mice (Fig. 1, G and H, and fig. S2G). Moreover, by a combination of laser reflection and fluorescence confocal microscopy (reflection microscopy) we confirmed the increase of crystal deposition in spinal cord lesions of old mice (Fig. 1, I and J). Crystals were similarly observed in two other models of myelin injury (fig. S2).

Toxic overload of cholesterol drives the formation of foamy macrophages and maladaptive immune responses in atherosclerosis. We hypothesized that the accumulation of cholesterol, the major component of myelin, may overwhelm the cholesterol transport capacity of phagocytes, thereby forming a bottleneck for successful repair in the aged CNS. Because cholesterol cannot be broken down it needs to be transferred from the phagocytes back to the extracellular space using the transporters ATP-Binding Cassette A1 and G1 (ABCA1 and ABCG1) in the plasma membrane where it binds high-density lipoprotein particles (e.g., APOE) (*8*). Real-time quantitative reverse transcription PCR revealed that the expression of *ApoE*, *Abca1* and *Abcg1*, was reduced in 4 dpi lesions of old compared to young mice (Fig. 1, K to M, and fig. S3). Oxysterols (hydroxylated cholesterol metabolites) such

as 24S- and 27-hydroxycholesterol are endogenous ligands for liver X receptor (LXR), thereby controlling the expression of genes involved in cholesterol efflux in cholesterol-loaded cells (*9*). Relative amounts of 24S-hydroxycholesterol did not differ in lesions of young and old animals, but 27-hydroxycholesterol levels were reduced in lesions of old mice (fig. S3). One possible explanation for lesion restitution failure in old mice is the inability to clear excessive myelin-derived cholesterol from phagocytes. Thus, we examined whether the LXR agonist, GW3965 (*10*) improve lesion recovery in old mice by inducing the expression of genes involved in lipid efflux, such as *Abca1*, *Abcg1* and *ApoE* (fig. S3). GW3965 led to markedly improved lesion regeneration in old mice with a reduction in the number of IBA1-positive and MAC2-positive phagocytes (Fig. 1, A to C). In addition, the number of phagocytes containing myelin debris, the number of foam cells and the amount of cholesterol crystals was reduced by treatment with GW3965 (Fig. 1, A to J).

Because accumulation of cholesterol in phagocytes may pose a barrier for successful tissue regeneration, we analyzed the regenerative capacity of mouse mutants lacking central factors of the reverse cholesterol transport pathway. We induced demyelinating lesions in 3 month old NR1H3 (or LXRα) knockout mice and observed, as in aged wild-type mice, impaired lesion restitution and sustained phagocyte infiltration at 21 dpi (fig. S4, A to C). In addition, we detected accumulation of myelin debris in lysosomes of phagocytes and crystal deposition in lesions of LXRα KO mice (fig. S4, D to G).

Next, we analyzed the role of apolipoprotein E (APOE), the major CNS cholesterol carrier that supports lipid efflux from cells (*11*). We induced focal demyelination in the corpus callosum of 12-week old APOE knockout (APOE KO) and wild-type control mice and quantified lesion size and recovery. Lesion size did not differ initially, at 4 dpi (fig. S4, H to J). However, when lesions were analyzed at 21 dpi, we observed impaired lesion restitution. We detected an increased number of IBA1-positive, MAC2-positive and MHCII-positive phagocytes, crystal deposition and myelin debris accumulation within lysosomes of phagocytes in spinal cord and corpus callosum lesions of APOE KO animals as compared to control mice (Fig. 2 and fig. S5). Because APOE has functions beyond cholesterol transport (*11*), we tested the efficacy of cyclic oligosaccharide 2-hydroxypropyl-β-cyclodextrin (HβCD), a compound that increases cholesterol efflux and solubility (*12*); and found that HβCD treatment attenuated the phenotype of APOE KO animals (Fig. 3 and fig. S6).

ApoE represents together with *Abca1* and *Abcg1* the major nuclear liver X receptor regulated genes that are involved in mediating cholesterol efflux from phagocytes. We thus crossbred CX3CR1CreER animals with $Abca1^{fl/fl}$ and $Abcg1^{fl/fl}$ mice to obtain microglia/macrophage specific double knockout mice (ABCA1/G1 KO). We observed an increased number of IBA1-positive and MHCII-positive phagocytes, an increase in crystal deposition and fewer myelinated axons in 21 dpi lesions of ABCA1/G1 KO animals as compared to control (fig. S7).

Because excessive cholesterol accumulation in phagocytes limits lesion recovery, we turned to cell culture experiments to determine the mechanisms involved. We prepared phagocytes (primary microglia or bone marrow-derived macrophages) from APOE KO and wild-type mice and examined the phagocytic uptake of myelin debris, which did not differ in cells prepared from wild-type or APOE KO mice (fig. S8, A and B). Because APOE is also produced by astrocytes, we incubated cells in the presence of serum-free conditioned media prepared from either wild-type or APOE KO astrocytes and observed the clearance of the internalized myelin particles from phagocytes. Myelin debris persisted within lysosomes of APOE KO cells that were incubated with conditioned media from APOE KO astrocytes. Clearance could be improved by an APOE-derived mimetic peptide, ATI5261 (*13*), which contains an amphipathic α-helical motif responsible for lipid binding and cholesterol efflux (Fig. 3, E and F). Moreover, myelin debris treatment resulted in crystal formation, which was increased in APOE KO macrophages and reduced by GW3965 treatment (fig. S8, C to G).

In atherosclerosis, cholesterol crystals can induce inflammation by phagolysosomal membrane rupture and subsequent stimulation of the caspase-1-activating NLRP3 (NALP3 or cryopyrin) inflammasome and secretion of interleukin (IL)-1 cytokines (*14*, *15*). Myelin debris treatment resulted in lysosomal permeabilization and caspase-1 cleavage in wild-type, but not in NLRP3-deficient macrophages (Fig. 4, A to H, and fig. S9, A and B). More pronounced caspase-1 activation was observed in APOE KO as compared to wild-type macrophages, which was confirmed in vivo in APOE KO mice after lysolecithin injection (Fig. 4E and fig. S9C). Myelin overloading induced cell death, which resulted in DNA fragmentation (detected by TUNEL assay), was cholesterol-dependent (fig. S9, D and E), and rescued by caspase-1 inhibitors pointing to an inflammasome-mediated pyroptotic cell death pathway (Fig. 4G and fig. S10). Thus, cholesterol derived from myelin debris can activate the NLRP3 inflammasome in macrophages when toxic levels build up intracellularly in the absence of sufficient lipoprotein carriers.

Because jamming the lysosomal system with myelin debris resulted in cholesterol crystallization and inflammasome activation, we asked whether this pathway was responsible for limiting regeneration in old mice. To examine whether increased inflammasome activation contributed to the poor recovery of old mice, we analyzed spinal cord lesions of aged wild-type and NLRP3-deficient mice. As in GW3965 treated old animals (Fig. 4, I and J), we found significantly improved

remyelination in aged NLRP3-deficient mice as compared to aged wild-type mice at 21 dpi. Thus, inflammasome activation possibly downstream of cholesterol accumulation drives a maladaptive immune response impairing inflammation resolution and repair in aged mice.

Self-resolving inflammation is essential for a proper restorative process after tissue damage, while uncontrolled inflammation can leave lasting marks that permanently alter tissue homeostasis (*16*). Here, we made the surprising finding that the self-limiting inflammatory response, which is necessary to initiate a regenerative process, is maladaptive in the CNS of aged mice. It appears that the inability of aged phagocytes to clear the enormous amounts of cholesterol that are released from myelin after myelin breakdown in demyelinating diseases results in a phase transition of free cholesterol into crystals, inducing lysosomal rupture and inflammasome stimulation, which is consistent with the beneficial effects of nuclear receptor agonists in remyelination (*17*, *18*). The unexpected link between lipid metabolisms and tissue regeneration provides opportunities for the development of regenerative medicines for remyelination and for improving functional recovery after CNS injury (*19*).

REFERENCES AND NOTES

1. P. Patrikios, C. Stadelmann, A. Kutzelnigg, H. Rauschka, M. Schmidbauer, H. Laursen, P. S. Sorensen, W. Brück, C. Lucchinetti, H. Lassmann, Remyelination is extensive in a subset of multiple sclerosis patients. *Brain* **129**, 3165–3172 (2006). doi:10.1093/brain/awl217 Medline
2. F. J. Najm, M. Madhavan, A. Zaremba, E. Shick, R. T. Karl, D. C. Factor, T. E. Miller, Z. S. Nevin, C. Kantor, A. Sargent, K. L. Quick, D. M. Schlatzer, H. Tang, R. Papoian, K. R. Brimacombe, M. Shen, M. B. Boxer, A. Jadhav, A. P. Robinson, J. R. Podojil, S. D. Miller, R. H. Miller, P. J. Tesar, Drug-based modulation of endogenous stem cells promotes functional remyelination in vivo. *Nature* **522**, 216–220 (2015). doi:10.1038/nature14335 Medline
3. F. Mei, S. P. J. Fancy, Y.-A. A. Shen, J. Niu, C. Zhao, B. Presley, E. Miao, S. Lee, S. R. Mayoral, S. A. Redmond, A. Etxeberria, L. Xiao, R. J. M. Franklin, A. Green, S. L. Hauser, J. R. Chan, Micropillar arrays as a high-throughput screening platform for therapeutics in multiple sclerosis. *Nat. Med.* **20**, 954–960 (2014). doi:10.1038/nm.3618 Medline
4. V. A. Deshmukh, V. Tardif, C. A. Lyssiotis, C. C. Green, B. Kerman, H. J. Kim, K. Padmanabhan, J. G. Swoboda, I. Ahmad, T. Kondo, F. H. Gage, A. N. Theofilopoulos, B. R. Lawson, P. G. Schultz, L. L. Lairson, A regenerative approach to the treatment of multiple sclerosis. *Nature* **502**, 327–332 (2013). doi:10.1038/nature12647 Medline
5. J. M. Ruckh, J.-W. Zhao, J. L. Shadrach, P. van Wijngaarden, T. N. Rao, A. J. Wagers, R. J. M. Franklin, Rejuvenation of regeneration in the aging central nervous system. *Cell Stem Cell* **10**, 96–103 (2012). doi:10.1016/j.stem.2011.11.019 Medline
6. S. Shen, J. Sandoval, V. A. Swiss, J. Li, J. Dupree, R. J. M. Franklin, P. Casaccia-Bonnefil, Age-dependent epigenetic control of differentiation inhibitors is critical for remyelination efficiency. *Nat. Neurosci.* **11**, 1024–1034 (2008). doi:10.1038/nn.2172 Medline
7. V. E. Miron, A. Boyd, J.-W. Zhao, T. J. Yuen, J. M. Ruckh, J. L. Shadrach, P. van Wijngaarden, A. J. Wagers, A. Williams, R. J. M. Franklin, C. Ffrench-Constant, M2 microglia and macrophages drive oligodendrocyte differentiation during CNS remyelination. *Nat. Neurosci.* **16**, 1211–1218 (2013). doi:10.1038/nn.3469 Medline
8. K. J. Moore, I. Tabas, Macrophages in the pathogenesis of atherosclerosis. *Cell* **145**, 341–355 (2011). doi:10.1016/j.cell.2011.04.005 Medline
9. X. Fu, J. G. Menke, Y. Chen, G. Zhou, K. L. MacNaul, S. D. Wright, C. P. Sparrow, E. G. Lund, 27-hydroxycholesterol is an endogenous ligand for liver X receptor in cholesterol-loaded cells. *J. Biol. Chem.* **276**, 38378–38387 (2001). doi:10.1074/jbc.M105805200 Medline
10. C. Hong, P. Tontonoz, Liver X receptors in lipid metabolism: Opportunities for drug discovery. *Nat. Rev. Drug Discov.* **13**, 433–444 (2014). doi:10.1038/nrd4280 Medline
11. R. W. Mahley, Apolipoprotein E: Cholesterol transport protein with expanding role in cell biology. *Science* **240**, 622–630 (1988). doi:10.1126/science.3283935 Medline
12. S. Zimmer, A. Grebe, S. S. Bakke, N. Bode, B. Halvorsen, T. Ulas, M. Skjelland, D. De Nardo, L. I. Labzin, A. Kerksiek, C. Hempel, M. T. Heneka, V. Hawxhurst, M. L. Fitzgerald, J. Trebicka, I. Björkhem, J.-A. Gustafsson, M. Westerterp, A. R. Tall, S. D. Wright, T. Espevik, J. L. Schultze, G. Nickenig, D. Lütjohann, E. Latz, Cyclodextrin promotes atherosclerosis regression via macrophage reprogramming. *Sci. Transl. Med.* **8**, 333ra50 (2016). doi:10.1126/scitranslmed.aad6100 Medline
13. A. Hafiane, J. K. Bielicki, J. O. Johansson, J. Genest, Apolipoprotein E derived HDL mimetic peptide ATI-5261 promotes nascent HDL formation and reverse cholesterol transport in vitro. *Biochim. Biophys. Acta* **1841**, 1498–1512 (2014). doi:10.1016/j.bbalip.2014.07.018 Medline
14. P. Duewell, H. Kono, K. J. Rayner, C. M. Sirois, G. Vladimer, F. G. Bauernfeind, G. S. Abela, L. Franchi, G. Nuñez, M. Schnurr, T. Espevik, E. Lien, K. A. Fitzgerald, K. L. Rock, K. J. Moore, S. D. Wright, V. Hornung, E. Latz, NLRP3 inflammasomes are required for atherogenesis and activated by cholesterol crystals. *Nature* **464**, 1357–1361 (2010). doi:10.1038/nature08938 Medline
15. K. Rajamäki, J. Lappalainen, K. Oörni, E. Välimäki, S. Matikainen, P. T. Kovanen, K. K. Eklund, Cholesterol crystals activate the NLRP3 inflammasome in human macrophages: A novel link between cholesterol metabolism and inflammation. *PLOS ONE* **5**, e11765 (2010). doi:10.1371/journal.pone.0011765 Medline
16. A. Aguzzi, B. A. Barres, M. L. Bennett, Microglia: Scapegoat, saboteur, or something else? *Science* **339**, 156–161 (2013). doi:10.1126/science.1227901 Medline
17. J. K. Huang, A. A. Jarjour, B. N. Oumesmar, C. Kerninon, A. Williams, W. Krezel, H. Kagechika, J. Bauer, C. Zhao, A. Baron-Van Evercooren, P. Chambon, C. Ffrench-Constant, R. J. M. Franklin, Retinoid X receptor gamma signaling accelerates CNS remyelination. *Nat. Neurosci.* **14**, 45–53 (2011). doi:10.1038/nn.2702 Medline
18. D. Meffre, G. Shackleford, M. Hichor, V. Gorgievski, E. T. Tzavara, A. Trousson, A. M. Ghoumari, C. Deboux, B. Nait Oumesmar, P. Liere, M. Schumacher, E.-E. Baulieu, F. Charbonnier, J. Grenier, C. Massaad, Liver X receptors alpha and beta promote myelination and remyelination in the cerebellum. *Proc. Natl. Acad. Sci. U.S.A.* **112**, 7587–7592 (2015). doi:10.1073/pnas.1424951112 Medline
19. F. Bei, H. H. C. Lee, X. Liu, G. Gunner, H. Jin, L. Ma, C. Wang, L. Hou, T. K. Hensch, E. Frank, J. R. Sanes, C. Chen, M. Fagiolini, Z. He, Restoration of visual function by enhancing conduction in regenerated axons. *Cell* **164**, 219–232 (2016). doi:10.1016/j.cell.2015.11.036 Medline
20. J. A. Piedrahita, S. H. Zhang, J. R. Hagaman, P. M. Oliver, N. Maeda, Generation of mice carrying a mutant apolipoprotein E gene inactivated by gene targeting in embryonic stem cells. *Proc. Natl. Acad. Sci. U.S.A.* **89**, 4471–4475 (1992). doi:10.1073/pnas.89.10.4471 Medline
21. G. Liang, J. Yang, J. D. Horton, R. E. Hammer, J. L. Goldstein, M. S. Brown, Diminished hepatic response to fasting/refeeding and liver X receptor agonists in mice with selective deficiency of sterol regulatory element-binding protein-1c. *J. Biol. Chem.* **277**, 9520–9528 (2002). doi:10.1074/jbc.M111421200 Medline
22. M. Westerterp, S. Gourion-Arsiquaud, A. J. Murphy, A. Shih, S. Cremers, R. L. Levine, A. R. Tall, L. Yvan-Charvet, Regulation of hematopoietic stem and progenitor cell mobilization by cholesterol efflux pathways. *Cell Stem Cell* **11**, 195–206 (2012). doi:10.1016/j.stem.2012.04.024 Medline
23. S. Yona, K.-W. Kim, Y. Wolf, A. Mildner, D. Varol, M. Breker, D. Strauss-Ayali, S. Viukov, M. Guilliams, A. Misharin, D. A. Hume, H. Perlman, B. Malissen, E. Zelzer, S. Jung, Fate mapping reveals origins and dynamics of monocytes and tissue macrophages under homeostasis. *Immunity* **38**, 79–91 (2013). doi:10.1016/j.immuni.2012.12.001 Medline
24. S. Safaiyan, N. Kannaiyan, N. Snaidero, S. Brioschi, K. Biber, S. Yona, A. L. Edinger, S. Jung, M. J. Rossner, M. Simons, Age-related myelin degradation burdens the clearance function of microglia during aging. *Nat. Neurosci.* **19**, 995–998 (2016). doi:10.1038/nn.4325 Medline
25. E. O. Samstad, N. Niyonzima, S. Nymo, M. H. Aune, L. Ryan, S. S. Bakke, K. T.

Lappegård, O.-L. Brekke, J. D. Lambris, J. K. Damås, E. Latz, T. E. Mollnes, T. Espevik, Cholesterol crystals induce complement-dependent inflammasome activation and cytokine release. *J. Immunol.* **192**, 2837–2845 (2014). doi:10.4049/jimmunol.1302484 Medline
26. C. Oberle, J. Huai, T. Reinheckel, M. Tacke, M. Rassner, P. G. Ekert, J. Buellesbach, C. Borner, Lysosomal membrane permeabilization and cathepsin release is a Bax/Bak-dependent, amplifying event of apoptosis in fibroblasts and monocytes. *Cell Death Differ.* **17**, 1167–1178 (2010). doi:10.1038/cdd.2009.214 Medline
27. N. Snaidero, W. Möbius, T. Czopka, L. H. P. Hekking, C. Mathisen, D. Verkleij, S. Goebbels, J. Edgar, D. Merkler, D. A. Lyons, K.-A. Nave, M. Simons, Myelin membrane wrapping of CNS axons by PI(3,4,5)P3-dependent polarized growth at the inner tongue. *Cell* **156**, 277–290 (2014). doi:10.1016/j.cell.2013.11.044 Medline
28. D. Lütjohann, C. Hahn, W. Prange, T. Sudhop, M. Axelson, T. Sauerbruch, K. von Bergmann, C. Reichel, Influence of rifampin on serum markers of cholesterol and bile acid synthesis in men. *Int. J. Clin. Pharmacol. Ther.* **42**, 307–313 (2004). doi:10.5414/CPP42307 Medline
29. K. M. Thelen, K. M. Rentsch, U. Gutteck, M. Heverin, M. Olin, U. Andersson, A. von Eckardstein, I. Björkhem, D. Lütjohann, Brain cholesterol synthesis in mice is affected by high dose of simvastatin but not of pravastatin. *J. Pharmacol. Exp. Ther.* **316**, 1146–1152 (2006). doi:10.1124/jpet.105.094136 Medline

ACKNOWLEDGMENTS

We thank L. Vaculčiaková for help with the calculations of 3D reconstructions. The technical assistance of A. Kerksiek is gratefully acknowledged. The work was supported by an ERC CoG Grant (M.S.) and grants from the German Research Foundation (SI 746/9-1,10-1, SPP1757, TRR128, TRR43), the Tschira-Stiftung, the Adelson Foundation, the Cluster of Excellence and DFG Research Center CNMBP (W.M.) and SyNergy (M.S.). W.M. is supported by an ERC Grant to K.-A. Nave. M.B.Q. is supported by a Boehringer Ingelheim stipend. All data are presented in the main text and supplementary materials.

SUPPLEMENTARY MATERIALS

www.sciencemag.org/cgi/content/full/science.aan4183/DC1
Materials and Methods
Figs. S1 to S10
References (*20–29*)

10 April 2017; resubmitted 5 November 2017
Accepted 11 December 2017
Published online 4 January 2018
10.1126/science.aan4183

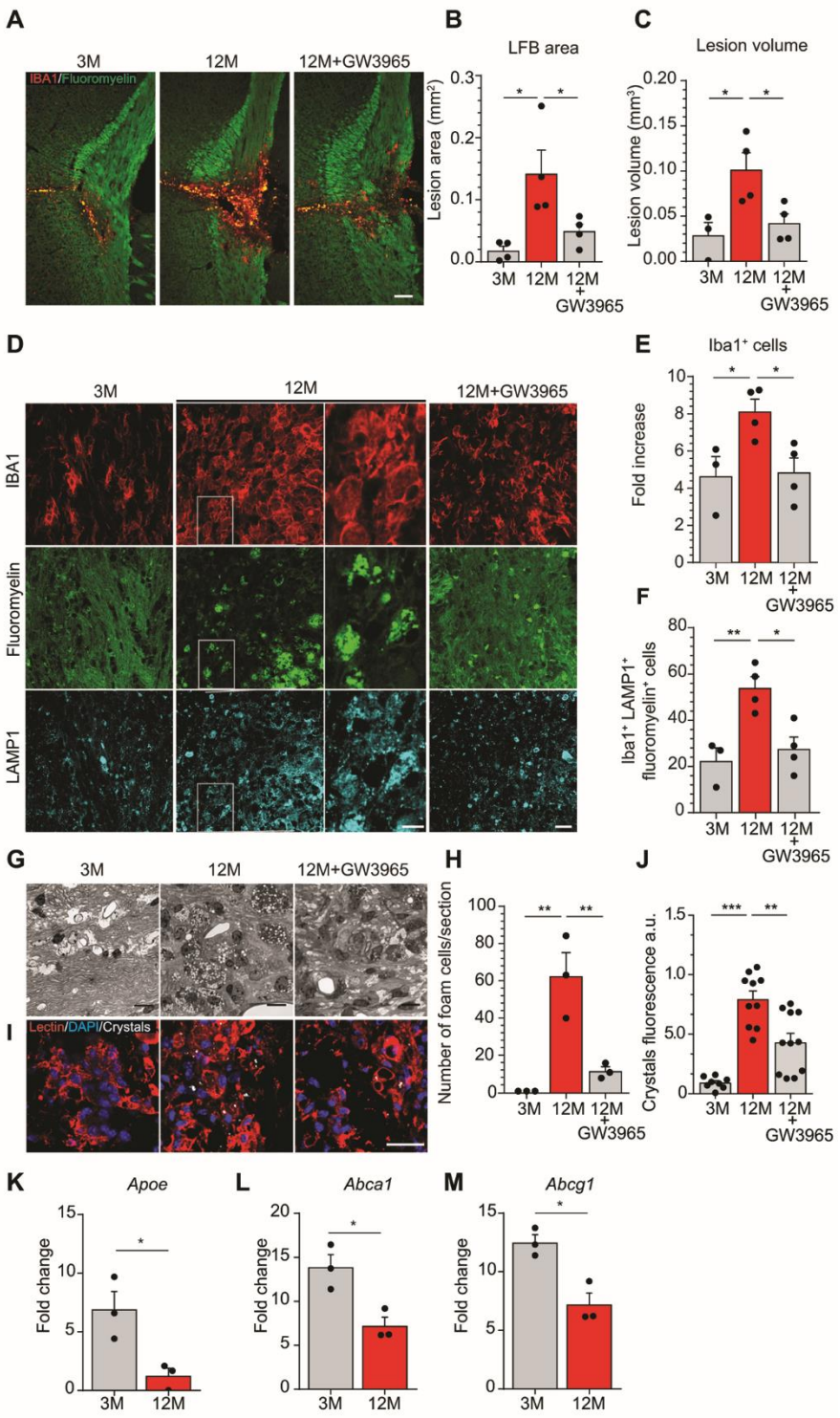

Fig. 1. Defective cholesterol clearance limits lesion regeneration in aged mice. (**A**) Images of corpus callosum lesions stained with fluoromyelin (green) and IBA1 (red) in 3 month old (3M), 12 month old (12M) and 12 month old mice treated with GW3965 (12M+GW3965) at 14 dpi. Scale bar, 100 µm. (**B** and **C**) Quantification of lesion area in mm^2 determined by luxol fast blue (LFB) and in mm^3 by fluoromyelin staining at 14 dpi. (**D**) Confocal images of 3M, 12M and 12M+GW3965 corpus callosum lesions showing IBA1 (red), fluoromyelin (green) and LAMP1 (cyan). Scale bar, 40µm. Magnified images of the boxed areas are show next to the images. (**E**) Change in number of IBA1⁺ cells in corpus callosum lesions compared to contralateral unlesioned side. (**F**) Number of IBA1⁺/fluoromyelin⁺/LAMP1⁺ cells in lesioned corpus callosum at 14 dpi. (**G**) Semithin section and (**H**) quantification of foam cells of 3M, 12M and 12M+GW3965 corpus callosum lesions. Scale bar, 10 µm. (**I**) Reflection microscopy images of spinal cord lesions, showing crystals (white) in lectin⁺ phagocytes (red), and (**J**) relative quantification of the fluorescence intensity of the reflected light. Scale bar, 25 µm. (**K** to **M**) Quantitative PCR analysis of *Apoe*, *Abca1* and *Abcg1* in 4 dpi lesions of 3M and 12M mice. All data are mean ± SEM; *P < 0.05, **P < 0.01, ***P < 0.001 by one way ANOVA test, with Tukey's multiple comparison test.

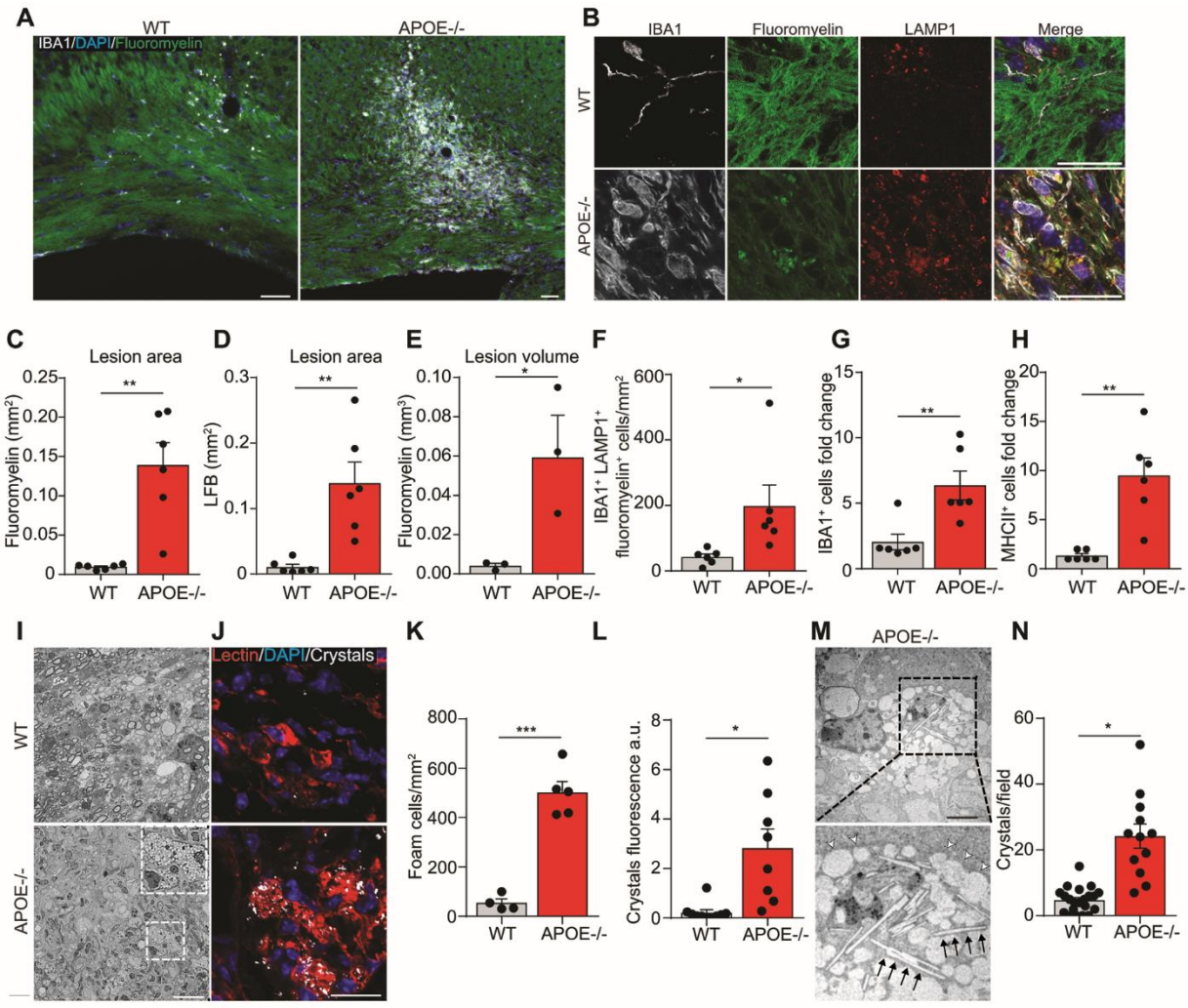

Fig. 2. APOE is required for cholesterol clearance in demyelinating lesions. (**A** and **B**) Images of corpus callosum lesions in WT and APOE−/− mice at 21 dpi showing fluoromyelin staining (green), IBA1 (white), DAPI (blue) and LAMP1 (red). (**C** and **D**) Quantification of lesion area in mm^2 at 21 dpi as determined by fluoromyelin and luxol fast blue (LFB) staining. (**E**) Lesion volume in mm^3 measured by fluoromyelin staining in consecutive sections. (**F**) Number of IBA1⁺/fluoromyelin⁺/LAMP1⁺ cells per mm^2 in lesions at 21 dpi. (**G** and **H**) Change in the number of IBA1⁺ and MHC II⁺ cells in the lesioned corpus callosum as compared to the contralateral unlesioned side. (**I**) Representative images (boxed area shown at larger magnification in right corner) and (**K**) quantification of foam cells in spinal cord lesions in WT and APOE−/− mice at 21 dpi. (**J**) Reflection microscopy images of 21 dpi lysolecithin lesions, showing crystals (white) in lectin⁺ phagocytes (red), and (**L**) relative quantification of the fluorescence intensity of the reflected light. (**M**) Transmission electron microscopy images of foam cells in 21 dpi lesions of APOE−/− mice (boxed area shown below at higher magnification), showing needle-like cholesterol crystals (black arrows) and lipid droplets (white arrowheads), and (**N**) relative quantification of crystals. All data are mean ± SEM; *P < 0.05, **P < 0.01, ***P < 0.001, two-tailed Student's *t*-test. Scale bars in (A, B, I, and J) are 25 μm; scale bar in (K) is 2.5 μm.

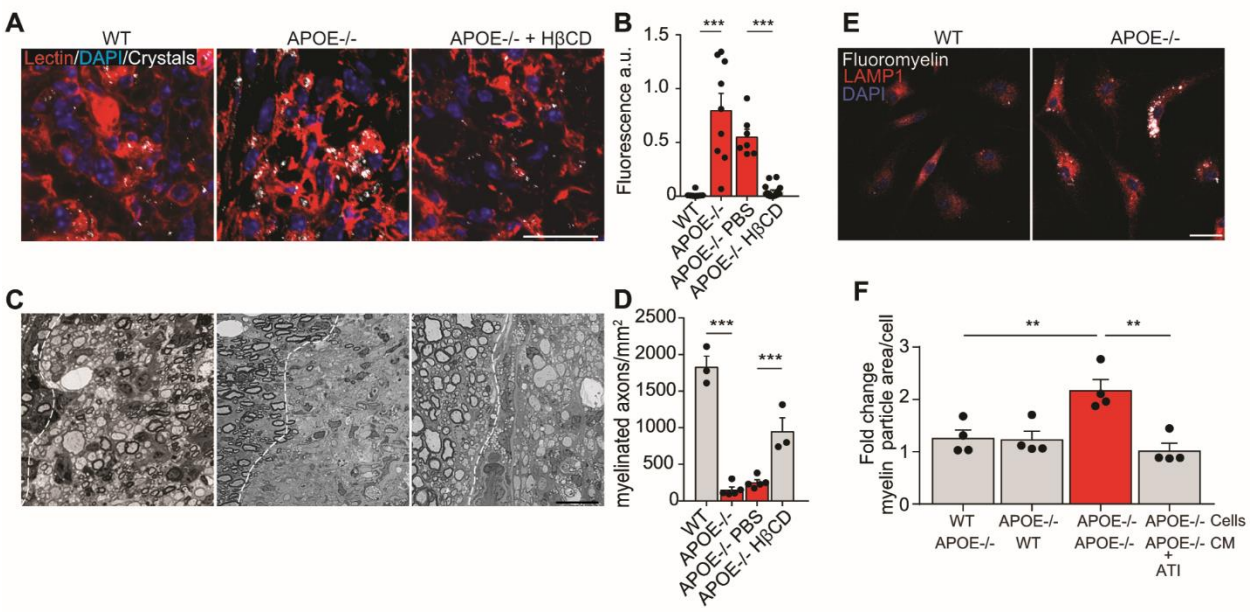

Fig. 3. Enhancing cholesterol clearance prevents lysosomal storage of myelin debris and crystal formation. (**A**) Representative images with crystals (white) and lectin⁺ phagocytes (red); and (**B**) quantification of cholesterol crystals in lysolecithin lesions of WT, APOE−/− and APOE−/− mice treated with HBCD or PBS. (**C**) Representative images of Methylenblue-Azur II staining and (**D**) quantification of remyelination in lysolecithin lesions at 21 dpi. The edges of the lesions are identified by a dashed line. (**E**) Confocal images of primary microglial cell cultures prepared from WT or APOE−/− mice, treated with myelin debris and stained for LAMP1 (red), fluoromyelin (white) and DAPI (dark blue) at 24 hours post-treatment. Microglia from WT or APOE−/− mice were treated with myelin debris and subsequently transferred in media conditioned (CM) either by WT or APOE−/− astrocytes. APOE−/− microglia cells in APOE−/− conditioned media were additionally treated with APOE mimetic peptide (ATI). (**F**) Change in the area of myelin particles per cell as compared to WT cells in WT conditioned media. All data are mean ± SEM; *P < 0.05, **P < 0.01, ***P < 0.001, by two way ANOVA, with Tukey's multiple comparison test. Scale bar is 25 μm in (A); scale bar is 100 μm in (B).

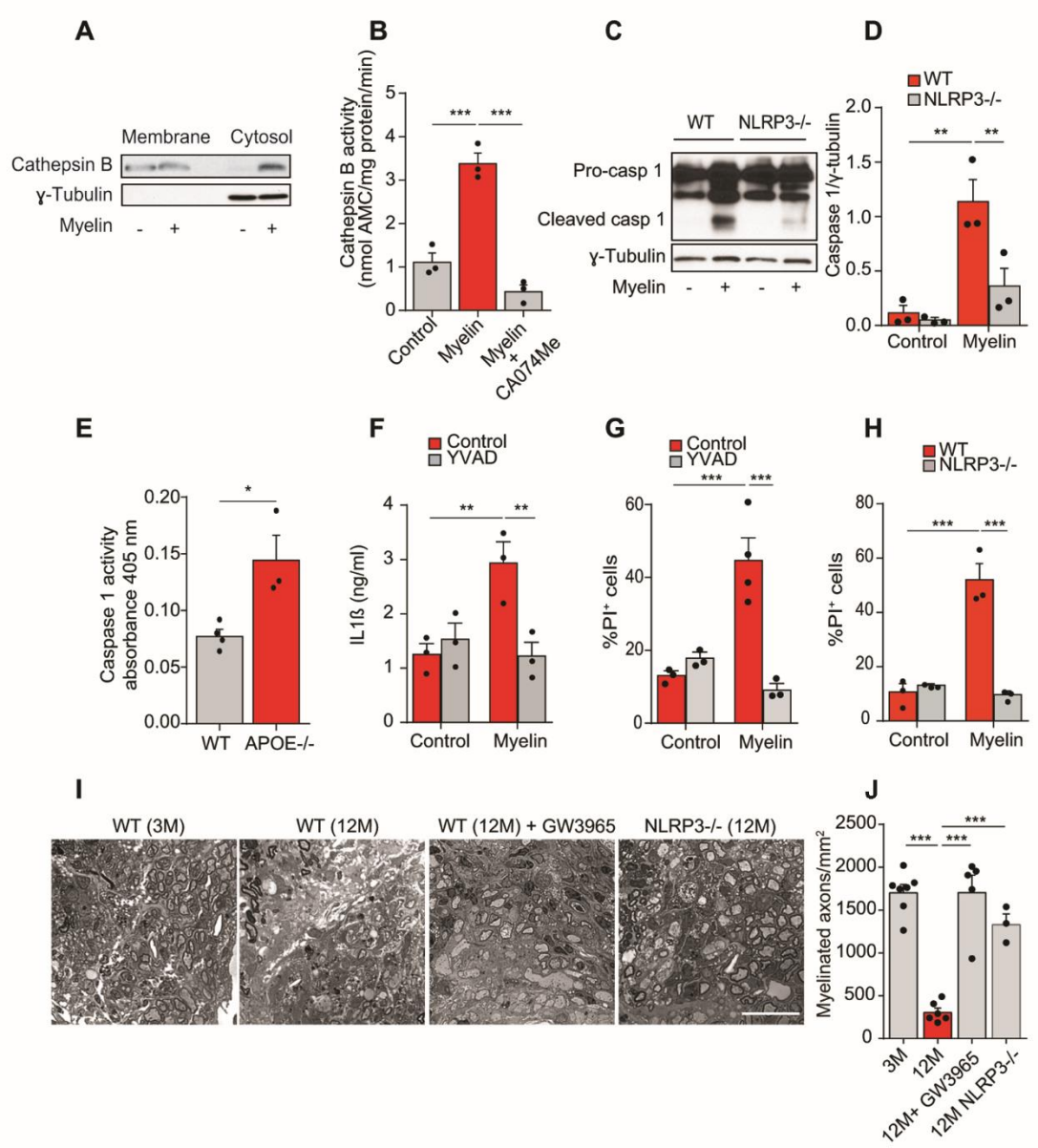

Fig. 4. Defective myelin debris clearance activates the NLRP3 inflammasome. (**A**) Immunoblot of cytosol and membrane fractions of primary bone marrow-derived macrophages (BMDM) 12 hours after treatment with myelin debris for cathepsin B and γ-tubulin. (**B**) Cathepsin B activity assay of the cytosolic fraction of control macrophages 12 hours after treatment with myelin debris in the presence or absence of the cathepsin B inhibitor, CA074me (10μM). (**C** and **D**) Immunoblot and quantification of the active subunit of caspase 1 (p20) after myelin debris treatment of WT or NLRP3−/− BMDM. The intensity of the p20 band was normalized to γ-tubulin. (**E**) Caspase 1 activity in lysates from lysolecithin lesions of WT and APOE−/− mice at 21 dpi. (**F**) ELISA for IL1β release in WT BMDM, after treatment with myelin debris with or without YVAD. (**G**) Quantification of the percentage of dead cells (propidium iodide positive, PI^+) after myelin debris treatment (12 hours) in the presence or absence of caspase 1 inhibitor (YVAD). (**H**) Quantification of PI^+ cells after treatment of WT and NLRP3−/− BMDM with myelin debris for 12 h. (**I**) Methylenblue-Azur II staining of remyelinating lesions in the spinal cord of 3M, 12M, GW3965 treated 12 M, and 12M old NLRP3−/− mice and (**J**) relative quantification of myelinated fibers. All data are mean ± SEM; *P < 0.05, **P < 0.01, ***P < 0.001 by one way ANOVA test, with Tukey's multiple comparison test and two-tailed Student's *t*-test (E). Scale bar, 25 μm.

Cite as: E. A. Costa *et al*., *Science* 10.1126/science.aar3607 (2018).

Defining the physiological role of SRP in protein-targeting efficiency and specificity

Elizabeth A. Costa,[1] Kelly Subramanian,[2] Jodi Nunnari,[2] Jonathan S. Weissman[1,3]*

[1]Department of Cellular and Molecular Pharmacology, University of California, San Francisco, San Francisco, CA, USA. [2]Department of Molecular and Cellular Biology, University of California, Davis, Davis, CA, USA. [3]Howard Hughes Medical Institute, University of California, San Francisco, San Francisco, CA, USA.

***Corresponding author. Email: jonathan.weissman@ucsf.edu**

The signal recognition particle (SRP) enables cotranslational delivery of proteins for translocation into the endoplasmic reticulum (ER), but its full in vivo role remains incompletely explored. We combined rapid auxin-induced SRP degradation with proximity-specific ribosome profiling to define SRP's in vivo function in yeast. Despite the classic view that SRP recognizes N-terminal signal sequences, we show that SRP was generally essential for targeting transmembrane domains regardless of their position relative to the N terminus. By contrast, many proteins containing cleavable N-terminal signal peptides were efficiently cotranslationally targeted in SRP's absence. We also revealed an unanticipated consequence of SRP loss: Normally ER-targeted transcripts were mistargeted to mitochondria, leading to mitochondrial defects. These results elucidate SRP's essential roles in maintaining the efficiency and specificity of protein targeting.

Regardless of their ultimate destination, nuclear encoded genes are translated in the cytosol. In non-plant eukaryotes, two cellular locations serve as the major sites of translocation across lipid bilayers: the mitochondrial outer membrane and the surface of the endoplasmic reticulum (ER), the latter being the entry point for proteins in the secretory pathway. The role of the signal recognition particle (SRP) in mediating cotranslational ER targeting is well established. SRP recognizes N-terminal hydrophobic signals of nascent polypeptide chains and, via interaction with the ER-localized SRP receptor, directs them to the translocon (*1*).

This classical model, however, fails to capture the full diversity of SRP targeting strategies and SRP function, leaving open several unanswered questions. A substantial fraction of proteins containing N-terminal targeting sequences do not require SRP for translocation (*2*, *3*), and in vitro, these are capable of post-translational ER translocation (*4*, *5*). However, SRP was recently shown to be comparably associated with SRP-independent and SRP-dependent nascent chains (*6*); whether this engagement is important for cotranslational targeting of SRP-independent proteins (*6*, *7*) is unknown. Recent studies have also pointed to several non-conventional modes of SRP interaction with nascent chains in vivo. For example, SRP can be recruited to mRNAs before the targeting signal is accessible (*6*, *8*, *9*), and in bacteria SRP has been found to bind internal transmembrane domains (TMDs) (*8*). However, a general role of SRP in enabling cotranslational targeting of eukaryotic proteins lacking N-terminal targeting sequences is not established. Furthermore, targeting to either the ER or mitochondria is highly specific with minimal mistargeting or dual targeting of proteins (*10*). In metazoans, the nascent polypeptide-associated complex (NAC) plays a critical role in this specificity by preventing mistargeting of mitochondrial proteins to the ER (*11*). It is not understood how cells prevent mistargeting of ER proteins to mitochondria.

To address these issues, we sought to monitor cotranslational protein targeting following rapid SRP depletion. We used the plant based auxin-induced degradation (AID) system (*12*) to induce acute and robust loss of one of the subunits of SRP, Srp72 (Fig. 1, A and B). The depletion of Srp72 was rapid, with a half-life of approximately 5 min (Fig. 1C). We used proximity-specific ribosome profiling (*7*), which utilizes a biotin ligase (BirA) localized to a subcellular location such as the surface of the ER or the mitochondrial outer membrane to label ribosomes at this location. Subsequent affinity purification of labeled ribosomes and sequencing of ribosome-protected mRNA fragments provides a snapshot of translation at that subcellular location.

To identify proteins that rely on SRP for efficient ER targeting in yeast, we performed a time course of proximity-specific ribosome profiling in the presence of cycloheximide (CHX) following Srp72 depletion using two ER-localized BirA fusions: Sec63-BirA (Fig. 1D) and BirA-Ubc6 (fig. S1A). Upon loss of SRP, transcripts of proteins previously predicted to be SRP-dependent (*3*) showed time-dependent depletion at the ER, validating our system. Genes encoding internal TMDs but lacking N-terminal targeting signals, also depleted from the ER upon loss of SRP in a similar timescale (Fig. 1D and fig.

S1A) and magnitude (Fig. 1E and fig. S1B). Thus, with the prominent exception of tail anchored (TA) proteins and SND substrates whose TMDs are at or near the C terminus, respectively (*13–15*), SRP is essential for targeting TMDs to the ER regardless of their distance to the N terminus.

By contrast, a prominent subset of mRNAs predicted to be SRP-independent remained at the ER throughout the one-hour auxin treatment (Fig. 1D and fig. S1A). A small group of mRNAs is known to be cotranslationally targeted to the ER in the presence of CHX, which uncouples the kinetics of translation and ER targeting (*7*). To ensure that the observed cotranslational targeting in the absence of SRP was not due to this effect, we performed a time course of Srp72 depletion and proximity-specific ribosome profiling without CHX treatment (Fig. 2A). In absence of auxin treatment, the extent of ER enrichment for secretory protein transcripts was reduced as compared to that observed in CHX-treated cells (fig. S2), as expected (*7*). Proteins containing targeting TMDs were nearly universally SRP-dependent, whereas a prominent group of proteins containing cleavable signal peptides with low hydrophobicity remained efficiently cotranslationally targeted following prolonged SRP depletion (fig. S3).

The ER enrichment of transcripts encoding SRP-independent proteins observed at later time points theoretically could be due to polysome tethering of mRNAs, although the one hour duration of our time course was considerably longer than typical yeast mRNA half lives (~10 min) (*16*). To examine the impact of SRP depletion on de novo mRNA targeting, we induced expression of reporter mRNAs with β-estradiol under conditions of SRP depletion (Fig. 2B) focusing on five genes representing of a range of targeting signals (fig. S4). In our ribosome profiling experiments, transcripts of three genes (SWP1, PST1, and FET3) displayed efficient ER targeting in SRP's absence (Fig. 2A). However, FET3 is predicted to be SRP-dependent and its localization is independent of SEC72 (*3*), a factor implicated in translocation of some SRP-independent substrates (*17*, *18*). All three proteins showed ER localization by fluorescence microscopy even when SRP was depleted (Fig. 2C). By contrast, two proteins whose targeting was observed to be SRP-dependent, Erg5 and Tsc13, which have an N-terminal or an internal targeting TMD, respectively, failed to localize to the ER when SRP was depleted (Fig. 2C). Consistent with the microscopy, in cells depleted of SRP, Fet3, but not Erg5, was glycosylated indicating translocation into the ER (Fig. 2D). Thus, SRP-independent proteins can be de novo cotranslationally targeted and translocated into the ER even in the prolonged absence of SRP.

We next examined if loss of SRP can lead to mistargeting of proteins. While the ER and mitochondria are connected (*19*), targeting to these organelles is exquisitely specific (*10*). To explore if SRP contributes to this specificity, we performed the proximity-specific ribosome profiling experiment using a mitochondrial-localized BirA fusion (Fig. 3A). Mitochondrial protein targeting was unaffected by loss of SRP (fig. S5). By contrast, a number of mRNAs were newly targeted to mitochondria, and the majority encoded for proteins normally co-translationally targeted to the ER (Fig. 3A). Transcripts that remained efficiently targeted to the ER in the absence of SRP were generally not mistargeted to mitochondria (Fig. 3B). We observed the same set of mistargeted mRNAs in multiple replicates and with two different mitochondrial-localized BirA fusions (Tom20 and Om45) and strain backgrounds (Fig. 3C). Thus, a prominent subset of SRP-dependent substrates, including proteins with N-terminal and internal targeting sequences, were cotranslationally targeted to the mitochondrial surface in SRP's absence.

We next used our estradiol-inducible system (Fig. 2B) to visualize protein localization of six gene products (fig. S4) consisting of five (Ole1, Erg5, Sct1, Orm1, and Nsg2) that displayed SRP-dependent ER targeting and one (Swp1) that was SRP-independent. In our ribosome profiling experiments, OLE1, ERG5, and SCT1 transcripts were consistently mistargeted to mitochondria, while ORM1 and NSG2 transcripts were not. In SRP-depleted cells, Ole1, Erg5, and Sct1 co-localized with mitochondria (Fig. 3D and fig. S6), although whether these proteins cross the mitochondrial membranes is an open question. By contrast, Swp1, Nsg2, and Orm1 were predominantly co-localized with the ER or were observed in focal structure adjacent to the ER (Fig. 3D and fig. S6), which might represent cytosolic aggregates.

In cells depleted of SRP for an hour, mitochondria lost their normal tubular structure and instead were more fragmented (Fig. 3D). To examine how proximal this morphological defect is to SRP depletion, we imaged cells at various time points after auxin treatment (Fig. 4A and fig. S7A) and categorized mitochondrial morphology (fig. S7B). Mitochondrial morphology defects were observed at early time points (Fig. 4B), prior to detection of ER stress (fig. S7C) and while ER morphology appeared normal (fig. S8). The rapid emergence of mitochondrial morphology defects in cells suggests that they are not a secondary consequence of ER morphological defects; however it is possible that the later, severe mitochondrial defects are impacted by the ER defects. The observed mitochondrial fragmentation required synthesis of new proteins, because cells depleted of SRP and treated with CHX possessed predominantly tubular mitochondria (fig. S9). Thus, mistargeting of SRP-dependent proteins to mitochondria disrupts mitochondrial structure.

Three important principles of SRP action now emerge (Fig. 4C). First, a prominent subset of proteins with cleavable N-terminal signal peptides is efficiently cotranslationally targeted to the ER in the complete and extended absence of SRP. Second, with the exception of proteins only containing TMDs

at or near to the C terminus (*13*–*15*), targeting and translocation of proteins with anchoring TMDs, regardless of their position relative to the N terminus, are fully dependent on SRP. Together with work in bacteria (*8*), our findings suggest that a universal feature of SRP's action is to engage TMDs across the length of the nascent chain. Third, our results reveal an unanticipated role for SRP in maintaining the specificity of organelle targeting. Without SRP, a subset of proteins becomes susceptible to aberrant cotranslational targeting to mitochondria reminiscent of the mistargeting of some TA proteins to mitochondria in absence of GET3/TRC40 ER targeting factors (*13*). This may reflect a more general tendency of hydrophobic or aggregation-prone proteins to be recruited to mitochondria (*20*). Mistargeting in the absence of SRP triggered rapid mitochondrial fragmentation, an indicator of mitochondrial dysfunction. Consistent with SRP playing a role in maintaining mitochondrial integrity, yeast adapted for SRP deletions acquire *rho*$^-$ (respiration-deficient) phenotypes (*21*, *22*). This role of SRP parallels that of NAC, which can prevent mistargeting of mitochondrial proteins to the ER in metazoans (*11*). Together, these observations illustrate the critical role of maintaining specificity of protein targeting for proper organellar function.

REFERENCES AND NOTES

1. X. Zhang, S.-O. Shan, Fidelity of cotranslational protein targeting by the signal recognition particle. *Annu. Rev. Biophys.* **43**, 381–408 (2014). doi:10.1146/annurev-biophys-051013-022653 Medline
2. D. T. Ng, J. D. Brown, P. Walter, Signal sequences specify the targeting route to the endoplasmic reticulum membrane. *J. Cell Biol.* **134**, 269–278 (1996). doi:10.1083/jcb.134.2.269 Medline
3. T. Ast, G. Cohen, M. Schuldiner, A network of cytosolic factors targets SRP-independent proteins to the endoplasmic reticulum. *Cell* **152**, 1134–1145 (2013). doi:10.1016/j.cell.2013.02.003 Medline
4. M. G. Waters, G. Blobel, Secretory protein translocation in a yeast cell-free system can occur posttranslationally and requires ATP hydrolysis. *J. Cell Biol.* **102**, 1543–1550 (1986). doi:10.1083/jcb.102.5.1543 Medline
5. W. Hansen, P. Walter, Prepro-carboxypeptidase Y and a truncated form of pre-invertase, but not full-length pre-invertase, can be posttranslationally translocated across microsomal vesicle membranes from *Saccharomyces cerevisiae*. *J. Cell Biol.* **106**, 1075–1081 (1988). doi:10.1083/jcb.106.4.1075 Medline
6. J. W. Chartron, K. C. L. Hunt, J. Frydman, Cotranslational signal-independent SRP preloading during membrane targeting. *Nature* **536**, 224–228 (2016). doi:10.1038/nature19309 Medline
7. C. H. Jan, C. C. Williams, J. S. Weissman, Principles of ER cotranslational translocation revealed by proximity-specific ribosome profiling. *Science* **346**, 1257521 (2014). doi:10.1126/science.1257521 Medline
8. D. Schibich, F. Gloge, I. Pöhner, P. Björkholm, R. C. Wade, G. von Heijne, B. Bukau, G. Kramer, Global profiling of SRP interaction with nascent polypeptides. *Nature* **536**, 219–223 (2016). doi:10.1038/nature19070 Medline
9. R. M. Voorhees, R. S. Hegde, Structures of the scanning and engaged states of the mammalian SRP-ribosome complex. *eLife* **4**, e07975 (2015). doi:10.7554/eLife.07975 Medline
10. C. C. Williams, C. H. Jan, J. S. Weissman, Targeting and plasticity of mitochondrial proteins revealed by proximity-specific ribosome profiling. *Science* **346**, 748–751 (2014). doi:10.1126/science.1257522 Medline
11. M. Gamerdinger, M. A. Hanebuth, T. Frickey, E. Deuerling, The principle of antagonism ensures protein targeting specificity at the endoplasmic reticulum. *Science* **348**, 201–207 (2015). doi:10.1126/science.aaa5335 Medline
12. K. Nishimura, T. Fukagawa, H. Takisawa, T. Kakimoto, M. Kanemaki, An auxin-based degron system for the rapid depletion of proteins in nonplant cells. *Nat. Methods* **6**, 917–922 (2009). doi:10.1038/nmeth.1401 Medline
13. M. Schuldiner, J. Metz, V. Schmid, V. Denic, M. Rakwalska, H. D. Schmitt, B. Schwappach, J. S. Weissman, The GET complex mediates insertion of tail-anchored proteins into the ER membrane. *Cell* **134**, 634–645 (2008). doi:10.1016/j.cell.2008.06.025 Medline
14. S. Stefanovic, R. S. Hegde, Identification of a targeting factor for posttranslational membrane protein insertion into the ER. *Cell* **128**, 1147–1159 (2007). doi:10.1016/j.cell.2007.01.036 Medline
15. N. Aviram, T. Ast, E. A. Costa, E. C. Arakel, S. G. Chuartzman, C. H. Jan, S. Haßdenteufel, J. Dudek, M. Jung, S. Schorr, R. Zimmermann, B. Schwappach, J. S. Weissman, M. Schuldiner, The SND proteins constitute an alternative targeting route to the endoplasmic reticulum. *Nature* **540**, 134–138 (2016). doi:10.1038/nature20169 Medline
16. C. Miller, B. Schwalb, K. Maier, D. Schulz, S. Dümcke, B. Zacher, A. Mayer, J. Sydow, L. Marcinowski, L. Dölken, D. E. Martin, A. Tresch, P. Cramer, Dynamic transcriptome analysis measures rates of mRNA synthesis and decay in yeast. *Mol. Syst. Biol.* **7**, 458 (2011). doi:10.1038/msb.2010.112 Medline
17. D. Feldheim, R. Schekman, Sec72p contributes to the selective recognition of signal peptides by the secretory polypeptide translocation complex. *J. Cell Biol.* **126**, 935–943 (1994). doi:10.1083/jcb.126.4.935 Medline
18. S. Panzner, L. Dreier, E. Hartmann, S. Kostka, T. A. Rapoport, Posttranslational protein transport in yeast reconstituted with a purified complex of Sec proteins and Kar2p. *Cell* **81**, 561–570 (1995). doi:10.1016/0092-8674(95)90077-2 Medline
19. B. Kornmann, E. Currie, S. R. Collins, M. Schuldiner, J. Nunnari, J. S. Weissman, P. Walter, An ER-mitochondria tethering complex revealed by a synthetic biology screen. *Science* **325**, 477–481 (2009). doi:10.1126/science.1175088 Medline
20. L. Ruan, C. Zhou, E. Jin, A. Kucharavy, Y. Zhang, Z. Wen, L. Florens, R. Li, Cytosolic proteostasis through importing of misfolded proteins into mitochondria. *Nature* **543**, 443–446 (2017). doi:10.1038/nature21695 Medline
21. F. Felici, G. Cesareni, J. M. Hughes, The most abundant small cytoplasmic RNA of *Saccharomyces cerevisiae* has an important function required for normal cell growth. *Mol. Cell. Biol.* **9**, 3260–3268 (1989). doi:10.1128/MCB.9.8.3260 Medline
22. B. C. Hann, P. Walter, The signal recognition particle in *S. cerevisiae*. *Cell* **67**, 131–144 (1991). doi:10.1016/0092-8674(91)90577-L Medline
23. R. Rothstein, Targeting, disruption, replacement, and allele rescue: Integrative DNA transformation in yeast. *Methods Enzymol.* **194**, 281–301 (1991). doi:10.1016/0076-6879(91)94022-5 Medline
24. M. Morawska, H. D. Ulrich, An expanded tool kit for the auxin-inducible degron system in budding yeast. *Yeast* **30**, 341–351 (2013). doi:10.1002/yea.2967 Medline
25. M. Ares, Isolation of total RNA from yeast cell cultures. *Cold Spring Harb. Protoc.* **2012**, 1082–1086 (2012). doi:10.1101/pdb.prot071456 Medline
26. R. Di Santo, S. Aboulhouda, D. E. Weinberg, The fail-safe mechanism of post-transcriptional silencing of unspliced *HAC1* mRNA. *eLife* **5**, e20069 (2016). doi:10.7554/eLife.20069 Medline
27. A. Murley, L. L. Lackner, C. Osman, M. West, G. K. Voeltz, P. Walter, J. Nunnari, ER-associated mitochondrial division links the distribution of mitochondria and mitochondrial DNA in yeast. *eLife* **2**, e00422 (2013). doi:10.7554/eLife.00422 Medline
28. N. J. McGlincy, N. T. Ingolia, Transcriptome-wide measurement of translation by ribosome profiling. *Methods* **126**, 112–129 (2017). doi:10.1016/j.ymeth.2017.05.028 Medline
29. J. G. Dunn, J. S. Weissman, Plastid: Nucleotide-resolution analysis of next-generation sequencing and genomics data. *BMC Genomics* **17**, 958 (2016). doi:10.1186/s12864-016-3278-x Medline
30. L. Käll, A. Krogh, E. L. L. Sonnhammer, A combined transmembrane topology and signal peptide prediction method. *J. Mol. Biol.* **338**, 1027–1036 (2004). doi:10.1016/j.jmb.2004.03.016 Medline
31. M. Elstner, C. Andreoli, T. Klopstock, T. Meitinger, H. Prokisch, The mitochondrial proteome database: MitoP2. *Methods Enzymol.* **457**, 3–20 (2009). doi:10.1016/S0076-6879(09)05001-0 Medline

ACKNOWLEDGMENTS

We thank members of the Weissman and Nunnari labs for discussion; C. Jan, M. Jost, and M. Shurtleff for critical reading of the manuscript; and the UCSF Center for Advanced Technology for technical assistance. This work was supported by Howard Hughes Medical Institute (J.S.W.), and NIH grants: R01AG041826 (J.S.W.), P50GM102706 (J.S.W.), R01GM062942 (J.N.), R01GM097432 (J.N.), and R01GM106019 (J.N.). E.A.C. was supported by NSF Graduate Research Fellowship 1144247. J.N. serves on the scientific advisory board of Mitobridge, Inc. Data are deposited in Gene Expression Omnibus under accession number GSE106329.

SUPPLEMENTARY MATERIALS

www.sciencemag.org/cgi/content/full/science.aar3607/DC1
Materials and Methods
Figs. S1 to S9
Tables S1 to S3
References (*23*–*31*)

30 October 2017; accepted 4 January 2018
Published online 18 January 2018
10.1126/science.aar3607

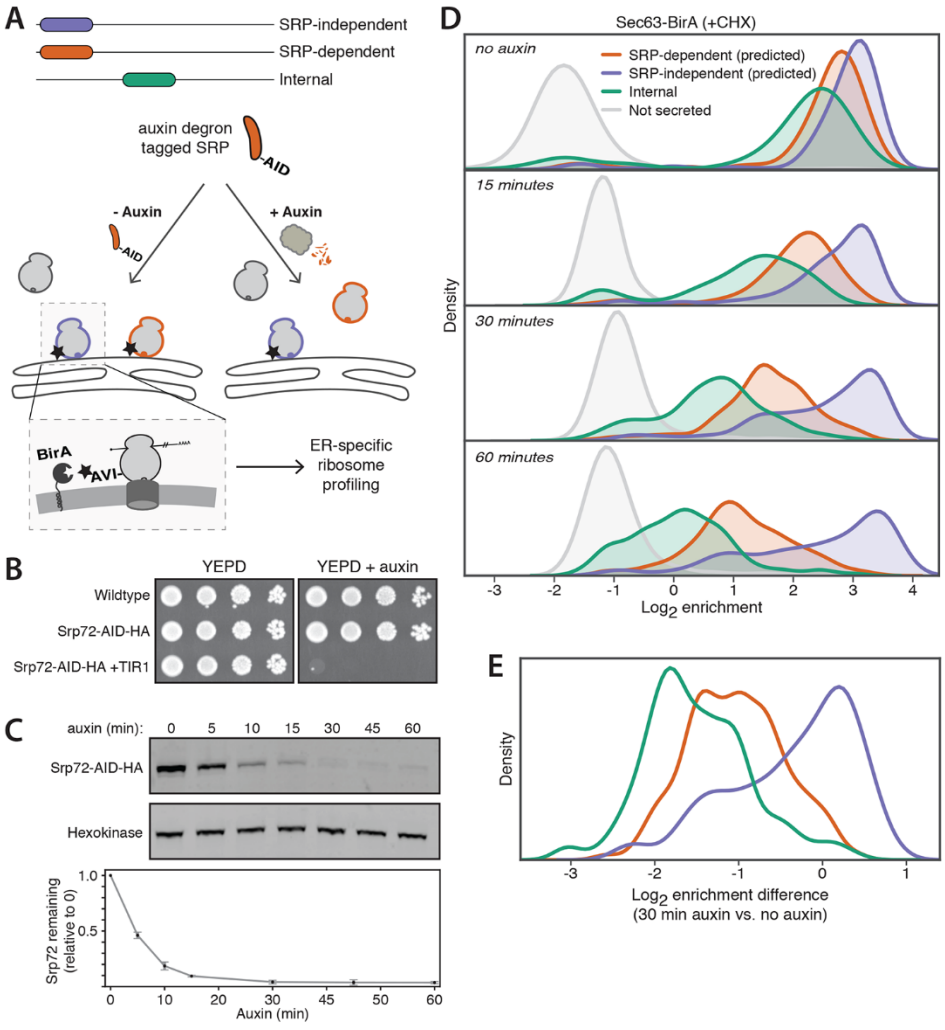

Fig. 1. A strategy to functionally probe acute loss of SRP. (**A**) Schematic of experimental setup using auxin-induced degradation (AID) and proximity-specific ribosome profiling. (**B**) Growth of degron-tagged Srp72 (Srp72-AID) strains in the absence or presence of auxin. (**C**) Immunoblots (IBs) and quantification of Srp72-AID depletion upon auxin addition (mean ± SD, *N*=3). (**D**) Density distributions of Sec63-BirA $\log_2$ enrichments with Srp72-AID after indicated times of auxin treatment. Genes are separated by predictions of SRP-dependence from (*3*). (**E**) Density distributions of $\log_2$ enrichment differences comparing 30 min auxin to no auxin for each gene. Genes are categorized as in (D).

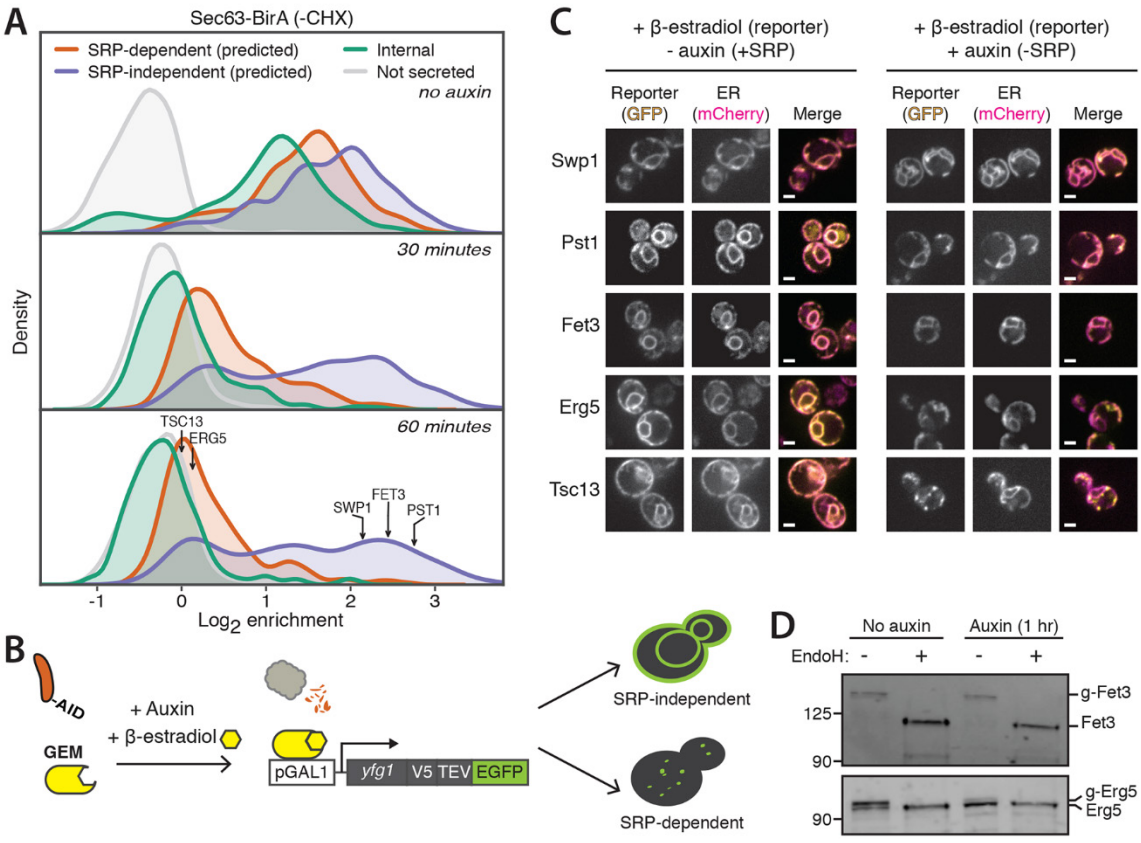

Fig. 2. Efficient cotranslational ER targeting in the absence of SRP. (**A**) Density distributions of Sec63-BirA log_2 enrichments with Srp72-AID after indicated times of auxin treatment. Arrows indicate enrichments of reporter genes. (**B**) Schematic of β-estradiol-inducible reporter system. GEM is a fusion protein consisting of GAL DNA binding domain, β-estradiol-binding domain, and Msn2 activation domain. (**C**) Single plane confocal fluorescence microscopy images of yeast with Srp72-AID expressing reporter-EGFP (yellow) and ER mCherry-HDEL (magenta) in the absence (left) or presence (right) of auxin. Scale bar, 2 µm. (**D**) IBs of reporters in the absence or presence of auxin. Where indicated, lysates were treated with EndoH.

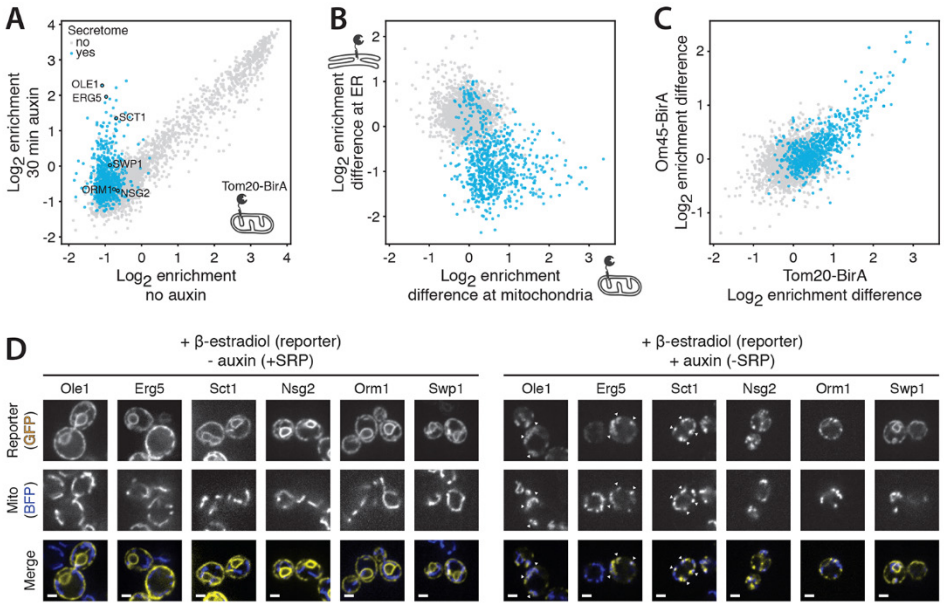

Fig. 3. Secretory proteins are mistargeted to mitochondria in absence of SRP. (**A**) Scatter plot of Tom20-BirA log_2 enrichments with Srp72-AID comparing the absence or treatment with auxin. Genes encoding secretory proteins are shown in blue. (**B**) Scatter plot comparing log_2 enrichments differences of 30 min auxin treatment relative to no auxin treatment. Mitochondria (Tom20-BirA, x-axis) is in the presence of CHX, and ER (Sec63-BirA, y-axis) is in the absence of CHX. Colors as in (A). (**C**) Scatter plot comparing log_2 enrichment differences of 30 min auxin treatment relative to no auxin treatment. Tom20-BirA (x-axis) uses W303 strain background, and Om45-BirA (y-axis) uses BY4741 strain background. Colors as in (A). (**D**) Single plane confocal fluorescence microscopy images of yeast with Srp72-AID expressing reporter-EGFP (yellow) and mitochondrial Su9-TagBFP (blue) in the absence (left) or presence (right) of auxin. Scale bar, 2 μm.

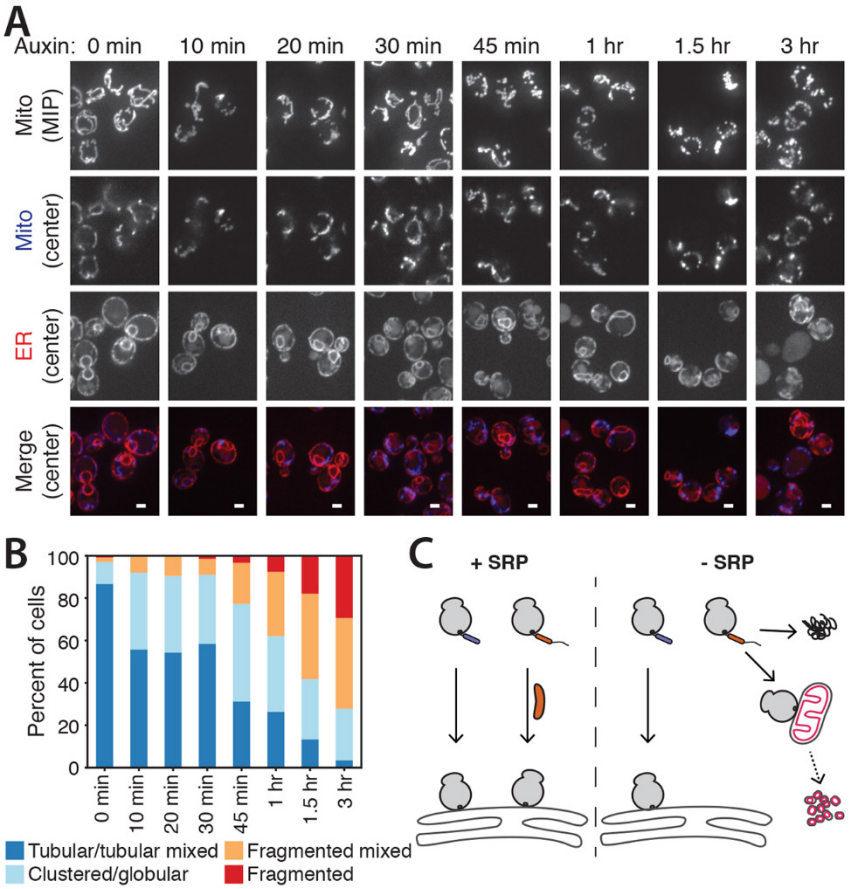

Fig. 4. Loss of SRP leads to rapid mitochondrial defects. (**A**) Confocal fluorescence microscopy of mitochondrial and ER morphology with Srp72-AID after indicated times of auxin treatment. Mitochondrial Su9-TagBFP is shown as a maximum intensity projection (MIP, top) or a single plane (blue, below) with ER mCherry-HDEL (red). Scale bar, 2 μm. (**B**) Quantification of mitochondrial morphologies from (A). (**C**) Summary of physiological consequences of loss of SRP.

PSYCHIATRIC GENOMICS

Shared molecular neuropathology across major psychiatric disorders parallels polygenic overlap

Michael J. Gandal,[1,2,3,4] Jillian R. Haney,[1,2,3] Neelroop N. Parikshak,[1,2,3] Virpi Leppa,[1,2,3] Gokul Ramaswami,[1,2,3] Chris Hartl,[1,2,3] Andrew J. Schork,[5] Vivek Appadurai,[5] Alfonso Buil,[5] Thomas M. Werge,[5,6,7] Chunyu Liu,[8,9] Kevin P. White,[10,11] CommonMind Consortium,* PsychENCODE Consortium,* iPSYCH-BROAD Working Group,* Steve Horvath,[3] Daniel H. Geschwind[1,2,3]†

The predisposition to neuropsychiatric disease involves a complex, polygenic, and pleiotropic genetic architecture. However, little is known about how genetic variants impart brain dysfunction or pathology. We used transcriptomic profiling as a quantitative readout of molecular brain-based phenotypes across five major psychiatric disorders—autism, schizophrenia, bipolar disorder, depression, and alcoholism—compared with matched controls. We identified patterns of shared and distinct gene-expression perturbations across these conditions. The degree of sharing of transcriptional dysregulation is related to polygenic (single-nucleotide polymorphism–based) overlap across disorders, suggesting a substantial causal genetic component. This comprehensive systems-level view of the neurobiological architecture of major neuropsychiatric illness demonstrates pathways of molecular convergence and specificity.

Despite remarkable success identifying genetic risk factors for major psychiatric disorders, it remains unknown how genetic variants interact with environmental and epigenetic risk factors in the brain to impart risk for clinically distinct disorders (*1*, *2*). We reasoned that brain transcriptomes—a quantitative, genome-wide molecular phenotype (*3*)—would allow us to determine whether disease-related signatures are shared across major neuropsychiatric disorders with distinct symptoms and whether these patterns reflect genetic risk.

We first analyzed published gene-expression microarray studies of the cerebral cortex across five major neuropsychiatric disorders (*3*–*11*) using 700 cerebral cortical samples from subjects with autism (ASD) (n = 50 samples), schizophrenia (SCZ) (n = 159), bipolar disorder (BD) (n = 94), depression (MDD) (n = 87), alcoholism (AAD) (n = 17), and matched controls (n = 293) (*12*). These disorders are prevalent and disabling, contributing substantially to global disease burden. Inflammatory bowel disease (IBD) (n = 197) was included as a non-neural comparison.

Individual data sets underwent stringent quality control and normalization (Fig. 1) (*12*), including rebalancing so as to alleviate confounding between diagnosis and biological (such as age and sex) or technical (such as post mortem interval, pH, RNA integrity number, batch, and 3′ bias) covariates (figs. S1 and S2). Transcriptome summary statistics for each disorder were computed with a linear mixed-effects model so as to account for any sample overlap across studies (*12*). Comparison of differential gene expression (DGE) $\log_2$ fold change ($\log_2$FC) signatures revealed a significant overlap among ASD, SCZ, and BD and SCZ, BD, and MDD (all Spearman's $\rho \geq 0.23$, $P < 0.05$, 40,000 permutations) (Fig. 2A). The regression slopes between ASD, BD, and MDD $\log_2$-FC effect sizes compared with SCZ (5.08, 0.99, and 0.37, respectively) indicate a gradient of transcriptomic severity with ASD > SCZ ≈ BD > MDD (Fig. 2B). To ensure robustness, we compared multiple methods for batch correction, probe summarization, and feature selection, including use of integrative correlations, none of which changed the qualitative observations (fig. S3) (*12*). Results were also unaltered after first regressing gene-level RNA degradation metrics, suggesting that systematic sample quality issues were unlikely to drive these correlations (fig. S3). Further, the lack of (or negative) overlap between AAD and other disorders suggests that similarities are less likely due to comorbid substance abuse, poor overall general health, or general brain-related post-mortem artefacts.

Disease-specific DGE summary statistics (data table S1) provide human in vivo benchmarks for determining the relevance of model organisms, in vitro systems, or drug effects (*13*, *14*). We identified a set of concordantly down- and up-regulated genes across disorders (fig. S4) as well as those with more specific effects. Complement component 4A (*C4A*), the top genome-wide association study (GWAS)–implicated SCZ disease gene (*15*), was significantly up-regulated in SCZ ($\log_2$FC = 0.23, $P = 6.9 \times 10^{-6}$) and in ASD [RNA sequencing (RNA-seq); $\log_2$FC = 0.91, P = 0.014] (data table S1) but not in BD, MDD, or AAD. To investigate potential confounding by psychiatric medications, we compared disease signatures with those from nonhuman primates treated with acute or chronic dosing of antipsychotic medications. Significant negative overlap (fig. S5) (*12*) was observed, indicating that antipsychotics are unlikely to drive, but rather may partially normalize, these transcriptomic alterations, whereas the psychotomimetic phencyclidine partially recapitulates disease signatures.

To validate that these transcriptomic relationships are generalizable, we generated independent RNA-seq data sets for replication for three out of the five disorders (fig. S6) (*12*). We identified 1099 genes whose DGE is replicated in ASD [odds ratio (OR) 6.4, $P = 3.3 \times 10^{-236}$, Fisher's exact test] (table S2), 890 genes for SCZ (BrainGVEX; OR 4.5, $P = 7.6 \times 10^{-155}$), and 112 genes for BD (BrainGVEX; OR 3.9, $P = 4.6 \times 10^{-26}$), which is likely due to the relatively smaller RNA-seq sample size for BD (*12*). We observed similarly high levels of transcriptomic overlap among ASD, SCZ, and BD and a similar gradient of transcriptomic severity (Fig. 2C and fig. S7). The SCZ and BD patterns were further replicated in the CommonMind data set, although gene-level overlap was lower (fig. S7) (*12*, *16*). The ASD signature was qualitatively consistent across the four major cortical lobules, indicating that this pattern is not caused by regional differences (Fig. 2D).

To more specifically characterize the biological pathways involved, we performed robust weighted gene coexpression network analysis (rWGCNA) (*12*, *17*), identifying several shared and disorder-specific coexpression modules (Fig. 3). Modules were stable (fig. S8), showed greater association with disease than other biological or technical covariates (fig. S9), and were not dependent on corrections for covariates or batch effects (fig. S10). Moreover, each module was enriched for protein-protein interactions (fig. S8) and brain enhancer-RNA co-regulation (fig. S11) derived from independent data, which provides anchors for dissecting protein complexes and regulatory relationships.

An astrocyte-related module (CD4 and hubs *GJA1* and *SOX9*) was broadly up-regulated in ASD, BD, and SCZ [false discovery rate (FDR)–corrected $P < 0.05$] (Fig. 3C and data table S2) (*12*) and enriched for glial cell differentiation

[1]Program in Neurobehavioral Genetics, Semel Institute, David Geffen School of Medicine, University of California, Los Angeles, Los Angeles, CA 90095, USA. [2]Department of Neurology, Center for Autism Research and Treatment, Semel Institute, David Geffen School of Medicine, University of California, Los Angeles, 695 Charles E. Young Drive South, Los Angeles, CA 90095, USA. [3]Department of Human Genetics, David Geffen School of Medicine, University of California, Los Angeles, Los Angeles, CA 90095, USA. [4]Department of Psychiatry, Semel Institute, David Geffen School of Medicine, University of California Los Angeles, 695 Charles E. Young Drive South, Los Angeles, CA 90095, USA. [5]Institute of Biological Psychiatry, Mental Health Services Copenhagen, Copenhagen, Denmark. [6]The Lundbeck Foundation Initiative for Integrative Psychiatric Research, iPSYCH, Denmark. [7]Department of Clinical Medicine, University of Copenhagen, Copenhagen, Denmark. [8]Department of Psychiatry, University of Illinois at Chicago, Chicago, IL 60607, USA. [9]The State Key Laboratory of Medical Genetics, Central South University, Changsha, Hunan, China. [10]Department of Human Genetics, University of Chicago, Chicago, IL 60637, USA. [11]Tempus Labs, 600 W. Chicago Avenue, Chicago, IL 60654, USA.
*For each consortium, authors and affiliations are listed in the supplementary materials.
†Corresponding author. Email: dhg@mednet.ucla.edu

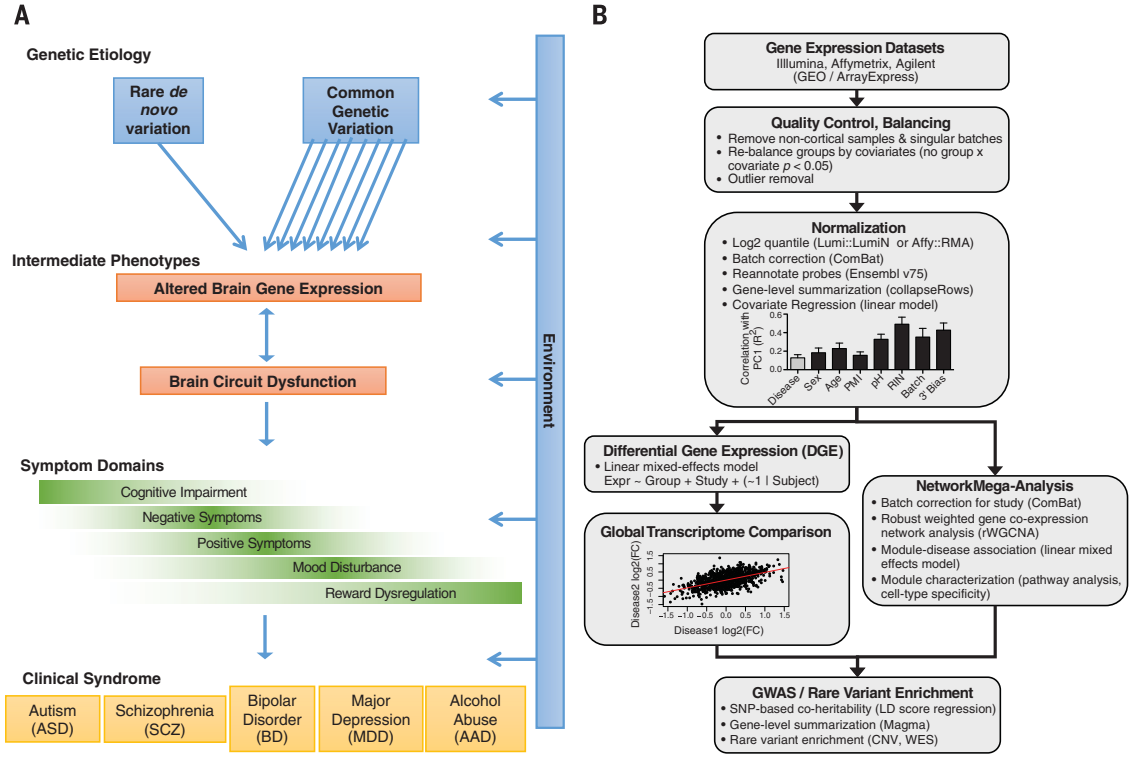

Fig. 1. Experimental rationale and design. (**A**) Model of psychiatric disease pathogenesis. (**B**) Flowchart of the cross-disorder transcriptome analysis pipeline (*12*). Cortical gene expression data sets were compiled from cases of ASD (n = 50 samples), SCZ (n = 159), BD (n = 94), MDD (n = 87), AAD (n = 17), and matched non-psychiatric controls (n = 293) (table S1) (*12*).

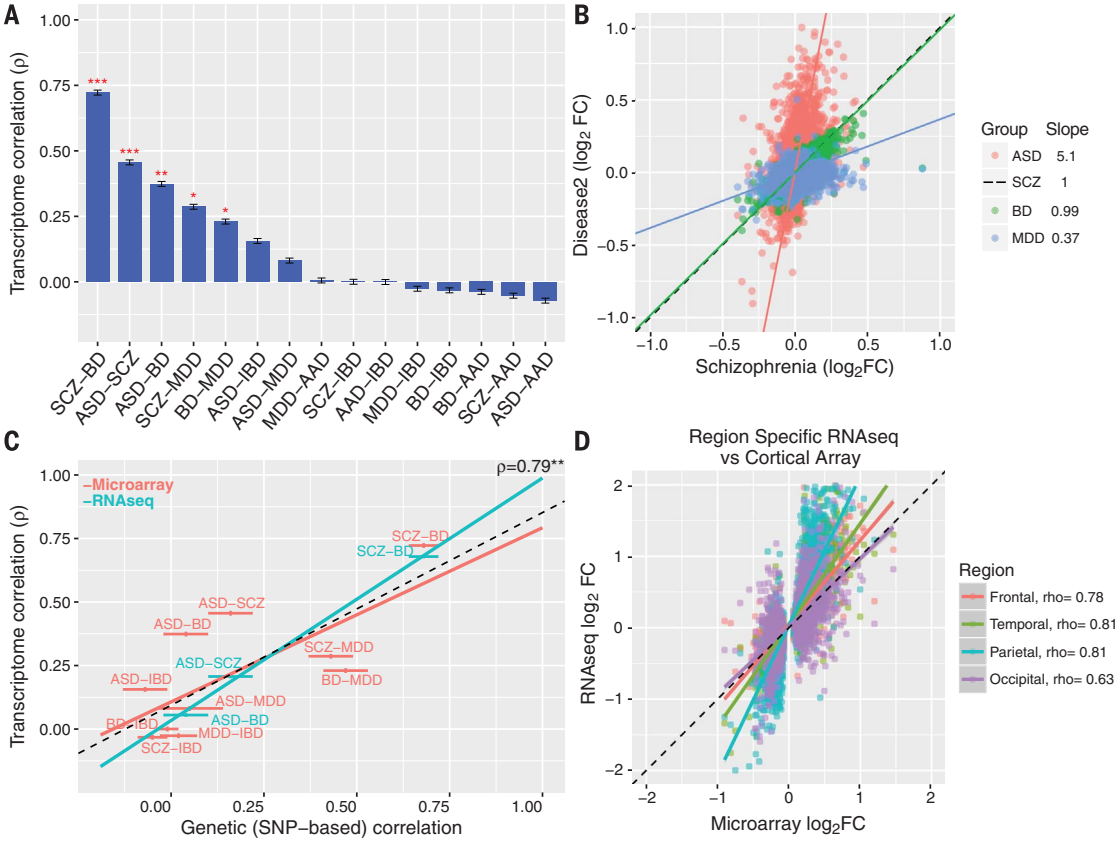

Fig. 2. Cortical gene expression patterns overlap. (**A**) Rank order of microarray transcriptome similarity for all disease pairs, as measured with Spearman's correlation of differential expression log_2FC values. (**B**) Comparison of the slopes among significantly associated disease pairs indicates a gradient of transcriptomic severity, with ASD > SCZ ~ BD > MDD. (**C**) Overlapping gene expression patterns across diseases are correlated with shared common genetic variation, as measured with SNP coheritability (*22*). The y axis shows transcriptome correlations using microarray-based (discovery, red) and RNA-seq (replication, blue) data sets. (**D**) RNA-seq across all cortical lobes in ASD replicates microarray results and demonstrates a consistent transcriptomic pattern. Spearman's ρ is shown for comparison between microarray and region-specific RNA-seq replication data sets (all $P < 10^{-14}$). Plots show mean ± SEM. *P < 0.05, **P < 0.01, ***P < 0.001.

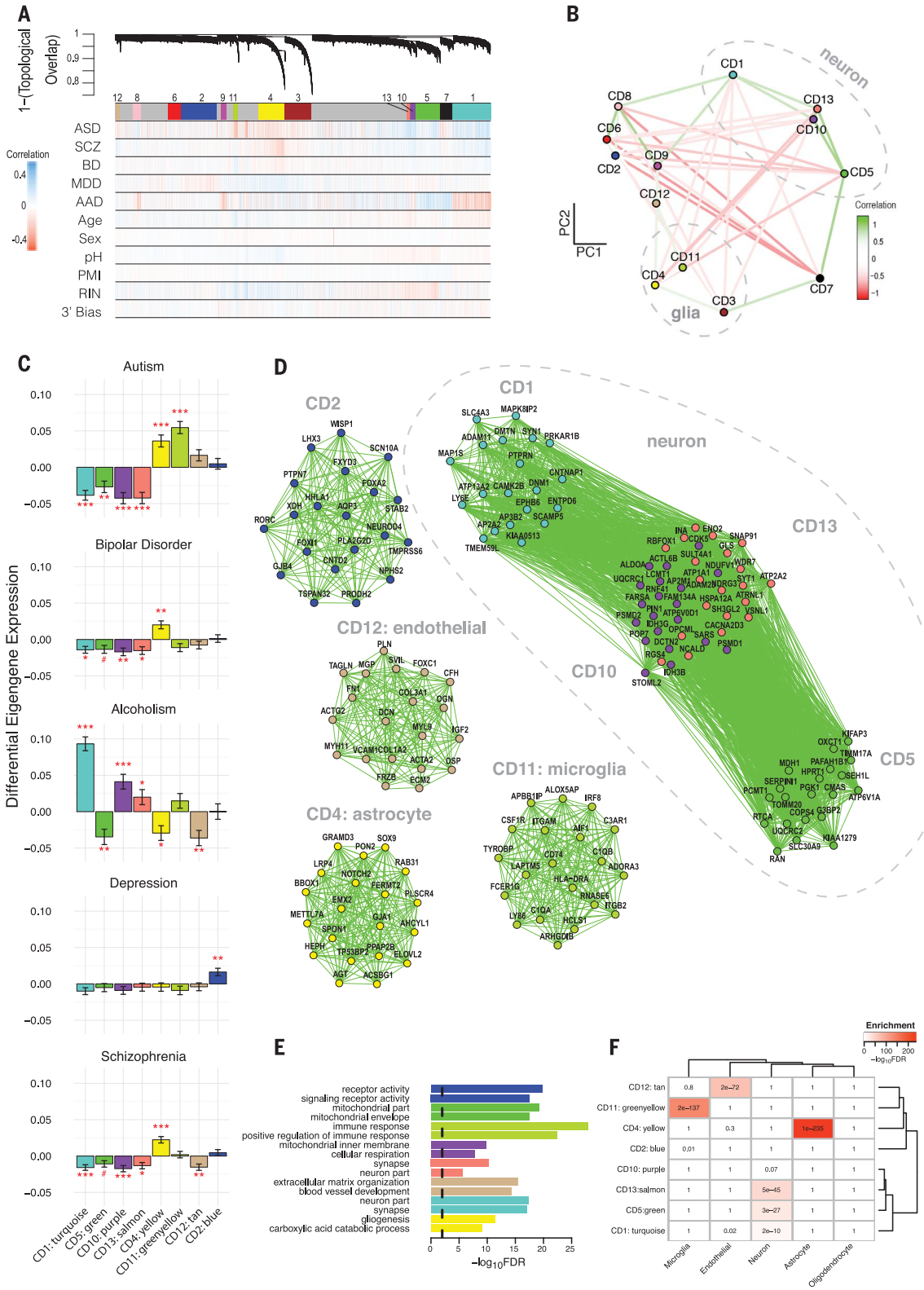

Fig. 3. Network analysis identifies modules of coexpressed genes across disease. (**A**) Network dendrogram from coexpression topological overlap of genes across disorders. Color bars show correlation of gene expression with disease status, biological, and technical covariates. (**B**) Multidimensional scaling plot demonstrates relationship between modules and clustering by cell-type relationship. (**C**) Module-level differential expression is perturbed across disease states. Plots show β values from linear mixed-effect model of module eigengene association with disease status (FDR-corrected $\#P < 0.1$, $*P < 0.05$, $**P < 0.01$, $***P < 0.001$). (**D**) The top 20 hub genes are plotted for modules most disrupted in disease. A complete list of genes' module membership (kME) is provided in data table S2. Edges are weighted by the strength of correlation between genes. (**E** and **F**) Modules are characterized by (E) Gene Ontology enrichment (top two pathways shown for each module) and (F) cell-type specificity, on the basis of RNA-seq of purified cell populations from healthy human brain samples (*25*).

and fatty-acid metabolism pathways. By contrast, a module strongly enriched for microglial markers (CD11) was up-regulated specifically in ASD (two-sided *t* test, FDR-corrected $P = 4 \times 10^{-9}$). Hubs include canonical microglial markers (*HLA-DRA* and *AIF1*), major components of the complement system (*C1QA* and *C1QB*), and *TYROBP*, a microglial signaling adapter protein (*18*). Results fit with convergent evidence for microglial up-regulation in ASD and an emerging understanding that microglia play a critical role regulating synaptic function during neurodevelopment (*19*).

One module, CD2, was up-regulated specifically in MDD (FDR-corrected $P = 0.009$) (data table S2) and was enriched for G protein–coupled receptors, cytokine-cytokine interactions, and hormone activity pathways, suggesting a link between inflammation and dysregulation of the

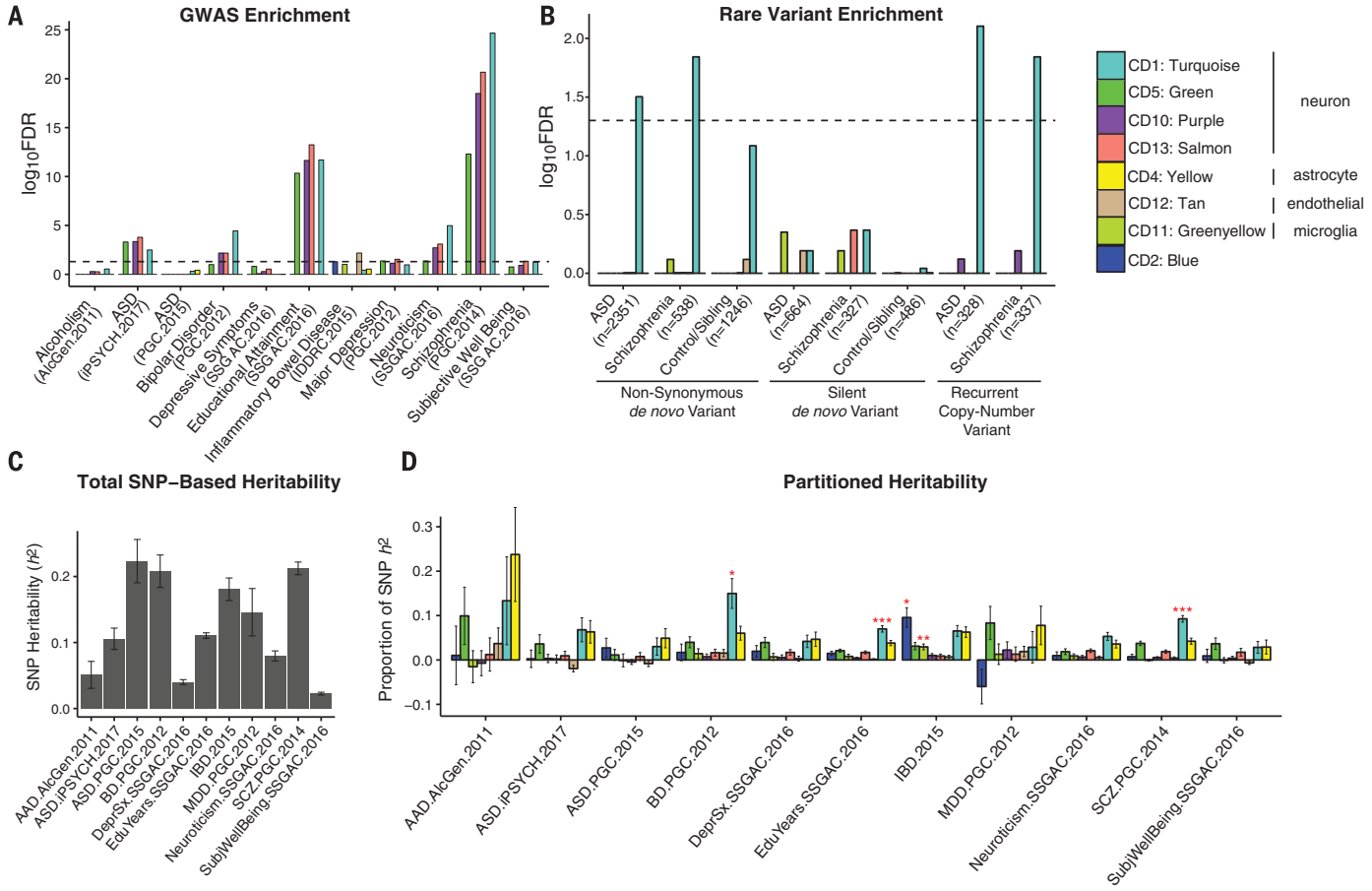

Fig. 4. Down-regulated neuronal modules are enriched for common and rare genetic risk factors. (**A**) Significant enrichment is observed for SCZ-, ASD-, and BD-associated common variants from GWAS among neuron/synapse and mitochondrial modules (*12*). GWAS data sets are listed in table S3. (**B**) The CD1 neuronal module shows significant enrichment for ASD- and SCZ-associated nonsynonymous de novo variants from whole-exome sequencing. The number of genes affected by different classes of rare variants is shown in parentheses. Significance was calculated by using logistic regression, correcting for gene length. *P* values are FDR-corrected. (**C**) Total SNP-based heritability (liability scale for psychiatric diagnoses) calculated from GWAS by using LD-score regression. (**D**) Proportion of heritability for each disorder or trait that can be attributed to individual coexpression modules. Significance (FDR-corrected $*P < 0.05$, $**P < 0.01$, $***P < 0.001$) is from enrichment statistics comparing the proportion of SNP heritability within the module divided by the proportion of total SNPs represented. The CD1 module shows significant enrichment in SCZ, BD, and educational attainment.

hypothalamic-pituitary (HPA) axis, which is consistent with current models of MDD pathophysiology (*20*). Several modules annotated as neuronal/mitochondrial were down-regulated across ASD, SCZ, and BD (CD1, CD10, and CD13) (Fig. 3C and data table S2) (*12*). The overlap of CD10 with a mitochondrial gene-enriched module previously associated with neuronal firing rate (*21*) links energetic balance, synaptic transmission, and psychiatric disease (data table S2).

The transcriptome may reflect the cause or the consequence of a disorder. To refine potential causal links, we compared single-nucleotide polymorphism (SNP)–based genetic correlations between disease pairs (*22*) with their corresponding transcriptome overlap. SNP coheritability was significantly correlated with transcriptome overlap across the same disease pairs (Spearman's $\rho = 0.79$, 95% confidence interval 0.43 to 0.93, $P = 0.0013$) (Fig. 2C), suggesting that a major component of these gene-expression patterns reflects biological processes coupled to underlying genetic variation.

To determine how disease-associated variants may influence specific biological processes, we investigated whether any modules harbor genetic susceptibility for specific disorders or for relevant cognitive or behavioral traits (*12*). We identified significant enrichment among several of the down-regulated, neuronal coexpression modules (CD1, CD10, and CD13) for GWAS signal from SCZ and BD, as well as for educational attainment and neuroticism (FDR-corrected $P < 0.05$, Spearman) (Fig. 4A) (*12*). We also observed enrichment for the three down-regulated neuronal coexpression modules in the iPSYCH Consortium (*23*) ASD GWAS cohort (Fig. 4A and table S3) (*12*). By contrast, these modules showed no enrichment for MDD, AAD, or IBD. Further, none of the microglial- or astrocyte-specific modules showed psychiatric GWAS enrichment. Extending this analysis to disease-associated rare variants (data table S3) (*2*, *12*), we found that the CD1 neuronal module was enriched for genes harbouring rare, nonsynonymous de novo mutations identified in ASD (OR 1.36, FDR-corrected $P = 0.03$, logistic regression) and SCZ cases (OR 1.82, FDR-corrected $P = 0.014$) but not unaffected controls (Fig. 4B). A similar CD1-enrichment was observed for genes affected by rare, recurrent copy-number variation (CNV) in ASD (OR 2.52, FDR-corrected $P = 0.008$) and SCZ (OR 2.46, FDR-corrected $P = 0.014$). These results suggest convergence of common and rare genetic variation acting to down-regulate synaptic function in ASD and SCZ.

We next used LD score regression (*24*) to partition GWAS heritability (Fig. 4C and data table S4) into the contribution from SNPs located within genes from each module (Fig. 4D) (*12*). CD1 again showed significant enrichment for SCZ (2.5-fold, FDR-corrected $P = 8.9 \times 10^{-11}$), BD (3.9 fold, FDR-corrected $P < 0.014$), and educational attainment (1.9-fold, FDR-corrected $P < 0.0008$; χ^2 test) GWAS, accounting for ~10% of SNP-based heritability within each data set, despite containing only 3% of the SNPs. This illustrates how gene network analysis can begin

to parse complex patterns of common variants, each of small effect size, to implicate specific biological roles for common variant risk across neuropsychiatric disorders.

These data provide a quantitative, genome-wide characterization of the cortical pathology across five major neuropsychiatric disorders, providing a framework for identifying the responsible molecular signaling pathways and interpreting genetic variants implicated in neuropsychiatric disease risk. We observed a gradient of synaptic gene down-regulation, with ASD > SZ ≈ BD. BD and SCZ appear most similar in terms of synaptic dysfunction and astroglial gene up-regulation, which may represent astrocytosis, activation, or both. ASD, an early-onset disorder, shows a distinct up-regulated microglial signature, which may reflect the role for microglia in regulation of synaptic connectivity during neurodevelopment (*19*). MDD shows neither the synaptic nor astroglial pathology but does exhibit dysregulation of HPA-axis and hormonal signaling not observed in the other disorders.

Our data suggest that shared genetic factors underlie a substantial proportion of cross-disorder expression overlap. Given that a minority of these relationships represent expression quantitative trait loci (fig. S12), most of the genetic effects are likely acting indirectly, through a cascade of developmental and cell-cell signaling events rooted in genetic risk. Genetic variation is also not the only driver of expression variation; there is undoubtedly a contribution from environmental effects. Hidden confounders could introduce a correlation structure that matches SNP-level genetic correlations, but parsimony and hidden covariate correction suggests that this is unlikely. Diagnostic misclassification could artificially elevate shared signals, but the results are robust to disorder removal (fig. S13), and misclassification would not account for the substantial overlap we observed with ASD, which has a highly distinct phenotypic trajectory from later onset disorders. Last, we have replicated broad transcriptomic and cell type–specific patterns independently for ASD, SCZ, and BD, providing an organizing pathological framework for future investigation of the mechanisms underlying specific gene- and isoform-level transcriptomic alterations in psychiatric disease.

REFERENCES AND NOTES

1. D. H. Geschwind, J. Flint, *Science* **349**, 1489–1494 (2015).
2. M. J. Gandal, V. Leppä, H. Won, N. N. Parikshak, D. H. Geschwind, *Nat. Neurosci.* **19**, 1397–1407 (2016).
3. I. Voineagu *et al.*, *Nature* **474**, 380–384 (2011).
4. K. Garbett *et al.*, *Neurobiol. Dis.* **30**, 303–311 (2008).
5. M. L. Chow *et al.*, *PLOS Genet.* **8**, e1002592 (2012).
6. C. Chen *et al.*, *Mol. Psychiatry* **18**, 1308–1314 (2013).
7. P. R. Maycox *et al.*, *Mol. Psychiatry* **14**, 1083–1094 (2009).
8. K. Iwamoto, M. Bundo, T. Kato, *Hum. Mol. Genet.* **14**, 241–253 (2005).
9. S. Narayan *et al.*, *Brain Res.* **1239**, 235–248 (2008).
10. L.-C. Chang *et al.*, *PLOS ONE* **9**, e90980 (2014).
11. I. Ponomarev, S. Wang, L. Zhang, R. A. Harris, R. D. Mayfield, *J. Neurosci.* **32**, 1884–1897 (2012).
12. Materials and methods are available as supplementary materials.
13. D. Prilutsky *et al.*, *Trends Mol. Med.* **20**, 91–104 (2014).
14. J. Lamb *et al.*, *Science* **313**, 1929–1935 (2006).
15. A. Sekar *et al.*, *Nature* **530**, 177–183 (2016).
16. M. Fromer *et al.*, *Nat. Neurosci.* **19**, 1442–1453 (2016).
17. P. Langfelder, S. Horvath, *BMC Bioinformatics* **9**, 559 (2008).
18. B. Zhang *et al.*, *Cell* **153**, 707–720 (2013).
19. M. W. Salter, B. Stevens, *Nat. Med.* **23**, 1018–1027 (2017).
20. P. W. Gold, *Mol. Psychiatry* **20**, 32–47 (2015).
21. K. D. Winden *et al.*, *Mol. Syst. Biol.* **5**, 291 (2009).
22. S. H. Lee *et al.*, *Nat. Genet.* **45**, 984–994 (2013).
23. C. B. Pedersen *et al.*, *Mol. Psychiatry* **23**, 6–14 (2018).
24. H. K. Finucane *et al.*, *Nat. Genet.* **47**, 1228–1235 (2015).
25. Y. Zhang *et al.*, *Neuron* **89**, 37–53 (2016).
26. P. Du, W. A. Kibbe, S. M. Lin, *Bioinformatics* **24**, 1547–1548 (2008).
27. L. Gautier, L. Cope, B. M. Bolstad, R. A. Irizarry, *Bioinformatics* **20**, 307–315 (2004).
28. G. K. Smyth, *Stat. Appl. Genet. Mol. Biol.* **3**, e3 (2004).
29. M. C. Oldham, P. Langfelder, S. Horvath, *BMC Syst. Biol.* **6**, 63 (2012).
30. W. E. Johnson, C. Li, A. Rabinovic, *Biostatistics* **8**, 118–127 (2007).
31. S. Durinck, P. T. Spellman, E. Birney, W. Huber, *Nat. Protoc.* **4**, 1184–1191 (2009).
32. J. A. Miller *et al.*, *BMC Bioinformatics* **12**, 322 (2011).
33. P. Langfelder, B. Zhang, S. Horvath, *Bioinformatics* **24**, 719–720 (2008).
34. N. N. Parikshak *et al.*, *Cell* **155**, 1008–1021 (2013).
35. M. J. Mason, G. Fan, K. Plath, Q. Zhou, S. Horvath, *BMC Genomics* **10**, 327 (2009).
36. A. C. Zambon *et al.*, *Bioinformatics* **28**, 2209–2210 (2012).
37. J. Reimand, T. Arak, J. Vilo, *Nucleic Acids Res.* **39** (suppl. 2), W307–W315 (2011).
38. J. D. Dougherty, E. F. Schmidt, M. Nakajima, N. Heintz, *Nucleic Acids Res.* **38**, 4218–4230 (2010).
39. X. Xu, A. B. Wells, D. R. O'Brien, A. Nehorai, J. D. Dougherty, *J. Neurosci.* **34**, 1420–1431 (2014).
40. Schizophrenia Working Group of the Psychiatric Genomics Consortium, *Nature* **511**, 421–427 (2014).
41. Psychiatric GWAS Consortium Bipolar Disorder Working Group, *Nat. Genet.* **43**, 977–983 (2011).
42. S. Ripke *et al.*, *Mol. Psychiatry* **18**, 497–511 (2013).
43. Autism Spectrum Disorders Working Group of The Psychiatric Genomics Consortium, *Mol. Autism* **8**, 21 (2017).
44. G. Schumann *et al.*, *Proc. Natl. Acad. Sci. U.S.A.* **108**, 7119–7124 (2011).
45. J. Z. Liu *et al.*, *Nat. Genet.* **47**, 979–986 (2015).
46. A. Okbay *et al.*, *Nat. Genet.* **48**, 624–633 (2016).
47. A. Okbay *et al.*, *Nature* **533**, 539–542 (2016).
48. C. A. de Leeuw, J. M. Mooij, T. Heskes, D. Posthuma, *PLOS Comput. Biol.* **11**, e1004219 (2015).
49. P. Munk-Jørgensen, P. B. Mortensen, *Dan. Med. Bull.* **44**, 82–84 (1997).
50. C. B. Pedersen *et al.*, *JAMA Psychiatry* **71**, 573–581 (2014).
51. B. N. Howie, P. Donnelly, J. Marchini, *PLOS Genet.* **5**, e1000529 (2009).
52. B. Howie, J. Marchini, M. Stephens, *G3 (Bethesda)* **1**, 457–470 (2011).
53. N. Patterson, A. L. Price, D. Reich, *PLOS Genet.* **2**, e190 (2006).
54. A. Manichaikul *et al.*, *Bioinformatics* **26**, 2867–2873 (2010).
55. C. C. Chang *et al.*, *Gigascience* **4**, 7 (2015).
56. J. de Ligt *et al.*, *N. Engl. J. Med.* **367**, 1921–1929 (2012).
57. S. De Rubeis *et al.*, *Nature* **515**, 209–215 (2014).
58. M. Fromer *et al.*, *Nature* **506**, 179–184 (2014).
59. S. L. Girard *et al.*, *Nat. Genet.* **43**, 860–863 (2011).
60. S. Gulsuner *et al.*, *Cell* **154**, 518–529 (2013).
61. I. Iossifov *et al.*, *Nature* **515**, 216–221 (2014).
62. I. Iossifov *et al.*, *Neuron* **74**, 285–299 (2012).
63. B. M. Neale *et al.*, *Nature* **485**, 242–245 (2012).
64. B. J. O'Roak *et al.*, *Nature* **485**, 246–250 (2012).
65. A. Rauch *et al.*, *Lancet* **380**, 1674–1682 (2012).
66. S. J. Sanders *et al.*, *Nature* **485**, 237–241 (2012).
67. B. Xu *et al.*, *Nat. Genet.* **44**, 1365–1369 (2012).
68. G. Mi, Y. Di, S. Emerson, J. S. Cumbie, J. H. Chang, *PLOS ONE* **7**, e46128 (2012).
69. D. Moreno-De-Luca *et al.*, *Mol. Psychiatry* **18**, 1090–1095 (2013).
70. S. J. Sanders *et al.*, *Neuron* **87**, 1215–1233 (2015).
71. B. K. Bulik-Sullivan *et al.*, *Nat. Genet.* **47**, 291–295 (2015).
72. S. Akbarian *et al.*, *Nat. Neurosci.* **18**, 1707–1712 (2015).
73. K. D. Hansen, R. A. Irizarry, Z. Wu, *Biostatistics* **13**, 204–216 (2012).
74. A. E. Jaffe *et al.*, *Proc. Natl. Acad. Sci. U.S.A.* **114**, 7130–7135 (2017).
75. V. Reinhart *et al.*, *Neurobiol. Dis.* **77**, 220–227 (2015).
76. L. Cope, X. Zhong, E. Garrett, G. Parmigiani, *Stat. Appl. Genet. Mol. Biol.* **3**, e29 (2004).
77. G. Parmigiani, E. S. Garrett-Mayer, R. Anbazhagan, E. Gabrielson, *Clin. Cancer Res.* **10**, 2922–2927 (2004).
78. M. V. Martin, K. Mirnics, L. K. Nisenbaum, M. P. Vawter, *Mol. Neuropsychiatry* **1**, 82–93 (2015).
79. P. Yao *et al.*, *Nat. Neurosci.* **18**, 1168–1174 (2015).
80. K. G. Ardlie *et al.*, *Science* **348**, 648–660 (2015).
81. A. van B. Granlund *et al.*, *PLOS ONE* **8**, e56818 (2013).
82. C. L. Noble *et al.*, *Gut* **57**, 1398–1405 (2008).
83. S. Girirajan *et al.*, *Am. J. Hum. Genet.* **92**, 221–237 (2013).
84. D. Malhotra, J. Sebat, *Cell* **148**, 1223–1241 (2012).
85. S. J. Sanders *et al.*, *Neuron* **70**, 863–885 (2011).
86. L. A. Weiss *et al.*, *N. Engl. J. Med.* **358**, 667–675 (2008).
87. C. R. Marshall *et al.*, *Am. J. Hum. Genet.* **82**, 477–488 (2008).
88. D. Moreno-De-Luca *et al.*, *Am. J. Hum. Genet.* **87**, 618–630 (2010).
89. J. T. Glessner *et al.*, *Nature* **459**, 569–573 (2009).
90. E. K. Green *et al.*, *Mol. Psychiatry* **21**, 89–93 (2016).
91. J. T. Glessner *et al.*, *PLOS ONE* **5**, e15463 (2010).
92. H. Stefansson *et al.*, *Nature* **455**, 232–236 (2008).
93. J. L. Stone *et al.*, *Nature* **455**, 237–241 (2008).
94. D. F. Levinson *et al.*, *Am. J. Psychiatry* **168**, 302–316 (2011).
95. V. Vacic *et al.*, *Nature* **471**, 499–503 (2011).
96. D. Rujescu *et al.*, *Hum. Mol. Genet.* **18**, 988–996 (2009).
97. S. E. McCarthy *et al.*, *Nat. Genet.* **41**, 1223–1227 (2009).
98. J. G. Mulle *et al.*, *Am. J. Hum. Genet.* **87**, 229–236 (2010).

ACKNOWLEDGMENTS

The work is funded by the U.S. National Institute of Mental Health (NIMH) (grants P50-MH106438, D.H.G.; R01-MH094714, D.H.G.; U01-MH103339, D.H.G.; R01-MH110927, D.H.G.; R01-MH100027, D.H.G.; R01-MH110920, C.L.; and U01-MH103340, C.L.), the Simons Foundation for Autism Research Initiative (SFARI) (SFARI grant 206733, D.H.G., and SFARI Bridge to Independence Award, M.J.G.), and the Stephen R. Mallory schizophrenia research award at the University of California, Los Angeles, (UCLA) (M.J.G.). The study was supported by The Lundbeck Foundation Initiative for Integrative Psychiatric Research (grant R102-A9118) and by the Novo Nordisk Foundation. Published microarray data sets analyzed in this study are available on Gene Expression Omnibus (accession nos. GSE28521, GSE28475, GSE35978, GSE53987, GSE17612, GSE12649, GSE21138, GSE54567, GSE54568, GSE54571, GSE54572, GSE29555, and GSE11223), ArrayExpress (accession no. E-MTAB-184), or directly from the study authors (*4*). New RNA-seq data (available on Synapse with accession numbers syn4590909 and syn4587609, with access governed by NIMH Repository and Genomics Resource) were generated as part of the PsychENCODE Consortium, supported by grants U01MH103339, U01MH103365, U01MH103392, U01MH103340, U01MH103346, R01MH105472, R01MH094714, R01MH105898, R21MH102791, R21MH105881, R21MH103877, and P50MH106934 awarded to Schahram Akbarian (Icahn School of Medicine at Mount Sinai), Gregory Crawford (Duke), Stella Dracheva (Icahn School of Medicine at Mount Sinai), Peggy Farnham (USC), Mark Gerstein (Yale), Daniel Geschwind (UCLA), Thomas M. Hyde (LIBD), Andrew Jaffe (LIBD), James A. Knowles (USC), Chunyu Liu (UIC), Dalila Pinto (Icahn School of Medicine at Mount Sinai), Nenad Sestan (Yale), Pamela Sklar (Icahn School of Medicine at Mount Sinai), Matthew State (UCSF), Patrick Sullivan (UNC), Flora Vaccarino (Yale), Sherman Weissman (Yale), Kevin White (UChicago), and Peter Zandi (JHU). RNA-seq data from the CommonMind Consortium used in this study (Synapse accession no. syn2759792) was supported by funding from Takeda Pharmaceuticals Company, F. Hoffman-La Roche and NIH grants R01MH085542, R01MH093725, P50MH066392, P50MH080405, R01MH097276, RO1-MH-075916, P50M096891, P50MH084053S1, R37MH057881, R37MH057881S1, HHSN271201300031C, AG02219, AG05138, and MH06692. Brain tissue for the study was obtained from the following brain bank collections: the Mount Sinai NIH Brain and Tissue Repository, the University of Pennsylvania Alzheimer's Disease Core Center, the University of Pittsburgh NeuroBioBank and Brain and Tissue Repositories, the Harvard Brain Bank as part of the Autism Tissue Project (ATP), the Stanley Medical Research Institute, and the NIMH Human Brain Collection Core. Summary statistics for the ASD GWAS performed on data from the iPSYCH consortium are available in data table S5. Data and analysis code are available at https://github.com/mgandal/Shared-molecular-neuropathology-across-major-psychiatric-disorders-parallels-polygenic-overlap. The authors thank S. Parhami, H. Won, J. Stein, D. Poliodakis, J. Flint, R. Ophoff, and members of the D.H.G. laboratory for critical reading of earlier versions of this manuscript. The authors also thank B. Pasaniuc for his helpful comments and for assistance with module heritability analyses.

SUPPLEMENTARY MATERIALS

www.sciencemag.org/content/359/6376/693/suppl/DC1
Materials and Methods
Supplemental Text
Figs. S1 to S13
Tables S1 to S3
Consortia
References (*26-98*)
Data Tables S1 to S5

10 February 2016; resubmitted 21 June 2017
Accepted 20 November 2017
10.1126/science.aad6469

PROTEIN BIOCHEMISTRY

Atomic structures of low-complexity protein segments reveal kinked β sheets that assemble networks

Michael P. Hughes,[1] Michael R. Sawaya,[1] David R. Boyer,[1] Lukasz Goldschmidt,[1] Jose A. Rodriguez,[2] Duilio Cascio,[1] Lisa Chong,[1] Tamir Gonen,[3] David S. Eisenberg[1]*

Subcellular membraneless assemblies are a reinvigorated area of study in biology, with spirited scientific discussions on the forces between the low-complexity protein domains within these assemblies. To illuminate these forces, we determined the atomic structures of five segments from protein low-complexity domains associated with membraneless assemblies. Their common structural feature is the stacking of segments into kinked β sheets that pair into protofilaments. Unlike steric zippers of amyloid fibrils, the kinked sheets interact weakly through polar atoms and aromatic side chains. By computationally threading the human proteome on our kinked structures, we identified hundreds of low-complexity segments potentially capable of forming such interactions. These segments are found in proteins as diverse as RNA binders, nuclear pore proteins, and keratins, which are known to form networks and localize to membraneless assemblies.

Membraneless organelles, such as P bodies, nuclear paraspeckles, and stress granules (SGs), form and redissolve in mammalian cells in response to stimuli (*1*, *2*). Such phase separation is a property of macromolecules that are capable of multivalent interactions with each other, yielding a liquid phase having ~100 times the concentration of the macromolecule compared to the bulk liquid (*3*, *4*). This type of phase separation is often seen with proteins that bind nucleic acids and contain low-complexity domains (LCDs) (*1*, *2*, *5*–*8*). For example, the SG-associated proteins hnRNPA1, hnRNPA2, and FUS undergo liquid-liquid phase separation (*9*–*12*), and they contain LCDs that transition into reversible semisolid phase hydrogels over time or at higher protein concentration (*1*, *5*, *9*). LCDs are common in the human proteome; they are largely intrinsically disordered (*13*), and dramatically underrepresented in the Protein Data Bank (PDB) of known three-dimensional (3D) structures (*14*).

Electron microscopy reveals that such hydrogels contain protein fibrils, and x-ray diffraction of the hydrogel yields a cross-β pattern (fig. S1, C to E) (*5*, *15*) reminiscent of amyloid. However, whereas the fibrils found in FUS hydrogels are heat and SDS-sensitive (*5*), amyloid fibrils resist denaturation by SDS and boiling. The spines of amyloid fibrils contain pairs of closely mating β sheets along the fibril axis. Residue side chains tightly interdigitate with side chains of the opposing β sheet to form a dry interface called a steric zipper, as seen in the structure of NKGAII from amyloid beta (Aβ) (Fig. 1A) (*16*, *17*). The steric zipper explains the extraordinary stability of some pathogenic amyloid. Apparently, the relatively labile multivalent interactions of the hydrogel-forming proteins are different; their atomic-level details are largely unknown, although, importantly, solid-state nuclear magnetic resonance has shown that 57 of the 214 residue LCDs of FUS form an ordered protofilament core, with the remaining residues dynamically disordered (*18*).

To investigate relatively weak adhesion between LCDs of proteins recruited to SGs, we sought relevant atomic structures. Guided by studies of the LCDs of FUS and RBM14, which show that successive replacement of tyrosine residues by serine lowers their capacity to form hydrogels (*1*, *5*), we scanned the LCD of FUS for tandem sequence motifs of the form [G/S]Y[G/S], finding two such segments: FUS-^{37}SYSGYS^{42} and FUS-^{54}SYSSYGQS^{61} (fig. S1A). Both segments crystallized as micron-sized needles, and both atomic structures were determined, in addition to structures of three other segments identified by 3D profiling (see below): ^{243}GYNGFG^{248} from protein hnRNPA1, ^{77}STGGYG^{82} from FUS, and ^{116}GFGNFGTS^{123} from nup98 (Fig. 1). Confirming the relevance of these structures to adhesion and multivalency of LCDs, a labile hydrogel is formed by a 26-residue synthetic peptide construct linking the three above segments of FUS (Fig. 2). Powder diffraction patterns of all five crystalline segments, this hydrogel, and the FUS-LCD hydrogel suggest that they all share cross-β architecture (figs S2 and S3).

All five segments crystalized as pairs of kinked β sheets (Fig. 1). Each β sheet runs the length of the crystal, formed from the stacking of about 300,000 segments, and all structures show kinks at either glycines or aromatic residues instead of being extended (fig. S4). The structures share common adhesive features, including hydrogen bonds in-register to an identical segment below it (Fig. 1, B to F, and fig. S5). Aromatic residues predominate, both for intersheet stabilization and intrasheet stabilization. Within sheets, the aromatic side chains stack in an energetically favorable conformation, with the planes of the rings stacked parallel at a separation of 3.4 Å (*19*–*21*) (fig. S5). These aromatic "ladders" enhance the stability of each β sheet. The kinks allow close approach of the backbones, providing favorable van der Waals or hydrogen-bond interactions between the sheets (fig. S5). These close interactions are quantified by the structural complementarity (Sc) (Fig. 1), reflecting adhesion between the sheets. However, the kinks prevent side chains from interdigitating across the β-sheet interface so that the kinked interfaces bury smaller surface areas than found in pathogenic amyloid fibrils and presumably have lower binding energies. Because of the distinction of the kinked structures from pathogenic steric zippers, we term them low-complexity aromatic-rich kinked segments (LARKS).

Calculations and experiments support our structural inference that LARKS have smaller binding energies than steric zippers. We estimated energies of separation of the pairs of β sheets in LARKS and steric zippers by applying atomic solvation parameters (*22*, *23*) to our structures: The mean atomic solvation energy for separation of our LARKS interfaces is 567 ± 556 cal/mol/β strand, whereas it is 1431 ± 685 cal/mol/β strand for 75 steric zipper structures (fig. S6). These crude estimates suggest that the adhesive energy of one pair of β strands in a LARKS is of the order of thermal energy, so that pairs of β sheets adhere only through multivalent interactions of strands. In contrast, the adhesive energy of one pair of strands in a steric zipper is several times that of thermal energy. Consistent with calculations, the synthetic multi-LARKS construct of Fig. 2 dissolves when gently heated. Thus, paired kinked β sheets of LARKS are less strongly bound than the paired β sheets in amyloid fibrils, yet still produce fibrils with the cross β-diffraction pattern of pathogenic amyloid.

To identify potential LARKS in the human proteome, we used computational 3D profiling, a method that tests the compatibility of query sequences with a template structure (*24*, *25*). Here, we threaded human sequences onto the backbones of SYSGYS, GYNGFG, and STGGYG, placed and optimally repacked side chains, and then evaluated the Rosetta energy (Fig. 3A) (*26*). We advanced the threading by one residue and repeated the procedure until the end of the query sequence was reached. This 3D profiling predicted that nucleoporin proteins are enriched in LARKS (Fig. 3C). Our confidence in this prediction was bolstered by the success of earlier predictions that GYNGFG and STGGYG could form LARKS, based on threading with only the SYSGYS template. Here, again, we were able to validate our profiling algorithm by determining the structure

[1]Department of Biological Chemistry and Department of Chemistry and Biochemistry, University of California Los Angeles (UCLA), Howard Hughes Medical Institute (HHMI), UCLA–Department of Energy (DOE) Institute for Genomics and Proteomics, Los Angeles, CA 90095, USA. [2]Department of Chemistry and Biochemistry, UCLA, UCLA-DOE Institute for Genomics and Proteomics, Los Angeles, CA 90095, USA. [3]HHMI and Department of Physiology, UCLA, Los Angeles, CA 90095, USA.
*Corresponding author. Email: david@mbi.ucla.edu

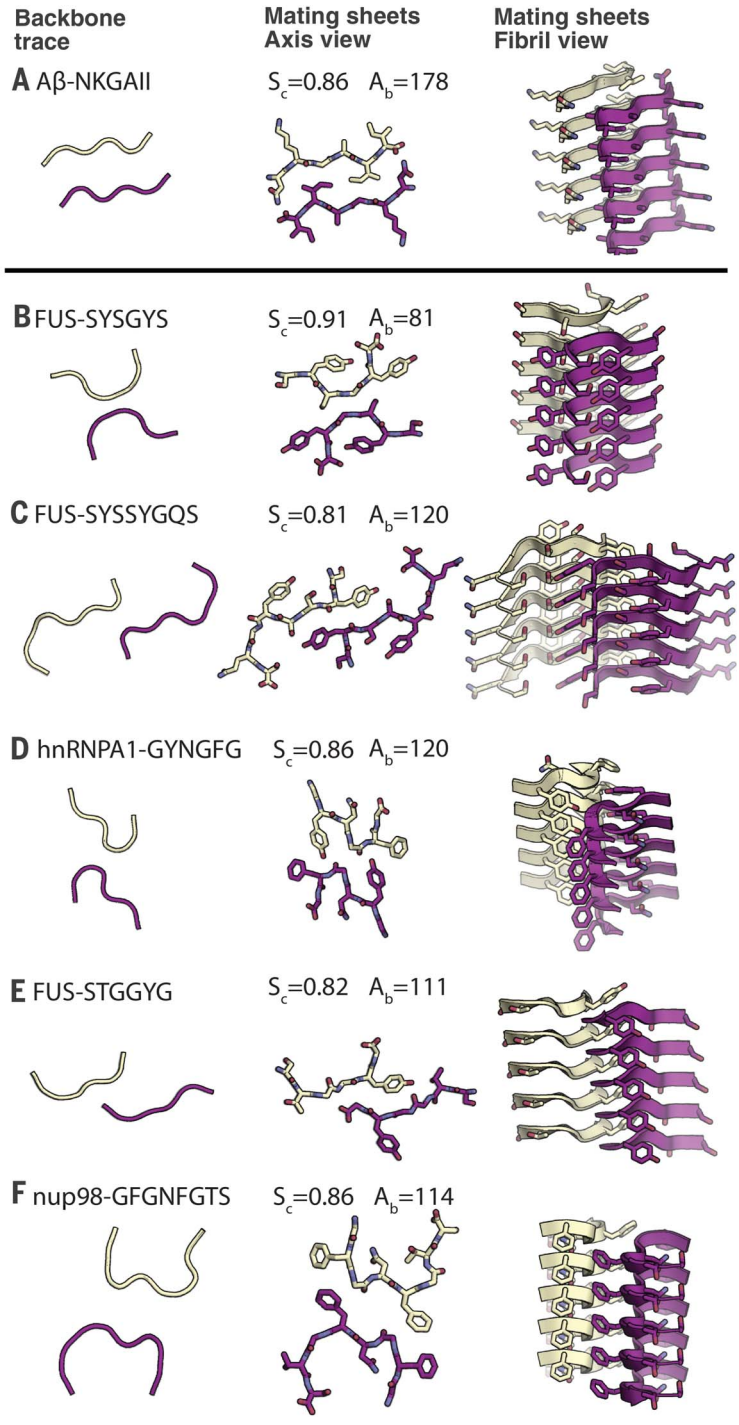

Fig. 1. Structures of LARKS compared to a steric zipper. (**A**) Steric zipper. (**B**) to (**F**) Structures of LARKS. All structures are composed of two mating β sheets, one purple and the other yellow. The left-hand column shows the trace of the backbones of mating sheets to highlight kinks in the backbones of LARKS and the pleating of the classical β sheets in steric zippers. The second column shows the atomic structures of mating sheets viewed down the fibril axes. The third column shows cartoons of the mating β sheets viewed nearly perpendicular to the fibril axes. Each interface is characterized by the shape complementarity score (Sc = 1.0 for perfect complementarity) and buried solvent-accessible surface area (Ab) in Å^2 between the mated sheets. Carbon atoms are colored purple or yellow, nitrogen is blue, and oxygen is red. Five layers of β sheets are shown of the hundreds of thousands in the crystals. The kinked structures of LARKS are rare among mating β sheets; dozens of other paired β sheets form steric zippers (*35*).

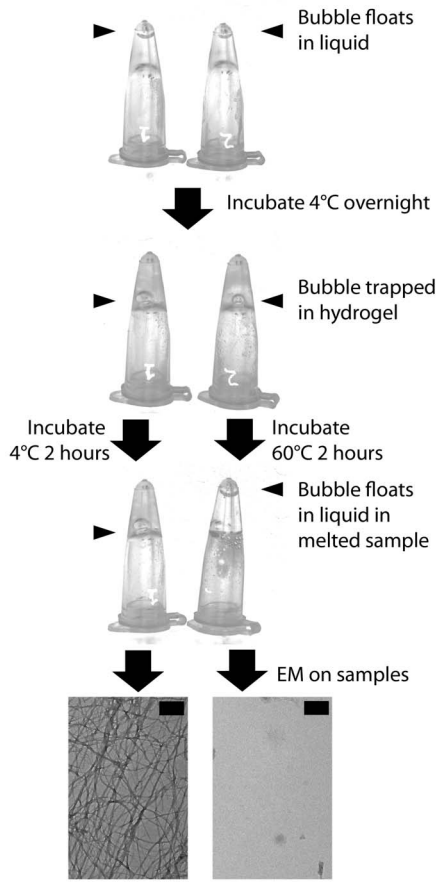

Fig. 2. Synthetic LARKS construct forms a labile hydrogel. A synthetic LARKS construct with the sequence SYSGYSGDTSYS-SYGQSNGPSTGGYG (underlined sequences correspond to LARKS) forms a labile hydrogel when dissolved in water at 50 mg/ml and left overnight at 4°C. The hydrogel melts upon heating the sample to 60°C for 2 hours. A bubble (blue arrow) was introduced to the sample to show the difference between the liquid state (bubble rises) and hydrogel state (bubble does not rise). Electron microscopy confirms that fibrils were indeed melted. The hydrogel-forming property of this triple-LARKS sequence suggests that it is the multiple LARKS found in many LCDs that endow their unusual property of forming hydrogels. Scale bars, 200 nm. Single-letter abbreviations for the amino acid residues are as follows: A, Ala; C, Cys; D, Asp; E, Glu; F, Phe; G, Gly; H, His; I, Ile; K, Lys; L, Leu; M, Met; N, Asn; P, Pro; Q, Gln; R, Arg; S, Ser; T, Thr; V, Val; W, Trp; and Y, Tyr.

of GFGNFGTS from the porin nup98, confirming LARKS architecture (Fig. 1F) and providing evidence that LARKS are present in a different type of membraneless organelle (*27*).

Analyzing the nonredundant human proteome of 20,120 sequences from UniProt, we found 5867 proteins with LCDs. Of these, 2500 proteins contain at least one LARKS and 1725 proteins contain two or more LARKS and thus are able to

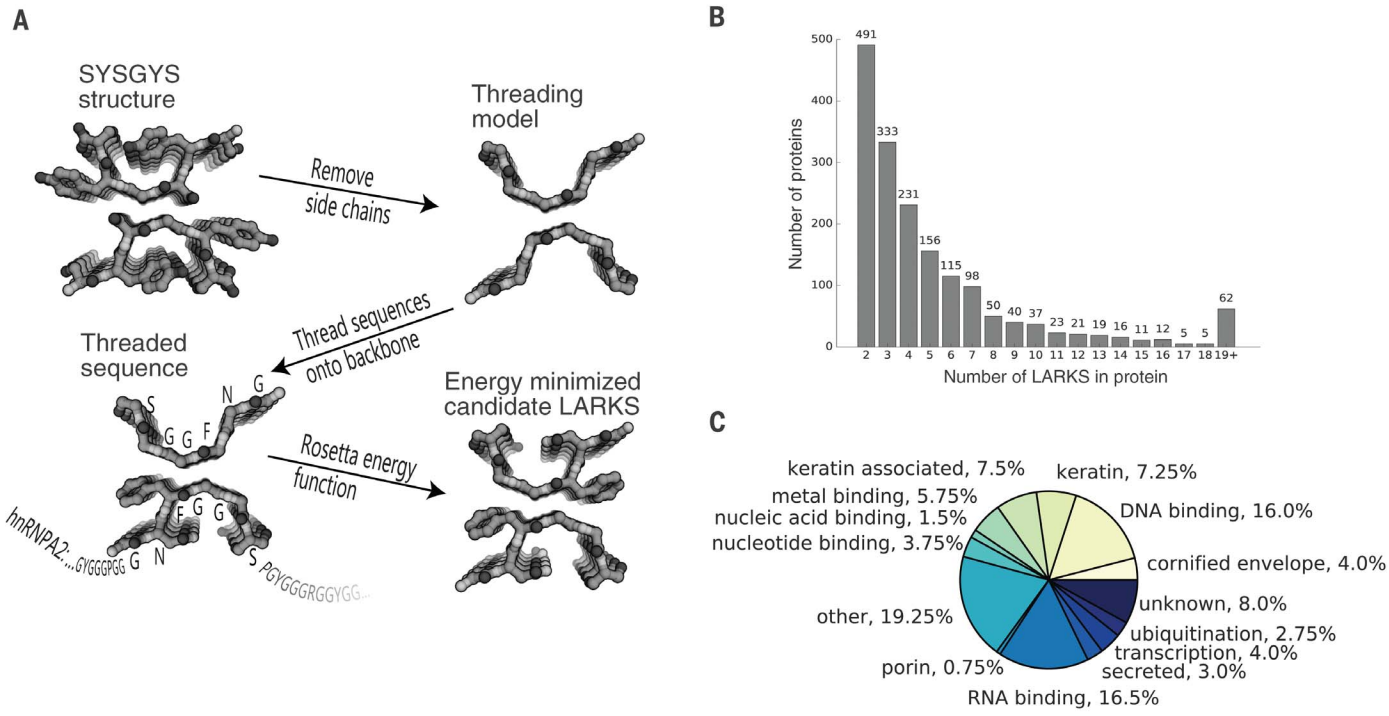

Fig. 3. Three-dimensional profiling to identify LARKS in LCDs of human proteins. (**A**) Side chains are removed from the backbones of one of our atomic structures of a LARKS. Then the sequence of interest (hnRNPA2 shown) is threaded through the six-residue template by placing the query side chains on the template backbone. Side chains are repacked and a Rosetta energy function is used to estimate whether the structure is favorable for the threaded sequence. The sequence then advances through the template by one-residue increments, producing successive models. (**B**) The frequency of the number of LARKS in 1725 human proteins predicted to house at least two LARKS. Proteins having two or more LARKS are predicted to have the capacity to form networks and possibly gels. (**C**) The annotated functions of the 400 proteins with the most predicted LARKS.

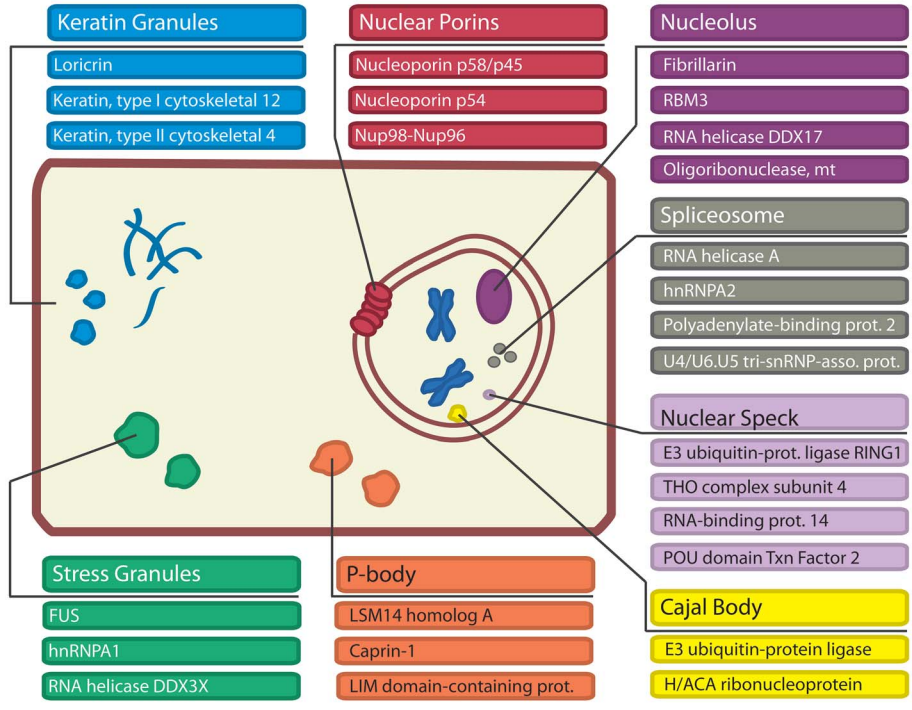

Fig. 4. Functions of proteins among the 400 proteins most enriched in LARKS and dynamic intracellular bodies of which they are known to be a part.

form multivalent interactions and hence protein networks and gels. Hundreds of proteins house three or more LARKS (Fig. 3B). The 400 human LCDs most enriched in LARKS average 14 LARKS, with a median of 10 LARKS.

We assigned cellular function to these 400 proteins based on their UniProt annotations (Fig. 3C): 16% are DNA binding, 17% are RNA binding, and 4% are nucleotide binding, consistent with reports of nucleotide binding proteins in membraneless organelles (*2*, *8*). Keratins (5%), keratin-associated (9%), and cornified envelope proteins (4%) are also enriched in LARKS. The finding of keratins is consistent with experiments (*28*) showing that keratin granules are trafficked to the cell cortex, where they merge and eventually mature into filaments. Also rich in LARKS are proteins found in ribonucleoprotein particles such as the spliceosome or nucleolus (Fig. 4). Nucleoporins including nup54 and nup98 with FG repeats are enriched in predicted LARKS, and purified FG repeats form a hydrogel (*27*, *29*). The possibility that the FG repeats of nucleoporins may form LARKS in the diffusion barrier of the pore is supported by our structure of GFGNFGTS from nup98. We assigned additional cellular functions to these 400 proteins from their associated gene ontology (GO) terms. We found GO terms enriched in the human proteome

for RNA transport, processing localization, SG assembly, and epithelial cell differentiation due to the numerous keratins enriched in LARKS. Therefore, we propose 3D profiling for LARKS as a tool to identify proteins that may form networks and gels by multivalent interactions and may participate in membraneless organelles (fig. S10).

In conclusion, the prevalence of LCDs within eukaryotic proteomes has long been recognized (*30*), but the role of these domains has not been fully defined. Previous discoveries include the following: LCDs can "functionally aggregate" (*31*); proteins with LCDs typically form more protein-protein interactions (*32*, *33*); and proteins can interact homotypically and heterotypically through LCDs (*1*, *5*, *34*). Our atomic structures support the hypothesis that LCDs have the capacity to form gel-like networks. LARKS possess three properties that are consistent with their functioning as adhesive elements in protein gels formed from LCDs: (i) high aqueous solubility contributed by their high proportion of hydrophilic residues: serine, glutamine, and asparagine; (ii) flexibility ensured by their high glycine content; and (iii) multiple interaction motifs per chain (Fig. 3B), endowing them with multivalency, enabling them to entangle, forming networks as found in gels (Fig. 2). That each LARKS provides adhesion only comparable to thermal energy suggests that numerous LARKS must cooperate in gel formation and that the interactions must be concentration dependent and may be transient. If steric zippers act as molecular glue, then LARKS in LCDs act as Velcro. These properties are compatible with the hypothesis that LARKS are a protein interaction motif that provides adhesion of LCDs in protein gels and in membraneless assemblies (fig S10).

REFERENCES AND NOTES

1. S. Hennig *et al.*, *J. Cell Biol.* **210**, 529–539 (2015).
2. A. Aguzzi, M. Altmeyer, *Trends Cell Biol.* **26**, 547–558 (2016).
3. S. F. Banani, H. O. Lee, A. A. Hyman, M. K. Rosen, *Nat. Rev. Mol. Cell Biol.* **18**, 285–298 (2017).
4. P. Li *et al.*, *Nature* **483**, 336–340 (2012).
5. M. Kato *et al.*, *Cell* **149**, 753–767 (2012).
6. S. Elbaum-Garfinkle, C. P. Brangwynne, *Dev. Cell* **35**, 531–532 (2015).
7. Y. Lin, D. S. W. Protter, M. K. Rosen, R. Parker, *Mol. Cell* **60**, 208–219 (2015).
8. A. F. Harrison, J. Shorter, *Biochem. J.* **474**, 1417–1438 (2017).
9. T. Murakami *et al.*, *Neuron* **88**, 678–690 (2015).
10. A. Patel *et al.*, *Cell* **162**, 1066–1077 (2015).
11. A. Molliex *et al.*, *Cell* **163**, 123–133 (2015).
12. S. Xiang *et al.*, *Cell* **163**, 829–839 (2015).
13. B. Kumari, R. Kumar, M. Kumar, *Mol. Biosyst.* **11**, 585–594 (2015).
14. J. C. Wootton, *Comput. Chem.* **18**, 269–285 (1994).
15. J. C. Schwartz, T. R. Cech, R. R. Parker, *Annu. Rev. Biochem.* **84**, 355–379 (2015).
16. R. Nelson *et al.*, *Nature* **435**, 773–778 (2005).
17. M. R. Sawaya *et al.*, *Nature* **447**, 453–457 (2007).
18. D. T. Murray *et al.*, *Cell* **171**, 615–627.e16 (2017).
19. M. O. Sinnokrot, E. F. Valeev, C. D. Sherrill, *J. Am. Chem. Soc.* **124**, 10887–10893 (2002).
20. G. B. McGaughey, M. Gagné, A. K. Rappé, *J. Biol. Chem.* **273**, 15458–15463 (1998).
21. E. Arunan, H. S. Gutowsky, *J. Chem. Phys.* **98**, 4294 (1992).
22. D. Eisenberg, A. D. McLachlan, *Nature* **319**, 199–203 (1986).
23. D. E. Eisenberg, M. Wesson, M. Yamashita, *Chem. Scr.* **29A**, 217–221 (1989).
24. J. U. Bowie, R. Lüthy, D. Eisenberg, *Science* **253**, 164–170 (1991).
25. L. Goldschmidt, P. K. Teng, R. Riek, D. Eisenberg, *Proc. Natl. Acad. Sci. U.S.A.* **107**, 3487–3492 (2010).
26. A. Leaver-Fay *et al.*, *Methods Enzymol.* **487**, 545–574 (2011).
27. S. Frey, R. P. Richter, D. Görlich, *Science* **314**, 815–817 (2006).
28. R. Windoffer, S. Wöll, P. Strnad, R. E. Leube, *Mol. Biol. Cell* **15**, 2436–2448 (2004).
29. C. Ader *et al.*, *Proc. Natl. Acad. Sci. U.S.A.* **107**, 6281–6285 (2010).
30. K. L. Sim, T. P. Creamer, *Mol. Cell. Proteomics MCP* **1**, 983–995 (2002).
31. J. A. Toretsky, P. E. Wright, *J. Cell Biol.* **206**, 579–588 (2014).
32. A. Coletta *et al.*, *BMC Syst. Biol.* **4**, 43 (2010).
33. V. N. Uversky, C. J. Oldfield, A. K. Dunker, *Annu. Rev. Biophys.* **37**, 215–246 (2008).
34. I. Kwon *et al.*, *Cell* **155**, 1049–1060 (2013).
35. D. S. Eisenberg, M. R. Sawaya, *Annu. Rev. Biochem.* **86**, 69–95 (2017).

ACKNOWLEDGMENTS

D.S.E. is on the scientific advisory board and holds equity in ADRx, Inc. X-ray diffraction data were collected at the Northeastern Collaborative Access Team beamline 24-ID-E, which is funded by the National Institute of General Medical Sciences from the National Institutes of Health (P41 GM103403). This research used resources of the Advanced Photon Source, a U.S. Department of Energy (DOE) Office of Science User Facility operated for the DOE Office of Science by Argonne National Laboratory under contract no. DE-AC02-06CH11357. We thank NSF MCB-1616265, NIH AG-054022, DOE, and HHMI for support. Atomic coordinates and structure factors have been deposited in the PDB with the following accession codes: SYSGYS (6BWZ), SYSSYGQS (6BXV), STGGYG (6BZP), GYNGFG (6BXX), and GFGNFGTS (6BZM).

SUPPLEMENTARY MATERIALS

www.sciencemag.org/content/359/6376/698/suppl/DC1
Materials and Methods
Figs. S1 to S10
Tables S1 to S3
References (*36*–*47*)

13 May 2017; resubmitted 15 November 2017
Accepted 4 January 2018
10.1126/science.aan6398

Check out our exciting research Prize!

SCIENCE-PINS PRIZE FOR NEUROMODULATION

SCIENCE-PINS

$25, 000 Grand Prize!
Get published in *Science*!

The Prize is a new highly competitive international prize which honors scientists for their excellent contributions to neuromodulation research. For purposes of the Prize, neuromodulation is any form of alteration of nerve activity through the delivery of physical (electrical, magnetic, optical) stimulation to targeted sites of the nervous system."

For full details, judging criteria and eligibility requirements, visit:

www.sciencemag.org/prizes/pins

Submission Deadline: March 15, 2018

Science AAAS

PINS 品驰

want new technologies?

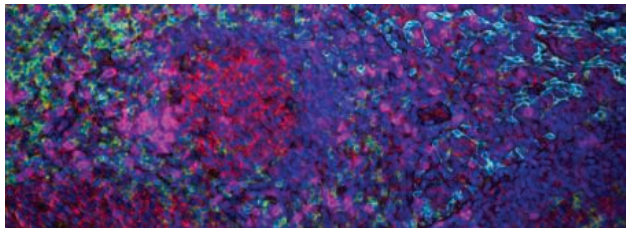

antibodies
apoptosis
biomarkers
cancer
cytometry
data
diseases
DNA
epigenetics
genomics
immunotherapies
medicine
microbiomics
microfluidics
microscopy
neuroscience
proteomics
sequencing
toxicology
transcriptomics

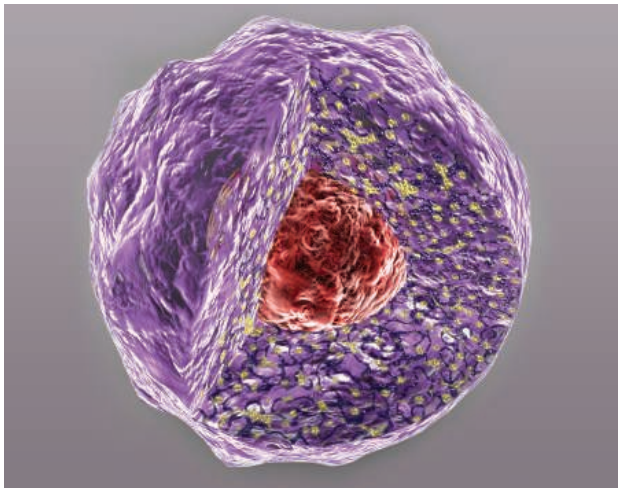

watch our webinars

Learn about the latest breakthroughs, new technologies, and ground-breaking research in a variety of fields. Our expert speakers explain their quality research to you and answer questions submitted by live viewers.

VIEW NOW!
webinar.sciencemag.org

Science
AAAS

Brought to you by the *Science*/AAAS Custom Publishing Office

@SciMagWebinars

eppendorf & Science

PRIZE FOR NEURO BIOLOGY

2017 Winner
Flavio Donato, Ph.D.
Kavli Institute
Norwegian University of
Science and Technology

For research on how neural networks mature during development to represent space in the brain

Application Deadline
June 15, 2018

Call for Entries

Eppendorf & Science Prize for Neurobiology
The annual Eppendorf & Science Prize for Neurobiology is an international award which honors young scientists for their outstanding contributions to neurobiological research based on methods of molecular and cell biology. The winner and finalists are selected by a committee of independent scientists, chaired by *Science's* Senior Editor, Dr. Peter Stern. To be eligible, you must be 35 years of age or younger.

As the Grand Prize Winner, you could be next to receive
> Prize money of US$25,000
> Publication of your work in *Science*
> Full support to attend the Prize Ceremony held in conjunction with the Annual Meeting of the Society for Neuroscience in the USA
> 10-year AAAS membership and online subscription to *Science*
> Complimentary products worth US$1,000 from Eppendorf
> An invitation to visit Eppendorf in Hamburg, Germany

It's easy to apply! Learn more at:

www.eppendorf.com/prize

eppendorf Science AAAS

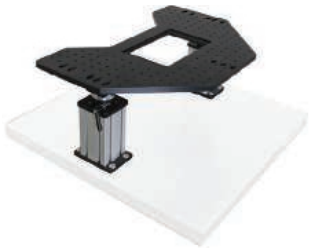

Quick-Adjust Neuroscience Platform

Prior Scientific's V-Deck is an ultrastable platform for neuroscience and electrophysiology, offering you the versatility to produce optimal images from thin sections up to whole-animal samples—all ensured through the availability of a wide range of height-adjustable, lockable platform posts. The V-Deck offers a large sample area, with an M6 × 25-mm breadboard that allows heating, cooling, perfusion, and incubation chambers, as well as micromanipulators, stereotaxic instruments, and other equipment, to be precisely mounted. Consequently, setting up microscopic imaging of an electrophysiology or neuroscience experiment to your exact specifications can be done rapidly and efficiently. Dovetail slides on the V-Deck enable quick, precise adjustment of your sample height. The entire V-Deck platform is compatible with almost any commercial vibration isolation table.

Prior Scientific
For info: +44-(0)-1223-881711
www.prior-scientific.co.uk

Real-Time PCR System

Forensic scientists who want to modernize their laboratories now have access to the Applied Biosystems QuantStudio 5 Real-Time PCR System for Human Identification (HID). The system is designed to deliver efficient performance with a smaller footprint and lower annual maintenance costs than previous systems. It uses HID Real-Time PCR Analysis Software v1.3, which enables data analysis with a virtual standard-curve feature, to minimize variation and reduce costs associated with using standards on every plate. The software also includes quantification and short tandem repeat (STR) setup features as well as data quality–review functionality, which integrate and streamline quantification and STR analysis. When combined with the Applied Biosystems Quantifiler HP and Quantifiler Trio DNA Quantification Kits, the entire solution offers a validated workflow that enables forensic labs to simultaneously acquire a quantitative and qualitative assessment of human DNA in their casework samples, to better determine downstream processing and successfully extract an STR profile.

Thermo Fisher Scientific
For info: 800-955-6288
www.thermofisher.com

RNA Methylation Analysis

Expand your understanding of RNA methylation with EpiGentek's complete suite of RNA methylation products. Recent data strongly suggest that m6A and 5-mC RNA methylation affects regulation of various biological processes such as RNA stability and mRNA translation, and that abnormal RNA methylation contributes to the etiology of human diseases. From directly quantifying the "fifth RNA base," N6-methyladenosine (m6A), to measuring global 5-methylcytosine (5-mC) RNA and more, our kits make it easy for you to determine how RNA methylation influences your research projects. We offer one m6A RNA kit [EpiQuik m6A RNA Methylation Quantification Kit (Colorimetric)] and three 5-mC RNA kits: MethylFlash 5-mC RNA Methylation ELISA Easy Kit (Fluorometric); EpiNext 5-mC RNA Bisulfite-Seq Easy Kit (Illumina); and Methylamp RNA Bisulfite Conversion Kit.

EpiGentek
For info: 877-374-4368
www.epigentek.com

Proximity Ligation Assay

Rely on Duolink PLA (proximity ligation assay) to amplify your protein signals by 1,000x and allow you to visually detect proteins and their interactions, all within a native cell. Our straightforward method provides visual protein interactions (both stable and transient); endogenous protein detection (no overexpression or genetic manipulation); high specificity (use of two antibodies/probes eliminates false positives); single-molecule sensitivity (rolling circle amplification makes proteins visible); and publication-ready results [compare image results from indirect methods (coimmunoprecipitation/Western blot)], with no special equipment needed—only standard immunofluorescence methods are used. Uncover the opportunities in your protein detection research with amplified performance and visual results.

Sigma Aldrich
For info: 800-325-3010
www.sigmaaldrich.com

Automated Sample Prep

QIAcube is a robotic workstation for automated purification of DNA, RNA, or proteins using well-established QIAGEN spin-column kits; it enables continued use of the kits and eliminates the need for tedious manual steps. QIAcube controls integrated components—including a centrifuge, heated shaker, pipetting system, and robotic gripper—allowing it to fully automate more than 40 QIAGEN spin-column kits. It uses advanced technology to process our spin columns, delivering seamless integration of automated, low-throughput sample prep into the laboratory workflow. No change of purification chemistry is required, assuring fast startup and immediate results. All steps in the purification procedure are fully automated—up to 12 samples can be processed per run. An integrated touchscreen simplifies protocol selection, and clear onscreen messages guide the user through worktable setup. In addition, a fully automated load check ensures that samples, reagents, and labware are correctly loaded.

QIAGEN
For info: 800-718-2056
www.qiagen.com

Hepcidin ELISA Kit

DRG's Hepcidin-25 ELISA Kit will help revolutionize future research, diagnosis, and treatment of anemias and iron overload diseases. Current diagnostic tests for iron do not provide adequate information for the diagnosis, monitoring, and treatment of current iron-related diseases. Hepcidin is a recently discovered hormone that controls iron absorption and distribution in the body. Unbalanced iron levels can lead to many common medical conditions, including anemia and hemochromatosis, and can cause chronic kidney disease, inflammation, or diabetes mellitus. The kit has analytical sensitivity from 0.153 ng/mL to 81 ng/mL, and uses a straightforward procedure—incubation time takes less than 2 hours and is done at room temperature with no shaking or assay buffer. Serum or plasma samples can be assessed.

DRG
For info: 973-564-7555
drg-international.com/products/hepcidin-25-bioactive-hs-v2

Electronically submit your new product description or product literature information! Go to www.sciencemag.org/about/new-products-section for more information.

Newly offered instrumentation, apparatus, and laboratory materials of interest to researchers in all disciplines in academic, industrial, and governmental organizations are featured in this space. Emphasis is given to purpose, chief characteristics, and availability of products and materials. Endorsement by *Science* or AAAS of any products or materials mentioned is not implied. Additional information may be obtained from the manufacturer or supplier.

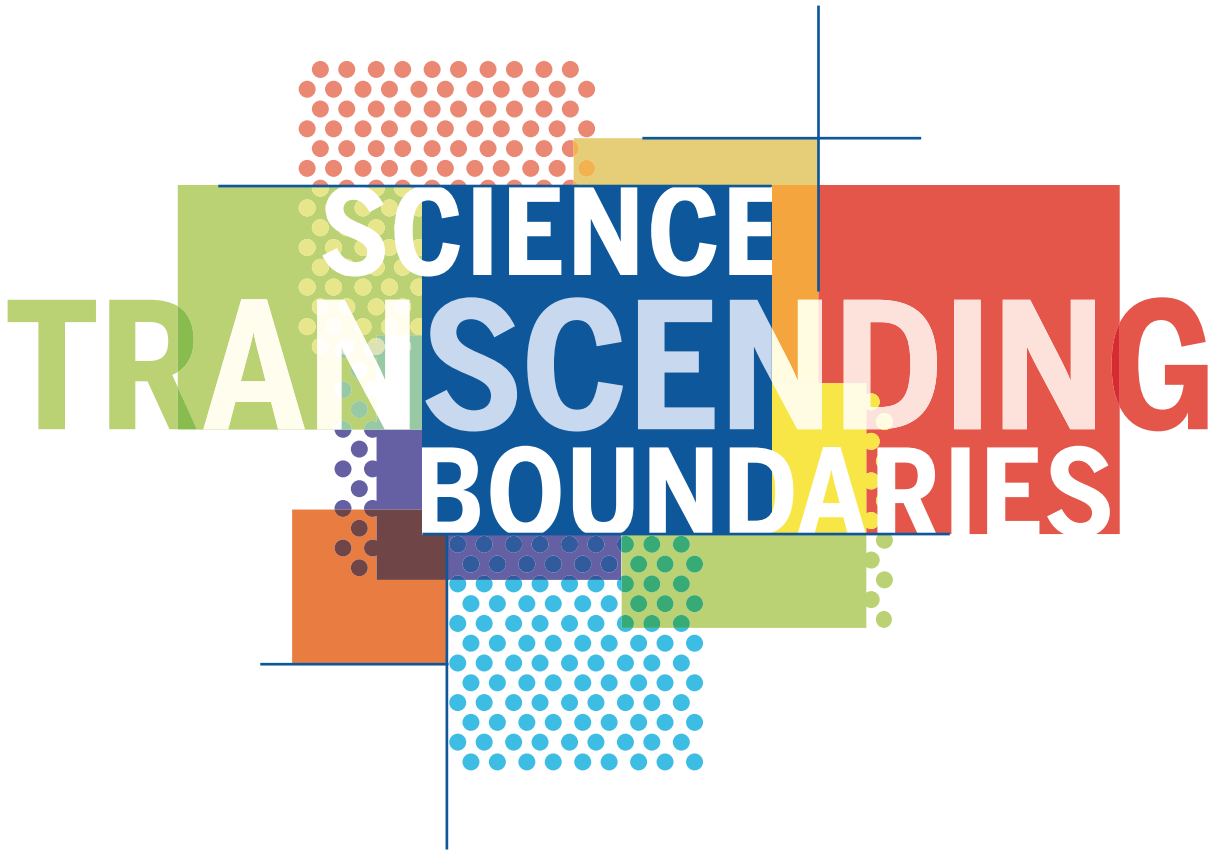

AAAS

ANNUAL MEETING

Feb. 14–18, 2019 | Washington, DC

How can science help address the many divisions in our communities, in global society, and in science itself? Science plays a unique and important role in how people see and understand the world, and how lines and distinctions are drawn. At this Annual Meeting, we look for ways science is bringing together people, ideas, and solutions from across real and artificial borders, disciplines, sectors, ideologies, and traditions. How can science working across boundaries improve its ability to find solutions to the pressing problems of our age? How can scientists, wherever they work, more effectively engage with the broader society? How can we find better ways to engage the public, especially in expanding access to science and scientific careers? At the international level, science diplomacy builds bridges between countries. How can we encourage more of this, and utilize science as a common ground more locally as well? Can science contribute information that might reduce or mitigate the starkly divergent interests of different populations and demographics, such as urban and rural communities? What boundaries most impede your research or your career? While acknowledging that some boundaries are useful and necessary, the meeting theme considers how research can be applied to problematic separations in the world, and how unhelpful boundaries within science are being addressed.

Positions Open
Toyota Technological Institute

Toyota Technological Institute has one opening for "Principal Professor" positions in its School of Engineering. For more information, please refer to the following website: **http://www.toyota-ti.ac.jp/english/employment/index.html**.

Research fields: ***Science and technology for advanced instrumentation and/or information processing***
Examples: New devices and systems for advanced information processing, communication, and/or sensing; Leading instrumentation technologies for ultra-sensitive measurements and/or bio-medical studies and diagnosis; Science and technology of cyber-physical systems.

Qualifications: A successful candidate must have a Ph. D. degree or the equivalent in a relevant field; he/she must possess outstanding competence to promote world-class research program(s) as well as to conduct excellent teaching and research supervision for graduate and undergraduate students, so as to fulfill his/her mission as a superb leader in research and education.

Positions: Principal Professor

The "Principal Professor" will serve as the head of a "unit laboratory", that consists of the Principal Professor, one associate professor, and three post-doctoral fellows. A start-up grant of about one hundred million Japanese yen (ca. one million US dollars) is available. In addition, a research budget of about ten million Japanese yen (ca. one hundred thousand US dollars) will be given each year to promote research programs for a period of five years. At the end of this five-year term, the principal professor will be given a formal evaluation.

Number of Positions Available: One

Start date: April 1, 2019 or on the date of the earliest convenience

Documents: Please refer to our website

Deadline: May 15, 2018

Inquiries: Search Committee Chair, Dr. Kazuo Hotate, Vice President & Professor
(Phone) +81-52-809-1821 (E-mail) **hotate-koubo@toyota-ti.ac.jp**

POSITIONS OPEN

POSTDOC POSITION

Postdoc position to study molecular mechanisms of oncogenic signaling, protein homeostasis, and cell metabolism. Candidates with Ph.D. and/or M.D. degrees and strong experience in biochemistry/molecular biology are encouraged to send their Curriculum Vitae and a list of three references to: **Wei-Xing Zong, PhD, Department of Chemical Biology, the Cancer Institute of New Jersey, Rutgers, The State University of New Jersey,164 Frelinghuysen Road, Piscataway, New Jersey 08854**. Website: **http://www.cinj.org/researcher-profiles/?id=807** Email: **bachorik@pharmacy.rutgers.edu.**

By **Paul C. Rogge**

My climate change crisis

Reading former Vice President Al Gore's *An Inconvenient Truth* in college awakened me to the widespread threat of climate change. Spurred to action, I joined a lab to develop alternative energy technologies. The result was an undergraduate project studying magnetic materials, which are important for electric vehicles and wind turbines. It got me hooked on research and left me wanting to make a bigger impact. I wanted my work to lead straight to solutions—but in the process, I veered off course.

While visiting prospective graduate programs, I found just the project I was looking for: creating a radically new type of solar cell using low-cost electrochemistry techniques. The chemistry my new project would require was fundamentally different from the methods I had learned while working on magnetic materials, and I hadn't really thought about chemistry since taking Chem 101 as a college freshman. But I was so driven by the potential social impact of the work that these realities did not worry me.

In my first week, it was clear that I was starting from scratch. Mixing my first solution, I dumped powdered copper sulfate into a dry beaker before adding water—a big no-no, as any chemist knows. The extreme heat given off nearly caused the beaker to explode. But I quickly learned the correct procedures and threw myself into my research.

However, 2 years of intense work did not lead to much progress. I found myself in the lab less, and my patience for troubleshooting experiments waned. I began to doubt my project and even my ability to graduate. To my adviser, the unexpected failure of the technique I was using offered a chance to dig deeper into the underlying chemistry. He was excited about what he saw as a silver lining, which made my enthusiasm sink even further. I didn't want to study electrochemistry techniques; I wanted to solve climate change.

In hindsight, the source of my dissatisfaction was clear. In choosing my research area, I had been blinded by my enthusiasm to tackle a pressing social and environmental problem. I hadn't critically considered my own scientific interests and whether I would enjoy working in an electrochemistry lab. I should have remembered how much I struggled in Chem 101. And I should have realized that the concepts and techniques I mastered in my undergraduate research on magnetic materials—the very things that got me hooked on research in the first place—were not particularly relevant for electrochemistry.

"I had been blinded by my enthusiasm to tackle a pressing ... problem."

Recognizing I was on the wrong path, I used the nuclear option: switching advisers midway through my Ph.D. While searching for a new adviser, I asked myself which scientific concepts and experimental techniques—the things I would engage with every day—excited me. Perhaps most important, I came to see science as an ecosystem of work ranging from investigating fundamentals to developing devices, all of which contribute to solving pressing problems. I realized I could make a meaningful contribution to combating climate change by working on something I was passionate about, even if it was less directly related to a specific technology.

I found a new home in a lab studying graphene, a material with promising electronic properties. Things clicked and my work took off immediately. There were still some bumps along the way, of course, but I found the day-to-day challenges in the lab less daunting because I was excited by the concepts and techniques I was working with.

Just as I came to see my research as part of a larger scientific ecosystem, today I understand that scientific advancements are just one part of the needed response to climate change. I've reduced my environmental impact by taking public transportation to work, significantly cutting my meat intake, and resisting my consumerist impulses. My lifestyle changes won't single-handedly reverse climate change, and neither will my individual scientific contributions. But we all need to work together to address such challenges, each of us contributing in the best way we can. ■

Paul C. Rogge is a postdoctoral researcher at Drexel University in Philadelphia, Pennsylvania. Send your career story to SciCareerEditor@aaas.org.

ILLUSTRATION: ROBERT NEUBECKER